UNITED KINGDOM · CHINA · MALAYSIA

MICROWAVE PROCESSING OF ORES

Baker Francis Giyani, BSc Eng, MSc Eng

Thesis submitted to the University of Nottingham for the degree of Doctor of Philosophy

June 2023

ABSTRACT

Copper is a widely used metal in applications ranging from electronics to building and construction. The demand for copper has increased more rapidly in recent years due to technological advancements, industrial development, and population growth. This is set against a backdrop where the global copper head grade is dropping because higher-grade ore bodies are already mined or becoming exhausted. This means that larger volumes of low-grade ores are being processed in plant operations to keep up with the growing demand. However, processing these low-grade ores using existing flowsheets is unlikely to be sustainable due to enhanced energy consumption and low process efficiency. Thus, innovative processing technologies must be explored to treat such ores if mineral processing is ever to become sustainable.

Microwave treatment of ores is one such processing technology that has been demonstrated to reduce ore competency and improve mineral liberation by inducing intergranular and transgranular fractures. Both these outputs, of course, leading to reduced energy consumption and higher process efficiency. The principal mechanism of microwave-induced fractures in ores is based on differential thermal stresses generated through rapid and selective heating of microwave-absorbent phases (e.g., sulphide minerals) within a microwave-transparent gangue matrix (rock-forming minerals). In hydrometallurgical processes, the induced fractures expose more sulphide grains to the leach solution, improving mass transfer and enhancing metal leach recovery. It has also been shown that a candidate ore should have suitable mineralogy and texture properties in order to support the creation and the effective transfer of induced stresses to enable crack propagation.

This study provides new findings that both support and extend the current understanding of microwave ore pre-treatment in leaching systems. The findings of leaching works reported by previous researchers were derived based on one ore type, and thus the influence of mineralogy and texture on the leaching performance of microwave ore pre-treatment is in no way explored. This research investigates five porphyry copper ores with varying mineralogy and texture, assessing for the first time the impact of texture and mineralogy on leachability following microwave exposure.

The results showed a significant ore strength reduction following point load testing, significant ultrasonic velocity reductions, coupled with a large fracture volume increase of over 500% and fracture openings of up to 1.0-2.5 mm wide as determined by X-ray CT imaging following microwave exposure. This proves that microwave treatment has induced fractures in treated ore samples, and the magnitude of these fractures was found to be dependent on ore mineralogy and texture, as well as microwave energy input (although microwave energy input optimisation was not an objective of this study and is reported elsewhere). Ores with a higher modal abundance of microwave heaters, coarse and/or clustered grains of microwave heaters, stiffer microwave heaters (e.g., pyrite), consistent texture of microwave heaters, and hard/brittle microwave-transparent gangue matrix (e.g., quartz) exhibited significant fractures.

In terms of leaching performance, ore samples with a large magnitude of microwave-induced fractures (i.e., those with amenable mineralogy and texture) achieved significant copper recovery enhancements of up to 28% (absolute) and faster leaching kinetics (by a factor of four or more) to achieve equivalent metal extraction at a microwave energy input of about 10-20 kWh/t. This demonstrates that mineralogy and texture have a significant impact on the leaching performance of microwave-treated ores. The leaching recovery improvement observed through assay results by ICP analysis is complemented by 3D X-ray Computed Tomography (XRCT) imaging, which revealed that microwave ore pre-treatment induces fractures in the direct

vicinity of sulphide mineralisation, and these fractures serve as leaching pathways to the interior of ore fragments, thereby improving metal leach extraction.

Furthermore, results showed that the effects of microwave treatment on ore fracturing and leaching improvement increase with particle size. These results suggest that the benefit of microwave treatment of ores can potentially be realised in leaching coarse ore fragments (e.g., heap leaching), where leaching is performed in coarse particles, but metal leach recoveries are typically low and leach durations are usually long. Several conceptual flowsheets incorporating microwave heating technology to assist mineral dissolution in heap leaching operations have been proposed, based on treating the whole ore or a portion of the feed with amenable mineralogy and texture for microwave treatment. To ensure effective treatment and avoid spread of power, a gravity-fed system was proposed in which ore fragments flow through a vertically aligned tube as a packed bed to interact with the high-intensity and well-confined microwave fields in a TE_{10} single mode cavity. This treatment system may require several applicators (connected in series) coupled to 100 kW generators to ensure homogeneous treatment of materials at higher throughput rates (e.g., >100 t/hr). A thorough techno-economic analysis should be performed to assess the economic viability of this technology in industrial heap leaching applications.

ACKNOWLEDGEMENTS

TABLE OF CONTENTS

LIST OF FIGURES

LIST OF TABLES

LIST OF ABBREVIATIONS

BBWI   Bond ball mill work index

BSE   Backscattered electrons

BTS   Brazilian tensile strength

BRWI   Bond rod Mill work index

CT   Computed tomography

D_e Equivalent core diameter (mm)

DWT   Drop weight test

EDX   Energy Dispersive X-ray

EDM   Euclidean Distance Map

EPMA   Electron probe microanalyzer

EMC   Electromagnetic Compatibility

FDI   Fluorescence dye impregnation

FOV   Field of view (with regards to X-ray CT imaging)

HPGR   High pressure grinding rolls

ICP-AES   Inductively coupled plasma atomic emission spectroscopy

IR   Infra-red

ISM   Industrial, Scientific, and Medical

$Is_{(50)}$ Point Load Index (MPa)

JKGem   JK geometallurgy index

JKRBT   JK rotary breakage tester

MIP   Mercury intrusion porosimetry

Mg   Geometrical magnification

MW   Megawatt

MLA   Mineral liberation analysis

NRPB   National radiological protection board UK

ORS   Object Research Systems

Pd   Power per unit volume (W/m^3)

PLT   Point load test

PUNDIT   Portable ultrasonic non-destructive digital indicating tester

TFT   Thin-film transistor

QEMSCAN	Quantitative evaluation of materials by scanning electron microscopy
SCM	Shrinking-core model
SDD	Source detector distance
SE	Secondary electrons
SEM	Scanning electron microscope
SOD	Source object distance
SX-EW	Solvent extraction - electrowinning
TE	Transverse electric
T&L	Microwave treated and leached samples
TM	Transverse magnetic
USGS	United States Geological Survey
UT	Microwave untreated samples
UT&L	Microwave untreated and leached samples
UCS	Uniaxial compressive strength
UPV	Ultra- pulse velocity
VNA	Vector network analyser
V_a	Pulse velocity of a specimen after microwave treatment (mm/µs)
V_b	Pulse velocity of a specimen before microwave treatment (mm/µs)
WR340	Rectangular waveguide (width x height = 86.4 x 43.2 mm)
WR430	Rectangular waveguide (width x height = 109.2 x 54.6 mm)
WR975	Rectangular waveguide (width x height = 247.6 x 123.8 mm)
WR2300	Rectangular waveguide (width x height = 584.2 x 292.1 mm)
XRD	X-ray diffraction
V_c	Volume of the empty cavity (m³)
V_s	Volume of the sample (m³)
Q_0	Quality factor of the empty cavity
Q_s	Quality factor of the cavity with the sample
f_0	Resonant frequency of the empty cavity (Hz)
f_s	Resonant frequency of the cavity with the sample (Hz)
J_1	First order Bessel function
C_p	Specific heat capacity of the material (J/kg°C)

LIST OF SYMBOLS

α_a	Atomic polarisation
α_e	Electronic polarisation
α_i	Interfacial polarisation
α_o	Orientation polarisation
ε	Complex permittivity
ε_0	Permittivity of free space (8.85×10^{-12} F/m)
ε'	Real part of the complex permittivity (dielectric constant)
ε''	Imaginary part of the complex permittivity (dielectric loss factor)
ε^*	Relative permittivity
ε''_{eff}	Effective loss factors
ε_s	Dielectric constant under static fields
ε_∞	Dielectric constant at very high frequencies
θ	Diffraction angle (degrees)
$\tan \delta$	Loss tangent (dissipation factor)
f	Frequency (Hz)
E	Electric field intensity (V/m)
β	Phase factor
D_p	Penetration depth (m)
λ	Wavelength (m)
λ_0	Free-space wavelength (m)
τ	Relaxation time (s)
ω	Angular frequency (radians per second)
μ	X-ray linear attenuation coefficient of the material
x_i	Length of X-ray path through material i
Z_e	Effective atomic number
E	Energy of X-ray beam
ρ	Bulk density of the material

f_i	Fraction of total number of electrons of element i
I_o	Initial intensity of X-ray beam
I	Final intensity of X-ray beam
δ_s	Skin depth (m)
σ	Electrical conductivity of the material (S/m)
μ_0	Permeability of free space ($4\pi \times 10^{-7}$ H/m)

1. INTRODUCTION

1.1   Background

Copper was one of the first metals used by ancient people, and it is still an essential metal today (Rötzer & Schmidt, 2018). Its unique properties (e.g., high thermal and electrical conductivity, corrosion resistance, and good machinability) make it applicable to multiple applications such as electrical power, electronics, transportation, plumbing, machinery, and metallurgy. In recent years, copper demand has increased rapidly due to the latest advances in technology, industrial development, and the growing world population. By 2050, the total copper demand is expected to increase by up to 350% compared to what it was in 2010 (Elshkaki et al., 2016).

Copper is produced from two major sources: primary (from mining and processing copper ores) and secondary (recycled from copper-bearing scrap). Copper is one of the most recycled metals; it is estimated that 30% of current global copper use comes from recycled copper scrap (ICSG, 2021). This means that recycled copper alone cannot meet the demand, and primary sources are critical to meeting future demand (Valenta et al., 2019). However, the global copper head grade continues to drop as higher-grade ore bodies are being mined and exhausted over time. Figure 1.1 indicates the trend for global copper head grade from 1990, projected forward to 2025. It can be seen that the copper head grades have dropped from about 1.6% in 1990 to around 0.9% in 2021, a drop of more than 40% in three decades. To keep up with the increasing copper demand, larger volumes of low-grade ores must be processed with significant knock-ons in terms of energy and water consumption.
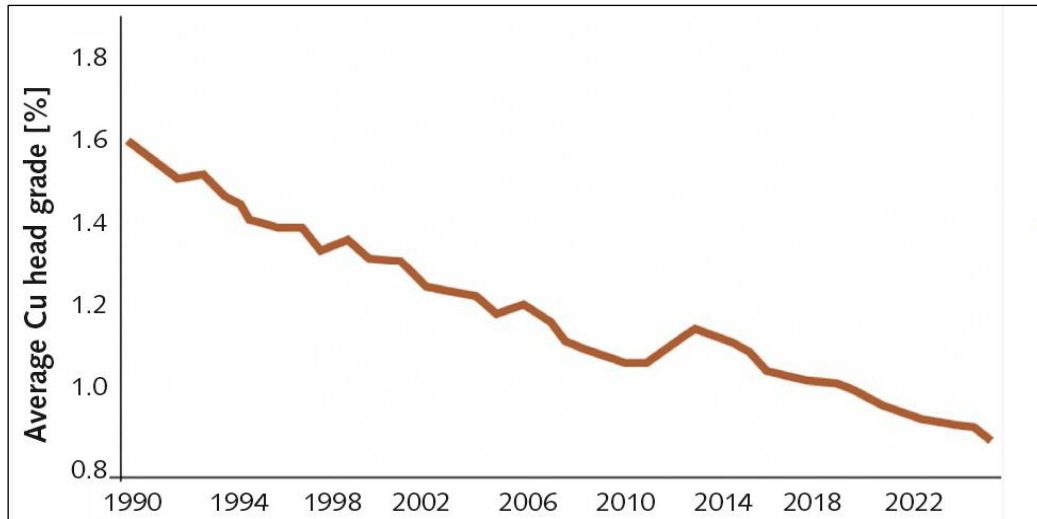
Figure 1.1. Global copper head grade trends (Harder, 2020 sourced from Brook-Hunt)

However, processing these low-grade ores using existing flowsheets is not economically attractive due to higher energy consumption and low process efficiency. To overcome future challenges in meeting the growing copper demand, innovative processing technologies must now be explored to treat low-grade ores more efficiently.

Currently, copper ores are processed via two principal routes: pyrometallurgy (for sulphide ores) and hydrometallurgy (for oxide or low-grade sulphide ores). The pyrometallurgical approach involves primary crushing followed by several stages of grinding to ensure effective mineral liberation. The ground product is subjected to froth flotation to concentrate the minerals, followed by smelting and refining processes to purify the concentrate into metallic copper. On the other hand, the hydrometallurgical approach involves primary crushing followed by mineral dissolution, normally through heap leaching. The leach solution is then concentrated in a solvent extraction-electrowinning system (SX-EW) to obtain the final copper product. Figure 1.2 shows the global trends in copper production from both processing methods from 1900 to 2020. It is estimated that copper production has almost doubled from about 9.0 million tonnes in the 1990s to 21.0 million tonnes in 2020 (ICSG, 2021), with pyrometallurgy alone accounting for more than 80% of total refined copper.
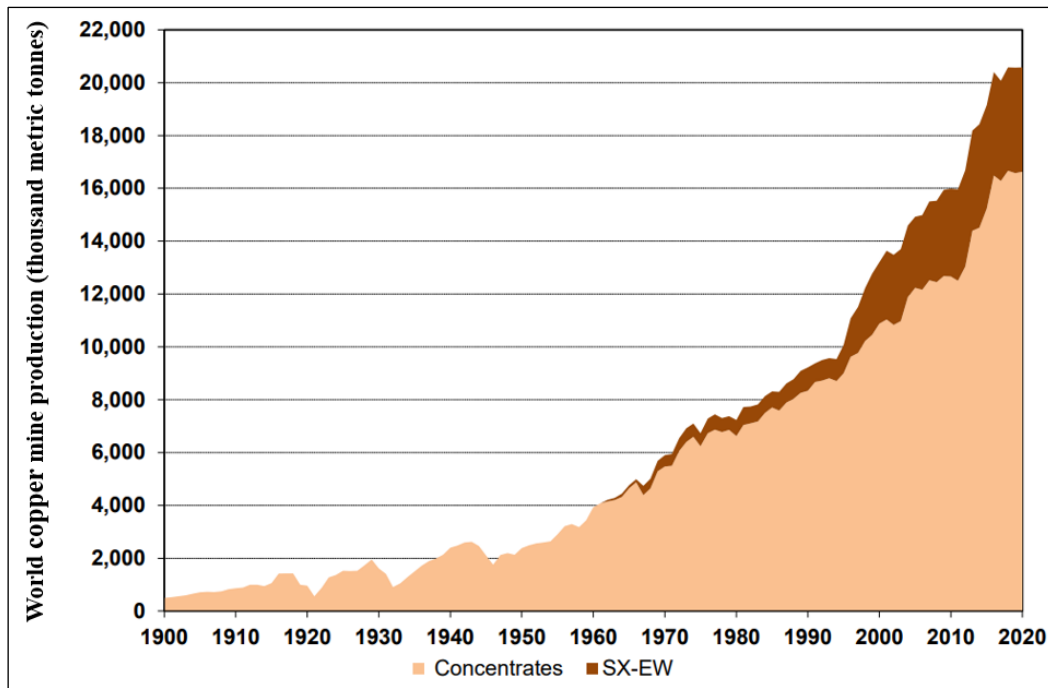
Figure 1.2. World copper mine production 1900-2020 (ICSG, 2021)

The low-grade copper sulphide ores encountered in the current mining operations are more difficult to process using the pyrometallurgical approach. This is due to the higher grinding energy requirements for maximum mineral liberation in these ores, which mostly consist of very fine grains of sulphide mineral. In addition to a finer grind size, grinding larger volumes of low-grade ores demands exponentially higher energy, which in turn significantly increases the energy consumption per tonne of copper produced.

Grinding is a very energy-intensive and inefficient process, with only 1% of the input energy contributing to the actual breakage, the rest of the energy being lost as heat and sound (Wills & Atkinson, 1993). Grinding energy alone accounts for approximately 40% of the total energy consumed by various unit operations in the mining industry (Powell & Bye, 2009). Figure 1.3 depicts a typical relationship between comminution energy input (or energy cost) and ore particle size. The comminution energy input increases exponentially as the ore particle size decreases. This is because the magnitude of existing flaws/defects in the particle decreases with particle size, making smaller particles stronger and thus requiring more comminution energy

to break. In addition to higher grinding energy requirements, higher mill throughputs increase liner wear and grinding media consumption, thereby increasing the cost per unit of metal produced even further.
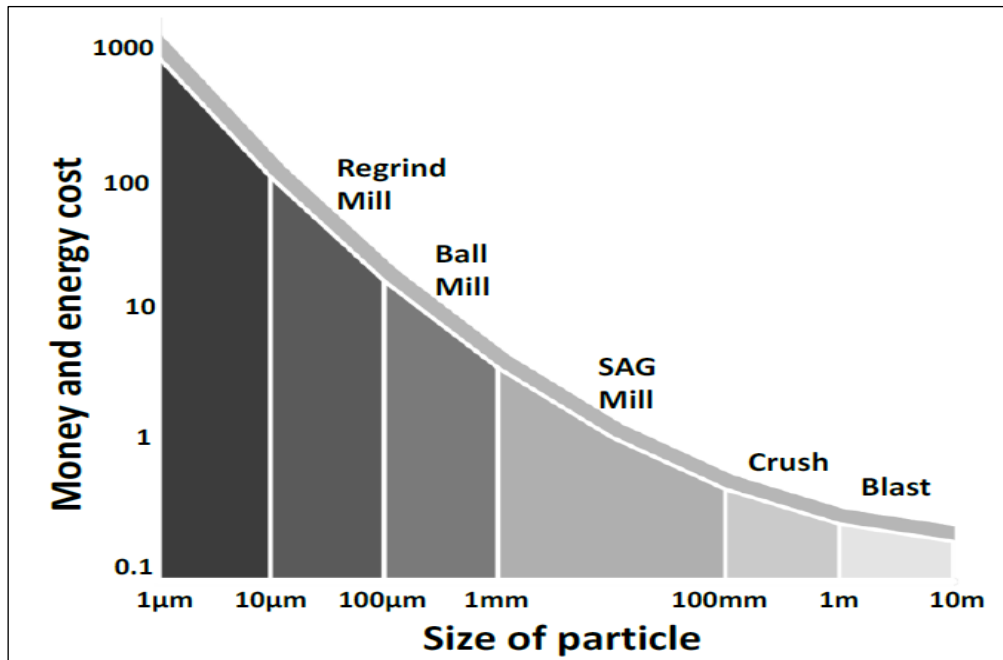
Figure 1.3. Comminution energy-particle size relationship (Adapted from Napier-Munn et al., 1996)

Normally, the low-grade copper sulphide ores are processed via the heap leaching approach because the mineral content does not justify the costs for grinding and metal concentration, and thus crushed ores typically below 25 mm are leached without grinding (Petersen, 2016). However, the leach recovery achieved in this process is typically low (>70%) compared to (>90%) in the crush-grind-float circuit, and the leach duration is relatively long, ranging from several months to more than a year (Brierley, 2008). This is because most of the sulphide grains are not readily exposed to the leach solution. A potential way to save energy while improving heap leach performance is to induce fractures along grain boundaries in crushed ore particles (leach feed). Microwave ore pre-treatment is one of the potential methods for inducing

fractures in sulphide ore samples, exposing more sulphide grains to the leach solution and thus improving leaching performance.

For the past 30 years, it has been demonstrated that microwave energy can reduce ore mechanical strength and improve mineral liberation (Walkiewicz et al., 1991; Kingman et al., 2000; Batchelor et al., 2017). The principal mechanism of microwave-induced fractures in sulphide ores is based on the rapid and selective heating of microwave-absorbing phases (mostly sulphide minerals) within a microwave transparent gangue matrix (mostly rock-forming minerals). This heating results in the thermal expansion of microwave-absorbing phases within the non-heating matrix, which creates tensile and shear stresses around grain boundaries, leading to micro-fractures along grain boundaries. This can be achieved when relatively low microwave energy is applied (Figure 1.4A).

In addition, if sufficient microwave energy is applied and the ore possesses suitable properties that support the initiation and propagation of fractures, the micro-fractures can combine (coalesce) to form macro-fractures (Figure 1.4B). These macro-fractures can act as leaching pathways to the inner part of the particle, thus allowing the dissolution of sulphide grains that could otherwise not be accessible to the leach solution, thereby improving the leaching performance. Furthermore, if fractures are made in large fragments that are subsequently crushed, the internal mineral may be exposed due to preferential breakage along induced fracture paths that would otherwise remain locked due to random breakage of the fragments. For example, in a recent study, a significant leaching recovery enhancement of 7-12% due to microwave treatment was achieved by Schmuhl et al. (2011) on a low-grade coarsely crushed copper sulphide ore sample.
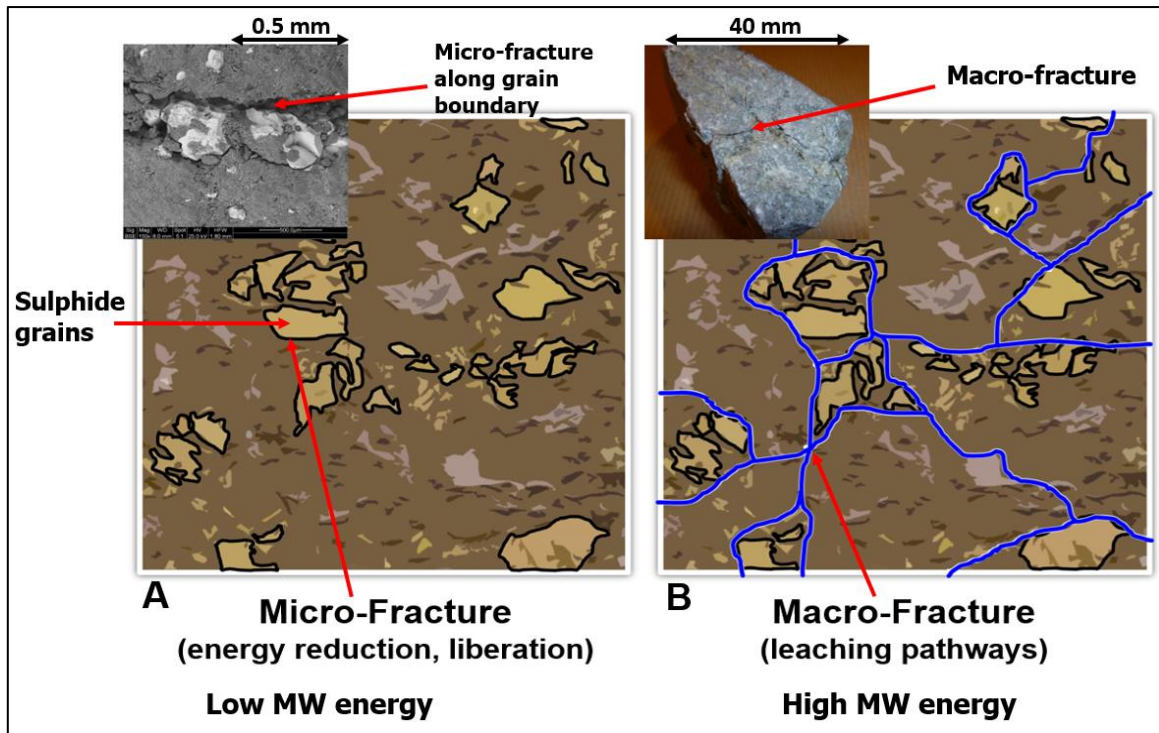
Figure 1.4. Microwave-induced fractures

Despite the improved leaching performance reported by previous researchers, the influence of ore properties (e.g., mineralogy and texture) on the leaching performance of microwave pre-treated copper sulphide ores has not been fully explored because their investigation was limited to one ore type. The current study aims to fill the existing gap in knowledge by using five copper sulphide ore samples of varying mineralogy and texture to assess the magnitude of microwave-induced fractures, followed by quantification of the enhanced metal extraction and improved leaching rate. In terms of practical application, this evaluation directs the potential ore candidates for microwave treatment in downstream processes such as heap leaching. Furthermore, this study has proposed potential alternative flowsheets and microwave treatment systems that can be coupled to a typical heap leaching flowsheet to reduce comminution energy and improve leaching performance, indicating opportunities and challenges.

1.2   Aims and Objectives

This research aims to provide a better understanding of the influence of ore mineralogy and texture on the extent of microwave-induced fractures. Thereafter, it explores the potential benefit of these fractures for the enhancement of mineral dissolution. These aims are achieved through the following specific objectives:

1. To characterise the mineralogy and texture of five different copper sulphide ores using the Mineral Liberation Analyzer (MLA) and X-ray Diffraction (XRD) techniques.

2. To quantify the extent of microwave-induced fractures on copper sulphide ores at various microwave energy levels using the point load and crushing techniques.

3. To develop a single-particle experimental method for visualising and quantifying microwave-induced fractures in ore specimens using the X-ray Computed Tomography (X-ray CT) imaging technique.

4. To evaluate the effect of microwave ore pre-treatment on leaching performance using X-ray CT imaging and the Inductively Coupled Plasma Atomic Emission Spectroscopy (ICP-AES) assay technique.

5. To assess the influence of microwave-induced fractures on the dissolution kinetics and overall metal extraction of coarse ore fragments (30-50 mm).

6. To propose alternative heap leaching flowsheets and microwave heating systems that incorporate microwave ore pre-treatment to improve mineral exposure and leaching performance.

1.3   Thesis Outline

This thesis is organised into nine chapters. Following a brief overview in this introductory chapter, the detail of this thesis is covered in Chapters 2-9, as summarised:

- Chapter 2 provides an overview of microwave fundamentals in industrial heating systems. This includes microwave-material interaction and heating mechanisms, dielectric properties and microwave heating relationship, dielectric properties measurement techniques, microwave power density and penetration depth, essential components in industrial microwave heating systems, as well as microwave safety and emission aspects.

- Chapter 3 presents a review of relevant literature on microwave ore pre-treatment in mineral processing applications to date, with an emphasis on comminution and leaching processes. In addition, this chapter has presented theoretical studies that explain the fundamental mechanisms of ore fracturing upon microwave treatment, as well as the influence of ore mineralogy, texture, and microwave power density on microwave-induced damage.

- Chapter 4 describes the main experimental techniques used in this study, including mineral liberation analysis (MLA), X-ray diffraction (XRD), point load test (PLT), ultra-pulse velocity (UPV), Inductively coupled plasma - atomic emission spectroscopy (ICP-AES), and X-ray computed tomography (X-ray CT).

- Chapter 5 evaluates the mineralogy and texture of five different copper sulphide ores used in the current study in order to identify potential ore candidates for microwave treatment.

- Chapter 6 presents results that demonstrate the effect of microwave energy input on the extent of ore pre-damage using the point load and crushing tests.

- Chapter 7 describes the experimental design and execution of a single-particle microwave treatment and leaching testwork. Thereafter, microwave treatment and leaching results based on X-ray CT imaging are presented, and the leaching results are correlated with the ICP-AES assay results.

- Chapter 8 presents results demonstrating the effect of microwave ore pre-treatment on the dissolution kinetics and overall metal extraction of coarse ore fragments of about 30-50 mm. In addition, this chapter proposes several alternative flowsheets incorporating microwave ore pre-treatment to reduce comminution energy and improve leaching performance in heap leaching operations, highlighting opportunities and challenges.

- Chapter 9 presents a summary of conclusions drawn from this work and the recommendations for future studies.

2. FUNDAMENTALS OF MICROWAVE HEATING

2.1 Introduction

Since their rapid development during World War II, microwaves have been widely used in various applications such as communications, radar detection, medical, scientific, electronic warfare, navigation, as well as microwave heating (Gupta & Leong, 2008). With regards to industrial heating applications, microwave energy is used in various industries including: food, rubber, textiles, tobacco, chemicals, and pharmaceuticals (Stuchly & Stuchly, 1983). For the past thirty years, researchers have shown the great potential of microwave energy in improving mineral processing systems (Walkiewicz et al., 1991; Kingman et al., 2000). This research will focus on the use of microwave energy in industrial heating applications for ore pre-treatment in order to improve comminution and subsequent downstream mineral recovery processes, particularly leaching.

Microwave heating of materials is essentially the result of direct molecular volumetric interaction with electromagnetic radiation, making it suitable for more rapid heating than conventional heating, which relies on convection, conduction, and radiation heat transfer mechanisms (Clark & Sutton, 1996; Haque, 1999). Crucially, microwave energy is transferred throughout the volume of the material (i.e., volumetric heating), reducing processing times and improving overall heating quality (Thostenson & Chou, 1999). This chapter provides an overview of microwave fundamentals in industrial heating systems, including material-microwave interaction, microwave heating mechanisms, measurements of dielectric properties, major microwave components, and safety aspects in industrial heating applications. A better understanding of microwave fundamentals is necessary for exploring the potential benefits of microwave heating and mitigating the challenges associated with microwave heating of materials, as well as scaling up such processes for use in the minerals industry.

2.1 Microwaves

Microwaves are electromagnetic waves of short wavelength ranging between 1 m to 1 mm with corresponding frequencies between 300 MHz and 300 GHz (Thostenson & Chou, 1999). In the electromagnetic spectrum, they are positioned between infrared and radio waves. They are self-propagating waves carrying electric and magnetic field components oscillating in phase and perpendicular to one another, and perpendicular to the propagation direction (Figure 2.1) (Metaxas & Meredith, 1983). Microwaves travel through vacuum at the same speed as visible light (3.0×10^8 m/s). When microwaves interact with matter, they can be absorbed, reflected, transmitted, or any combination of these three interactions.
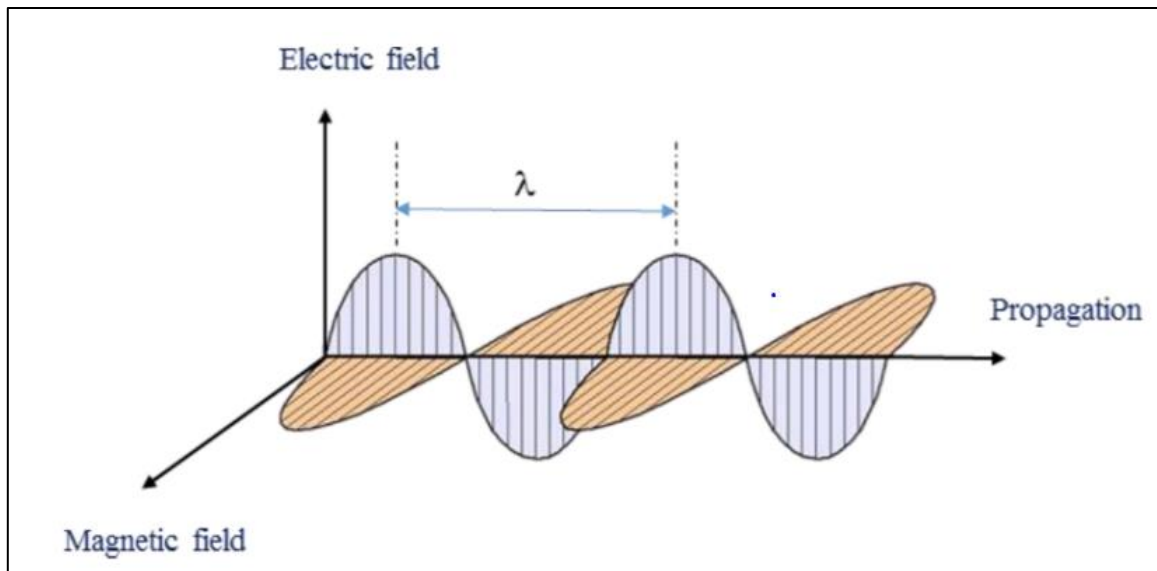
Figure 2.1. Propagation of electromagnetic waves (Staebler, 2017)

2.2 Classes of Materials Based on Microwave Interaction

Materials respond differently when subjected to microwave fields. In terms of microwave-matter interactions, there are three major classes of materials: insulators, conductors, and absorbers (Clark et al., 2000), as indicated in Figure 2.2. Insulators such as quartz are essentially microwave transparent (microwaves pass without being absorbed). Conductors such as aluminium in bulk form reflect most microwave energy, and heating occurs at the surface

(skin heating). Absorbers (dielectrics), on the other hand, absorb microwave energy and can be significantly heated depending on the dielectric properties of the material being treated.
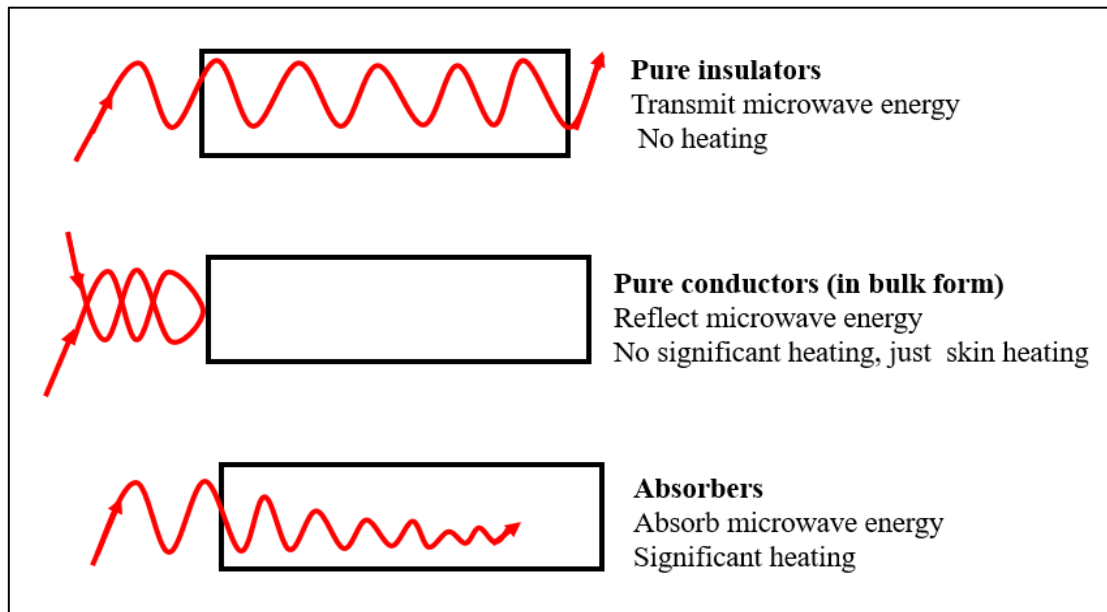
Figure 2.2. Material classes based on microwave interaction (adapted from Haque, 1999)

Materials composed of both absorbers and insulators in the same structure undergo selective heating when exposed to microwave fields. Sulphide ores are good examples of such materials, in which sulphide minerals (e.g., chalcopyrite) are selectively heated within a microwave transparent gangue matrix (e.g., quartz), and each of these minerals expands differently as a result of this heating. This uneven thermal expansion generates differential stresses, which leads to ore cracking, particularly at the grain boundary between the heated and non-heated phases. The microwave-induced cracks have the potential to improve comminution and subsequent mineral recovery processes (e.g., leaching), which is the focus of this research.

2.3 Microwave Heating Mechanisms

For nonmagnetic materials, microwave heating is only contributed by the electric field component of the electromagnetic wave via two main mechanisms: dielectric polarisation and direct conduction effects. Dielectric polarisation is caused by the ability of dielectrics to be polarised by the applied oscillating electric field and the inability of dipoles to precisely follow the rapid reversal of the electric field (Metaxas & Meredith, 1983). The direct conduction heating is caused by electrical resistance generated when electric current flows on the material upon microwave exposure. This is the most important mechanism in semiconducting materials, such as sulphide minerals.

In addition to the heating effect caused by the electric field component of an electromagnetic wave, ferromagnetic materials may couple with the magnetic component, resulting in additional heating mechanisms caused by magnetic losses (Clark & Sutton, 1996). According to Mishra & Sharma (2016), the heating mechanisms caused by magnetic losses are hysteresis, eddy current, domain wall resonance, and electron spin resonance. The heating effect due to magnetic losses is irrelevant in sulphide ores except when the ore is composed of ferromagnetic minerals (e.g., magnetite). The heating mechanisms caused by electric losses are discussed here.

2.3.1   Dielectric Polarisation

Dielectric polarisation is a slight relative displacement of positive and negative electric charges from their equilibrium position in a dielectric material in response to an external alternating electric field (Bain & Chand, 2017). In this process, the positive charges are displaced in the direction of the electric field, while negative charges are displaced in the opposite direction. Because of this charge separation, atoms within dielectrics acquire positive polarity at one end and negative polarity at the other. For materials with permanent dipoles, such as water molecules, which have positive polarity on the hydrogen atom and negative polarity on the

13

oxygen atom, the dipoles reorient/realign to some extent in response to the applied oscillating electric field.

Dielectric polarisation is classified into four mechanisms: electronic polarisation, atomic polarisation, orientation polarisation, and interfacial (spatial charge) polarisation (Metaxas & Meredith, 1983). The total dielectric polarisation is the sum of these four components, as expressed in Equation 2.1.

$$\alpha_{total} = \alpha_a + \alpha_e + \alpha_o + \alpha_i \tag{2.1}$$

Where, α is polarisation, and the subscripts a, e, o, and i, denote atomic, electronic, orientation, and interfacial, respectively.

However, each dielectric mechanism has a characteristic frequency range at which they contribute to dielectric heating, as indicated in Figure 2.3 (Agilent, 2005). At microwave frequencies, the orientation (dipolar) and interfacial heating are dominant (as indicated by higher dielectric properties), whereas the atomic and electronic polarisation are most significant in the infrared (IR) and ultraviolet (UV) frequency ranges, respectively.
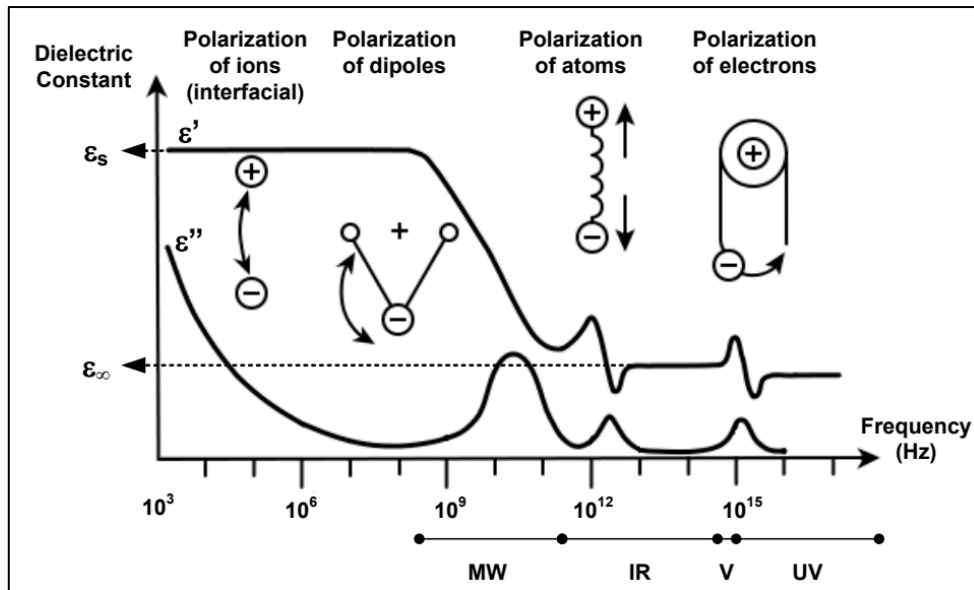
Figure 2.3. Characteristic frequencies of dielectric polarisation mechanisms (Agilent, 2005)

2.3.1.1 Electronic and Atomic Polarisation

Electronic polarization arises from the displacement of electron charges in relation to specific nuclei within a material in response to an applied electric field, as illustrated in Figure 2.4 (Peng & Hwang, 2015). Atomic polarization, on the other hand, results from a relative displacement of nuclei caused by unequal distribution of charge within a material. At microwave frequencies, the electronic polarization and atomic polarization occur rapidly enough to stay in phase with the rapid alternating field and thus do not contribute significantly to dielectric heating (Whittaker, 1997). Therefore, both electronic and atomic polarisation mechanisms are not relevant for the dielectric heating of minerals.

Figure 2.4. Electronic and Atomic polarisation (Gupta & Leong, 2008; Peng & Hwang, 2015)

2.3.1.2 Dipolar and Interfacial Polarisation

Dipolar polarisation arises from the reorientation/realignment of induced or permanent dipoles of molecules under the influence of an alternating electric field, as indicated in Figure 2.5. At low frequencies, the heating effect is not very significant because the dipoles have enough time to align in phase with the applied electric field, but the frequency is not sufficient to generate friction between rotating molecules for adequate heat formation. Also, negligible heat is generated at very high frequencies because the dipoles are too slow to respond to the fast oscillating electric field and thus no energy transfer (Whittaker, 1997). Between these two extremes (at relaxation frequency), the dipoles can respond, but they lag behind to some extent when attempting to align to the applied electric field; this causes collision and friction between rotating molecules, resulting in the generation of adequate heat (Meredith, 1998). Dipolar polarisation is more relevant for the dielectric heating of hydrated minerals, such as montmorillonite.
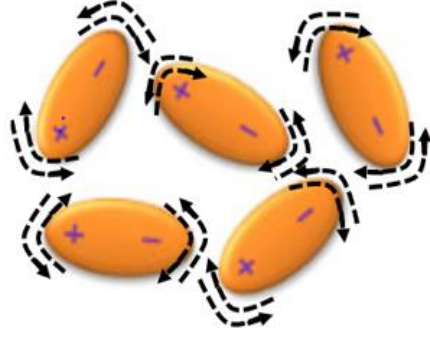
Figure 2.5. Dipolar polarisation (reproduced from Gupta & Leong, 2008; Peng & Hwang, 2015)

The electronic, atomic, and dipolar polarisation occur when charges are locally bound within atoms, molecules, or structures of solids or liquids. However, charge carriers (electrons, ions) can migrate over a distance within a material when a low-frequency electric field is applied (Agilent, 2005). Interfacial polarisation, also known as Maxwell-Wegner or space charge polarisation, occurs when the movement of charge carriers is hindered at interfaces/discontinuities or contact points between components within a heterogeneous material (Metaxas & Meredith, 1983). This causes charge accumulation on one side of the interface and the induction of a corresponding opposite charge on the other side of the interface (Figure 2.6), resulting in a dipolar heating effect.
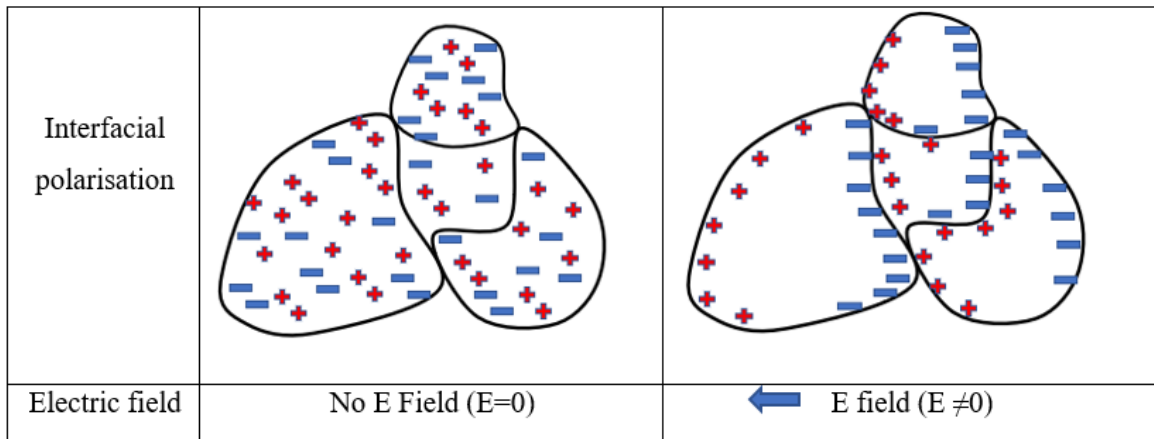
Figure 2.6. Interfacial (Maxwell-Wegner) polarisation

2.3.2 Direct Conduction Effect

In addition to dielectric polarisation, materials can heat when exposed to microwave fields via the direct conduction mechanism. This occurs when materials have free charge carriers (e.g., free electrons) that are set in motion when they interact with microwave fields. As a result, an electric current is induced that travels in phase with the field, thereby causing the material to heat due to electrical resistance (Whittaker, 1997). For materials with low electrical resistivity, such as copper metal (in bulk form), heating is limited at the surface (skin heating), because most microwave energy does not penetrate the material but is readily reflected. This has the potential to cause electrical arcing, which is discussed further in Section 2.9. The extent of microwave penetration within an electrical conductor (skin depth) is a function of the electrical conductivity of the material and microwave frequency, as expressed in Equation 2.2. This expression indicates that the skin depth of the material increases with the decrease in electrical conductivity and the decrease in the applied microwave frequency.

18

$$\delta_s = \sqrt{\frac{2}{\sigma\omega\mu_0}}, \qquad \text{where } \omega = 2\pi f \qquad \text{(2.2)}$$

Where;

δ_s = skin depth (m),

f = frequency (Hz),

σ = electrical conductivity of the material (S/m),

μ_0 = permeability of free space ($4\pi \times 10^{-7}$ H/m),

ω = angular frequency (rad/s).

For materials with electrical conductivity values falling between that of conductors and insulators (i.e., semiconductors) (see Table 2.1), the heating effect can be significant due to the limited free charge carriers that make them poor electrical conductors. Typical examples of semiconducting materials relevant to the current study are sulphide minerals (e.g., chalcopyrite), which have electrical conductivity values ranging from 1.0×10^0 and 1×10^5 S/m (Pridmore & Shuey, 1976).

Table 2.1. Conductivity and resistivity spectrum (reproduced from Mehdizadeh, 2015)

Conductivity S/m	Resistivity ohm-cm	Material class/ example
10^{-14}	10^{16}	Dielectrics, insulators (e.g., quartz)
10^{-12}	10^{14}	
10^{-10}	10^{12}	
10^{-8}	10^{10}	
10^{-6}	10^{8}	
10^{-4}	10^{6}	
10^{-2}	10^{4}	Semi conductive (e.g., sulphide minerals such as chalcopyrite)
10^{0}	10^{2}	
10^{2}	10^{0}	
10^{4}	10^{-2}	Highly conductive (e.g., copper metal)
10^{6}	10^{-4}	
10^{8}	10^{-6}	

2.4 Dielectric Properties

The extent to which nonmagnetic materials heat up when exposed to microwave fields is largely dictated by their dielectric properties (Nelson, 2006). Essentially, the dielectric properties of a material are defined in terms of electric permittivity (ε), which has a real part (ε') and an imaginary part (ε''), as shown in the complex algebraic Equation 2.3. The real part of electric permittivity is known as dielectric constant, which is a measure of a material's ability to be polarized and store energy when an external electric field is applied. The imaginary part is known as dielectric loss, which is a measure of the material's ability to dissipate the stored electrical energy into heat (Metaxas & Meredith, 1983). When the complex permittivity of the materials is normalized to the permittivity of vacuum, it is referred to as relative permittivity (Equation 2.4). Another parameter commonly used to assess the dielectric heating of materials is the loss tangent (tan δ), sometimes referred to as power loss factor. It is the ratio of the energy

dissipated as heat (ε'') to the energy stored (ε') as a result of microwave exposure, as expressed in Equation 2.5. Materials with a high loss tangent value typically heat more efficiently than those with a low value.

$$\varepsilon = \varepsilon' - j\varepsilon'' \tag{2.3}$$

$$\varepsilon^* = \frac{\varepsilon}{\varepsilon_0} \tag{2.4}$$

$$\tan \delta = \frac{\varepsilon''}{\varepsilon'} \tag{2.5}$$

Where;

    ε = permittivity (F/m),

    ε^* = relative permittivity,

    ε' = dielectric constant,

    ε'' = dielectric loss,

    $j = \sqrt{-1}$,

    δ = loss angle,

    ε_0 = permittivity of free space (8.85×10^{-12} F/m).

The dielectric properties of some sulphides and metal oxides relevant to the current study are shown in Tables 2.2 and 2.3, as reported by several researchers (Church et al., 1988; Kobusheshe, 2010; Batchelor, 2013). The dielectric measurements of these minerals were performed at ambient temperature and various frequencies using the cavity perturbation technique (discussed in Section 2.4.2). The frequencies used in this case are close to the ISM (Industrial, Scientific, and Medical) frequencies of 433, 896, and 2450 MHz, which are allocated for microwave heating applications in the United Kingdom. The results in these tables

show that most sulphides and metal oxides have relatively higher values of dielectric constant, loss factor, and loss tangent, implying that they are more susceptible to microwave heating than most silicates.

Table 2.2. Dielectric constant, loss factor and loss tangent of some sulphides and metal oxides (Batchelor, 2013 - reproduced by Ure, 2017)

	Mineral (Formula)	Dielectric Property	Frequency (MHz)			Reference
			400Mhz	910MHz	2450Mhz	
Sulphides	Chalcopyrite $CuFeS_2$	ε'	27.309	24.802	24.381	Batchelor (2013)
		ε''	6.329	4.093	3.046	
		$tan\delta$	0.232	0.165	0.125	
	Chalcocite Cu_2S	ε'	106.163	107.784	120.107	Batchelor (2013)
		ε''	2.218	4.144	10.722	
		$tan\delta$	0.021	0.038	0.089	
	Bornite Cu_5FeS_4	ε'	72.712	73.955	69.656	Batchelor (2013)
		ε''	3.809	7.723	15.414	
		$tan\delta$	0.052	0.104	0.221	
	Molybdenite MoS_2	ε'	28.293	27.558	26.074	Batchelor (2013)
		ε''	3.980	4.187	4.702	
		$tan\delta$	0.141	0.152	0.180	
	Pyrite FeS_2	ε'	23.138	21.675	21.497	Batchelor (2013)
		ε''	6.604	4.060	3.208	
		$tan\delta$	0.285	0.187	0.149	
Oxides	Magnetite Fe_3O_4	ε'	21.918	21.660	22.462	Batchelor (2013)
		ε''	0.731	0.371	0.424	
		$tan\delta$	0.033	0.017	0.019	
	Hematite Fe_2O_3	ε'	10.587	11.114	11.985	Batchelor (2013)
		ε''	1.690	0.843	0.495	
		$tan\delta$	0.160	0.076	0.041	
	Goethite $FeO(OH)$	ε'	23.807	26.312	26.783	Batchelor (2013)
		ε''	0.676	0.237	0.169	
		$tan\delta$	0.028	0.009	0.006	
	Ilmenite $FeTiO_3$	ε'	40.175	34.966	32.810	Batchelor (2013)
		ε''	2.072	2.318	2.597	
		$tan\delta$	0.052	0.066	0.079	
	Rutile TiO_2	ε'	17.993	17.829	18.484	Batchelor (2013)
		ε''	0.692	0.090	0.074	
		$tan\delta$	0.038	0.005	0.004	

Table 2.3. Dielectric constant, loss factor and loss tangent of some gangue minerals (Kobusheshe, 2010; Church et al., 1988; reproduced by Ure, 2017)

	Mineral (Formula)	Dielectric Property	Frequency (MHz)			Reference
			400Mhz	910Mhz	2450Mhz	
Silicates	Quartz SiO_2	ε'	3.782	3.708	3.813	Kobusheshe (2010)
		ε''	0.084	0.054	0.022	
		tanδ	0.022	0.015	0.006	
	Plagioclase $(Na,Ca)(Si,Al)_4O_8$	ε'	4.291	4.785	4.696	Kobusheshe (2010)
		ε''	0.001	0.001	0.001	
		tanδ	0.001	0.001	0.001	
	Orthoclase $KAlSi_3O_8$	ε'	5.250	4.767	4.772	Kobusheshe (2010)
		ε''	0.485	0.023	0.013	
		tanδ	0.092	0.005	0.003	
	Albite $NaAlSi_3O_8$	ε'	4.256	4.334	4.694	Kobusheshe (2010)
		ε''	0.000	0.026	0.023	
		tanδ	0.000	0.006	0.005	
Sheet Silicates	Muscovite $KAl_2(AlSi_3O_10)(F,OH)_2$	ε'	5.273	5.553	5.552	Kobusheshe (2010)
		ε''	1.146	0.250	0.110	
		tanδ	0.217	0.045	0.020	
	Biotite $K(Mg,Fe)_3AlSi_3O_{10}(F,OH)_2$	ε'	5.648	5.506	5.547	Kobusheshe (2010)
		ε''	0.414	0.413	0.241	
		tanδ	0.073	0.075	0.043	
	Na-Montmorillonite $(Na,Ca)_{0.33}(Al,Mg)_2(Si_4O_{10})(OH)_2.nH_2O$	ε'	7.112	6.654	6.387	Kobusheshe (2010)
		ε''	4.017	2.520	1.564	
		tanδ	0.565	0.379	0.245	
	Kaolinite $Al_2(Si_2O_5)(OH)_4$	ε'	6.478	6.105	6.018	Kobusheshe (2010)
		ε''	1.084	0.655	0.346	
		tanδ	0.167	0.107	0.057	
Carbonates	Calcite $CaCO_3$	ε'	8.890	8.840		Church (1988)
		ε''	0.077	0.500		
		tanδ	0.009	0.057		
	Dolomite $CaMg(CO_3)$	ε'	7.380	7.260		Church (1988)
		ε''	0.220	0.226		
		tanδ	0.030	0.031		
	Magnesite $MgCO_3$	ε'	6.710	6.610		Church (1988)
		ε''	0.122	0.104		
		tanδ	0.018	0.016		
	Siderite $FeCO_3$	ε'	7.160	7.100		Church (1988)
		ε''	0.193	0.190		
		tanδ	0.027	0.027		
Other	Apatite $Ca_5(PO_4)_3(OH,F,Cl)$	ε'	6.231	6.425	6.774	Kobusheshe (2010)
		ε''	0.226	0.045	0.012	
		tanδ	0.036	0.007	0.002	
	Zircon $ZrSiO_4$	ε'	6.165	6.915	7.064	Kobusheshe (2010)
		ε''	0.381	0.032	0.014	
		tanδ	0.062	0.005	0.002	

From Tables 2.2 and 2.3, a relationship of loss tangent versus loss factor ($\varepsilon"$) at a frequency of 910 MHz has been plotted (Figure 2.7). This plot categorises minerals into three groups based on their microwave heating response:

i.   Good heaters ($\varepsilon" > 1$) – they are located at the top right of the plot (mostly sulphides).

ii. Poor heaters ($0.2 < \varepsilon" < 1$) – they are located in the middle of the plot (mostly iron oxides).

iii. Non-heaters ($\varepsilon" < 0.2$) – they are located at the bottom left of the plot (mostly rock-forming minerals).

Mineral grouping based on microwave heating response is useful in assessing ore amenability to microwave treatment, and this method is used in the current study, as discussed further in Chapter 5 (Section 5.4).
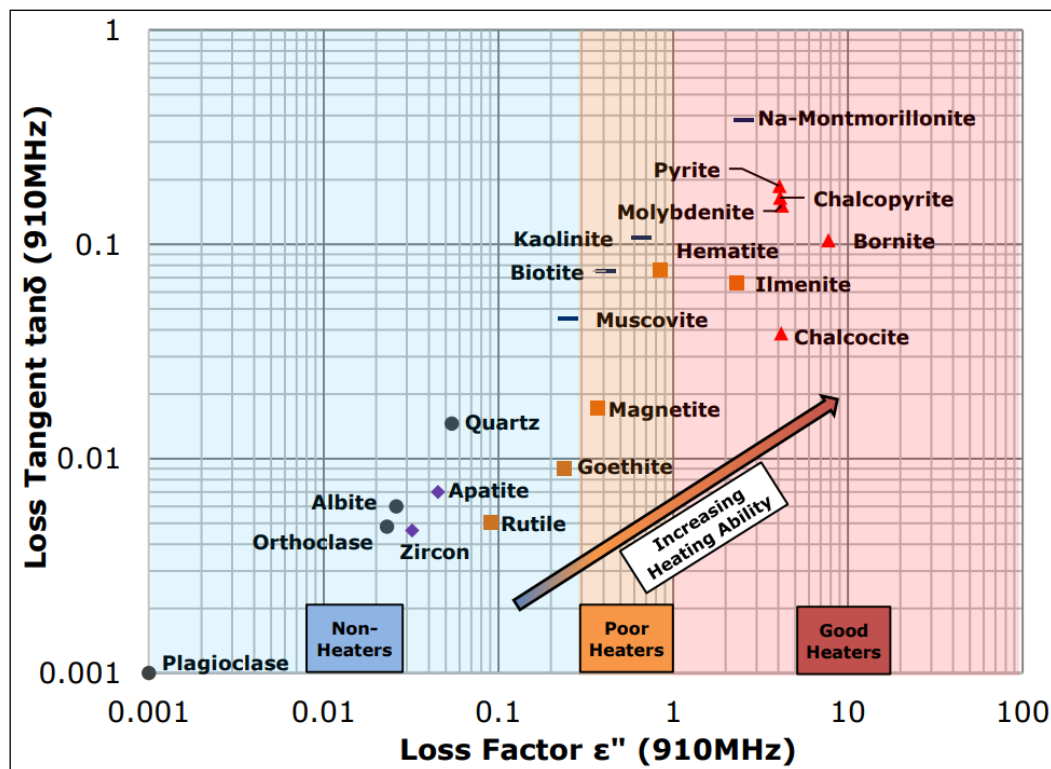
Figure 2.7. Dielectric loss tangent vs loss factor for selected minerals (Batchelor, 2013; Ure, 2017)

2.4.1 Factors Influencing Dielectric Properties of Materials

The dielectric properties of materials vary greatly depending on a variety of factors, including the frequency of the applied electric field, material temperature, and the chemical composition of the material (e.g., water content) (Nelson, 1994; Meredith, 1998). The variation of dielectric properties with frequency and temperature largely depends on the type of microwave heating mechanism exhibited by the material (Atwater & Wheeler, 2003; Pickles et al., 2005). The dielectric properties of the material may also vary significantly depending on the water content, which interacts strongly with microwave energy via dipolar polarisation.

2.4.1.1 Temperature

For materials dominated by dipolar heating mechanisms (e.g., water), the nature of temperature dependency is related to dielectric relaxation processes (Nelson, 1994). Dielectric relaxation is the time required for dipoles to return to their random equilibrium position when the electric field is removed or the time required for dipoles to realign when the electric field is introduced (Agilent, 2005). Generally, an increase in temperature increases the mobility of dipoles which in turn decreases their relaxation time leading to an increase in ε' and/or ε'' to some extent. A significant increase in loss factor can be observed in some materials (e.g., ores or minerals) when a critical temperature is exceeded, which is caused by the changes in heating mechanisms enhanced by electrical conductivity due to phase transformation. The relationship between the dielectric loss factor of the material and its electrical conductivity is expressed in Equation 2.6.

$$\varepsilon'' = \frac{\delta}{2\pi f \varepsilon_0} \tag{2.6}$$

Where;

f = Microwave frequency (Hz),

δ = Electrical conductivity of the material (S/m),

ε_0 = permittivity of free space (8.85 x 10^{-12} F/m),

ε''= relative dielectric loss factor.

Figures 2.8 and 2.9 illustrate the effect of temperature on the dielectric constant and loss factor of some sulphide minerals, respectively, as reported by Batchelor (2013). It appears that most sulphides are thermally stable up to a temperature of about 350°C, after which oxidation alters the dielectric properties. Though chalcocite began to exhibit significant changes in dielectric properties at a low temperature of about 100°C. In contrast, the dielectric properties of gangue minerals, such as quartz and orthoclase appeared to be thermally stable up to 600°C, as shown in Figures 2.10 and 2.11 (Cumbane, 2003).
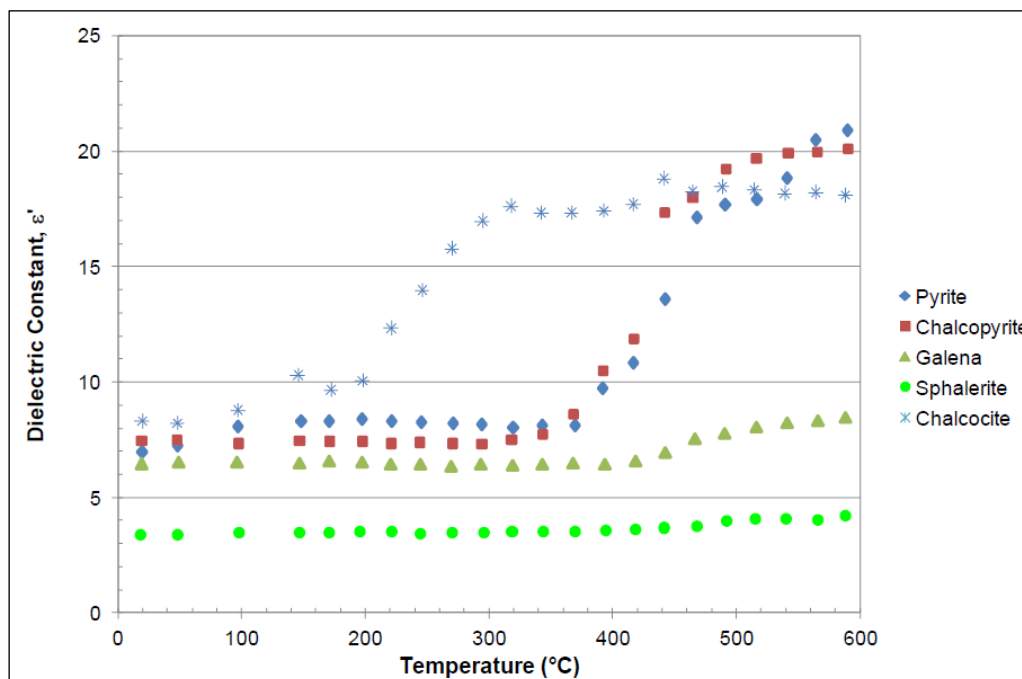
Figure 2.8. Variation of dielectric constant with temperature for some sulphides at 2.21 GHz (Batchelor, 2013)
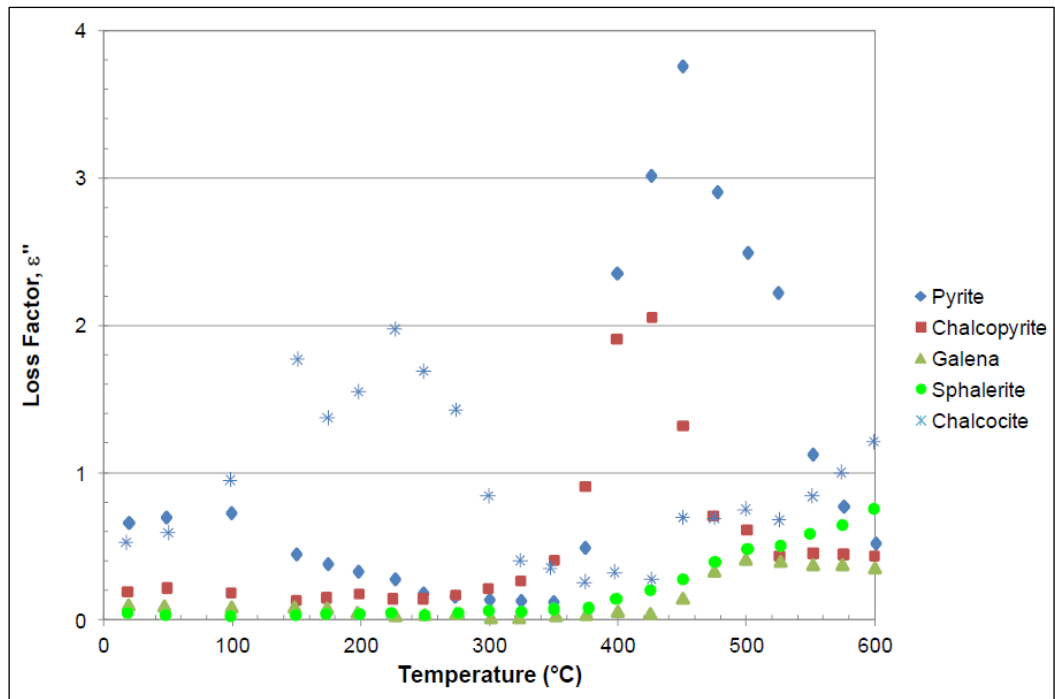
Figure 2.9. Variation of loss factor with temperature for some sulphides at 2.21 GHz (Batchelor, 2013)
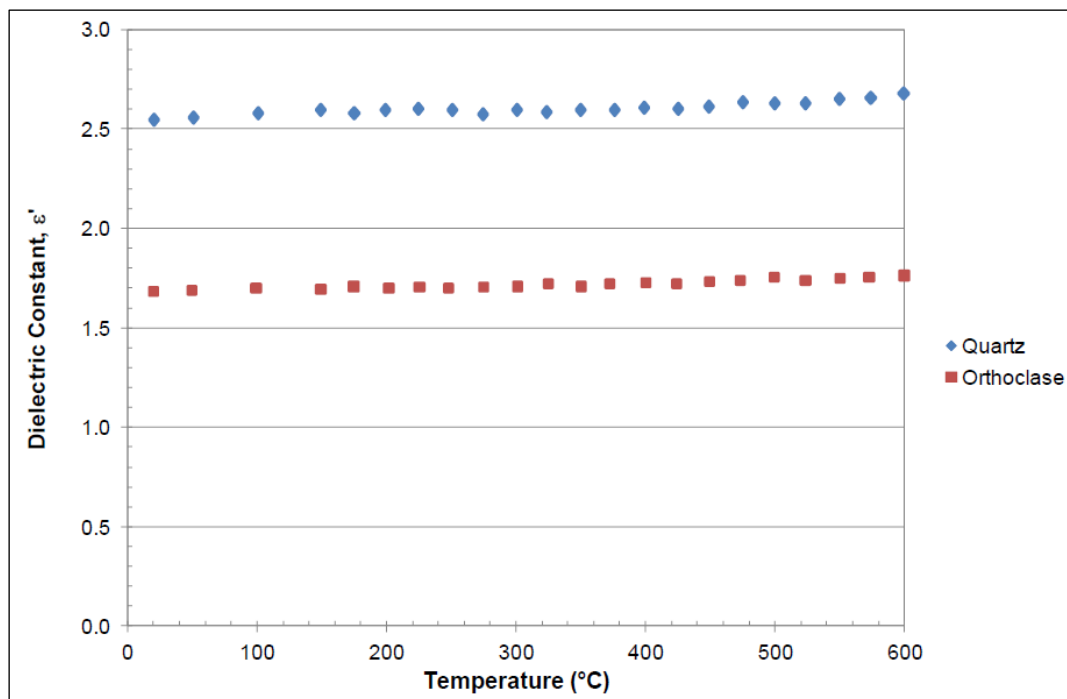
Figure 2.10. Variation of dielectric constant with temperature for some gangue minerals at 2.21 GHz (Cumbane, 2003; Batchelor, 2013)
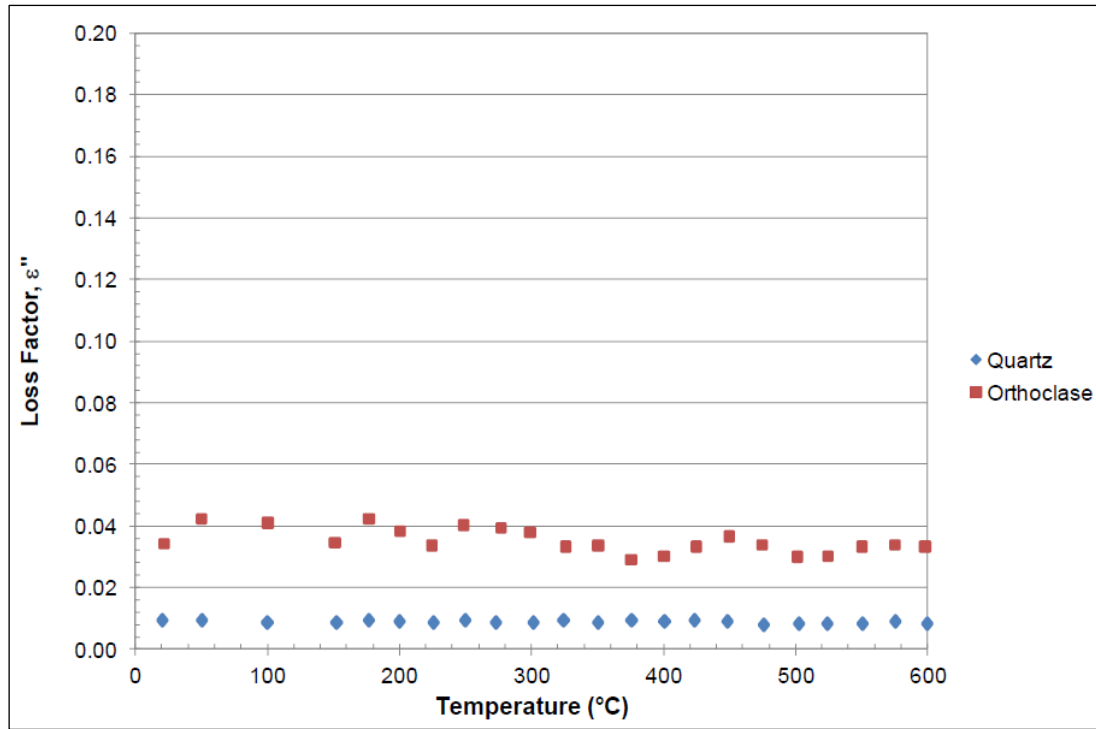
Figure 2.11. Variation of loss factor with temperature for some gangue minerals at 2.21 GHz (Cumbane, 2003; Batchelor, 2013)

2.4.1.2 Frequency

For polar materials, the nature of frequency dependency is also related to dielectric relaxation processes (Nelson, 1994). This dependency is governed by Debye relations (Equations 2.7 and 2.8), which can also be used for qualitative understanding of the effect of microwave frequency on permittivity for some solids (Hotta et al., 2009; Bobicki et al., 2020). The relationship described by these expressions can be illustrated in Figure 2.12. At very low frequencies, the dipoles have sufficient time to respond to the applied electric field hence high storage (ε_r'), but the frequency is so low to impart sufficient losses (ε_r''). At very high frequencies, the dipoles do not have sufficient time to cope with the electric field, hence low storage (ε_r') and low loss (ε_r''). At intermediate frequency (i.e., relaxation frequency), there is a phase lag between the dipole alignment and the applied electric field, hence intermediate storage (ε_r') but the loss (ε_r'') reaches its peak value (Nelson, 1994; Agilent, 2005).

$$\varepsilon'(\omega) = \varepsilon_\infty + \frac{\varepsilon_s - \varepsilon_\infty}{1 + \omega^2 \tau^2} \tag{2.7}$$

$$\varepsilon''(\omega) = \frac{(\varepsilon_s - \varepsilon_\infty)\omega\tau}{1 + \omega^2 \tau^2} \tag{2.8}$$

Where;

ε' = dielectric constant,

ε'' = dielectric loss factor,

ε_s = dielectric constant under static fields,

ε_∞ = dielectric constant at very high frequencies,

ω = angular frequency ($2\pi f$ rad/s),

τ = relaxation time (s).
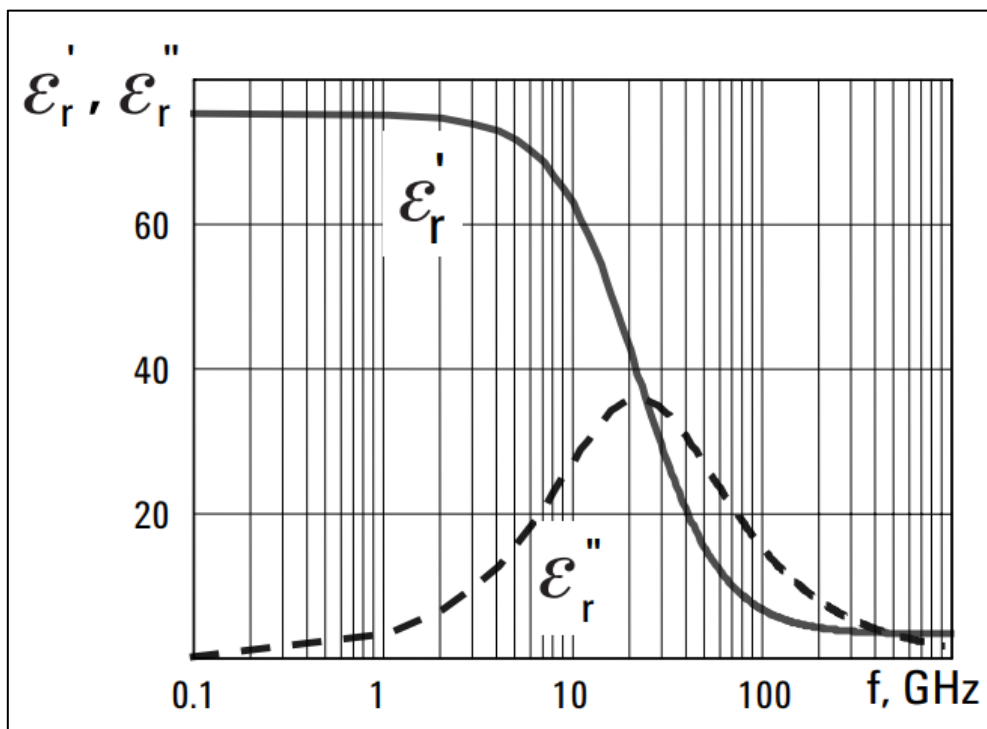
Figure 2.12. The Debye model for water at 30°C with a single relation time (Nelson, 1994; Agilent, 2005)

Bobicki et al. (2020) demonstrated the effect of microwave frequency on dielectric properties using chromite ore. There was a weak frequency dependency at low temperatures, which became more significant as temperature increased due to increases in both the electrical conduction effect and lattice spacing at high temperatures. The effect of microwave frequency on the dielectric properties of such chromite ore at 1000°C is shown in Figure 2.13, indicating a decrease of both the real and imaginary permittivities with increasing frequency.
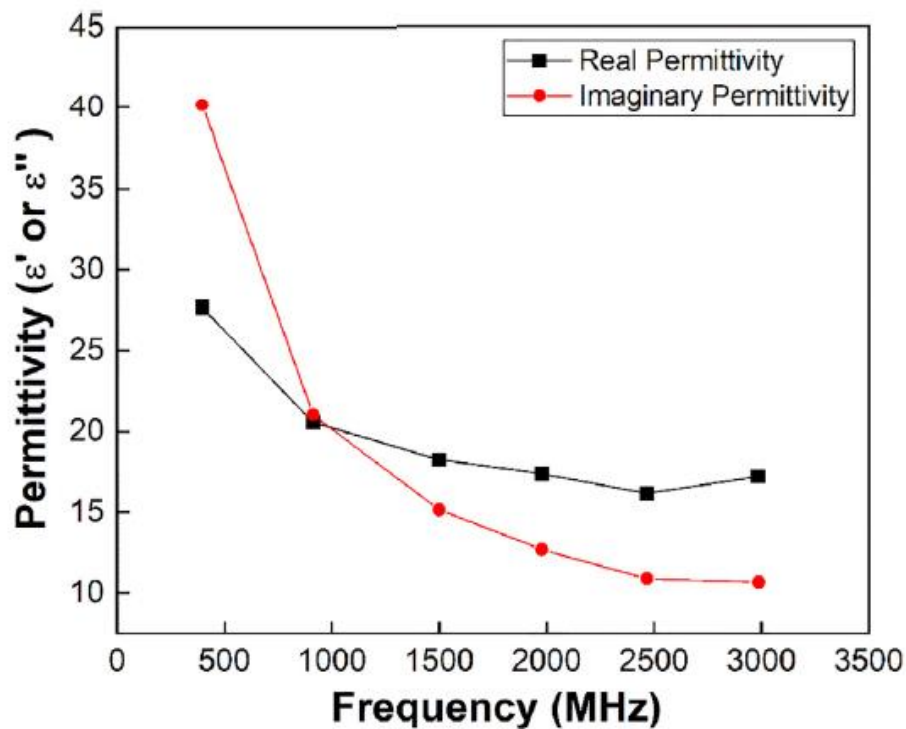
Figure 2.13. Real and imaginary permittivity of chromite ore at 1000°C (Bobicki et al., 2020)

2.4.1.3 Water Content in the Material

Ores may contain water in various forms (free, or chemically bound). The presence of water in the ore can have a significant impact on the ore's dielectric properties, and this is due to its higher permittivity values than other materials contained in the ore (Bobicki et al., 2020). Basically, free water is weakly bonded to the material and can be removed easily by evaporation at about 100°C. In contrast, chemically-bound water is more difficult to remove

than free water, requiring higher temperatures of about 100-300°C to breakdown the water in the crystal lattice of the material or about 200-600°C to remove hydroxyl group (dehydroxylation) from the material.

In general, water removal from materials (e.g., ores) is associated with a decrease in permittivity values at the temperatures at which the water is expelled. This effect is more significant during the dehydroxylation of some ores (e.g., gibbsite) or the removal of interlayer water from some ores (e.g., vermiculite, or hydrated silicates). Using hydrated silicate minerals, Kobusheshe (2010) observed a significant decrease in dielectric properties and mass loss due to the removal of bound water at temperatures ranging from 100°C to 300°C (Figures 2.14 and 2.15).
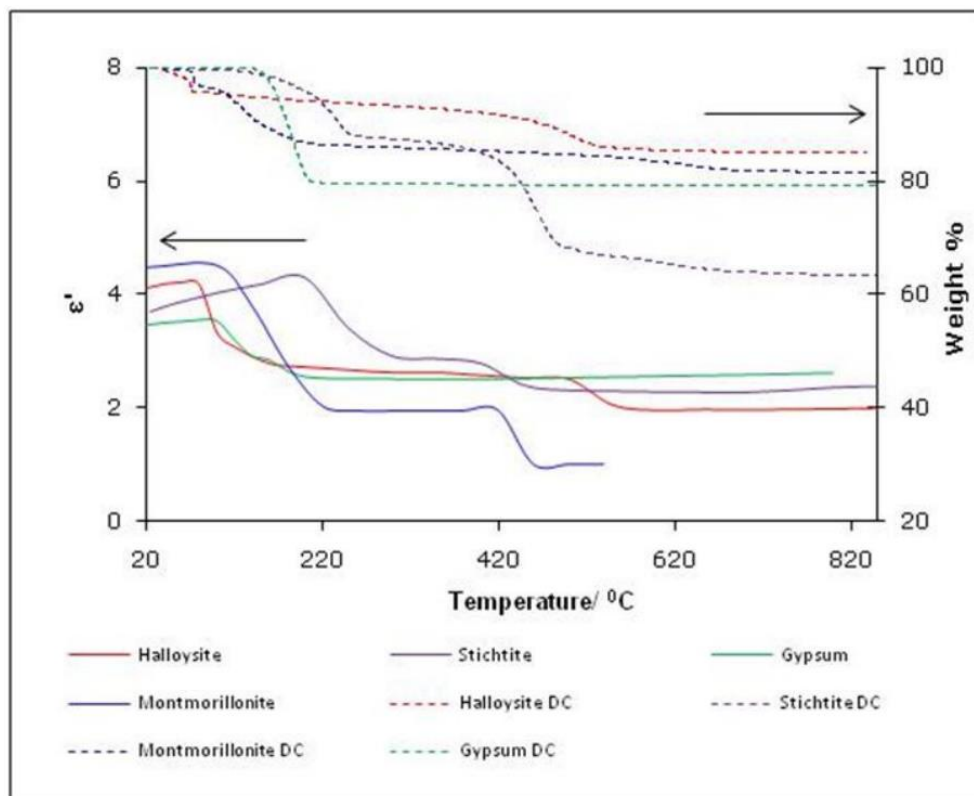
Figure 2.14. Comparison between dielectric constant and dehydration curves of some hydrated silicate minerals (Kobusheshe, 2010)
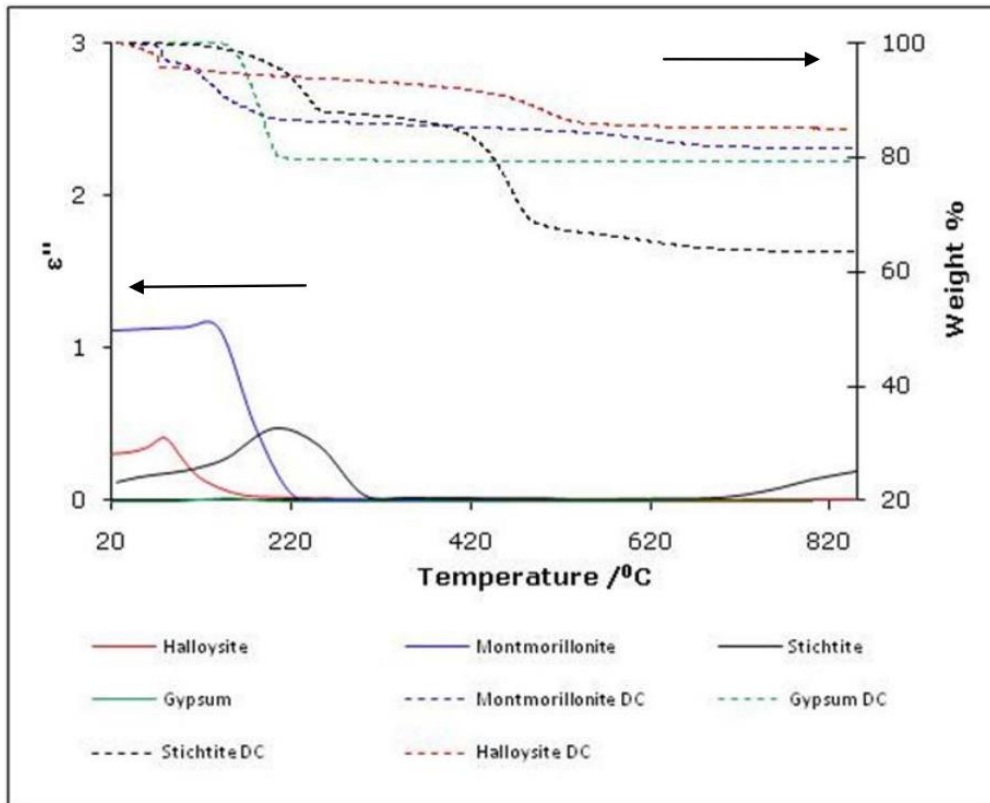
Figure 2.15. Comparison between loss factor and dehydration curves of some hydrated silicate minerals (Kobusheshe, 2010)

2.4.2   Measurements of Dielectric Properties of Materials

There are several techniques for measuring the dielectric properties of materials, but the most common ones used for ores and minerals are open-ended coaxial probe, waveguide transmission line, and resonant cavity (e.g., cavity perturbation). These measurement techniques are briefly described here.

2.4.2.1 Open-ended Coaxial Probe

The open-ended coaxial probe is a quick and non-destructive technique for measuring the dielectric properties of high-loss materials, particularly fluids or well-machined solid surfaces. Typically, the setup consists of a vector network analyser (VNA) that generates a microwave signal and sends it to the material under test (e.g., cored or powdered ore samples) via a metallic probe (Figure 2.16a). The field at the probe fringes into the material (Figure 2.16b) and the

reflected signal (S_{11}) from the material is then measured and related to its dielectric properties (Agilent, 2005). It is critical that the probe make direct contact with the specimen to avoid signal loss, which could lead to incorrect results; thus, the specimen should have a flat surface at the contact point with the probe. In addition, the specimen should have a sufficient thickness (semi-infinite) to allow the reflection of the incident signal for VNA detection.
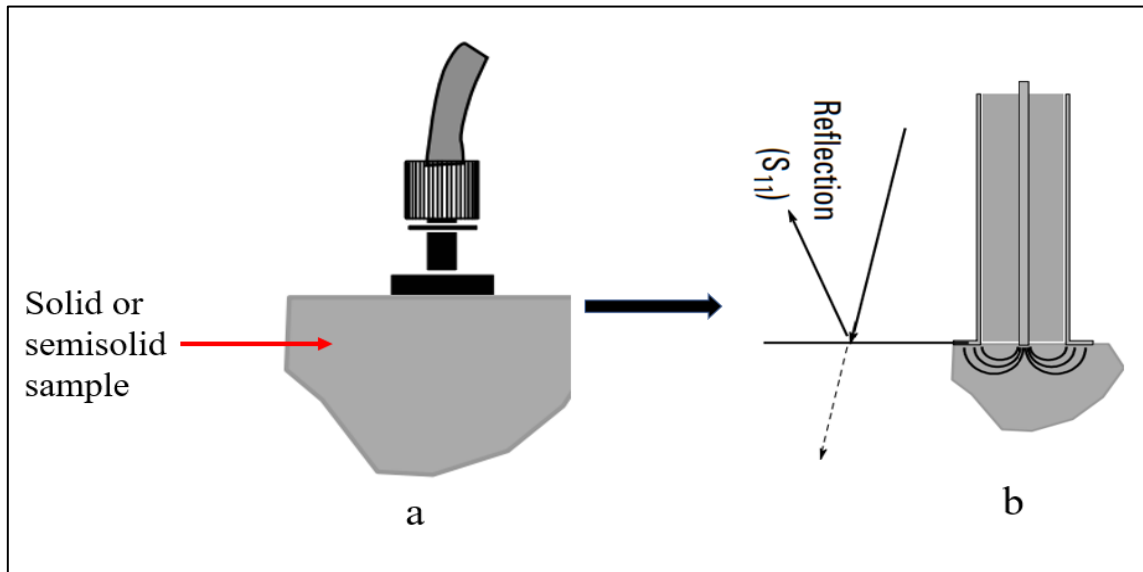
Figure 2.16. Open-ended coaxial probe (Agilent, 2005)

2.4.2.2 Waveguide Transmission Line

A typical waveguide transmission line system consists of a VNA and a waveguide section loaded with a sample. During dielectric measurements, the VNA generates a microwave signal that is transmitted through the material packed in the waveguide. The dielectric properties of the material are then determined based on the transmitted and reflected signal by numerical techniques using a software. This method is limited by practical sample dimensions (i.e., larger sample size at lower frequencies), and the sample should completely fill the waveguide cross-section (Agilent, 2005). The method is suitable for lossy to low-loss materials and can effectively measure the bulk dielectric properties of materials (e.g., crushed ore). Figure 2.17

shows an image of the waveguide cell developed at the University of Nottingham for measuring the dielectric properties of coarsely crushed ore fragments (e.g., -45 mm) at ISM frequencies of 896/915/922 MHz. Fine ore fragments (e.g., -16 mm) can be measured in a small cell coupled to a WR340 waveguide (not shown here) at the higher ISM frequency of 2.45 GHz.
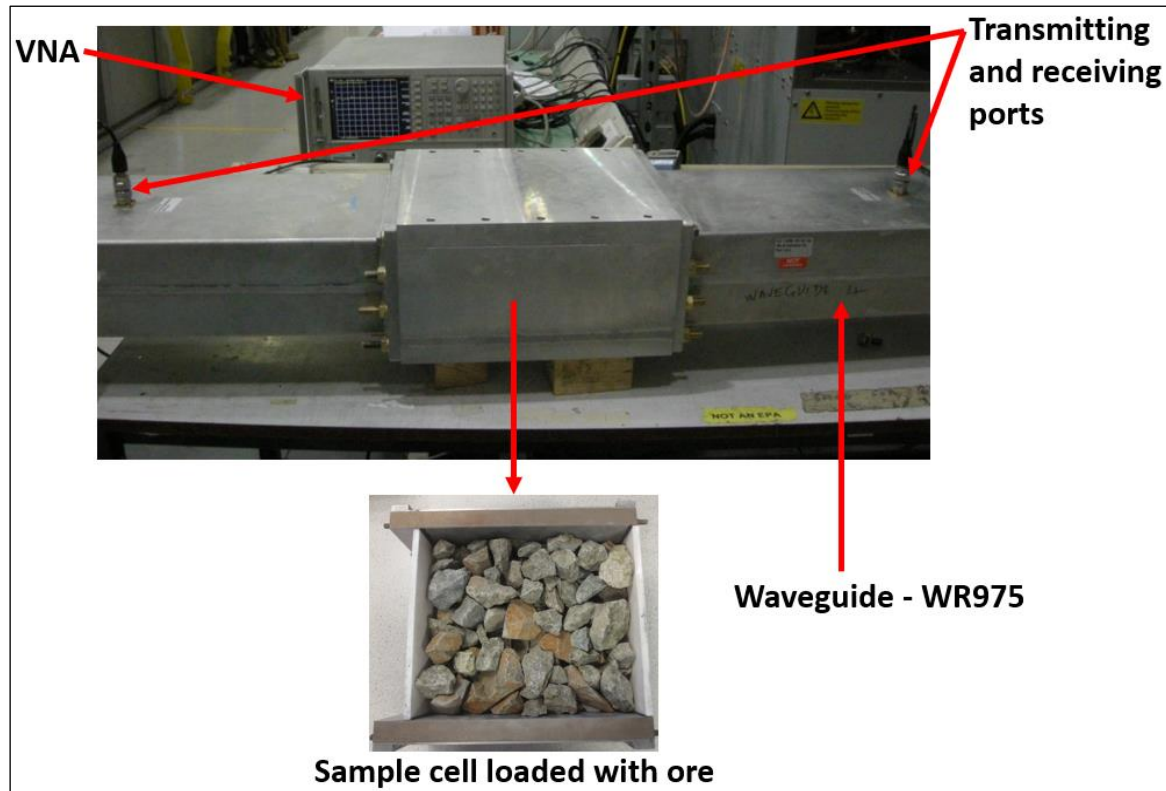
Figure 2.17. Waveguide transmission line (adapted from Batchelor, 2013)

2.4.2.3 Resonant Cavity

The resonant cavity technique (e.g., cavity perturbation) is used for measuring the dielectric properties of very small samples and low-loss materials that cannot be measured using the previously mentioned techniques. The dielectric properties are measured based on the shift in resonant frequency and the change in quality factor (Q) caused by the introduction of a small sample in the cavity, which produces a negligible perturbation of the electromagnetic field distribution inside the cavity (Meng et al., 1995). Essentially, the quality factor of a resonant

cavity is defined as the ratio of the energy stored in the cavity to the energy dissipated to the walls of the cavity per cycle (Metaxas & Meredith, 1983), as expressed in Equation 2.9.

$$\text{Quality factor (Q)} = 2\pi \frac{\text{Energy stored in the cavity}}{\text{Energy dissipated per cycle}} \qquad (2.9)$$

A typical setup of the cavity perturbation technique is shown in Figure 2.18. To allow dielectric measurements at elevated temperatures, this setup is equipped with a furnace together with a cylindrical cavity and other accessories. The furnace is well insulated, and the cavity is incorporated with a cooling system to ensure minimal heat transfer from the furnace to the cavity. Depending on temperature settings, a programmed robotic arm moves a quartz tube (loaded with a small sample e.g., finely ground ore) upward to the furnace to be heated to a desired temperature and then immediately downward to the cavity to interact with the microwave fields. The shift in resonant frequency and the change in quality factor are then determined based on the measurements of the empty tube and that of the loaded tube using a vector network analyser.
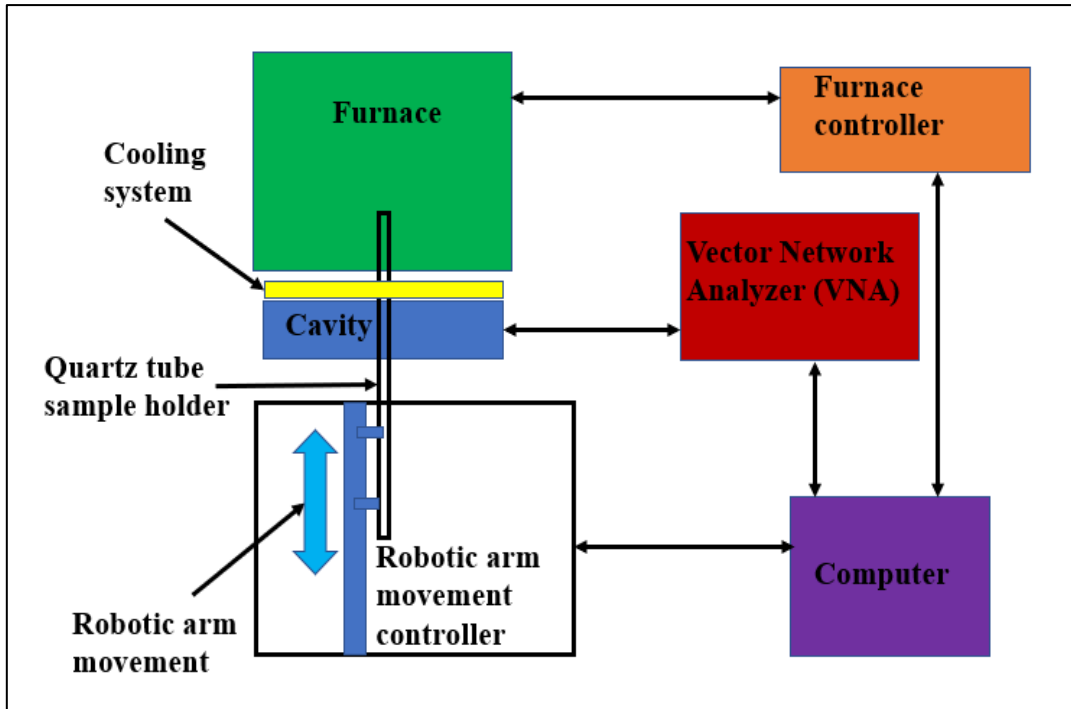
Figure 2.18. Cavity perturbation setup for dielectric measurements

With the aid of computer software, the dielectric constant (ε') and the loss factor (ε'') of the sample under investigation are determined based on the shift in resonant frequency and the change in quality factor using Equations 2.10 and 2.11, respectively (Smith et al., 2010).

$$\varepsilon' = 1 + 2J_1{}^2(X_{l,m})\frac{V_c}{V_s}\left(\frac{f_0 - f_s}{f_0}\right) \tag{2.10}$$

$$\varepsilon'' = 2J_1{}^2(X_{l,m})\frac{V_c}{V_s}\left(\frac{1}{Q_s} - \frac{1}{Q_0}\right) \tag{2.11}$$

Where;

V_c = Volume of the empty cavity (m³),

V_s = Volume of the sample (m³),

Q_0 = Quality factor of the empty cavity,

Q_s = Quality factor of the cavity with the sample,

f_0 = Resonant frequency of the empty cavity (Hz),

f_s = Resonant frequency of the cavity with the sample (Hz),

J_1 = First order Bessel function.

The cavity perturbation technique has been utilized by several researchers at the University of Nottingham to determine the dielectric properties of various minerals. Some results relevant to the current study have been reported by Kobusheshe (2010) and Batchelor (2013), and have previously been presented in Tables 2.2 and 2.3.

2.5 Microwave Penetration Depth

The amplitude of electromagnetic waves diminishes as they penetrate inside dielectric materials due to the energy lost in heating the material. As a result, the field intensity and power flux density decrease exponentially with distance from the surface. Microwave penetration depth is defined as the distance into the dielectric material at which the power drops to 1/e (0.368) of its value at the surface, this is determined by Equation 2.12 (Meredith, 1998). This expression indicates that microwave penetration depth increases with the decrease in microwave frequency and/or dielectric properties (dielectric constant and dielectric loss). This parameter gives an indication of heating uniformity and heating efficiency of the workload when exposed to microwave fields.

$$D_p = \frac{\lambda_0}{2\pi\sqrt{(2\varepsilon')}} \frac{1}{\sqrt{\left[\left[1 + \left(\frac{\varepsilon''}{\varepsilon'}\right)^2\right]^{0.5} - 1\right]}}, \qquad \text{where } \lambda_0 = \frac{c}{f} \qquad (2.12)$$

Where;

     D_p= penetration depth (m),

     λ_0 = free space wavelength (m),

     ε' =dielectric constant,

     ε''= dielectric loss,

     c = speed of electromagnetic waves in free space (3×10^8 m/s),

     f = frequency (Hz).

Batchelor (2013) estimated the penetration depth of several minerals relevant to this work at different microwave frequencies (Table 2.4). It is clear that the penetration depth of microwave-transparent minerals (e.g., quartz) is relatively large (more than a metre) at nearly 2.45 GHz, compared to a low penetration depth of 28 mm for pyrite (microwave-absorbing mineral) at the same frequency. Since most sulphide ores are composed of a large proportion of microwave-transparent minerals (e.g., over 90% by weight), microwaves can penetrate deeper into the ore fragments and selectively and volumetrically heat the absorbing minerals, potentially resulting in differential thermal stresses and ore fracturing. In the case of massive sulphide ores, using a higher frequency of 2.45 GHz can inhibit the treatment performance of coarsely crushed fragments (e.g., -50+30 mm) due to lower penetration depth. This challenge can be addressed using the lower ISM frequencies, such as 433 or 896 MHz, which can penetrate deeper into such fragments.

Table 2.4. Microwave penetration depth for selected minerals (Batchelor, 2013)

Mineral	Penetration Depth (mm) at Frequency (MHz)				
	400	910	1,427	1,949	2,470
Plagioclase	-	-	4,013	1,554	41,861
Apatite	1,318	2,953	5,686	7,859	4,190
Orthoclase	564	4,977	2,346	4,436	3,246
Zircon	778	4,309	-	-	3,667
Quartz	2,762	1,870	-	1,901	1,715
Albite	-	4,198	4,690	4,729	1,820
Muscovite	240	494	583	401	414
Biotite	685	298	273	212	189
Kaolinite	281	198	211	156	137
Montmorillonite	82	55	45	38	31
Rutile	731	2,460	1,350	1,826	1,122
Goethite	861	1,135	1,757	1,463	592
Magnetite	764	658	452	300	216
Hematite	230	208	155	152	135
Ilmenite	365	134	79	57	43
Chalcopyrite	99	64	48	39	31
Pyrite	88	60	45	35	28
Molybdenite	160	66	41	28	21
Chalcocite	554	131	56	31	20
Bornite	267	58	25	14	11

2.6 Microwave Power Density

The amount of microwave energy absorbed by the dielectric material (per unit volume) that is dissipated as heat depends on its dielectric properties and the magnitude of the applied electrical energy (Equation 2.13). This expression indicates that the power density is linearly proportional to microwave frequency, loss factor and the square of electric field intensity inside the material (Meredith, 1998). This implies that a small change in electric field intensity has a significant influence on power density, since the relationship involves a square term. The effective dielectric loss factor (ε''_{eff}) includes a combination of different heating mechanisms i.e., electric conduction losses and various polarisation losses.

The heating rate of a material subjected to microwave energy is related to the applied power density and material properties (e.g., specific heat capacity and density); this relationship is simply expressed by Equation 2.14. In this expression, it is assumed that the electric field strength is uniform throughout the material and the dielectric properties of the material do not change with temperature. However, these assumptions may not apply to heterogeneous materials (e.g., ores), which contain a variety of minerals with different microwave responses and specific heat capacities within the same material. Typically, the influence of power density on the heating rate of ores has been studied using numerical simulations of binary ores of varying mineralogy and texture to develop a better understanding of the ore fracture mechanism when exposed to microwave fields.

$$P_d = 2\pi f \varepsilon_0 \varepsilon''_{eff} E^2 \tag{2.13}$$

$$\frac{dT}{dt} = \frac{2\pi f \varepsilon_0 \varepsilon''_{eff} E^2}{\rho C_p} \tag{2.14}$$

Where;

P_d = power per unit volume (W/m^3),

ε_0 = permittivity of free space (8.854 x 10^{-12} F/m),

ε''_{eff} = effective loss factors,

f = frequency (Hz),

E = root mean square electric field strength within the material (V/m),

dT/dt = heating rate of the material (°C/s),

C_p = specific heat capacity of the material (J/kg°C),

ρ = density of the material (kg/m^3).

Microwave power density is a critical parameter in applicator design because it dictates ore treatment performance. Numerical simulation studies (discussed further in the literature review in Section 3.5.2) have shown that microwave treatment performed at higher power densities (e.g., $1x10^9$-$1x10^{11}$ W/m^3) within a shorter irradiation time (e.g., < 2 sec) generate significant thermal stresses due to minimal temperature gradient between the absorbent and non-absorbent phases (Jones et al., 2005; Ali & Bradshaw, 2009). As a result, significant fractures can potentially be induced on ore specimens using relatively low microwave energy (e.g., 1 kWh/t), depending on ore mineralogy, texture, and the thermal-mechanical properties of minerals present in the ore. Single mode applicators, which are discussed further in Section 2.7.3, can achieve such higher power densities.

2.7 Main Components of Microwave Heating Systems

In general, microwave heating systems consist of three major components:

   i.   The source – for generating microwave energy. Magnetrons are the most common source of microwave energy for domestic and industrial heating applications due to their higher power output and efficiency, frequency stability, and lower capital cost (Metaxas & Meredith, 1983).

  ii.   The cavity – for holding the sample and exposing it to the microwave fields in order to be heated.

 iii.   The waveguide – for transmitting microwave energy from the generator to the cavity with minimal losses.

2.7.1 Magnetron

A magnetron is a vacuum tube used to generate microwaves; its operation principle is based on the movement of electrons under the influence of combined electric and magnetic fields. Figure 2.19a shows the essential components of a magnetron, which include: (1) a central cathode surrounded by an anode, consisting of an array of equally spaced radial slots; (2) a permanent magnet which is aligned parallel to the cathode and perpendicular to the electric field between the anode and the cathode; (3) a high voltage DC source, with the anode at positive potential; (4) an antenna which is connected to one of the cavities (Meredith, 1998).

Electrons are emitted from the hot filament (cathode) by a process known as thermionic emission and have an accelerating field that moves them toward the anode. But the magnetic field decelerates these electrons, causing them to spiral around the cathode (see Figure 2.19b), imparting energy to microwave oscillations as they make their way to the anode (Metaxas & Meredith, 1983). As a result, alternating positive and negative charges are induced at the tips of the cavities (which act as capacitor plates) and currents are induced around the curved surfaces of the cavities (which act as inductors), as shown in Figure 2.19c (Nave, 2021). This capacitor-inductor (LC) oscillation leads to the radiation of electromagnetic waves at the natural frequency of the cavity via the antenna.
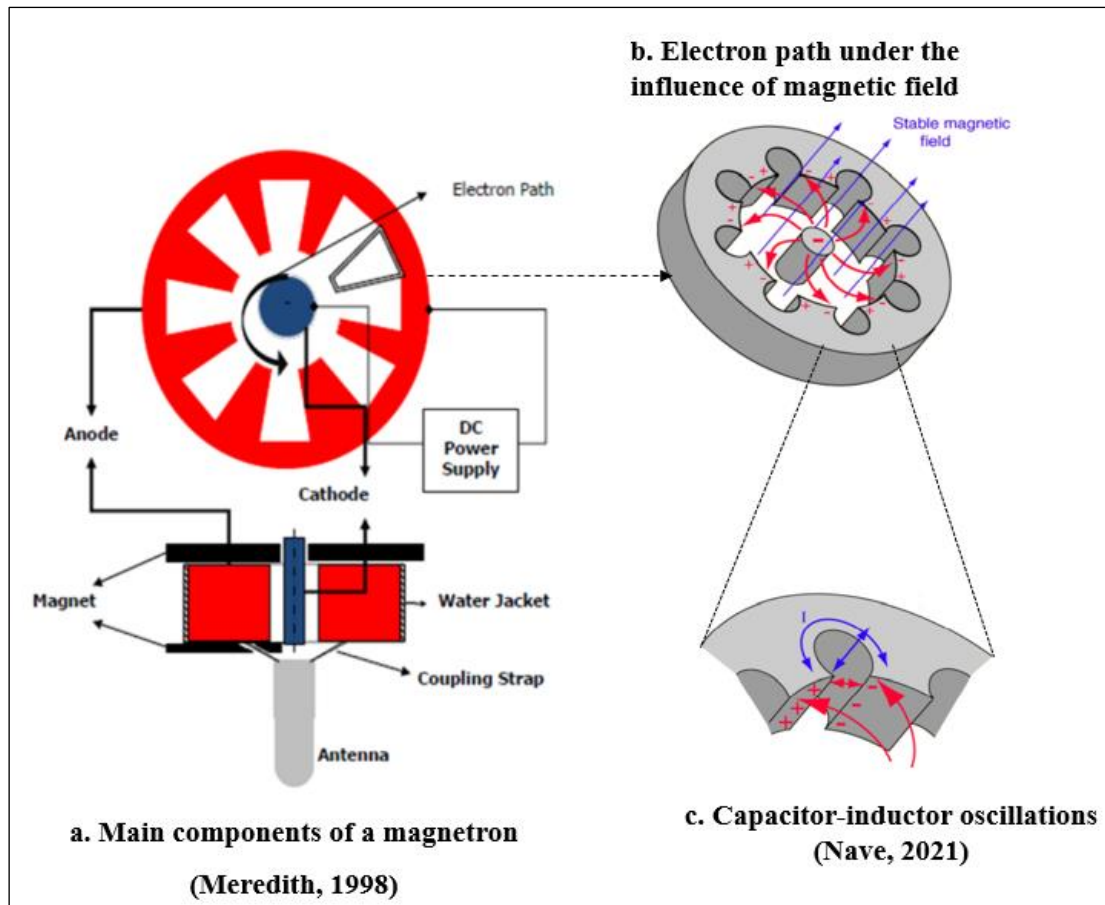
Figure 2.19. Working principle of a magnetron

2.7.2 Microwave Transmission

In industrial microwave heating systems, magnetrons are connected to the applicators by waveguides. A waveguide is essentially a hollow metallic pipe with a uniform cross-section (e.g., rectangular) that is used to transmit microwave energy from one point to another with minimal energy losses. The inner walls of a waveguide are made of highly conducting materials such as copper or aluminium to allow microwave reflection during propagation. In a rectangular waveguide, there are two main modes of propagation: transverse electric (TE) or H mode and transverse magnetic (TM) or E mode. The electric field component in the direction of propagation is zero for the TE mode, while the magnetic field component in the direction of propagation is zero for the TM mode (Metaxas & Meredith, 1983).

The size of the waveguide is dependent on the wavelength (or frequency) of the incident wave. The electromagnetic field cannot propagate if the wavelength is too long (frequency too low) in comparison to the size of the waveguide. Thus, there exists a cut-off wavelength above which the wave cannot propagate in a particular waveguide. For the TE_{10} mode, the cut-off wavelength is twice the dimension of the broad side of the rectangular waveguide (Meredith, 1998). Table 2.5 lists some standard waveguide dimensions and their corresponding frequency ranges. In the current study, microwave treatment tests were performed using a generator (operating at a frequency of 2.45 GHz) connected to the WR430 or WR340 waveguides.

Table 2.5. Some standard rectangular waveguide dimensions and frequency ranges (Metaxas & Meredith, 1983).

Official designation			Frequency range (GHz)	Dimensions	
EIA	RCSC	IEC		inches	mm (approx.)
WR975	WG4	-	0.75 - 1.12	9.75 x 4.875	248.0 x 124.0
WR770	WG5	-	0.96 - 1.45	7.7 x 3.85	196.0 x 98.0
WR430	WG8	R22	1.7 - 2.6	4.3 x 2.15	109.0 x 55.0
WR340	WG9A	R26	2.2 - 3.3	3.4 x 1.7	86.0 x 43.0

EIA: The Electronic Industries Alliance; RCSC: The Radio Components Standardization Committee; IEC: International Electrotechnical Commission.

2.7.3 Microwave Applicators

A microwave applicator, also known as a cavity, is a device usually a closed metal structure in which microwave energy interacts with the material to be heated in a controlled environment. A typical example of an applicator is a metallic box inside a domestic microwave oven where food is placed during heating. The most common applicators used for microwave heating are single mode cavities, multimode cavities, and travelling wave applicators.

2.7.3.1 Single Mode Applicators

Single mode applicators are designed with dimensions such that the standing waves create one well-defined mode inside the cavity, where the electric field strength is maximum. This is established based on the solution of the Maxwell's equations given the geometry of the

applicator and the appropriate boundary conditions (Thostenson & Chou, 1999). The size of a single mode applicator is in the order of one wavelength (e.g., <122 mm at 2.45 GHz), with one resonant mode for maximum electric field strength, and the sample should be placed in this region (the hot spot) to ensure maximum power delivery. To achieve this, a single mode cavity must stay tuned, and the impedance of the generator and transmission line be matched to that of the applicator and its load. Since the microwave power is confined within a small volume, single mode cavities can achieve higher power densities than other applicator types for a given power input. This makes them suitable for applications requiring higher heating rates in a shorter exposure time (a few seconds), such as ore fracturing to reduce ore competency and improve comminution. This has been demonstrated by several researchers both theoretically (Whittles et al., 2003; Ali & Bradshaw, 2010) and experimentally (Kingman, 2004a; Batchelor, 2013).

A typical example of a single mode cavity consists of a rectangular waveguide with an opening in one or both broad faces (Figure 2.20). These openings provide access for the positioning or continuous flow of the workload to interact with microwave fields in the region of maximum electric field intensity. In this type of setup, the size of the cavity and that of the workload are limited by the waveguide dimensions, which are dictated by microwave frequency, as discussed in Section 2.7.2. For example, the size of the cylindrical cavity at 2.45 GHz is approximately 80 mm, 200 mm at 896/915/922 MHz, and 480 mm at 433 MHz (Batchelor, 2013). This means that increasing the applicator size to accommodate higher throughput rates, such as those encountered in mining operations (say, over 100 t/hr), will require treatments to be performed at lower ISM frequencies, such as 896 or 433 MHz in the UK. Furthermore, using lower ISM frequencies in such systems enables deeper microwave penetration into the material, which improves the overall treatment process.
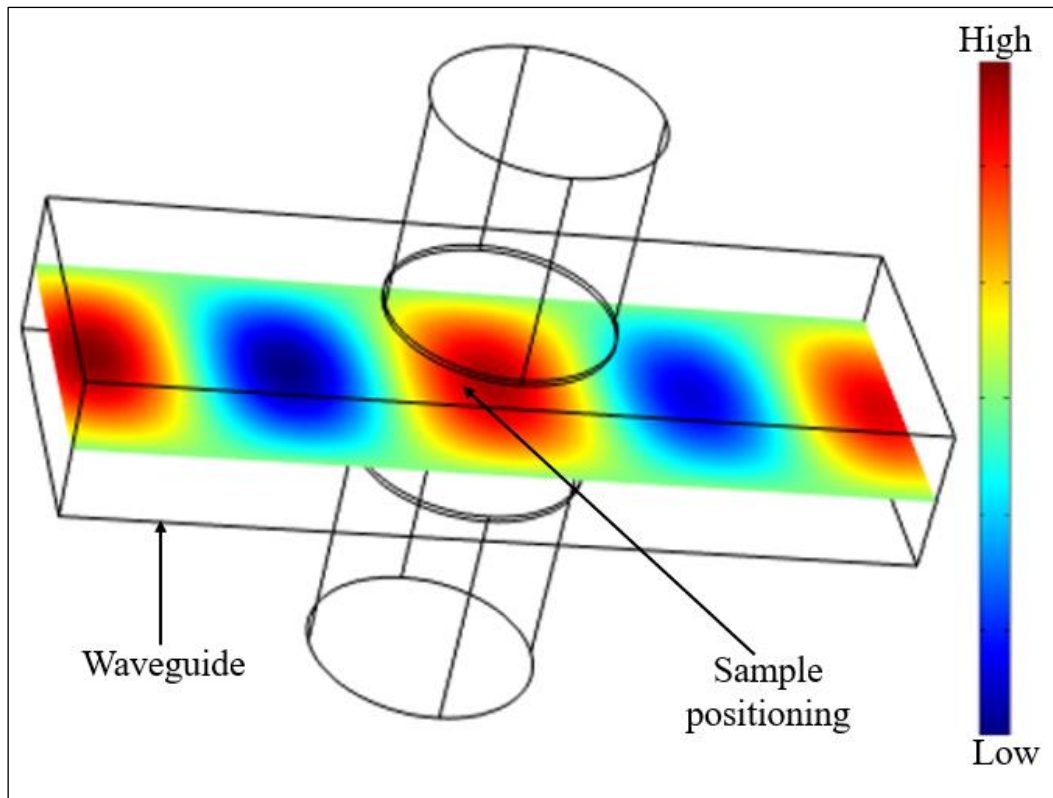
Figure 2.20. Electric field distribution in a rectangular waveguide - TE$_{10}$ single mode cavity

2.7.3.2 Multimode Applicators

Multimode cavities are the most commonly used microwave heating applicators; a typical example is a domestic kitchen microwave oven in our homes. Unlike single mode cavities, multimode cavities support multiple resonant modes at the same time, forming a complex electric field pattern within a cavity, as illustrated in Figure 2.21. Since the number of possible resonant modes increases with cavity size, its dimensions on each side are typically greater than one or two wavelengths (Thostenson & Chou, 1999). The inside walls of the cavity are made of highly conducting materials (mostly aluminium) to support the reflection of microwave energy with minimal losses, and thus most of the incoming energy is delivered for heating the workload.

However, the presence of multiple resonant modes causes several hot spots at various locations within the cavity, resulting in poor heating uniformity. In addition, the larger size of the applicator and the non-uniform distribution of the electric field strength within the cavity results in a lower power density when compared to single mode cavities. Several techniques are used to improve heating uniformity in multimode cavities, such as turning either the workload (e.g., using turntables) or the microwave fields (e.g., using mode stirrers). Turntables improve microwave heating uniformity by randomly and continuously exposing every portion of the workload in regions of high and low electric field strength, resulting in more uniform heating throughout the workload. On the other hand, mode stirrers are metallic devices (with rotating blades) placed within the cavity, when they turn, they reflect and redistribute continuously the electromagnetic fields throughout the workload, resulting in more uniform heating (Mehdizadeh, 2015).
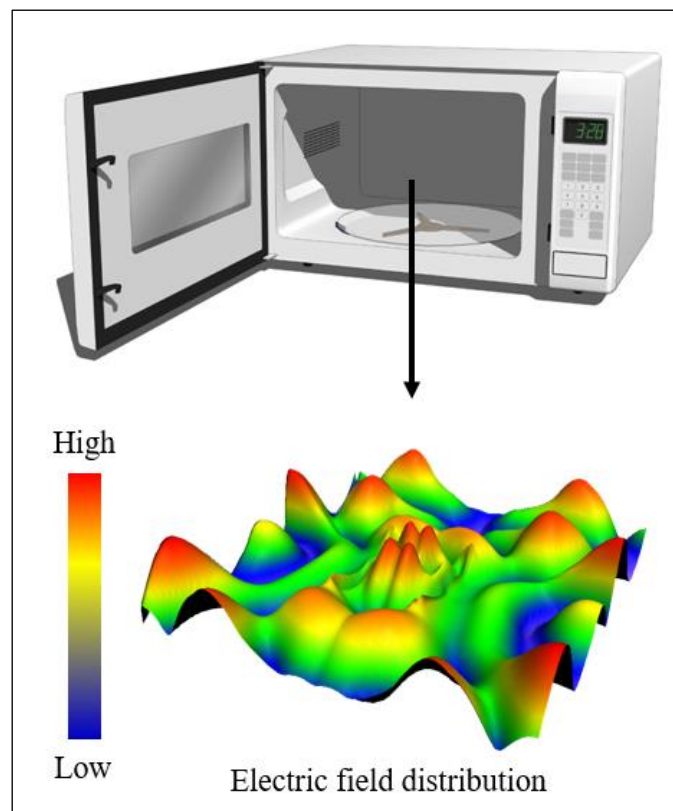
Figure 2.21. Electric field distribution in a multimode cavity

Most researchers have utilized multimode cavities (particularly kitchen microwave ovens) for ore pre-treatment studies because they are widely available commercially. These studies are reviewed in Chapter 3 to demonstrate their applications in ore pre-treatment to assist comminution and mineral dissolution.

2.7.3.3 Travelling Wave Applicators

Travelling wave applicators allow microwave energy to interact with the workload in continuous operations, which is typically preferred when high throughput is required. In this type of applicator, the microwave power is fed into a confined chamber to make an interaction with the workload as it moves forward, and the residue power is dissipated into a dummy load (typically water) (Metaxas & Meredith, 1983). There are two main configurations of microwave travelling applicators used in continuous operations: longitudinal (standing wave applicator) and meandering waveguide applicators (Figure 2.22).
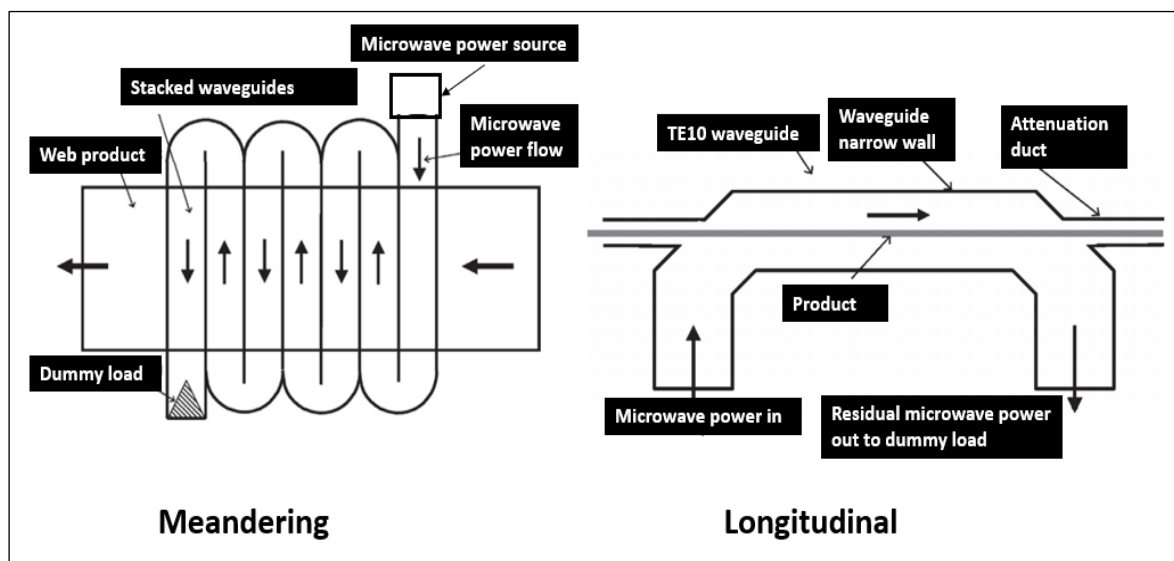
Figure 2.22. Main configurations of travelling wave applicator (Mehdizadeh, 2015)

The heating efficiency of travelling wave applicators is dependent on the applicator's cross-sectional area as well as the dielectric properties and throughput rate of the workload. A common challenge associated with the travelling wave applicators is the emission of microwave radiation at the product's entry and exit ports, particularly when the dimensions of the opening at these ports are much larger than the operating wavelength (Mehdizadeh, 2015). Choking structures are typically installed at these ports to reflect the escaping radiations back to the workload in order to improve the heating efficiency and comply with radiation legislation, as discussed further in Section 2.11.

Previous research on microwave ore pre-treatment at the University of Nottingham using a continuous longitudinal configuration (i.e., material flowing along a TE_{10} waveguide applicator) showed that only materials in the centre of the conveyor are effectively treated, while the rest receive very little or no microwave energy dose at all. This is because, in TE_{10} single mode cavities, the electric field intensity is maximum at the centre of the cavity and diminishes to zero at the cavity extremes. Arcing is also a common challenge in continuous systems operating at higher microwave power due to material segregation on the conveyor belt (i.e., air gaps between particles) as well as the air gap existing between the top of the particle bed and the top of the applicator. Both the non-homogeneous treatment and arcing effects lower the overall ore treatment performance. One potential solution to this problem is to use gravity-fed systems to keep the cavity volume full during treatment and reduce particle-particle segregation by using ore particles of varying size classes. A continuous ore treatment gravity-fed system with a capacity of up to 150 t/hr has been demonstrated at the University of Nottingham, and this system is discussed further in Section 3.5.4.

2.8 Auxiliary Components in Microwave Heating Systems

In addition to the major components described in the previous section, microwave industrial heating systems consist of auxiliary components such as circulators, directional couplers with power meters, and tuners (e.g., stub tuners, short circuit tuners). The function and the working principle of each of these devices are described.

2.8.1   Circulator

A circulator is a waveguide component with three ports that protects a microwave generator from excessive reflected power from the cavity. This device allows microwave propagation from one port to the next in only one direction. It is made of ferrite, which is a mixture of iron oxide and rare-earth elements such as yttrium (Meredith, 1998). In the presence of a strong magnetic field provided by a permanent magnet, the ferrite rotates the plane of polarisation of the applied electromagnetic waves at an angle depending on the direction of propagation. This allows the transmission of the incident power from the generator to the cavity, while the reflected power coming back from the cavity is diverted to the circulating water load and fully absorbed there (Figure 2.23), thereby protecting the generator. The benefit of diverting the reflected power away from the generator is twofold: it reduces the internal heating of the magnetron and improves magnetron frequency stability (Meredith, 1998).
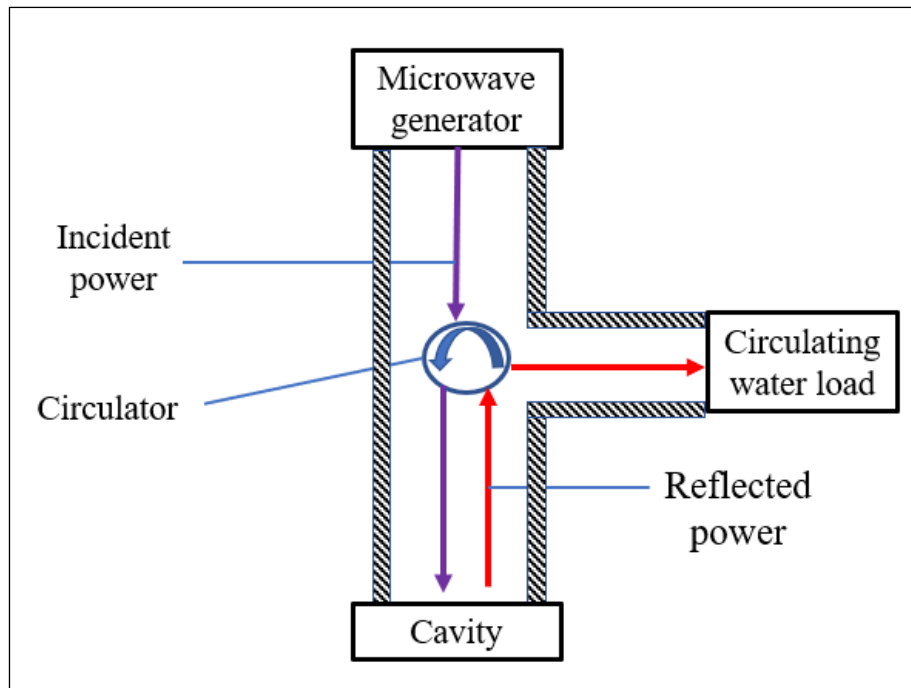
Figure 2.23. Working principle of a circulator

2.8.2 Directional Couplers

A microwave heating system is sometimes equipped with a directional coupler, a device that samples out a small portion of microwave power in a main waveguide and measures it with power meters in an auxiliary waveguide, depending on propagation direction. Essentially, a directional coupler has four ports with one or two coupling holes/slots in each of the main and auxiliary waveguides. As illustrated in Figure 2.24, if the generator is connected to port 1 and the load to port 2, then port 3 is the coupled port and port 4 is the isolated port. Conversely, if the generator is connected to port 2 and the load to port 1, then port 4 is the coupled port and port 3 is the isolated port (Microwaves101, 2011). This power coupling based on propagation direction in the main waveguide allows measurement of both forward and reflected powers without disrupting the power flowing in the main waveguide. The power is weakly coupled, allowing power meters in the milliwatt range to measure higher powers of up to tens of kilowatts (Meredith, 1998).

51
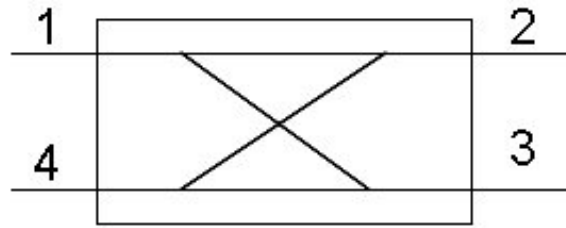
Figure 2.24. A simple schematic of directional coupler operation (Microwaves101, 2011)

In the initial work reported in Chapter 6 of this dissertation, the power meters (attached to a directional coupler) were used to measure the forward and reflected powers during microwave treatment. The power absorbed by the sample was then calculated by subtracting the reflected power from the forward power.

2.8.3   Tuners

Industrial and laboratory microwave heating systems are equipped with stub tuners for impedance matching to ensure maximum power delivery to the workload. The device is placed between the microwave generator and the applicator. The three-stub tuner is commonly used due to its simplicity in operation. It consists of three capacitive stubs spaced a quarter or one-eighth of guide wavelength apart along the broad face centreline of a rectangular waveguide (Collin, 2007; Bilik & Bezek, 2010), with only two adjacent stubs adjusted at a time during the matching (e.g., 1 and 2, or 2 and 3). The tuning involves the insertion of the stubs (manually or automatically) at different lengths into the waveguide, which adjusts the impedance of the generator and transmission line to match that of the workload, minimizing the reflected power and ultimately maximizing power delivery to the workload. The automatic tuners typically have built-in power meters that allow them to calculate and adjust the stub positions to minimize reflected power. Microwave treatment tests in Chapters 7 and 8 used an experimental set-up equipped with automatic tuners to maximise power delivery to the workload.

In addition to stub tuners, a single mode cavity microwave heating system incorporates a short circuit tuner, which is simply a waveguide with a metal plate attached to a piston at the end of the transmission line. The plate reflects the forward power back to the cavity, forming a standing wave due to the superposition of forward and reflected waves. The plate can be moved back and forth along the guide and fixed in place to adjust the location of the maxima and minima of the standing wave pattern of the electric field within the cavity. The plate is adjusted until the region of maximum electric field strength (hot spot) is positioned where the workload is located within the cavity. This position varies depending on the dielectric properties of the material being heated, implying that tuning is necessary whenever a workload with varying dielectric properties is to be heated (Meredith, 1998). The tuning process is aided by a vector network analyser (VNA) by sending a signal through a sample and then analysing the reflected and transmitted signals.

2.9 Electrical Breakdown and Arcing

Microwave treatment of materials (e.g., sulphide ores) may cause electrical breakdown (discharge) of the surrounding medium such as air. The electrical discharge in air occurs when the air is ionised and current flows through it. This occurs when the applied electric field exceeds the dielectric strength of air, which is approximately 30 kV/cm in a uniform field at ambient atmospheric pressure and temperature (18°C) (Meredith, 1998). This phenomenon is more pronounced when ores with high surface sulphide mineralisation are subjected to high-energy microwave irradiation. Given their low microwave penetration ability, these materials can accumulate more surface charges that may acquire enough kinetic energy, which can ionize the surrounding air (e.g., air in the gaps between the touching or nearby particles). This causes an electrical discharge (electric arc or spark), forming high-temperature hot spots which can damage the equipment and destroy the sample being treated (Sun et al., 2016). The air gaps formed between ore particles during microwave treatment can be a source of electrical arcing,

especially for ores with high surface sulphide mineralisation. These air gaps can be minimized to some extent by using a feed that contains particles of varying size classes.

2.10   Thermal Runaway

As discussed in Section 2.4.1, the electromagnetic absorption ability of dielectric materials increases sharply with temperature. The rise in temperature may accelerate the microwave heating rate of these materials, potentially leading to the undesirable effect known as thermal runaway. This thermal phenomenon occurs when the power dissipated in a small volume within a workload exceeds the heat transferred to its surroundings (Meredith, 1998). This causes an increase in the loss factor, which promotes further heating, and the temperature will continue to rise until the material is decomposed. Typically, this phenomenon is accompanied by the formation of hot spots in the workload (Semenov & Zharova, 2006), which can seriously damage the sample being treated and the equipment if no detection systems and control measures are in place (Vriezinga et al., 2002).

2.11   Microwave Safety and Exposure Standards

Microwave energy is non-ionizing radiation, as opposed to gamma rays, which have enough energy to eject electrons from atoms and molecules, resulting in the formation of harmful free radicals in human bodies (Kitchen, 2001). However, microwave exposure to human bodies can cause severe burn injuries because human tissues are highly receptive to microwave radiation (Catalá-Civera et al., 2006). This effect can be very significant, particularly in industrial heating systems due to higher microwave power levels used in such systems, which can reach up to 100 kW. In addition, microwave leakage into the surrounding environment can cause interference with other systems (e.g., telecommunication).

Typically, there are two types of safety standards for microwave irradiation: one that accounts for human exposure and the other for a leakage into the environment (Kitchen, 2001). According to the UK National Radiological Protection Board (NRPB), the exposure limit is

0.4 watts per kg of tissue, whereas the acceptable limit of leakage power-flux density is 5.0 mW/cm^2 measured at a distance of 50 mm from equipment, with a maximum of up to 10 mW/cm^2 under abnormal conditions (British-Standards, 2011). Therefore, industrial microwave heating systems should be subjected to leakage tests regularly, and sensors should be installed to take continuous measurements and shut down the system if the acceptable radiation levels are exceeded. Thus, ensuring that the process complies with the regulatory requirements outlined in the health and safety and Electromagnetic Compatibility (EMC) legislation.

Microwave leakage through open ports (e.g., at the entrance and exit points of conveyor belts) can be suppressed using resistive and/or reactive choking structures (Metaxas & Meredith, 1983). Resistive chokes utilize lossy materials (e.g., carbon foam) to absorb microwave energy that leaks into the environment. Reactive chokes, on the other hand, use repetitive metallic structures (i.e., corrugated choke) to reflect back the microwave energy that has escaped from the cavity, minimizing the residual microwave leakage to an acceptable level while simultaneously maximizing power delivery to the workload. Sometimes a combination of reactive and resistive chokes is considered to further minimize microwave leakage and improve system performance, as illustrated in Figure 2.25. Noting that the resistive (absorptive) choke is positioned farthest away from the heating chamber so that it does not affect the heating efficiency of the workload, given its high microwave absorptive ability (Mehdizadeh, 2015).
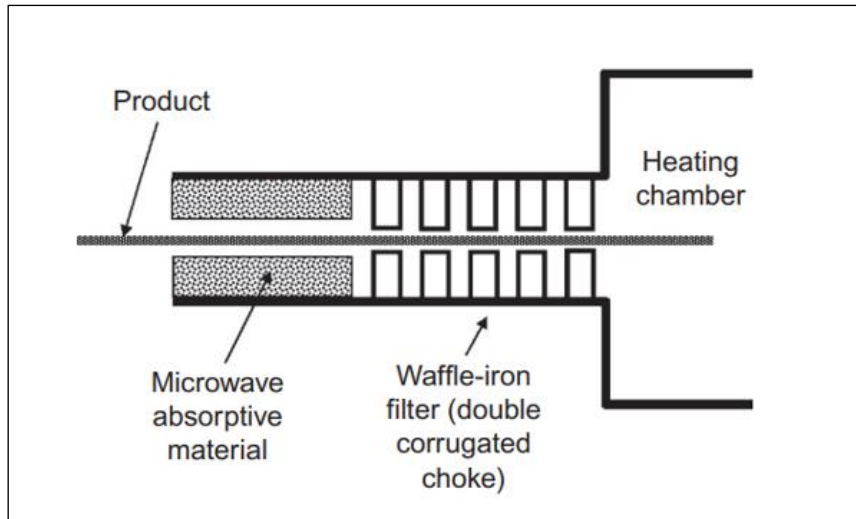
Figure 2.25. An illustration of a combination of reactive (corrugated) and absorptive chokes (Mehdizadeh, 2015)

2.12 Summary

Microwaves are electromagnetic waves with short wavelengths ranging from 1 m to 1 mm. They are widely used in a variety of applications, the heating of materials being the most familiar example. Microwave heating of dielectric materials occurs via one or both of two main mechanisms: dielectric polarisation (e.g., dipolar losses) and direct conduction effect (conduction losses). Dipolar losses generate heat due to frictional and molecular interaction forces resulting from charge redistribution or polarisation under the influence of an alternating external electric field. On the other hand, direct conduction heating is caused by electrical resistance generated when semi-conducting materials (e.g., sulphide minerals) are exposed to microwave fields.

The ability of a material to heat in microwave fields is dictated by its dielectric properties, which can be measured using various techniques such as waveguide transmission line, resonant cavity (e.g., cavity perturbation), and open-ended coaxial probe. The dielectric properties of materials can also be used to estimate microwave penetration depth and power density, which

are two design parameters that indicate heating uniformity and treatment performance. Generally, most sulphides and metal oxides have relatively higher dielectric values (loss factor and loss tangent), implying that they can heat up more rapidly when exposed to microwave fields than most silicates. In contrast, the microwave penetration depth of most silicates (due to their low dielectric values) is relatively large (>1 metre at 2.45 GHz) compared to tens of millimetres for sulphide minerals. This suggests that microwaves can penetrate deeper into the gangue matrix in most ores and selectively and volumetrically heat the sulphide grains, inducing thermal stresses and causing ore fracturing, potentially reducing ore competency and improving mineral exposure. In the case of massive sulphide ores, microwave treatment can be performed at lower ISM frequencies (e.g., 896 MHz) to allow deeper microwave penetration, which is useful in industrial applications because lower frequencies necessitate a large magnetron, waveguide system, and cavity. However, laboratory experiments are limited to higher ISM frequencies (2.45 GHz) because the sample size is comparable to the size of the waveguide and cavity.

Microwave heating systems typically consist of three major components: the source, such as a magnetron (for microwave generation), the waveguide (for microwave transmission), and the cavity (for exposing material to microwave fields). A single mode applicator provides higher power density than other applicators because microwaves are confined in a small volume, and the workload is placed in this region of maximum electric field intensity. This makes it suitable for applications requiring rapid and selective heating (within a few seconds) e.g., for inducing fractures in ore samples to improve comminution. Single mode applicator systems are usually pre-matched to ensure maximum power delivery to the workload and improve system performance. In industrial heating systems, microwave emissions should be regularly monitored, and control systems installed to minimize emissions in order to comply with health and safety and electromagnetic compatibility legislation.

3. REVIEW OF MICROWAVE TREATMENT OF ORES IN MINERAL PROCESSING

3.1 Introduction

Mineral processing is a method of recovering commercially valuable minerals from their ores. This process involves two fundamental operations, namely comminution (size reduction) and concentration (separation of valuable minerals from the waste gangue minerals). The most important role of comminution is not merely size reduction, but to liberate valuable minerals from their host rocks prior to all subsequent concentration processes (Wills & Atkinson, 1993). However, the process is extremely energy-intensive, inefficient, and costly (Walkiewicz et al., 1991; Tromans, 2008). Furthermore, the loss of valuable minerals caused by inefficient comminution processes can be significant.

Microwave ore pre-treatment has shown potential application for improving the comminution process (Walkiewicz et al., 1991; Kingman et al., 2000). The aim is to pre-weaken the ore at low specific energy input so that less energy might be required in subsequent downstream comminution processes. Also, microwave treatment of ores can increase the effective liberation size, resulting in higher mineral recovery at a coarser particle size (Orumwense et al., 2004; Scott, 2006; Batchelor et al., 2017). Furthermore, microwave ore pre-treatment can improve metal leach recovery from ores or concentrates by increasing the accessibility of minerals for lixiviant attack via a network of induced cracks (Haque 1987; Amankwah & Pickles, 2009; Charikinya et al., 2015). However, the effectiveness of this process is largely dictated by microwave treatment conditions (specific energy input and power density) and inherent ore properties such as mineralogy, texture, and the thermal-mechanical properties of microwave-absorbing grains and transparent gangue matrix.

This chapter provides a review of the studies on microwave heating of minerals and ore breakage mechanisms resulting from this heating. The review also highlights key findings from previous studies on microwave heating technology to assist comminution (reduce ore competency and enhance mineral exposure) and improve leaching performance.

3.2 Microwave Heating of Minerals

Minerals heat up differently upon exposure to microwave fields. This is due to the differences in dielectric properties, electrical conductivities, and bonding properties that exist in the different mineral phases (Hua & Liu, 1996). Several studies have been conducted to assess the heating response of minerals when exposed to microwave fields, and some of these studies are discussed here.

Ford & Pei (1967) irradiated certain oxide and sulphide compounds in a microwave oven for different exposure times of between 0.1 and 40 minutes at variable powers of up to 1.6 kW at 2.45 GHz. General observations from this early work indicated that dark-coloured compounds heated faster (to temperatures around 1000°C) than light-coloured compounds.

Chen et al. (1984) assessed the relative transparency of forty mineral types (natural and synthetic) to microwave energy in a waveguide applicator, which allowed the mineral samples to be placed in an area of high electric field strength. These authors reported that most silicates, carbonates, sulphates, some oxides, and some sulphides are transparent to microwave radiation. They also discovered that the majority of sulphides, sulphosalts, and sulphoarsenides heat up rapidly. Their results are in good agreement with those of another study reported by Walkiewicz et al. (1988).

McGill et al. (1988) studied the effect of microwave power level on the heating characteristics of a variety of powdered minerals and reagent-grade chemicals. Each experiment used a 25-gram sample that was exposed to various microwave power inputs ranging from 500 to 2000 Watts at 2.45 GHz. Results showed that the heating rates of minerals increased with increasing

microwave power input, except for the low-lossy minerals such as quartz, which did not heat significantly irrespective of power input. In addition, a study reported by Chunpeng et al. (1990) showed that most oxide and sulphide minerals heated more efficiently than carbonate minerals when exposed to microwave fields.

Kingman et al. (2000) investigated the microwave heating responses of various minerals over a range of exposure times using a microwave power of 2.6 kW at a frequency of 2.45 GHz. Similar findings were reported in this later study that sulphides (mostly valuable minerals) heat up faster than most metal oxides and silicates (gangue minerals) due to their semiconducting properties (Table 3.1). Magnetite heats up faster than most sulphides and other metal oxides because it interacts with both the magnetic and electric field components of microwave fields due to its ferrimagnetic properties.

Table 3.1. Heating rate of selected minerals (adapted from Kingman et al. 2000)

Mineral	Composition	Temperature (°C) after Time (s)						
		10	30	60	90	100	120	
Phlogopite	$KMg_3(Si_3Al)O_{10}(F,OH)_2$	19	21	22	23	25	26	Non-sulphide (gangue minerals)
Quartz	SiO_2	18	21	23	26	28	28	
K-Feldspar	$KAlSi_3O_8$	18	21	24	25	27	31	
Dolomite	$CaMg(CO_3)_2$	21	23	25	29	30	33	
Plagioclase	$(Na,Ca)(Si,Al)_4O_8$	21	24	25	28	32	34	
Ilmenite	$FeTiO_3$	32	46	64	77	81	90	Mostly sulphide (valuable) minerals with few oxides
Chalcopyrite	$CuFeS_2$	61	98	124	146	148	165	
Pyrite	FeS_2	75	134	177	189	197	202	
Chalcocite	Cu_2S	68	126	153	194	211	245	
Galena	PbS	211	341	422	436	441	453	
Magnetite	Fe_3O_4	200	324	351	403	452	463	

Salsman et al. (1996) employed a short pulse microwave system to evaluate the influence of sulphide content and sulphide particle size on heating response using a mixture of pure minerals i.e., chalcopyrite ($CuFeS_2$) - a high microwave-absorbent sulphide mineral, and quartz (SiO_2) - a relatively non-microwave-absorbent mineral. The proportion of $CuFeS_2$ in

the mixture varied from 0% to 7%. In additional experiments, $CuFeS_2$ with particle sizes 53, 178, 357, and 601 µm were mixed with SiO_2 powder finer than 150 µm. Thereafter, 100-gram samples of each mixture were exposed in a multimode cavity for 120 seconds at a microwave power of 1 kW. Results showed that the microwave energy absorbed by the sample (which correlates with the degree of heating) is proportional to the mass of $CuFeS_2$ grains present in the mixture, as indicated in Figure 3.1. In addition, the heating rate decreases significantly with the decrease in $CuFeS_2$ grain size because the heat absorbed by the smaller $CuFeS_2$ grains dissipates more rapidly into the surrounding SiO_2 than that dissipated by the larger grains, and the temperature of the smaller grains does not rise as rapidly.
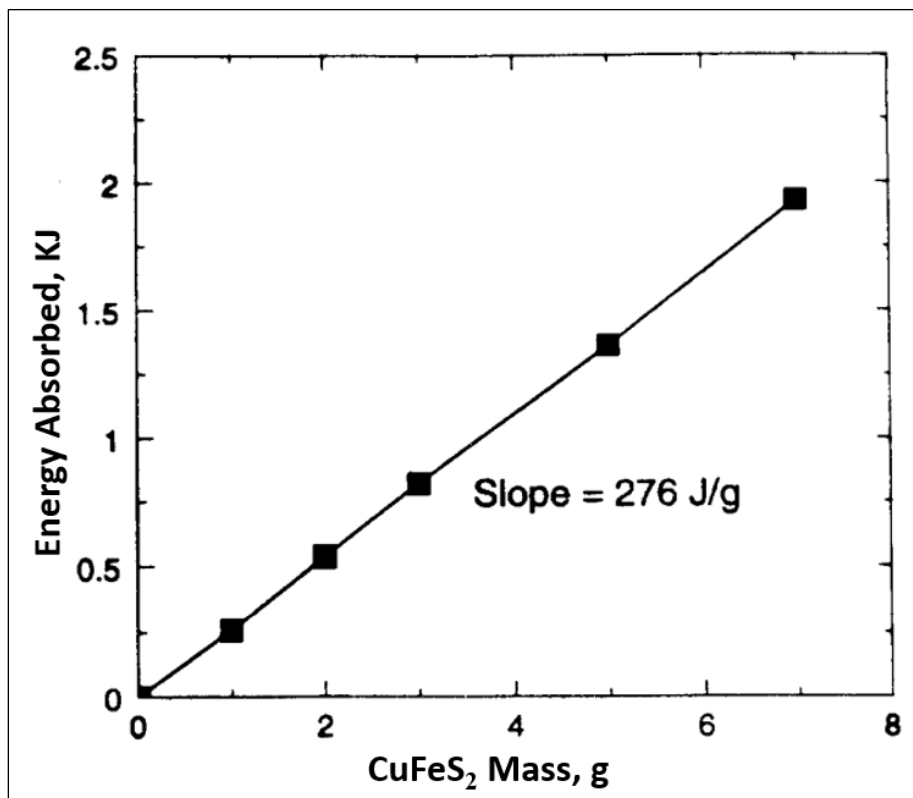
Figure 3.1. Energy absorbed by SiO_2-$CuFeS_2$ mixture at 1 kW, 120 sec (Salsman et al., 1996)

3.3 Microwave-induced Ore Fracture Mechanism

Unlike conventional heating which relies on conduction heat transfer mechanism to heat the bulk sample, microwave heating is rapid, selective, and volumetric because microwave energy is delivered directly to materials through molecular interaction with the electromagnetic field. As a result, extremely large but localised temperature gradients can be created within and around mineral grains (Ali & Bradshaw, 2010). Ores are essentially heterogeneous materials containing various mineral phases, and the fracture mechanism upon microwave irradiation is based on selective heating and thermal expansion mismatches between these mineral phases. The expansion of microwave absorbent phases stretches the transparent gangue matrix, causing tensile and shear stresses around grain boundaries, which can lead to microfractures when the magnitude of these stresses exceeds the ore strength (Salsman et al., 1996).

Jones et al. (2005) used a binary ore of pyrite (microwave-absorbent phase) and calcite (microwave-transparent gangue) to conduct a theoretical study to simulate the thermal stresses formed and resulting damage when an ore is exposed to microwave fields. The following conclusions were derived from the study:

i.   The stress regime inside a heated mineral particle is compressive, whereas shear and tensile stresses predominate outside the boundary.

ii. Material weakening is caused by elevated shear stresses outside the grain boundary that exceed the material's strength.

iii. As the heated particle size decreases, more energy is required to raise the temperature sufficiently to generate thermal stresses sufficient for crack formation.

It is worth mentioning that ore samples containing hydrated mineral phases can also exhibit significant fractures when exposed to microwave fields. In this case, ore fracturing is attributed to the dehydration of water (an excellent microwave absorber) contained within the ore. The

fractures formed are thought to be caused by one or more of the following mechanisms (Kobusheshe, 2010):

i. Internal pressure caused by steam generated when microwaves interact with hydrated phases within the ore.

ii. Expansion of hydrated clay minerals (e.g., smectite, halloysite, montmorillonite).

iii. Thermal decomposition of certain mineral phases and loss of water of crystallisation, resulting in lattice structural defects.

The microwave-induced fracture patterns on ore samples can be inter-granular (occurring along grain boundaries) or trans-granular (across grains). The SEM images of a microwave pre-treated nickel sulphide sample reported by Batchelor et al. (2015) showed evidence of both inter- and trans-granular fractures. The fractures originated at the sulphide grain boundaries and propagated towards the microwave transparent gangue matrix of pyroxene and felspar (see Figure 3.2). A similar pattern of both inter-granular and trans-granular fractures was also observed by other researchers in microwave ore treatment studies (Andriese et al., 2011; Charikinya et al., 2015). This suggests the possibility of improving mineral liberation at a relatively coarser grind size or improving metal leach recoveries of coarsely crushed fragments, particularly in heap leaching.
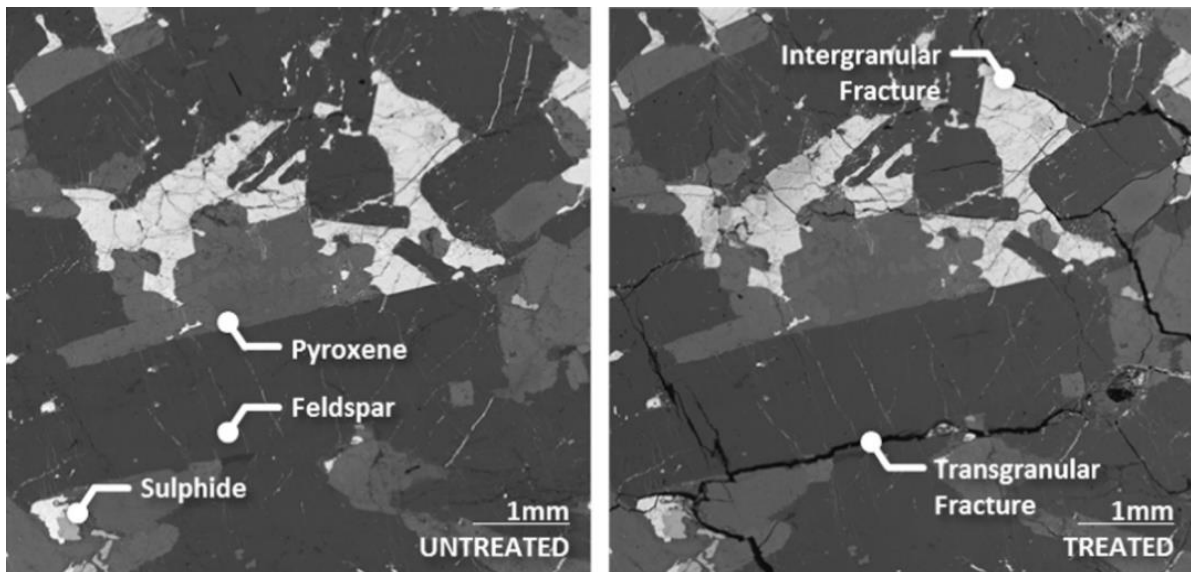
Figure 3.2. Microwave-induced fracture pattern (Batchelor et al., 2015)

3.4 Microwave-induced Damage Quantification

The extent of ore pre-damage due to microwave treatment can be quantified using various techniques. This is performed by comparing the mechanical strength or physical properties of treated versus untreated ore samples. Table 3.2 summarises the principles, capabilities, and limitations of the most commonly used methods for determining the magnitude of microwave-induced damage. These techniques have been employed by several researchers in microwave ore pre-treatment studies, and they are mentioned in the review discussed in Section 3.5.

Table 3.2. Common testing techniques for assessing microwave-induced damage

Technique	Principles	Capabilities	Limitations
UCS	Rock breakage resistance under axially compression loading between two flat platens.	Widely accepted technique in assessing rock strength.	Regular specimens with dimensions (Height/Diam $\geq$ 2).
BTS	Rock breakage resistance under radially compression loading between two round platens.	A simple way to determine the tensile strength of a rock sample.	Regular specimens with dimensions (Diam /thickness $\geq$ 2).
PLT	Rock breakage resistance under compression loading between two tip cones.	Irregular specimens can be tested, and index corrected to the standard equivalent core size of 50 mm [$Is_{(50)}$]. The index correlates with UCS. Portable-easy to carry on site.	Many specimens are required ($\geq$ 20 irregular particles, $\geq$ 10 for block samples), less effective for weak ores.
BBWI/ BRWI	Rock breakage resistance upon grinding, it involves grinding and classification.	Popular and widely accepted, results are reliable and reproducible.	Requires large sample mass (10-15 kg), very time-consuming.
DWT	Impact breakage by releasing a known weight from a pre-determined height to impact the sample.	Provides breakage parameters, simple operation, flexibility and extended input energy range.	Time-consuming, more than a day to complete a sample (Zuo & Shi, 2016), require 60-100 kg.
JKRBT	Particles of known velocities are projected to the stationary anvils for impact breakage.	Rapid breakage test, takes up to 1/10th of the time to complete a DWT (Shi et al., 2009).	
JKGem ci	Constrained jaw crushing a narrow-sized ore at a fixed ratio of mean particle size to CSS (2.5:1).	Rapid test, provides indices which correlate with impact breakage parameters and grindability.	Requires coarse feed particle size (-31.5 + 26.5 mm).
MIP	Mercury is intruded into porous rock samples under controlled pressure.	Rapid porosity test, detect pore/crack up to 400 μm (Rouquerol et al., 2012).	Cannot measure closed pores/cracks, measures the largest entrance towards the pore.
UPV	Ultrasonic velocity attenuation due to rock discontinuities.	The same sample can be tested before and after treatment, portable-easy to carry on site, inexpensive, and repeat measurements on the same sample for accuracy.	No internal microfracture details, requires good contact between specimen surface and transducer.
XRCT	Variations of X-rays attenuation based on materials contained in a rock sample.	3-D visualized image, measurement of internal features non-destructively.	Scanning artefacts, very expensive.
SEM (BSE)	Bombarding a specimen with a high-energy focused beam of electrons to produce images.	Provide high-quality and detailed surface images with the highest magnification.	Stereological effects, prolonged sample preparation, expensive.
FDI	Observing the fluorescence dye intruded in the microfractures under UV radiation.	Less expensive.	Detect cracks open to the surface only, photobleaching.

3.5 Microwave Ore Pre-treatment to Improve Comminution

This section presents a review of studies on microwave ore pre-treatment to assist comminution. This review is divided into two main sections: experimental studies using real ores (conducted at low and high microwave power density) and theoretical studies using binary ores (mostly numerical simulations). A pilot scale microwave ore pre-treatment plant tested at the University of Nottingham between 2010 and 2015 is also briefly reviewed to indicate scale-up possibilities.

3.5.1 Experimental Studies - Low Microwave Power Density

Many researchers have used low microwave power density to improve comminution or reduce ore strength. These studies were conducted in multimode cavities with microwave powers ranging from 100 W to 7 kW for longer irradiation times (10 seconds to more than 10 minutes), and their findings are discussed here.

Walkiewicz et al. (1991) investigated the influence of microwave treatment on the grindability of iron ores. The ore weighing 350 g was treated at 3 kW for 3.5 minutes in a multimode cavity. A significant reduction in the Bond ball mill work index (BBWI) of between 10-24% was achieved. In a subsequent study, no significant reductions were observed when the power was increased to 6 kW (Walkiewicz et al., 1993). This indicates that there is an optimum energy above which no additional grinding benefit is achieved irrespective of the microwave energy input.

Tavares & King (1999) assessed whether microwave pre-treatment could reduce the strength of three ore types (titanium, taconite and iron) using an ultrafast load cell (UFLC) and microscopic techniques. The ores were irradiated in a multimode mode cavity at different power levels of up to 1.2 kW. It was found that microwave energy induces fractures on such ore samples and the degree of induced damage was dependent on the applied power, with

coarser particles demonstrating higher strength reductions than finer particles for a given treatment condition. This is because coarser particles have a larger volume of the transparent matrix (surrounding absorbent minerals) than finer particles, which promotes crack propagation. Also, coarser particles have a large number of pre-existing flaws that can be extended when sulphide grains expand due to microwave irradiation.

Kingman et al. (2000) reported significant reductions in the Bond rod mill work index (BRWI) of 91% and 70% for ilmenite and carbonatite ores, respectively. Such impressive strength reductions were attributed to the coarse mineralogy of the excellent heaters encapsulated in a transparent gangue matrix which supported a larger thermal gradient (less conduction). In other studies, Vorster et al. (2001) and Koleini & Barani (2008) reported significant reductions in BRWI of up to 70% (massive copper ore) and 46% (iron ore), respectively.

Amankwah et al. (2005) reported a reduction in BBWI of about 11.5% and a strength reduction from a Chatillon tester of 10.6% when the free-milling gold ore was subjected to microwave treatment in a multimode cavity for up to 5 minutes at 1.5 kW. Also, Kumar et al. (2010) reported an increase in the specific rate of breakage of iron ore of about 12% after 60 sec of irradiation time using a 0.9-kW multimode cavity. The significant comminution improvements reported in these studies have been attributed to the presence of good microwave heaters (magnetite) in a transparent gangue matrix (e.g., quartz). Wang & Forssberg (2005), on the other hand, investigated the effect of microwave pre-treatment on the grindability of dolomite, limestone, and quartz. Because of their microwave transparency characteristics, these materials showed a very marginal grindability improvement even at a higher microwave power of 7 kW and a longer irradiation time of 30 minutes.

Omran et al. (2015) compared the grindability of microwaved versus conventionally heated iron ore samples containing high phosphorous mineral contents. Batches of 100-gram samples were subjected to microwave heating at different exposure times (30-60 minutes) in a multimode cavity at 900 Watts, 2.45 GHz. Likewise, 100-gram samples were heated in a conventional furnace for one hour at three different temperatures i.e., 400, 500, and 600°C. After heating, the samples were ground and the fraction passing 125 µm determined. Grindability results showed that the fraction of fines (-125 µm) progressively increased with microwave exposure time from 46.6% (untreated) to about 59.8% (treated at 60 sec). Whereas conventional heating at 600°C for 1 hour increased the grind fineness to 50.8% while consuming more power (224 times) than that consumed via microwave heating.

In a similar study, Cai et al. (2018) reported an increase in ore grind fineness (-38 µm) with increasing microwave irradiation time, from 31.7% (untreated) to about 55% after 45 seconds. However, there was a decrease in grind product fineness for samples irradiated for more than 45 seconds. The improved grinding results in both studies are attributed to differential thermal stresses between hematite (a good microwave heater) and fluoroapatite, chamosite (microwave transparent gangue matrix). The decrease in grind fineness observed after prolonged irradiation time, on the other hand, could be attributed to sintering effects that increased the strength of oolitic hematite mineral grains. In both studies, SEM images of microwaved samples revealed the presence of intergranular fractures between hematite and fluoroapatite/chamosite grains.

Marion et al. (2016) investigated the effect of microwave irradiation on the grindability of a copper-nickel sulphide ore containing chalcopyrite, pentlandite, and pyrrhotite. Prior to microwave irradiation, the ore was pre-crushed to -3.36 mm. Microwave treatment was performed in batches of 250 grams, which were irradiated for 30, 60, and 90 seconds at 3 kW (2.45 GHz) in a multimode cavity. The extent of ore pre-damage due to microwave irradiation was quantified using the Berry & Bruce (1966) grindability technique. A significant reduction

in BBWI of up to 22 % was observed after 60 seconds of microwave irradiation. The observed strength reduction was attributed to microwave-induced fractures caused by differential thermal stresses between sulphide mineral grains and gangue matrix. The SEM images of pre-treated samples revealed the presence of microwave-induced fractures.

Singh et al. (2017) evaluated the influence of microwave pre-treatment on the milling of three samples (manganese ore, iron ore, and coal). Fifty grams (-3.35 mm) from each of the three samples were subjected to microwave heating in a multimode cavity at 180, 540, and 900 Watts for 1,3, and 5 minutes. Thereafter, samples were ground for 2 minutes in a planetary mill (225 ml capacity) and sieved through (3.35, 1, 0.5, and 0.15 mm), and the P_{80} was determined. Grinding of iron and manganese ore samples resulted in P_{80} reductions of 47.8% and 20.8%, respectively, at 900 Watts after 5 minutes of exposure time. The coal sample showed a reduction of 18% at 180 Watts for 1 min, no further significant grinding improvement was achieved after prolonged exposure times.

Bobicki et al. (2018) explored the effect of microwave treatment on the grindability of two low-grade ultramafic nickel ores. Batch samples (425–1000 μm) weighing 100 grams were treated in a multimode cavity at 1 kW (2.45 GHz) for different exposure times of up to 15 minutes. Treated samples were then wet ground at 30% solids in a stirred media attrition mill for 15 minutes. The relative work index by Berry & Bruce (1966) was used to assess the extent of ore pre-damage. The most microwave-amenable ore of the two ores tested had a decrease in product size (P_{80}) from 606 μm (untreated) to 19 μm after 15 minutes of microwave exposure, equivalent to a relative work index of about 3.6%. Such ore had a consistent texture and released water vapour due to serpentine dehydroxylation at 730°C, corresponding to a mass loss of 11.8%. The higher heating rates and larger thermal expansion of microwave-absorbing grains such as pentlandite and magnetite, as well as pressure build-up due to water expansion,

promoted fractures in such ore. The SEM analysis of unground pre-treated fragments revealed the presence of these fractures.

Jiawang et al. (2020) studied the influence of microwave pre-treatment of iron ore (containing magnetite) on impact breakage. The ore was sawn to form cuboid specimens of 50 mm × 50 mm ×100 mm. These specimens were subjected to microwave treatment for up to 7 minutes at 1.2-2.8 kW, and the extent of induced damage was determined using the DP-1200 drop hammer impact device. The ore dynamic strength decreased with the increase in irradiation power and time. For instance, after 5 minutes of microwave exposure, the ore dynamic strength decreased from 100% (untreated) to 79% and 43% at 1.2 and 2.8 kW, respectively. On the other hand, when the microwave power was maintained at 2 kW, the ore strength decreased from 100% (untreated) to 76% and 51% at 3 and 5 minutes of microwave exposure, respectively. Suggesting that greater ore damage can be achieved by maximizing the microwave power than extending the treatment duration (i.e., maximizing the thermal shock).

Yu et al. (2021) studied the effect of microwave treatment on lead-zinc ore grindability. Two hundred-gram subsamples (1-2 mm) were microwave-treated using a multimode cavity at 0.8 kW (70 sec) and 7 kW (15 sec) at 2.45 GHz. The microwave-treated samples were then ground for 10 minutes using a planetary mill and % passing 74 µm was determined, and results were compared with that of the untreated sample (baseline). Grinding results showed an increase in ore fineness (-74 µm) due to microwave treatment from 36% (untreated) to 41% and 49% treated at 0.8 kW (70 sec) and 7 kW (15 sec), respectively. The improved grinding results are attributed to ore weakening caused by microwave-induced fractures, which were visible in the SEM images of treated samples. The grinding improvement due to microwave treatment has also been reported by He et al. (2021) for a polymetallic ore composed of several microwave heaters such as jamesonite, pyrite, cassiterite, and sphalerite, particularly for coarse particle size fractions (-3.2+2, -2+1 mm).

Barani et al. (2021) assessed the influence of microwave treatment of copper sulphide ore on ball milling and bed breakage. The main minerals present in this ore were chalcopyrite, galena, and quartz. Eighty-gram subsamples (-3.36 mm) were microwave treated for 10 minutes in a multimode cavity at 0.9 kW (2.45 GHz). The bed breakage tests were carried out in a piston-die device. For each test, 350 grams of the sample was poured into a piston-die cylinder and pressed to 1950 kN, and the pressed cake was collected and sieved through a 250-µm sieve. The remaining materials on the sieve were pressed again, and this process was repeated until the entire sample passed through a 250-µm sieve. Similarly, the samples were repeatedly ground in a ball mill and sieved through a 250-µm. Thereafter, the bed breakage and ball milling products (-250 µm) were separately dry sieved into 8 size fractions ranging from -250+177 µm to -37 µm. Although the particle size distribution of the treated sample in both breakage methods was similar to that of the untreated sample, a slight increase in chalcopyrite liberation of 2% (on average) was observed in the bed breakage treated sample, with higher liberation observed in the coarse size fractions. General observation indicates that the influence of microwave ore pre-treatment on comminution decreases with particle size.

Pickles & Lu (2022) recently performed a comparative study of the dewatering and weakening of gibbsite-type bauxite ores using conventional and microwave heating methods. The ore was in the form of roughly spherical bauxite ore pisoids (−6.68+4.70 mm) and coarse irregular fragments (-4.5+2.5 cm). Essentially, the dehydroxylation of bauxite ores involves the removal of loosely bound water at low temperatures, followed by the removal of more strongly bonded water at higher temperatures, potentially reducing the ore strength. The conventional heating was carried out in a laboratory resistance furnace at 1200 Watts (120 V, 10 A), and ten-gram samples were heated for 20 minutes at 200°C, 500°C, 700°C and 900°C.

For the microwave heating tests, fifty-gram samples were microwaved in a multimode cavity for 2 minutes at 825, 1000 and 1200 Watts. The compressive strengths were measured using a

Chatillon compression tester, and 80 bauxite particles were tested in each sample. Higher strength reductions of up to 73.8% (900°C, 20 minutes) and 58.6% (1.2 kW, 2 minutes) were achieved for the pisolitic sample by conventional and microwave heating, respectively. Also, the moisture loss was higher (12-70%) for the conventionally heated sample than for the microwaved (1.6-5.4%). The low performance of microwaved samples could be attributed to non-homogeneous heating, as some fragments received a higher microwave energy dose than others, indicating that only a fraction of the particles were effectively treated.

In the case of coarsely crushed fragments, which involved single-particle treatment in both treatment methods, results indicate that the microwaved sample was relatively weaker than the conventionally-heated and as-received samples, for all size fractions tested (Figure 3.3). Despite the higher strength reduction achieved on the microwaved sample, the water removal extent was lower than that of the conventionally heated sample, indicating that the water removal process with microwave heating resulted in high internal water vapour pressures, which promoted significant ore fracturing. Also, for the microwaved sample, the ore strength decreased with increasing particle size, which is consistent with the findings reported by other researchers mentioned earlier in this review. Furthermore, the energy requirements for microwave heating were significantly lower than those for conventional heating. In microwave heating systems, only the sample is heated (i.e., selective heating), and very little heat is lost to the surrounding environment, as opposed to conventional heating, which involves heating the entire furnace in order to heat the sample.
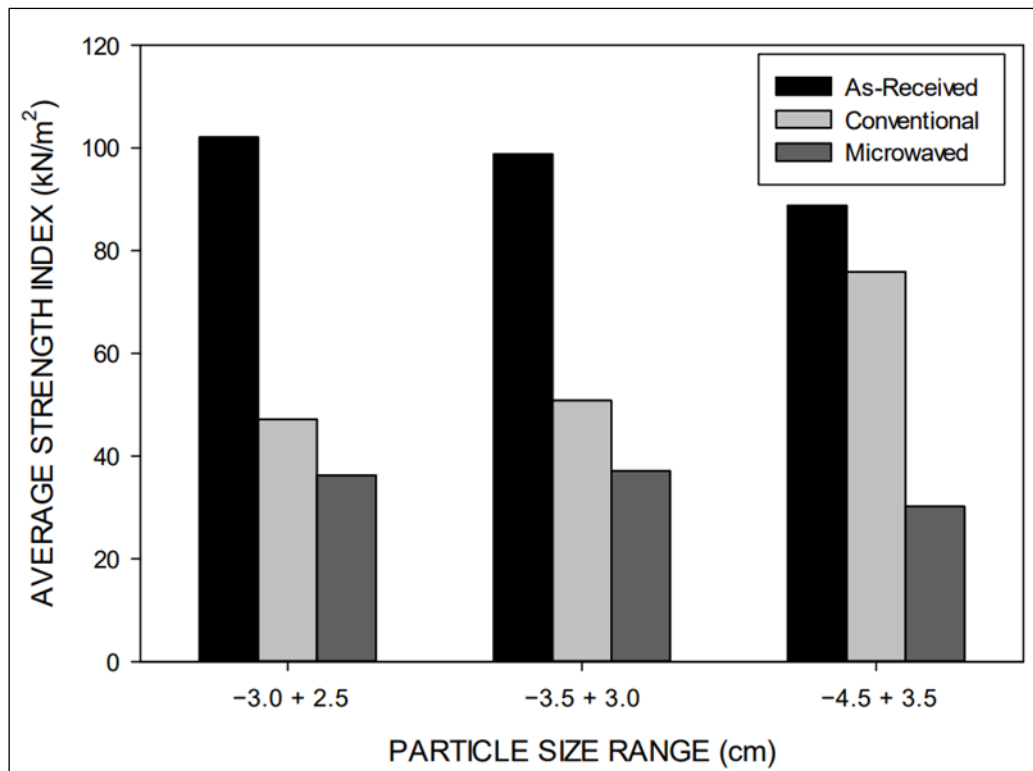
Figure 3.3. Ore strength results as-received, microwaved, and conventionally heated samples (Pickles & Lu, 2022)

3.5.2   Theoretical studies - Microwave ore pre-treatment

A number of researchers have conducted theoretical studies on the microwave treatment of ores in order to provide a fundamental understanding of ore fracturing when exposed to microwave fields. Several variables influencing the performance of microwave-induced fractures could be assessed individually, and the resulting damage quantified using numerical simulation of binary ores, which could not be assessed experimentally using real ores due to their heterogeneous and complex texture. In this section, some theoretical studies on microwave treatment of ores to improve comminution are discussed.

Whittles et al. (2003) evaluated the influence of microwave power density on ore strength reduction by numerical simulation. The modal domain was a binary ore of calcite (transparent gangue) and pyrite (microwave-absorbent phase), with the pyrite grains randomly distributed to simulate a simplified ore sample. The extent of ore pre-damage was simulated using the uniaxial compressive strength test (UCS) model. Initially, microwave treatment tests were simulated using a multimode cavity operating at 2.6 kW (2.45 GHz) for 1, 5, 15, and 30-second treatment times, resulting in power densities ranging from $3x10^9$ W/m^3 at 300K to $9x10^9$ W/m^3 at temperatures greater than 600K. The microwave treatment tests were then simulated using a single mode cavity at high power of 15 kW (2.45 GHz) with much shorter heating times of 0.05, 0.25, 0.5, and 1 second to evaluate the effect of increasing the microwave power density on strength reduction.

Results showed that the higher microwave power density of $1x10^{11}$ W/m^3 in a single-mode cavity generates a significantly larger reduction in strength of up to 55% (from 126 to 57 MPa) within a short exposure time of 0.05 seconds. In contrast, a strength reduction of 37% (from 126 to 79 MPa) was achieved in a multimode cavity at 2.6 kW after 30 seconds of microwave exposure, with little effect on the UCS strength reduction at heating intervals of 1 and 5 seconds due to insufficient stresses for ore fracturing. The higher strength reduction was possible in the single mode cavity at $1x10^{11}$ W/m^3 due to a higher temperature gradient between the pyrite grains and calcite matrix (i.e., less time for conduction effect), which maximizes the induced stresses that exceed the ore strength.

Jones et al. (2005) used the 2D finite difference simulation method to investigate the effect of microwave power density on ore strength reduction and propose the ore weakening mechanism due to microwave treatment. The simulation used a binary ore of a single circular pyrite grain (microwave-absorbent phase) within a calcite matrix (transparent gangue). Microwave treatment tests were simulated at four different power densities ranging from $1x10^8$ W/m^3 to

$1x10^{11}$ W/m^3. The effect of particle size on induced stresses and ore weakening was investigated by modelling ten different particle diameters ranging from 50 μm to 500 μm varied by a 50 μm increment. Results showed that the weakening of this binary ore occurs due to radial tensile stresses within the calcite matrix and shear stresses along the calcite-pyrite grain boundary. The pyrite grain exhibited little or no damage due to the high compressive stresses existing within the interior of the grain. Also, for a given exposure time, the maximum temperature attained by the sample increases linearly with microwave power density. Furthermore, smaller particle sizes require higher microwave power densities to attain higher temperatures, which can induce sufficient stresses for ore fracturing.

In another study, Jones et al. (2007) assessed the effect of microwave power density and exposure time on ore strength using a quasi-static thermo-mechanical 2D model of a simplified pyrite-calcite system. The models were assigned 1% pyrite grains of the total sample area, which were randomly distributed throughout a cylindrical sample of 37 mm (diameter) by 74 mm (height). The ore strength was quantified using simulations of the uniaxial compressive strength (UCS) test. Results showed that higher strength reductions were achieved at higher microwave power density and in a shorter exposure time. For instance, the higher UCS strength reduction of 35% was achieved in 0.4 seconds at a power density of 1×10^{10} W/m^3, compared to the same strength reduction of 35% achieved after 10 seconds at 2×10^9 W/m^3. Also, these results showed that a five-fold increase in power density resulted in a five-fold reduction in the total energy required to achieve the same strength reduction of 35%. The better performance of a single mode cavity in a short exposure time is attributed to less time for conduction from the absorbent phase to the adjacent gangue matrix, which maximizes the induced thermal stresses, resulting in significant ore fracturing and higher strength reduction. These results are consistent with earlier simulation work reported by Whittles et al. (2003).

Ali & Bradshaw (2009) quantified damage around grain boundaries of microwave-treated ore using numerical simulation. The effects of power density, treatment time, mineralogy, and texture were also investigated. This study used two binary ores i.e., galena-calcite and magnetite-dolomite, each with a composition of 10% microwave-absorbing mineral and 90% transparent matrix by volume. For each binary ore, two textures were simulated: coarser-grained (1.0-2.5 mm) and finer-grained (0.125–0.25 mm). Results showed that for a given power density and ore type, the damage incurred in the sample increases with microwave exposure time, and there is an optimum exposure time range where the benefit of microwave irradiation is maximum. Also, for both binary ores tested, the damage decreases significantly as the absorbent-grain size decreases. It was also evident that a higher microwave power density is required, in addition to higher energy input in order to achieve significant damage, implying that there is a power density level below which no further increase in ore damage is possible by increasing irradiation time.

In another study, Ali & Bradshaw (2010) evaluated the effects of microwave power density and absorbent grain size on the extent of ore pre-damage and crack pattern using numerical simulation. The simulations were performed using binary ores of 10% galena (a microwave-absorbing mineral) and 90% calcite (a transparent matrix) by area. Two different textures were simulated: coarser-grained (1–2.5 mm) and finer-grained (0.1–0.25 mm). The extent of ore pre-damage was quantified using a simulated Brazilian test. Results showed that the extent of ore pre-damage increased with microwave power density, absorbent grain size and exposure time (Figures 3.4 - 3.7). For example, for a given power density of 1×10^9 W/m^3, the coarse-grained texture suffered greater damage (2164 microcracks at 0.2 sec) than the fine-grained texture (456 microcracks at 0.4 sec). In addition, for the coarse-grained texture, the number of microcracks increased from 2164 (at 1×10^9 W/m^3, 0.2 sec) to 3600 (at 1×10^{11} W/m^3, 0.2 sec). It is also apparent that the fine-grained texture requires more microwave energy or higher

power density in order to induce significant fractures. A close examination of crack patterns revealed that micro-fractures occurred around the grain boundary and on the calcite matrix regardless of the shape of the absorbent phase (galena). Also, there were no significant differences in crack patterns observed for different shapes of the microwave-absorbent phase.
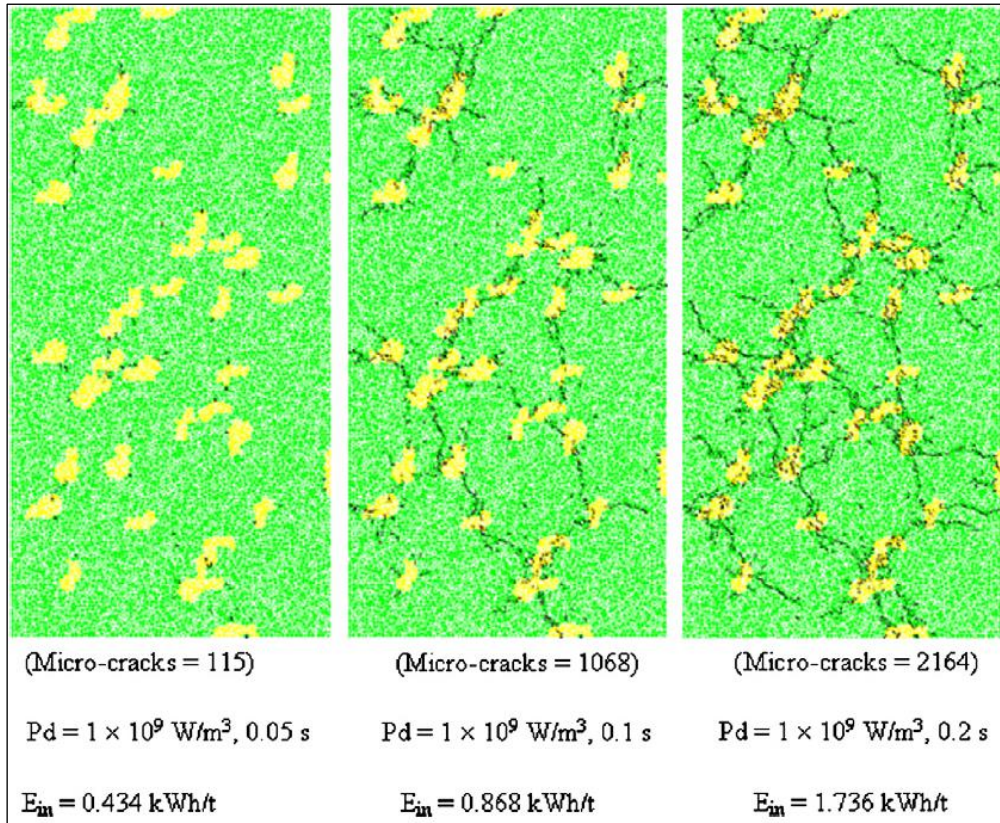
Figure 3.4. Micro-cracks in coarse-grained galena in calcite matrix at $1x10^9$ W/m^3 (Ali & Bradshaw, 2010)

Figure 3.5 Micro-cracks in fine-grained galena in calcite matrix at 1×10^9 W/m^3(Ali & Bradshaw, 2010)
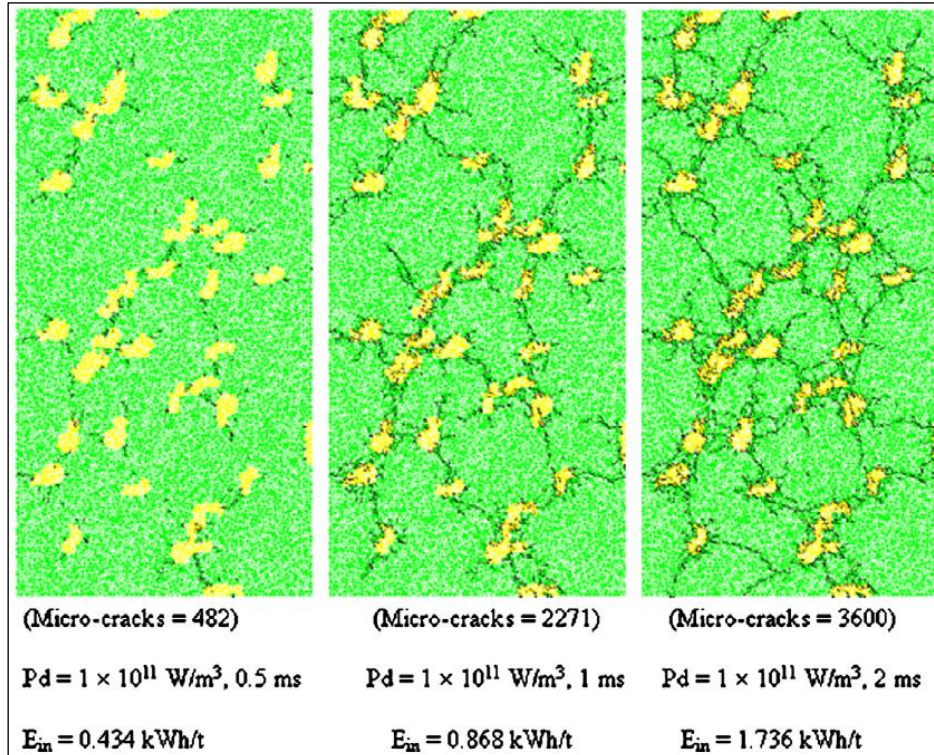
Figure 3.6. Micro-cracks in coarse-grained galena in calcite matrix at 1x1011 W/m3 (Ali & Bradshaw, 2010)

Figure 3.7. Micro-cracks in fine-grained galena in calcite matrix at 1×10^{11} W/m³ (Ali & Bradshaw, 2010)

Ali (2010) conducted a numerical simulation microwave treatment study to assess the influences of several variables on ore strength reduction and identify ores that are more amenable to microwave treatment. These variables include the thermo-mechanical properties of minerals, absorbent phase grain size, microwave power density, absorbent phase dissemination, and absorbent modal area. It was shown that higher strength reductions are achieved by increasing the microwave power density. Also, ores with some of these properties achieved higher strength reductions:

    i.   Microwave-absorbing mineral with a high thermal expansion coefficient.

    ii.   Microwave-absorbing mineral constrained in a strong transparent gangue matrix.

    iii.   Coarse-grained microwave-absorbing grains.

    iv.   Poorly disseminated microwave-absorbing phase.

    v.   High modal area of a microwave-absorbent phase.

Yang et al. (2020) studied the effect of microwave treatment on the fragmentation of synthetic ore (briquettes) made of alundum cement (as a microwave-transparent gangue) and pyrite (as a microwave-absorbing phase). The briquettes were made by mixing 22-28 grams of alundum cement (P_{80} = 48.6 µm) with pyrite grains (0-8 grams) of a given size fraction and water (5 grams). This mixture was then compacted at 35 MPa and dehydrated at 120°C for five days to cure. The cured briquettes were microwaved in a multimode cavity at 0.6-1.0 kW, and the failure load was determined using the Chatillon compression tester. Results showed that the extent of microwave heating of briquettes increases with pyrite content, attaining a maximum surface temperature of 358°C (21% pyrite) against 96°C (0% pyrite) at 0.9 kW and 120 seconds irradiation time. Extensive fractures were also observed on the treated specimens, particularly those with a high pyrite content and coarse pyrite grains. The XRD results of the powdered treated specimens indicated the presence of corundum, hematite, pyrrhotite, pyrite, and quartz, suggesting that some pyrite has been oxidised to hematite and pyrrhotite.

Figure 3.8 shows the failure load of briquettes as a function of pyrite average grain size. In this case, each briquette had the same pyrite content of 18% and was microwaved at the same conditions i.e., 0.9 kW for 120 seconds. The failure load decreased with increasing pyrite grain size. This is because the heat absorbed by the coarse pyrite grains is not dissipated more rapidly into the surrounding gangue matrix, resulting in much higher thermal stresses and thus significantly weakening the ore.
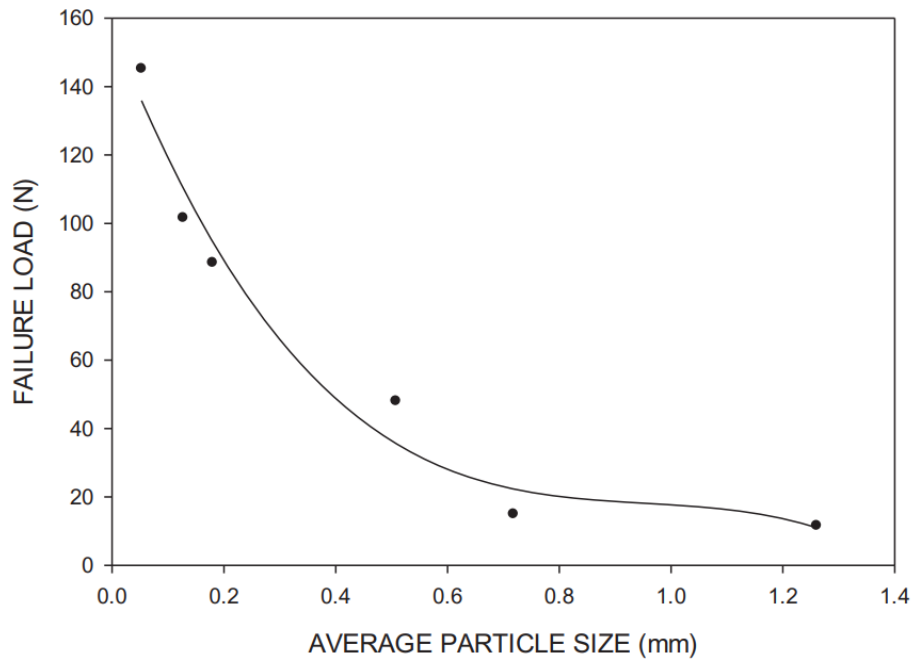
Figure 3.8. Failure load versus pyrite grain size (Yang et al., 2020)

The effect of pyrite content on failure load is shown in Figure 3.9. In this case, each briquette had the same pyrite grain size (-20+28 mesh = 841-600 µm) and was microwaved at the same conditions i.e., 0.9 kW for 120 seconds. It can be seen that, within the range of pyrite content tested of about 3-20%, the failure load decreased with increasing pyrite content, which is attributed to larger thermal stresses caused by the increased amount of microwave heaters within the ore. Moreover, the 2D ImageJ analysis revealed that the degree of ore fragmentation increased with increasing pyrite content, pyrite grain size, and incident microwave power, which is consistent with the failure load results.
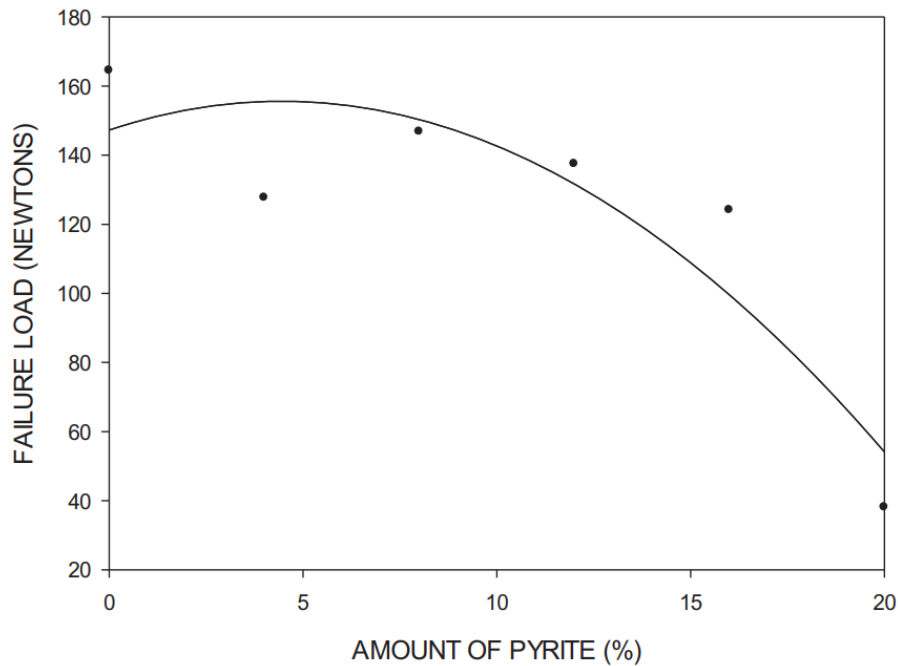
Figure 3.9. Failure load versus pyrite content (Yang et al., 2020)

A theoretical study reported by Djordjevic (2014) showed that the modulus of elasticity (stiffness) of minerals has a significant influence on the extent of ore fracturing. Figure 3.10 shows the modulus of elasticity of some common minerals found in sulphide ores, indicating that pyrite, magnetite, and rutile have higher elastic modulus values than most gangue minerals or other sulphides (e.g., chalcopyrite). The model is composed of sulphide grains embedded in a matrix of feldspar (Figure 3.11). In the first case, pyrite properties were assigned to the sulphide phase (A), while chalcopyrite properties were used in the second case (B), and both binary ores were loaded under identical conditions. Fractures (dark phase) can be seen on the gangue matrix in case A but not in case B. This is because pyrite can effectively transfer induced stresses to the feldspar gangue matrix, whereas chalcopyrite cannot. This is due to the fact that the elastic moduli of chalcopyrite and feldspars are comparable, whereas the elastic modulus of pyrite is much higher than that of feldspar. These observations suggest that ore

samples containing a high proportion of stiffer microwave heaters (e.g., pyrite, magnetite) are more amenable to microwave-induced fractures, given suitable texture (e.g., coarse grain size).
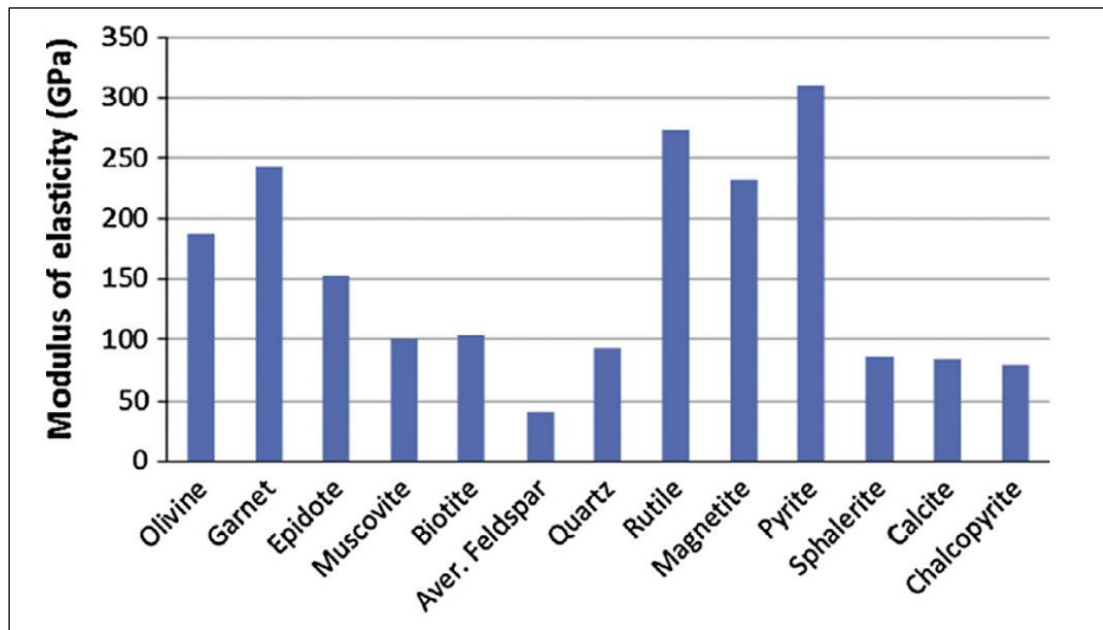
Figure 3.10. Modulus of elasticity of some common minerals (Mavko et al., 2009; Djordjevic, 2014)
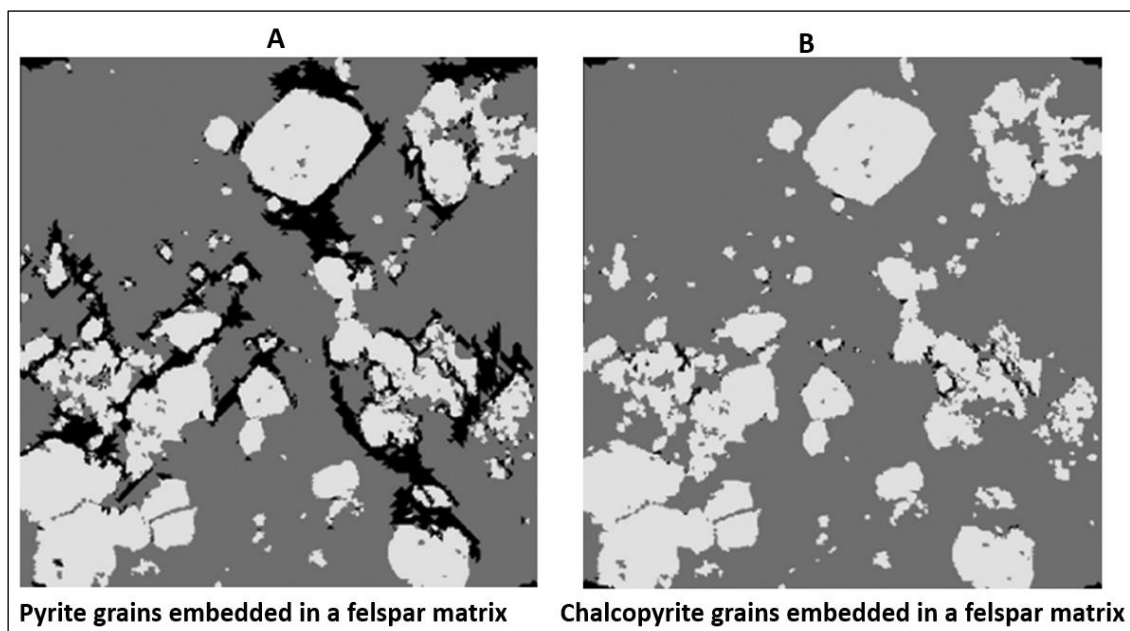
Figure 3.11. The extent of feldspar matrix failure in the presence of pyrite or chalcopyrite grains (Djordjevic, 2014)

3.5.3   Experimental Studies – High Microwave Power Density

Following the earlier numerical simulation observations by Whittles et al. (2003), Kingman et al. (2004a) conducted experimental studies to prove the hypothesis that higher microwave power density increases the magnitude of ore fracturing. To achieve this objective, microwave treatment experiments were performed using lead-zinc ore samples employing a single mode (5-10 kW for 0.1-1 sec) and a multimode (5-15 kW for 1-10 sec) cavity. A strength reduction in terms of median $Is_{(50)}$ of about 43% was achieved in the multimode cavity at 10 kW after 1 sec of irradiation time, whereas a similar strength reduction (43%) was achieved in the single mode cavity after a short duration of 0.1 sec.

In a subsequent study, Kingman et al. (2004b) reported an $Is_{(50)}$ reduction of about 40% at 10 kW within 0.1 sec with no further reduction achieved at 15 kW (Figure 3.12). The breakage rate improved by over 40%, and strength reduction from a drop weight test (DWT) in terms of A*b of 41.1% was achieved at 15 kW in 0.2 sec. It was concluded that significant strength reductions can be achieved at higher microwave powers at shorter exposure times, and there is an optimum energy above which no further significant damage is induced. Similarly, Rizmanoski (2011) reported a strength reduction following DWT (A*b) of 29% for a copper ore treated at 5 kW of modulated power. However, no significant strength reduction was achieved at 1 kW, suggesting that such a low power was not adequate to induce noticeable damage.
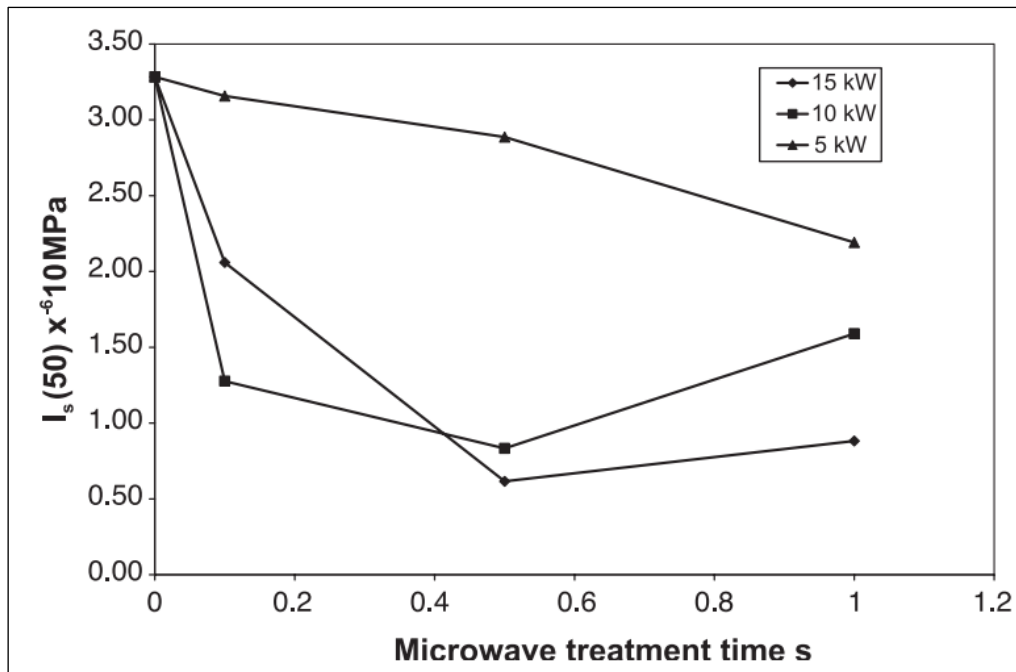
Figure 3.12. Is(50) as a function of microwave exposure time for material -53+45 mm (Kingman et al., 2004b)

Grinding results reported by Kingman et al. (2004b) showed that the difference in the specific rate of breakage between treated and untreated samples decreases with particle size (see Figure 3.13). The largest particle size fraction of -19+16 mm demonstrated the greatest breakage improvement, with a difference of over 70% compared to a difference of about 11% for the smallest size fraction (-4.75+3.35 mm). The decrease in breakage improvement with particle size can be attributed to a decrease in the gangue matrix surrounding the microwave absorbers in the smaller fragments. Essentially, fractures propagate more effectively when the microwave-absorbing grains expand through a large volume of the microwave-transparent gangue matrix. As particle size decreases, some microwave absorbers expand through free space, reducing the induced thermal stresses and the degree of ore fracturing. As a result, the benefit of microwave ore pre-treatment on grinding performance diminishes as particle size decreases.
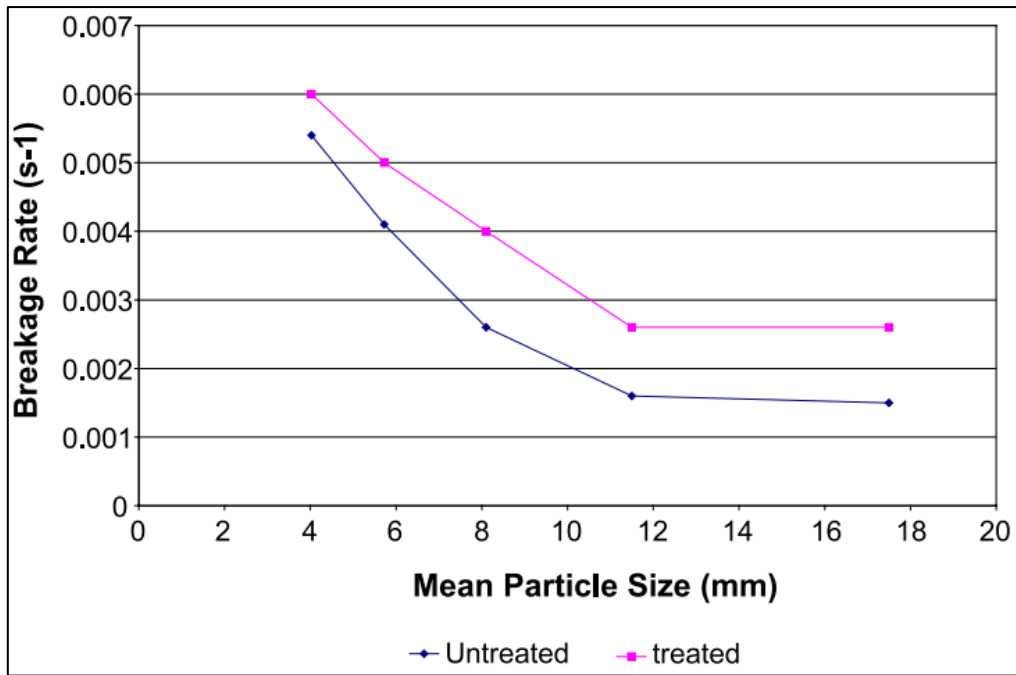
Figure 3.13. Specific rate of breakage versus mean particle size (Kingman et al., 2004b)

In another study, Sahyoun et al. (2004) reported significant reductions in BRWI of copper carbonate ore (containing copper sulphides, magnetite, and carbonate minerals), ranging from 10.1 kW/t (untreated) to 2.73-1.75 kWh/t (treated), equivalent to a reduction of 73-83%. This was achieved in a short irradiation time of 0.5 sec using a single mode cavity at a microwave power of 10-15 kW, equivalent to 1.4-2.1 kWh/t specific energy input (see Table 3.3). Furthermore, copper sulphide liberation increased from 30% (untreated) to 70% (treated) in the coarse-size fractions (+500 µm), and evidence of intergranular fractures due to microwave treatment was observed by scanning electron microscopy (SEM).

Table 3.3. Rod mill grinding results after microwave treatment in a single mode cavity (Sahyoun et al., 2004)

Microwave Exposure Time (s)	Power Level (kW)	% Reduction in Bond Work Index	Reduction in Bond Work Index (kWh/t)	Energy Expended (kWh/t)
0	0	0	0	0
0.5	10	78.4	7.92	1.39
0.5	13	75.7	7.65	1.81
0.5	14	82.7	8.35	1.94
0.5	15	73	7.37	2.08

In general, the impressive strength reduction reported in these microwave treatment studies using single mode cavities, within very short durations and high microwave power inputs, is attributed to the higher temperature gradient developed between the microwave-absorbing phases and the non-absorbing matrix. As a result, significant damage is induced, which can significantly reduce ore strength. On the other hand, if the ore is slowly heated with low microwave power, more heat is transferred by conduction from the microwave-absorbing phases to the adjacent gangue matrix, resulting in small thermal stresses and less ore weakening (Kingman et al., 2004b).

Batchelor (2013) employed both single mode batch and conveyor applicator systems of 15-30 kW to quantify the extent of microwave-induced damage on nickel, copper and lead-zinc ore samples using ultra pulse velocity (UPV) and point load test (PLT) techniques. A strength reduction of point load index $Is_{(50)}$ (corrected to the standard equivalent core size of 50 mm) of up to 33% and sonic velocity reductions of 9.1% were achieved at low microwave specific energies of about 2.4 kWh/t. In another study, Kobusheshe (2010) reported the $Is_{(50)}$ and sonic velocity reductions in hydrated minerals of up to 40% and 70%, respectively, at 9 kWh/t. The impressive results observed in this latter study were attributed to the selective heating of the hydrobiotite layer (excellent microwave heater), which turned into steam, resulting in localised pressure buildup within the ore. As a result, significant fractures are induced, resulting in the observed reductions in ore strength and sonic velocity measurements.

In another study, Batchelor et al. (2015) investigated the influence of mineralogy and texture on microwave ore pre-treatment using 13 sulphide ores of varying mineralogy and texture. The ores were treated at high power (15-25 kW) in a single mode cavity with an energy input of 0.5-10 kWh/t, and the extent of ore pre-damage was quantified using the PLT method. Figure 3.14 compares the grain size distribution of microwave heaters composed in these ores. Notice that the 50% passing (D_{50}) of the nearest sieve size of 425 µm (~500 µm) was selected to

represent the average grain size of the microwave heaters. This arbitrary size was selected because it ideally separated the ores into two size classes: coarse-mineralization (blue and red plots) and fine-mineralization (other plots), with coarse-mineralized ores expected to exhibit significant strength reduction after microwave treatment.
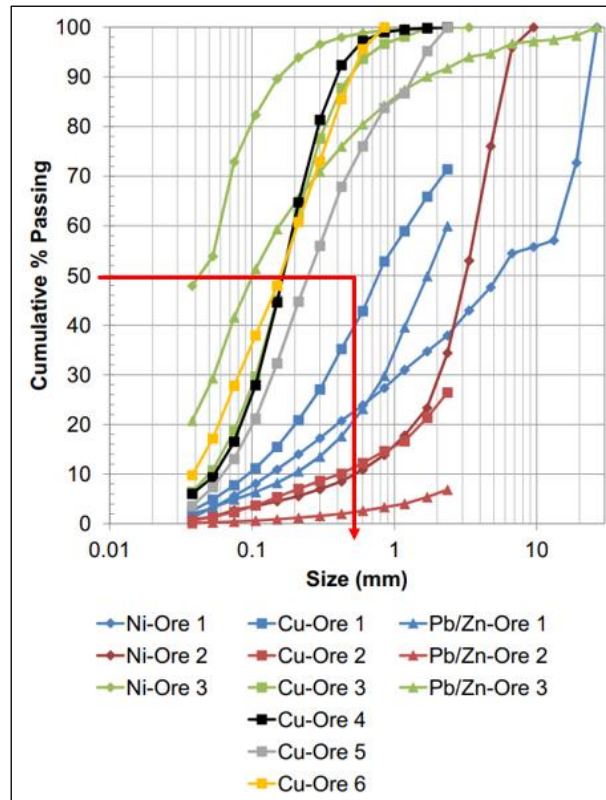
Figure 3.14. Apparent good microwave-heating phases grain size distributions (adapted from Batchelor et al., 2015)

Figure 3.15 compares the grain size (% passing 425 µm) and modal mineralogy of microwave heaters in these ores. The PLT results in Figure 3.16 shows that ores that demonstrated the highest average reductions in $Is_{(50)}$ (>20%) at low microwave energy of up to 5 kW/t contained a significant proportion of magnetite (mostly coarse-grained) coupled with a partially hard matrix (e.g., Ni-Ore 3, Pb/Zn-Ore 2 and Pb/Zn-Ore 3). The next best-performing ores (>10% reduction at less than 5 kWh/t) contained a significant proportion of coarse iron sulphides (e.g., Ni-Ore 2, Cu-Ore 2, Pb/Zn-Ore 1 and Pb/Zn-Ore 4). Finally, the ores that achieved less than

10% in strength reductions contained fine grains of microwave-absorbing phases, a high proportion of soft gangue minerals, and/or a significant proportion of barren fragments (Ni-Ore 1, Cu-Ore 1, Cu-Ore 3, Cu-Ore 4, Cu-Ore 5 and Cu-Ore 6).
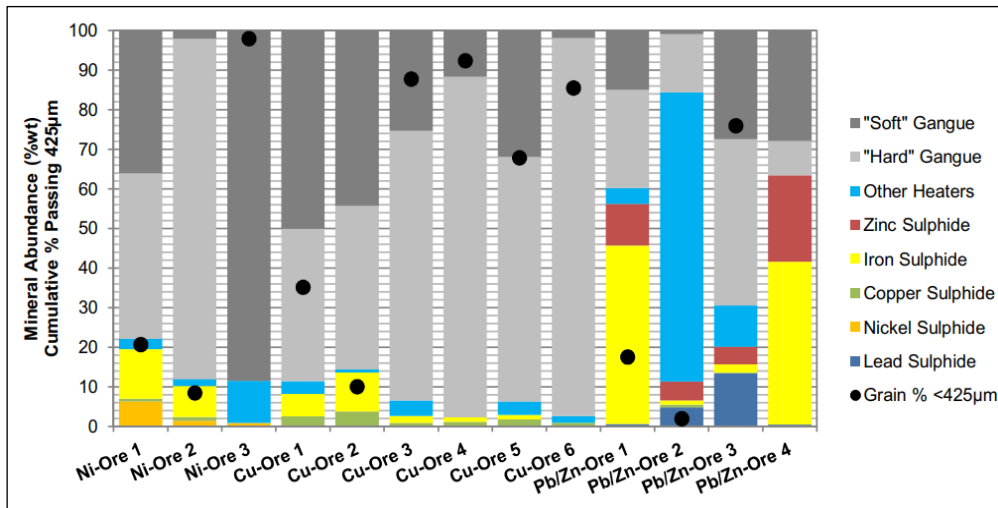
Figure 3.15. Modal mineralogy and microwave heaters grain size comparison (Batchelor et al., 2015)
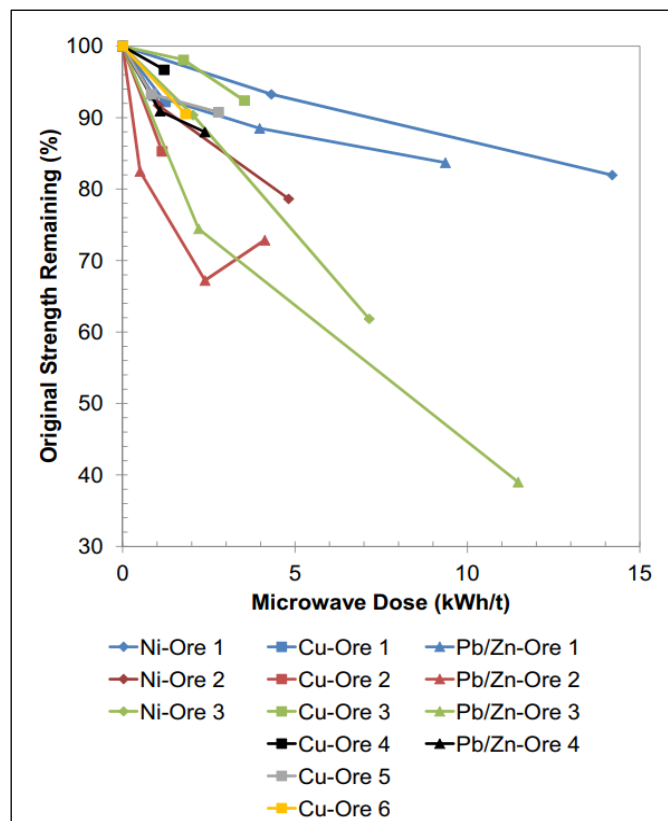
Figure 3.16. Point load test results summary (Batchelor et al., 2015)

The authors concluded that ores that achieved higher strength reduction due to microwave treatment met the following criteria:

i.   Contain the highly microwave-absorbent phases such as magnetite or sulphides of iron, lead, nickel, and copper.

ii.   Consist of a high modal abundance of total good microwave heaters of 2-20 wt%. Ores with >20% microwave-absorbing phases (e.g., massive sulphide deposits) do not exhibit significant fractures at low energies because the microwave energy available to thermally expand the grains is reduced as it must be shared amongst the microwave-heating phases present. The low-grade or barren ores, on the other hand, do not have sufficient microwave heaters to induce significant fractures.

iii. Contain at least 50% abundance of hard gangue matrix ($\geq$6 Mohs) that surrounds the microwave-absorbing phases, which supports the effective transfer of stresses and ore fracturing. The soft gangue matrix tends to undergo ductile deformation to absorb thermal shock, requiring high microwave energy to initiate and propagate fractures.

iv.   Have a coarser grain size of microwave absorbent phases, with grain sizes d_{50} >0.5-1.0 mm.

v.   Have a consistent texture of microwave-absorbing phases, with a high proportion of amenable texture in most fragments.

Charikinya et al. (2015) used sphalerite ore to assess the influence of microwave treatment on the severity of induced damage on crushed ore products using a combination of XRCT and QEMSCAN techniques. Three different size fractions of HPGR and cone crusher products were used i.e., large (-25+19 mm), medium (-16+9.5 mm) and small (-5+4.75 mm). The microwave treatment tests were carried out in a single mode cavity with a specific energy input of 2-3 kWh/t. Microwave treatment resulted in an increase in the crack volume of over 500%

for both modes of prior comminution at all particle sizes tested. Furthermore, microwave-treated samples exhibited both trans-granular and inter-granular crack patterns.

Ure (2017) quantified the microwave-induced damage on copper sulphide ore samples using Fluorescence Dye Impregnation (FDI) in combination with a stereomicroscope imaging technique. The ore fragments (-50+25.4 mm) were treated in a single mode cavity using a pilot-scale batch microwave treatment system. An increase in the fractured area of up to 26-75% was achieved at a microwave specific energy input of 0.7-2.2 kWh/t, with higher energies generating larger fractured areas.

3.5.4 Scale-up Possibilities - A Case Study of Microwave Ore Pre-treatment

All of the studies discussed in Sections 3.5.1 to 3.5.3 were carried out in batch mode using lab-scale microwave cavities capable of treating a few grams to less than 25 kg per batch. Recently, researchers at the University of Nottingham (UK) designed, constructed and tested a pilot plant for microwave ore pre-treatment capable of operating continuously at a throughput rate of up to 150 t/hr (Buttress et al., 2017; Batchelor et al., 2017). The aim was to demonstrate the viability of a pilot-scale system that could then be scaled up to a large-scale system that could be deployed for mine site operations. The applicator design criteria for this system are briefly discussed, a flowsheet is described, and the comminution results derived from this system are summarised in this section.

The applicator design was one of the most important aspects of this system because it dictates the treatment performance. Unlike other high-throughput microwave heating systems that use conveyor belts to expose the sample to the applicator, this system utilised a vertically aligned tube through which materials flow as a packed bed to interact with microwave fields. Furthermore, the applicator incorporated corrugated circular chokes (reactive) and resistive

chokes (filled with carbon foam). This configuration was preferred because it maximizes the system performance in the following ways:

i.   Reactive chokes - confine the electric fields by reflecting the escaping power back to the applicator.

ii. Resistive chokes - prevent microwave leakage to the environment at the top and bottom sections of the tube in order to comply with Electromagnetic Compatibility (EMC) legislation.

iii. The packed bed of ore fragments and fines – minimize air gaps which can be a potential source of electrical arcing during microwave treatment, which could damage the sample and the treatment tube, thereby lowering the system's performance.

This configuration ensures that the electric field is confined to a small region in the applicator (the hot spot), lowering the heat conduction effect of the heated phases to the bulk ore. This effect maximizes the temperature gradient between the heated and non-heated phases, which in turn maximizes the induced stresses (thermal shock) and causes ore fracturing at a low microwave energy input. The tube was connected to one single mode applicator (phase I), then to two single mode applicators connected in series (phase II), each of which was coupled to a 100-kW generator (operating at 896 MHz) via a WR975 waveguide (Figure 3.17). The dual applicator configuration increased the homogeneity of the electric field distribution through the cross-sectional area of the applicator, which maximizes the chances for each fragment to receive an equal energy dose.

The treatment tube is made of Ultra-High Molecular Weight Polyethylene (UHMW-PE). This material was preferred because of its microwave-transparent properties and greater mechanical robustness. The inner diameter of the tube was chosen to be 200 mm for effective material flow without blockage. This size is at least five times the coarsest ore fragment tested (-50.8+25.4 mm), as recommended by Jenike (1964).
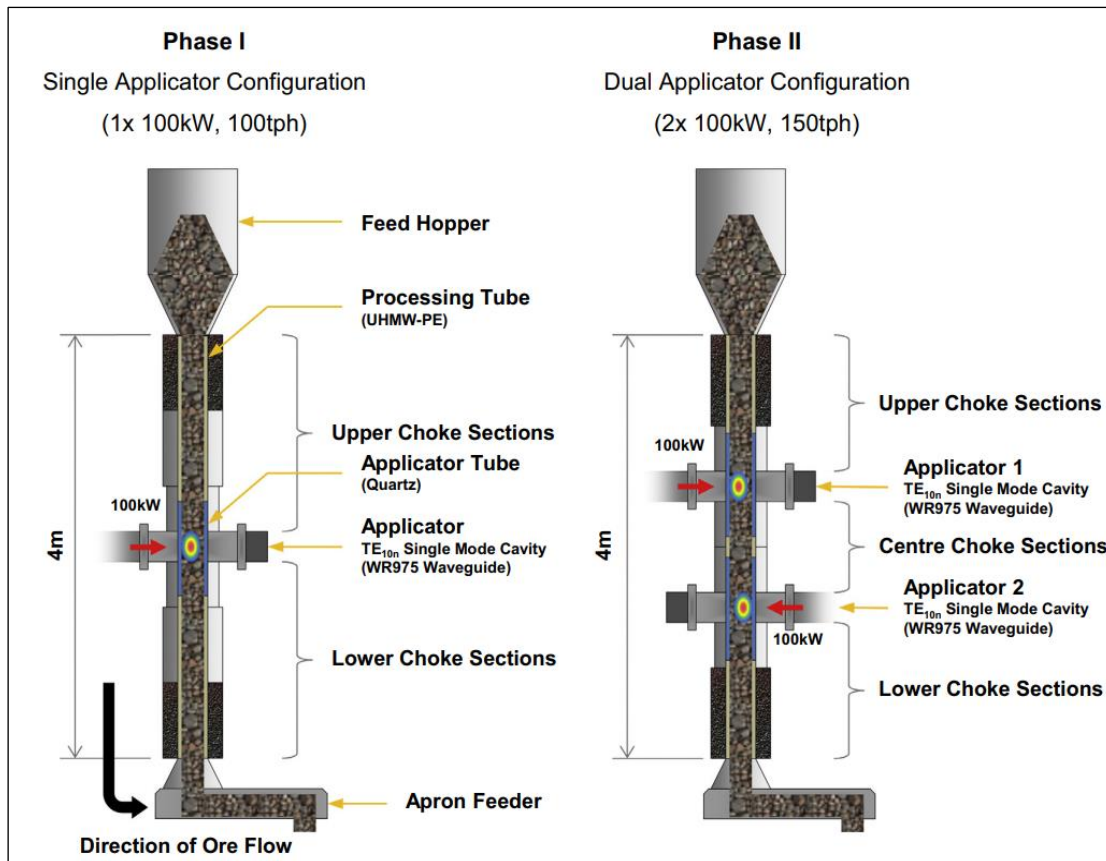
Figure 3.17. Vertical flow configuration of the 100 tph single applicator (left) and 150 tph dual applicator systems (right) (Buttress et al., 2017)

Figure 3.18 depicts the pilot plant system layout. Feed materials (ore and ore fines) were loaded from bags into separate feed bins A01-A04 using a jig crane J01. These materials are transferred by the bin discharge conveyors C01-C04 at different rates to the main feed conveyor C05. Thereafter, materials are transferred by the bucket elevator E01 to the feed hopper A05 via a transfer conveyor C06. From the feed hopper, materials flow down as a packed bed to the applicator AT01 to interact with microwave energy supplied by two generators M01 and M02. The flow of material through the tube is controlled by the apron feeder FD01. Finally, the treated materials are transferred to the discharge bins DB01-DB04 via discharge conveyor C08.
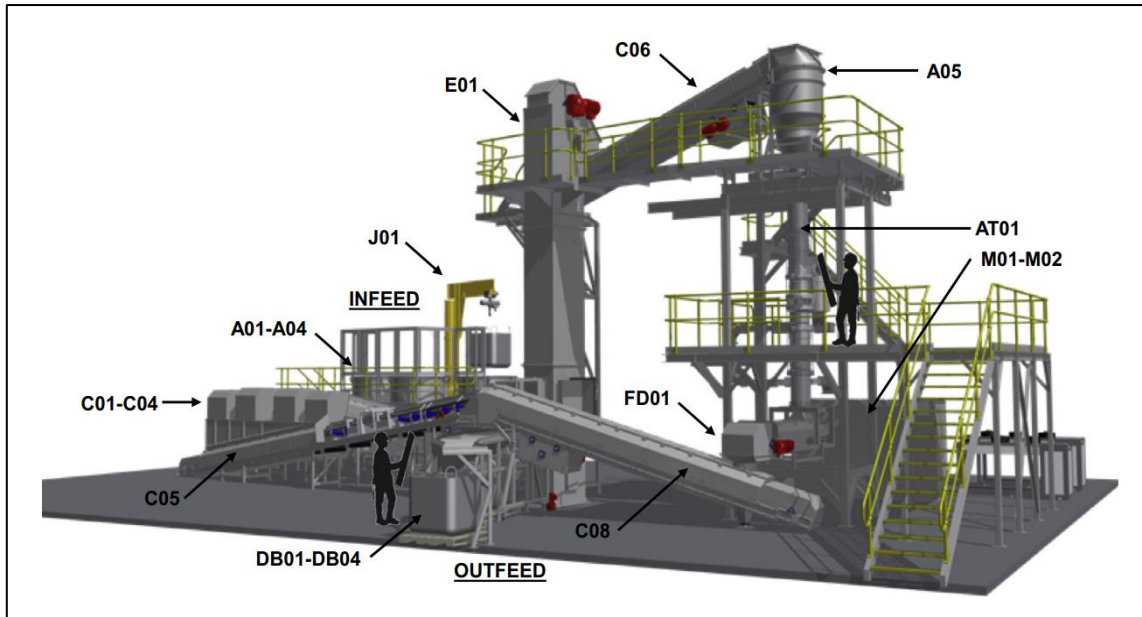
Figure 3.18. Pilot plant layout of microwave ore pre-treatment (Buttress et al., 2017)

Batchelor et al. (2017) evaluated the performance of this treatment system using three different porphyry copper ore types. The extent of microwave-induced damage was quantified using BBWI, DWT, and JKGem Ci techniques. As stated earlier, the testwork was conducted in two phases using a throughput rate of about 30-150 t/h at low specific energy inputs of between 0.3-3 kWh/t to achieve bulk microwave power densities of about 3.3×10^6 - 6.6×10^6 W/m^3. Table 3.4 provides a summary of microwave treatment conditions in both phases. The BBWI and the JKGem ci tests were conducted based on the standard procedure described by Bond (1961) and Kojovic et al. (2010), respectively. Due to mass constraints, a modified DWT was performed using a -31.5+26.5 mm fraction only.

Table 3.4. Microwave treatment conditions in both phases (Batchelor et al., 2017)

Test ID	Power (kW)	Throughput (t/h)	Dose (kWh/t)	Average power density (W/m³)
Phase I				
Ore 1				
T1	1×100	70	1.4	$6.6×10^6$
T2	1×100	50	2.0	$6.6×10^6$
T3	1×100	30	3.3	$6.6×10^6$
Ore 2				
T1	1×100	70	1.4	$6.6×10^6$
T2	1×100	50	2.0	$6.6×10^6$
T3	1×100	30	3.3	$6.6×10^6$
Ore 3				
T1	1×100	70	1.4	$6.6×10^6$
T2	1×100	50	2.0	$6.6×10^6$
T3	1×100	30	3.3	$6.6×10^6$
Phase II				
Ore 1				
T4	2×50	150	0.7[2×0.3]	$3.3×10^6$
T5	2×75	150	1.0[2×0.5]	$5.0×10^6$
T6	2×100	150	1.3[2×0.7]	$6.6×10^6$
Ore 2				
T4	2×50	150	0.7[2×0.3]	$3.3×10^6$
T5	2×75	150	1.0[2×0.5]	$5.0×10^6$
T6	2×80	120	1.3[2×0.7]	$5.3×10^6$

The grinding results of ore 2 showed a reduction in BBWI of 5.0-8.7% for the dual applicator (at $3.3\text{-}5.3\text{x}10^6$ W/m³) against a reduction of 2.6% for the single applicator (at $6.6 \text{ x}10^6$ W/m³), as shown in Table 3.5. This suggests that exposing more ore to a region of high electric field strength promotes more fractures and thus higher strength reduction is achieved. The DWT results of ores tested showed a strength reduction (A*b) of 7% to 14% (Table 3.6), and the JKGem Ci results showed a beneficial change of up to 35% in terms of percentage passing 4.75 mm sieve size. Also, mineral liberation results on the treated ore showed that equivalent liberation may be achieved for a grind size of about 40–70 µm coarser than that of untreated ore.

Based on the comminution results derived from this pilot system, flow sheet simulations indicated that the reduced ore competency following microwave treatment at 0.7–1.3 kWh/t could potentially yield up to a 9% reduction in specific comminution energy (Ecs) at a nominal

plant grind of P_{80}=190 µm, or up to 24% reduction at a grind size of P_{80}=290 µm. Furthermore, depending on grind size and ore type, throughput could be increased by up to 30%.

Table 3.5. BBWI test summary (Batchelor et al., 2017)

Test ID	F_{80}(µm) Mean	σ	P_{80}(µm) Mean	σ	Gbp (g/rev) Mean	σ	BBMWi (kWh/t) Mean	σ	CoV (%)	Beneficial change (%)	Confidence level (%)
Ore 1											
UT2	2061	16	161	0.6	3.393	0.098	9.27	0.21	2.3	-	-
T4	2038	3	162	0.6	3.445	0.047	9.19	0.08	0.9	0.9	44
T5	2057	24	161	0.6	3.501	0.030	9.03	0.06	0.7	2.5	86
T6	2047	3	162	0.6	3.421	0.016	9.23	0.02	0.3	0.4	24
Ore 2											
UT1	2108	11	113	0.0	1.716	0.003	13.76	0.03	0.2	-	-
T2	2121	25	113	0.0	1.770	0.006	13.41	0.06	0.4	2.6	98
UT2	2140	37	156	0.6	2.028	0.026	13.69	0.17	1.3	-	-
T4	2112	14	157	0.6	2.284	0.030	12.50	0.10	0.8	8.7	100
T5	2135	21	157	0.6	2.181	0.041	13.00	0.21	1.6	5.0	99
T6	2134	17	158	1.0	2.255	0.025	12.69	0.11	0.8	7.3	100

Table 3.6. JKDW test A*b values (Batchelor et al., 2017)
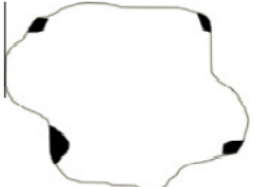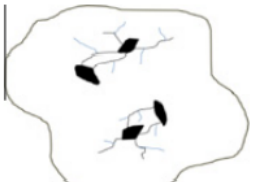
Test ID	Modified JKDW	Full JKDW	Calculated JKDW A*b	Change (%)
Ore 1				
UT	-	56.3	56.3	-
T	-	-	60.2	7
UT2	43.0	44.9	44.9	-
T4	46.7	N/A	48.1	7
T5	40.1	N/A	41.3	-8
T6	40.3	N/A	41.5	-8
Ore 2				
UT	-	36.6	36.6	-
T	-	-	39.2	7
UT2	45.8	39.3	39.3	-
T4	46.2	N/A	39.6	1
T5	45.8	N/A	39.3	0
T6	52.2	N/A	44.8	14
Ore 3				
UT	-	73.8	73.8	-
T	-	-	79.0	7

The investigation performed in this pilot-scale plant has demonstrated the potential of scaling up microwave ore pre-treatment continuous systems by integrating electromagnetic design with material handling systems. Since only porphyry copper ores were tested in this system, other ore types should be investigated in order to gain a better understanding of the system's performance. Furthermore, higher throughputs than 150 t/h should be tested in a system like this to explore the possibilities and limitations, given that most mines are currently operating at higher throughputs to maximize metal productivity due to the declining ore grades.

3.6 Microwave Ore Pre-treatment to Assist Leaching

In the context of mineral processing, leaching can be defined as a chemical process in which minerals are selectively dissolved from ores using appropriate chemicals, such as sulphuric acid for copper oxide ores or sodium cyanide for gold ores. Prior to leaching, the ore is crushed and ground in several stages to expose minerals of interest for effective dissolution. The kinetics of mineral dissolution is dependent on the accessibility of leach solution to the mineral grains and the rate of chemical reaction (Marsden & House, 2006). Table 3.7 shows five different classes of mineral grains based on their accessibility to leach solution (Ghorbani et al., 2011). Microwave treatment of ores can potentially improve mineral accessibility through a network of induced fractures, which can be represented by classes (b) and (c).

Table 3.7. Classification of mineral grains based on their accessibility to leach solution (Ghorbani et al., 2011)

Classes	Illustration
(a) Grains exposed to the leach solutions at the surface of particles	
(b) Grains exposed to the leach solutions via pores or cracks	
(c) Grains which become exposed to the leach solutions only after other grains have reacted	
(d) Grains from which pores or fissures that do not extend to the particle surface depart	
(e) Grains located inside the particles and not connected to a pore	

The kinetics of mineral dissolution is commonly described using the shrinking-core model (SCM), which assumes a particle as a sphere with an unreacted core that shrinks in size as leaching progresses (Crundwell, 1995). According to this model, the extent of mineral grain dissolution is dependent on their position within the particle, so mineral grains near the edge leach faster than those in the centre (Ghorbani et al., 2013a). Fractured particles (e.g., from microwave treatment) can provide leaching pathways to dissolve some of the mineral grains located at the core via a network of induced cracks (e.g., grains marked X, Y, Z in Figure 3.19), resulting in improved leaching kinetics and overall metal extraction.
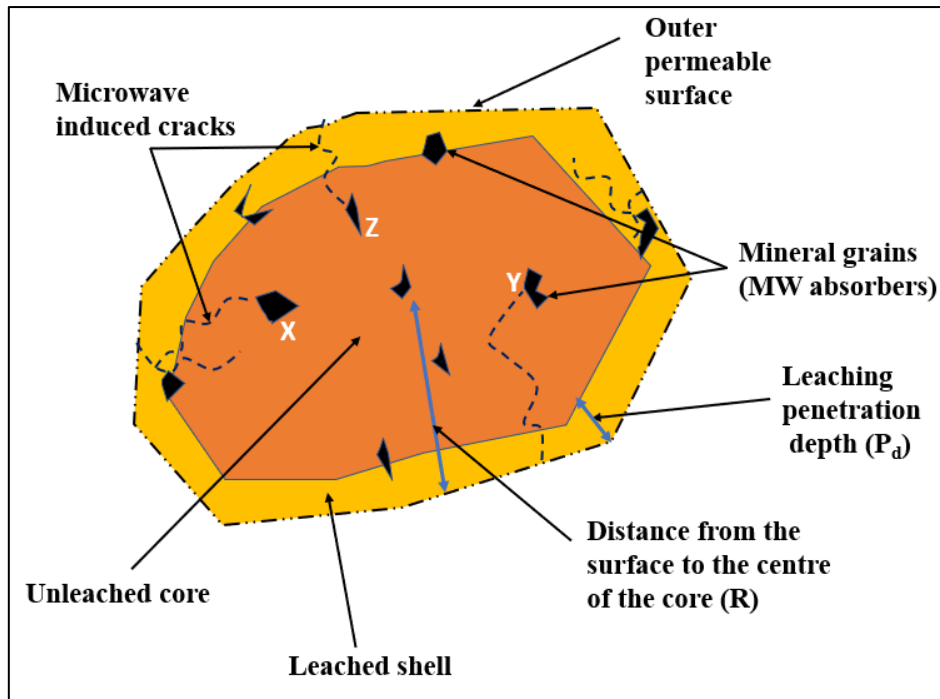
Figure 3.19. Leaching of a cracked particle (adapted from Ghorbani et al., 2013a)

Using various ore types and leaching methodologies, several researchers have demonstrated that microwave ore pre-treatment can potentially improve metal leach extraction. The findings of those studies are briefly discussed in this section.

Olubambi et al. (2007) tested whether microwave pre-treatment could improve the dissolution of low-grade complex sulphide ore. Batches of 100 grams of ore samples were irradiated in a multimode cavity at 1100 Watts for 5 minutes. The dissolution rate was investigated using the potentiodynamic polarisation technique in sulphuric and hydrochloric acids, both at a concentration of 1 molar. The microwave-treated and untreated samples (each weighing 0.4 grams) were individually powdered, mixed with powdered graphite (0.6 grams) and silicon oil (0.7 mls). This mixture was compressed under pressure using a carbon paste electrode holder to make working electrodes in the electrochemical cell. Results showed that higher dissolution rates of up to 2.1×10^{-2} mm/yr were achieved for the treated sample versus 9.2×10^{-3} mm/yr for the untreated sample. The authors suggested that the observed mineral dissolution enhancement could be attributed to microwave-induced cracks that serve as electrochemical sites (regions

where leach solution interacts with exposed minerals). Furthermore, the increase in pyrite phases detected by XRD analysis of microwaved samples could have promoted galvanic interaction, facilitating covellite and galena dissolution.

Galvanic interaction exists when two sulphide minerals with different rest potentials are in direct contact with each other in an acid-aqueous solution. In such a system, a mineral with a higher rest potential (e.g., pyrite) acts as the cathode and is preserved, whereas a mineral with a lower rest potential (e.g., covellite) acts as the anode and is oxidised (Mehta & Murr, 1983; Ghorbani et al., 2013b). This suggests that the anodic reaction takes place on the covellite surfaces, whereas the fast-cathodic reduction occurs on the pyrite surface, because pyrite has a higher rest potential than covellite, see Table 3.8 (Kocabag & Smith, 1985; Dixon & Tshilombo, 2010).

Table 3.8. Rest potential at pH 4 (Mehta & Murr, 1983; Kocabag & Smith, 1985)

Mineral	Chemical formula	Rest potential (V, SHE)
Pyrite	FeS_2	0.66
Marcasite	FeS_2	0.63
Chalcopyrite	$CuFeS_2$	0.56
Sphalerite	$(Zn,Fe)S$	0.46
Covellite	CuS	0.45
Bornite	Cu_5FeS_4	0.42
Galena	PbS	0.40
Argentite	Ag_2S	0.28
Stibnite	Sb_2S_3	0.12

In another study, Olubambi (2009) examined the effect of microwave treatment of a low-grade complex sulphide ore on bioleaching using mixed mesophilic bacteria. Microwave treatment tests were carried out in a multimode cavity at a maximum power of 0.11 kW with 5 minutes of irradiation time. Leaching tests were conducted in an incubator shaker at a temperature of 32-35°C. Higher metal recoveries of up to 92.4% zinc and 51.7% copper were achieved after 18 days of leaching time for the microwaved sample, compared to a recovery of 84.3% zinc

and 38.2% copper for the untreated sample. The higher metal recoveries observed in the microwave-treated samples were attributed to an increase in electrochemical sites (i.e., induced cracks), and an increase in pyrite phases which promoted galvanic interactions.

Schmuhl et al. (2011) used a copper sulphide ore to study the effect of microwave treatment on copper dissolution for two different size fractions (+9.2-12.5 mm and +13-19 mm). Batches of 50-200 grams were microwave irradiated in a single mode cavity using a continuous or pulse mode, which were then combined to obtain 6-kg batches of each size fraction for continuous column leach tests. The leach solution containing sulphuric acid and ferric sulphate was pumped from the bottom to flood the column, ensuring consistent and total wetting of the ore particles by the leach solution. Leaching tests were carried out at ambient temperature (25°C) for a period of up to 25 days.

Results showed that after an initial increase, the degree of copper enhancement due to microwave treatment for the finer size fraction (+9.2-12.5 mm) stabilised at around 7% over a period of 11 days. On the other hand, the enhancement for the coarse fraction (+13-19 mm) stabilised at around 12% for 25 days. Suggesting that coarse particles are more susceptible to microwave irradiation than fine particles. This is due to the larger volume of microwave-absorbing phases contained in the coarse particles, which are mostly surrounded by the microwave-transparent gangue matrix, supporting the formation and propagation of fractures. It was concluded that microwave ore pre-treatment has the potential to improve metal leach recovery for coarse particles (with fine sulphide mineralization), which may improve the economics of heap leaching of low-grade ores.

Amankwah & Ofori-Sarpong (2011) evaluated the effect of microwave treatment of free-milling gold ore on mineral dissolution. The ore contained quartz and aluminosilicate (microwave transparent matrix) together with magnetite and hematite (microwave absorbent

minerals). The ore (-3.4+0.25 mm) was microwave pre-treated for up to 5 minutes at 700 Watts in a multimode cavity. The ore was then crushed and wet milled to $P_{80} = 75$ µm, before being subjected to bottle roll cyanide leaching at 40% solids at an alkaline pH of 10.5. The cyanide concentration was 500 ppm and the leach duration was 24 hours. The gold recovery for the treated sample was 70% after 4 hours of leaching and increased to 97% after 12 hours, compared to a recovery of 42% after 4 hours and 92% after 24 hours for the untreated sample. The leaching enhancement observed in the treated sample was attributed to microwave-induced fractures due to selective heating and differential thermal expansion between the excellent microwave heaters (e.g., magnetite) and transparent gangue minerals (e.g., quartz). It was concluded that microwave treatment of ores can potentially improve the mineral dissolution in free-milling gold ores.

Charikinya & Bradshaw (2017) used coarsely crushed sphalerite ore to demonstrate whether microwave energy could improve metal recovery in heap leaching operations. Three different size fractions (25+19 mm, 16+9.5 mm, 5+4.75 mm) were individually subjected to microwave treatment in a single mode cavity at specific microwave energies between 2 and 5 kWh/t. Leaching was carried out in flooded bed reactors operated in a continuous mode. The leach solution containing ferrous ions and sulphuric acid was pumped from the bottom using a peristaltic pump. This mode of operation was selected in order to eliminate the channelling and spatial distribution of microorganisms that could influence leaching results. The leach columns were inoculated with a mixed culture of mesophilic acidophilic chemolithotrophs. The leach temperature was maintained at 30°C for a long period of 350 days. Results showed that microwave ore pre-treatment improved the overall zinc recovery by 23-26% for the size fractions tested. The improved zinc recovery is attributed to microwave-induced fractures, which were observed on the X-ray CT scans of the same sample in a parallel study reported by Charikinya et al. (2015). It was concluded that microwave treatment has the potential to

improve metal recovery in heap leach leaching operations, which typically achieve poor metal recoveries despite longer leach duration.

Several authors have demonstrated in Section 3.5 that mineralogy and texture play an important role in dictating the extent of microwave-induced fractures. However, most leaching studies discussed here have used a single ore to evaluate the leaching performance of microwave pre-treated ores. For a better understanding, the current study has used five different copper porphyry ores to investigate the influence of mineralogy and texture on the leaching performance resulting from microwave-induced fractures.

3.7 Roasting Pre-treatment of Refractory Gold Ores

Refractory gold ores contain gold that is locked within pyrite or arsenopyrite, making it inaccessible to cyanide solution. These ores may also contain naturally carbonaceous materials that adsorb the solubilized gold cyanide complex from the leach solution. Consequently, such ores do not give economic recoveries upon the conventional cyanidation process (La Brooy et al., 1994). Low gold recoveries of up to 20% have been achieved from the highly carbonaceous ores (Stenebråten et al., 2000), the worst recovery of 0% was reported by Pyke et al. (1999).

Roasting as a pre-treatment is the most attractive technique for ores that contain both sulphides and carbonaceous components. The aim is to produce a highly porous iron oxide calcine in which gold is highly liberated and free of carbonaceous materials that could otherwise inhibit gold dissolution or adsorption processes. The roasting process of refractory ores under oxidizing conditions involves complete oxidation of the sulphide minerals and carbonaceous material, as represented by the chemical Equations 3.1 to 3.4 (Komnitsas & Pooley, 1989).

i. Oxidation of pyrite or arsenopyrite to magnetite

$$3FeS_2 + 8O_2 \rightarrow Fe_3O_4 + 6SO_2 \tag{3.1}$$

$$12FeAsS + 29O_2 \rightarrow 4Fe_3O_4 + 6As_2O_3 + 12SO_2 \tag{3.2}$$
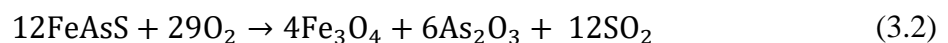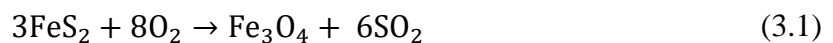
Then, magnetite is further oxidized to hematite

$$4Fe_3O_4 + O_2 \rightarrow 6Fe_2O_3 \tag{3.3}$$

ii.   Oxidation of carbonaceous components to carbon dioxide

$$C + O_2 \rightarrow CO_2 \tag{3.4}$$

The optimum roasting conditions vary depending on ore mineralogy, ore particle size, and oxygen flow rate. Typical roasting temperatures of about 500-700°C and oxygen supplies of 6-8% in excess of stochiometric requirement are desirable. The calcine is not fully oxidised at low temperatures (400°C), whereas at high temperatures (>700°C), the calcine is sintered, forming impenetrable coatings that render the gold inaccessible in subsequent recovery processes (Figure 3.20). The particle size distribution of roaster feed should be narrow to avoid over-roasting of fine particles or under-roasting of coarse particles, typically in the range of 75-150 μm (Marsden & House, 2006).
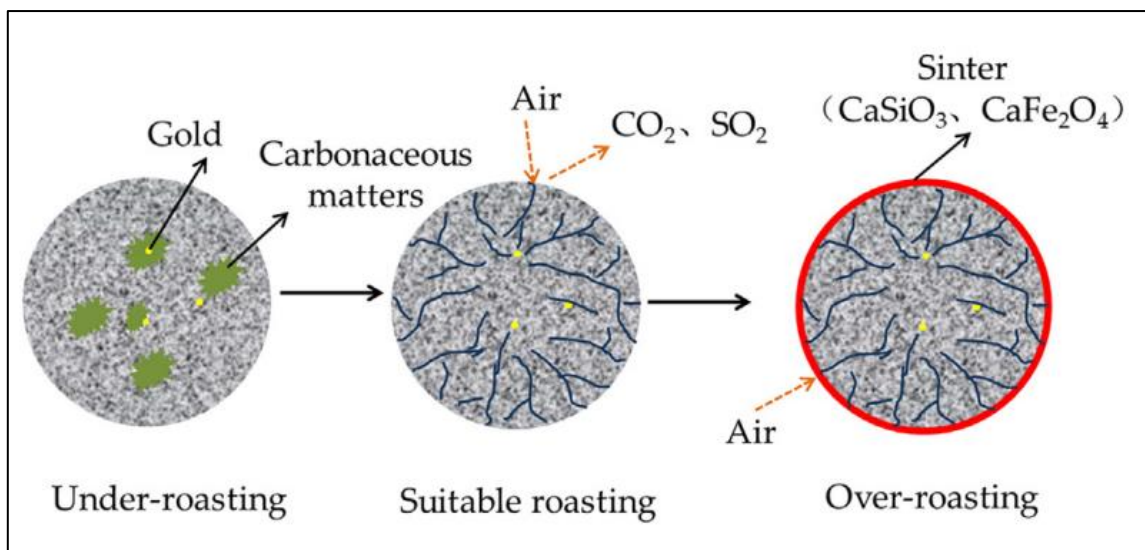
Figure 3.20. Three possible calcine products (Jin et al., 2019)

Depending upon the ore mineralogy of the roaster feed, the off-gases may contain significant amounts of various gases of environmental concern (e.g., sulphur dioxide and arsenic trioxide), which must be extensively cleaned before discharge to meet stringent environmental legislation. Lime or limestone can be added to the ore to react with SO_2 to form gypsum, a stable and inert compound. Also, the naturally occurring carbonates in the ore may fix SO_2 during oxidation, reducing lime consumption (Fraser et al., 1991). The SO_2 generated during roasting can be coupled with the cyanide detoxification (INCO SO_2/air) process to minimize cyanide levels in the tailings before discharge.

3.7.1 Microwave Roasting of Refractory Gold Ores and Concentrates

The carbonaceous materials in refractory gold ores that reduce gold recovery are mostly crystalline graphite (Helm et al., 2009). According to Hotta et al. (2011), the loss factor (ε_r'') of carbonaceous materials increases with the degree of graphitization. The sulphide minerals that occlude gold in refractory ores, on the other hand, are excellent microwave heaters due to their semiconducting properties. The heating response of sulphide and carbonaceous rocks has been investigated by Van Weert & Kondos (2007). The fragments were irradiated, and the maximum temperature attained was measured using an infrared (IR) gun. Based on the maximum temperature attained, the fragments were classified as hot, medium, or cold. Both sulphidic and carbonaceous fragments were classified as hot material.

The higher microwave heating response of sulphide minerals and carbonaceous (graphitic) materials suggests that refractory gold ores or concentrates should heat up faster when exposed to microwave fields, producing porous calcines that are easy to leach and potentially improving metal extraction. Several researchers have used microwave energy to pre-treat (roast) the refractory gold ores or concentrates in order to improve mineral dissolution. These studies are reviewed in this section.

Haque (1987) applied microwave energy to treat refractory arsenopyritic concentrates prior to leaching. More than 80% of arsenic and sulphur were volatilized as As_2O_3 and SO_2, producing a hematite (Fe_2O_3) calcine at 550°C, resulting in higher metal recoveries of up to 98% (Au) and 60% (Ag) by cyanidation leaching. To prevent the oxidation of arsenic and sulphur, the concentrate was then irradiated in an N_2 atmosphere in a sealed silica tube. In this case, the sulphur and arsenic were mostly volatilized off as As_2S_3 and iron remained in the calcine as pyrrhotite (FeS). However, the gold recovery following cyanidation was only 89%, indicating that almost complete calcination of the concentrate is required for efficient gold extraction. It was concluded that microwave energy has a sound technological potential in the pre-treatment of refractory arsenopyritic gold ores or concentrates.

Nanthakumar et al. (2007) compared the effect of microwave roasting versus conventional roasting on cyanide leaching using a refractory gold ore. Microwave roasting tests were carried out in a multimode cavity at 700 Watts for up to 84 minutes. However, the preg-robbers could not be eliminated even after such a long irradiation time. The reason for this could be linked to the poor heating response of this ore upon microwave irradiation due to its low loss factor (ε''= 0.07-0.02) over a wide temperature range at 2.45 GHz. An attempt was then made to indirectly roast the ore by microwaves using magnetite as a susceptor. In this case, magnetite is strongly heated by microwave energy, and this heat is then transferred to the ore via conduction. The indirect microwave roasting of this ore reduced the total carbon content from 6% to about 1% (i.e., 83% reduction) after 40 minutes of irradiation, with a rapid initial decrease and a slow decrease thereafter beyond 20 minutes. The sulphide sulphur was also eliminated after 5 minutes. As a result, the gold recovery by cyanidation increased to over 98%, whereas the same recovery was achieved after 24 hours of conventional roasting.

In connection to the initial work by Nanthakumar et al. (2007), a study was conducted by Amankwah & Pickles (2009) using another gold ore sample. The loss factor of this ore was higher than that of the initial work (up to $\varepsilon''=70$) after the critical temperature (400°C) at 2.45 GHz, such that the indirect roasting was unnecessary because the ore heated strongly when directly exposed to microwave fields. The total carbon content removal at 600 Watts was over 75% in less than one hour of irradiation, whereas the same degree of carbon removal required up to 8 hours of conventional roasting at 600°C. Also, the sulphur removal was 90% after 30 minutes of microwave exposure versus 75% achieved by conventional roasting at 600°C. The heating rate by the conventional method was 31°C/min versus 110°C/min by the microwave method. Direct cyanidation of the microwaved calcine gave a poor gold recovery of 82%, this could be attributed to sintering. When the calcine was ground to remove the sintered coating, the gold recovery increased to 97%. Gold recoveries from calcine roasted in the conventional furnace at 600°C and 710°C were 85% and 96%, respectively. The authors concluded that microwave roasting facilities could potentially be incorporated into gold leaching plants for the rapid treatment of refractory gold ores.

Hua et al. (2006) used microwave energy for oxidative roasting of copper sulphide concentrate (containing chalcopyrite and pyrite) in the presence of calcium carbonate ($CaCO_3$) as a sulphur retention reagent. The roaster feed were pellets (3 mm diameter) made of a mixture of copper sulphide concentrate (65-76 µm) and $CaCO_3$ (43-65 µm) at a ratio of 1:1 to 1:4 by weight, respectively. These pellets were roasted in a microwave oven or conventional tube furnace, then ground to 76-50 µm prior to leaching by $NH_3-(NH_4)_2CO_3$ solution. Thirty-gram subsamples of pellets were irradiated for 10 minutes at three different power levels i.e., 452, 575, and 750 Watts. The conventional roasting was performed for 60 minutes at 600-900°C using 33 grams of pellets. Microwave roasting resulted in higher roasting kinetics (4–17 times larger) than conventional roasting, and the copper recovery attained by microwave roasting

was relatively higher (90-96.6%) than that of conventional roasting (71-77%). The copper recovery increased with increasing microwave power up to a point where a further power increase resulted in poor recovery due to sintering.

Choi et al. (2017) studied the influence of microwave roasting of flotation concentrate (38-45 µm) on gold recovery by thiourea leaching. Microwave roasting was carried out in a multimode cavity for 10-70 minutes at 1 kW (2.45 GHz), and leaching experiments were conducted for 1 hour at 70°C. The sulphur content was reduced by over 94% after 30 minutes of microwave exposure. The XRD pattern of the raw concentrate identified pyrite and quartz as the main mineral phases, whereas that of the calcine revealed the presence of hematite, pyrrhotite, and quartz, suggesting that pyrite was oxidised to hematite and pyrrhotite. Almost 100% gold recovery was achieved within 1 hour of leach time for the calcine product irradiated for 70 minutes, as opposed to a recovery of 78.1% from the raw concentrate.

Wang et al. (2019) assessed the effect of microwave roasting pre-treatment of refractory gold concentrate on leaching performance. Roasting experiments were carried out at a microwave power of 2.5 kW for 10-30 minutes, with the sample reaching a temperature of 300-500°C. The sulphur and carbon contents in the gold concentrate decreased as the roasting temperature increased. The carbon content decreased from 6.6% (untreated) to 5.9% (treated at 500°C), while the sulphur content decreased from 0.51% (untreated) to 0.39% (treated at 500°C). As a result, gold extraction increased significantly, from 65.8% (untreated) to 95.2% (treated at 500°C) for the same cyanidation leaching conditions. In a related study, Wang et al. (2020) reported higher gold extractions of up to 90.1% due to microwave roasting pre-treatment at 500°C versus a poor recovery of less than 70% for the untreated sample. The improved gold extraction due to microwave roasting in both studies is attributed to the reduction of sulphur and carbonaceous materials, as well as the formation of fractures on the calcines, thereby

weakening the preg-robbing effect and exposing the encapsulated gold to facilitate lixiviant permeability.

Amankwah & Ofori-Sarpong (2020) used a flash flotation concentrate to assess the effectiveness of microwave roasting and compare results with that of conventional roasting upon cyanide leaching. The as-received ore (containing carbonaceous matter, pyrite and arsenopyrite) was crushed and milled to $P_{80} = 220\,\mu m$, then floated to get the concentrate, which was then roasted prior to cyanide leaching. Microwave roasting was carried out in a multimode cavity using 800 Watts at 2.45 GHz for 20 to 60 minutes. The conventional roasting was performed in an electrical resistance furnace at 650-750°C for up to 8 hours. Over 90% of the sulphide sulphur was oxidised within 60 minutes of microwave roasting, compared to 76% and 88% sulphur oxidation achieved by conventional roasting at 650°C and 750°C, respectively. The gold recovery of up to 95.6% was achieved for the microwaved calcine, compared to a recovery of 84% and 91% for the conventionally roasted calcine at 650°C and 750°C, respectively.

3.7.2 Chlorination Roasting

Certain metals (e.g., gold and silver) can be readily volatilized from their ores by heat treatment in the presence of alkali halide salts. Varley et al. (1923) reported some of the earliest work conducted at the US Bureau of Mines on ore chlorination roasting. Higher losses of gold (>90%) and silver (>80%) were reported by roasting gold-silver bearing ores with alkali chloride salt at a concentration of 5.0-7.5%wt at elevated temperatures (750-1050°C) for 30-60 minutes. The loss of gold and silver is attributed to the formation of gold chloride and silver chloride in the vapour, respectively. The findings from these early studies provide possibilities for metal recovery from their ores via the adsorption of exhaust gases collected during chlorination roasting. Recently, several researchers have employed microwave energy for chlorination roasting of gold ores, and their findings are briefly discussed.

Zhu et al. (2018) compared the efficiency of microwave chlorination roasting with that of conventional roasting by a muffle furnace. The sample used for their work was gold tailings containing hematite and quartz. Calcium chloride ($CaCl_2$) was used as a chlorination agent, which decomposes to form chlorine gas that reacts with gold to form gaseous gold chloride. The testworks were conducted using various combinations of roasting times (15-40 minutes), temperatures (700-950°C), $CaCl_2$ concentrations (1-11%), and tailings particle size (200-1450 mesh). Microwave roasting results showed an increase in gold recovery from 69% to 96%, compared to 35% and 85% for conventional roasting at 700°C and 850°C, respectively. The higher gold recovery observed in microwave roasting was attributed to the induced microcracks on the calcine, which may have facilitated the reaction between chlorine and gold. These cracks were revealed in the SEM images of the microwave-calcine products.

Similarly, Li et al. (2020) examined the effect of microwave roasting of gold tailings (containing hematite, quartz and corundum) in the presence of calcium chloride. The procedure involved mixing gold tailings with anhydrous $CaCl_2$ and water, then pressing the pulp to form pellets with sizes ranging between 2 to 12 mm. The dried pellets weighing 30 grams were roasted in a microwave tube furnace at an average power of 1.2 kW for 15 minutes, and the exhaust gas was adsorbed by activated carbon soaked in an alkaline solution. The gold recovery was then determined based on the amount of gold in the raw tailings and the amount that remained in the calcine after roasting. The pellets' temperature reached up to 900°C after 16 minutes of microwave irradiation, resulting in a maximum gold recovery of 85%. The same gold recovery was achieved by conventional roasting at 1000°C, but at the expense of higher energy consumption (i.e., twice that of microwave roasting). The rapid heating rate observed in microwave roasting is likely attributed to the presence of hematite in the sample. It was concluded that microwave chlorination roasting is a potential and non-polluting method of recovering gold from gold-bearing tailings.

In a subsequent investigation, Li et al. (2021) conducted experiments on diagnostic roasting of gold tailings using microwave and conventional heat treatment methods. The aim was to identify the type of gold carriers contained within the tailings matrix. An electron probe microanalyzer (EPMA) showed that the gold in this sample exists in three forms: (1) Free gold, (2) Bare gold - gold located at the edges of the gangue matrix, (3) Locked gold - fully locked gold within pyrrhotite and quartz.

Roasting results indicated that gold recovery increases with an increase in roasting temperature. At 400°C, the recovery was about 22%, indicating that free gold was recovered. Following that, at 800°C, the recovery was 58%, indicating that free gold plus bare gold were recovered, with 36% belonging to bare gold alone. Finally, at 1100°C, the proportion of locked gold alone was 41%. Furthermore, microwave roasting yielded higher gold recovery and sulphur removal rate than conventional roasting. The authors suggested that a combination of microwave-induced defects caused by thermal stress and de-stabilization of the stable covalent bond of gangue matrix caused by microwave non-thermal effect may have contributed to the observed recovery improvement.

Despite the higher recovery improvements reported in these studies, localized heating or non-uniform heating is a common challenge encountered in microwave roasting of metal concentrates. This undesirable effect may cause over-roasting that may lead to sintering or under-roasting (incomplete oxidation), both effects lead to poor metal recovery. One potential solution to this problem is to use microwave-roasting fluidised bed systems to uniformly distribute heat and increase contact areas between the oxidation gas and solids.

3.8 Summary

Microwave treatment of ores has shown great potential in improving mineral processing systems such as comminution and leaching. The ore fracture mechanism due to microwave treatment is a result of thermal stresses caused by the rapid and selective heating of different mineral phases composed in the ore. For hydrated ores, fractures occur due to internal pressure resulting from steam generated when microwaves interact with the hydrated phases present in the ore. The extent of microwave-induced fractures is highly dependent on microwave treatment conditions (microwave power density and specific energy input) and intrinsic ore properties such as mineralogy, texture, and the thermal-mechanical properties of microwave-absorbent phases and transparent gangue matrix.

Using single mode cavities, significant comminution improvement can be achieved at higher microwave power density within a shorter irradiation time, which maximizes the temperature gradient (thermal shock) between the microwave-absorbent phases and the transparent gangue matrix within the ore, thereby promoting ore fracturing. In the context of mineralogy and texture, ores with good microwave heaters, coarse-grained, and/or poorly disseminated absorbent phases constrained in a hard gangue matrix promote the formation and propagation of induced fractures, thereby reducing ore strength and improving comminution. In terms of leaching, microwave-induced fractures in ore samples can provide extra surface area for mineral-lixiviant interactions, potentially improving metal extraction.

Moreover, microwave roasting pre-treatment of refractory gold ores or concentrates rapidly oxidises the sulphide and carbonaceous minerals that encapsulate gold, making it accessible to the leach solution and reducing the preg-robbing effect, thereby maximizing the gold leach extraction. However, the treatment time required for roasting is longer than that required in ore fracturing. This is because the aim of roasting pre-treatment is to heat the ore/concentrate until

the sulphides and carbonaceous minerals are oxidised, whereas in ore fracturing, only a thermal shock is required to induce fractures through rapid and selective heating of microwave-absorbent phases within a microwave-absorbent gangue matrix (i.e., maximising temperature gradient). In terms of microwave energy requirements, this suggests that roasting pre-treatment requires more energy than microwave-assisted ore fracturing.

Despite encouraging leaching results reported in the literature, the influence of mineralogy and texture on the leaching performance of microwave-treated ores (particularly copper sulphide ores) has not been fully investigated, given the fact that most microwave-assisted leaching studies were conducted using a single ore type. The current study investigates and quantifies the influence of mineralogy and texture on the extent of microwave-induced fractures and leaching performance using five porphyry copper sulphide ores of varying lithology. Furthermore, for the first time, the current study employs the X-ray CT technique to visualize and quantify microwave-induced fractures, as well as assess the leaching improvement resulting from these fractures using both image processing and assay results, thereby extending the current understanding of microwave heating technology in mineral processing systems.

4. EXPERIMENTAL TECHNIQUES

4.1 Introduction

As stated in Chapter 1, the aim of this research is to investigate the influence of ore mineralogy and texture on the extent of microwave-induced fractures and leaching performance. This is accomplished through several experimental techniques, including ore characterisation, microwave treatment and induced damage quantification, as well as elemental analysis. Ore characterisation was performed using the Mineral Liberation Analyser (MLA) and X-ray Diffraction (XRD) techniques. The magnitude of microwave-induced damage was quantified using three different techniques: point load test (PLT), ultra-pulse velocity (UPV), and X-ray computed tomography (X-ray CT). The inductively coupled plasma-atomic emission spectroscopy (ICP-AES) technique was used to quantify the extent of leaching improvement due to microwave treatment. This chapter provides a brief description of each of these techniques, with X-ray CT being covered in greater detail due to its significant role in this research.

4.1 Mineral Liberation Analyzer (MLA)

The Mineral Liberation Analyzer (MLA) is an effective characterisation technique that was chosen for this study because it provides qualitative and semi-quantitative mineralogical and textural information about ore specimens, which can help to assess the amenability of ores to microwave treatment. The MLA is essentially a scanning electron microscope (SEM) equipped with an energy-dispersive X-ray (EDX) spectrometer and software (for data acquisition and system automation) (Pszonka & Sala, 2018).

The working principle of the SEM-EDX system is illustrated in Figure 4.1. An electron gun emits electrons by thermionic emission from a V-shaped tungsten filament (cathode). The emitted electrons are accelerated down the column and then focused on a specimen by a set of magnetic lenses. Scanning coils (not shown in this figure) deflect the beam in a rastered fashion (back and forth) over a rectangular area of the specimen (Hafner, 2007). The interaction of the incident beam of electrons within the specimen produces three major effects: secondary electrons (SE), backscattered electrons (BSE), and characteristic X-rays radiation. A signal generated by each of these effects is measured by a separate detector, giving a distinct type of information about the sample.

The SE are generated by inelastic scattering of incoming electrons, leading to an ejection of weakly-bound electrons near the surface of the sample. The SE are responsible for the topographical and morphological contrast of the specimen. On the other hand, the BSE are generated by elastic scattering of the incoming electrons with the nucleus of the specimen atom. Materials with higher atomic numbers scatter more of the incoming electrons, and these materials appear brighter in the SEM image. Thus, the BSE provides compositional maps that relate to the differences in the average atomic number of materials in a specimen. The characteristic X-ray radiation is generated when a beam of incoming electrons penetrates and interacts with volume beneath the surface of the specimen (Mohammed & Abdullah, 2018), knocking off an electron from the specimen's atom innermost shell (K-shell). When an electron from the outer shell transits to fill the vacancy, energy is released in the form of X-ray photons. Measurements of the energies of X-ray radiations (EDX) give information about the chemical composition of the specimen by comparison to a library of reference spectra (Vernon-Parry, 2000).
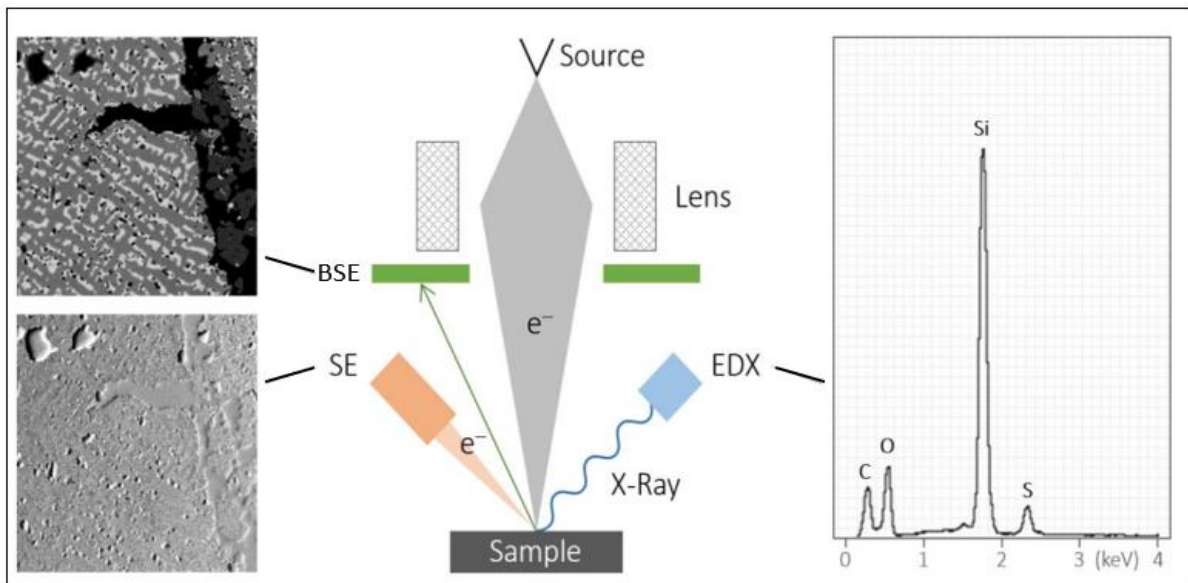
Figure 4.1. SEM-EDX system working principle (Heneka, 2019)

4.2 X-ray Diffraction (XRD)

X-ray diffraction (XRD) is a rapid analytical technique widely used for phase identification of crystalline materials (Westlake et al., 2012), and it was used in this study to quickly check the major mineral phases in the ores to support the MLA results. The XRD works by irradiating a sample with X-rays, and the X-rays are diffracted by the sample and collected at the detector. X-rays are used in XRD measurements because their wavelengths are comparable to the interplanar atomic spacing of crystalline materials (0.2-10 nm) (Speakman, 2011). Figure 4.2 illustrates the X-ray reflection in a crystalline material with two successive planes of atoms. If the X-rays from the top path and bottom path are in phase with each other, constructive interference occurs. This type of interference occurs when the relationship between interplanar atomic spacing (d-spacing), the wavelength of incident radiation (λ), and the angle of diffraction (θ) satisfies Bragg's law (Elton & Jackson, 1966), given in Equation 4.1. Thus, diffracted waves will interfere constructively if the path lengths of the two X-ray beams vary by a multiple of wavelengths.
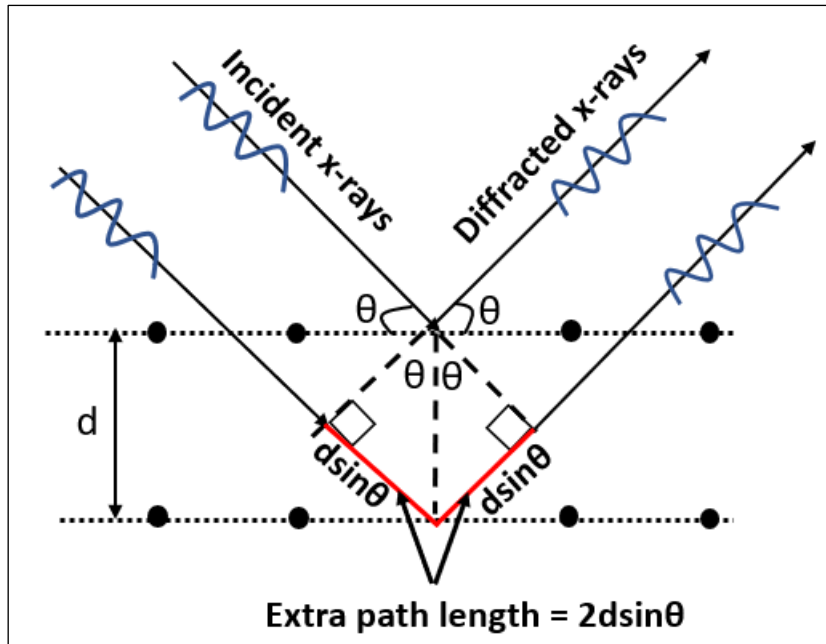
Figure 4.2. Illustration of X-ray reflection in a crystalline material (adapted from Unruh & Forbes, 2019)

$$n\lambda = 2d\sin\theta \qquad (4.1)$$

Where;

n = Integer,

λ = Wavelength (Å),

θ = Diffraction angle (degrees),

d = Interplanar spacing.

X-ray diffractometers work by positioning a crystalline specimen in a path of a monochromatic X-ray beam. To satisfy the conditions of Bragg's law for diffraction, both the X-ray source and the X-ray detector rotates to allow scanning the sample through a range of diffraction angles (2θ), and thus all possible diffraction directions of the lattice should be attained due to the random orientation of the powdered specimen (Bunaciu et al., 2015). The diffracted X-rays are recorded and counted by the detector, producing a distinct diffraction pattern which relates to the crystal lattice of the specimen, since each crystalline material has a different atomic

arrangement. Material identification is accomplished by comparing the measured diffraction pattern with standard reference patterns.

4.1 Point Load Test (PLT)

The point load test (PLT) is a widely accepted technique for determining the mechanical strength of rock specimens. This technique was used in this study to quantify the extent of microwave-induced damage by comparing the strength of treated and untreated ore samples. The test device essentially consists of a rigid loading frame with two-tip conical hardened-steel platens of standard dimensions, hydraulic ram assembly and a digital readout display. The width and depth of the specimen are measured, and the specimen is compressed between the two tips until it fails (Figure 4.3), and the maximum load before failure is recorded. The loading system shall have a loading frame with a platen-to-platen clearance that allows testing of rock specimens in the required size range so that an adjustable distance is available to accommodate both small and large specimens (ASTM, 1995). Also, the loading capacity should be sufficient to break the strongest specimens.
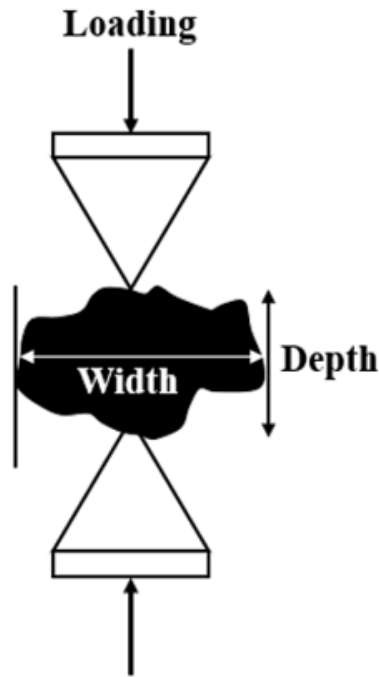
Figure 4.3. Point load test working principle

The PLT technique can be used to test both regular (e.g., cores and cut blocks) and irregular rock specimens, so irregular fragments do not require machining before measurements. The most important limitation of this technique is that the loading is applied in a small area that does not adequately represent the entire rock specimen, which is variably heterogeneous and anisotropic. To minimize the effect of sample variability on the PLT results, many rock specimens should be tested in each size fraction (>20 fragments) (Broch & Franklin, 1972; ASTM, 1995). The test determines the point load index (Is - uncorrected) for the standard 50 mm core diameter using Equation 4.2. For rock samples of other dimensions and shapes, the index is corrected to the standard equivalent core size of 50 mm using Equation 4.3. The constants F and D_e represent the size correction factor and equivalent diameter, respectively, as defined by Equations 4.4 and 4.5 (Brook, 1985). The final expression for the corrected point load index $Is_{(50)}$ is shown in Equation 4.6.

$$Is = \frac{P}{D^2} \tag{4.2}$$

$$Is_{50} = F\frac{P}{D_e{}^2} \tag{4.3}$$

$$F = [\frac{D}{50}]^{0.45} \tag{4.4}$$

$$D_e = [\frac{4 \times W \times D}{\pi}]^{0.5} \tag{4.5}$$

$$Is_{(50)} = \left[\frac{P \times \left(\frac{D}{50}\right)^{0.45}}{\frac{4 \times W \times D}{\pi}}\right] \tag{4.6}$$

Where;

P = Load at failure (N),

D = Depth dimension (mm),

W= Width dimension (mm),

D_e = Equivalent core diameter,

$Is_{(50)}$ = Point Load Index (MPa),

F = Size correction factor.

4.2 Ultra-Pulse Velocity (UPV) Testing

Ultra-pulse velocity (UPV) testing is a non-destructive method for detecting discontinuities (internal defects) in solid structures (e.g., rock samples) using high-frequency sound waves above the upper limit of human hearing (>20 kHz) (Krautkrämer & Krautkrämer, 2013). Sound waves travel at different speeds through different mediums, and the dominant factors influencing the velocity of sound waves for a given material are its density and elasticity, as expressed by Equation 4.7 (Hellier, 2003). The velocity of sound through a solid material (e.g.,

ore specimen) is reduced to some extent due to a change in medium (e.g., air voids or defects) along its path length because the speed of sound in air is lower than in solids. Thus, making UPV testing applicable for detecting and quantifying microwave-induced fractures. This technique has also been used by other researchers in microwave ore pre-treatment studies (Kobusheshe, 2010; Batchelor, 2013).

$$V_c = \sqrt{\frac{E}{\rho}\frac{1-\sigma}{(1+\sigma)(1-2\sigma)}} \qquad (4.7)$$

Where;

V_c = Compression wave velocity (m/s),

E = Young's modulus of elasticity (N/m^2),

ρ = material density (kg/m^3),

σ = Poisson's ratio.

The principle of operation of UPV device is illustrated in Figure 4.4. The pulse generator creates repetitive electrical pulses, which are then converted to mechanical vibrations by the transmitted transducer. These vibrations travel through the specimen (e.g., ore sample) to the receiving transducer, which converts the vibrations back to an electrical signal and amplifies it prior to measurement. The electronic timing circuit measures the transit time across the ore specimen with a known path length, which helps in determining the velocity of longitudinal waves (the fastest mode of propagation).
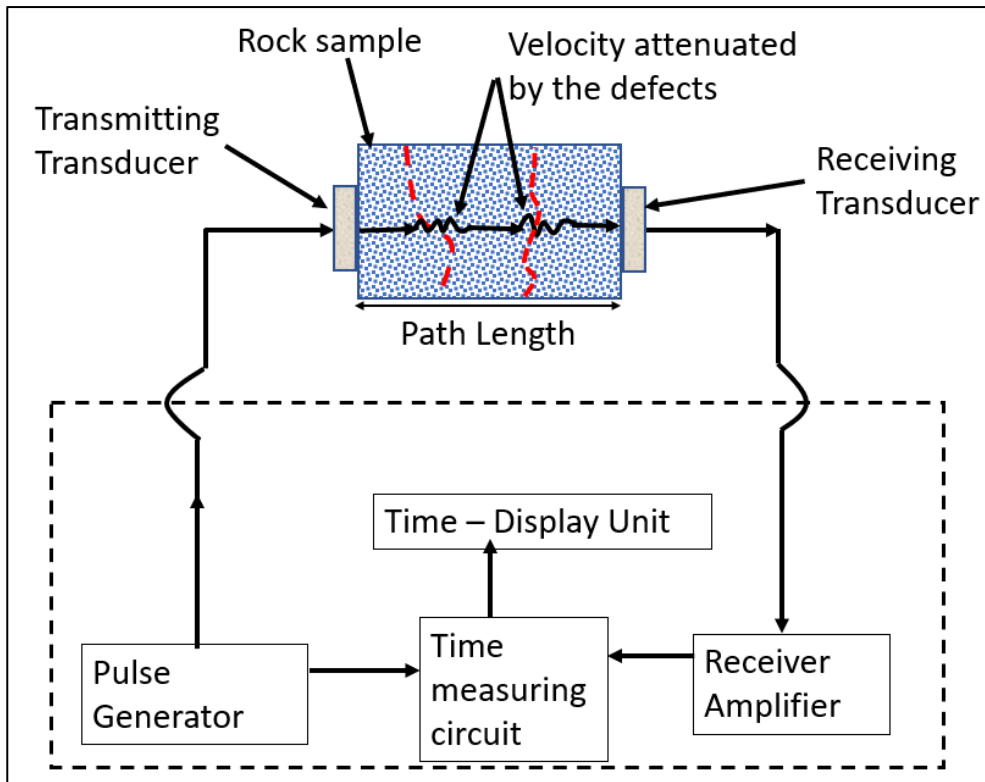
Figure 4.4. Essential components of UPV tester (adapted from Hellier, 2003)

4.3 Inductively Coupled Plasma Atomic Emission Spectroscopy

Inductively coupled plasma atomic emission spectroscopy (ICP-AES) is an analytical technique used to determine the elemental composition of analytes. It is a widely accepted technique due to its low detection limit (i.e., ppm - ppb range), multi-elemental capability, and high sample throughput (Tyler & Jobin Yvon, 1995). The ICP-AES technique was preferred in the current study because the work involved over a hundred analytes and each analyte required the analysis of two elements (copper and iron).

The ICP-AES works on the principle that excited atoms and ions emit energy of their own characteristic wavelengths as they return to their ground state (Murray et al., 2000). This instrument is composed of three major components: the sample introduction system, the torch assembly, and the spectrometer (Figure 4.5). A peristaltic pump introduces the sample into a nebulizer, where it combines with argon carrier gas to form a mist (aerosol) as it enters a spray

chamber. The fine mist is introduced into the torch assembly via the inner tube. Argon gas is also introduced via two separate concentric tubes: 1. As a cooling gas (fed tangentially) for preventing the torch from melting, 2. As an auxiliary gas for plasma formation.

The torch is surrounded by copper induction coils that are powered by a radio frequency (RF) generator. To initiate the plasma, a high-voltage discharge (tesla spark) is applied to ionize the argon atoms, forming ions and electrons in the auxiliary gas. The magnetic field surrounding the induction coils forces these ions and electrons to move rapidly in an annular path, causing them to collide with other argon atoms, resulting in intense heat formation of up to 10,000 Kelvin (Wilschefski & Baxter, 2019). When the mist from the spray chamber is introduced to this heat, it is vaporised, atomised, and ionised. This excites electrons in atoms and ions to higher energy levels, which in turn emit photons of characteristic wavelengths as they return to their ground state. The emitted light is focused on a diffraction grating and prism, allowing the spectrum to be split into its component wavelengths (Cherevko & Mayrhofer, 2018). The intensity of light with different wavelengths is measured by the detector, which is then correlated with the concentrations of elements in the analyte. Thus, by determining which wavelengths are emitted by the sample and at what intensities, the concentrations of elements in the sample can be quantified based on reference standards (Murray et al., 2000).
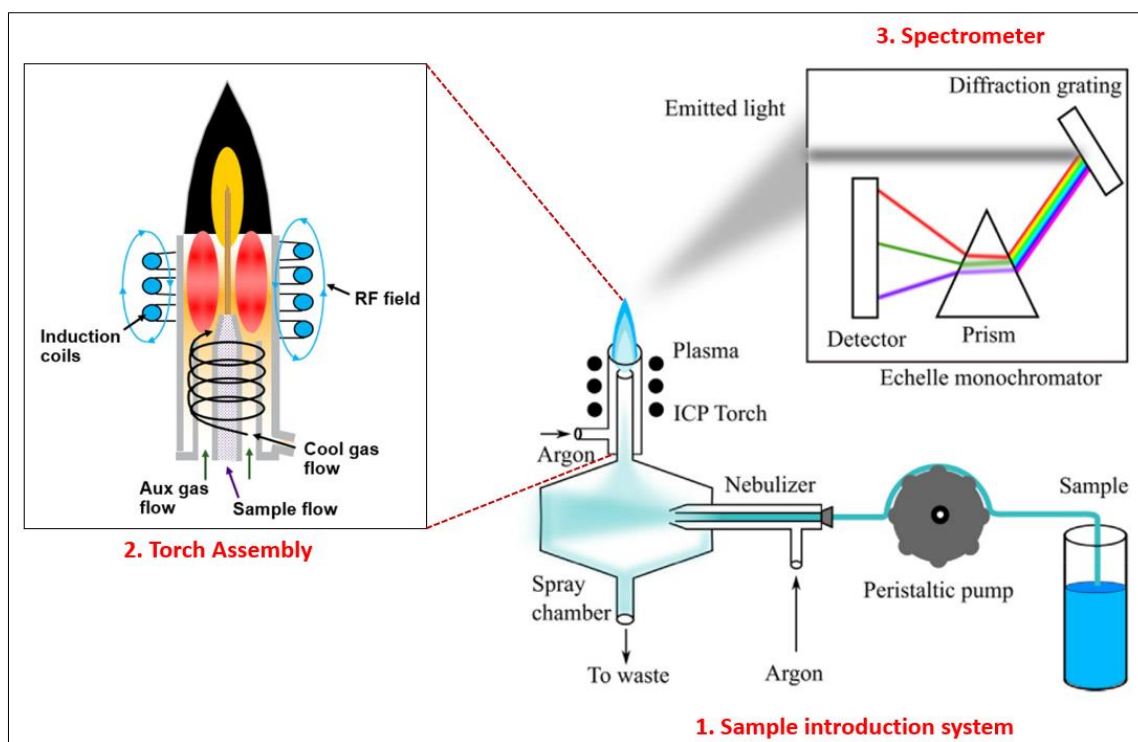
Figure 4.5. Operational principles of ICP-AES (adapted from Cherevko & Mayrhofer, 2018)

4.4 X-ray Computed Tomography

X-ray Computed Tomography (X-ray CT) is a non-destructive technique used to visualize the internal features of solid specimens. This technique was initially used in medicine for imaging soft tissue and bones to supplement 2D X-ray images (Sun et al., 2012). Over the years its application has been subsequently extended to a wide range of industrial tasks, including ore characterisation (e.g., microstructures) at higher resolutions of up to less than 10 µm.

This study has employed the X-ray CT technique to visualise and quantify microwave-induced fractures, as well as to assess the extent of leaching improvement resulting from these fractures. This technique can provide both 2D and 3D qualitative information about microwave-induced damage (e.g., fracture size and pattern), which can then be linked to mineral exposure for lixiviant interaction. Thereby, extending the current understanding of the use of microwave energy to improve mineral dissolution in sulphide ores.

The X-ray CT system is essentially composed of three important components: an X-ray source for generating X-rays, a sample stage for positioning the specimen during scanning, and a series of detectors for detecting the extent of X-ray attenuation (Ketcham & Carlson, 2001). The basic principles of X-ray CT involve directing the X-rays through a specimen at different angular positions and recording the linear attenuations of the transmitted X-rays to form a series of 2D projection images (radiographs). The radiographs are then computerized reconstructed to form a series of 2D slices that can be stacked together to form a 3D image of the scanned specimen (Figure 4.6).
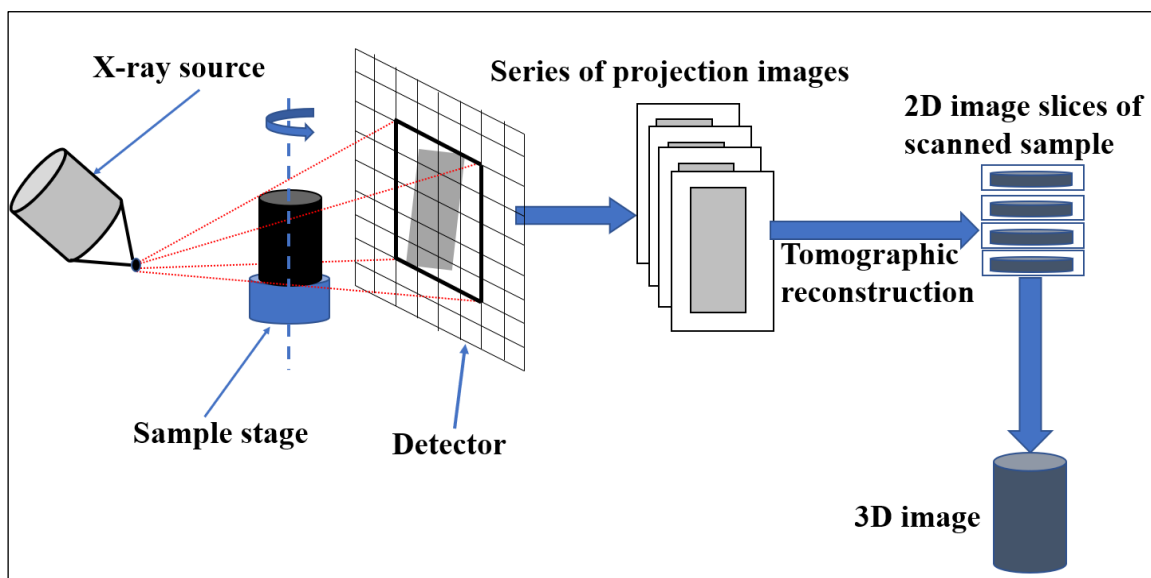
Figure 4.6. X-ray CT imaging – working principles

4.4.1   X-ray Generation

X-rays are electromagnetic waves with very short wavelengths in the Angstrom range (10^{-10} metres) (Als-Nielsen & McMorrow, 2011). The X-ray photons are highly energetic, which makes them penetrative through a wide range of objects, including denser materials such as geological samples. It is this penetrating ability that makes it useful in imaging the internal features of various objects. X-rays are essentially generated by the sudden deceleration of accelerated electrons into a metal target in a vacuum tube (Figure 4.7). The process involves

releasing electrons from the heated filament (cathode) through a process known as thermionic emission, which occurs when metals are heated to high temperatures (over 1000 Kelvin) (Haase & Go, 2016). The released electrons accelerate towards a metal target (anode) when a high voltage (typically, 50–150 kV for CT scans) is applied between the two electrodes (Seibert, 2004). When the electrons strike the metal target, they lose their kinetic energy in the form of heat (99%) and X-ray radiation (1%) (Zink, 1997). The copper stem (coupled to a water-cooling system) serves as a heat sink.

The whole unit is enclosed in a protective lead housing to contain the X-rays, and a small window allows X-rays to exit towards the specimen being scanned. A circular aperture or collimating plates at the window exit shapes the beam geometry, forming a conical beam or a fan beam, respectively (Kruth et al., 2011). A thin metal plate of copper or aluminium is typically placed at the X-ray tube window to filter very low energies of an X-ray spectrum (Ketcham & Carlson, 2001), as these can be fully absorbed by the specimen, leading to the beam hardening artefact (described in Section 4.5.1.1).
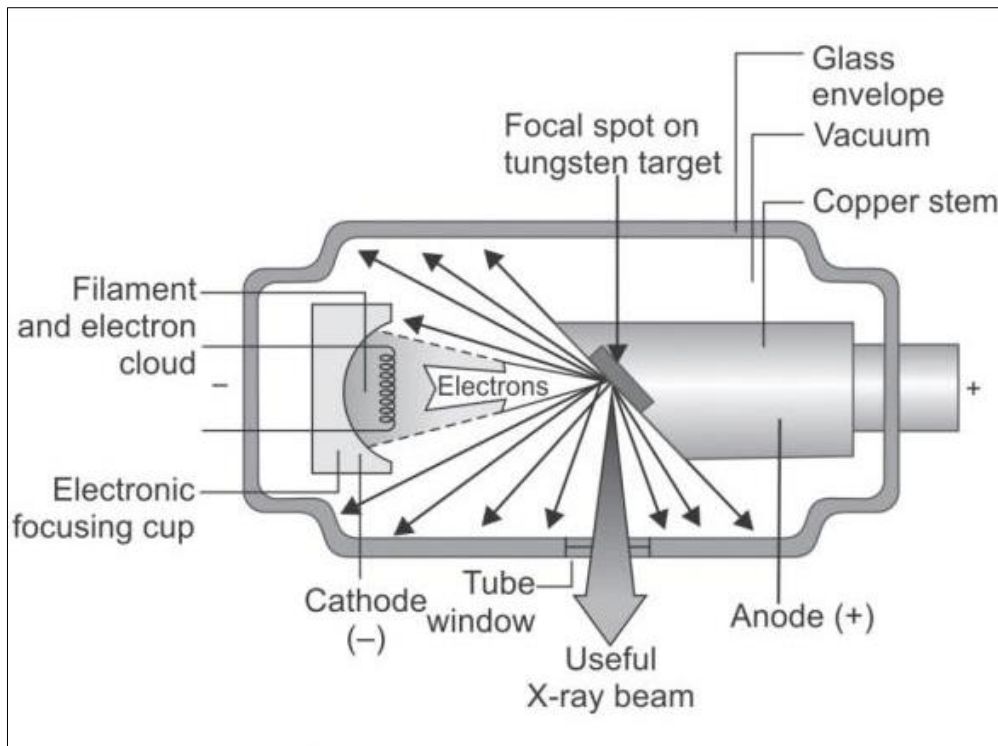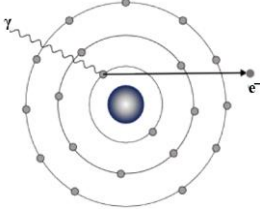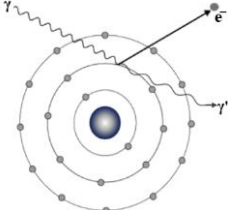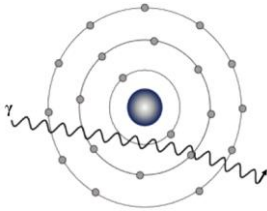
Figure 4.7. X-ray tube components for CT imaging (Karjodkar, 2019)

4.4.2   X-ray Interaction with Matter and Attenuation

The intensity of a beam of X-rays gradually decreases (attenuates) as it traverses through matter, and the extent of attenuation is material dependent. The image contrast that we observe on the CT image is a result of the X-ray attenuation of different materials composed in the specimen being scanned. The attenuation of X-rays as they interact with matter is a result of several physical effects, and the most relevant ones for X-ray imaging are photoelectric absorption, Compton (incoherent) scattering, and Rayleigh (coherent or elastic) scattering (ASTM E1441, 1992). The description of each of these effects is summarised in Table 4.1. Other interactions, such as pair production and photodisintegration, have not been considered here because they occur at higher energies (>1.02 MeV) (Bushberg, 1998), which are beyond the typical energy range (< 450 keV) used for industrial CT scanners (Kruth et al., 2011).

Table 4.1. X-ray photon-matter interaction (adapted from Maier et al., 2018)

Illustration	Description
Photoelectric Absorption	• Incident X-ray photon interacts with the inner shell electron of an atom. The photon is totally absorbed, and the electron is ejected from its orbit. The outer shell electron fills the vacancy, leading to secondary (low energy) X-ray characteristic radiation. • It depends on the atomic number (Z) of the material and incident energy (E). • It is the most dominant contributor to total attenuation.
Compton Scattering	• Incident X-ray photon interacts with the outer shell or weakly bound electrons, forming a recoil electron and the photon is scattered with partial loss of its initial energy. • It is the second most dominant contributor to total attenuation.
Rayleigh Scattering	• Incident X-ray photon of low energy (<10 keV) interacts with the cloud of electrons (whole atom). The energy is not large enough to eject an electron, but the whole atom is set to vibrations momentarily, leading to the release of another X-ray photon with the same energy as that of the incident photon with a small deflection in its path. • Minor contribution to the total attenuation.

The attenuation of a monoenergetic beam of X-rays through a homogeneous material is expressed by Beer's-Lambert law (Equation 4.8) (Wellington & Vinegar, 1987), which is modified to Equation 4.9 when the specimen is composed of various materials with different X-ray attenuation properties. The line integral is the sum of all linear attenuations along a ray path. The X-ray attenuation coefficient of a material essentially depends on X-ray energy, atomic number, and the density of the material being inspected (Kyle & Ketcham, 2015), as expressed in Equation 4.10. This expression indicates that the attenuation coefficient of a

material increases as the effective atomic number and material density increase, and decreases as the applied X-ray energy increases (Van Geet et al., 2000).

$$I = I_0 e^{-\mu x} \tag{4.8}$$

$$I = I_0 e^{-\int \mu_i x_i} \tag{4.9}$$

$$\mu = \rho \left(a + \frac{b Z_e^{3.8}}{E^{3.2}} \right) \tag{4.10}$$

Where;

I_o, I = Initial and final intensity of X-ray beam,

μ_i = Linear attenuation coefficient of material i,

x_i = Length of X-ray path through material i,

Z_e = Effective atomic number,

E = Energy of X-ray beam,

ρ = Bulk density of the material,

a and b = Energy-dependent coefficients.

4.4.3 X-ray Detection

The X-ray photons that have been transmitted through a specimen are collected on the detector for visualization. A typical design of a CT detector consists of three essential layers (Shefer et al., 2013): scintillator (for converting X-ray photons to visible light), photodiode (for converting visible light to electric current), and substrate (for providing mechanical and electrical infrastructure). The most scintillating materials used in CT detectors are cesium iodide (doped with thallium as an activator), cadmium tungstate, or ceramic materials based on yttrium–gadolinium oxides (Michael, 2001). These materials convert X-ray photons into

visible light via three consecutive stages (i.e., conversion, transport, and luminescence), as illustrated in Figure 4.8 (Nikl, 2006):

i. Conversion – the absorption of X-ray photons in the scintillator leads to the formation of many electron-hole pairs. The electrons (e) jump to the conduction band, leaving the holes (h) in the valence band.

ii. Transport - electrons and electron holes migrate through the material.

iii. Luminescence - electrons and electron holes are trapped in the activation sites (luminescence centres) and recombine to produce scintillation photons in the visible wavelength range.
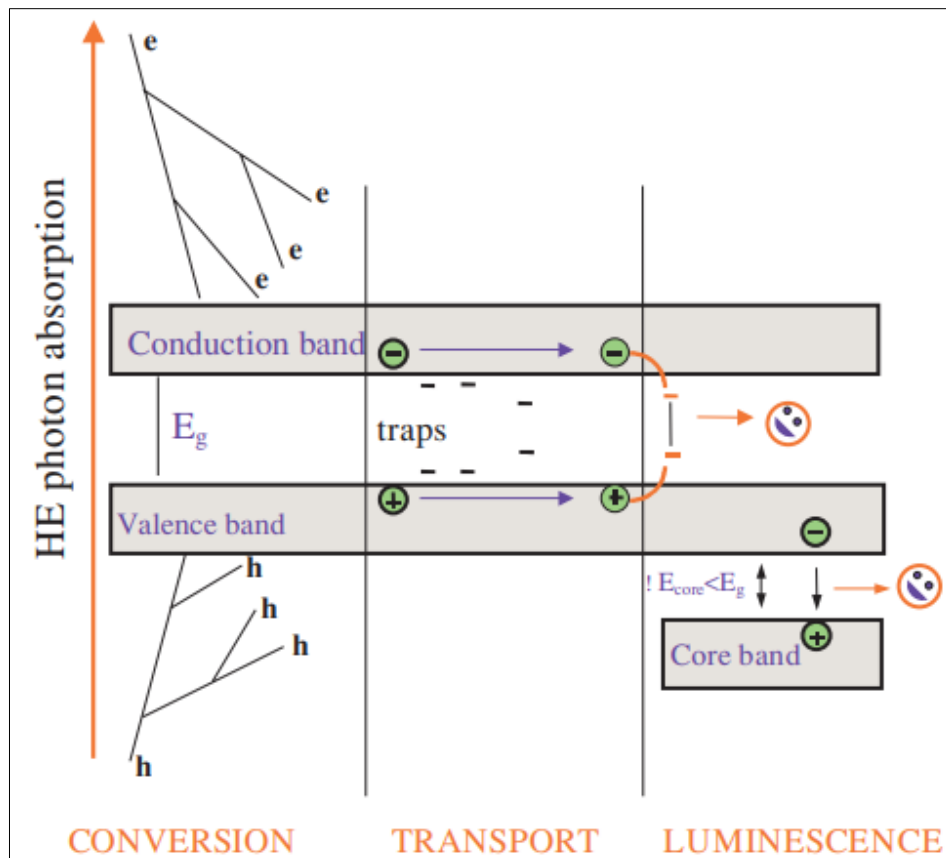
Figure 4.8. Scintillation mechanism in a single crystal solid-state (Nikl, 2006)

The visible light is then converted to an electric current in a pixelized matrix of photodiodes (Spahn, 2013), with each photodiode generating a current in response to the absorption of light originating from the scintillator. The current is then amplified and digitized using transistors such as amorphous silicon thin-film transistor (TFT). The signal is then transmitted from the detector system to acquisition circuitry to generate radiographs, which are then reconstructed using a computer software to generate the final image of the scanned specimen.

In the current study, a high-resolution (DXR-250) 2024 x 2024 - pixel flat-panel detector, with a 200-µm pixel pitch was used. This detector utilizes the amorphous silicon TFT coupled to the cesium iodide scintillator.

4.4.4   Application of X-ray CT for Assessing Microstructures in Ore Specimens

Several studies in the field of mineral processing have used the X-ray CT technique as a characterization tool for 3D visualization and quantification of internal microstructures in ore samples (Garcia et al., 2009; Charikinya et al., 2015). Other studies have employed this technique to assess the extent of mineral dissolution in sulphide ores (Kodali et al., 2011; Dobson et al., 2017; Ghadiri et al., 2020).

The application of the X-ray CT technique in mineral processing studies is possible because ore samples are naturally heterogeneous, consisting of mineral grains with varying densities and atomic numbers, as well as voids or cracks of different sizes. The high-density mineral grains (e.g., chalcopyrite) attenuate more X-ray photons than voids (air) or gangue minerals (e.g., quartz), and due to their high contrast of X-ray attenuations, these phases can be easily distinguished in CT images. Normally, the sulphide grains appear brighter than their associated gangue minerals, whereas the cracks or voids appear darker than the adjacent solid ore phases. Figure 4.9 shows an example of a 2D slice of a microwave-treated specimen in the current

study, indicating distinct peaks of grey values that correspond to different phases along line AB.
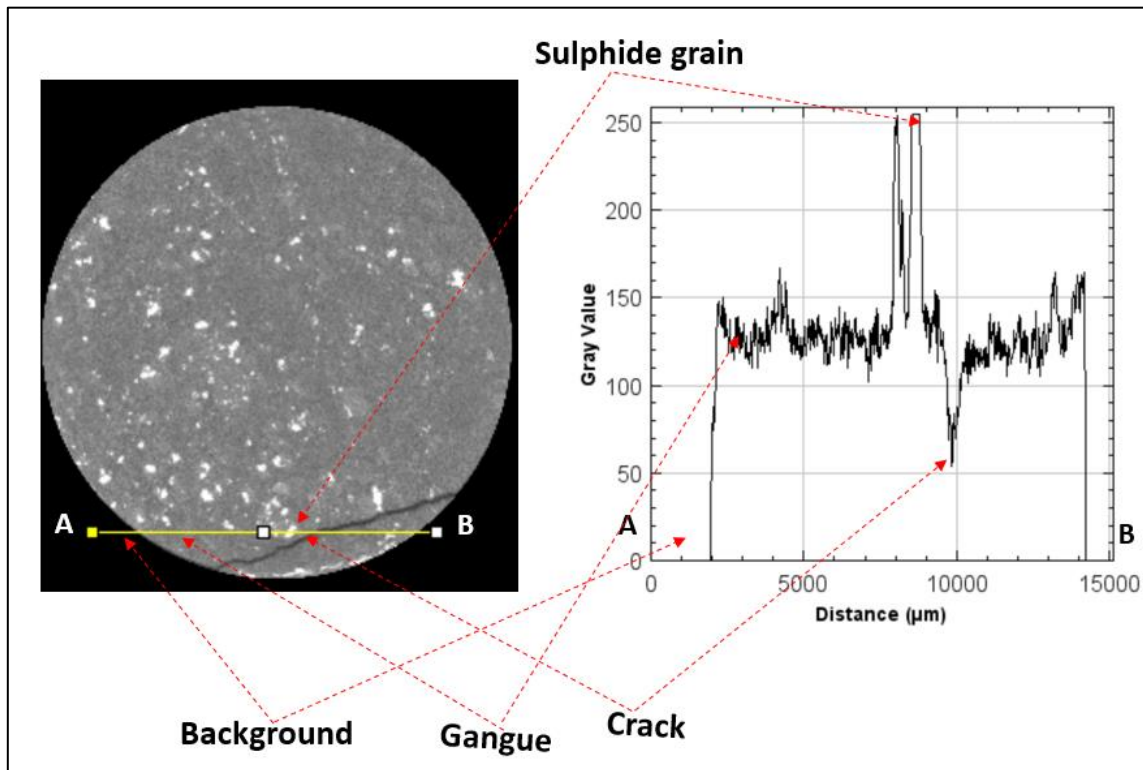
Figure 4.9. Different ore phases with their corresponding peaks on a grey scale

Figure 4.10 shows the plots of the linear attenuation coefficient versus X-ray energies of common minerals found in typical porphyry copper ores (Reyes et al., 2017). These plots indicate a significant gap in attenuation coefficients between the rock-forming minerals (e.g., quartz) and the sulphide minerals (e.g., chalcopyrite) over a broad range of X-ray energies. In contrast, the X-ray attenuation coefficients of rock-forming minerals (e.g., quartz vs muscovite) or sulphide minerals (e.g., chalcocite vs bornite) differ only slightly (narrow gap). This implies that the sulphide minerals can be easily distinguished and segmented from the gangue minerals, allowing quantitative and qualitative analysis. However, the gangue minerals or the sulphide minerals cannot be distinguished from each other in CT images, thus making their segmentation impossible. This challenge can be addressed by using other analytical techniques,

such as the Mineral Liberation Analyser - MLA (described in Section 4.1) to complement the X-ray CT results.
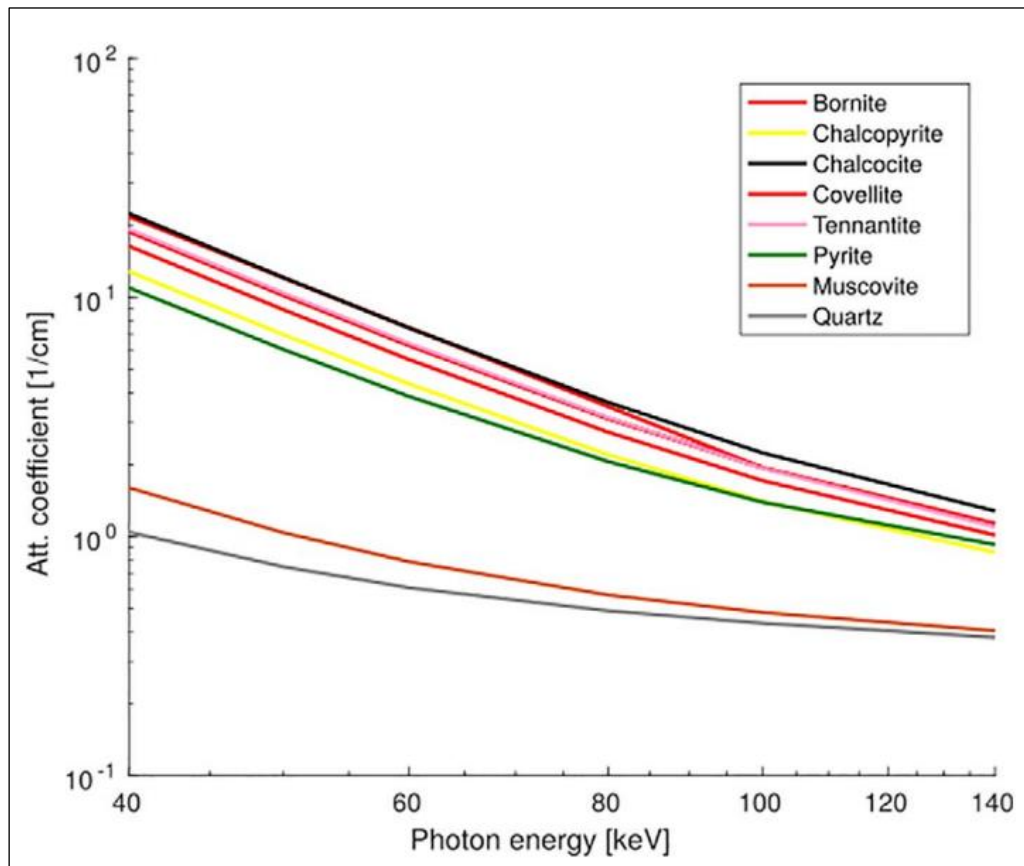
Figure 4.10. Linear attenuation coefficients versus X-ray energies - common minerals found in porphyry copper ores (Reyes et al., 2017)

Another limitation of the X-ray CT technique is that larger ore specimens (e.g., >75 mm) cannot be scanned in full at a higher resolution (e.g., <10 µm) in a single scan because the whole specimen cannot fit in the field of view (FOV) during scanning. Thus, requiring multiple scans and then merging the data to produce a full scanned image, but this procedure is both time-consuming (several hours to days) and costly. Furthermore, larger ore specimens are too thick for X-rays to penetrate, so only a small fraction is transmitted for detection, resulting in poor image quality.

4.5.1 CT Artefacts

Although X-ray CT imaging is a powerful tool for non-destructively detecting and characterising internal microstructures of materials, it is prone to image artefacts. The term artefact as applied to X-ray CT imaging refers to any discrepancy between the reconstructed image and the actual features of an object being scanned (Makins, 2014). Artefacts degrade the quality of the CT image, which may lead to erroneous interpretation of features of interest, so measures should be taken to minimize or correct them. The most common CT artefacts encountered in geological materials are beam hardening, ring artefacts, motion artefacts, and the partial volume effect (Ketcham & Carlson, 2001), as well as the Feldkamp (cone-beam) artefact.

4.5.1.1 Beam Hardening

Beam hardening occurs when an X-ray beam with polychromatic energies (consisting of a range of energy spectrums) passes through an object. In this case, the lower X-ray energies are highly attenuated compared to the higher X-ray energies, resulting in a beam with lower overall intensity but higher mean energy than the incident beam (Helliwell et al., 2013). For a cylindrical specimen, the beam hardening effect can cause cupping, where the edge appears brighter than the interior even if the object is the same at all points since the X-rays passing through the middle section encounter more materials than those at the periphery (see Figure 4.11) (Barrett & Keat, 2004; Stauber & Müller, 2008). The beam hardening effect can be reduced by placing a thin plate of metallic filter (copper or aluminium) between the X-ray source and the specimen to pre-filter the very low energies in the energy spectrum before they reach the specimen. This effect can also be minimized using a software correction algorithm during the reconstruction process. The beam hardening artefact was corrected in the current study during image reconstruction, as stated in the image processing methodology in Section 7.5.2.
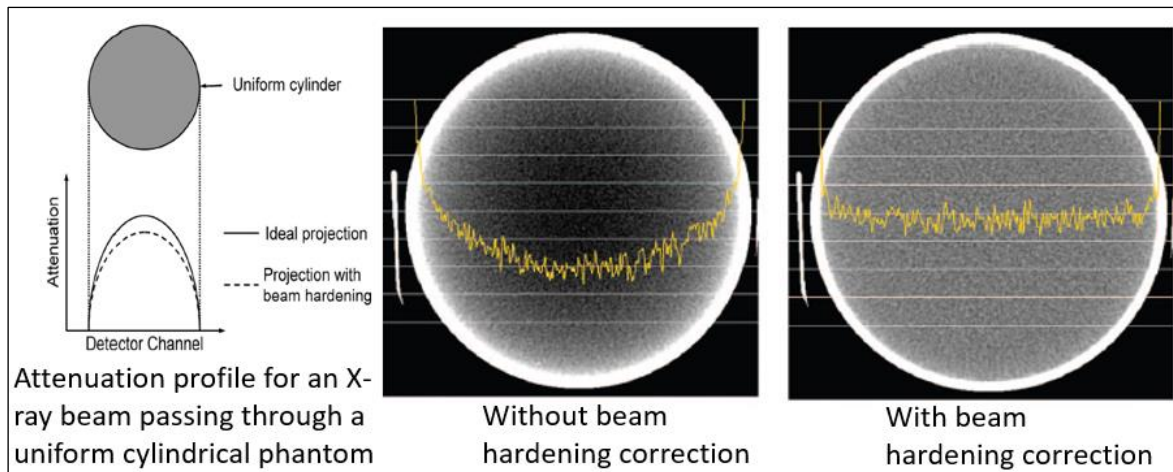
Figure 4.11. Beam hardening effect - uniform cylindrical water phantom (Barrett & Keat, 2004)

4.5.1.2 Ring Artefacts

Ring artefacts is a defect in tomographic imaging in which the quality of the CT image is distorted by the appearance of concentric rings (around the centre of rotation) on the reconstructed images (see Figure 4.12). This problem is caused by defects in one or more detector elements, poor detector calibration, a defect in the scintillator, or contamination (e.g., dust) on the detector system. Any of these defects cause erroneous readings in each angular position, resulting in the formation of rings or half-rings around the rotation centre of the reconstructed image (Barrett & Keat, 2004; Stauber & Müller, 2008). For defects related to detector or scintillator systems, a repair or calibration may be required, and in the case of dust contamination, this effect can be reduced by cleaning the system. In addition, this artefact can be detected and minimised using a software algorithm prior to image reconstruction (Ketcham & Carlson, 2001).
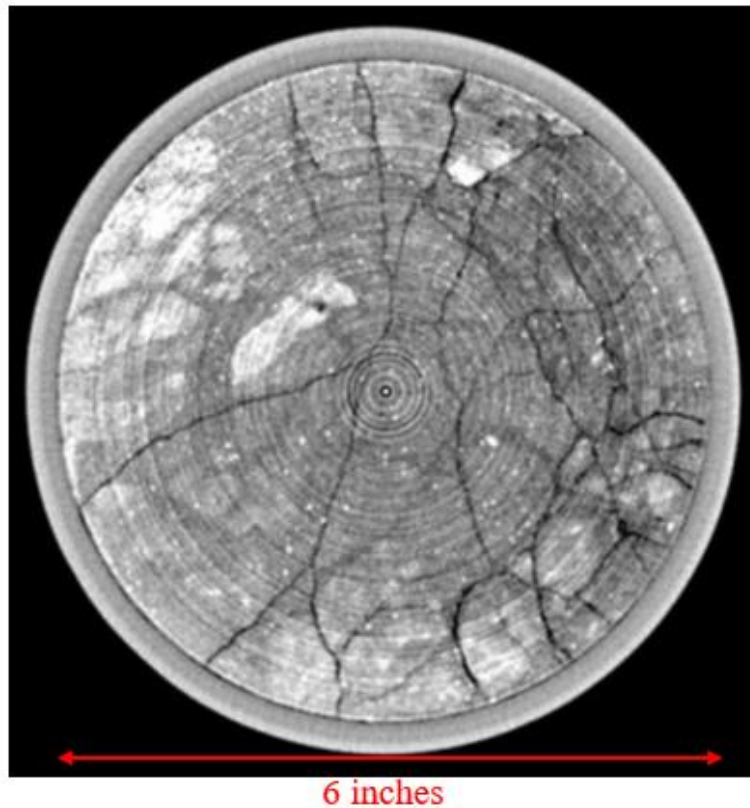
Figure 4.12. Ring artefacts on a saprolite core encased in a PVC pipe (Ketcham & Carlson, 2001)

4.5.1.3 Motion Artefacts

Motion artefacts occur when the specimen shifts from the centre of rotation during scanning, such that the projections do not fit together during reconstruction because the shift is not accounted for in the reconstruction process (Schulze et al., 2011). As a result, the reconstructed image usually appears with shading or streaking (Barrett & Keat, 2004), which does not represent the actual features in the specimen being scanned. Figure 4.13 demonstrates the effect of motion artefacts using a simulation of a phantom cylinder (9.6 mm diameter by 2 mm high) with four circular holes of 0. 8 mm diameter and a 2-mm square cut-out (Davis & Elliott, 2006). To avoid motion artefacts, a specimen should be securely fastened on the sample stage prior to image acquisition.
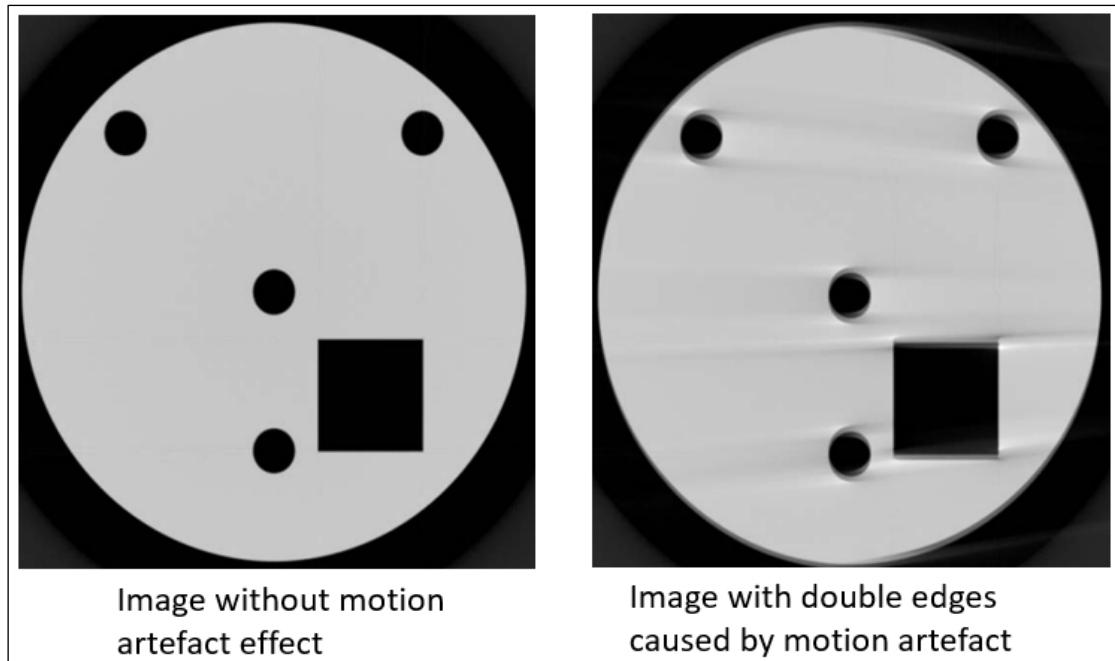
Figure 4.13. Motion artefact demonstration (Davis & Elliott, 2006)

4.5.1.4 Partial Volume and Cone Beam Effects

Partial volume artefact occurs when two or more different materials of wide X-ray attenuation properties reside in the same voxel, resulting in a grey-scale intensity that is the average attenuation of their properties (Ketcham & Carlson, 2001). This averaging of grey-scale intensities within a voxel causes blurred transitions between these materials or phases, which can lead to erroneous measurements if not minimized during image processing. Normally, morphological filters can be used to smooth or sharpen the blurs, improving image quality for further analysis.

Many modern CT scanners use X-ray sources with cone-beam geometry (Der Sarkissian et al., 2019) due to their fast image acquisition. The diverging cone shape of the X-ray beam allows image acquisition of the entire field of view in a single rotation, as opposed to a fan-shaped X-ray beam, which scans a small field of view in a single rotation (i.e., a single slice per rotation), requiring multiple rotations to scan the entire specimen.

However, the cone-beam scanning geometry typically leads to a distinct type of artefact known as cone-beam image artefacts, also known as Feldkamp artefacts (Cnudde & Boone, 2013; Müller et al., 2015). This effect is more pronounced at high cone angles because the detector in these regions does not collect a complete set of data required for image reconstruction. The missing data results in image distortion, streaks, and noise in the peripheral (Scarfe & Farman, 2008). This artefact can be minimized using a well-known Feldkamp reconstruction algorithm technique, either in its original form or in various modifications (Schulze et al., 2011). This artefact was minimized in the current study by using the Feldkamp algorithm during image reconstruction, though a few slices (<10 slices) showed this effect at the top and bottom sections of the cores, accounting for less than 1% of all slices.

4.5.2 Image Processing

Image processing is a method of performing some operations on an image to extract some useful information from its content (Konstantinidis et al., 2009), which can then be interpreted qualitatively or quantitatively. In the current study, several image operations were performed to allow the identification, extraction, and quantification of features of interest (e.g., microwave-induced cracks and sulphide mineral grains). The most important operations used in this study were thresholding, voxel connectivity, and volume thickness, as described in the following sections.

4.5.2.1 Thresholding

Image thresholding is an important step in image processing because it allows extracting features of interest by clustering the image into foreground and background based on the selected (threshold) grey-scale value. Thus, any pixel with an intensity above the threshold is considered foreground; otherwise, it is background (Goh et al., 2018). Normally, manual selection of the threshold grey value is prone to human biases, potentially affecting subsequent image processing operations; therefore, automatic thresholding techniques should be

considered to avoid human biases. There are several techniques for automatic thresholding, but the most common and widely used are Otsu and Maximum Entropy (Zhang & Hu, 2008).

In the current study, the Otsu technique was used to distinguish voids/cracks (air) from other ore phases, while the Maximum Entropy technique was used to distinguish sulphide grains, as described in detail in Section 7.5.2. The Otsu algorithm determines the threshold value that separates features in an image into two classes (background and foreground) by minimizing the within-class variance or maximizing the between-class variance (Otsu, 1979). The Maximum Entropy, on the other hand, works by maximizing the sum of the two class entropies (background and foreground) (Kapur et al., 1985). Normally, the optimum threshold value by Otsu, Maximum Entropy, or other algorithms is determined after several iterations using computer software.

The concept of entropy originated in the physical and engineering sciences, but it is now used in a variety of scientific and non-scientific disciplines (Robinson, 2008). The entropy of an image is essentially, a measure of randomness that can be used to evaluate its texture, and it can simply be expressed by Equation 4.11 (Shannon & Weaver, 1949). The higher the entropy, the greater the texture variation in an image.

$$\text{Entropy} = -\sum_{i=1}^{n-1} P_i \log_2 P_i \tag{4.11}$$

Where;

   n = Number of grey levels (e.g., 256 for 8-bit images),

   P_i = Probability of occurrence of grey level i in the image.

Figure 4.14 illustrates the entropy concept using two 2D images (1460 x 1467 pixels) with varying textures, namely Specimens 1 and 2. The grey intensity data set generated by ImageJ Fiji was used to calculate the entropies using Equation 4.11. Figure 4.15 shows the plots of Cum $[-(PiLog_2Pi)]$ versus grey intensity level, with the final values on the plots indicating the entropies of these images. These results show that specimen 1, which has a more random texture (more phases), has a wider distribution of intensity histogram and thus a higher entropy.
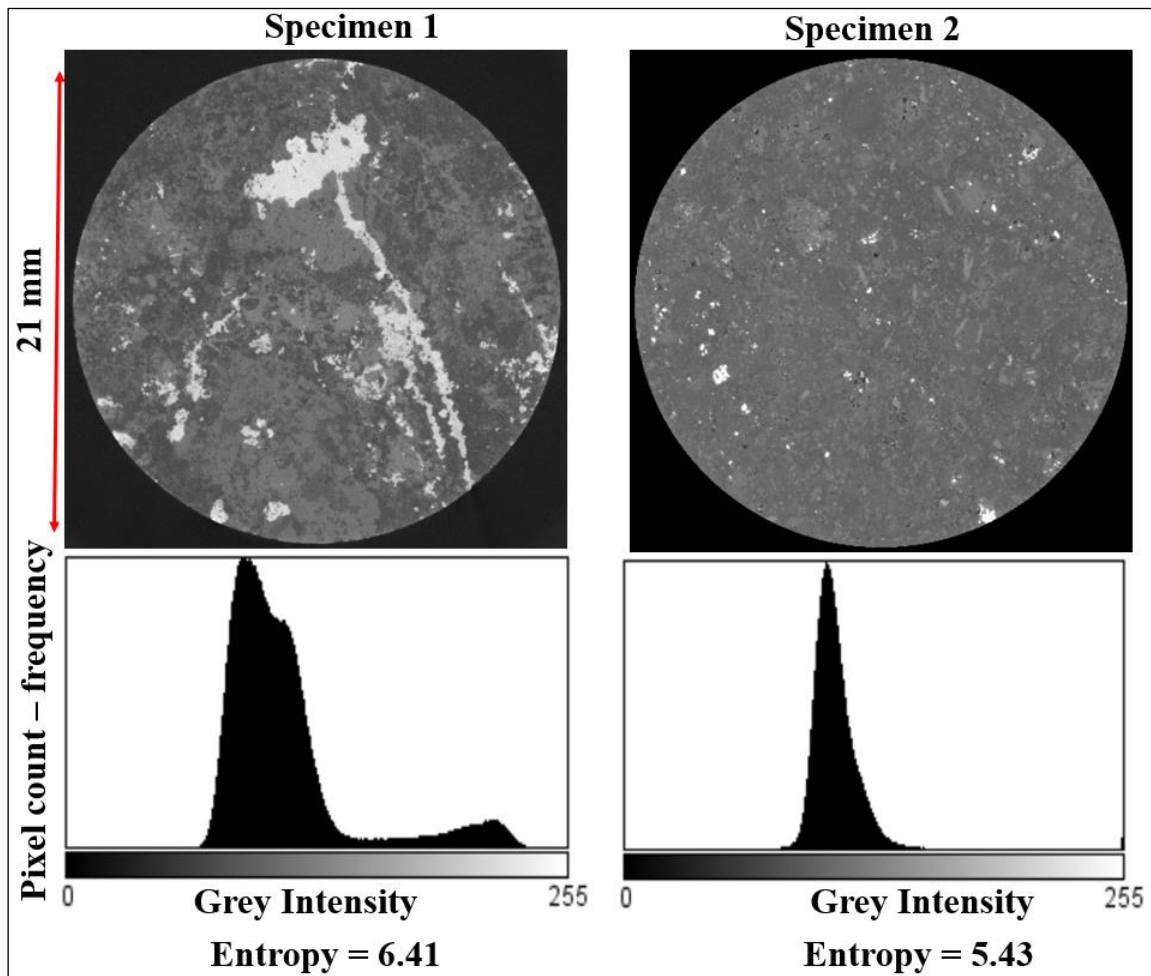
Figure 4.14. The entropy concept illustrated using ore specimens with varying textures
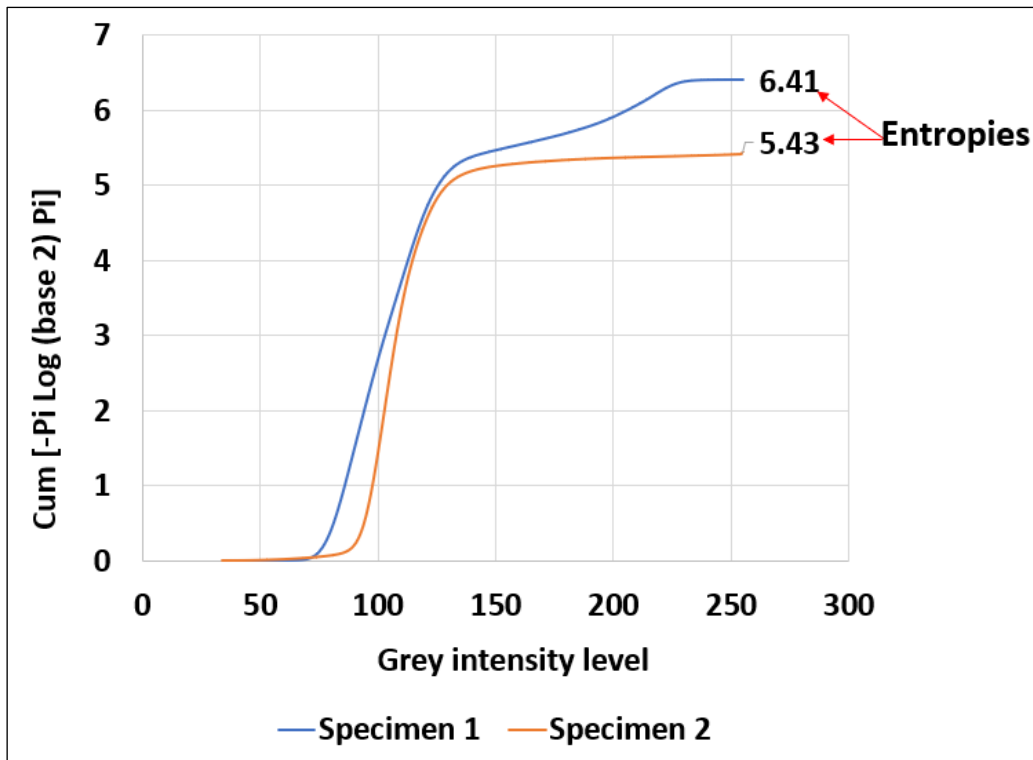
Figure 4.15. Plots illustrating the entropy concept using grey intensity profiles

4.5.2.2 Voxel Connectivity and Labelling

Voxel connectivity and labelling is the concept of grouping objects in an image and assigning them labels based on their neighbourhood. The idea is to group pixels that belong to the same connected component and then label them as a single object, simplifying subsequent image analysis tasks (e.g., quantification and characterisation) (Borgefors et al., 1997). This concept is illustrated in Figure 4.16, where 43 small components (left) have been connected to form three large components (right).
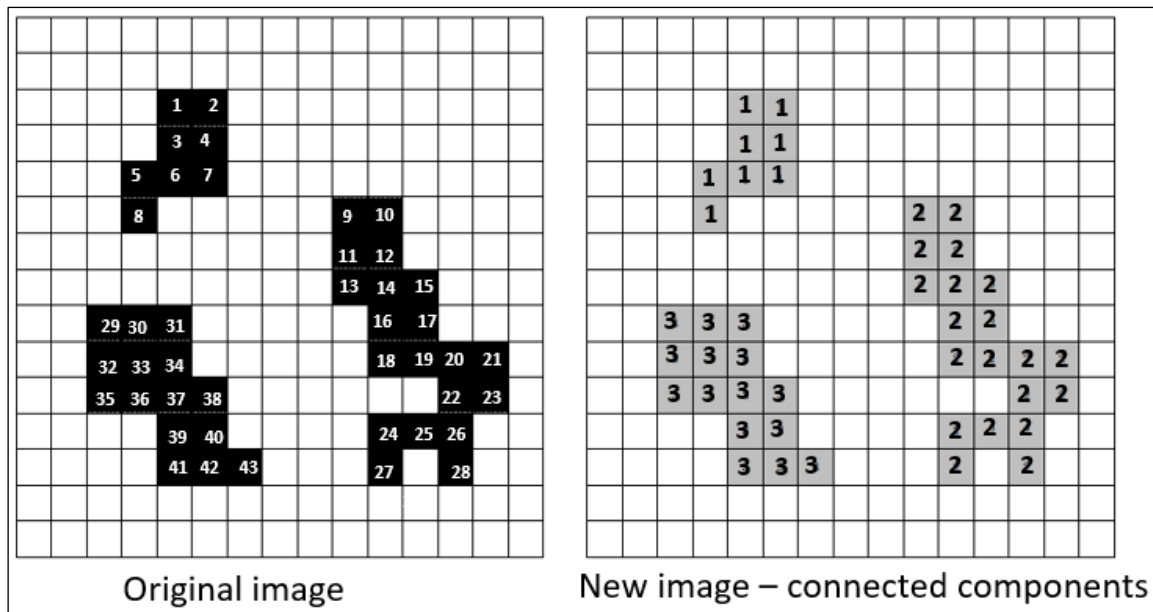
Figure 4.16. Connected components illustration (adapted from Schwenk & Huber, 2015)

In a 2-dimensional image, pixels with the same intensity value can be grouped through either 4-connectivity (i.e., group pixels touching each other on any of the 4 faces) or 8-connectivity (i.e., group pixels touching each other on any of the 4 faces or 4 corners). For a 3-dimensional image, voxel connectivity can be performed via three possible options (Figure 4.17) (Toriwaki & Yonekura, 2002):

- 6-connectivity – group all voxels touching each other on either of their six faces.

- 18-connectivity – group all voxels touching each other on either of their six faces or twelve edges.

- 26-connectivity – group all voxels touching each other on either of their six faces, twelve edges or eight corners.
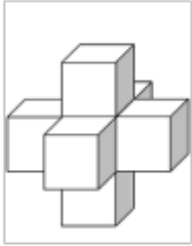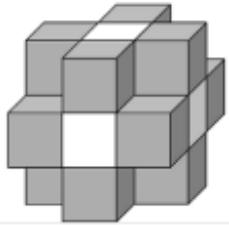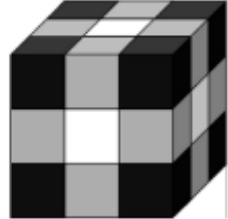
6-connected		6 faces
18-connected		6 faces + 12 edges
26-connected		6 faces + 12 edges + 8 corners

Figure 4.17. Voxel connectivity (Toriwaki & Yonekura, 2002; Fonseca, 2011)

In the current study, the concept of voxel connectivity aims to reduce the number of individual items (e.g., sulphide grains or cracks) in a binary image by grouping them into separate and manageable components before analysis. In this case, the 6-connectivity algorithm was selected. The 26-connectivity option was avoided in this study because of the lengthy computation time. The 18-connectivity was not considered because this option is currently unavailable in the software used for image processing (ORS Dragonfly - Version 2021.3).

4.5.2.3 Volume/Local Thickness Determination

The volume thickness algorithm can be used to characterize 3-dimensional binary images of complex objects, such as micro-fractures in ore specimens. This technique has been described by Hildebrand & Rüegsegger (1997) using Figure 4.18. Let Ω be the set of all data points of a

143

3D object, and p be an arbitrary point within this object. The local thickness is determined by fitting maxima spheres to the object, and thus the local thickness at any point (e.g., point p) is the diameter of the largest sphere that fits inside the object and contains the point. The centre and radius of the sphere in this figure are denoted by x and r, respectively. This technique is used in the current study to determine the magnitude and mapping of microwave-induced fractures in the cores using the ORS Dragonfly software by comparing the volume thickness of cracks/voids in the pre-treated and post-treated scans.
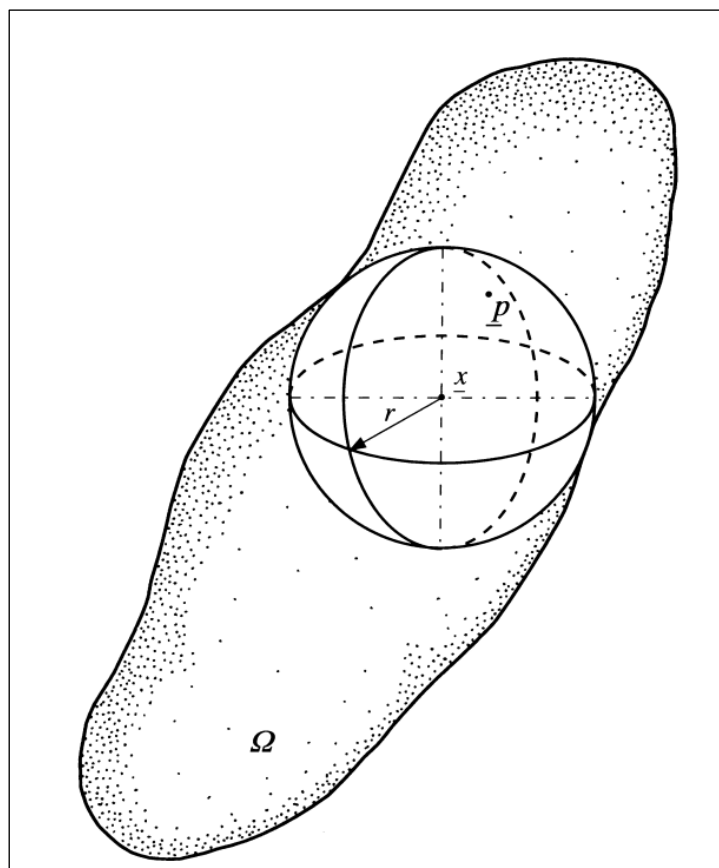
Figure 4.18. Local thickness determination by fitting maxima spheres to the object (Hildebrand & Rüegsegger, 1997)

4.6 Summary

This chapter has described several experimental techniques used in the current study, including MLA, XRD, PLT, UPV, ICP-AES, and X-ray CT. The MLA and XRD techniques are used in this study to assess the mineralogy and texture of ore samples in order to determine the ore's amenability to microwave-induced fractures, which aids in the interpretation of microwave treatment and leaching results. The PLT, UPV, and X-ray CT techniques are used to quantify the extent of microwave-induced damage. The leaching improvement caused by microwave-induced fractures is assessed using the ICP-AES and X-ray CT imaging techniques. The sample preparation and experimental procedure are described in Chapters 5-8.

5. ORE CHARACTERISATION AND EVALUATION

5.1 Introduction

It has been well established in the literature review in Chapter 3 that the magnitude of microwave-induced damage on ores not only depends on microwave treatment conditions (i.e., power density), but also on ore properties. These properties include: mineralogy, texture, and the thermal-mechanical properties of the microwave-transparent gangue matrix and microwave-absorbent grains. Five porphyry copper sulphide ore samples with varying mineralogy and texture are characterised in this chapter to evaluate their mineralogy and texture. This evaluation is critical because it gives a clue of potential ore candidates for microwave treatment to improve comminution and enhance mineral exposure, based on the previous studies in the literature. The five ore types used in this study are:

a. Ore 1 – porphyritic monzonite ore

b. Ore 2 – quartzite ore

c. Ore 3 – limestone skarn ore

d. Ore 4 – porphyry ore

e. Ore 5 – alkalic porphyritic ore

Ores 1, 2, and 3 are three ore types of varying mineralogy and texture extracted from a mine in the United States. Ore 4 is from a mine in Chile, while Ore 5 is from a mine in Canada. The ores can not be identified due to confidentiality restrictions. The mineralogical and textural analysis of these ore samples was performed using the mineral liberation analyser (MLA). Because these samples were recently used in other microwave treatment studies at the University of Nottingham, their MLA results are available in the records. Ores 1, 2, and 3 were investigated in a microwave treatment study reported by Ure (2017) and were used in the pilot plant trials (discussed in Section 3.5.4) designated as Ores 2, 1, and 3, respectively (Batchelor

et al., 2017). Ores 4 and 5 have recently been investigated in other microwave treatment research works in the group at the University of Nottingham. These results are presented in this chapter and then used in subsequent chapters to interpret the microwave treatment and leaching results. The XRD analysis was performed in the current study as an alternative method to quickly check the major mineral phases present in these ores in order to support the MLA results.

5.2 Materials and Methods for MLA Analysis

This section briefly describes the MLA measurement procedure as described by Ure (2017). Twenty ore fragments (~25mm) were collected from representative samples of each ore type for MLA measurements. More fragments could be selected to improve the level of confidence; however, twenty fragments were adequate to give an indication of the ore mineralogy and texture, given equipment availability and measurement time constraints. These fragments were carefully selected based on visual observation by considering their differences in terms of texture and sulphide mineralisation to represent the bulk of the ore sample. The average mineral abundance and grain size distribution of these twenty fragments are reported.

Each of the selected ore fragments was sawn using a diamond-impregnated saw to expose a fresh surface for analysis. The sawn piece was trimmed off at the edges to fit into a 30 mm diameter polyethylene mounting cup. Some fragments did not require sawing because their cross-section would fit in the 30 mm mount without trimming. Epoxy resin mixed with a hardener was filled to the mounting cups to the desired level. Vacuum impregnation was carried out in a Struers (Epovac) chamber for about 15 minutes to remove air bubbles and ensure all pores are filled with resin. The mounts were then placed in a pressure curing unit (Technomat) overnight to facilitate the removal of air bubbles and allow curing. Mounts were finally set in an oven at 60°C. A vacuum oven may also typically be used for mount preparation. Normally, SEM analysis requires a flat and highly polished surface for optimum imaging (Stutzman &

Clifton, 1999). To achieve this, the hardened solid specimens were subjected to several stages of grinding and thereafter polishing, performed with progressively finer abrasives to remove surface roughness. The polished specimens were then carbon coated to a thickness of about 25-30 nm to make the sample surface conductive. The non-conductive surface will accumulate electric charges during scanning that will distort the image (Cheremisinoff, 1989). The specimens were then loaded in the SEM chamber, ready for examination.

It should be noted that only four fragments of Ore 5 were selected for MLA measurements based on their textural differences. These fragments were used to indicate a variety of textures existing in this sample, but they do not adequately represent the bulk sample. However, the modal abundance presented in this study is more accurate because it is based on the MLA results of a representative sample of ground particles of five size fractions ranging from +300 to -106 µm.

The mineralogical and textural analysis was conducted using the FEI Quanta 600 SEM (Figure 5.1) located at the University of Nottingham, UK. This system is equipped with a circular sample holder capable of holding up to fourteen round sample mounts at a time, each with a diameter of 30 mm. The samples were scanned using an accelerating voltage of 20 kV, a beam current of 40 nA, and a spot size of 7 units.
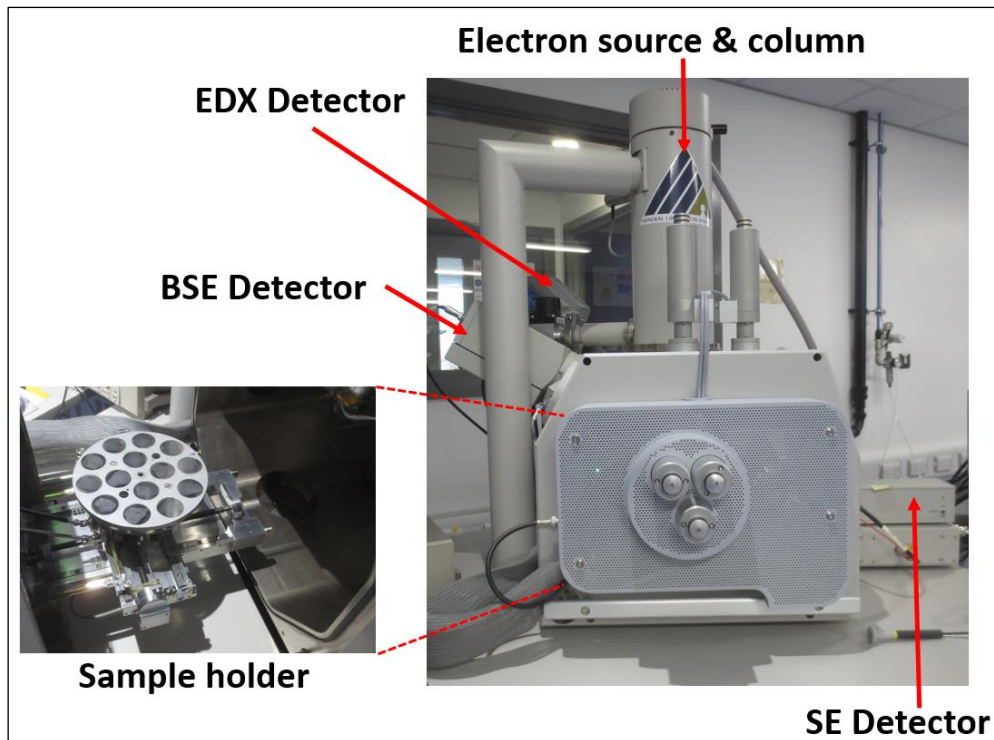
Figure 5.1. MLA setup - FEI Quanta 600

The MLA measurements of three samples (Ores 1, 2, and 3) were conducted using a combination of XMOD (X-ray Modal) and SPL_Lt (Sparse Phase Liberation_Lite) measurement modes. The XMOD method, which is based on X-ray point counting of an evenly spaced grid of points across the fragment, was used for rapid mineral identification. The SPL_Lt was used to generate grouped maps of microwave heaters (mostly sulphides or metal oxides), which appear as bright phases on the BSE image. The mineral association data and grain size distribution of microwave heaters were also determined using this method, avoiding the more time-consuming measurement of all phases composed in a particle. The MLA measurements of Ores 4 and 5 were performed using the XBSE (Extended Back-scattered Electron) technique, which is based on a single X-ray analysis per grain identified in the BSE image. The major steps involved in the XBSE measurement mode are summarised in Figure 5.2.
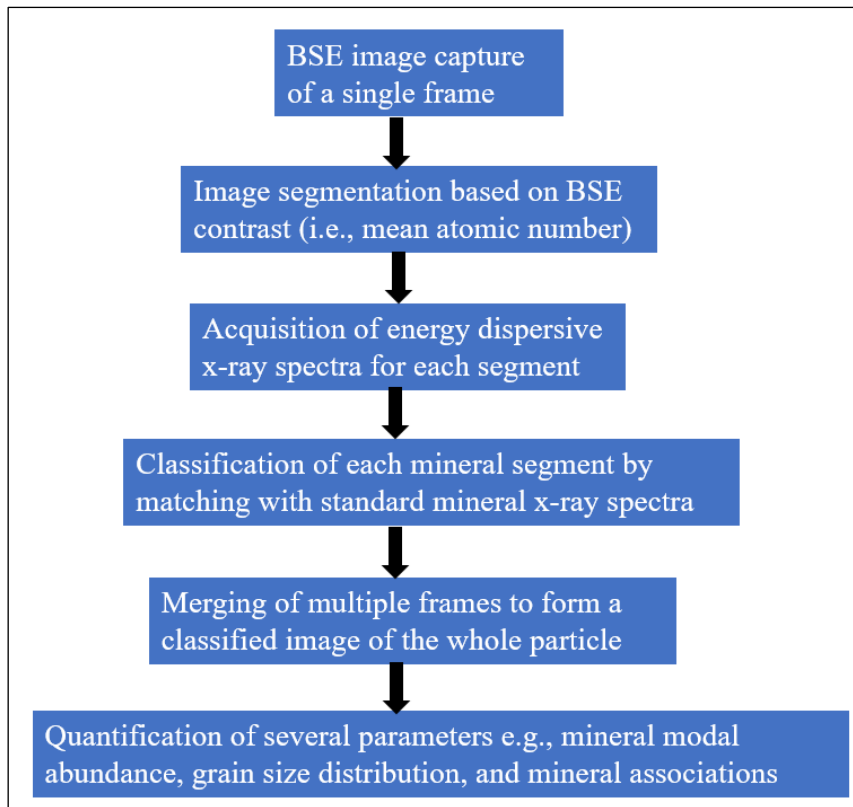
Figure 5.2. Major steps involved in the MLA measurements XBSE mode

5.3 Materials and Methods for XRD Analysis

The XRD analysis was performed using Bruker D8 Advance with Davinci design, with Cu K-alpha radiation source of wavelength $\lambda = 1.5420$ Å (Figure 5.3). The procedure involved crushing of ore samples followed by several stages of rifle splitting to get small representative subsamples of about 100 grams from each ore type. These subsamples were then ground to -106 µm using a TEMA mill (a ring and puck pulverizer). The ground product was further split to get about 2-3 grams of which a small portion was evenly packed and levelled in a sample holder prior to XRD analysis. The XRD spectra were acquired over a range of 2θ from $10°$ to $70°$ at $0.02°$ increments, with a step time of 0.1 sec. Mineral identification was carried out by matching the peaks of the measured XRD patterns with those of reference databases using DIFFRAC EVA software.
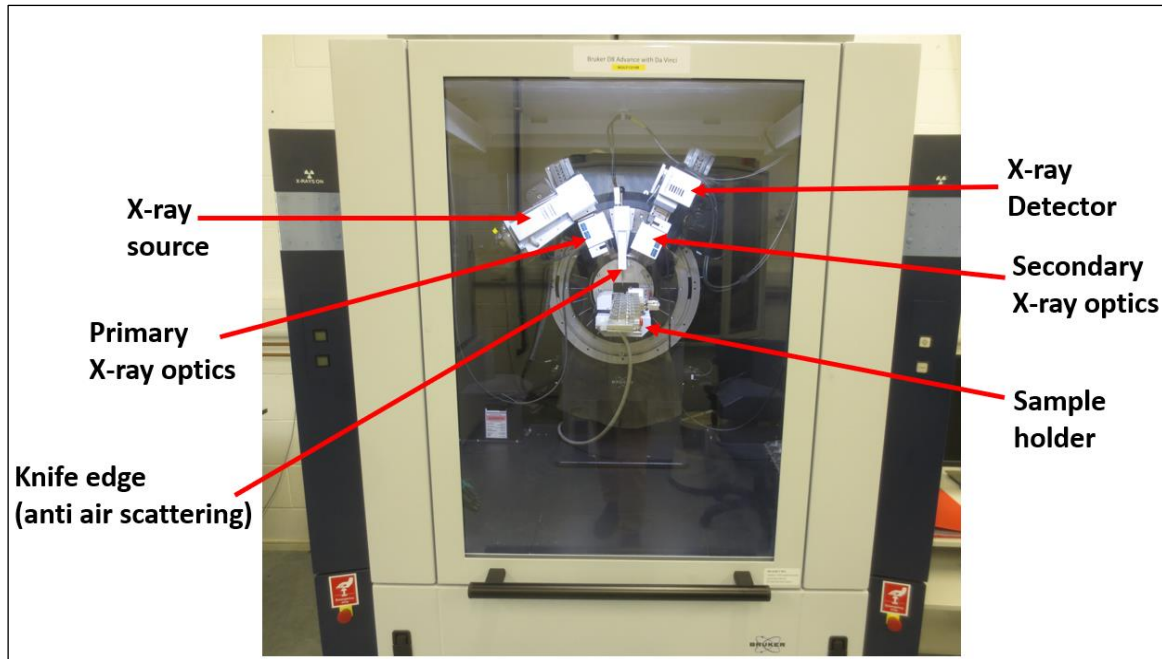
Figure 5.3. XRD setup – Bruker D8 Advance

5.4 Mineral Groupings and Evaluation

Minerals were grouped based on their microwave heating response to assess the amenability of each ore type to microwave treatment. As previously stated in Section 2.4, minerals can be grouped into three categories based on their microwave heating response: good, poor, and non-microwave heaters. The good microwave heaters are mostly sulphide minerals (which have semi-conducting properties), such as chalcopyrite, bornite, chalcocite, covellite, pyrite, and molybdenite. The non-sulphide minerals included in the good microwave heaters are magnetite (ferrimagnetic material) and montmorillonite (hydrated phyllosilicate mineral). The poor microwave heaters include hematite, ilmenite and rutile. The non-heating gangue minerals (rock-forming minerals) include quartz, feldspars, pyroxenes, micas (e.g., muscovite, biotite) and carbonates (e.g., calcite). Table 5.1 summarises the mineral classification system based on the microwave heating response used in the current study.

In addition to microwave heating response, the non-heating minerals were classified based on their hardness to assess ore amenability for microwave treatment. Mineral hardness can be expressed in a variety of ways, such as tensile and compressive strengths, as well as fracture toughness. In the current study, the Mohs hardness scale, which is a relative measure of resistance to scratching, was used as a simple method of mineral classification based on their resistance to local deformation due to microwave treatment. The scale consists of ten reference minerals arranged in increasing order of hardness such that each mineral will scratch the one on the scale below it, but will not scratch the one above it (Tabor, 1970). Minerals with Mohs hardness ≥6 (e.g., quartz, feldspars, and pyroxenes) have been classified as hard, while those with Mohs hardness <6 have been classified as soft (e.g., muscovite, phlogopite, biotite, and calcite and similar carbonates minerals). This technique has been used by other researchers in microwave treatment studies (Batchelor et al., 2015; Ure, 2017).

Table 5.1. Mineral groupings (reproduced from Ure, 2017)

Mineral Groupings		
Good Heaters	Copper Sulphides	Chalcopyrite
		Bornite
		Chalcocite
		Covellite
	Other Sulphides	Pyrite
		Molybdenite
		Sphalerite
	Non-Sulphide	Montmorillonite
Other Heaters	Non-Sulphides	Fe-Oxides
		Ilmenite
		Rutile
Non-Heating Gangue	Hard Gangue (Mohs≥6)	Quartz
		Plagioclase Feldspar
		Orthoclase Feldspar
		Pyroxene/Amphibole
		Dravite
	Soft Gangue (Mohs<6)	Micas (muscovite, biotite, phlogopite)
		Chlorites
		Hornblende
		Calcite and similar minerals

In general, ore samples with a higher modal abundance of good and coarse-grained microwave heaters constrained in a large proportion of hard and brittle gangue matrix (e.g., quartz) are more likely to be amenable to microwave-induced fractures. Moreover, the presence of stiffer microwave heaters (e.g., pyrite) in the ore promotes crack propagation even further, as demonstrated in the literature review in Figure 3.11. This is because such heaters are more efficient stress raisers and can effectively transfer the stresses to the gangue matrix, resulting in significant ore fracturing that can liberate other sulphide minerals associated with pyrite (e.g., chalcopyrite). The extent of microwave-induced fractures, on the other hand, is reduced to some extent when the ore is mostly composed of less stiff microwave heaters (e.g., chalcopyrite), which has a low or comparable elastic modulus value to most gangue minerals. The extent of microwave-induced fractures is expected to decrease even further when the ore is mostly composed of chalcocite or bornite, which have a lower modulus of elasticity than that of chalcopyrite due to their higher copper content and lack of iron (Djordjevic, 2014).

5.5 Mineralogy and Texture Results

5.5.1 Ore 1

Ore 1 is a quartz monzonite porphyry copper ore, and the grouped modal mineralogy MLA results of this sample are shown in Table 5.2. This ore contains chalcopyrite as the dominant copper sulphide mineral and pyrite as the dominant iron sulphide mineral, both iron and copper sulphides are good microwave heaters. The ore also consists of a non-sulphide microwave-heating mineral (montmorillonite), and a small proportion of poorly heating minerals such as hematite and ilmenite. The combined weight of all microwave heaters is about 6%. The non-heating gangue is dominated by quartz and felspar, both are hard gangue minerals (>6 on the Mohs hardness scale). The combined weight of these hard gangue minerals is approximately 65%. The soft gangue mostly consists of phlogopite, muscovite, and biotite. Further analysis

showed that the microwave heaters have a ~31% association with soft gangue, ~54% with hard gangue and 10% with free space.

Table 5.2. Average modal mineralogy- Ore 1 (Ure, 2017)

Grouped Minerals			Modal (wt%)	Total modal (wt%)
Good MW heaters		Chalcopyrite	0.71	
		Other copper sulphides	0.02	
		Pyrite	2.78	
		Other sulphides	0.01	
		Montmorillonite	2.64	6.16
Other MW heaters		Iron oxides (magnetite, hematite, ilmenite)	0.17	
		Rutile	0.00	0.17
Non-heating gangue	**Hard gangue ≥6 (Mohs scale)**	Quartz	37.01	
		Feldspar	28.03	
		Dravite	0.00	
		Other hard gangue	1.43	66.47
	Soft gangue <6 (Mohs scale)	Phlogopite	11.08	
		Muscovite	4.75	
		Biotite	7.64	
		Chlorite	2.46	
		Other soft gangue	1.27	27.20

The XRD pattern of Ore 1 is shown in Figure 5.4. Based on this pattern, the ore consists of quartz, feldspar, phlogopite, biotite, chalcopyrite, and pyrite. Though the proportion of these minerals is not indicated, the major phases identified on the XRD pattern were also detected in the MLA results of this sample, as reported by Ure (2017). The mineral matching in these two studies suggests that the ore samples are identical because they came from the same lot though studied at different times. This justifies the use of MLA results shown in Table 5.2 and Figure 5.5 to describe the mineralogy and texture of the Ore 1 sample used in the current study.
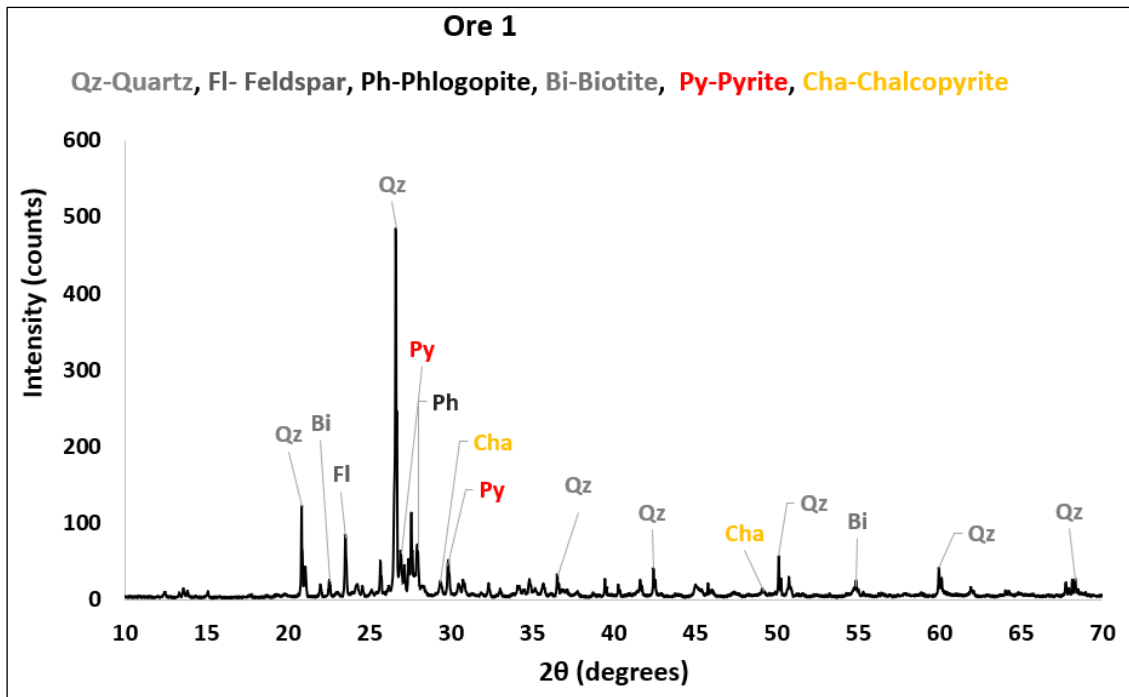
Figure 5.4. XRD pattern – Ore 1

Figure 5.5 shows examples of MLA grouped mineral maps of Ore 1 fragments. These images show that pyrite occurs as disseminated finer grains, coarse discrete grains of up to 1.5 mm (fragment E) or as micro-vein (fragment F). Similarly, the copper sulphide grains occur as micro-veins (see fragments G and H) or as finely disseminated grains. Also, copper sulphides have little association with iron sulphides (pyrite).
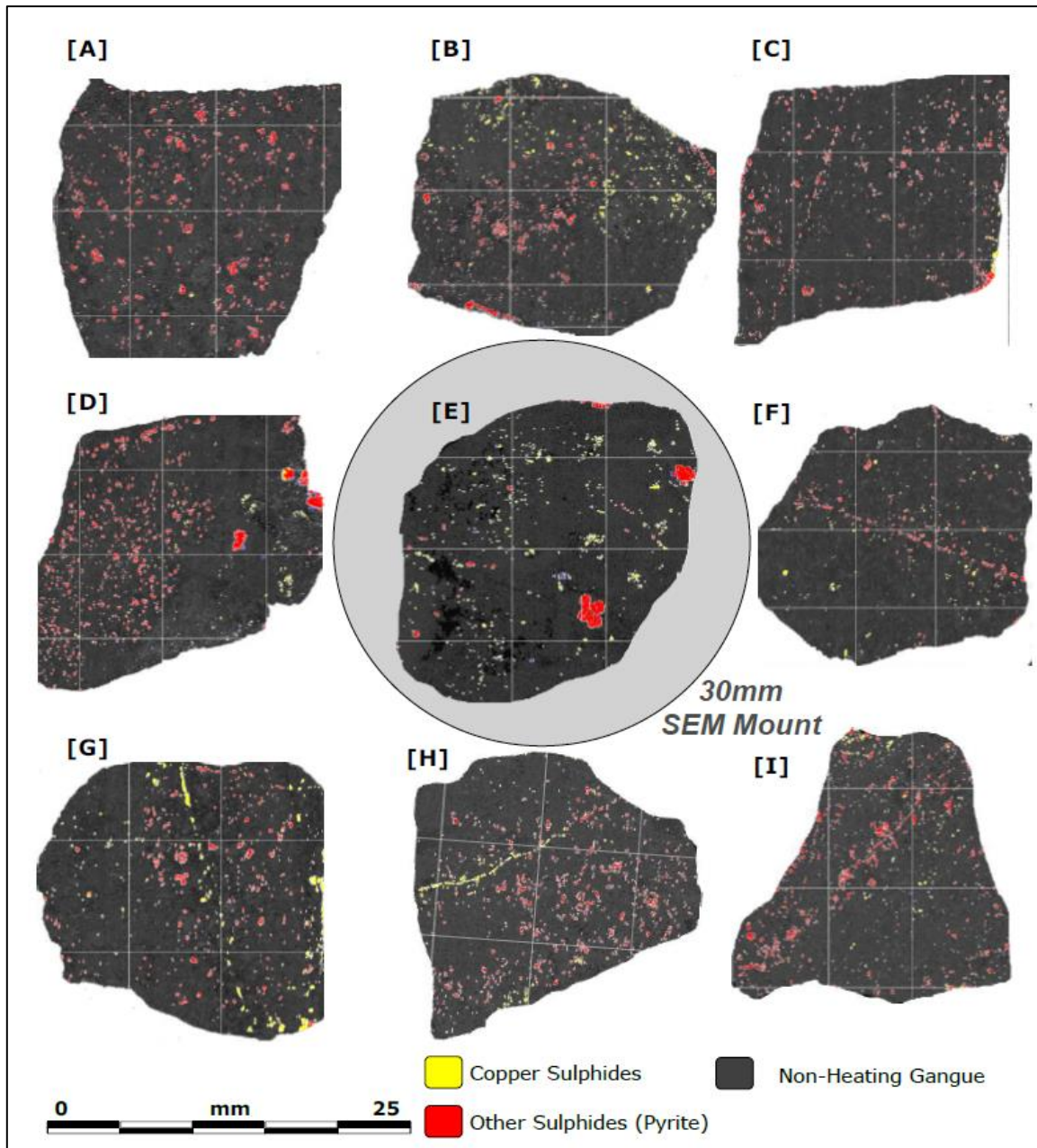
Figure 5.5. Example textural images from MLA (false colour) – Ore 1 (Ure, 2017)

Figure 5.6 shows the grain size distribution of microwave heating phases in Ore 1. These results show that pyrite grains (a large proportion of other sulphides) are relatively coarser than copper sulphide grains or other heaters. The D_{50} of pyrite grains is approximately 190 µm, whereas those of copper sulphides and other microwave heaters are about 130 µm and 47 µm, respectively.
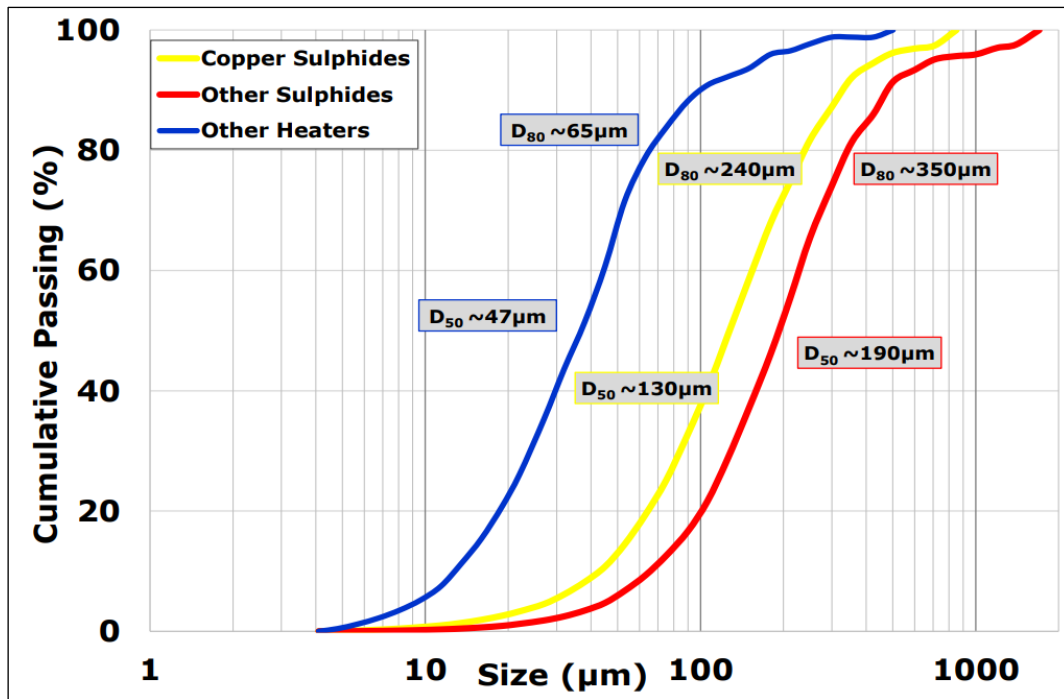
Figure 5.6. Grain size distribution of MW heating phases – Ore 1 (Ure, 2017)

Based on mineral modal abundance and textural observations, this ore should be amenable to microwave-induced fracture. This is due to the combined effects of the high modal abundance of good microwave heaters, the coarse grain size of microwave heaters, and a large proportion of hard gangue non-heating matrix. This texture promotes intense local heating, and the hard (brittle) gangue matrix does not undergo ductile deformation to absorb the thermal expansion of microwave heaters. As a result, larger stresses are generated, leading to increased ore fracturing.

Furthermore, crack propagation will be facilitated by the pyrite grains present in this ore. This is because pyrite has a much higher modulus of elasticity (i.e., stiffer) than the gangue minerals present in this ore (quartz and feldspar), and thus during microwave treatment, it can effectively transfer the induced stresses to the surrounding gangue matrix. As a result, greater damage is induced in the gangue matrix, which reduces the ore strength and increases the mineral exposure of other sulphide minerals (e.g., chalcopyrite).

A study conducted by Batchelor et al. (2017) and Ure (2017) indicated that Ore 1 (designated as Ore 2) achieved a higher strength reduction of JKDWT (A*b) of 7-14%, and a significant reduction in BBWI of 2.6-8.7% at a microwave treatment dose of 0.7-1.3 kWh/t.

5.5.2 Ore 2

Ore 2 is a quartzite copper ore consisting of chalcopyrite as the main copper sulphide mineral and pyrite as the main iron sulphide mineral as indicated in Table 5.3. The ore also contains small proportions of other microwave heaters such as bornite, covellite, and montmorillonite. The combined proportion of microwave heaters is about 2%. The non-heating gangue is dominated by the hard gangue matrix, mainly quartz (~90%). The total proportion of the soft gangue matrix is about 5% only.

Table 5.3. Average modal mineralogy - Ore 2 (Ure, 2017)

Grouped Minerals		Modal (wt%)	Total modal (wt%)
Good MW heaters	Chalcopyrite	0.82	
	Other copper sulphides	0.27	
	Pyrite	0.56	
	Other sulphides	0.05	
	Montmorillonite	0.30	2.00
Other MW heaters	Iron oxides (hematite, ilmenite)	0.00	
	Rutile	0.00	0.00
Non-heating gangue	Hard gangue ≥6 (Mohs scale) — Quartz	90.76	
	Feldspar	1.61	
	Other hard gangue	0.07	92.44
	Soft gangue <6 (Mohs scale) — Phlogopite	3.14	
	Muscovite	1.15	
	Biotite	1.16	
	Chlorite	0.07	
	Carbonates	0.00	
	Other soft gangue	0.04	5.56

Figure 5.7 shows the XRD pattern of the Ore 2 sample. The major phases identified in this pattern are quartz, muscovite, phlogopite, pyrite, and chalcopyrite. These major phases were also detected in the MLA results shown in Table 5.3 and Figure 5.8 which supports the use of these MLA results to describe the mineralogy and texture of Ore 2 in the current study.
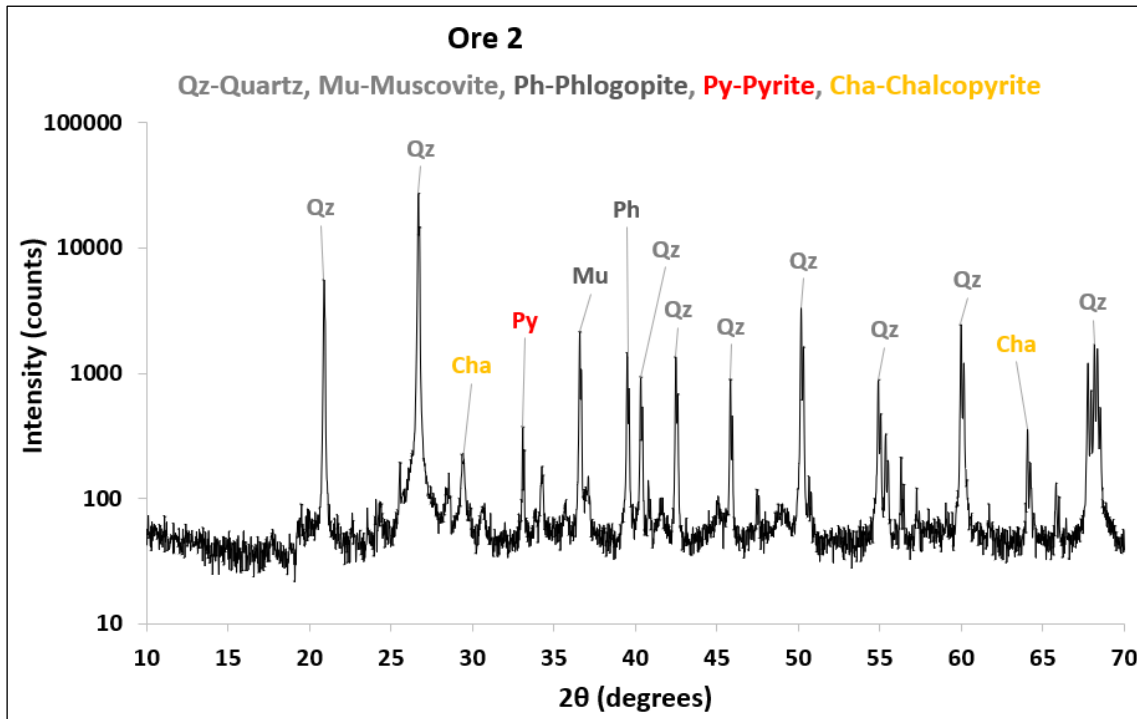
Figure 5.7. XRD pattern – Ore 2

Figure 5.8 shows examples of grouped textural images of Ore 2 fragments. It can clearly be seen that this ore is dominated by copper sulphide grains, and these grains are disseminated throughout the fragments, or deposited as discrete grains along the naturally fractured planes (fragment G). Since the fragments were selected based on their textural differences to represent the bulk ore, some had mixed phases of copper and iron sulphides, while others had mostly a single phase of either copper sulphide (fragments A and H) or pyrite (fragment E). This variation in mineralogy or texture between fragments within an ore indicates that some fragments are more amenable to microwave-induced fractures than others. As a result, the

proportion of more amenable fragments within an ore dictates the extent of overall induced damage.

The average grain size distribution of microwave heaters in these fragments shows that both copper and iron sulphides have a D_{50} of around 160-170 µm (Figure 5.9). Other microwave heaters are relatively finer, having a D_{50} of about 38 µm. It can also be noticed that Ore 2 is comprised of a large proportion of voids, see the dark spots in most of the fragments in Figure 5.8. Though it is possible that some sulphide grains were dislodged during sample preparation, leaving the large voids (vugs) seen in these images. The association data shows that the microwave-absorbing grains have a 19% association with free space (including the vugs), 65% with the hard gangue and 8% with the soft gangue. Also, in some fragments, copper sulphides have a good association with pyrite (fragments C&F).
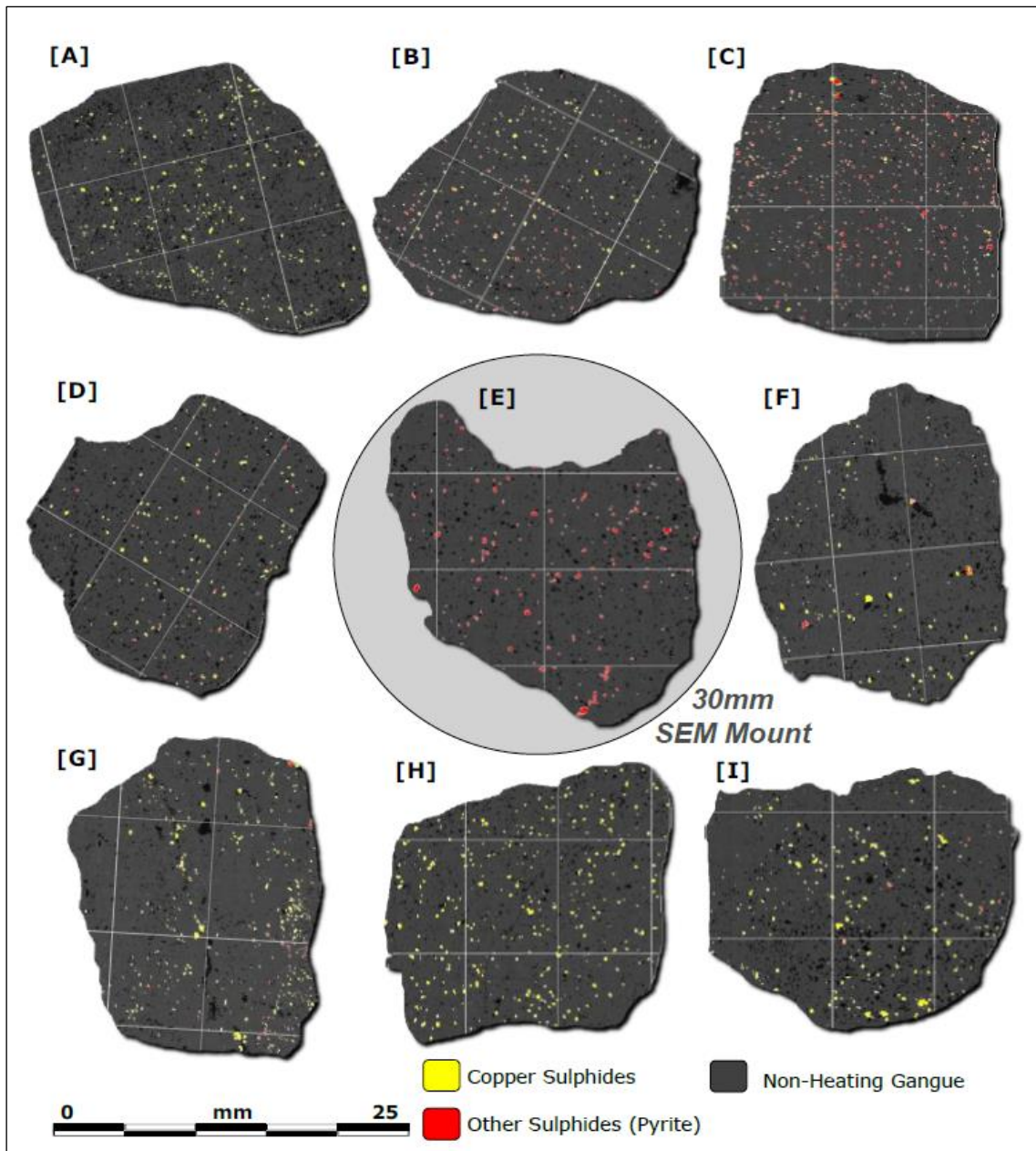
Figure 5.8. Example textural images from MLA (false colour) – Ore 2 (Ure, 2017)
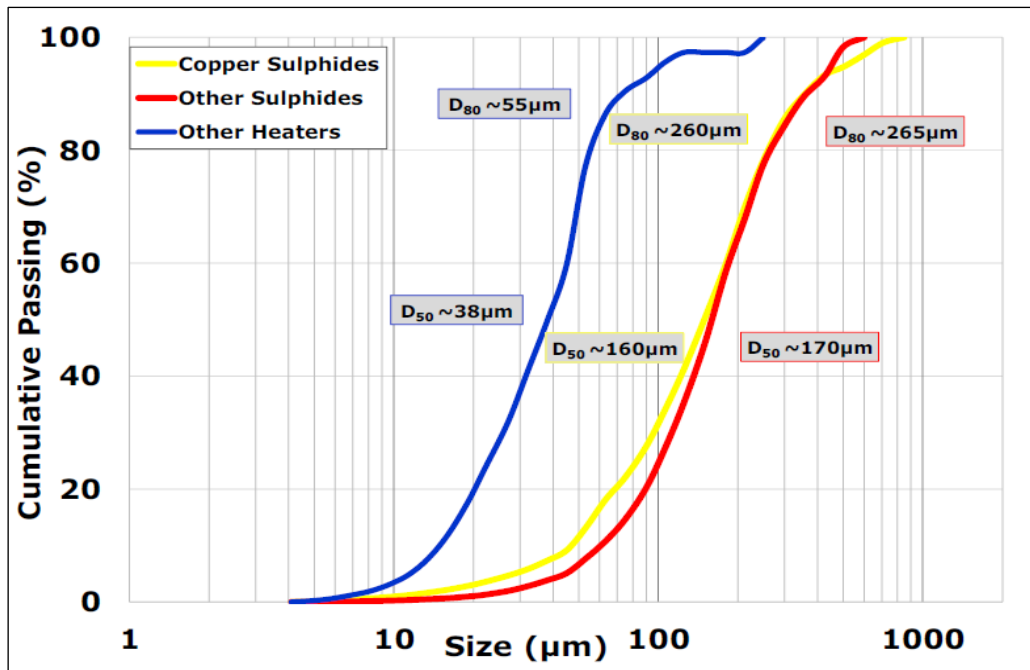
Figure 5.9. Grain size distribution of MW heating phases – Ore 2 (Ure, 2017)

Based on mineralogical and textural observations, Ore 2 should be amenable to microwave-induced fractures to some extent. This is due to a reasonable proportion of good microwave heaters (2%) and the hard gangue matrix surrounding these heaters. Also, microwave heating is expected to exacerbate the existing fractures in some fragments, particularly if sulphide grains are deposited along these fractures.

However, the magnitude of microwave-induced fractures in this ore will most likely be reduced due to the combined effect of the finer grain size of microwave heaters, the low content of stiffer microwave heaters (e.g., pyrite), and the high association of microwave heaters with free space (contributed by inherent voids). This texture does not effectively promote the generation and transfer of larger thermal stresses during microwave heating, resulting in minimal fractures. The inherent voids within the ore can reduce the induced fractures to some extent because some microwave-absorbing grains expand through free space during microwave treatment. Essentially, the microwave-absorbing grains should be enclosed within a transparent gangue matrix for the effective transfer of stresses and propagation of fractures.

162

Using Ore 2 (designated as Ore 1), Batchelor et al. (2017) and Ure (2017) achieved a strength reduction of JKDWT (A*b) of up to 7% and a reduction in BBWI of 2.5% at microwave treatment dose of 1 kWh/t.

5.5.3   Ore 3

Ore 3 is a limestone skarn low-grade copper ore, and Table 5.4 shows the grouped modal abundance of this sample. This ore is composed of chalcopyrite as the dominant copper sulphide mineral and pyrite as the dominant iron sulphide mineral. Other microwave heaters composed in this ore though in small proportions are montmorillonite and iron oxides (magnetite, hematite). The combined weight proportion of microwave heaters in this ore is approximately 7%, dominated by pyrite (5.3%). The non-heating phase consists of soft minerals (mostly chlorite) and small proportions of biotite and carbonate minerals e.g., calcite. The non-heating hard gangue matrix consists of feldspars (plagioclase and orthoclase) and quartz. The hard and soft minerals have combined weight proportions of approximately 33% and 59%, respectively. The microwave heaters in this ore have a 51% association with the soft gangue, 28% with the hard gangue and 4% with free space.

Table 5.4. Average modal mineralogy - Ore 3

Grouped Minerals			Modal (wt%)	Total modal (wt%)
Good MW heaters		Chalcopyrite	0.55	
		Other copper sulphides	0.11	
		Pyrite	5.31	
		Other sulphides	0.00	
		Montmorillonite	0.06	**6.03**
Other MW heaters		Iron oxides (magnetite, hematite, ilmenite)	1.27	
		Rutile	0.00	**1.27**
Non-heating gangue	**Hard gangue ≥6 (Mohs scale)**	Quartz	11.72	
		Orthoclase	19.71	
		Other hard gangue	1.88	**33.31**
	Soft gangue <6 (Mohs scale)	Chlorite, biotite, hornblende	54.40	
		Carbonates	3.30	
		Other soft gangue	1.69	**59.39**

The XRD pattern of the Ore 3 sample is shown in Figure 5.10. This ore appears to be composed of six major phases: pyrite, quartz, felspars (orthoclase), biotite, hornblende and carbonates (calcite). These phases were also detected in the MLA results of the Ore 3 sample available in our records, supporting the use of Table 5.4 and Figure 5.11, in the current work to describe the mineralogy and texture of this sample.
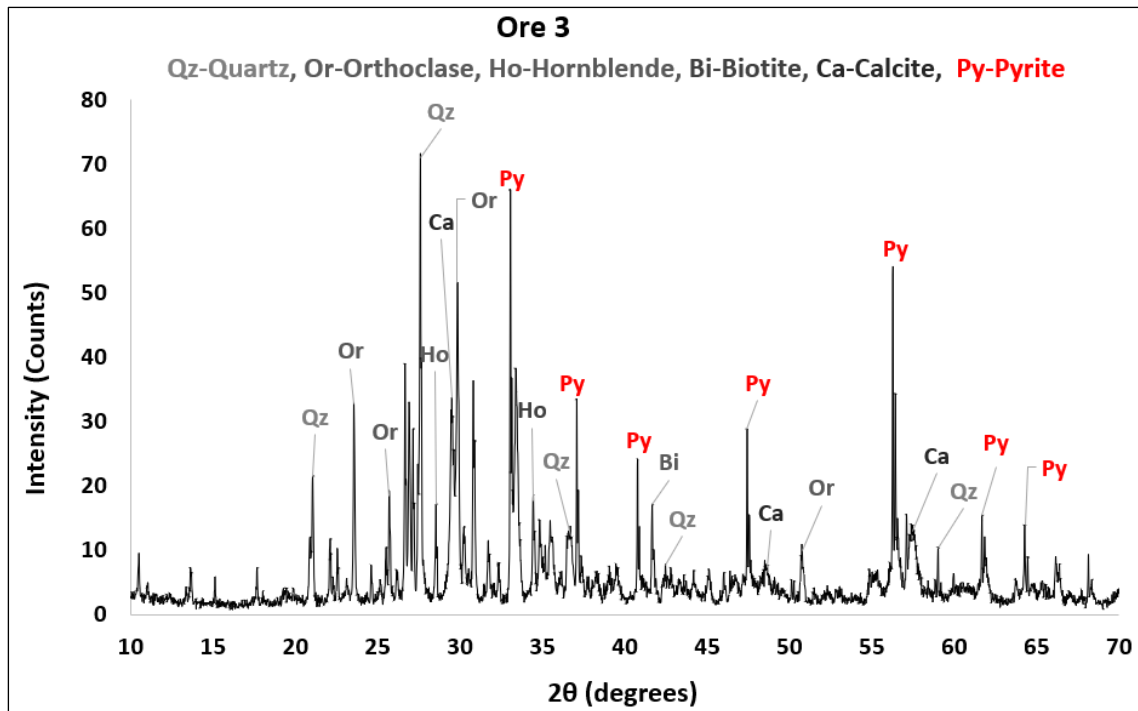
Figure 5.10. XRD pattern – Ore 3

The simplified grouped textural images of Ore 3 fragments are shown in Figure 5.11, indicating two major phases: microwave heaters (dominated by pyrite) and non-heating gangue matrix. This figure shows that the microwave heaters occur as coarse discrete grains or macro-veins (see fragments A to E). Some fragments consist of fine grains of microwave heaters which are mostly disseminated or occur as microveins (see fragments F to I). The grain size distribution of microwave heaters in this ore type is shown in Figure 5.12. The ore contains relatively larger grains of microwave heaters (e.g., pyrite) with D_{50} of up to 500 µm. Because of the higher modal abundance of good microwave heaters and the coarser grain size of these heaters in most of the fragments, Ore 3 is a potential candidate for microwave-induced fractures. During microwave treatment, this texture promotes faster heating and higher thermal stresses. The higher pyrite content in this ore type facilitates crack propagation because it is both a good and stiffer microwave heater.

165

However, this ore contains a high percentage of soft gangue matrix (59%), which can absorb induced thermal and undergo ductile deformation, thereby reducing the magnitude of microwave-induced fractures to some extent. Furthermore, fragments with high surface sulphide mineralisation will most likely reflect microwave energy, potentially resulting in electrical arcing and decreased ore fracturing.
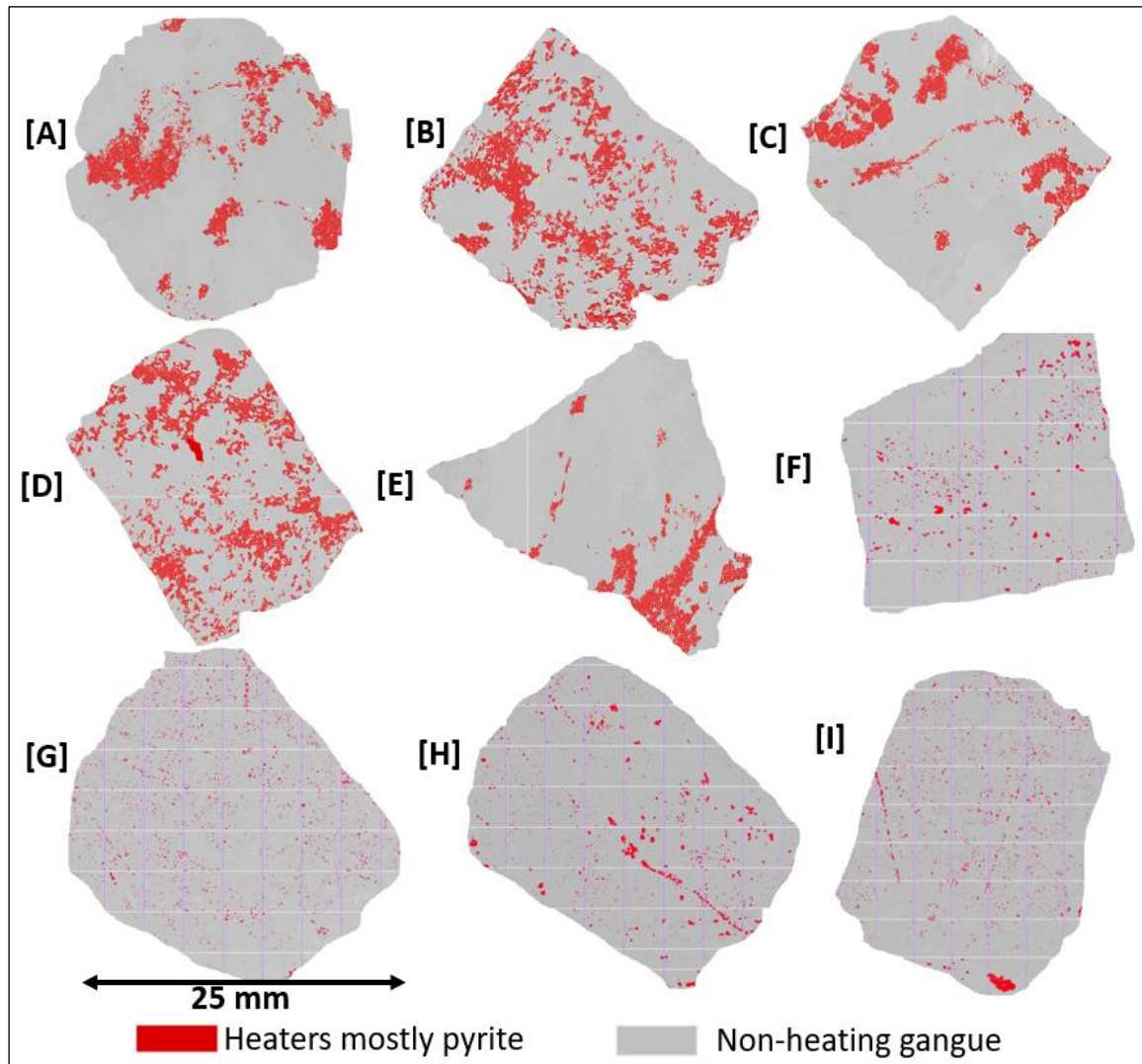
Figure 5.11. Example textural images from MLA (false colour) – Ore 3
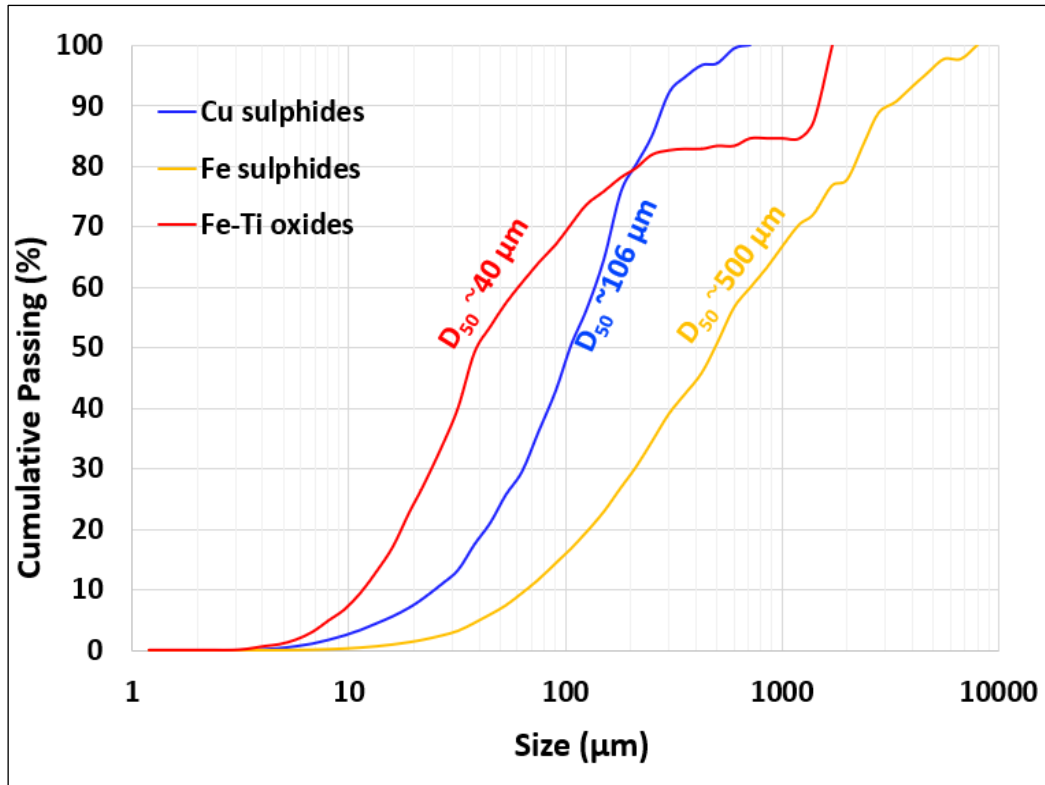
Figure 5.12. Grain size distribution of MW heating phases – Ore 3

5.5.4 Ore 4

Ore 4 is a porphyry copper ore, and the modal abundance of this sample is presented in Table 5.5. The main copper sulphide mineral in this ore is chalcopyrite. It can be noticed that this ore contains a significant amount of good microwave heaters, predominantly pyrite (~11%) followed by magnetite (~1%) and chalcopyrite (~0.7%). Other microwave heaters though in small proportions include hematite, ilmenite, and rutile. The combined weight of all microwave heaters is relatively high (~13%). The non-heating phases consist of hard and soft minerals, with almost equal proportions. The hard and soft gangue minerals are dominated by quartz and muscovite respectively. The microwave heaters in this ore have a 47% association with the soft gangue, 40.5% with the hard gangue and 4.3% with free space.

Table 5.5. Average modal mineralogy - Ore 4

Grouped Minerals			Modal (wt%)	Total modal (wt%)
Good MW heaters		Chalcopyrite	0.68	
		Other copper sulphides	0.02	
		Pyrite	11.75	
		Other sulphides	0.00	
		Magnetite	1.19	13.64
Other MW heaters		Other iron oxides (hematite, ilmenite)	0.23	
		Rutile	0.14	0.37
Non-heating gangue	Hard gangue ≥6 (Mohs scale)	Quartz	39.03	
		Feldspar	0.85	
		Dravite	4.30	
		Other hard gangue	0.96	45.14
	Soft gangue <6 (Mohs scale)	Phlogopite	0.00	
		Muscovite	38.64	
		Biotite	1.09	
		Chlorite	1.06	
		Other soft gangue	0.06	40.85

Figure 5.13 shows the XRD pattern of the Ore 4 sample. This pattern indicates that the ore consists of four major phases i.e., quartz, muscovite, pyrite, and magnetite. These phases were also found in the MLA results of the Ore 4 sample in our records, which supports the use of the MLA results shown in Table 5.5 and Figure 5.14 to describe the mineralogy and texture of this sample.
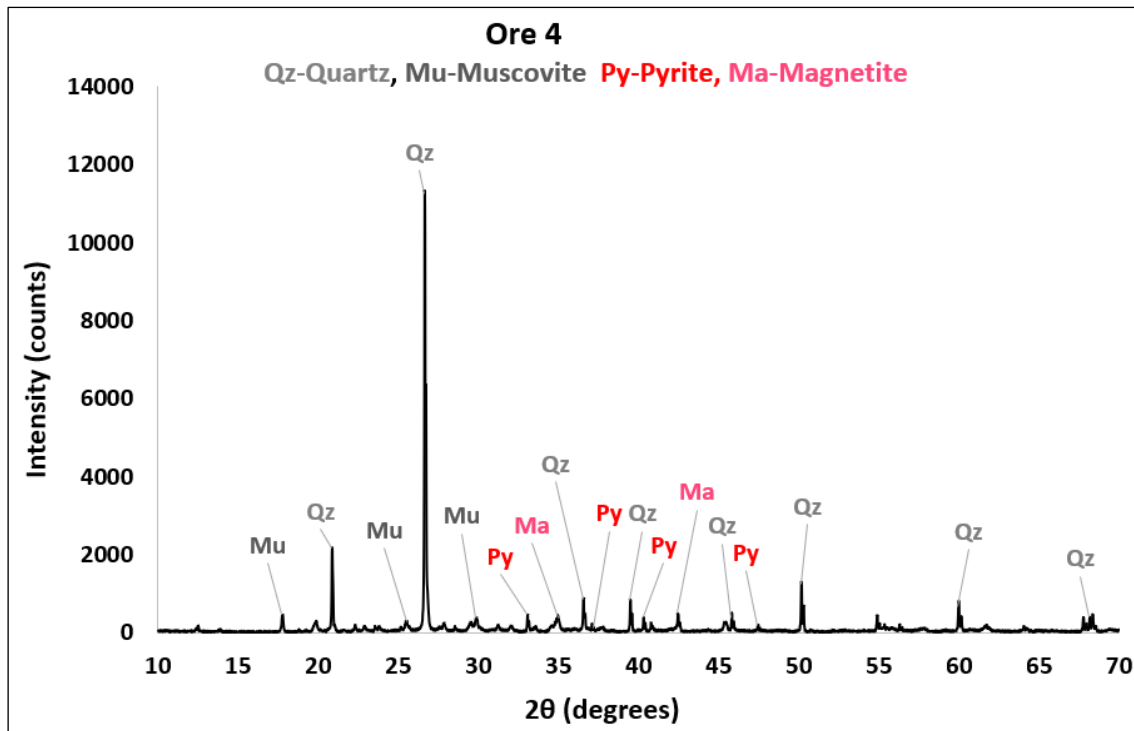
Figure 5.13. XRD pattern – Ore 4

Figure 5.14 shows examples of grouped textural images of Ore 4 fragments. It can clearly be seen in these images that iron sulphide (mainly pyrite) occurs as macro-vein (fragment C), clustered grains (fragment D), or as finely disseminated grains over the entire fragment (fragment B). On the other hand, magnetite occurs as coarse discrete grains in a mutual association with iron-titanium oxides (fragments D and G). There were few fragments which had relatively lower sulphide and iron oxide contents (e.g., fragments H and I), fragments with this type of texture are expected to exhibit minimal or no induced fractures upon microwave treatment.
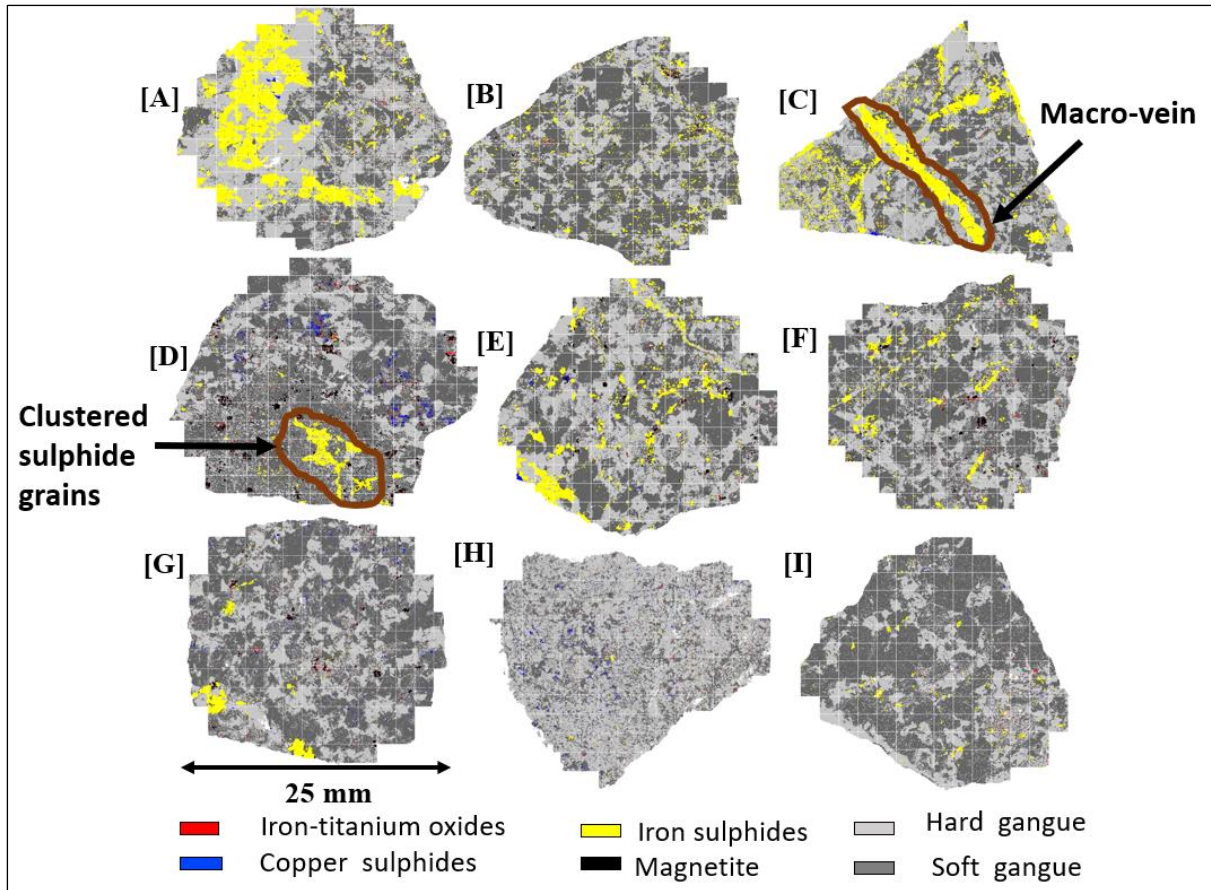
Figure 5.14. Example textural images from MLA (false colour) – Ore 4

The grain size distribution shown in Figure 5.15 indicates that iron sulphides (mainly pyrite) have a coarser grain size (D_{50}) of approximately 600 µm. This grain size does not represent a native grain size of pyrite but a combination of several grains joining together to form mineralised veins. Other microwave heaters such as magnetite and copper sulphides have native grain sizes of about 90-125 µm. The iron-titanium oxides have a relatively finer grain size of about 25 µm.
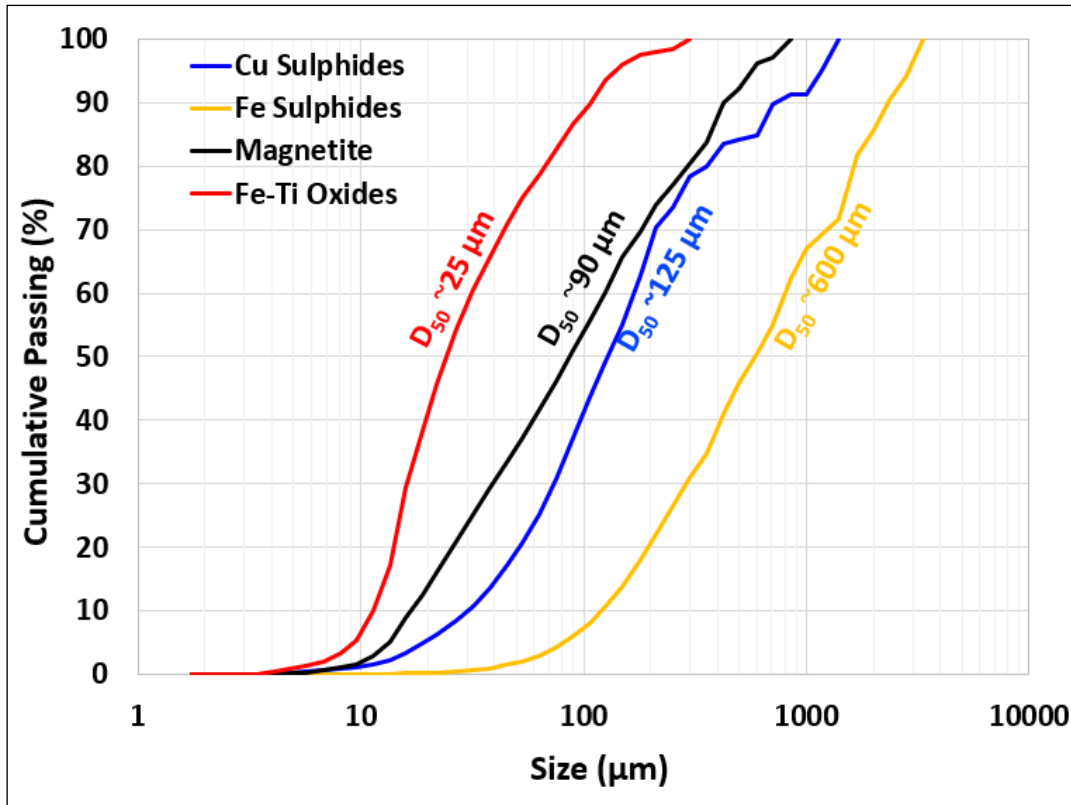
Figure 5.15. Grain size distribution of MW heating phases – Ore 4

Ore 4 is a potential candidate for microwave treatment due to the higher modal abundance and coarser grain size of good microwave heaters, which appear as clustered grains (fragment D) or macro-veins (fragment C) (see Figure 5.14). The stiffness of pyrite and magnetite, the dominant microwave heaters in this ore, will promote crack propagation even further. However, the soft gangue matrix present in this ore can absorb some of the induced stresses and undergo ductile deformation, reducing the degree of microwave-induced fractures to some extent. Some ores with mixed phases of hard and soft gangue matrix investigated in the previous microwave studies (e.g., Ore 1) have achieved a higher strength reduction of JKDWT (A*b) of 7-14% at a microwave dose of about 1 kWh/t (Batchelor et al., 2017). Similarly, Ore 4 is most likely one of the best ore candidates for microwave-induced fractures in this study, given the higher modal abundance and coarser grain size of good microwave heaters.

In terms of leaching, Ore 4 is expected to achieve higher metal extraction due to microwave-induced fractures, which are enhanced by the favourable mineralogy and texture of this ore. These fractures which mostly occur in the vicinity of sulphide grains, will maximize the mineral exposure to the leach solution, leading to higher metal leach extraction.

5.5.5 Ore 5

Ore 5 is an alkalic porphyry copper ore. As stated in Section 5.2, the modal mineralogy of this ore was determined using a finely ground sample of five size fractions with particles ranging from +300 to -106 µm. The average modal abundance of these five size fractions is presented in Table 5.6. This is the more accurate modal mineralogy because it represents the whole ore rather than just a few fragments. The ore consists of bornite and chalcopyrite as the main copper sulphide minerals. It also contains a large proportion of iron oxides (3.3%), dominated by magnetite and a negligible proportion of pyrite. The combined weight proportion of all microwave heaters is approximately 5%. The ore is composed of both hard and soft non-heating gangue minerals, dominated by feldspar and muscovite, respectively. The combined weight proportions of hard and soft gangue minerals are about 64% and 31%, respectively. The microwave heaters in this ore have a 91% association with the hard gangue, 4% with the soft gangue, and 4% with free space.

Table 5.6. Average modal mineralogy - Ore 5

Grouped Minerals		Modal (wt%)	Total modal (wt%)
Good MW heaters	Chalcopyrite	0.48	
	Bornite	0.60	
	Other copper sulphides	0.01	
	Pyrite	0.06	
	Other sulphides	0.03	
	Montmorillonite	0.00	1.18
Other MW heaters	Iron oxides (magnetite, hematite, ilmenite)	3.32	
	Rutile	0.56	3.88
Non-heating gangue	**Hard gangue ≥6 (Mohs scale)** Quartz	2.98	
	Feldspar	59.84	
	Other hard gangue	1.09	63.91
	Soft gangue <6 (Mohs scale) Phlogopite	0.00	
	Muscovite	22.77	
	Biotite	0.00	
	Carbonates	2.12	
	Chlorite	5.88	
	Other soft gangue	0.26	31.03

The XRD pattern of Ore 5 is shown in Figure 5.16. This pattern indicates that the ore is composed of magnetite, feldspar-muscovite mixed phases, quartz, chlorite, and carbonate minerals (e.g., calcite and copper carbonate). In general, most of the major mineral phases indicated on the XRD pattern were also detected in the MLA results of this ore.
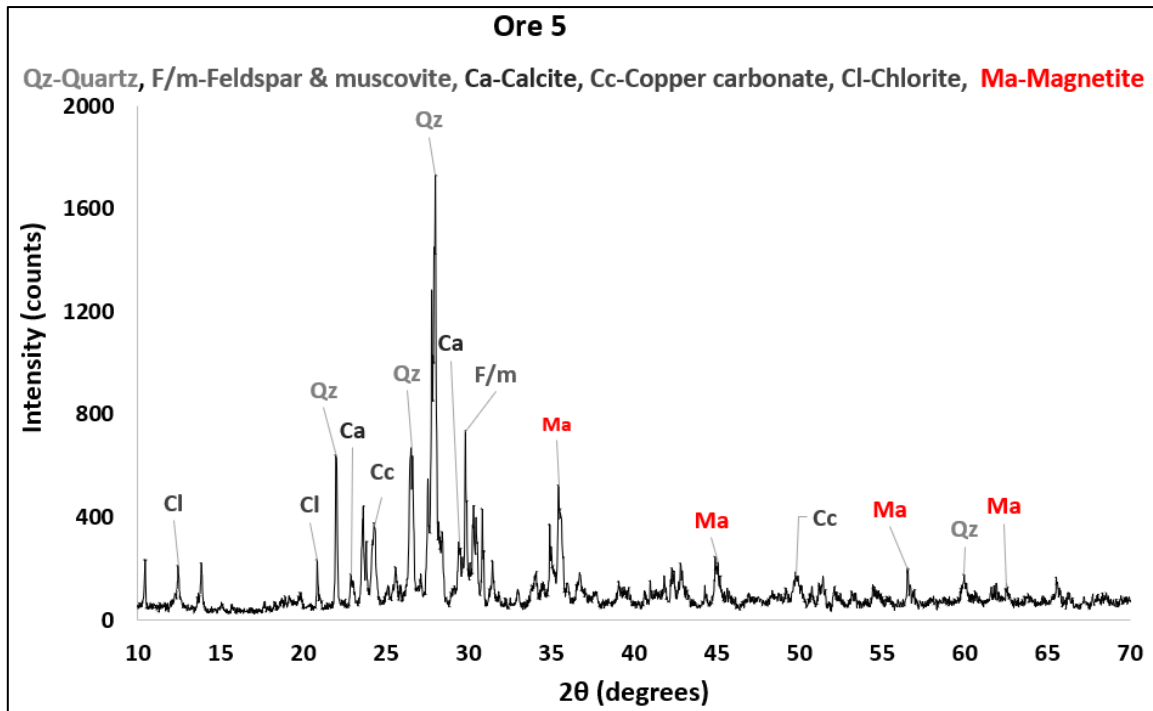
Figure 5.16. XRD pattern – Ore 5

Examples of grouped textural images of Ore 5 fragments are shown in Figure 5.17. It is worth noting that only four fragments were selected from this ore. Of course, these four fragments do not adequately represent the texture of the entire ore, but they are presented here to demonstrate the textural variations present in this sample. This figure shows that the copper sulphide mineralisation is in the form of finely disseminated grains (fragment A), micro-veins (fragments B and C), or coarse discrete grains and macro-veins (fragment D). It can also be seen that magnetite has a good association with iron-titanium oxides but little or no association with copper sulphides.
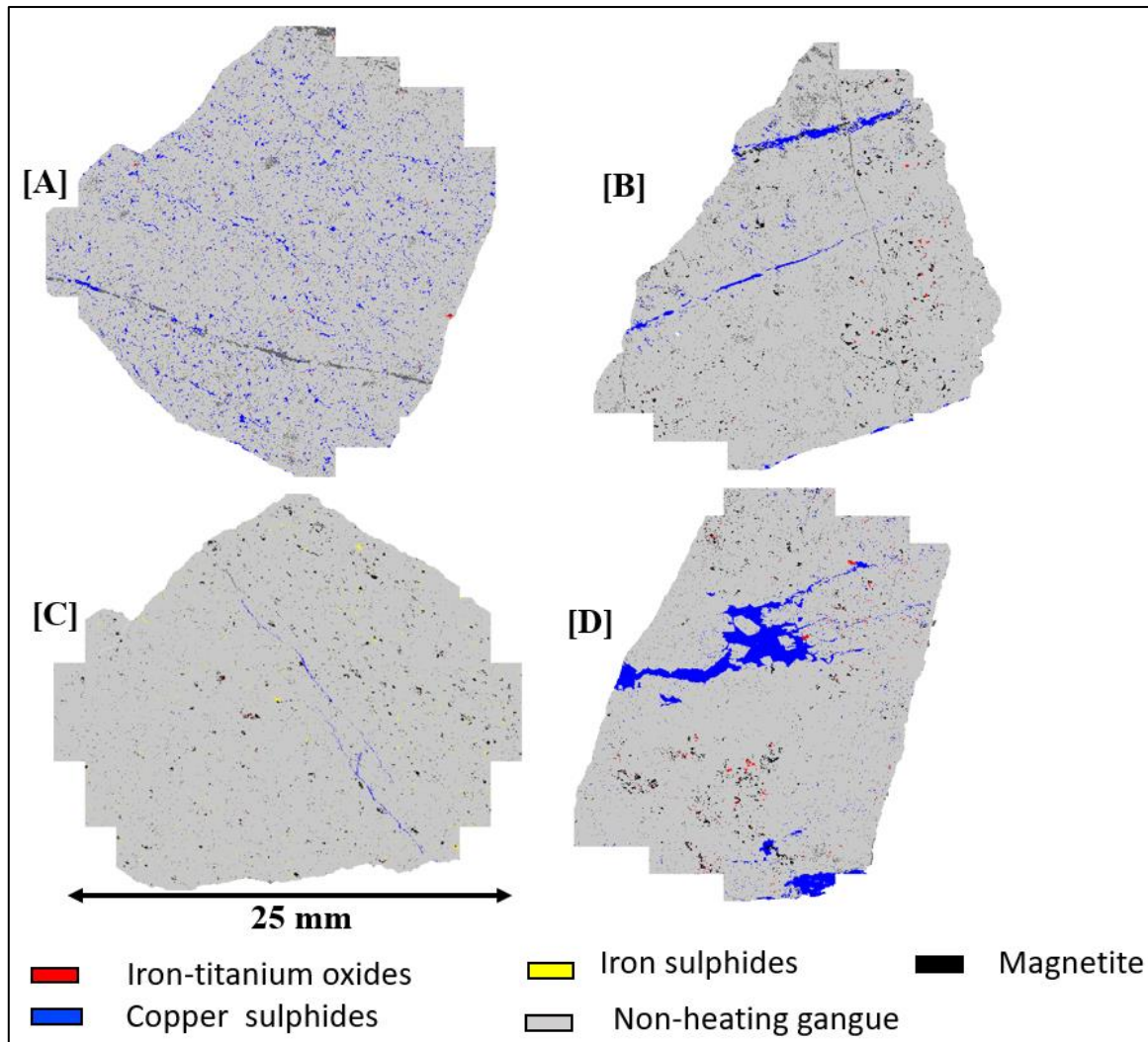
Figure 5.17. Example textural images from MLA (false colour) – Ore 5

Figure 5.18 shows the average grain size distributions of microwave heating phases derived from the four fragments shown in Figure 5.17. Though these distributions were generated using only a few fragments, it can generally be seen that most microwave heating phases, such as iron sulphides (pyrite), magnetite, and iron-titanium oxides, are relatively finer (D_{50} = 38-75 μm). The average grain size of copper sulphide is about 212 μm. It is also important to mention that visual observation showed that only a small proportion of Ore 5 fragments had a texture with coarse sulphide mineralisation (~1%.)
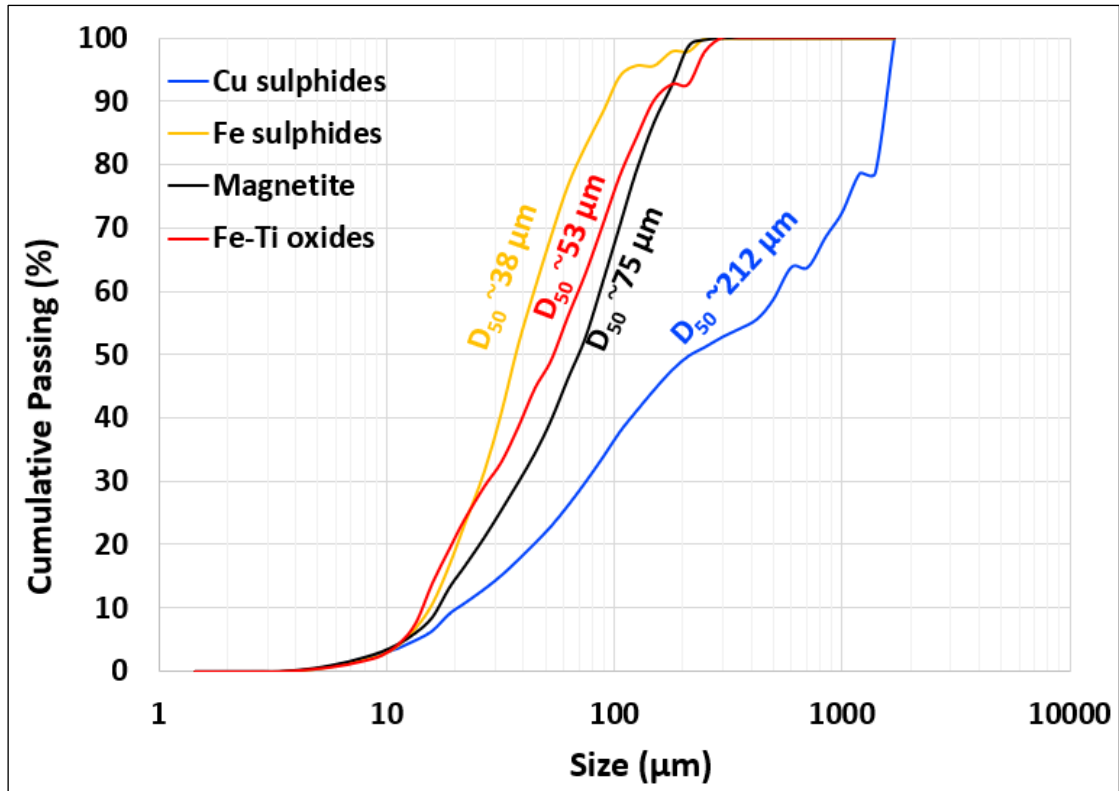
Figure 5.18. Grain size distribution of MW heating phases – Ore 5

The mineralogical and textural observations indicate that Ore 5 should be amenable to microwave-induced fractures. This is due to the higher modal abundance of good microwave heaters and the harder gangue matrix surrounding these heaters. However, the extent of microwave-induced fractures is likely to be reduced to some degree due to the finer grain size of the microwave heaters in most fragments, which account for over 99% of the sample. Although the ore contains a reasonable proportion of magnetite (the stiffer microwave heater), the grain size in most fragments is relatively finer. A few fragments with coarse discrete grains of good microwave heaters or micro-veins are expected to exhibit significant fractures.

5.6 Summary

The mineralogical and textural features of five copper sulphide ores have been evaluated using the MLA and XRD techniques. This evaluation aims to give an indication of the potential ore candidates for microwave treatment in order to improve comminution (reduce ore competency) and enhance mineral exposure to assist leaching. The following mineralogical and textural features have been evaluated in this work: the modal abundance of minerals, the grain size distribution of microwave heaters, and the extent of dissemination and association of microwave heaters within ore fragments.

Figure 5.19 shows a summary of key mineralogical and textural features of all five ore types used in the current study. The evaluation of each sample against the criteria for ore amenability to microwave treatment proposed by Batchelor et al. (2015) shows that:

i.   Each ore type has a modal abundance of microwave heaters in the range of 2-20%, with the Ore 4 sample having the highest abundance of 14% and Ore 2 having the lowest abundance of 2%.

ii. Ores 3 and 4 met the criteria of having the coarsest grain size of microwave heaters of D_{50}>500 µm. The other three samples have the coarsest grain size within a range of 170-212 µm, with Ore 2 having the smallest grains (170 µm).

iii. The modal abundance of hard gangue matrix in each ore is greater than 50%, with the exception of Ore 4 (45%) and Ore 3 (33%). Ore 2 has the hardest gangue matrix, with a modal abundance of 92%. The association data shown in Figure 5.20 (normalised to 100%) indicates that the microwave heaters in Ores 1, 2, and 5 have over 57% association with the hard gangue. The microwave heaters in Ore 2 have a high association of ~20% with free space, whereas the microwave heaters in other ore types have a 4-10% association with free space.

iv.   The microwave heaters are more clustered or occur as micro-veins in most fragments for Ores 4, 3, and 1, whereas those in Ores 2 and 5 are mostly finely and highly disseminated.
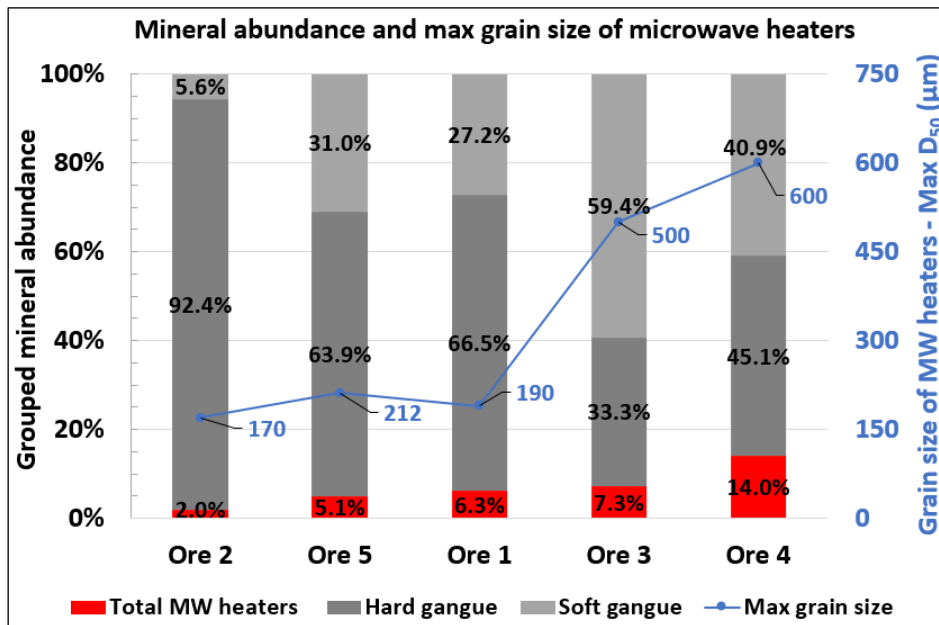
Figure 5.19. Mineral abundance and grain size of microwave heaters summarised
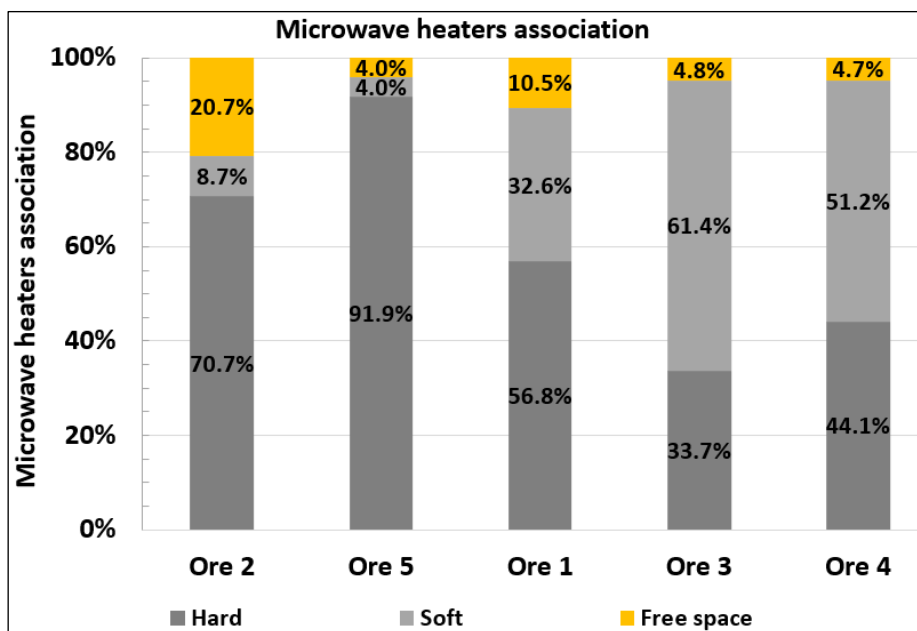
Figure 5.20. Microwave heaters association

178

Based on the listed criteria, all five ore samples are generally potential candidates for microwave-induced fractures. However, the mineralogical and textural differences between these ore types suggest that some should be more amenable to microwave-induced fractures than others. Ore types with some of the following properties are expected to exhibit significant fractures:

i.   Have a high modal abundance of good microwave heaters.

ii. Consist of coarse/clustered grain size or microveins of microwave heaters.

iii. Consist of microwave heaters enclosed within a hard and brittle gangue matrix.

Given a sufficient microwave energy dose, this type of mineralogy and texture promotes intense heating and thermal stresses within the ore, resulting in micro/macro-fractures. Also, the presence of stiffer microwave heaters (e.g., pyrite and magnetite) in the ore is advantageous because they can effectively transfer induced stresses in the low-strength gangue matrix (e.g., feldspar), increasing the degree of ore fracturing. However, the magnitude of microwave-induced fractures is reduced to some extent when a large proportion of microwave absorbent phases are constrained within a soft gangue matrix or are exposed to free space. The soft gangue matrix absorbs the thermal shock and undergoes ductile deformation, which means less stress is available for ore fracturing. The high association of microwave heaters with free space (like in Ore 2) can reduce ore fracturing to some extent because less gangue matrix (crack propagation site) is available close to the microwave heaters, and thus the little stresses generated are mostly wasted to the free space.

Furthermore, it is worth noting that the proportion of amenable fragments in the ore determines its suitability for microwave treatment. Overall, ore types with a higher proportion of amenable fragments are better candidates for microwave treatment than those with a lower proportion.

In terms of leaching performance, ore types that exhibit significant microwave-induced fractures are expected to achieve higher metal leaching improvement than those with fewer induced fractures. This suggests that mineralogy and texture influence the leaching performance of microwave-treated ores. Therefore, higher metal leaching improvement should be achieved for ores with suitable mineralogy and texture for microwave-induced fractures. These properties include: higher modal abundance of microwave heaters, coarse/clustered grains of microwave heaters, stiffer microwave heaters, and hard/brittle gangue matrix (e.g., quartz). It is worth noting that the association of stiffer microwave heaters (e.g., pyrite) with copper sulphides would be expected to promote copper dissolution. This is because microwave-induced fractures increase pyrite exposure and the associated minerals (such as chalcopyrite) to the leach solution.

6. MICROWAVE TREATMENT OF MIXED-SIZE FRAGMENTS

6.1 Introduction

The objective of this preliminary work is to investigate the influence of microwave energy input on the extent of ore pre-damage using the copper sulphide ores described in Chapter 5. To achieve this objective, the ore fragments were coarsely crushed and split to obtain representative sub-samples, which were then subjected to microwave treatment at three separate energy levels. The extent of microwave-induced damage was quantified using two techniques: the point load test (PLT) and the crushing test. The general experimental procedure used in this investigation is summarized in Figure 6.1.
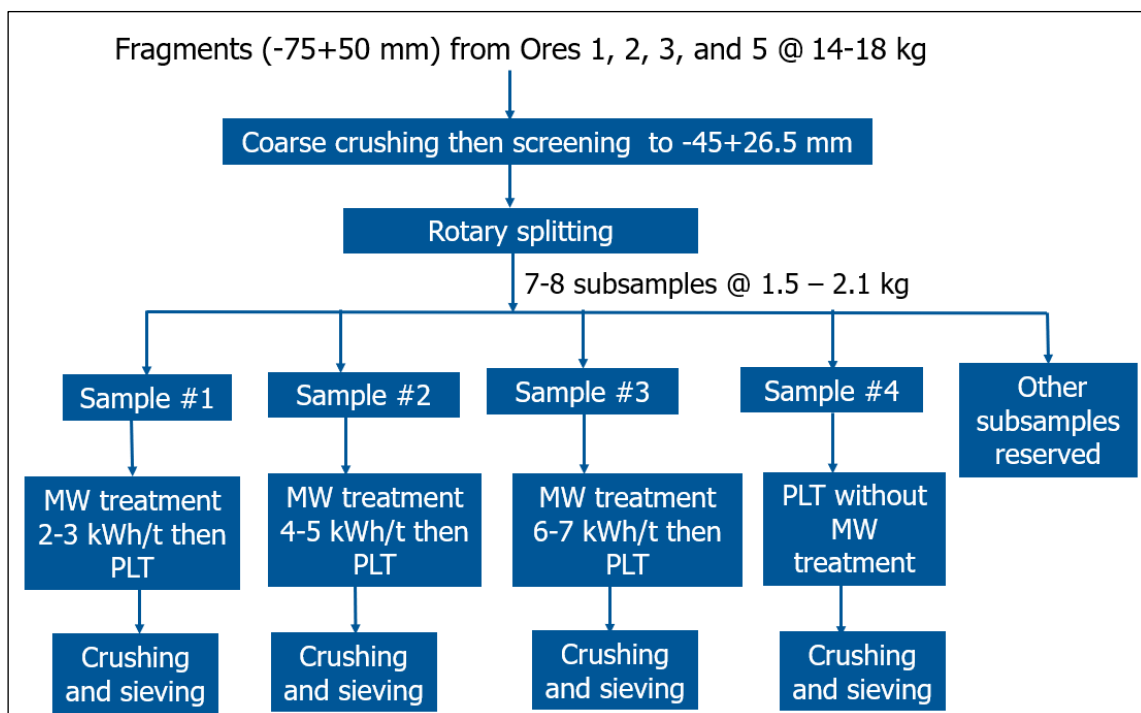
Figure 6.1. General experimental procedure

6.2 Experimental Methods

6.2.1 Sample Preparation

This investigation used the four copper sulphide ores described in Chapter 5, namely Ores 1, 2, 3, and 5. Ore 4 was not used in this initial work because it was not available when this investigation was conducted, but it was later used in the leaching work reported in Chapters 7 and 8. Ore fragments (-75+50 mm) of varying texture were selected from large batches of 50-100 kg samples based on physical observation to represent the bulk of the ore sample, making a total of 14-18 kg samples from each ore type. The large fragments from these samples were coarsely crushed by the jaw crusher before being screened to -45+26 mm and the fines were discarded. Crushing was performed to reduce the size of the fragments so that they could fit inside the microwave cavity during treatment. Each ore type was split into 7-8 subsamples (each weighing ~1.5-2.1 kg) using a rotary splitter, and the fragments from each subsample were numbered for identification during microwave treatment and point load tests (Figure 6.2).
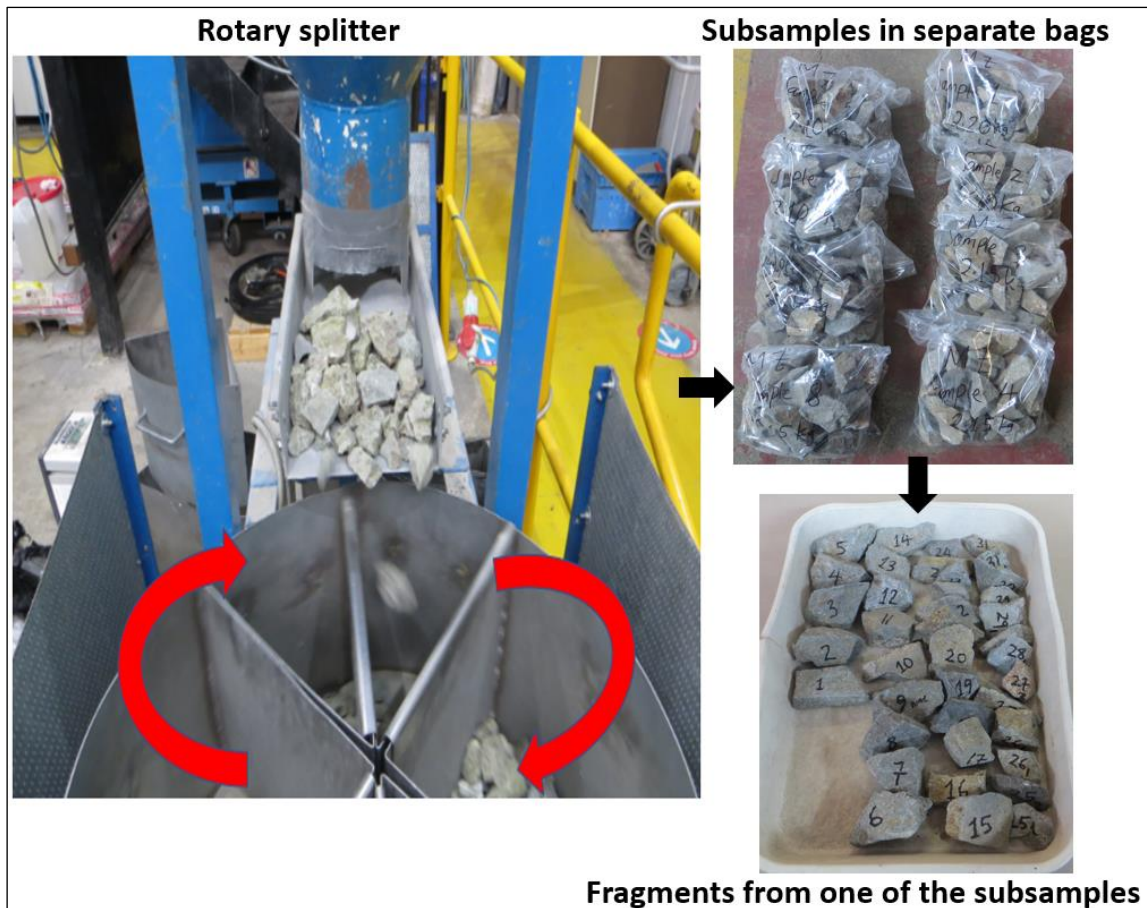
Figure 6.2. Sample preparation

6.2.2 Microwave Treatment Set-up and Methodology

Microwave treatment tests were performed in a TE_{10} single mode cavity using a 3-kW Richardson generator operating at a frequency of 2.45 GHz (Figure 6.3). The microwave power is transmitted from the Magnetron to the applicator through a rectangular waveguide (WR340/430). The circulator diverts the reflected power from the cavity to the recirculating water load and is absorbed there. To ensure maximum power delivery, the ore sample was placed in the region of maximum electric field strength by adjusting the 3-stub and short circuit tuners aided by a vector network analyser (VNA). The forward and reflected powers were measured using power metres, and the difference in their readings represents the power absorbed by the sample. The microwave energy input is determined using Equation 6.1.

$$E = \frac{P_{Abs} \times t}{m}$$ (6.1)

Where;

E = Specific microwave energy input (kWh/t),

P_{Abs} = Absorbed microwave power (kW),

t = Irradiation time (hrs),

m = Sample mass (tonnes).
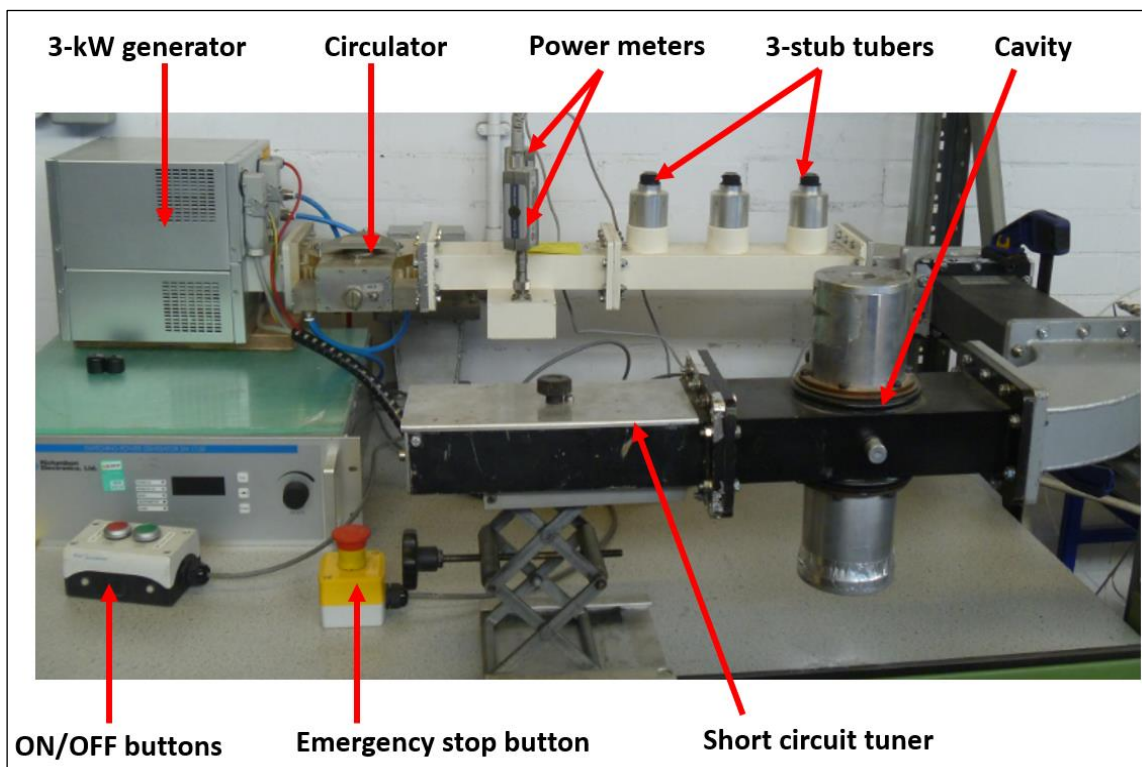
Figure 6.3. Microwave treatment set-up

The microwave treatment tests were carried out in small batches of 50-110 gram samples, using single or multiple fragments of -45+26 mm, depending on their size. To reduce the possibility of electrical arcing (described in Section 2.9), these fragments were placed in a glass quartz tube, and silica sand (the poor microwave absorber) was added to minimize the air gaps between fragments. Each ore type was treated at three different microwave energy levels of

about 2-3, 4-5, and 6-7 kWh/t, using a forward power of 1.5 kW and short treatment times of about 1, 2, and 3 seconds, respectively. A total of 338 treatment batches were performed in all four ore types. The microwave treatment conditions used in this investigation are summarised in Table 6.1, and the full energy profiles are shown in Appendix 11.1.1.

Table 6.1. Microwave treatment conditions summary

Ore type	Microwave Energy level	Total sample mass (g)	Number of treatment batches	Average sample mass per batch (g)	Average forward power (kW)	Average reflected power (kW)	Average absorbed power (kW)	Average Exposure time (sec)	Specific energy (Kwh/t) Weighted average	Max	Min
Ore 1	Low	2101.8	33	63.7	1.49	0.99	0.50	1.05	2.4	5.3	0.4
	Medium	2144.8	34	63.1	1.50	0.84	0.66	1.62	4.8	8.7	1.3
	High	2098.5	31	67.7	1.50	0.86	0.64	2.60	6.9	11.8	1.8
Ore 2	Low	1859.8	30	62.0	1.51	1.02	0.49	1.08	2.3	6.6	0.6
	Medium	1799.5	29	62.1	1.50	0.98	0.52	1.88	4.2	11.9	0.6
	High	1840.6	26	70.8	1.49	0.96	0.54	2.98	6.3	14.8	1.2
Ore 3	Low	1736.4	20	86.8	1.50	0.93	0.57	1.18	2.2	5.6	0.4
	Medium	1512.2	19	79.6	1.49	0.88	0.61	1.97	4.1	7.5	0.9
	High	1672.5	22	76.0	1.47	0.77	0.70	2.64	6.9	16.2	2.3
Ore 5	Low	2073.7	34	61.0	1.50	1.00	0.50	1.16	2.7	8.5	1.0
	Medium	2078.0	29	71.7	1.49	0.87	0.62	2.02	4.7	9.3	0.9
	High	2133.3	31	68.8	1.50	0.91	0.59	2.82	6.9	15.9	1.6
Total			338								

6.2.3   Quantification of Microwave-induced Damage

The magnitude of microwave-induced damage in ore samples was quantified using the point load test (PLT) and the crushing test, based on a decrease in ore strength and an increase in crusher product particle size fineness, respectively. These techniques were selected because they are available, simple and rapid. However, they cannot provide detailed information about the damage, such as fracture size; alternative techniques can be used to obtain such information (e.g., X-ray CT imaging).

An attempt was made in this initial work to examine microwave-induced fractures by X-ray CT technique using two fragments from Ore 3 of -45+26 mm (treated at 2.2 kWh/t). It was found that these fragments were too large to be scanned in full at a high resolution of 10-15

µm, and scanning them at a low resolution of 20-30 µm resulted in poor image quality. To address this challenge, these fragments were scanned in a small region (small field of view) at a resolution of 10-15 µm. However, when the pre- and post-treated scans were compared, there was no evidence of microwave-induced damage in the selected field of view. It could be possible that microwaves induced some damage, but they were not detected on the X-ray CT scans due to the limited field of view. Because of this challenge, the use of X-ray CT was suspended in this initial work, but it was later used in Chapter 7 to examine microwave-induced fractures and leaching effect in small cores of 21 mm diameter by 19-22 mm height, which were scanned in full at a resolution of 15 µm.

6.2.3.1 Point Load Test (PLT)

The PLT measurements were conducted using the device shown in Figure 6.4, and the fragments tested had a maximum dimension of 45-50 mm and a minimum dimension of about 10 mm. This particle size was small enough to fit in the gap between the two platens but large enough to allow adequate contact area with the two platens, resulting in the split of the entire specimen. The procedure involved determining the depth and width dimensions of each fragment using a Vernier calliper. Then, the fragment was positioned between the two platens and the maximum applied load on the specimen before failure was recorded. The standardized point load strength index $Is_{(50)}$ was then determined using Equation 4.6. The average $Is_{(50)}$ measurements of all fragments in each subsample were used to compare the extent of ore pre-damage at different microwave energy levels, with the strength index data from the untreated sample serving as the baseline for changes due to microwave treatment. A comparison was also made by plotting the spread of $Is_{(50)}$ measurements arranged in ascending order.
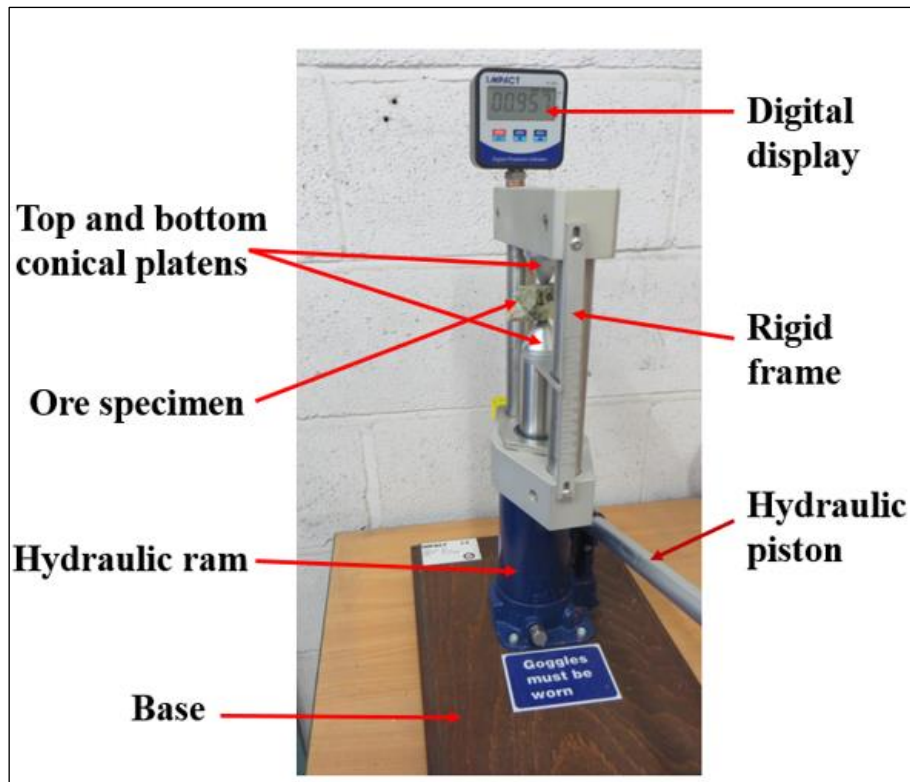
Figure 6.4. PLT device

6.2.3.2 Crushing Tests

Following PLT measurements, broken ore fragments from each subsample were collected and crushed, and the particle size distributions of crushed materials (treated versus untreated) were compared. The objective of this test was to determine the extent of microwave-induced damage left on the broken fragments following PLT measurements, which can be indicated by the increase in crusher product fineness. To achieve this objective, crushing was performed in a laboratory jaw crusher (Retsch BB200) shown in Figure 6.5, which has a maximum feed size of approximately 90 mm and product size of 2-30 mm. All subsamples, treated and untreated, were crushed separately using the same crusher settings and feed mode. The jaw gap was adjusted to yield a product top size of approximately 19 mm. Given the smaller sample size used in each subsample of 1.5-2.1 kg, the crusher was fed with one or two particles at a time (starvation feeding) to ensure consistent feeding in all subsamples. The crusher products were

then dry sieved using standard laboratory test sieves arranged in the root-two (Tyler) sequence from the top size of the feed down to 3.35 mm, and the particle size distributions of the treated and untreated samples were compared.

Figure 6.5. Laboratory jaw crusher

6.2.3.3 Statistical Analysis (t-test)

A t-test, also known as a Student's t-test, is a statistical test used to compare the averages of two groups and determine whether they differ from one another (Montgomery et al., 2009). The t-test was used in the current study to compare the average point load indices of the treated versus untreated fragments to determine whether the observed strength reduction due to microwave treatment is statistically significant. The t-test was also used to test the statistical significance of the leaching results presented in Chapter 8. This technique was chosen because it is a simple and quick way of interpreting statistical results using small data sets of at least n=10, provided the data is symmetrically distributed (Tebbs & Bower, 2003). One of the key

limitations of using a t-test with such a small sample size is that the true effect must be large in order to be statistically significant (De Winter, 2013).

The t-test works by comparing two different t-values (calculated and critical) to determine significant difference. The difference is considered significant (e.g., at 90% or 95% confidence level) if the calculated t-value is greater than the critical (threshold) t-value at that confidence level. The calculated t-value is the difference between the means of two data sets divided by the standard error (Equation 6.2) (Limentani et al., 2005; Montgomery et al., 2009). Based on this expression, the calculated t-value was determined by the differences in the mean strength index $Is_{(50)}$ or leach extraction of treated and untreated fragments, and their standard error using Equations 6.3 and 6.4. These expressions show that a larger t-value is obtained when the difference in the means of the two data sets is large and/or their standard deviations are small, and thus the larger the t-value, the more likely the difference is statistically significant.

The calculated t-value was compared to the critical t-value from the t-distribution table. The t-table is a reference table that lists critical t-values based on degrees of freedom and desired confidence levels. The degrees of freedom refer to the maximum number of logically independent values that are free to vary in the data set (Pandey & Bright, 2008). The degrees of freedom were determined based on the number of fragments tested on each ore type using Equation 6.5.

$$t_{calc} = \frac{\text{Difference of group averages}}{\text{Standard error of difference}} \tag{6.2}$$

$$t_{calc} = \frac{\overline{X}_T - \overline{X}_{UT}}{\sqrt{S_p{}^2 \times (\frac{1}{N_T} + \frac{1}{N_{UT}})}} \tag{6.3}$$

$$S_p{}^2 = \frac{(N_T - 1) \times s_T{}^2 + (N_{UT} - 1) \times s_{UT}{}^2}{N_T + N_{UT} - 2} \tag{6.4}$$

$$DF = N_T + N_{UT} - 2 \tag{6.5}$$

Where;

t_{calc} = Calculated t-value.

$\overline{X}_T$ and $\overline{X}_{UT}$ = Average $Is_{(50)}$ or leach extractions of treated and untreated fragments,

N_T and N_{UT} = Number of fragments in each sample set,

S_T and S_{UT} = Standard deviations of $Is_{(50)}$ or leach extraction of T and UT fragments,

S_p = Pooled variance,

DF = Degrees of freedom.

The t-test analyses of the PLT results from a microwave treatment study reported by Batchelor et al. (2015) showed that more than 100 fragments are typically required for less than a 10% average strength reduction to be statistically significant at >90% confidence level. When using fewer than 100 fragments, the average reduction may not be statistically significant. In the present work, only 30-60 fragments were used in each sub-sample because microwave treatment tests were performed in batches of one or two fragments. This means that treating more than 100 fragments would require at least 80 treatment batches per sub-sample, making treatment of all four ore types (16 sub-samples ~1280 batches) more time-consuming. Also,

due to equipment availability (e.g., ICP-AES) and the time constraints for sample preparation, only 10-12 fragments were used for each ore type (i.e., 5-6 pairs - treated vs untreated) in the leaching work in Chapter 8. Because only a few fragments were tested in this study, and smaller sample sizes typically have higher levels of variability, ore samples with little induced damage are more likely to exhibit statistically insignificant strength reductions.

6.3 Results and Discussion

6.3.1   Point Load Test

The PLT results of Ore 1 fragments are presented in Figure 6.6. This figure compares the point load indices of untreated and treated particles, arranged from weakest to strongest. A summary of statistical data is also provided here. The raw data of these results and the t-test analysis are provided in Appendices 11.1.2 and 11.1.2.5, respectively. The plots in Figure 6.6 show that microwave-treated particles (i.e., the lowest-ranked samples) are comparatively weaker (softer) than untreated particles. The t-test statistical analysis shows that treated particles at higher microwave energy inputs of 4.8 and 6.9 kWh/t are significantly weaker than untreated particles at >90% confidence level, achieving higher average strength reductions of about 15% and 23%, respectively. Also, most of the particles treated at a low energy of 2.4 kWh/t are weaker than untreated particles, as indicated by a gap on the plots of the treated versus untreated fragments. This sub-sample achieved a strength reduction of about 7%, which appears to be statistically insignificant at >90% confidence level, given the smaller number of fragments tested (37-41).

The higher strength reduction observed in this ore type is attributed to the high modal abundance of good microwave heaters (6%), as well as their moderate coarse grain size (max D_{50} = 190 µm), which promotes significant heating within the ore. Furthermore, the ore contains a high proportion of hard and brittle gangue matrix of quartz and feldspar (~65%),

which promotes ore fracturing by transferring stresses without undergoing ductile deformation to absorb thermal shock.

	Untreated (UT)	2.4 kWh/t	4.8 kWh/t	6.9 kWh/t
Mean	5.63	5.25	4.77	4.34
Median	5.48	5.33	4.86	4.14
Standard Deviation	2.19	2.44	1.90	2.26
Minimum	1.24	1.15	1.42	0.21
Maximum	10.77	10.30	8.13	10.82
Count	37	41	39	39
Average strength reduction		6.8%	15.3%	23.0%
T-test confidence level		52%	93%	99%
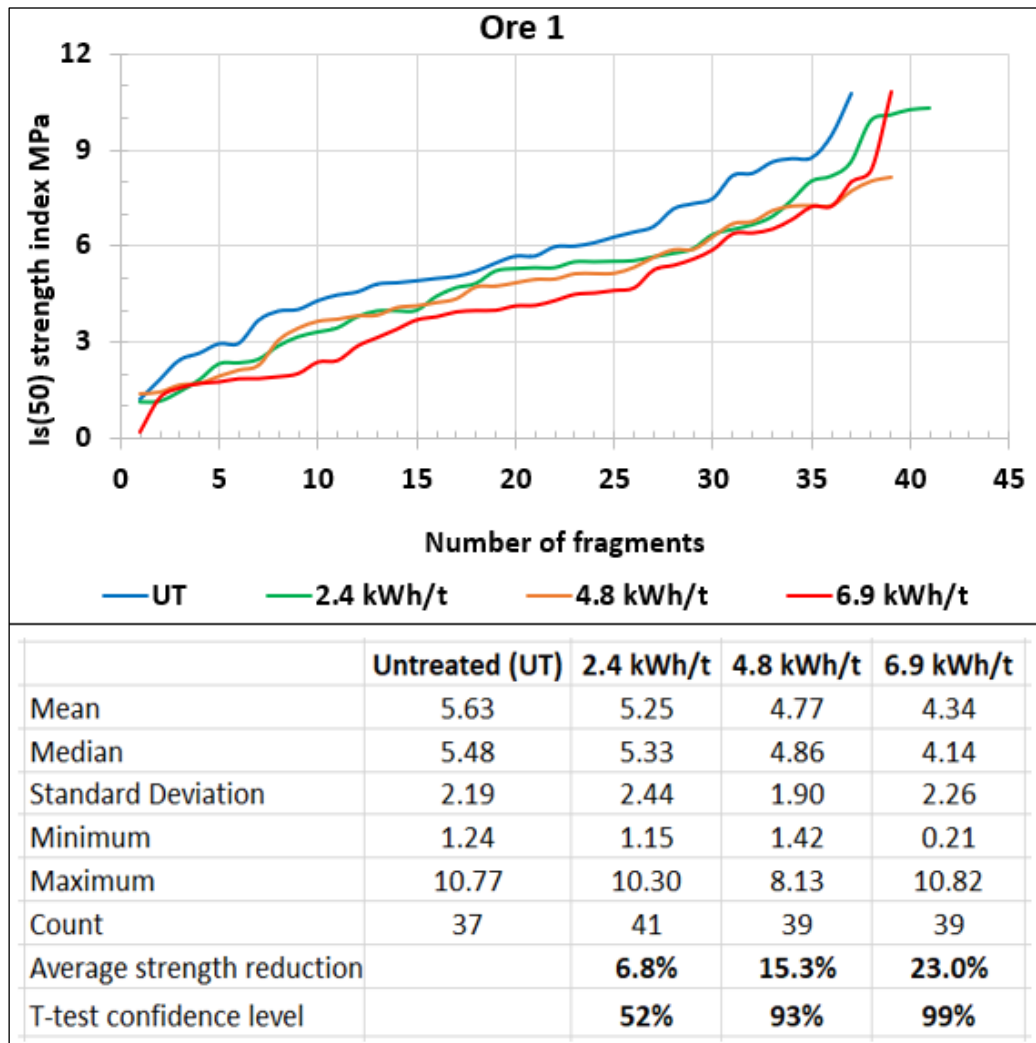
Figure 6.6. PLT results – Ore 1

Figure 6.7 shows the PLT results of the Ore 3 sample. These results show that treated particles are weaker than untreated particles, with a significant strength reduction of 19-21% at 90-93% confidence level achieved at a microwave energy input of 2.2-6.9 kWh/t. Also, visual inspection showed that 3 out of 30-32 fragments (10%) had fractures due to microwave treatment. The greater strength reduction observed in this ore type is attributed to the higher modal abundance of good microwave heaters of 7.3% and the larger grain size of these heaters,

which appear as coarse discrete grains or microveins with a maximum D_{50} of up to 500 µm. Also, the ore contains a high proportion of stiffer microwave heaters, such as pyrite (5.3%), which effectively transfers the induced thermal stresses to the gangue matrix, resulting in significant ore fracturing.

	Untreated (UT)	2.2 kWh/t	4.1 kWh/t	6.9 kWh/t
Mean	2.61	2.12	2.08	2.09
Median	2.56	2.02	1.91	1.58
Standard Deviation	1.14	1.07	1.07	1.30
Minimum	0.67	0.60	0.46	0.58
Maximum	5.37	4.32	4.74	5.91
Count	31	29	30	32
Average strength reduction		18.7%	20.6%	20.0%
T-test confidence level		90%	93%	90%
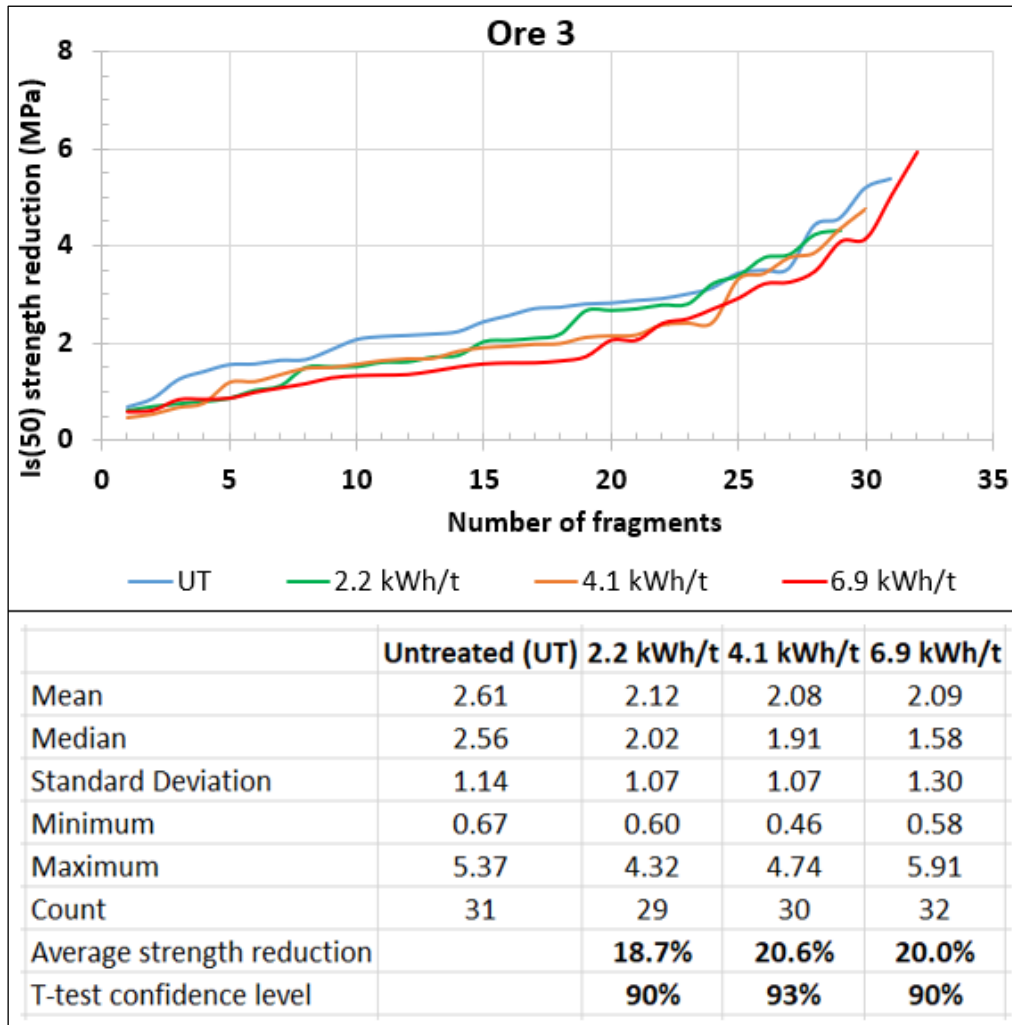
Figure 6.7. PLT results – Ore 3

The PLT results of Ore 5 fragments are shown in Figure 6.8. These results show a low strength reduction of up to 5% due to microwave treatment at 4.7 kWh/t, which appears to be statistically insignificant at a low confidence level of <72%. The poor performance of this ore is attributed to the combined effect of the finer grain size of microwave heaters in most of the particles and the high dissemination nature of these heaters. Despite the higher modal

abundance of good microwave heaters (5%) dominated by magnetite (the stiffer microwave heater), the grain sizes of magnetite and pyrite are finer, with D_{50} of about 75 and 35 µm, respectively, though copper sulphides had a coarser grain size of up to $D_{50} = 212$ µm. This type of texture promotes conduction heat losses from the microwave-absorbing grains to the adjacent gangue matrix, lowering the temperature gradient (thermal stresses) and leading to minimal ore fracturing.

Physical observation showed that 1 out of 61 fragments (1.6%) had some fractures as a result of microwave treatment at 4.7 kWh/t, and the image of the fractured fragment is shown in Figure 6.9. The low strength reduction observed at a higher microwave energy input of 6.9 kWh/t can probably be attributed to a low proportion of fragments with a suitable texture for microwave treatment in the sample. This suggests that the proportion of amenable fragments in the sample determines overall treatment performance.

Figure 6.8. PLT results – Ore 5

Ore 5

Is(50) strength index (MPa) vs Number of fragments

Legend: UT — 2.7 kWh/t — 4.7 kWh/t — 6.9 kWh/t

	Untreated (UT)	2.7 kWh/t	4.7 kWh/t	6.9 kWh/t
Mean	8.35	8.18	7.93	8.30
Median	8.64	8.05	7.23	7.77
Standard Deviation	3.60	3.22	3.80	3.46
Minimum	2.21	2.38	1.47	2.23
Maximum	19.86	14.82	19.91	16.52
Count	48	57	61	56
Average strength reduction		2.1%	5.0%	0.6%
T-test confidence level		60%	72%	53%
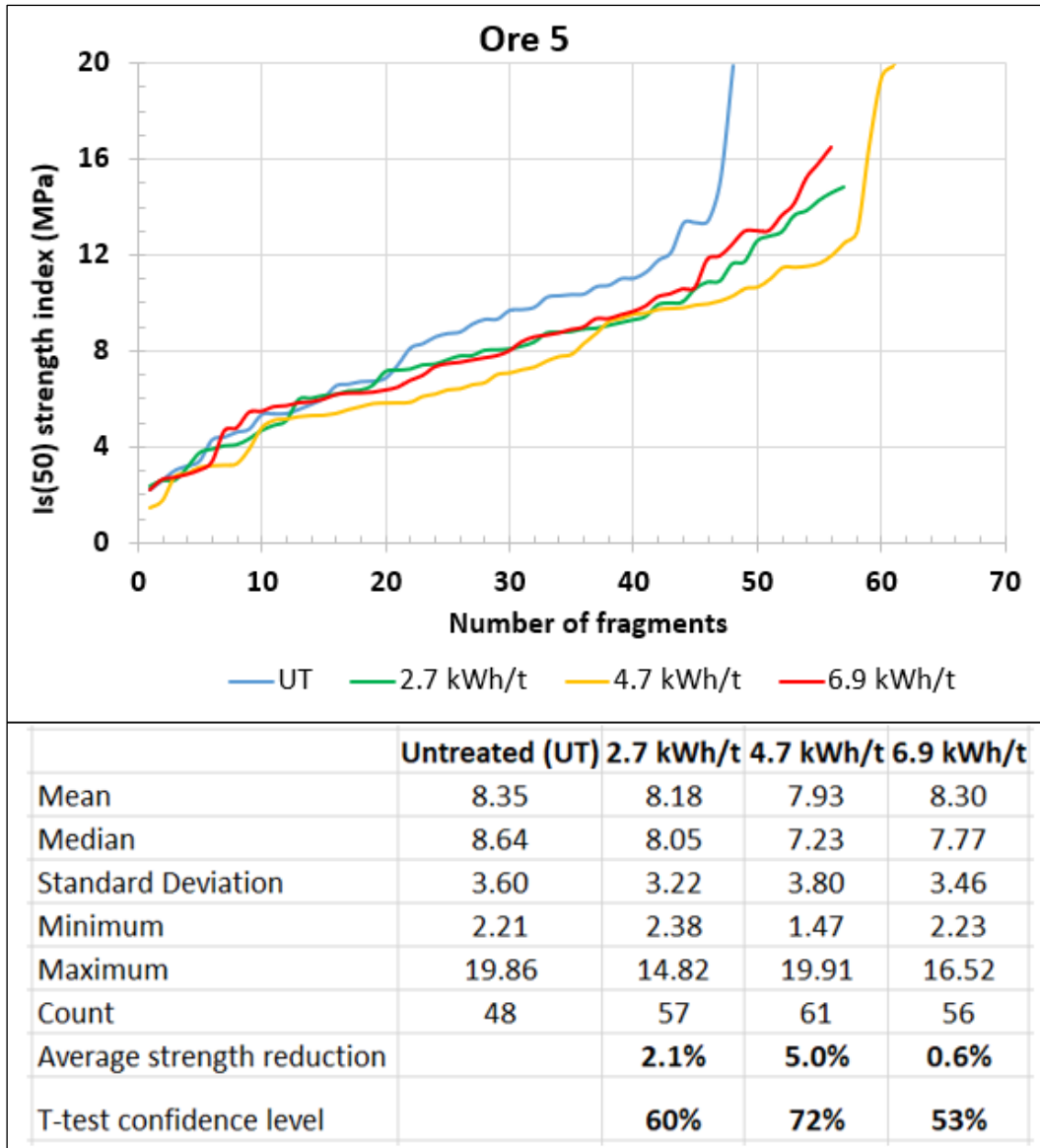
Figure 6.8. PLT results – Ore 5
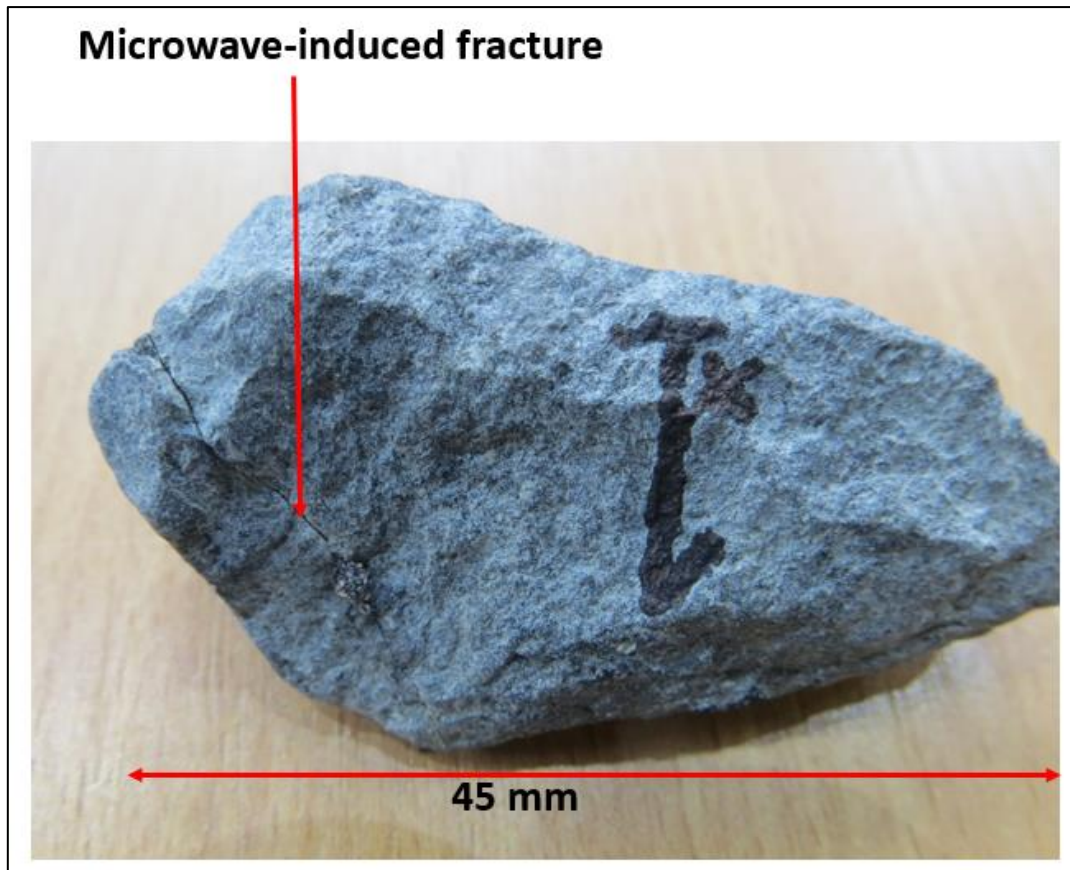
Figure 6.9. Example of Ore 5 fragments showing microwave-induced fractures

The PLT results of Ore 2 fragments show that microwave treatment at 2.3-6.3 kWh/t resulted in an average strength reduction of 5-10% at a low confidence level of <70% (Figure 6.10). Although the overall strength reduction in this sample is minimal, it is apparent that most of the fragments have shown a decrease in ore strength due to microwave treatment. This is indicated by a large gap between the plots of the treated and untreated fragments. The minimal induced damage observed in this ore is attributed to the low abundance of good microwave heaters of about 2%, which are mostly fine grains (up to $D_{50} = 170\,\mu m$) and the low content of stiffer microwave heaters (e.g., pyrite) of about 0.6%.
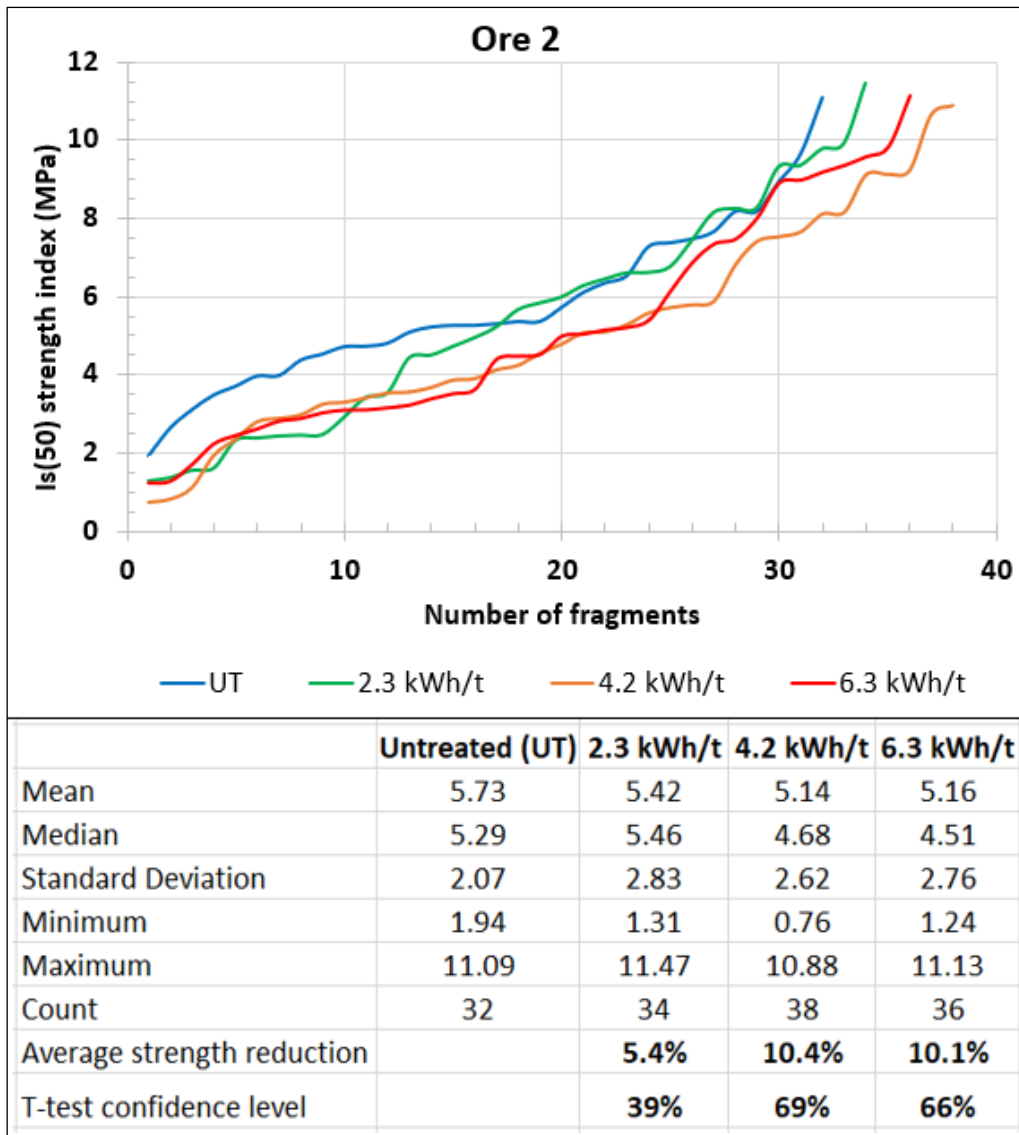
Figure 6.10. PLT results – Ore 2

Figure 6.11 presents a summary of the PLT results of all four ore types investigated in this initial work. These results indicate that the magnitude of ore strength reduction (induced damage) caused by microwave treatment varies between samples, which can be attributed to variations in ore mineralogy and texture properties. Furthermore, general observations show that the extent of ore strength reduction increases with microwave energy input.
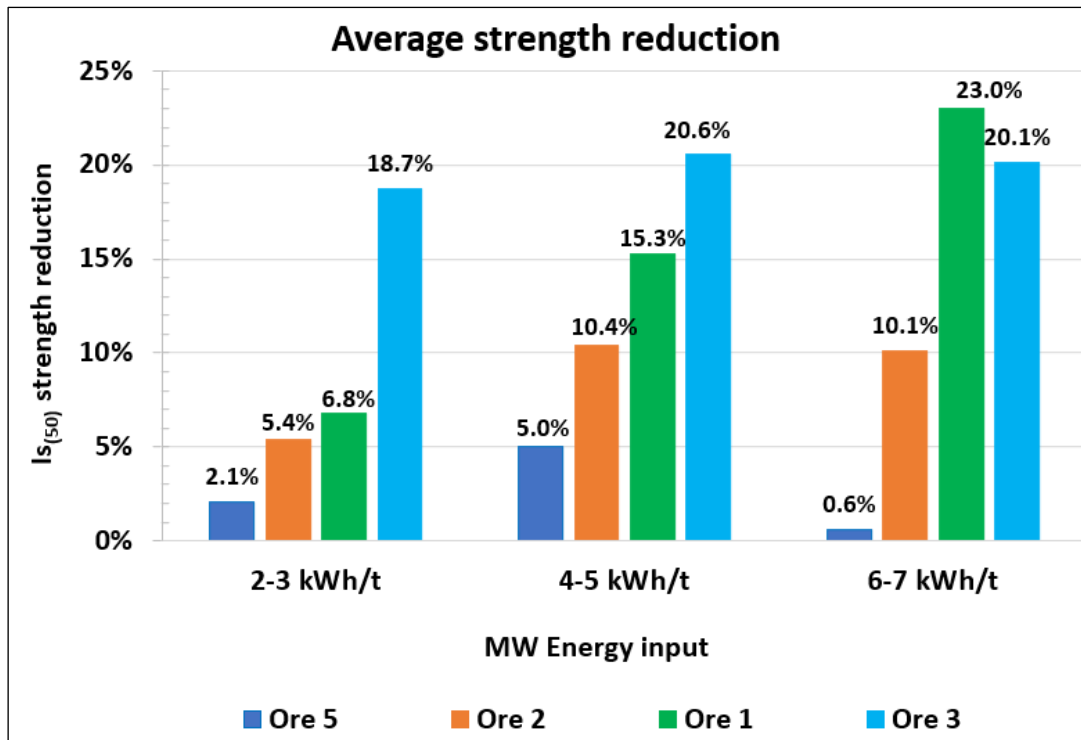
Figure 6.11. PLT results summary

6.3.2 Crushing Test

Following point load testing, the broken fragments were collected and then crushed using a jaw crusher to quantify the microwave-induced damage left on these fragments. The particle size distributions of the crusher feed and product of the four ores tested are shown in Figures 6.12-6.15. For comparison, the size distributions of the treated and untreated subsamples are shown. It can be seen in Figure 6.12 that Ore 3 fragments have shown an increase in product fineness size distribution from 10% (untreated) to 20% (treated) passing through 4 mm. Since this ore type exhibited a significant strength reduction in point load testing due to microwave treatment, it is likely that the jaw crusher exacerbated some microwave-induced damage, leading to the increase in fineness observed in the treated crushed materials. This suggests that the compressive loading mechanism of a jaw crusher caused cleavage breakage along the microwave-induced fractured planes, generating several large particles as well as some fine particles.
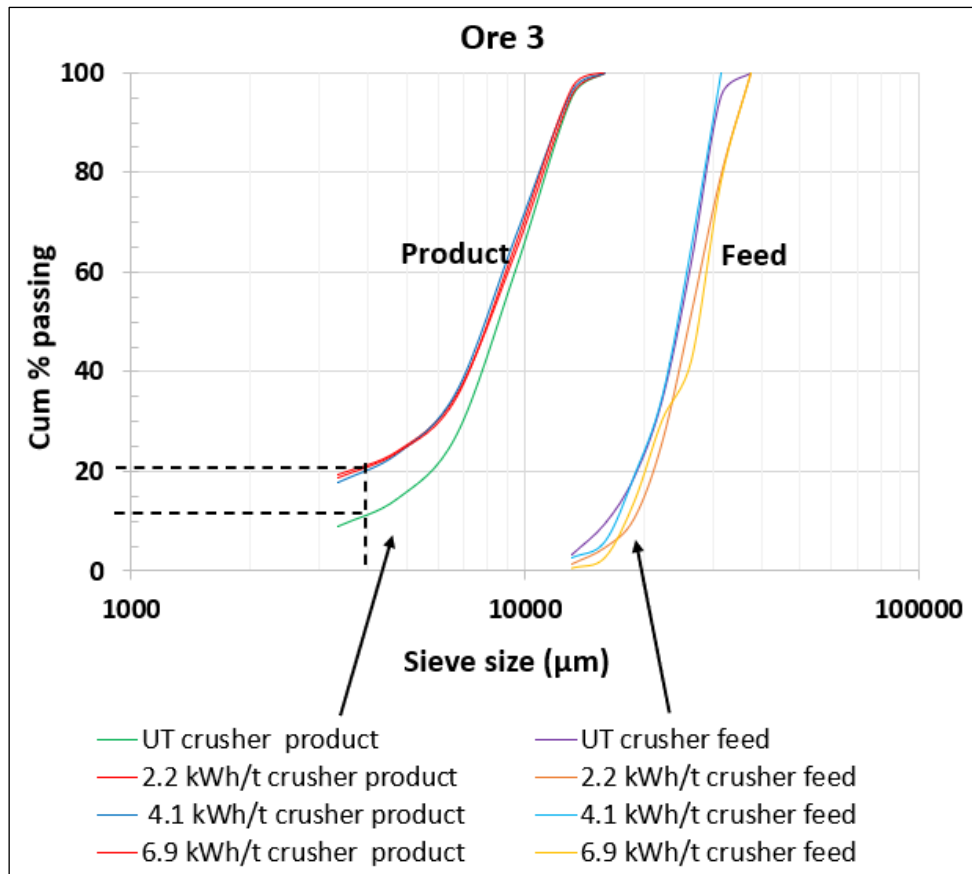
Figure 6.12. Crushing results – Ore 3

Other ore types did not show a noticeable increase in fineness of particle size due to microwave treatment, as indicated by the overlaps in the crusher product size distributions of the treated and untreated samples (Figures 6.13 - 6.15). This does not necessarily mean that microwaves did not induce fractures in these ore types. Some fragments had fractures, as evidenced by the decrease in ore strength in Figure 6.11, but the fractures that remained after PLT were not large enough to be reflected in the crushing product fineness because jaw crushers are more sensitive to ore breakage along macro-fractures (planes of weakness). It is possible that the benefit of microwave-induced damage in these ores could be observed in the mineral liberation results and crushing energy requirements due to increased mineral exposure and decreased ore competency, respectively.
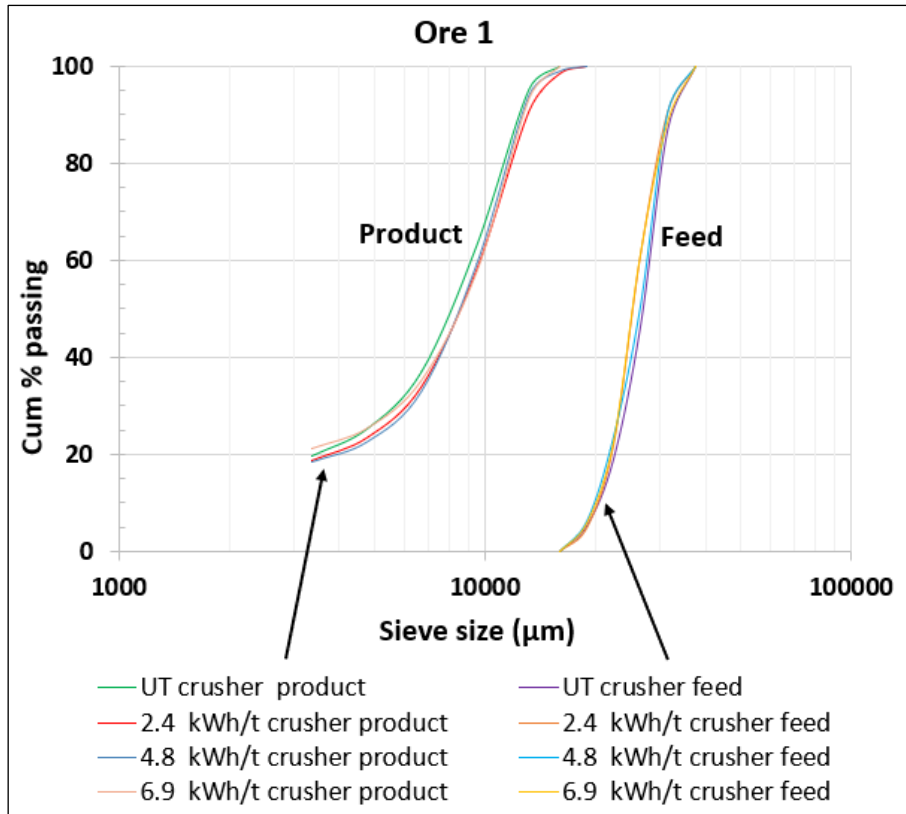
Figure 6.13. Crushing results – Ore 1
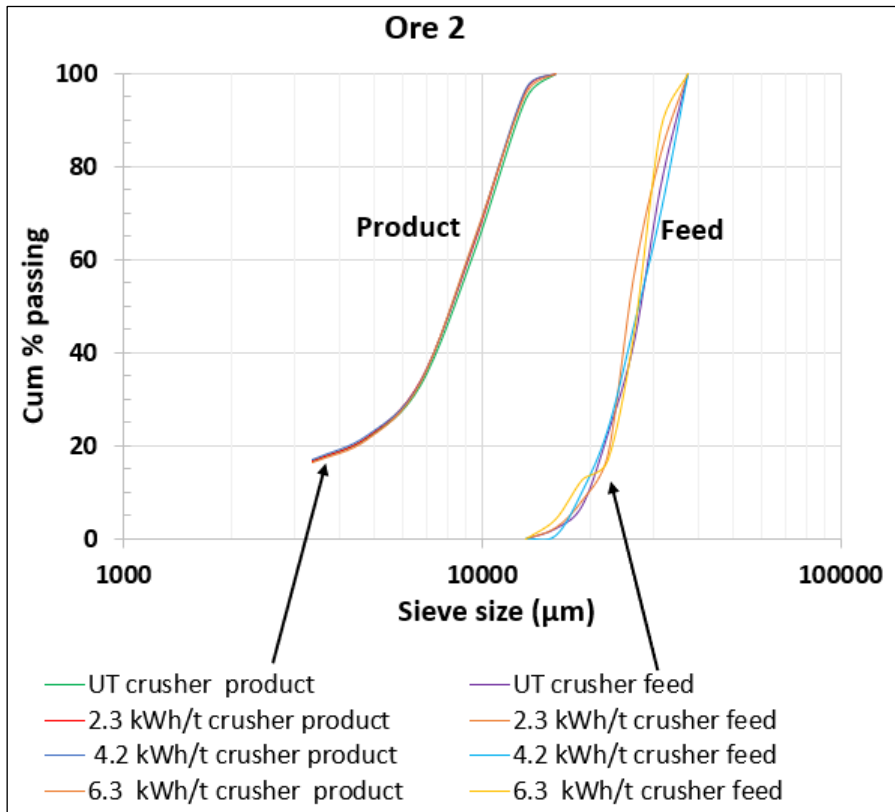
Figure 6.14. Crushing results – Ore 2
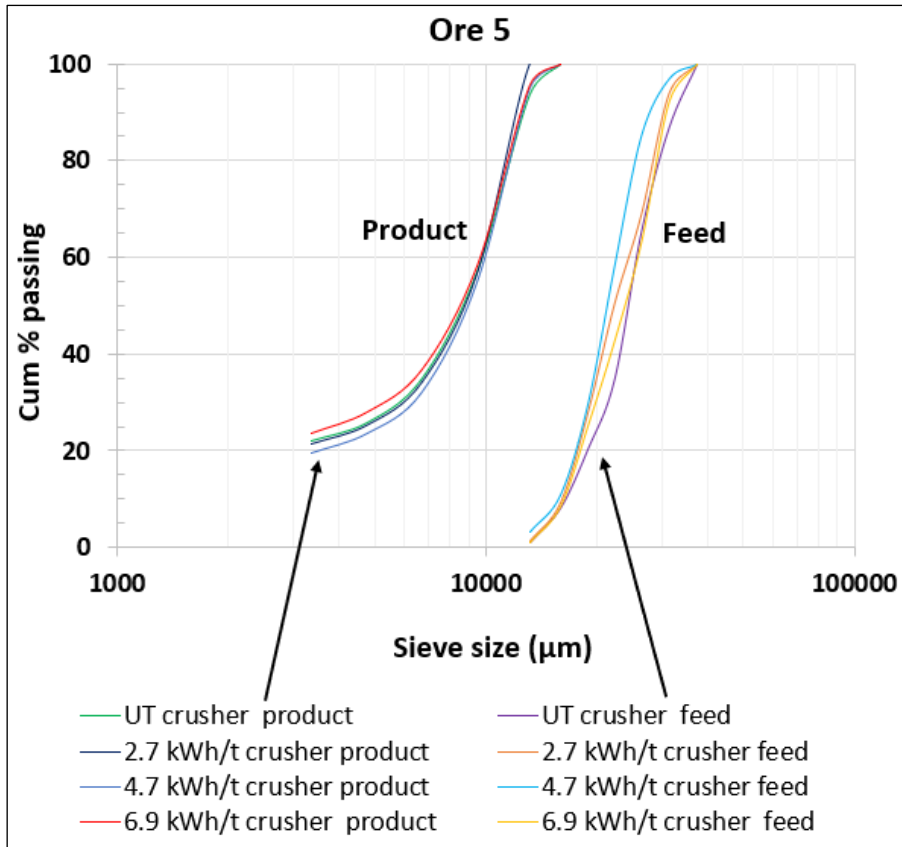
Figure 6.15. Crushing results – Ore 5

6.4 Conclusions

The influence of microwave energy input on the extent of ore pre-damage has been investigated using four porphyry copper sulphide ores of varying mineralogy and texture. Microwave treatment of these ores was performed at three different energy levels ranging from 2 to 7 kWh/t. The extent of ore pre-damage was quantified using the point loading and crushing tests. The presence of microwave-induced damage in the sample is indicated by a reduction in ore strength on the PLT results and an increase in ore fineness of the crusher product particle size distribution.

Results showed that the extent of ore pre-damage increases with the increase in microwave energy input, and the effect is more pronounced for ores with suitable mineralogy and texture properties for microwave-induced fractures. The best ore candidates, such as Ores 3 and 1, achieved a significant strength reduction of point load index of 7-23% at a microwave energy input of 2-7 kWh/t. These ore types had some of the following characteristics: a high modal abundance of good microwave heaters of about 6-7% that occurs as coarse discrete grains or microveins (D_{50} = 190-500 µm), stiffer microwave heaters (e.g., pyrite) of about >2.8%, and a hard (brittle) microwave-transparent gangue matrix. This type of mineralogy and texture promotes more rapid heating and thermal stresses, which facilitate ore fracturing. Other ore types, such as Ores 2 and 5, achieved a minimal or insignificant damage (0.6-10%) due to microwave treatment. Based on physical observation, these ore types had a lower proportion and/or finer grain size and higher dissemination of sulphide mineralization in the majority of the fragments.

The crushing results of Ore 3 fragments showed a slight increase in crusher product fineness due to microwave treatment, from 10% to 20% passing through 4 mm. The jaw crusher has most likely exacerbated some of the microwave-induced fractures in this sample, resulting in an increase in ore fineness on the crusher product particle size distributions of treated

fragments. However, the microwave-induced damage in other ore types (Ores 1, 2, and 5) was not large enough to be reflected in the crushing results.

Following this initial work, further investigation is conducted in Chapters 7 and 8 to assess the influence of ore mineralogy and texture on the extent of microwave-induced fractures. Thereafter, the extent of leaching improvement resulting from these fractures is quantified in order to identify potential ore candidates for microwave-assisted leaching of coarse fragments, such as heap leaching.

7. MICROWAVE TREATMENT AND LEACHING OF SMALL CORES

7.1 Introduction

It has been demonstrated in Chapter 6 that microwaves reduce ore competency (by inducing fractures), and the extent of induced damage is dependent on microwave energy input, microwave power density and intrinsic ore properties (e.g., mineralogy and texture). The objective of this chapter is to investigate the influence of mineralogy and texture on the leaching performance of microwave-treated ores using small cores (21 mm diameter) from the four porphyry copper sulphide ores described in Chapter 5, namely Ores 1, 2, 3, and 4. This investigation will give an indication of potential ore candidates for microwave treatment to assist leaching.

Microwave treatment tests were performed in a TE_{10} single-mode cavity. The magnitude of microwave-induced damage was quantified using two different techniques: X-ray computed tomography (XRCT) and ultra-pulse velocity (UPV). Leaching experiments were carried out in the 50-mL leaching tubes using aqua regia as a leaching chemical. The extent of mineral dissolution improvement due to microwave treatment was quantified using the ICP-AES technique, and the leaching results were supported by qualitative and quantitative results derived from X-ray CT imaging. A summary of the overall experimental procedure is shown in Figure 7.1.
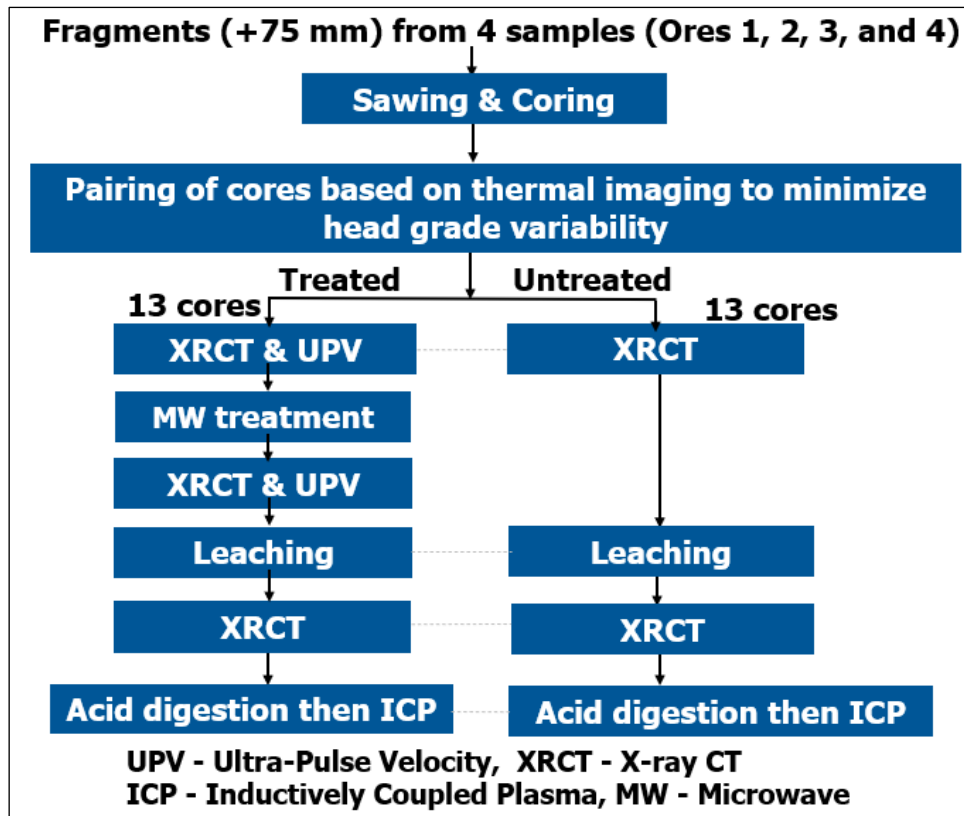
Figure 7.1. Overall experimental procedure – small cores

7.2 Sample Preparation

7.2.1 Sample Size and Geometry Selection Criteria

The ore specimen size and geometry used in this experimental work were selected based on the following criteria:

i.   The specimen should fit in the 80-mm diameter by 43-mm height microwave cavity.

ii.   The specimen should be small enough to be scanned in full by XRCT at a resolution of 15 µm within a reasonably shorter duration (e.g., 1 hour) to evaluate the microwave treatment and leaching effects. This resolution was preferred because over 90% of sulphide grains in each ore type tested could be detected as they were coarser than 15 µm (see the MLA results in Chapter 5). In addition, most microwave-induced fractures could be detected at this high resolution, given the high modal abundance and coarse

grain size of microwave-absorbing phases in the ores tested, together with the high microwave energy applied.

iii. The specimen should be large enough to be tested at various positions using 5-mm diameter ultrasonic transducers to quantify the damage due to microwave treatment.

iv. The specimen should fit into a 50-mL leaching tube of 30 mm diameter by 110 mm height.

v. The specimen should be representative of coarse particles found in crusher and SAG mill feed and that can be compared to other studies in the literature.

Based on these criteria, a cylindrical sample of 21 mm diameter and 19-22 mm height was deduced to be the best size and geometry for this work. Hence, fragments (+75 mm size) of Ores 1, 2, 3, and 4 were cored to obtain specimens for microwave treatment and leaching experiments. Ore 5 was not used in this investigation because the fragments were not large enough to be cored to obtain 21-mm diameter cores of sufficient height.

7.2.2 Coring and Marking

Ore fragments were cored using a pillar drill attached with a diamond-impregnated core bit of 25 mm diameter (Figure 7.2). Before coring, each fragment was sawn to trim off the edges to make it securely clamped on the vise to avoid any movement during coring. The table height was set, and the vise was properly adjusted to align the core bit to the ore fragment before being securely bolted to the table. The coring procedure was initiated, and water was applied using a spray bottle to remove the cuttings while also providing lubrication and cooling.
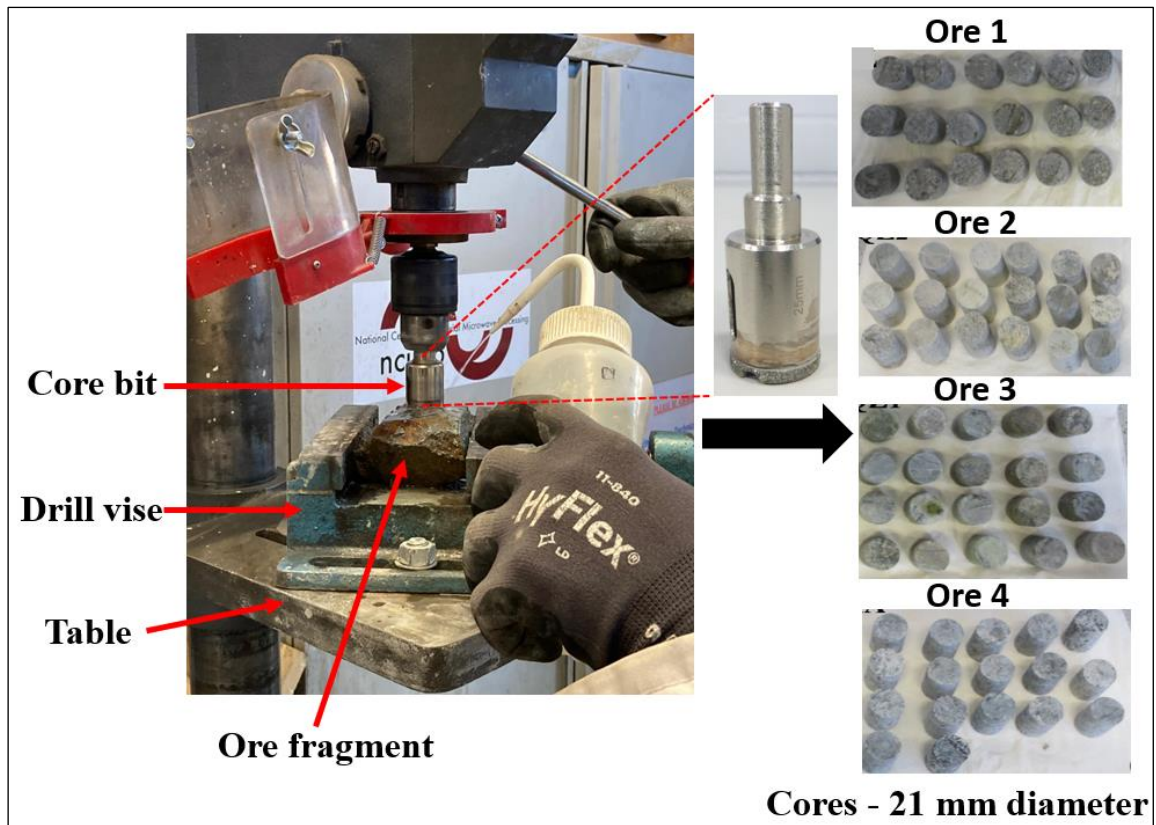
Figure 7.2. Coring procedure

7.2.3 Thermal Imaging

Previous studies conducted at the University of Nottingham have shown that microwave heating followed by infrared thermal imaging (MW-IR) can be used to distinguish low- and high-grade fragments based on temperature rise (Ferrari-John et al., 2016; Batchelor et al., 2016). This is possible because most valuable minerals (e.g., copper, nickel, and lead sulphides) heat up more rapidly in microwave fields than common microwave-transparent rock-forming minerals (e.g., quartz, feldspars). One important limitation of this technique is that low-grade materials containing significant proportions of microwave-absorbent gangue minerals (e.g., pyrite, magnetite, smectite clay), which heat up more rapidly in microwave fields, can be misplaced to high-grade materials.

In the current study, the cores were subjected to microwave heating followed by infrared imaging to determine the extent of sulphide mineralisation, allowing cores with almost similar sulphide content to be paired, one of which was microwave-treated before leaching and the other was leached without treatment. The pairing procedure was carried out to reduce the effect of metal head grade variability on mineral dissolution. This allowed the effect of microwave treatment on leaching performance to be quantified by comparing the leaching results of treated and untreated fragments.

All cores were irradiated at 250 Watts in a multimode cavity for 10 seconds. This power and irradiation time were sufficient to warm up the cores up to 35°C but insufficient to induce fractures detectable by UPV testing within a margin of error of less than 3.5% at >95% confidence level, based on the UPV repeatability results shown in Appendix 11.2.1. The cores were irradiated at two different orientations (i.e., facing up and down) and then imaged after each orientation using a thermal camera (NEC Avio H2640). Figure 7.3 shows the photographic image of 20 cores (from Ore 3), and the pairing illustration of these cores is shown in the thermal images in Figure 7.4 (e.g., A & P; B & G; and E & M). The thermal images demonstrating the pairing of cores from other ore types are available in Appendix 11.2.3.
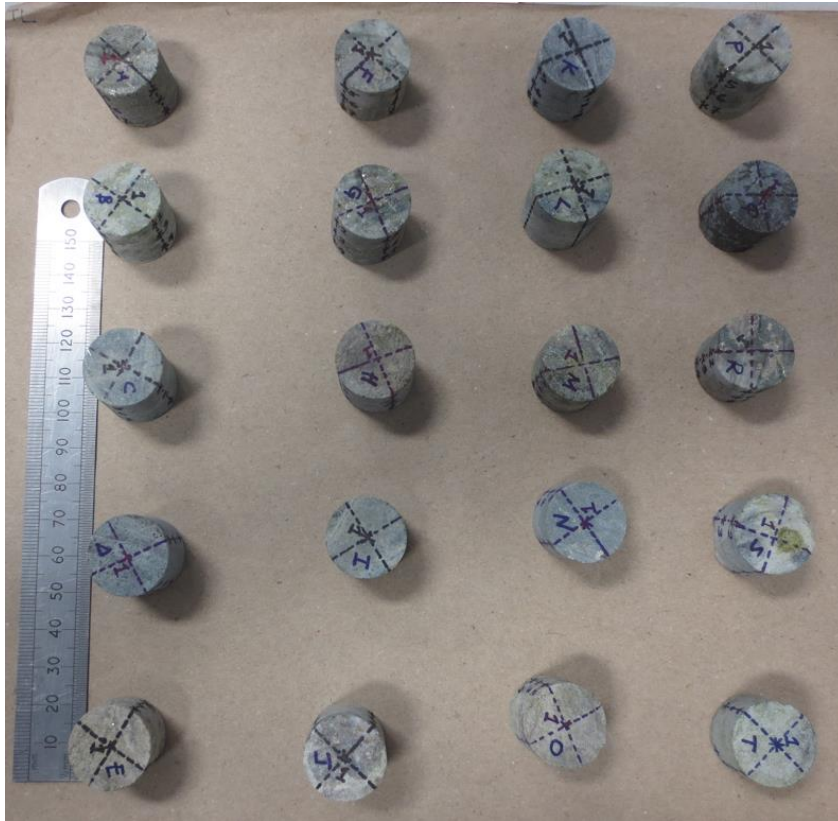
Figure 7.3. Photographic image of cores (Ore 3) - top view
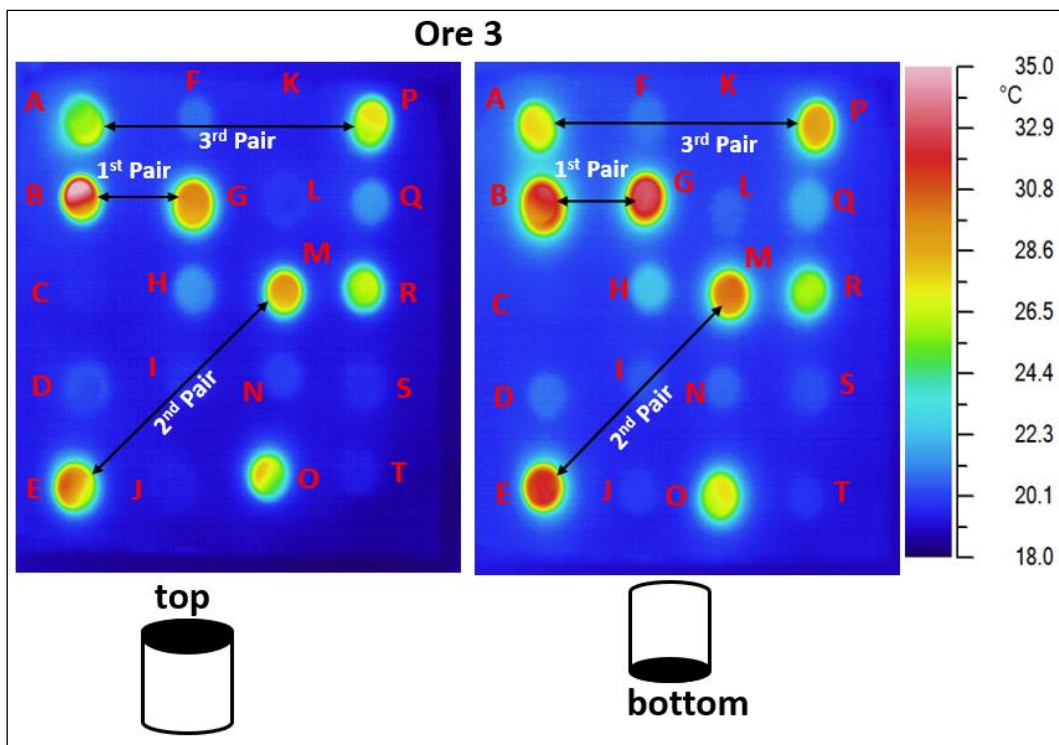
Figure 7.4. Thermal images of cores (Ore 3) – pairing illustration

Based on this procedure, thirteen hottest pairs of cores were selected from the four ore types. Table 7.1 shows a summary of temperature rise data for all selected cores, and the full temperature profiles are shown in Appendix 11.2.4. Figure 7.5 shows the average temperature rise and metal head grade (copper + iron) in each ore type, with error bars indicating the maximum and minimum values. The metal head grades were determined after leaching and digesting the cores, as described further in Section 7.4.1. The average metal head grades of treated-T and untreated-UT cores in Ores 1, 2, and 4 were relatively the same (within the margin of error), indicating that the pairing was good. In the case of Ore 3, the untreated cores had a higher average metal head grade than the treated cores, implying that the thermal images of the top and bottom sections of the cores were insufficient to indicate the overall metal content in these cores; the round section was also supposed to be imaged in multiple orientations.

It is worth noting that the temperature rise and metal head grades observed in Ores 3 and 2 suggest that the cores extracted from these ores contain a comparatively higher abundance of microwave heaters than that reported in the ore characterisation results in Chapter 5. Furthermore, although the MLA results reported in Chapter 5 show that Ore 1 contains a comparatively higher proportion of microwave-absorbing clay mineral (montmorillonite) (2.6% in Ore 1 versus <0.6% in other ores), its effect on microwave heating of this ore was not observed. This is due to the fact that the temperature rise indicated in Figure 7.5 is proportional to the average metal head grade (copper + iron), suggesting that the microwave heating effect of this ore is mostly contributed by copper/iron sulphides and oxides. This variation in temperature rise or metal head grade is probably attributed to sample variability, given that only a few cores (3-4 pairs) were used in this study, and the temperature measurements are based on the top and bottom sections of these cores.

Table 7.1. Temperature rise all cores summarised – thermal imaging

Ore type	T/UT	Max temp rise (°C)	Min Temp rise (°C)	Avrg temp rise in all pixels (°C)	Overall avrg temp rise (°C)
Ore 1	1T	6.7	3.8	5.5	4.3
	2T	5.0	4.9	4.1	
	3T	4.2	2.5	3.6	
	4T	4.7	3.1	3.9	
	1UT	6.7	4.4	5.7	4.6
	2UT	5.0	3.0	4.2	
	3UT	5.6	3.3	4.4	
	4UT	4.6	3.2	3.9	
Ore 2	1T	6.6	3.1	5.5	5.2
	2T	9.9	3.9	7.6	
	3T	3.3	1.3	2.4	
	1UT	7.2	2.5	5.6	5.0
	2UT	6.8	4.7	6.2	
	3UT	3.8	1.7	3.2	
Ore 3	1T	14.9	6.6	11.2	9.8
	2T	14.0	6.0	10.6	
	3T	9.7	4.6	7.7	
	1UT	17.6	5.6	11.9	10.2
	2UT	12.2	6.0	10.0	
	3UT	10.9	5.1	8.8	
Ore 4	1T	12.7	5.2	9.8	8.0
	2T	9.2	4.9	7.4	
	3T	7.9	4.6	6.9	
	1UT	12.8	6.1	9.8	7.6
	2UT	9.4	4.7	7.6	
	3UT	6.0	3.9	5.4	
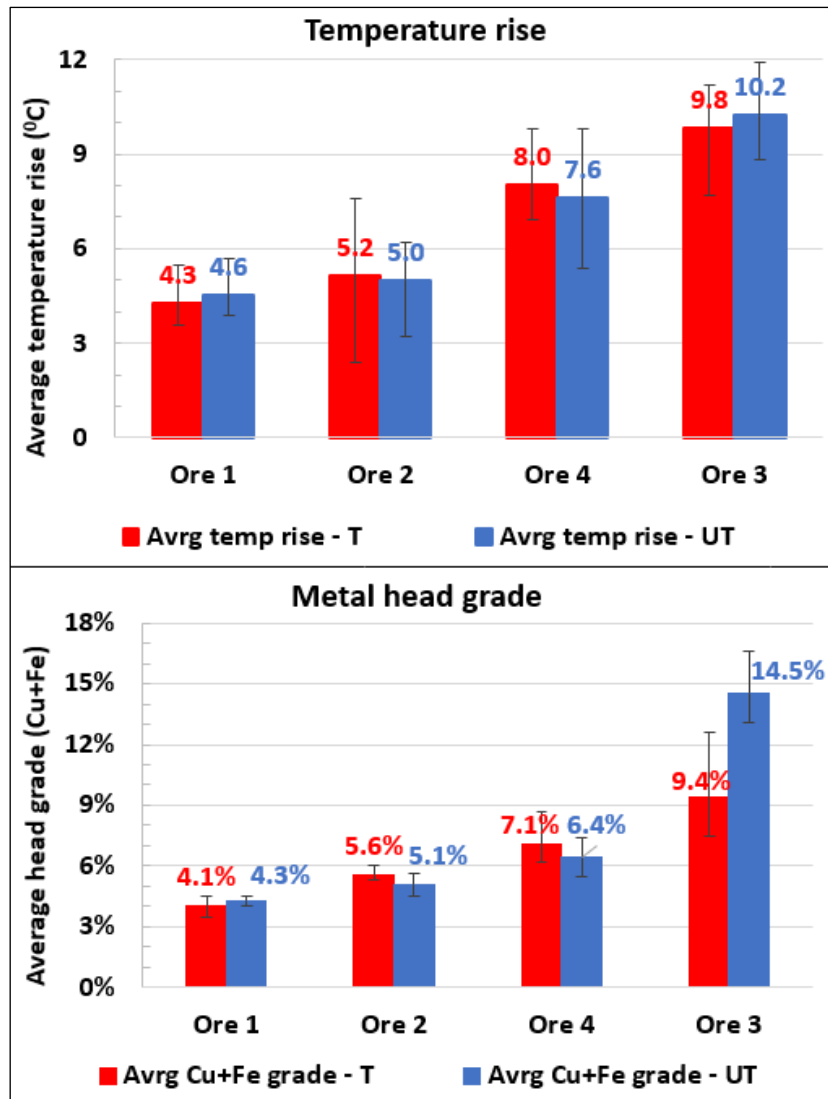
Figure 7.5. Average temperature rise and metal head grades

UPV measurements were performed using PUNDIT 7 (Figure 7.6). PUNDIT stands for

Portable Ultrasonic Non-destructive Digital Indicating Tester (CNS Farnell, 2006). Before

measurements, the device was calibrated using three calibration blocks with pulse transit times

of 4.65, 7.75, and 25.0 µsec. Each core was tested at seven (marked) locations using the 5-mm

rubber transducers, and a steel bar weighing 1 kg was used to compress these transducers by

gravity so that they make good contact with the specimen, minimizing signal losses. Due to the

non-destructive nature of this technique, measurements were performed on the same specimens

before and after microwave irradiation, and at the same marked positions, to minimise errors caused by non-homogeneity and anisotropy.

The thickness of ore specimen (i.e., distance between two opposite marked spots where the two transducers sit) was measured using a Vernier calliper. Six transit time measurements were taken at each location, and the average was used to calculate the pulse velocity at this location using Equation 7.1. The mean UPV values of the seven locations were determined before and after microwave treatment, and the extent of ore pre-damage due to microwave treatment was calculated using Equation 7.2.
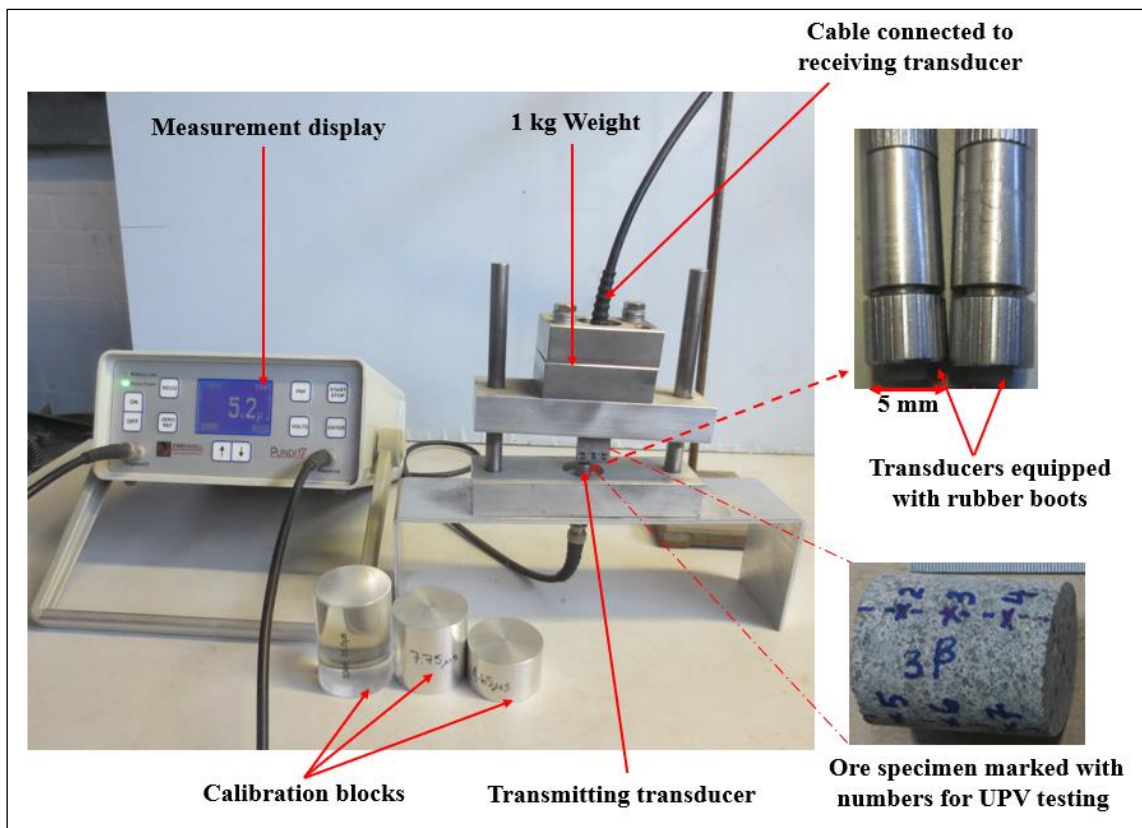
Figure 7.6. UPV measurement set-up

$$V = \frac{L}{T} \tag{7.1}$$

$$\text{UPV reduction (\%)} = \left(\frac{V_b - V_a}{V_b}\right) \times 100 \tag{7.2}$$

Where;

L = Path length between the two transducers (mm),

T = Time taken by the pulse to traverse the path length (µs),

V = Longitudinal pulse velocity (mm/µs),

V_b = Pulse velocity of the specimen before treatment (mm/µs),

V_a = Pulse velocity of the specimen after treatment (mm/µs),

UPV reduction = The extent of ore pre-damage (%).

7.3 Microwave Ore Pre-treatment Methodology

Microwave treatment of cores was performed in a single mode cavity using a 3-kW Richardson generator. The microwave treatment setup used in this investigation is identical to that described in Chapter 6 (Section 6.2.2), but an automatic stub-tuner was incorporated for pre-matching and power recording, as shown in Figure 7.7. Prior to each treatment, the core was placed in a region of maximum electric field strength to ensure maximum power delivery for effective treatment. This was done by adjusting the stub positions and short-circuit tuners with the help of a vector network analyser (VNA). After pre-matching, the waveguide switch was opened towards the cavity side to allow microwave propagation towards the sample.
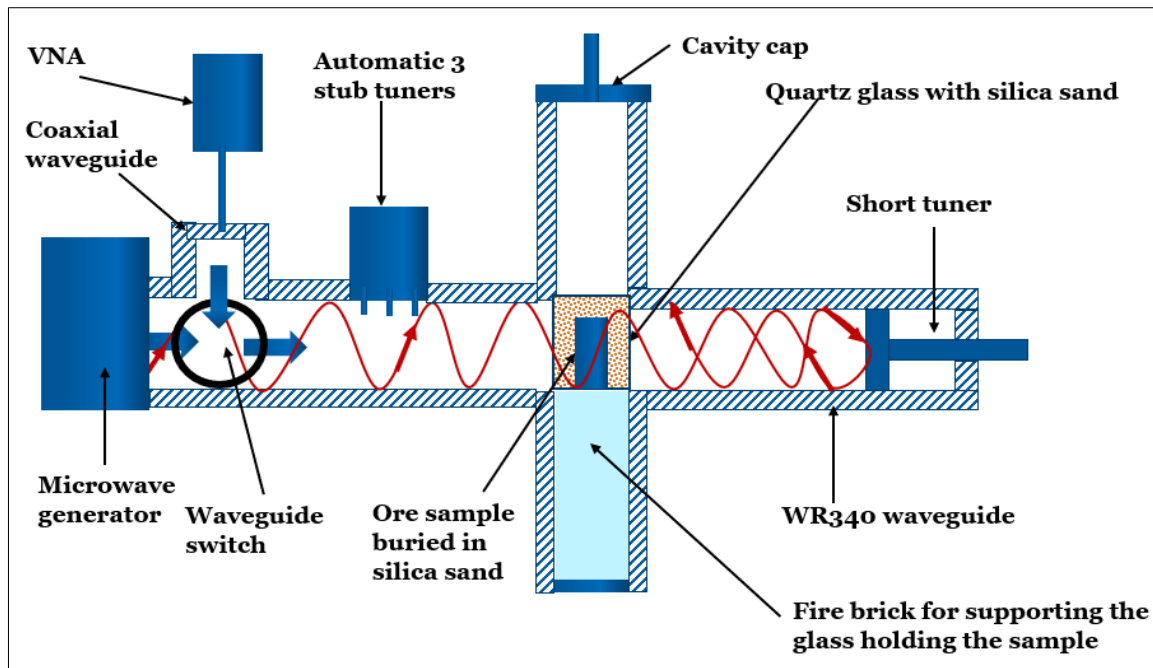
Figure 7.7. Microwave treatment setup

Table 7.2 shows a summary of the microwave treatment conditions used in this investigation. Each core was irradiated at 1 kW (forward power) for 2-4 sec and then checked for any damage by visual observation and UPV testing (>4% average UPV reduction). If no damage is observed in the first treatment attempt, the core was treated again for about 6-8 sec using the same power (1 kW). Most of the cores exhibited observable damage on the second attempt. The third treatment attempt of about 9-11 sec was only done for a few cores that did not show significant damage in the first two attempts. It is worth mentioning that the microwave energy input used in this investigation exceeds the probable economic range of 1-5 kWh/t proposed by Bradshaw et al. (2005), and no attempt was made to minimise microwave energy dose. This was done to maximise the degree of microwave-induced damage detectable on X-ray CT images at a resolution of 15 µm for all cores tested, in order to determine the influence of ore mineralogy and texture on the extent of microwave-induced fractures and leaching performance.

Table 7.2. Microwave treatment conditions – cores

Trial #	Core ID	Mass of core (g)	Forward power (kW)	Reflected power (kW)	Absorbed power (kW)	Exposure time (sec)	Treatment attempt to induce significant damage (>4% UPV reduction)
1	Ore 4-1T	21.95	1.08	0.06	1.02	6.6	Second
2	Ore 4-2T	22.57	1.06	0.18	0.89	6.5	Second
3	Ore 4-3T	23.67	1.07	0.15	0.92	6.6	Second
4	Ore 3-1T	19.57	1.09	0.37	0.72	8.4	Second
5	Ore 3-2T	22.14	1.08	0.18	0.90	9.0	Third
6	Ore 3-3T	21.64	1.12	0.28	0.84	8.8	Second
7	Ore 1-1T	20.38	1.07	0.15	0.92	6.9	Second
8	Ore 1-2T	21.37	1.06	0.18	0.88	6.0	Second
9	Ore 1-3T	20.50	1.06	0.24	0.82	11.1	Third
10	Ore 1-4T	19.88	1.07	0.22	0.85	11.5	Third
11	Ore 2-1T	20.70	1.07	0.22	0.86	7.4	Second
12	Ore 2-2T	20.40	1.07	0.18	0.89	10.9	Third
13	Ore 2-3T	21.29	1.06	0.25	0.81	10.6	Third

7.4 Leaching Methodology

7.4.1 Equipment and Methods

Ore samples were leached in a strongly acidic solution, namely aqua regia. This chemical can dissolve many metals, including noble metals like gold and platinum, hence the name 'aqua regia', which means royal water – the water that dissolves king of metals (Adams, 2005). So, it was used in the current study to dissolve metals (e.g., copper) from copper sulphide ore samples. Aqua regia is prepared by mixing two concentrated acids (hydrochloric and nitric) in a volume ratio of 3:1 (HCl:HNO$_3$), with each acid performing a different function. Nitric acidic serves as an oxidizing agent, whereas hydrochloric acid provides chlorine ions, which react with metal ions in the solution to form a soluble metallic compound. The dissolution of sulphide minerals in aqua regia can generally be expressed according to chemical Equation 7.3 (Moore, 1911; Huang et al., 2016).

$$3MS + 6HCL + 2HNO_3 \rightarrow 3MCl_2 + 4H_2O + 2NO + 3S \qquad (7.3)$$
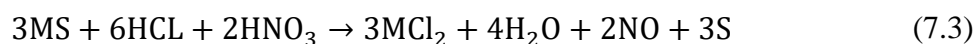
Apart from sample digestion for analytical purposes, aqua regia is not typically used for metal recovery in mineral processing industrial operations because preparing and handling large volumes of this solution is costly and raises safety concerns. Also, storing aqua regia for prolonged periods (several hours, days) without using it is not recommended because it quickly loses its effectiveness due to faster decomposition.

However, aqua regia was freshly prepared and utilised in this study to provide rapid leaching results (within a few hours), given the refractory nature of copper sulphide ores under weak acidic and oxidizing conditions (e.g., H_2SO_4 and $FeCl_3$). The refractoriness of copper sulphides (e.g., chalcopyrite) is caused by the formation of a passivating layer such as elemental sulphur (S^0), as indicated in chemical Equation 7.4, which inhibits the dissolution process (Dutrizac & MacDonald, 1974). Other common passivating agents include jarosites (insoluble sulphates), polysulphides, and metal-deficient sulphides (Klauber, 2008). This implies that the extent of leaching improvement due to microwave treatment based on aqua regia is overestimated, but it was used in this study to assess the role of ore mineralogy and texture on microwave-assisted leaching.

$$CuFeS_2 + 4Fe^{3+} \rightarrow Cu^{2+} + 5Fe^{2+} + 2S^0 \qquad (7.4)$$
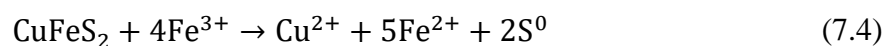
The leaching procedure involved placing each core in a 50-mL leaching tube and adding 18 mls of concentrated HCL (35% purity) followed by 6 mls of concentrated HNO_3 (70% purity). The samples were then leached for 4 hours at 100°C using the DigiPREP graphite block heater (Figure 7.8). Such a higher temperature and longer leach duration were selected to facilitate the dissolution kinetics of copper sulphides.

After leaching, the leachate was filtered using a syringe filter (0.45 µm openings) to remove any suspended solids. The filtered leachate was then analysed using the Inductively Coupled Plasma Atomic Emission Spectroscopy (ICP-AES) technique. The leach residue cores were rinsed with distilled water, dried, and scanned with an X-ray CT to examine the microstructural changes caused by leaching. Thereafter, the cores were pulverised in a ring and puck (TEMA) mill to -75 µm. The pulverized samples were split in several stages using a mini-rotary sample divider to obtain an appropriate weight for acid digestion (~1.0 gram). The acid digestion was performed to determine the grade of the leach residue and thus the back-calculated metal head grade of cores. The digestion process was carried out using the same set-up as that utilised for leaching the cores (Figure 7.8), but the leach duration was relatively short (90 minutes), and the volumes of acids used were comparatively small (HCl = 7.5 mls and HNO_3 = 2.5 mls). After acid digestion, the leachate was filtered through a syringe filter (with 0.45 µm openings) before ICP-AES analysis.
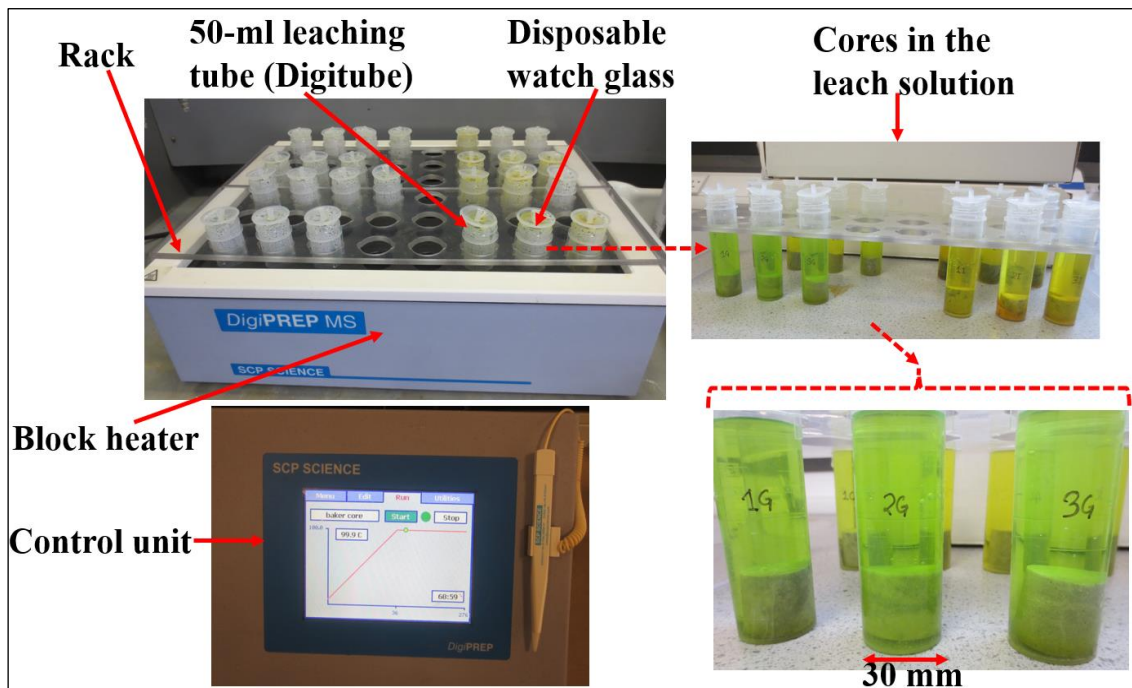
Figure 7.8. Leaching of cores using DigiPREP block heater

The leaching performance was evaluated in terms of copper and iron leach extractions, which were determined using Equations 7.5-7.7. The absolute leach extraction enhancement due to microwave treatment is the difference between treated and untreated extractions (Equation 7.8).

$$X_t = \frac{\text{Amount of metal dissolved at time t}}{\text{Total amount of metal in the fragment before leaching}} \times 100 \tag{7.5}$$

$$X_t = \frac{\text{Amount of metal dissolved at time t}}{\text{Total metal dissolved} + \text{Amount of metal remained in the residue}} \times 100 \tag{7.6}$$

$$X_t = \frac{V \times C_t}{V \times C_f + R} \times 100 \tag{7.7}$$

$$\Delta X = X_T - X_{UT} \tag{7.8}$$

Where;

X_t = Metal (copper/iron) leach extraction (%),

V = Total volume of leach solution (L),

C_t = Metal concentration at time t (g/L),

C_f = Metal concentration at the end of leaching (g/L),

R = Weight of metal remained in the residue after leaching (g),

ΔX = Absolute leach extraction enhancement due to microwave treatment (%),

X_T = Metal leach extraction of a treated fragment (%),

X_{UT} = Metal leach extraction of an untreated fragment (%).

The ICP-AES was calibrated to accurately determine the metal content in the leach solution. Six standard solutions with known copper and iron concentrations were prepared for the calibration process. The procedure involved pipetting 10 mls of 1000 ppm Cu standard and 10

mls of 10,000 ppm Fe standard, then making up to 100 mls to get a stock (intermediate) solution with 100 ppm Cu and 1000 ppm Fe. To match the acid concentration in the leach solution, a small portion of the intermediate stock solution was further diluted with a 10% aqua regia matrix (to make 15 mls) in six different combinations, as summarised in Table 7.3. The calibration plots used for the determination of copper and iron contents in the leach solution at wavelengths of 327.395 nm (Cu) and 234.350 nm (Fe) are indicated in Figure 7.9. It is worth noting that depending on the metal content range in the leach solution, several calibration solutions were prepared and sometimes dilution factors were applied.

Table 7.3. Example of calibration standard solutions used in this study

Standard ID	Dilution fraction	Volume of intermediate stock solution (ml)	Volume of matrix (10% aqua regia) (ml)	Cu (mg/L)	Fe (mg/L)
blank	0	0	15	0	0
a	0.8	12	3	80	800
b	0.6	9	6	60	600
c	0.4	6	9	40	400
d	0.2	3	12	20	200
e	0.1	1.5	13.5	10	100
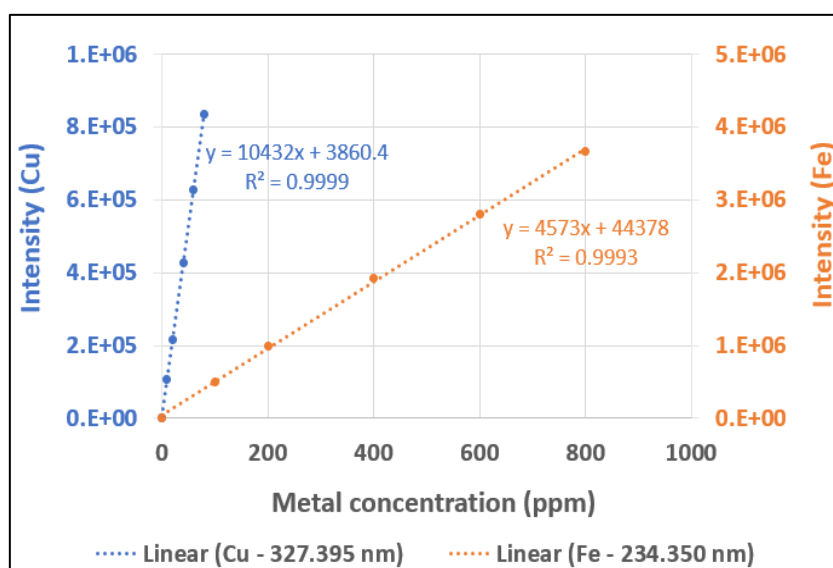
Figure 7.9. The ICP calibration curves for copper and iron

Table 7.4 indicates statistical data for ICP results (three repeats) of one of the leach solutions at 327.395 nm (Cu) and 234.350 nm (Fe) wavelengths. A margin of error of about 2% was achieved at 95% confidence level, other wavelengths indicated a similar margin error of about 2% (see Appendix 11.2.5).

Table 7.4. A summary of the ICP triplicate measurements

Sample ID	Cu (327.395 nm) ppm	Fe II (234.350 nm) ppm
1B run 1	89.00	2075.30
1B run 2	92.00	2139.10
1B run 3	89.30	2076.60
Mean	90.10	2097.00
STD	1.65	36.47
Margin error (95% conf level)	**2.08**	**1.97**

In addition, a few leach solutions were sent to another analytical laboratory to check the accuracy of assay results. Figure 7.10 shows the correlation plots of copper and iron leach results from the two analytical laboratories (lab A versus lab B), the raw data are available in Appendix 11.2.6. It can be seen that the data points for both copper and iron fall along the ideal unit correlation (dotted line), indicating that the assay results are accurate.
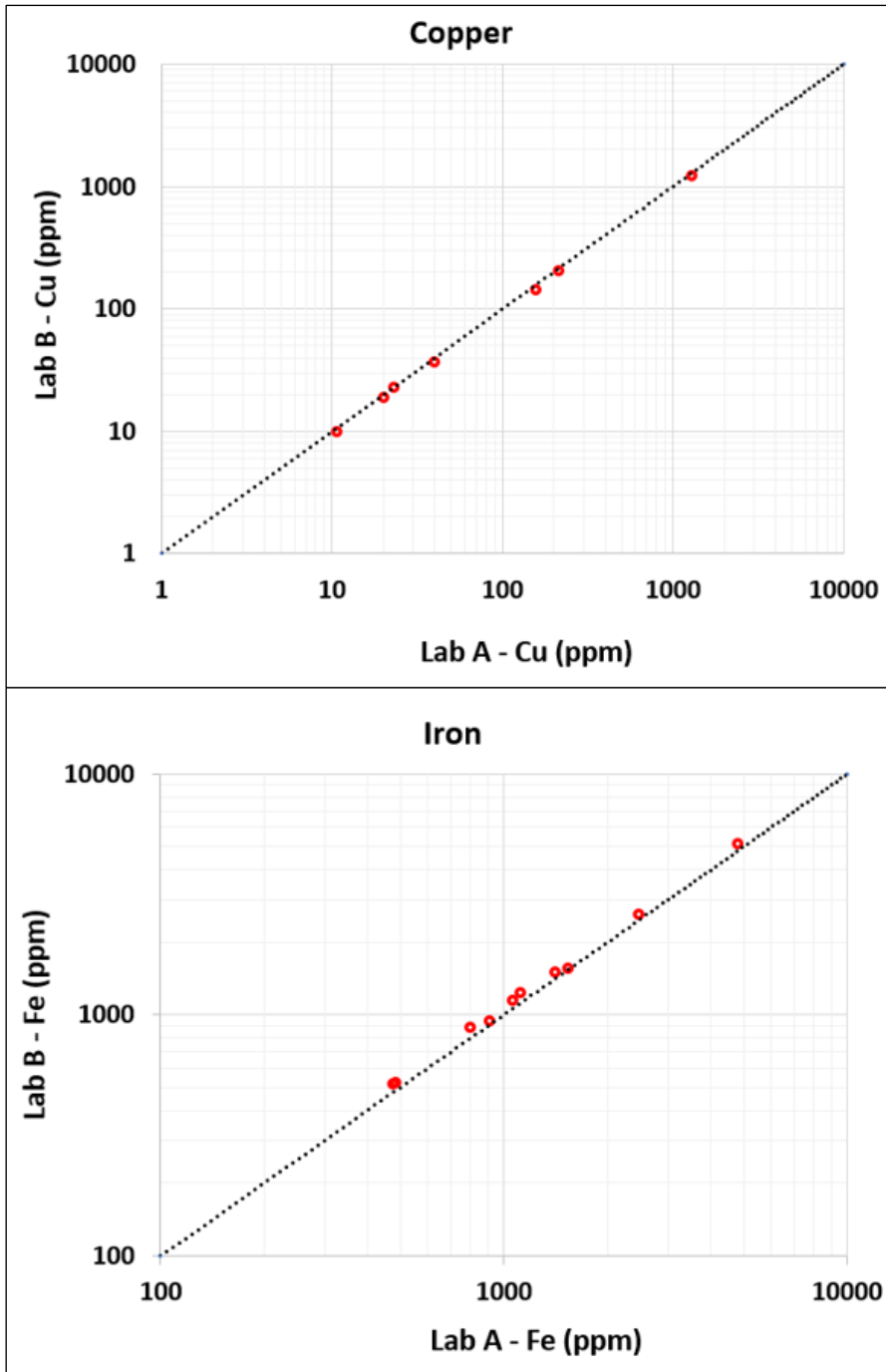
Figure 7.10. Comparison of ICP-AES results - two independent analytical laboratories

7.5 X-ray CT Equipment and Methods

7.5.1   Image Acquisition

Cores were scanned using a Phoenix v|tome|x m 240 kV X-ray CT scanner located at the Hounsfield Facility, University of Nottingham (Sutton Bonington Campus), UK. The system consists of a high-power 240 kV microfocus X-ray source (with a focal spot size of 13.1 µm), a sample stage, and a high resolution (DXR-250) 2024 x 2024 - pixel detector (Figure 7.11).

To ensure that the X-ray CT images of the cores are comparable before and after microwave irradiation/leaching, the cores were securely placed on the sample stage in the same orientation each time they were scanned. Each core was placed closer to the X-ray source to increase geometrical magnification. For a cone beam CT scanner, geometrical magnification is the ratio of Source Detector Distance (SDD) to Source Object Distance (SOD) (Müller et al., 2015). Each core was scanned at a geometrical magnification of 13.3, which was achieved at SOD and SDD of 61.3 mm and 817.4 mm, respectively. Each core was scanned at a spatial resolution of 15 µm, which was sufficient to detect most of the microwave-induced grains. Additionally, most of the sulphide grains could be detected because over 90% of the microwave-absorbing grains in the four ore types tested were coarser than 15 µm.
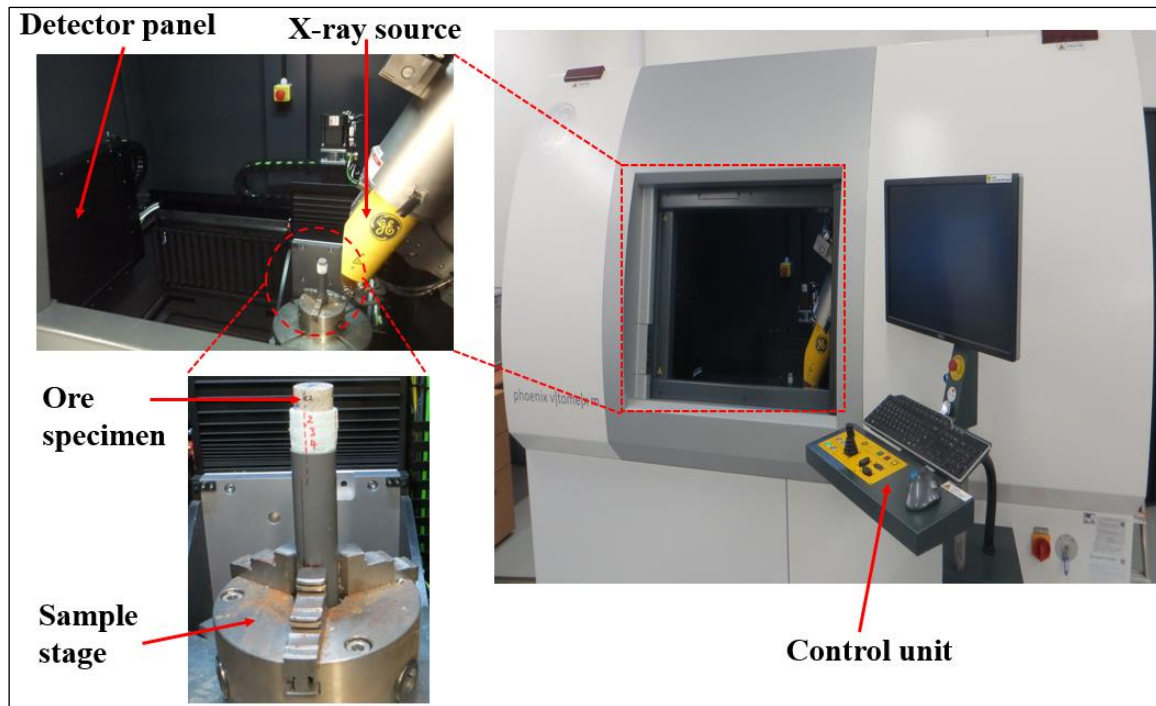
Figure 7.11. X-ray CT scanning set-up

The X-ray voltage and current were set at 164 kV and 80 µA, respectively. During scanning, a total of 2400 projection images were collected from each sample through 360° at 0.15° rotational increments. To reduce image noise, each projection image was an average of four frames with an exposure time of 333 milliseconds per frame. The scan duration for each core was 61 minutes, and all 13 pairs of cores were scanned multiple times, making a total of 65 scans (see Figure 7.12). Although only a few cores were scanned for each ore type, they were sufficient to provide an indication of the influence of ore mineralogy and texture on microwave-induced fractures and leaching performance, given the scanner's availability and budget constraints.

	T 4 cores	UT 4 cores	T 3 cores	UT 3 cores	T 3 cores	UT 3 cores	T 3 cores	UT 3 cores	
Scanning before MW treatment	✓	✓	✓	✓	✓	✓	✓	✓	
Scanning after MW treatment	✓	NA	✓	NA	✓	NA	✓	NA	
Scanning after leaching	✓	✓	✓	✓	✓	✓	✓	✓	
Total # of scans	12	8	9	6	9	6	9	6	65
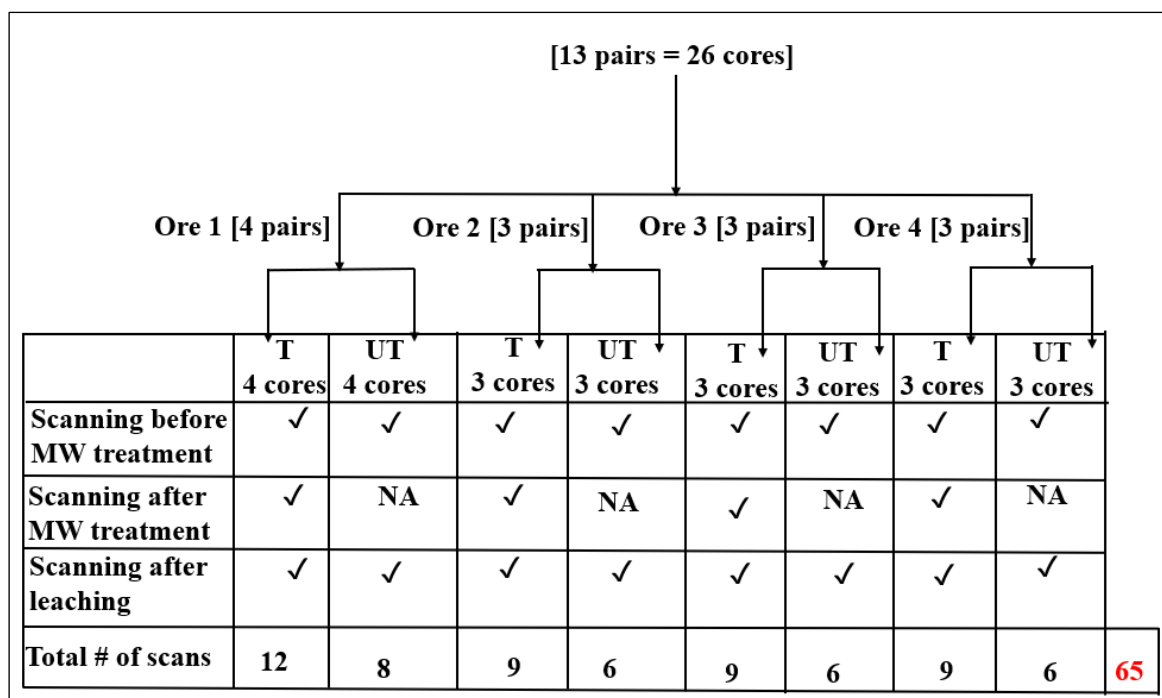
Figure 7.12. Schematic scanning workflow (Treated-T, Untreated -UT)

7.5.2 Image Processing Methodology

Each scan was reconstructed using the Phoenix proprietary software (Phoenix Datosx 2 Rec). Radiographs were visually assessed for sample movement before being reconstructed in 16-bit depth volumes with a beam hardening correction of 8.5. The reconstructed volumes were then post-processed using VG Studio MAX (version 2.2.0, Volume Graphics GmbH) for outputs of 2D slice image stacks. Thereafter, visualization and analysis of 3D images were performed using the ORS Dragonfly software through a powerful desktop computer (2 x Intel® Xeon® Gold 6142, 256GB RAM, NVIDIA Quadro P4000 GPU).

The 2D TIFF (Tag File Image Format) files (1500-2000 images) from each scan were loaded into the ORS Dragonfly software (Version 2021.3). The automatic global thresholding by Otsu (1979) was applied to convert an original image into a binary image to distinguish cracks/voids (air) from the rest of the ore phases. However, this technique was unable to distinguish sulphide grains from other ore phases. This limitation was addressed by loading the image files on an

225

open-source software ImageJ Fiji (Schneider et al., 2012) to check for the most suitable automatic algorithm that can threshold sulphide grains in this study. The ImageJ Fiji software consists of several automatic algorithm options for image thresholding.

More than six different automatic algorithms were tested using ImageJ Fiji software. The Maximum Entropy by Kapur et al. (1985) was able to threshold sulphide grains from the rest of the ore phases relatively well based on visual observation as compared to other entropy-based techniques (e.g., Renyi entropy), which could potentially overestimate the amount of sulphides grains to a certain extent (Figure 7.13). On the other hand, the cluster- or attribute-based methods (e.g., Otsu or moments) were unable to segment the sulphide grains more effectively (see Figure 7.14). The Maximum Entropy method has been used in the previous leaching study by Lin et al. (2016) for thresholding the sulphide grains from the rest of the ore phases. Therefore, the grey threshold value by the Maximum Entropy algorithm for each image data set was then applied to the Dragonfly software for further image analysis.
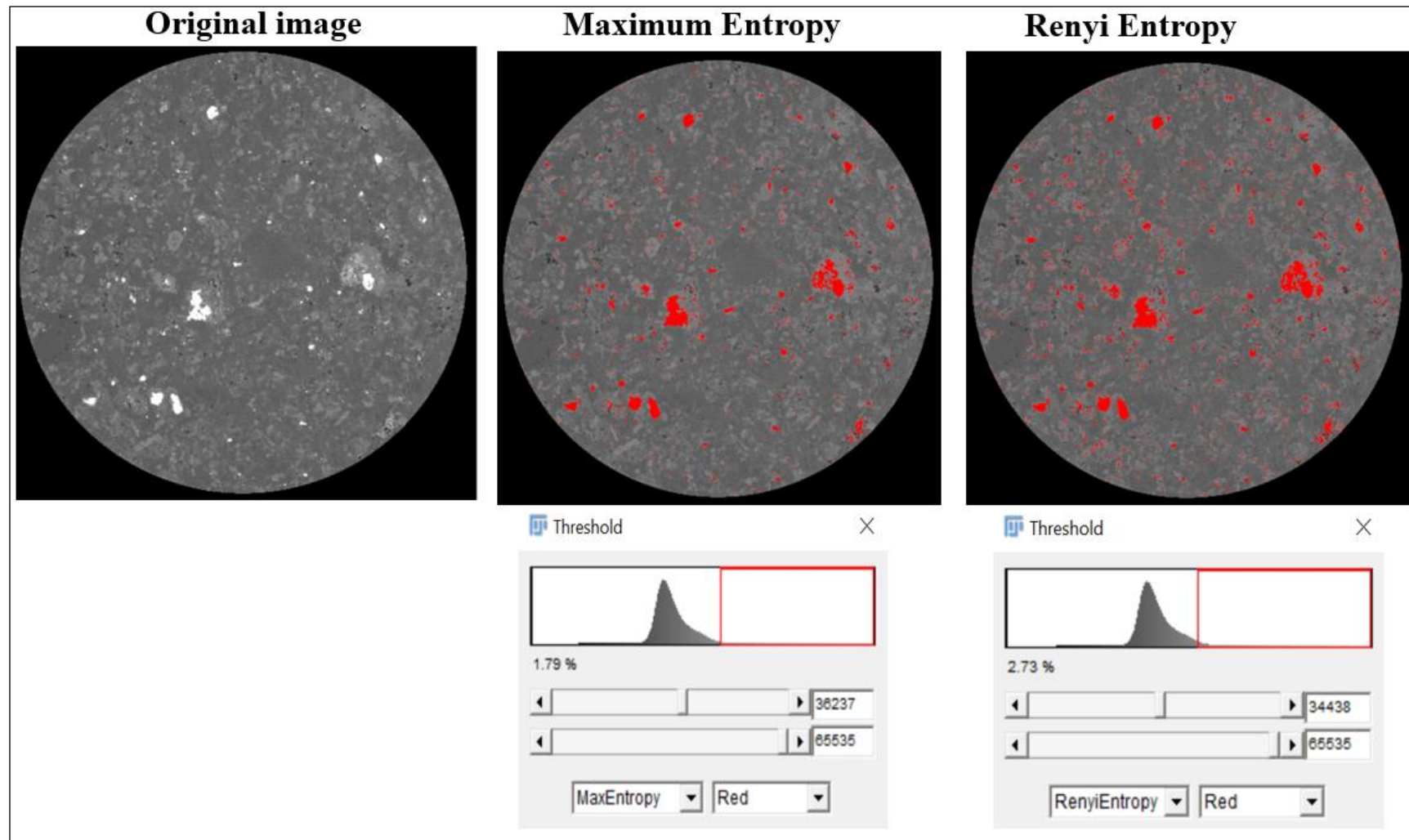
Figure 7.13. Automatic threshold algorithms (Maximum entropy and Renyi entropy)
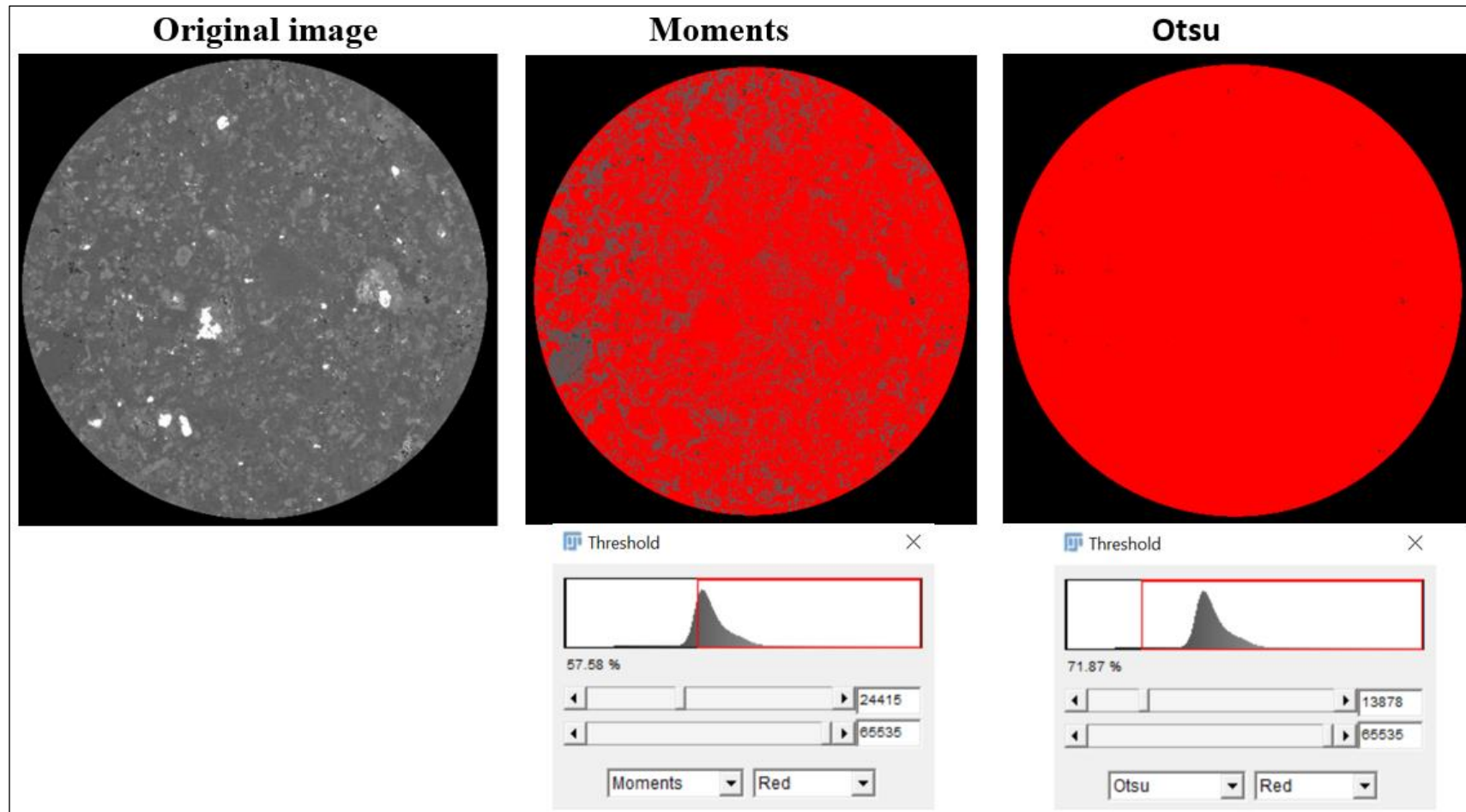
Figure 7.14. Automatic threshold algorithms (Moments and Otsu)

Quantitative analysis of features of interest on a 3D image requires a systematic procedure to generate reproducible results. Figure 7.15 outlines the general procedure developed in this study to determine several parameters, such as the volume of cracks/voids and sulphide grains, which were used to determine the extent of microwave-induced fractures and leaching performance, respectively. This procedure was tested in three different runs (image analysis sessions) using the same specimen to check whether the results are reproducible. In this case, 1500 (2D image) slices were loaded and analysed in three separate sessions. As indicated in Table 7.5, the results were reproducible with a margin error of about 3-4% at 95% confidence level. Therefore, for consistency, the procedure was applied to assess the extent of microwave-induced damage (increase in crack volume/thickness) and mineral dissolution (decrease in sulphide volume) by comparing the pre-treated and post-treated scans.

1. Import a stack of 2D TIFF (1500) images into the Dragonfly software to get a 3D image.	
2. Mask the image using a cylinder shape to remove regions of no interest at the peripherals.	
3. Threshold sulphide grains from the rest of the ore phases. In this case, the Maximum Entropy algorithm was applied.	
4. Apply the 6-connected components algorithm (described in Section 4.5.2.2), and then perform the analysis (e.g., volume of sulphide grains).	

Figure 7.15. The general procedure for image analysis workflow

Table 7.5. Void and sulphide volumes statistical parameters

Parameter	Run 1	Run 2	Run 3	Average	Standard deviation	Margin error (95% conf level)
Total voxels	3,510,718,848	3,510,718,848	3,506,455,680	3,509,297,792	2,461,341	
Total volume (mm^3)	11,847.73	11,847.73	11,833.34	11,842.93	8.31	
Voids labeled voxels	5,805,801	5,727,189	5,912,375	5,815,121.7	92,944	
Volume of voids labelled voxels (mm^3)	19.59	19.33	19.95	19.62	0.311	
Volume of voids labelled voxels (%)	0.17	0.16	0.17	0.17	0.0058	**3.9%**
Sulphide labeled voxels	118,219,068	118,284,499	113,120,524	116,541,363.67	2,962,715	
Volume of sulphide labelled voxels (mm^3)	398.96	399	381.75	393.30	9.95	
Volume of sulphide labelled voxels (%)	3.37	3.37	3.23	3.32	0.081	**2.8%**

7.6 Results and Discussion

7.6.1 Assessment of Microwave-induced Damage - UPV Testing

Figure 7.16 shows pictures of a few cores before and after microwave treatment to demonstrate the extent of microwave-induced damage in each of the four ores tested. These were the highly fractured cores from each ore type. The average, maximum, and minimum UPV reductions of each core tested at seven different positions are also shown to indicate the magnitude of induced damage. Although the treatment duration varied slightly between specimens, the extent of microwave-induced damage varied greatly. These pictures and their respective UPV reductions show that Ore 4-1T and Ore 3-3T cores exhibited much more damage than Ore 1-2T and Ore 2-1T cores.

To assess the overall damage in each ore type, the UPV reductions of all treated cores from each ore type were averaged, and the results are shown in Figure 7.17. The error bars indicate the maximum and minimum UPV reductions, and the raw data are provided in Appendix 11.2.2. As expected, Ores 4 and 3 were the best performers in terms of microwave-induced damage, exhibiting an average UPV reduction of about 28-31%, followed by Ore 1 with a reduction of ~23%. Ore 2 is the least performer, achieving a lower UPV reduction of approximately 14%.

		Ore 4-1T	Ore 1-2T	Ore 3-3T	Ore2-1T
UPV REDUCTION	Average	33.2%	23.9%	34.8%	24.3%
	Max	68.6%	68.4%	47.3%	29.6%
	Min	10.3%	0.4%	19.1%	16.2%
MW POWER, TIME		1 kW, 6.5 sec	1 kW, 6.0 sec	1 kW, 8.8 sec	1 kW, 7.4 sec
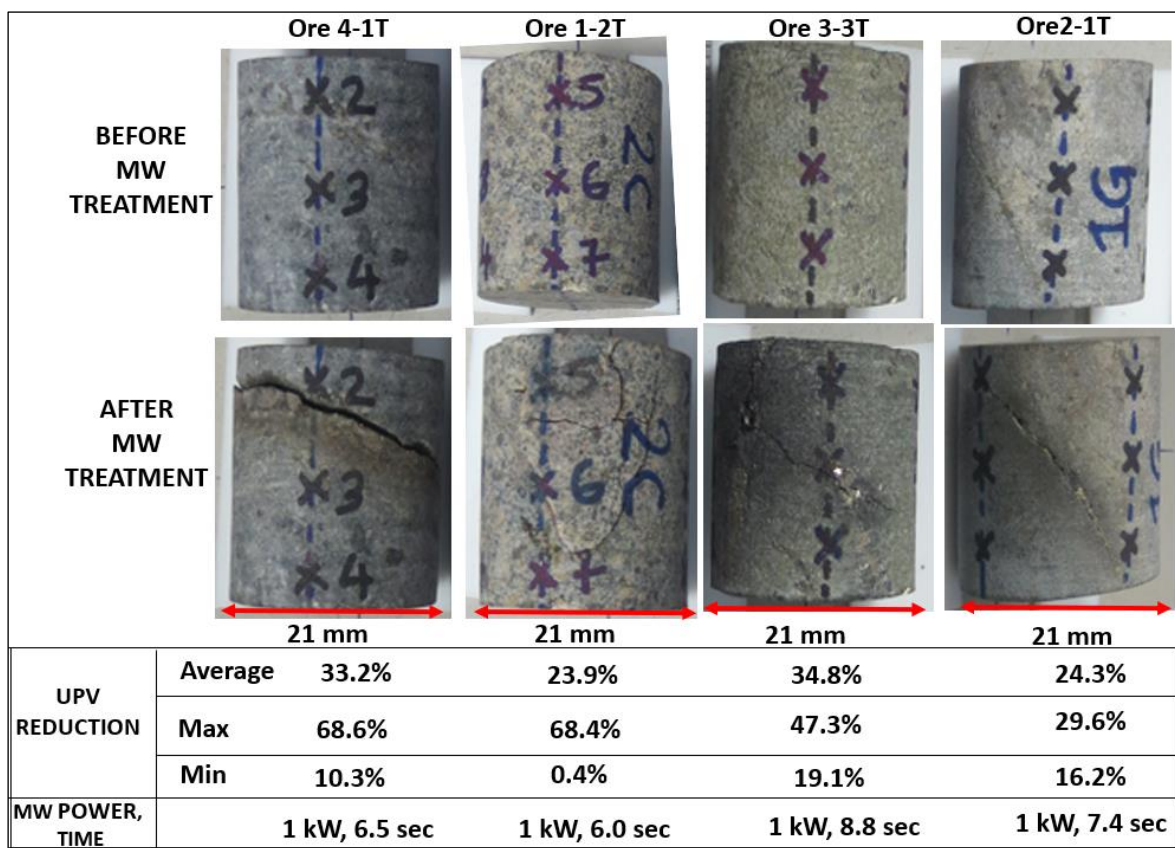
Figure 7.16. Pre- and post-treated cores (indicating MW-induced damage)
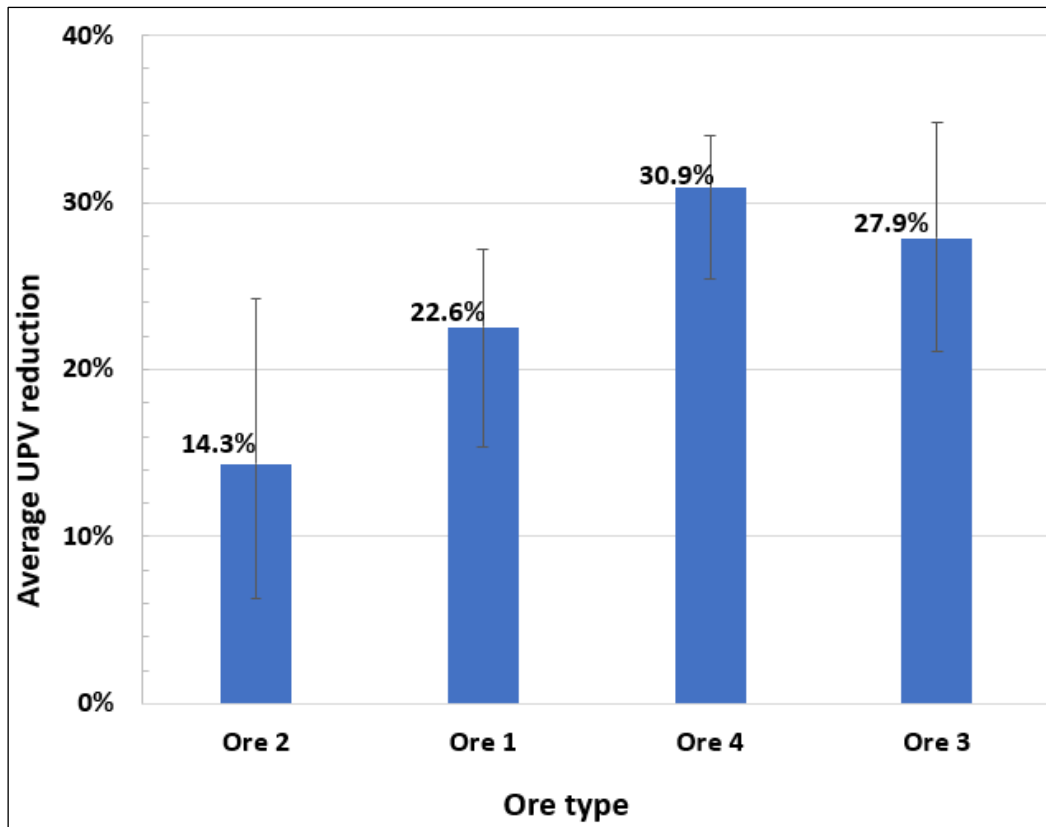
Figure 7.17. Microwave-induced damage – UPV reduction

Based on the MLA results presented in Chapter 5, the significant UPV reductions observed in both Ores 4 and 3 is attributed to the combined effect of a high modal abundance of good microwave heaters (~7-14%) and the large grain size of microwave heaters which occurs as coarse discrete grains or micro/macroveins (max D_{50} = 500-600 µm). Under microwave fields, this texture promotes intense heating and differential thermal stresses, which aid in ore fracturing. Moreover, these two ore types contain significant proportions of stiffer microwave heaters (e.g., pyrite) of 5-11%, which facilitate the effective transfer of induced stresses to the surrounding gangue matrix, resulting in significant ore fracturing.

The higher UPV reduction observed on Ore 1 is attributed to the high modal abundance of microwave heaters of 6%, with a grain size of D_{50} of up to 190 µm, as well as a large proportion of hard (brittle) gangue matrix (e.g., quartz) of about 66%. Essentially, ore samples with a high

abundance of good microwave heaters enclosed within a hard (brittle) non-heating gangue exhibit significant fractures due to effective generation and transfer of stresses without the gangue undergoing ductile deformation. The poor performance of Ore 2 in comparison to other ore types is attributed to the low proportion (2%) and finer grain size (max $D_{50} = 170$ µm) of good microwave heaters, as well as the low content of stiffer microwave heaters (e.g., pyrite and magnetite) of approximately 0.5%, combined with the high association of microwave heaters with free space (~20%).

7.6.2 Assessment of Microwave-induced Damage - X-ray CT Imaging

Although the UPV technique has been used to indicate the extent of microwave-induced damage, it does not provide qualitative information about the damage (e.g., fracture size and fracture maps) that can be directly linked to mineral dissolution performance. Instead, the X-ray CT technique was used to provide both qualitative and quantitative information about the damage. The crack/void volume increase was used to quantify the damage by comparing the pre-treated and post-treated scanning results, with pre-treated scans serving as the baseline for detecting changes caused by microwave treatment. For illustration, the X-ray CT results of a few cores shown in Figure 7.16 are presented here.

Figure 7.18 shows the 3D view and 3D rendered voids/cracks of Ore 3-3T core before and after microwave treatment. The 3D image depicts connected networks of cracks and voids of varying sizes, with the largest cracks for each scan shown in red and the smallest in blue. It can be observed that the total proportion of crack volume before microwave treatment was 0.04% and increased to 0.72% after treatment, which is equivalent to an increase of nearly 1700%. Further investigation revealed that the induced fractures account for roughly half of the damage, with the remainder being the void formed due to electrical arcing (see the region circled in red in Figures 7.18 and 7.19).
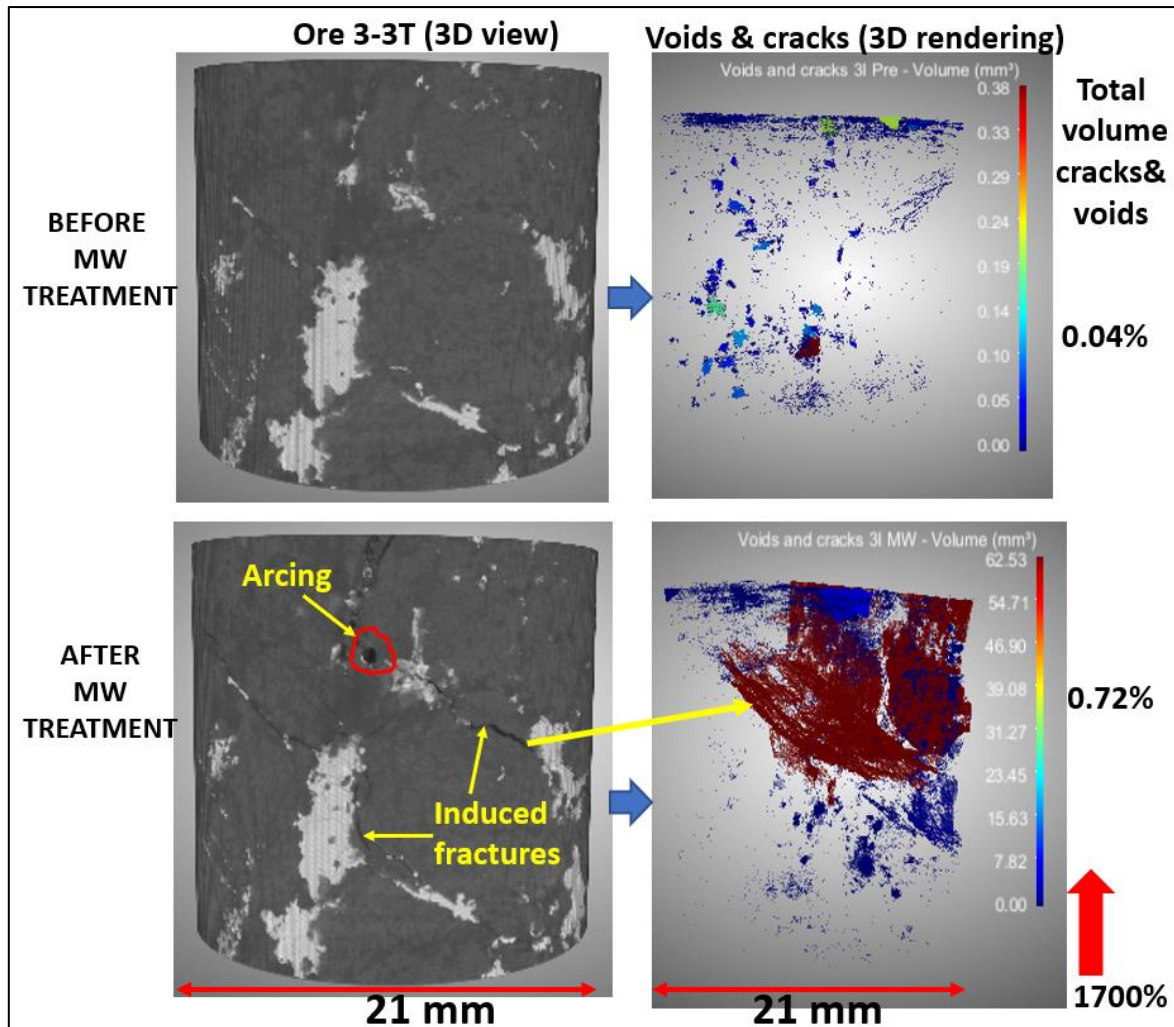
Figure 7.18. X-ray CT 3D scanning results - Ore 3-3T

As indicated on the XY and XZ planes in Figure 7.19, Ore 3-3T core sustained multiple fractures running across the entire specimen, with a crack length of more than 20 mm. It can be noticed that the specimen consists of coarse sulphide grains and macro/microveins of up to 2 mm wide, which have certainly contributed to the observed significant damage. It is also evident that microwave-induced fractures occur in the vicinity of mineralised regions (e.g., microveins). This observation supports previous findings in the literature, which suggests that the principal mechanism of microwave-induced fractures in ore samples is a result of selective heating and differential thermal stresses occurring between the heated phases and the non-heating matrix (Salsman et al., 1996; Jones et al., 2005; Ali & Bradshaw, 2010). It is also

apparent that the nature of the microwave-induced fractures in this specimen is both intergranular and transgranular, which can be exploited to improve mineral exposure at coarser particle sizes without or with minimal comminution. In the current study, this kind of fracture pattern has been exploited to provide leaching and mass transport pathways to improve mineral dissolution without further comminution.
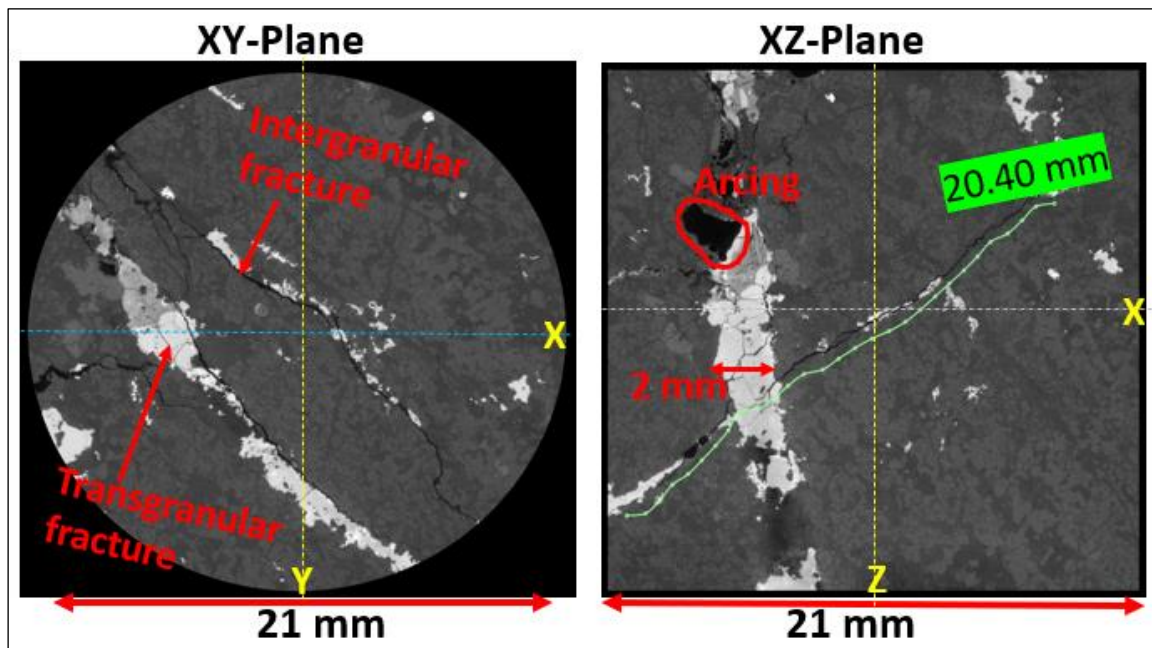
Figure 7.19. X-ray CT 2D scans of Ore 3-3T after microwave treatment

Figure 7.20 shows the 3D scanning results of Ore 4-1T core. This specimen is also highly fractured, indicating a crack volume increase of nearly 500% due to microwave treatment. The 2D view scanning results reveal that the specimen sustained multiple fractures of varying sizes. These fractures were attributed to the high modal abundance of good microwave heaters which occur as coarse discrete grains and macro/microveins (see the bright phases in Figures 7.20 and 7.21). It is also interesting to note that the induced fractures propagated along grain boundaries and across the gangue matrix, and in most cases, they could barely cut across the sulphide grains (the bright phases). This suggests that the sulphide grains were probably stiffer than the adjacent gangue matrix.
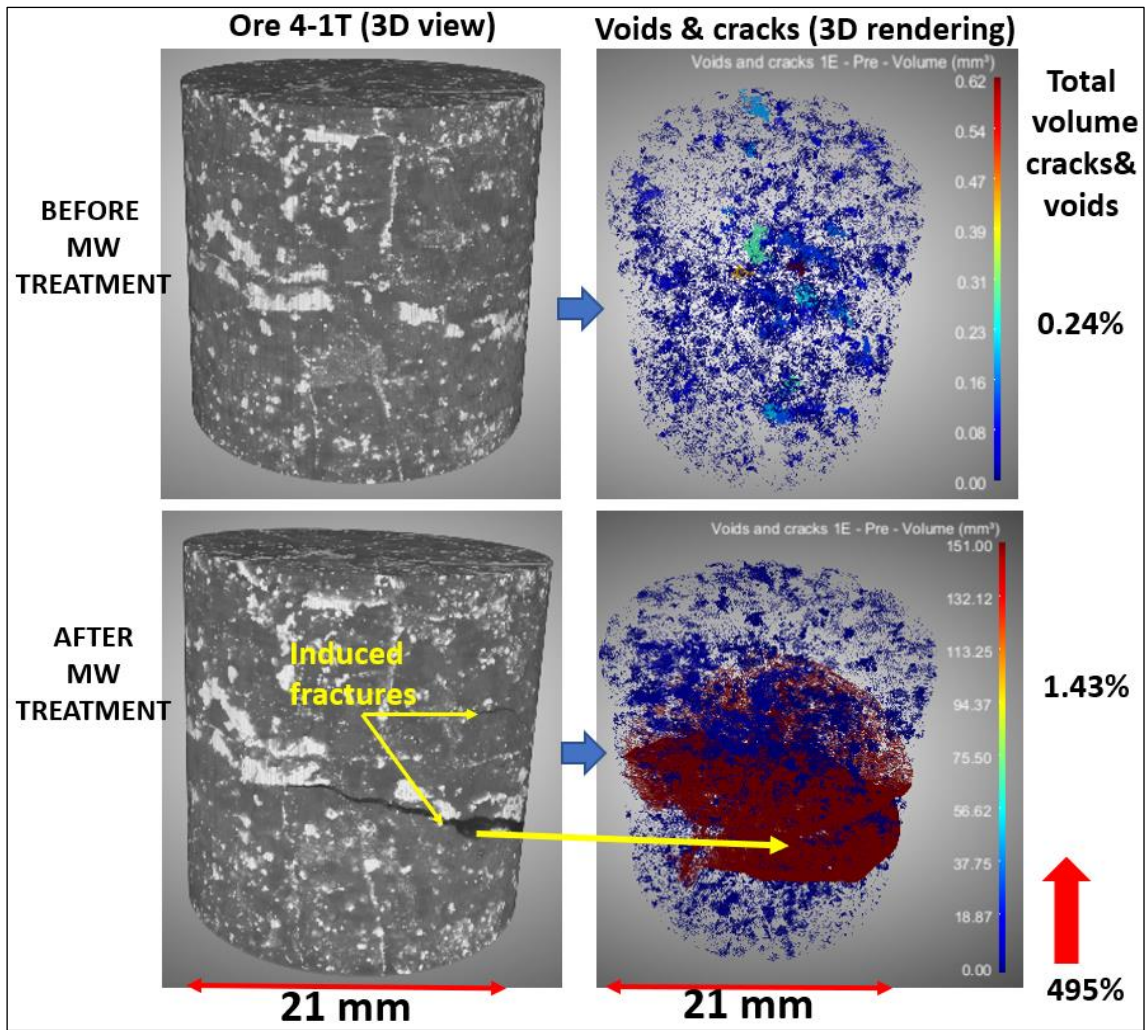
Figure 7.20. X-ray CT 3D scanning results - Ore 4-1T
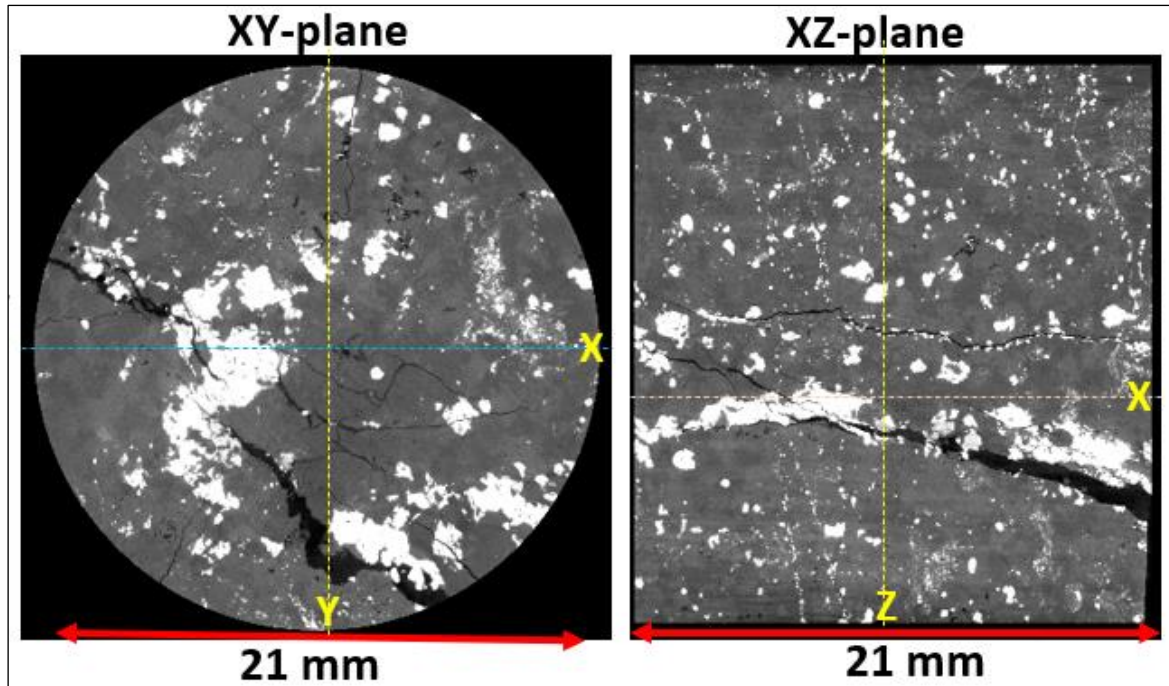
Figure 7.21 X-ray CT 2D scans of Ore 4-1T after microwave treatment

Figure 7.22 shows the 3D scanning results of Ore 1-2T core, which indicate a crack volume increase of 290% due to microwave irradiation. This lower induced damage is attributed to a lower proportion and finer grain size of microwave heaters compared to those of Ore 4-1T and Ore 3-3T cores shown previously. The induced damage could not spread throughout the core because the texture of microwave absorbing grains (bright phases) in this core is not more consistent and there are no mineralised veins (Figure 7.23), resulting in a lower damage that is more localised.
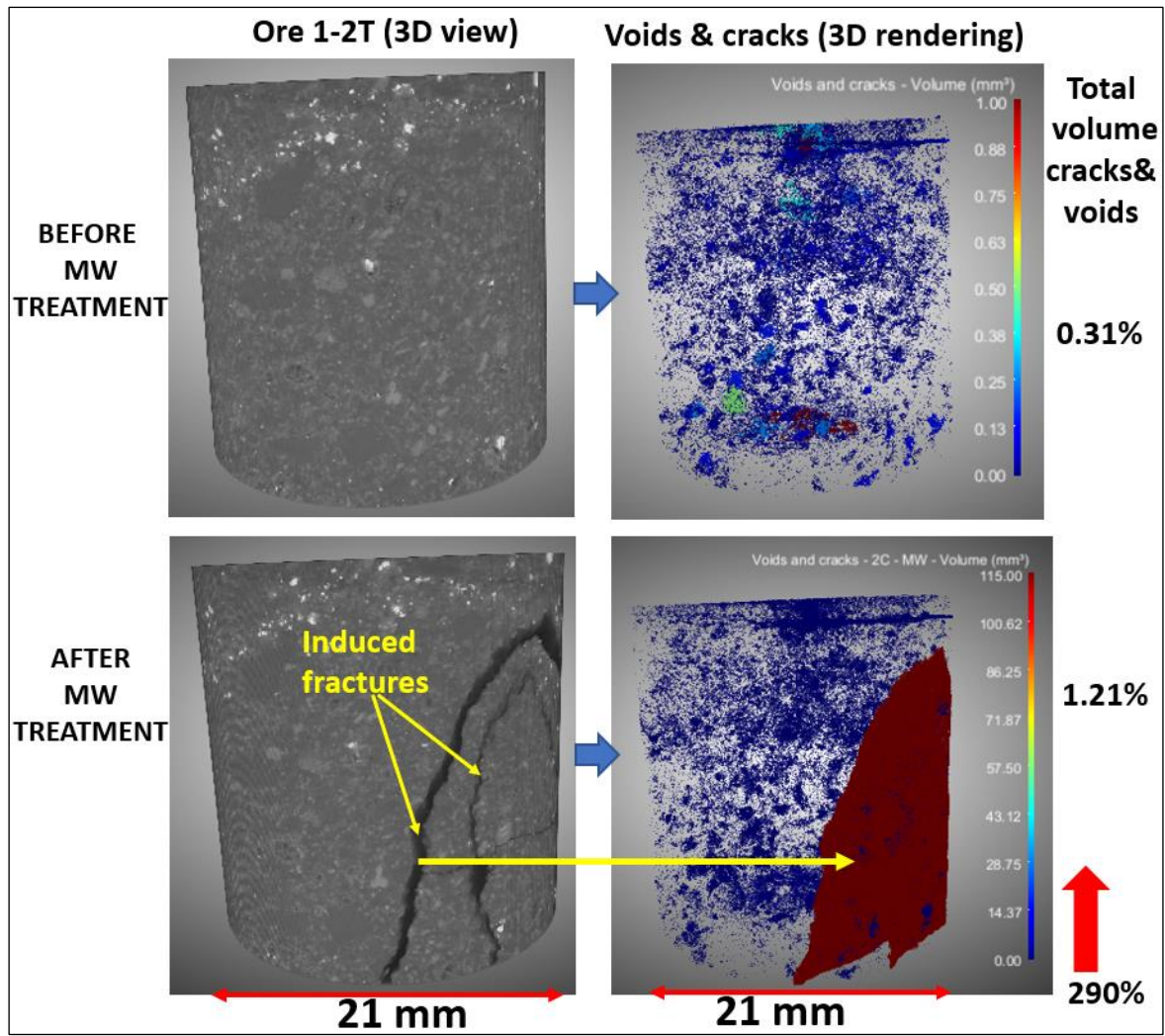
Figure 7.22. X-ray CT 3D scanning results - Ore 1-2T
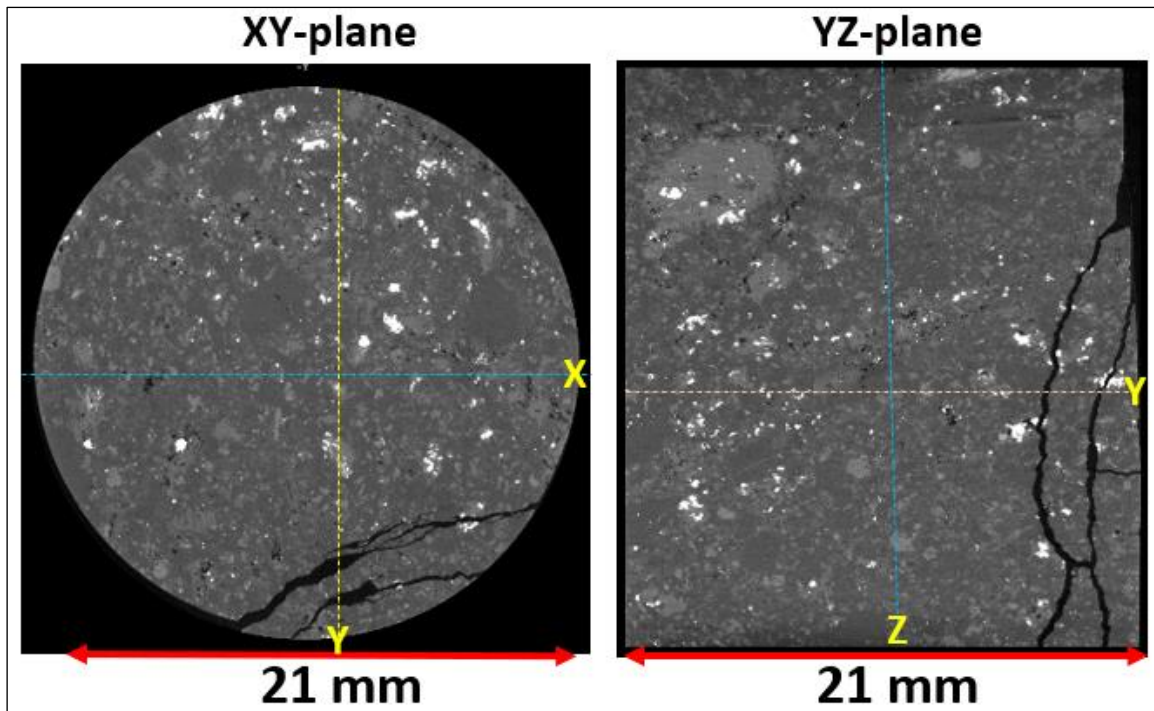
Figure 7.23. X-ray CT 2D scans of Ore 1-2T after microwave treatment

Figure 7.24 shows the 3D view and 3D rendered voids/cracks of Ore 2-1T core. This specimen performed poorly in terms of microwave-induced fractures in comparison to other specimens described previously, achieving a minimal crack volume increase of about 49%, from 0.55% (pre-treated) to 0.82% (post-treated). It is evident that narrow fractures have been formed due to microwave treatment (see the 3D view of the post-treated scan). Although the scale bar ranges differ, the increase in yellowish and reddish colours in the post-treated 3D rendered image shows the evidence that microwaves induced some fractures in this specimen.

A more detailed examination of the 2D slices reveals that sulphide minerals in this specimen occur as fine disseminated or coarse discrete grains, with some of these grains deposited along pre-existing fractures (see Figure 7.25). It can be seen that new fractures have been developed due to microwave treatment. In addition, some pre-existing fractures have been exacerbated by microwaves due to the expansion of microwave-absorbing grains along these fractures (planes of weakness). However, the size of the fractures generated in this specimen is smaller than that

previously observed in other ore types. This could be attributed to the lower proportion of stiffer microwave heaters (0.5%) and the comparatively finer grain size of these heaters (max D_{50} =170 µm).
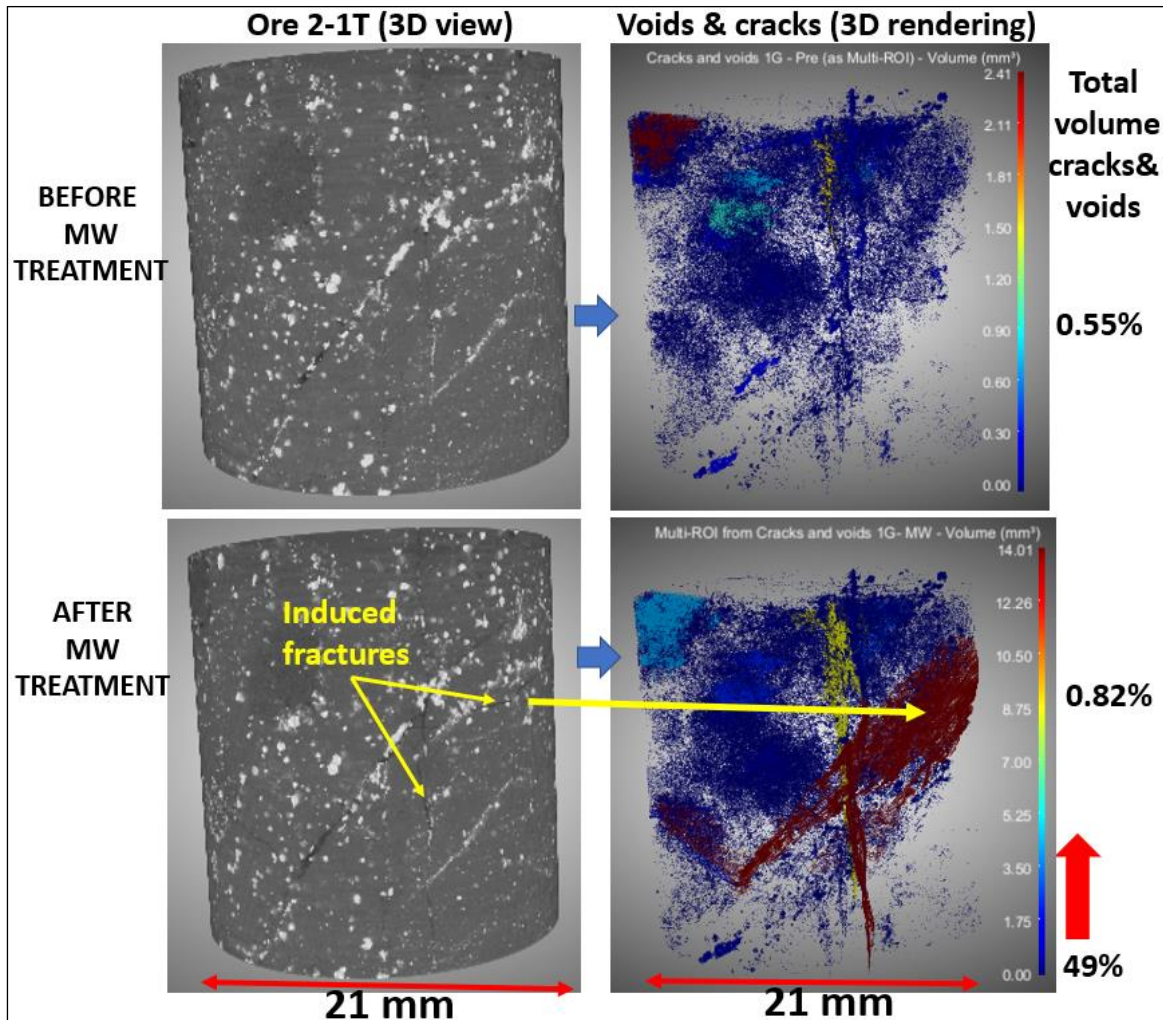
Figure 7.24. X-ray CT 3D scanning results - Ore 2-1T
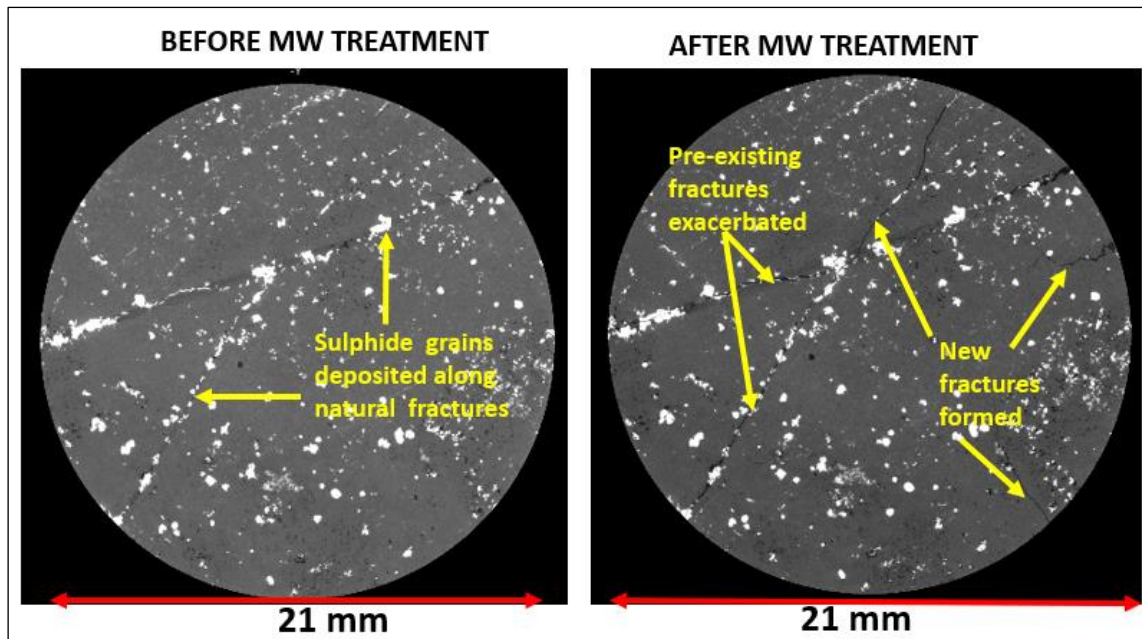
Figure 7.25. Ore 2-1T after microwave treatment

Based on the X-ray CT results of all treated cores, the average crack volume increase due to microwave treatment for each ore type is shown in Figure 7.26, and the raw data are presented in full in Appendix 11.2.8. The error bars represent the maximum and minimum crack volume increase percentages for each ore type. These results indicate that Ore 3 exhibited the greatest induced damage, with an average crack volume increase of around 652%. Ore 2, on the other hand, only exhibited minimal damage of about 19%. The long error bar seen in Ore 3 is attributed to the significant induced damage and void formed due to electrical arcing observed in the Ore 3-3T core, with other cores in this ore exhibiting comparatively lower damage. The trend in this figure follows a similar pattern to the UPV results observed in the previous section, indicating that, in addition to qualitative assessment, the X-ray CT technique can be used to quantify the magnitude of microwave-induced damage in ore specimens.
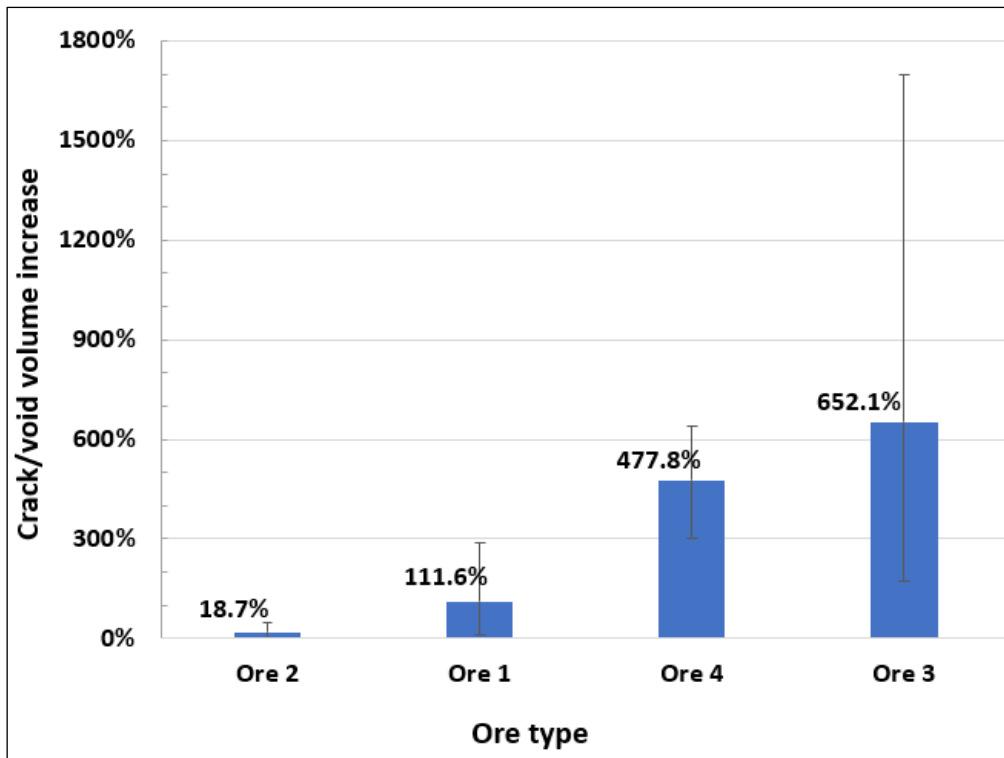
Figure 7.26. Microwave-induced damage - crack/void volume increase

In addition to crack volume analysis, the X-ray CT results were used to quantify the extent of ore fracturing using the volume thickness technique described in Section 4.5.2.3 by comparing the crack/void thickness before and after microwave treatment. Figures 7.27-7.30 show 3D visualisation of crack/void thickness in the pre-treated and post-treated scans. The red colour represents regions with the thickest cracks, while the blue colour indicates narrow fractured areas. It can be seen that most cores from Ores 1, 4, and 3 exhibited larger fractures due to microwave treatment, with some regions having crack thicknesses of more than 1.0-2.0 mm. Ore 2 cores, on the other hand, showed little or no microwave treatment effect, with narrow fractures of less than 0.25 mm. As previously stated, the larger induced damage (fracture thickness >2.0 mm) seen on Ore 3-3T core is partly due to the void formed as a result of electrical arcing.
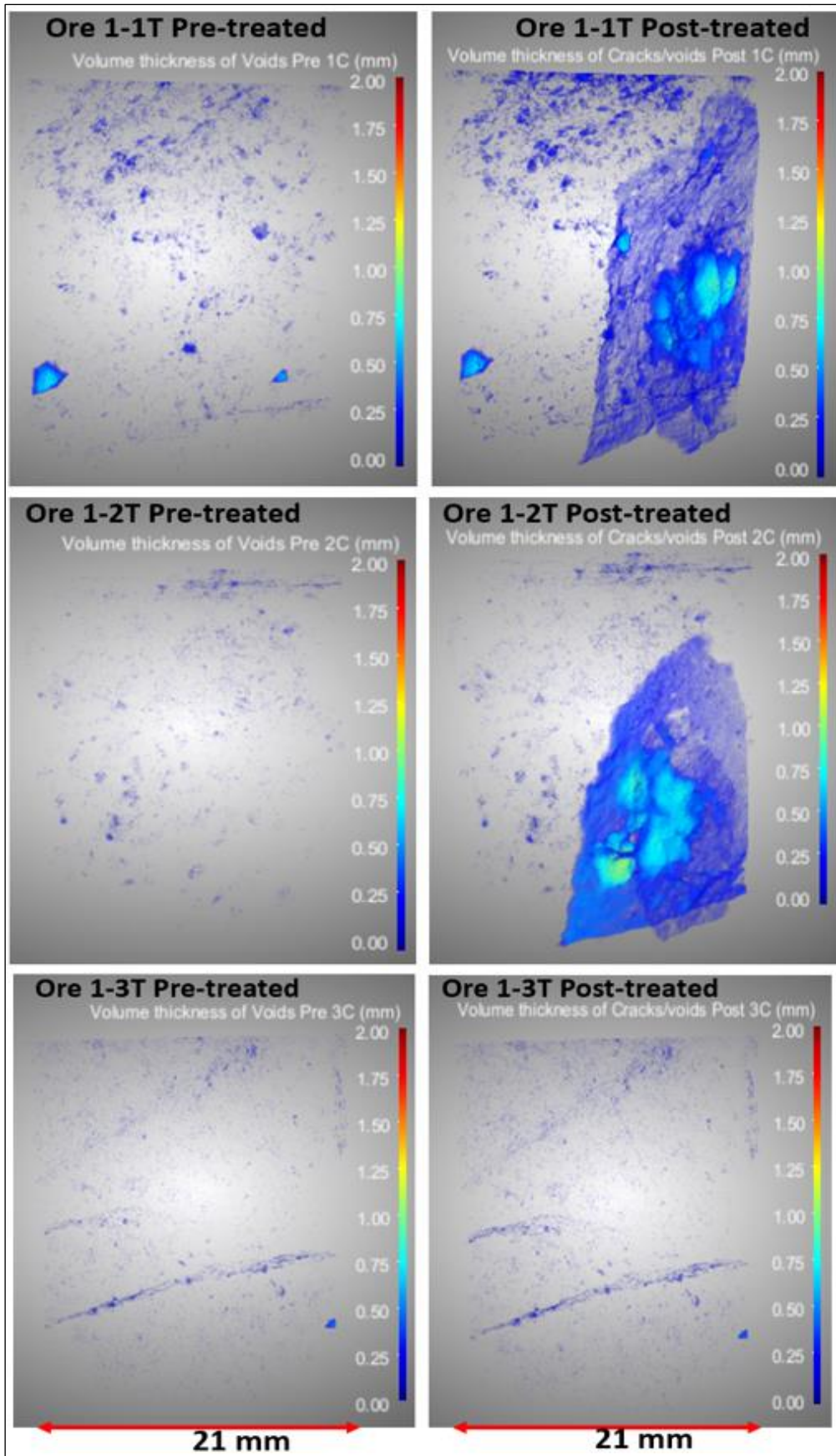
Figure 7.27. 3D-rendered cracks/voids thickness maps – Ore 1 (**4T see Appendix 11.2.8.2**)
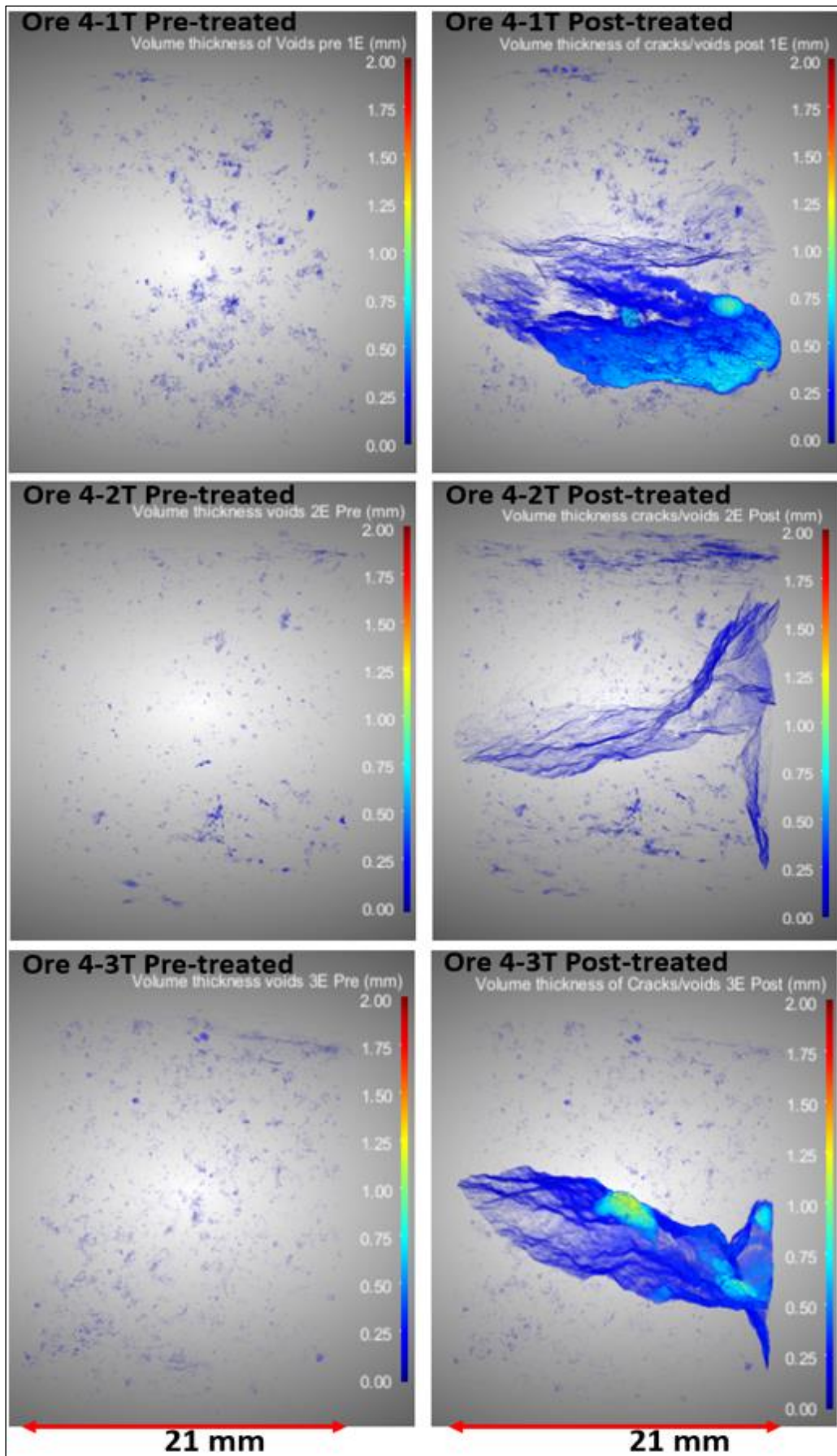
Figure 7.28. 3D-rendered cracks/voids thickness maps – Ore 4
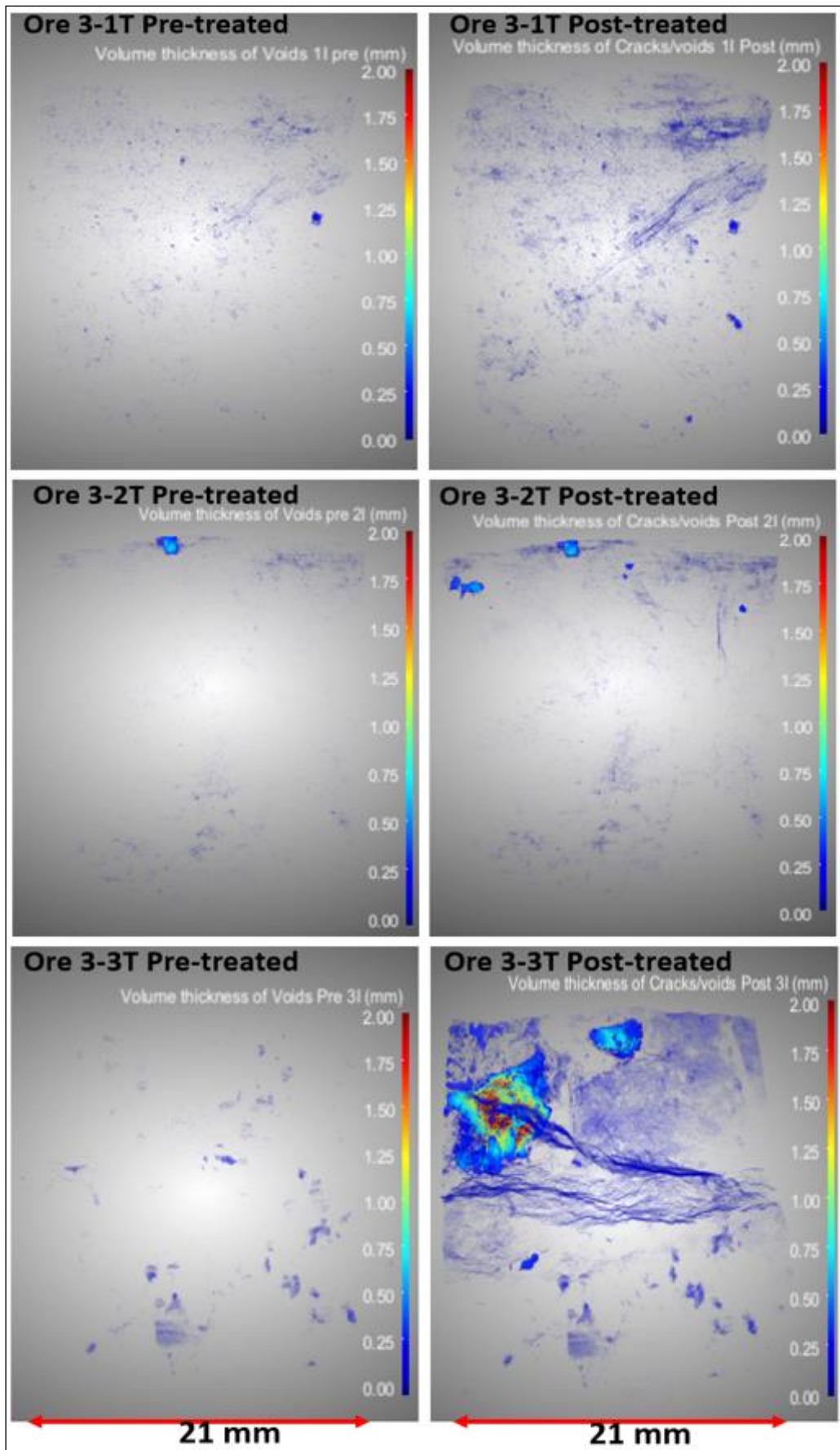
Figure 7.29. 3D rendered cracks/voids thickness maps – Ore 3
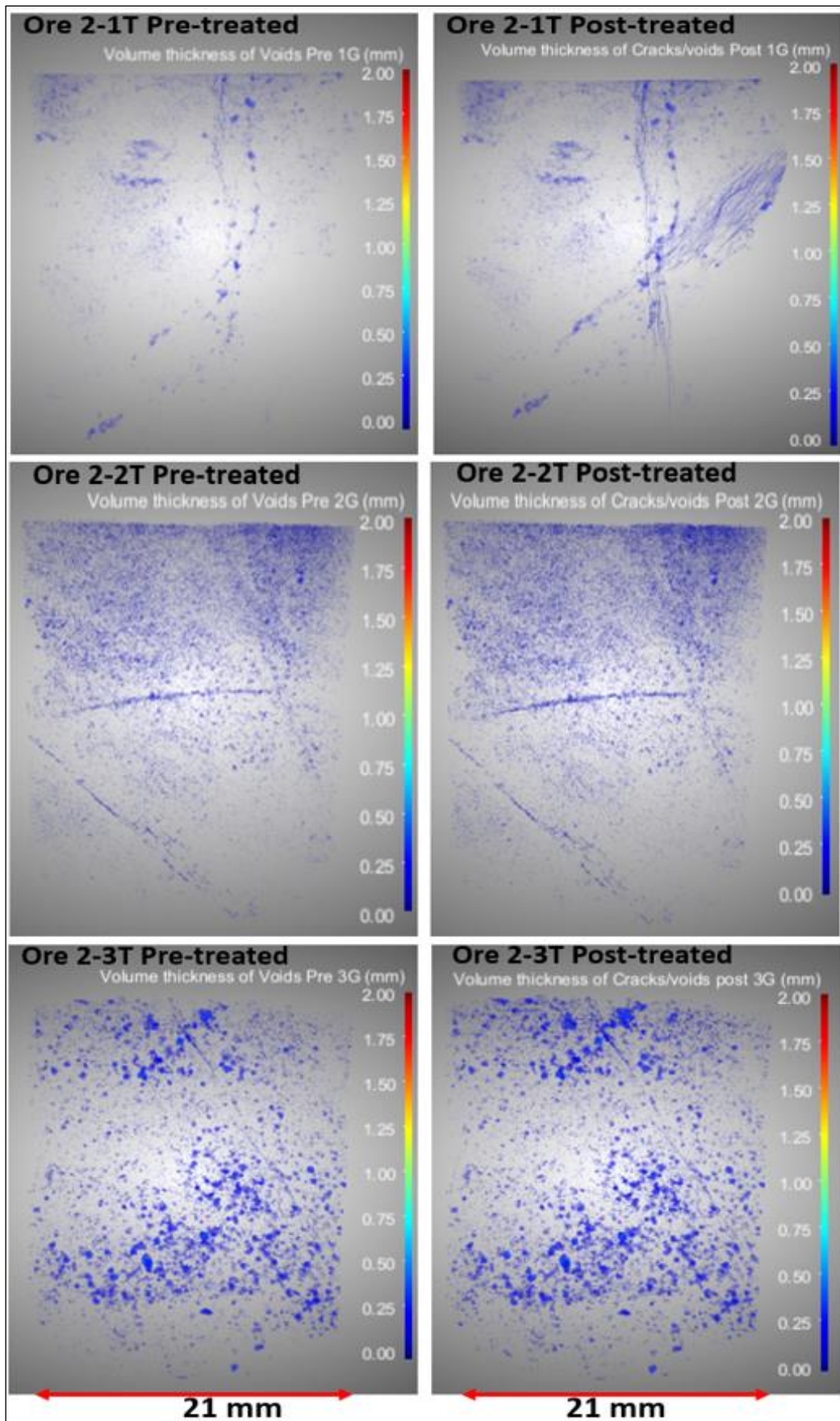
Figure 7.30. 3D-rendered cracks/voids thickness maps – Ore 2

Based on the results shown in Figures 7.27-7.30, the fracture size distribution for each core was constructed (see Appendix 11.2.8.3), and the average fracture thickness for each ore type before and after microwave treatment is shown in Figure 7.31. These results show that Ore 3 exhibited the largest fracture increase from $d_{80} = 0.05$ mm (pre-treated) to $d_{80} = 0.81$ mm (post-treated), equivalent to a 0.76 mm increase in crack thickness, which is partly due to electrical arcing observed on Ore 3-3T core. Other ore types that demonstrated greater damage due to microwave treatment were Ores 4 and 1, which exhibited an increase in the fracture thickness of about $d_{80} = 0.2\text{-}0.3$ mm. Although microwaves induced damage on some cores in Ore 2 sample (e.g., Ore 2-1T – see Figure 7.30), the overall increase in fracture thickness was negligible. As expected, these results are consistent with the fracture volume results seen in Figure 7.26, which show that ores with suitable mineralogy and texture for microwave treatment (e.g., Ores 4, 3, and 1) exhibit significant damage, as discussed in the previous section.
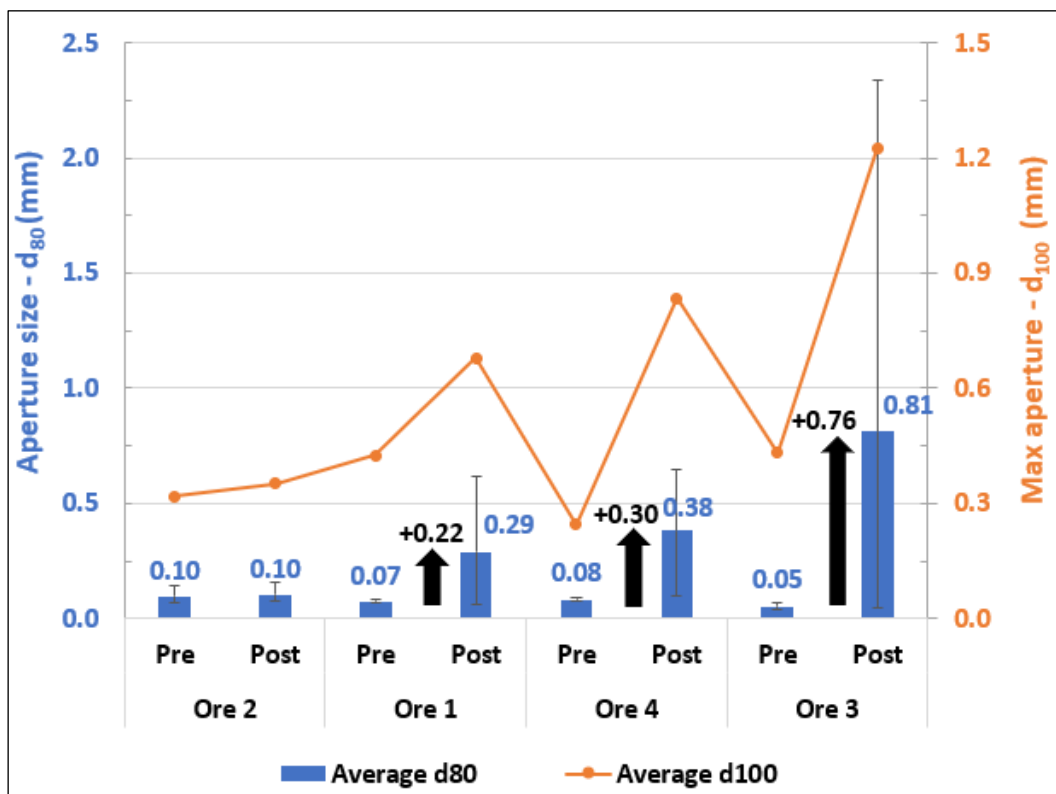
Figure 7.31. Average crack size comparison

In summary, both UPV and X-ray CT techniques demonstrated that microwave treatment effectively induced observable fractures in sulphide ores, and the magnitude of these fractures varies depending on ore mineralogy and textural properties. Larger fractures of more than 1.0-2.0 mm thick were induced in some regions on microwave-treated samples with suitable mineralogy and texture properties. It is obvious that these fractures are large enough to allow leaching chemicals to diffuse to the interior of the particle, potentially improving overall leaching performance. The next section investigates the extent of mineral dissolution improvement resulting from these fractures.

7.6.3   Effect of Microwave Ore Pre-treatment on Leaching Performance

The X-ray CT results have demonstrated that microwaves induce fractures in sulphide ores, and these fractures occur in the vicinity of sulphide mineralisation, indicating the possibility of improved mineral dissolution. The effect of microwave-induced fractures on the extent of acid penetration in copper sulphide ores is illustrated in Figure 7.32. Both the treated and untreated cores shown here were soaked in the acid solution for 4 hours. The greenish-yellow stains in the interior of the treated cores indicate that the acid solution penetrated more deeply in the treated cores than in the untreated cores. This simple observation suggests that microwave-induced fractures can increase access to internal sulphide mineralisation, which can be exploited to improve the leaching performance of coarsely crushed ore fragments. In another microwave treatment study, Ure (2017) reported a similar observation, indicating that fluorescence dye penetrated deeper into copper sulphide ore samples as a result of microwave treatment, and thus treated fragments exhibited longer fracture lengths.
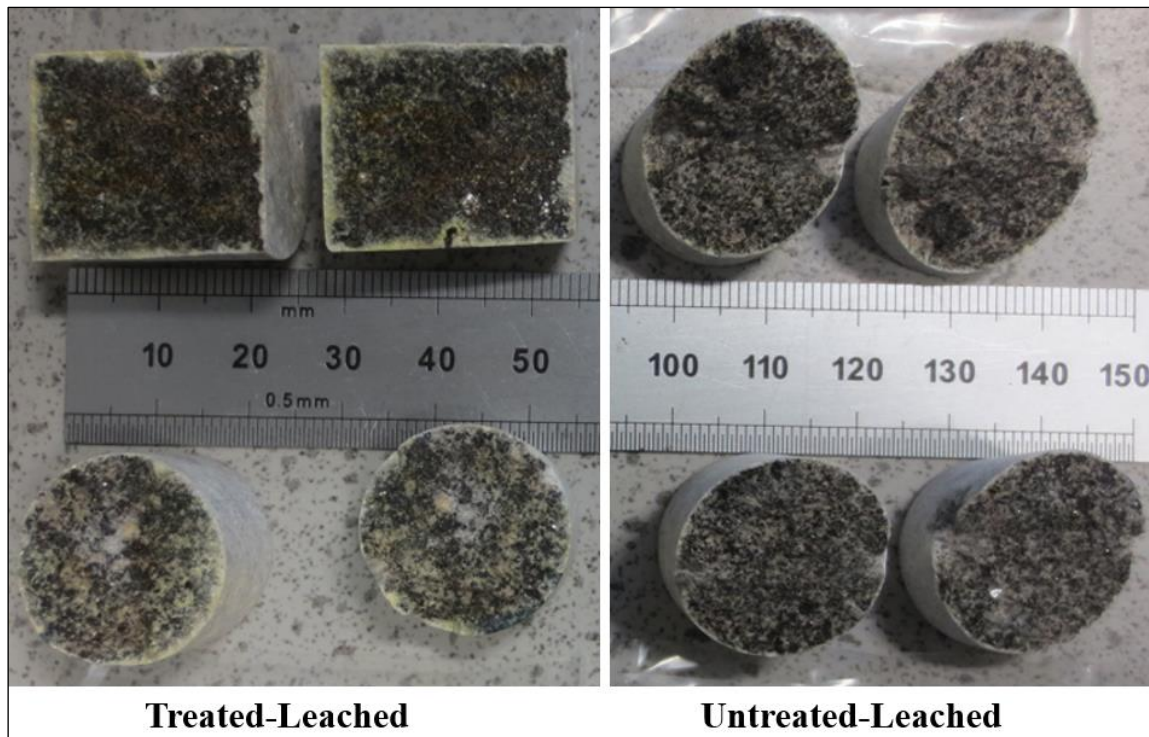
Figure 7.32. Physical observation of microwave treatment effect on acid penetration extent

The effect of microwave ore pre-treatment on mineral dissolution can be demonstrated using the X-ray CT imaging technique. Figure 7.33 shows the 2D slices of the pre- and post-treated scans of one of the Ore 4 cores. This specimen sustained multiple fractures due to microwave treatment, exposing internal sulphide grains to the leach solution. It can be observed that the acid solution penetrated deeply and dissolved most of the sulphide grains located along fractured surfaces, as indicated by the disappearance of bright phases along the fractures in the post-leached scan. This effect is more pronounced in large fractures than in small fractures, and thus large (wide opening) fractures are more beneficial in terms of leaching improvement than small (narrow opening) fractures.
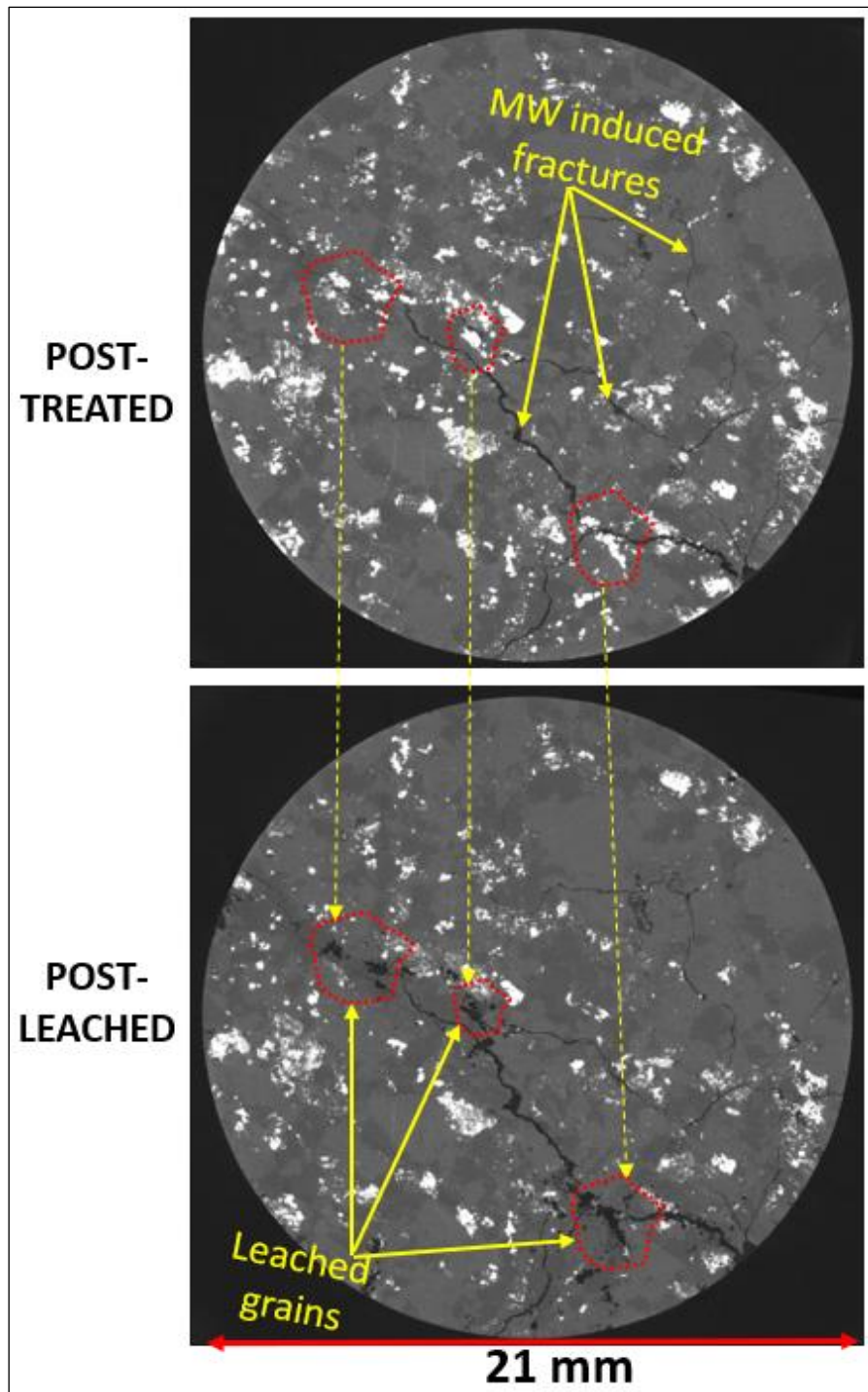
Figure 7.33. Leaching of sulphide grains along microwave-induced fractures

The volume decrease (disappearance) of sulphide grains after leaching was also determined quantitatively by X-ray CT technique to demonstrate the effect of microwave ore pre-treatment on mineral dissolution. Figures 7.34 to 7.37 show the comparison of the volume decrease of sulphide grains attained by the cores, arranged in pairs (treated versus untreated) based on

thermal imaging results described in Section 7.2.3. The error bars indicate a margin of error of 3% obtained in the triplicate runs of image analysis sessions shown in Table 7.5. The initial sulphide volume content before leaching for each core was determined and it is also presented here. The raw data are available in Appendix 11.2.8.1. Although there is a great variation of initial sulphide content in some pairs, it can generally be observed that treated cores achieved a higher sulphide volume decrease (beyond the image analysis error) than untreated cores, and the effect is more pronounced for Ores 3, 4, and 1. As observed in the previous section, these ore types exhibited significant induced damage, and thus the higher sulphide volume decrease observed here suggests that these ores are more likely to achieve greater leaching improvement.
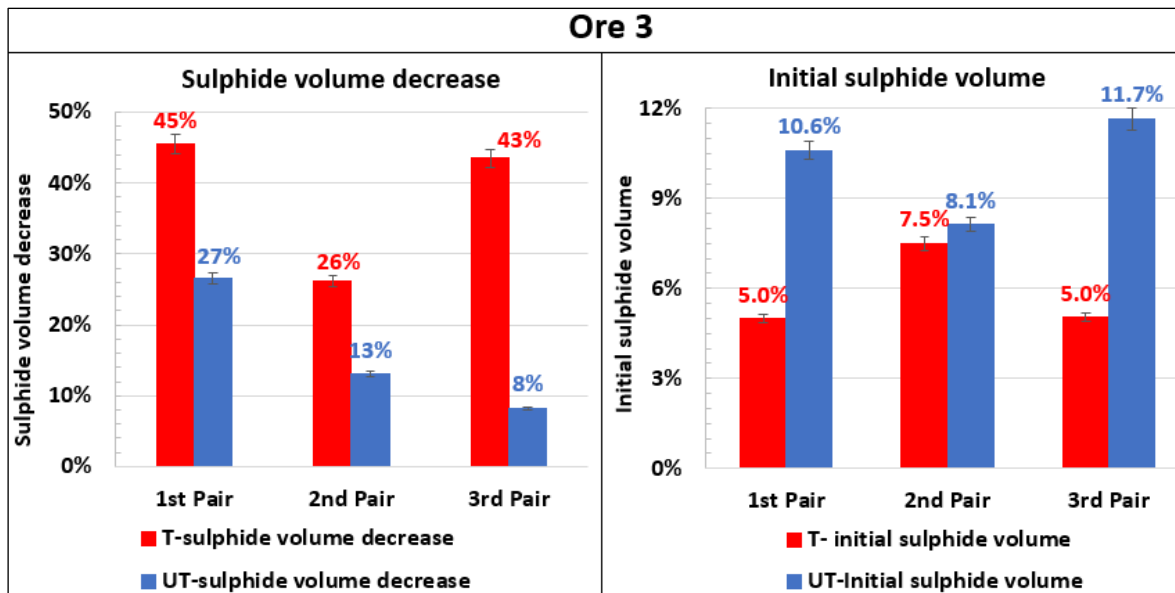
Figure 7.34. Sulphide volume decrease after leaching – Ore 3
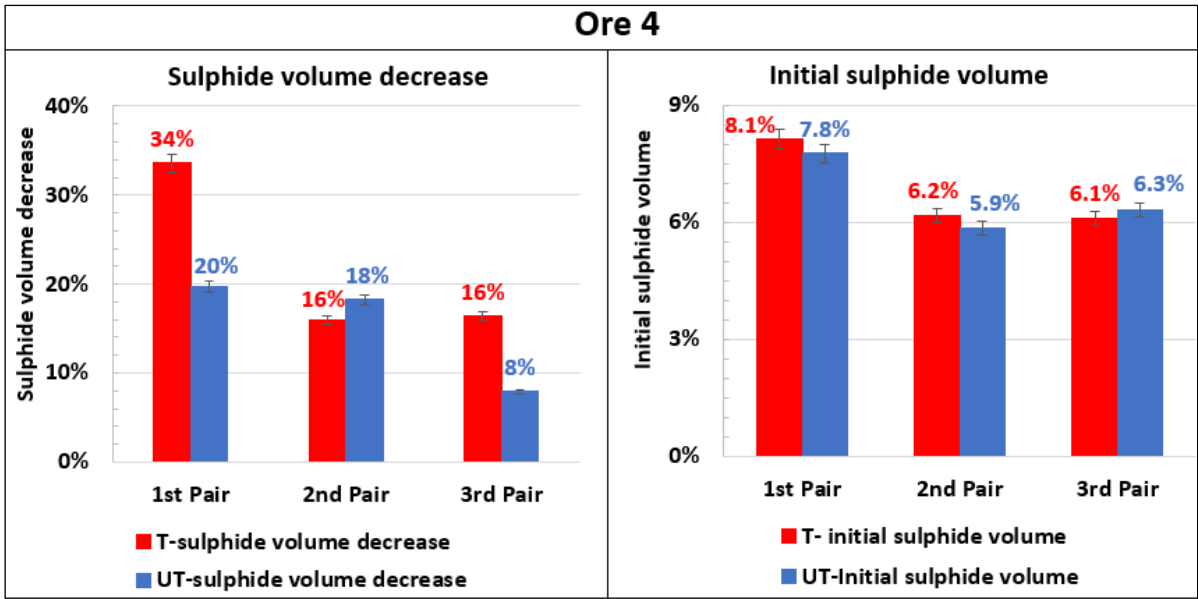
Figure 7.35. Sulphide volume decrease after leaching – Ore 4
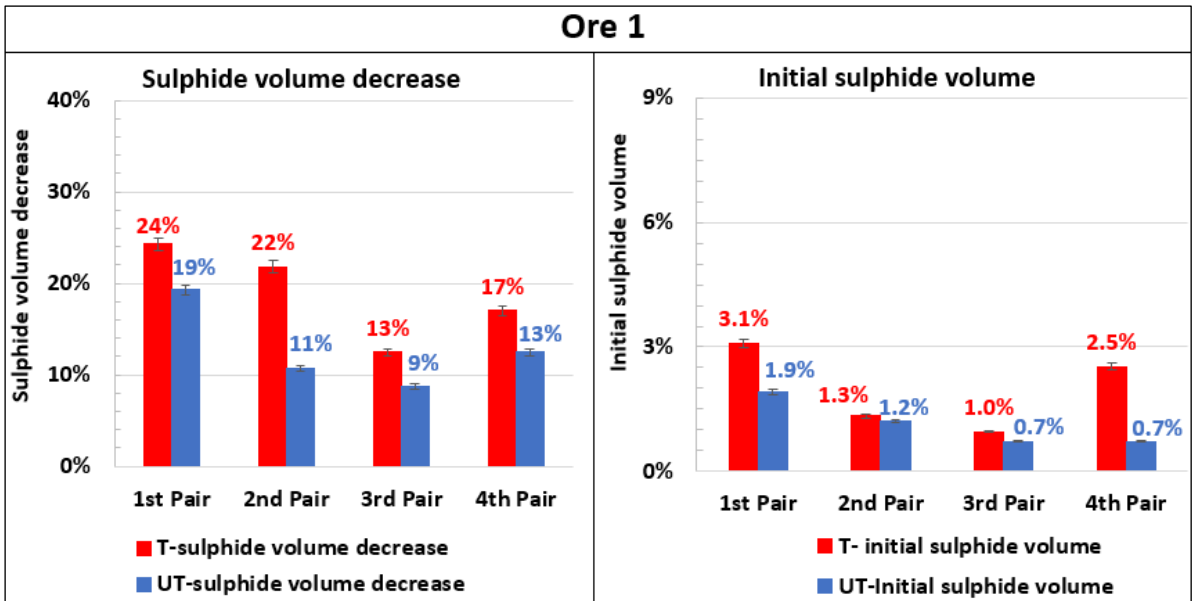
Figure 7.36. Sulphide volume decrease after leaching – Ore 1
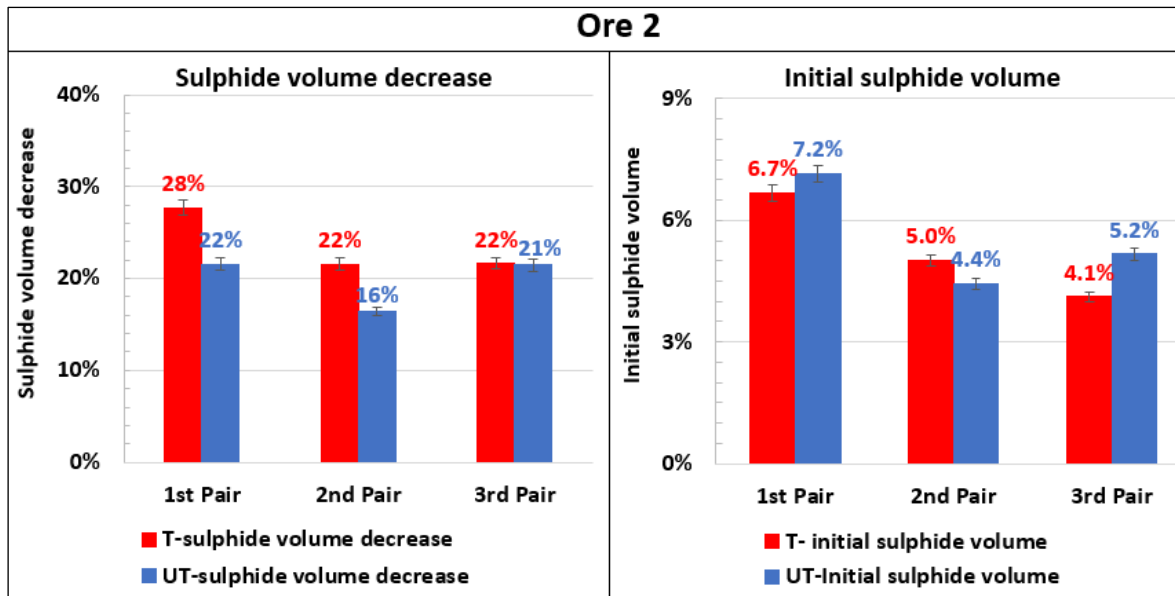
Figure 7.37. Sulphide volume decrease after leaching – Ore 2

The effect of microwave ore pre-treatment on copper and iron leach extractions for all pairs of cores tested is shown in Figures 7.38 to 7.41. The copper and iron head grades of treated and untreated cores are also shown to indicate the initial metal content before leaching. The error bars indicate the margin of error of ICP-AES analysis of about 2% shown in Table 7.4. Although there was a great variation of the metal head grades in some pairs, the general observation shows that treated cores achieved higher copper and iron extractions than untreated cores. As expected, the effect is more pronounced for Ores 3, 4, and 1 due to their favourable mineralogy and textural properties for microwave-induced fractures, such as high modal abundance of good and stiffer microwave heaters, as well as coarse grain size of these heaters. In general, these leaching results follow the same pattern as the sulphide volume decrease results derived from the X-ray CT scans shown in Figures 7.34 to 7.37, supporting the use of X-ray CT imaging to describe leaching phenomena.
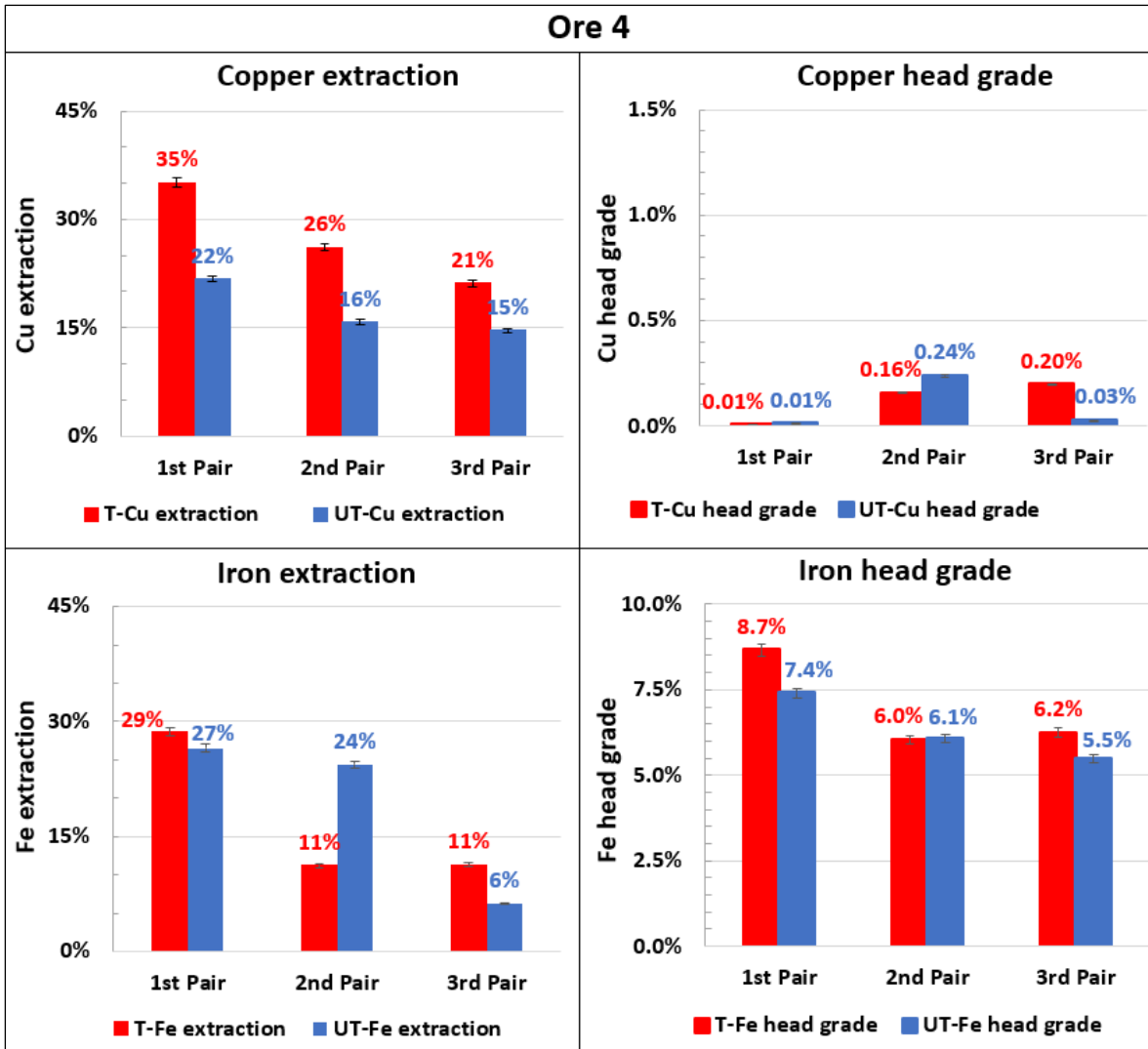
Figure 7.38. Copper/ iron leach extractions and head grades – Ore 4
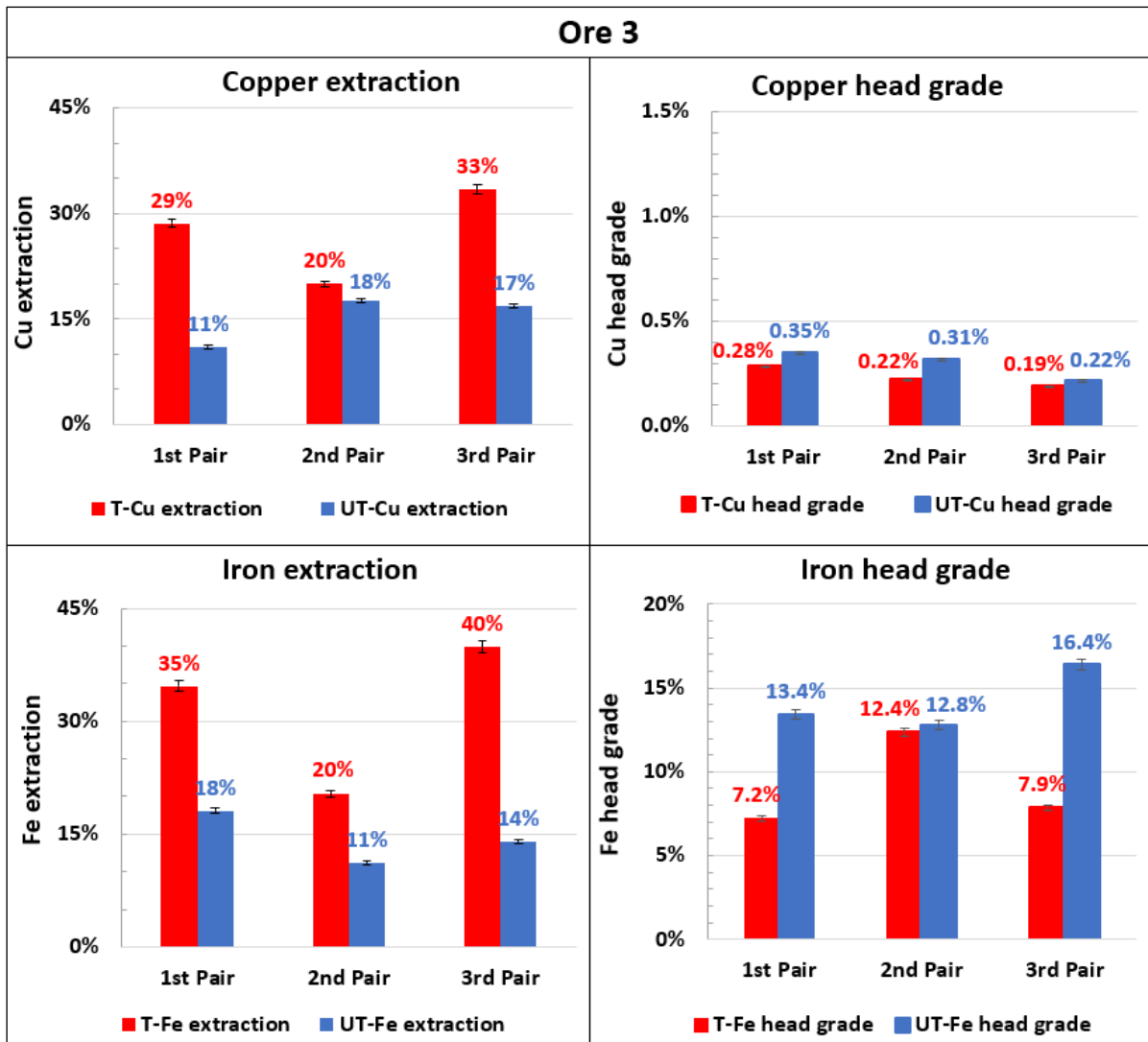
Figure 7.39. Copper/ iron leach extractions and head grades – Ore 3

According to Figures 7.40 and 7.41, although Ore 2 has almost a similar metal head grade to Ore 1 (copper + iron of about 4-5%), the extent of leaching improvement due to microwave treatment in Ore 2 is lower than that in Ore 1. This could be due to the lower content of stiffer microwave heaters in Ore 2 of 0.6% (against 2.8% in Ore 1) and the higher association of these heaters with free space (20% in Ore 2 versus 10% in Ore 1).
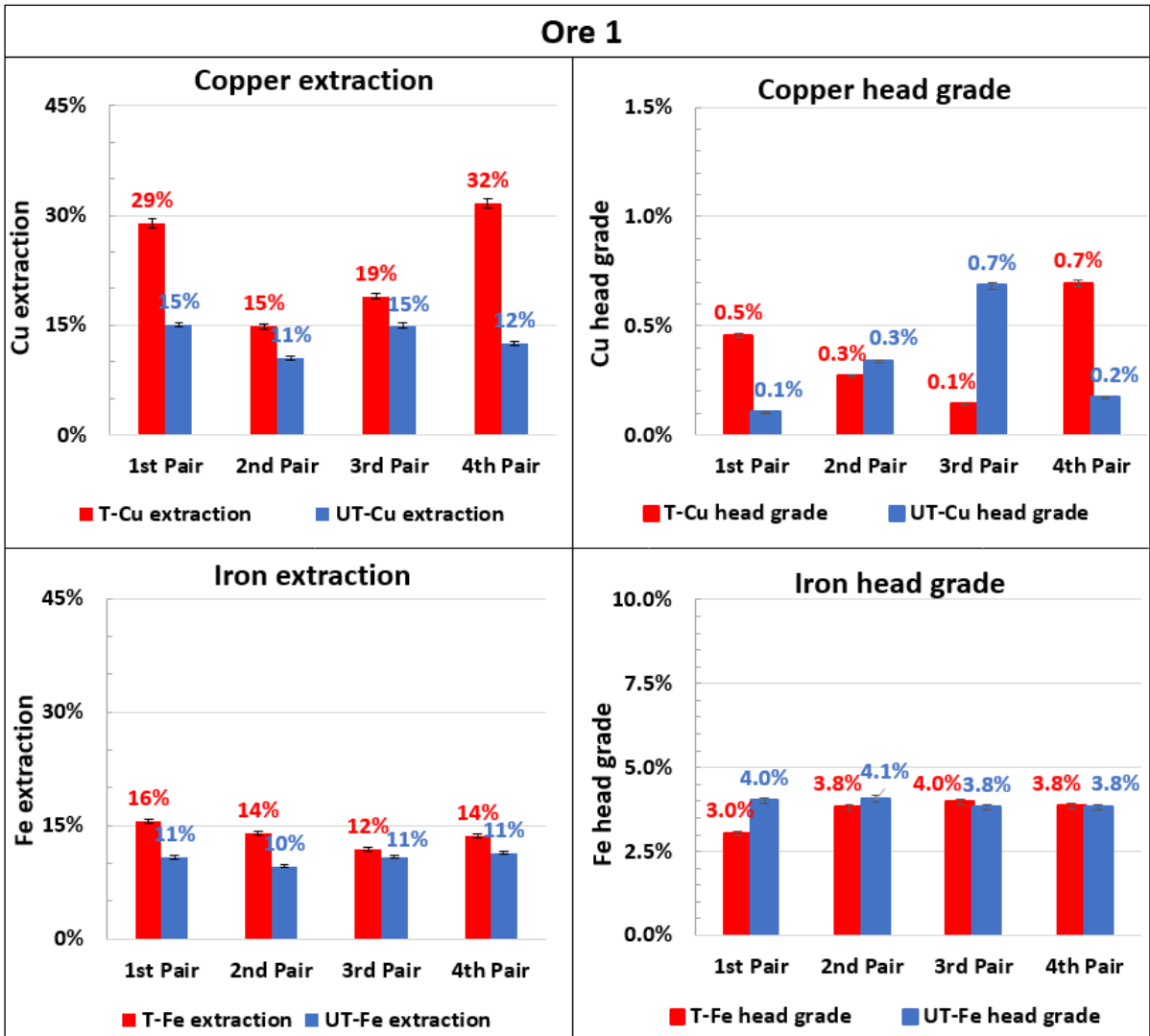
Figure 7.40. Copper/ iron leach extractions and head grades – Ore 1
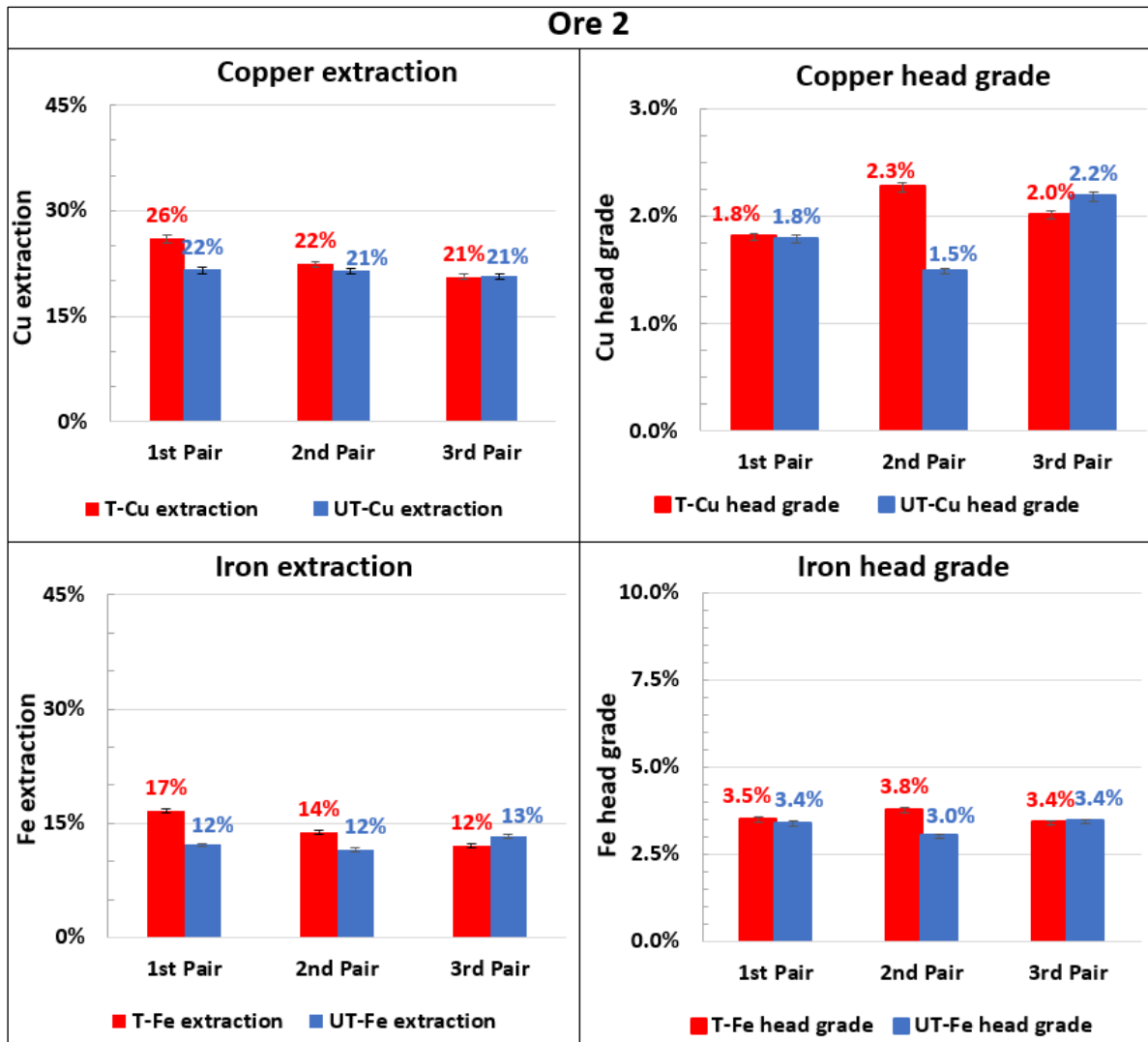
Figure 7.41. Copper/ iron leach extractions and head grades – Ore 2

It should be noted that the second pair of Ore 4 cores showed anomalous leaching results, indicating that the iron extraction of the untreated core is significantly higher than that of the treated core, and vice versa for copper extraction results. A close examination of CT images of this pair showed that although microwaves induced some fractures on the treated specimen, the untreated specimen had some interesting features that promoted iron extraction. As indicated in Figure 7.42, the untreated specimen had a large sulphide grain (probably pyrite) of ~3.65 mm wide with a volume of about 1.0 mm^3 located at the edge of the core, and next to this grain, there was a large opening of about 2.36 mm wide by 2.0 mm deep. During leaching, the acid was able to penetrate through this opening and completely leach out this large grain, as

indicated by the disappearance of this grain in the post-leached scan. This effect has probably led to higher iron extraction of the untreated core, which may have outweighed the effect of microwave-induced fractures on iron extraction of the treated core.
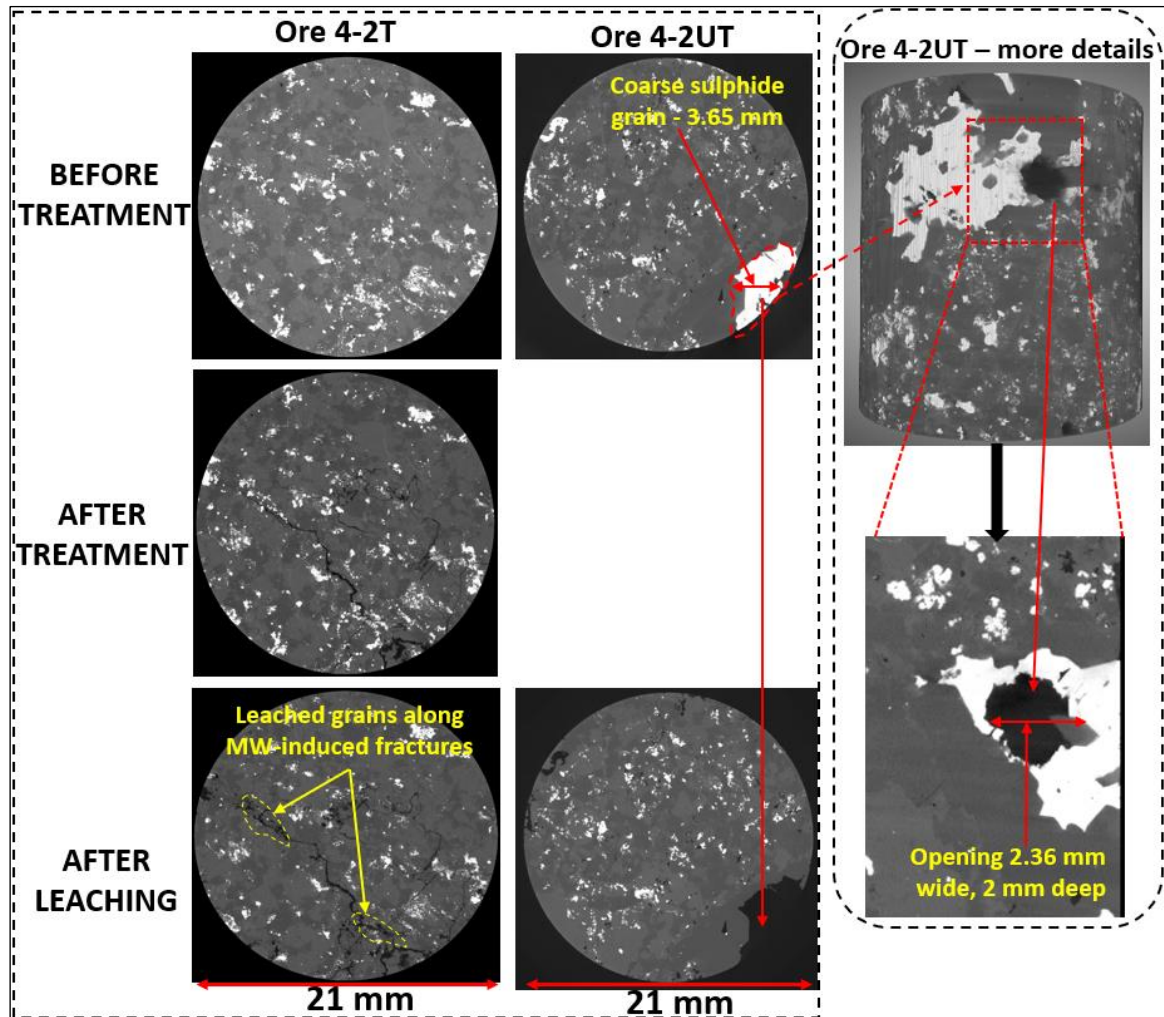
Figure 7.42. A close examination of the second pair of Ore 4 specimens

The average metal extractions and head grades of all cores in each ore type are presented in Figure 7.43. The error bars indicate the maximum and minimum values of metal leach extractions attained by each ore type. These results show that Ores 3 and 4 have higher iron grades than Ores 1 and 2. On the other hand, Ore 2 has a relatively higher copper grade than the other ores. In terms of microwave-induced fractures, the higher iron sulphide content in the ore, particularly pyrite, promotes significant fractures due to its higher modulus of elasticity.

This effect increases the exposure of pyrite and other sulphide minerals associated with it (e.g., chalcopyrite) to the leach solution. Thus, ore samples with higher pyrite content are expected to achieve higher metal leaching enhancement due to microwave treatment.

Also, these results show that Ores 1, 3, and 4 achieved higher copper leach extraction enhancements of 10-12% absolute, as opposed to the low enhancement of about 2% achieved by Ore 2. In the case of iron extraction, Ore 3 achieved the highest leaching enhancement of about 18%. The negligible iron enhancement in Ore 4 is mainly attributed to the anomaly leaching results in the second pair described in Figure 7.42, whereas the lower iron enhancement in Ore 1 could be linked to the lower iron head grade in this ore.
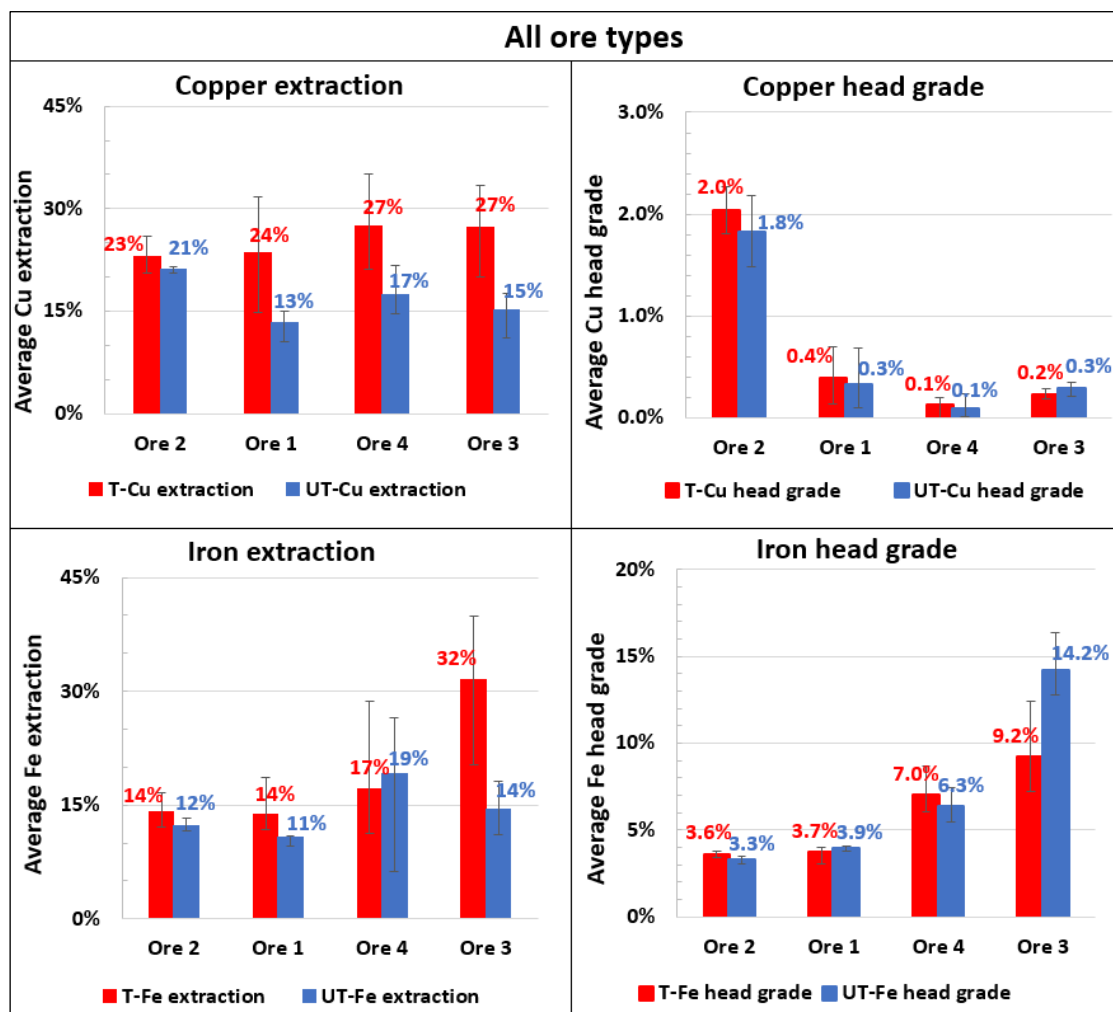
Figure 7.43. Average copper/iron leach extractions and head grades

Leaching results have shown that microwave ore pre-treatment can improve leaching performance to varying degrees, depending on mineralogy and texture properties. It is obvious that mineral dissolution (i.e., chemical erosion) increases the volume of induced fractures to some extent. Figure 7.44 presents the X-ray CT results that show the extent of crack volume increase due to leaching for treated and untreated cores, with the initial void/crack volume before treatment forming the baseline for changes. It is apparent that treated specimens achieved a higher crack volume increase due to mineral dissolution than untreated specimens, and the effect is more pronounced for Ores 3, 4, and 1, supporting the observed leaching results.
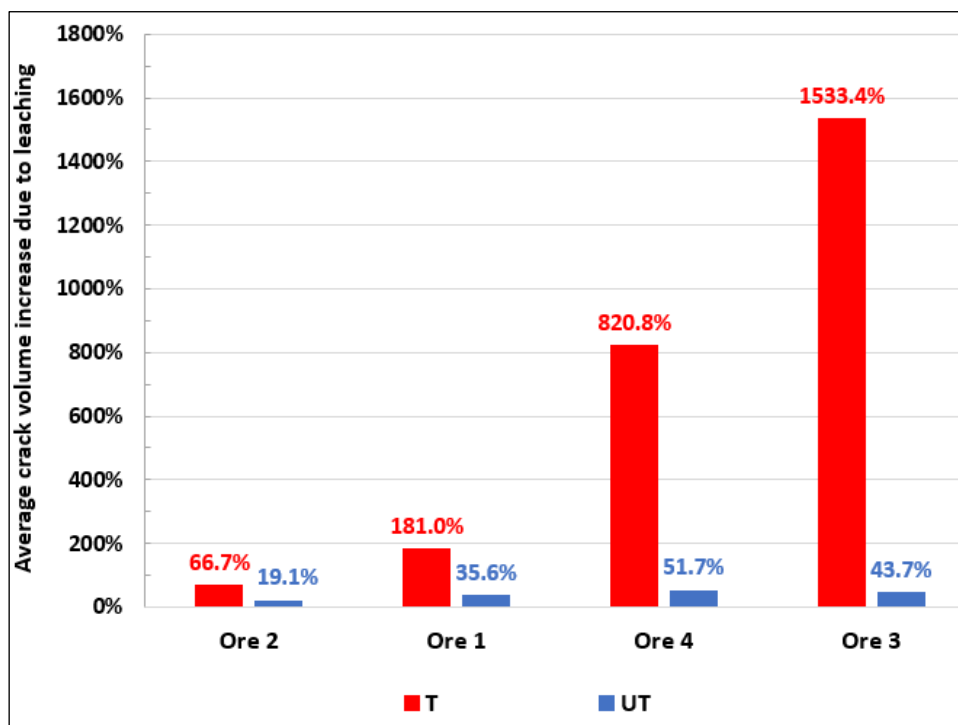
Figure 7.44. Fracture volume increase due to leaching

Although the crack volume increase due to leaching is linked to the dissolution of sulphide minerals, it can also be associated with the dissolution of acid-consuming gangue minerals (e.g., carbonates). This effect can be seen on post-leached CT images of Ore 3-3T core, where the crack volume increase is attributed to the dissolution of both sulphide grains and some acid-consuming gangue minerals (see Figure 7.45). According to the MLA results in Chapter 5,

Ore 3 contains a certain proportion of acid-consuming gangue minerals (e.g., carbonates - 3.3%). In the case of other samples (e.g., Ore 2), the crack volume increase due to leaching is mostly attributed to the dissolution of sulphide grains because a large proportion of the gangue matrix is quartz (~90%), which is essentially inert in the acid solution.
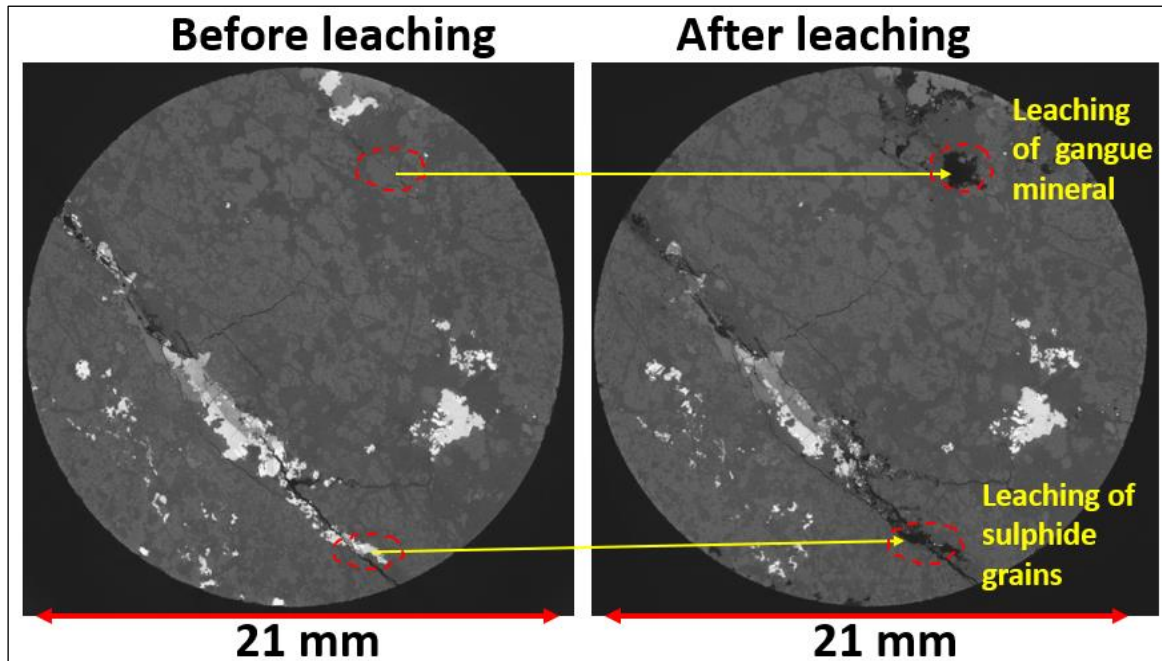
Figure 7.45. Cracks/voids growth due to leaching – Ore 3-3T

It is evident in Figures 7.44 and 7.45 that the aperture size or volume of microwave-induced fractures increases during leaching. It is also important to note that the dissolution of minerals is highest at the fracture entrance and decreases progressively towards the centre of the particle. This means that, given a longer leach duration, the effect of crack network growth due to leaching can further facilitate acid penetration into the interior of the treated particles, resulting in more effective mineral dissolution and improved metal extraction.

7.7 Conclusions

The objective of this chapter was to investigate the influence of ore mineralogy and texture on the extent of microwave-induced fractures and mineral dissolution improvement using four porphyry copper sulphide ores with varying mineralogy and texture. The extent of microwave-induced damage was quantified using two different techniques: ultrasonic pulse velocity (UPV) and X-ray computed tomography (XRCT). The extent of leaching improvement resulting from microwave-induced fractures was linked to the volume decrease of sulphide grains by X-ray CT imaging.

Results showed that the degree of microwave-induced damage varies greatly between ore samples. Ores with favourable mineralogy and texture properties for microwave-induced fractures (e.g., Ores 1, 3, and 4) achieved higher UPV reductions of about 28-31%, cracks volume increase of over 500%, and larger fractures with thicknesses of up to 1.0-2.5 mm as a result of microwave treatment. These ores possess some of these properties: 1. Contain a higher modal abundance of good microwave heaters (6-14%), which occur as coarse discrete grains or microveins (max ~D_{50}>190 µm), 2. Consist of stiffer microwave heaters (e.g., pyrite), 3. Have a consistent texture of microwave-absorbing phases, and 4. Contain a hard (brittle) microwave-transparent gangue matrix surrounding the microwave-absorbing grains.

Close examination of the X-ray CT images revealed that microwave-induced fractures in sulphide ores occur near mineralised regions (e.g., grain boundaries or microveins), supporting previous simulation and experimental findings that these fractures occur due to differential thermal stresses caused by selective heating of sulphide grains within a microwave-transparent gangue matrix. This mode of fracture maximizes mineral exposure for lixiviant interaction, promoting metal extraction. The post-leached CT scans indicated that large (wide) fractures allow deeper acid penetration, facilitating the dissolution of more sulphide grains. The ICP-AES analysis showed that ores with significantly large, induced fractures of up to 1.0-2.5 mm

thick, such as Ore 3, 4, and 1 achieved higher copper extraction enhancements of about 10-12% (absolute). These ore types had favourable mineralogy and texture properties for microwave-induced fractures, indicating that ore mineralogy and texture play an important role in dictating the extent of microwave-induced fractures and subsequent mineral dissolution improvement. This means that ore characterisation and evaluation in terms of mineralogy and texture are critical for selecting suitable ore candidates for microwave-assisted leaching.

8. MICROWAVE TREATMENT AND LEACHING OF COARSE FRAGMENTS

8.1 Introduction

As mentioned in the literature review (Chapter 3), microwave-induced fractures propagate more effectively when the microwave-absorbing phases are surrounded by a microwave-transparent gangue matrix. This suggests that the potential benefits of microwave ore pre-treatment are more likely to be realised in coarser size classes (e.g., >20 mm). This is because the microwave-absorbing phases in coarse particles are most likely surrounded by a large volume of microwave-transparent gangue matrix, which acts as crack propagation sites when thermal stresses are induced. The potential additional microwave-induced fractures in such coarse fragments may then be exploited to promote the dissolution of metals without further size reduction. This could be beneficial in heap leaching operations where leaching is performed on coarsely crushed materials. Furthermore, if the coarsely treated fragments are crushed, the internal mineral may be exposed due to preferential breakage along induced fracture paths, potentially promoting metal leach extraction.

Therefore, this chapter evaluates the influence of ore mineralogy and texture on the extent of microwave-induced fractures and leaching performance (ultimate extraction and dissolution kinetics) using coarse fragments (30-50 mm) of five copper sulphide ores described in Chapter 5. Thereafter, several possible conceptual flowsheets are proposed that incorporate microwave ore pre-treatment in a typical heap leaching flowsheet to reduce energy requirements and/or improve leaching performance. Finally, scale-up developments and conceptual designs for deploying microwave treatment technology in the mining industry (e.g., heap leaching) are discussed.

8.2 Experimental Methods

8.2.1   Sample Preparation - Sawing of Ore Fragments

Fifteen to twenty large fragments (75-110 mm) from each ore type were selected for this work. Each fragment was sawn (to 30-50 mm) to fit inside the glass quartz tube of 76 mm diameter that was used to hold the sample in the TE_{10} single mode cavity during microwave treatment. Also, fragments were sawn to make flat surfaces for UPV testing before and after microwave treatment to quantify the extent of induced damage.

The ore fragments were sawn using a wet sawing machine (Covington) shown in Figure 8.1B. The sawing procedure involves clamping the ore fragment tightly between the vise jaws to ensure that it stays in place during the sawing process. After loading the vise, the ore fragment is aligned in position for the first cut by adjusting the cross feed, making sure that the blade does not quite touch the ore fragment. The hood is closed and the motor is started to initiate the sawing process. During operation, the vise carriage advances towards the rotating blade, allowing the ore fragment to be cut in the desired position. After the first cut, the trimmed fragment is set for the second cut by adjusting the cross feed (without unclamping the fragment) to obtain a sawn piece with flat and parallel surfaces. The sawn fragments were then marked at different locations to allow UPV testing at those locations to quantify the extent of microwave-induced damage.
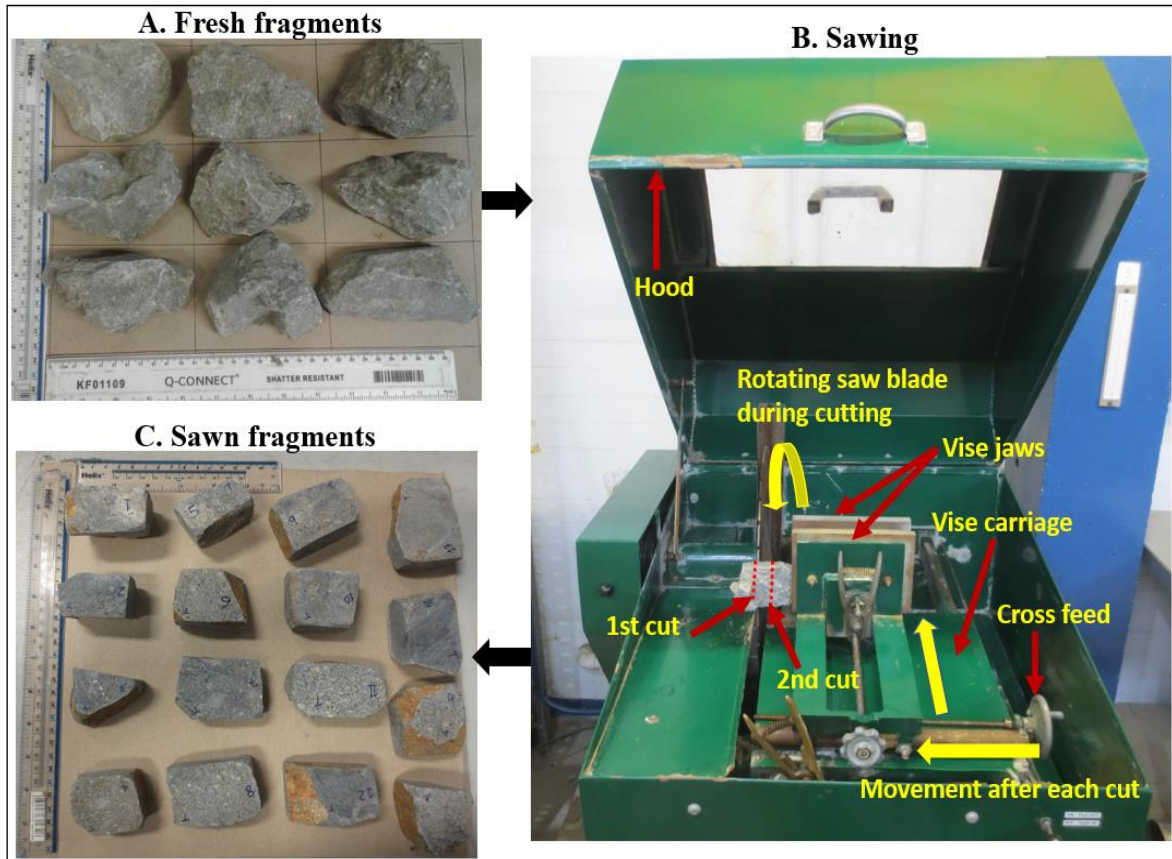
Figure 8.1. Sawing procedure

8.2.2 Thermal Imaging

As stated in Section 7.2.3, higher leach recoveries are typically achieved by ore fragments with higher metal grades due to their higher metal content. Therefore, it was necessary to select ore fragments with relatively the same metal content for the leaching work in order to make a fair comparison of the leaching results of treated versus untreated fragments, and this was achieved using a similar procedure described in Section 7.2.3. The fragments were warmed up in a multimode microwave applicator at a power of 250 Watts for 10 seconds, and the temperature attained by each fragment was observed using a thermal imaging camera (NEC Avio H2640), which helped to ascertain the content of microwave heaters in each fragment (predominantly sulphide minerals). Thereafter, fragments were paired based on their heating response to minimize the influence of ore grade variability on leaching extraction results. The pairing

procedure is illustrated in Figure 8.2 using Ore 1 fragments (i.e., 1 and 6; 4 and 10; 7 and 9; 11 and 15; 5 and 8). Based on this procedure, five to six pairs of fragments were obtained from each ore type, and one fragment in each pair was microwave treated before leaching while the other was leached without treatment to quantify the influence of microwave treatment on leach performance.

The sample pairing procedure can be evaluated by comparing the metal content of the treated and untreated fragments, which are determined based on the metal dissolved from the fragments during leaching plus the metal dissolved after pulverising the leached fragments, as shown in Appendix 11.3.2. The average copper and iron metal head grades of five/six treated (T) and untreated (UT) fragments are shown in Figure 8.3. The error bar indicates the maximum and minimum head grades. Despite differences in iron and copper content between treated and untreated fragments, it is clear that the average metal head grade (iron + copper) was comparable, with the exception of Ore 3, where untreated fragments appear to have a higher grade than treated fragments. These results suggest that the pairing procedure has reduced the ore grade variation between treated and untreated fragments, and thus the improved leaching performance observed on the treated samples can be linked to microwave-induced fractures. One potential limitation of this pairing technique is that the position of sulphide grains to the edge of the particle is not taken into account, but this can influence leaching results to some extent.
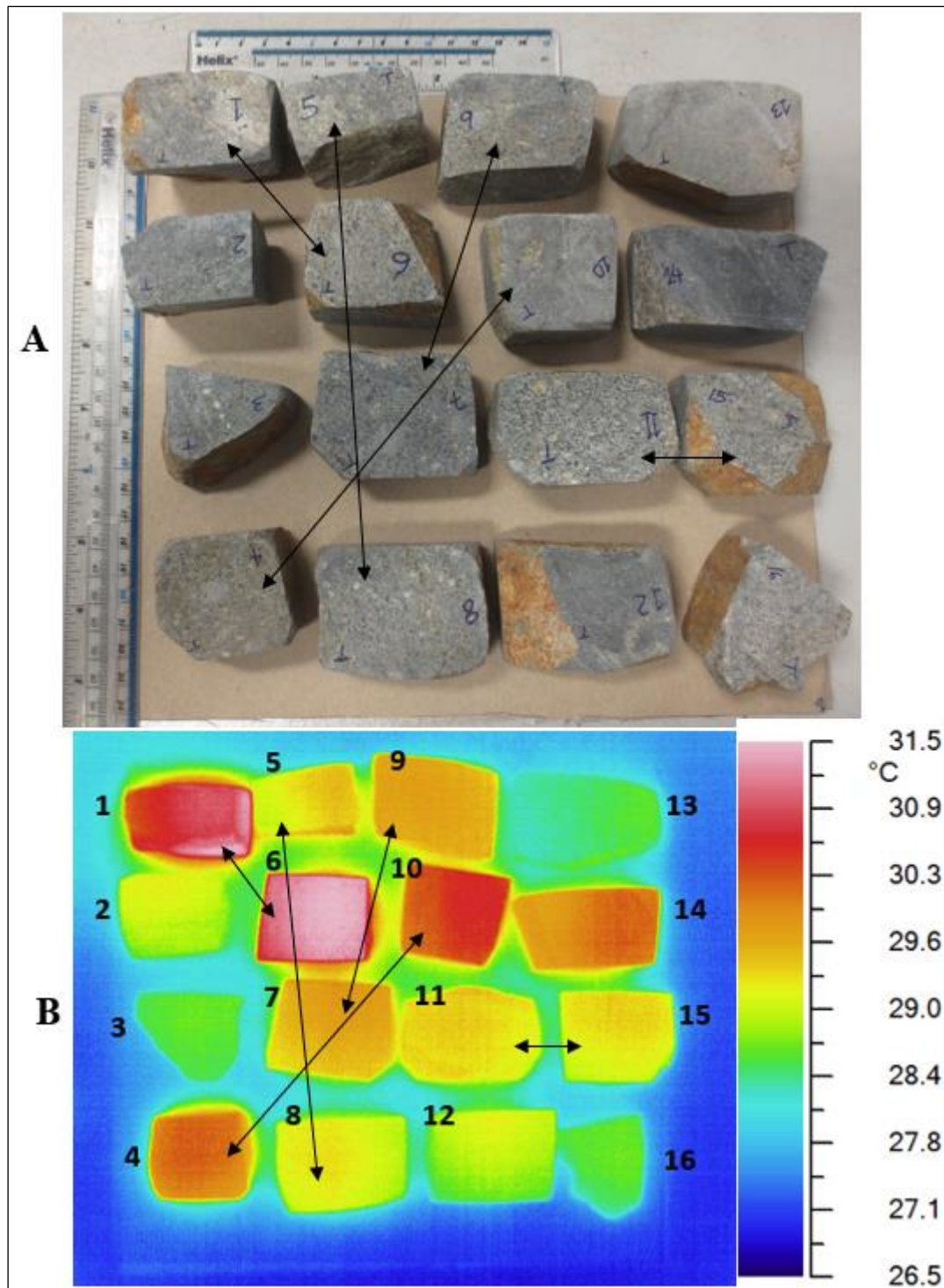
Figure 8.2. The pairing of Ore 1 fragments, A-photographic image, B-thermal image after microwave exposure
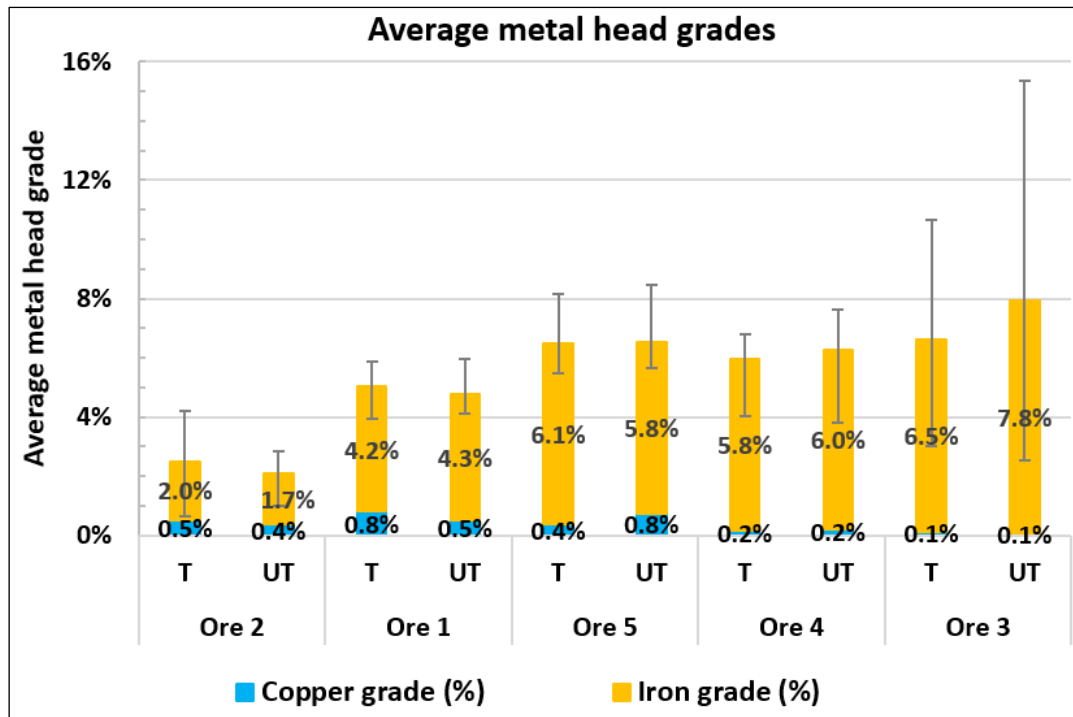
Figure 8.3. A comparison of average metal head grades (T-treated versus UT-untreated)

8.2.3 Microwave Treatment Methodology

Microwave treatments were performed using the experimental setup and the procedure described in Chapter 7 (Section 7.3). However, a higher forward power of about 3 kW was used in this case to induce macro-fractures that could be detected by visual observation or sonic velocity testing (i.e., >4% average UPV reduction). The treatment duration was approximately 4-5, 6-7, and 9-10 seconds in the first, second, and third treatment attempts, respectively, and no further treatment attempts were made if fractures were detected. The sample mass for each fragment was about 77-207 grams, with Ore 5 fragments having low sample masses due to their small original size before being sawn. A summary of microwave treatment conditions used for this investigation is presented in Table 8.1. The specific absorbed energy was calculated using Equation 6.1, which is based on microwave power absorbed by the sample (forward power minus reflected power), sample mass, and treatment duration.

It is apparent that the microwave energy input required to achieve significant damage varied greatly between samples, with Ore 5 fragments requiring more than twice the energy required by other ore types. It is worth noting that no attempt was made to minimise treatment energy, but the focus was to assess the role of mineralogy and texture on ore fracturing and leaching improvement. Previous research shows that fractures can be induced at microwave energy inputs of less than 1 kWh/t for ores with suitable mineralogy and texture properties for microwave treatment.

Table 8.1. A summary of microwave treatment conditions – Large fragments

Trial #	Sample ID	Mass of fragment (g)	Forward power (kW)	Reflected power (kW)	Absorbed power (kW)	Exposure time (sec)	Treatment attempt to induce significant damage	Specific absorbed energy (kWh/t)	Average absorbed energy (kWh/t)
1	Ore 1 - 1T	162.81	3.09	1.14	1.95	4.6	First	15.18	
2	Ore 1 - 2T	125.33	3.42	2.09	1.33	4.5	First	13.24	
3	Ore 1 - 3T	154.59	3.40	2.44	0.96	7.5	Second	12.94	13.70
4	Ore 1 - 4T	160.71	3.24	1.73	1.51	5.7	Second	14.73	
5	Ore 1 - 5T	180.52	3.38	2.41	0.97	6.7	Second	10.05	
6	Ore 1- 6T	161.84	3.34	2.32	1.02	9.2	Third	16.04	
7	Ore 3 - 1T	140.00	3.04	1.06	1.98	6.9	Second	27.15	
8	Ore 3 - 2T	148.18	2.95	1.01	1.94	4.4	First	15.93	
9	Ore 3 - 3T	156.11	3.04	1.28	1.76	4.1	First	12.98	21.5
10	Ore 3 - 4T	120.53	3.28	0.99	2.29	6.2	Second	32.45	
11	Ore 3 - 5T	116.26	3.03	1.45	1.58	5.0	First	18.96	
12	Ore 4 - 1T	192.89	3.04	0.43	2.61	5.3	First	19.88	
13	Ore 4 - 2T	207.75	3.00	0.74	2.26	6.3	Second	19.15	
14	Ore 4 - 3T	168.90	3.40	1.66	1.75	5.6	First	16.21	21.6
15	Ore 4 - 4T	153.61	3.07	0.80	2.27	6.3	Second	25.79	
16	Ore 4 - 5T	136.94	3.05	0.92	2.13	4.5	First	19.51	
17	Ore 4 - 6T	166.92	3.05	0.63	2.42	7.2	Second	29.09	
18	Ore 2 - 1T	155.86	3.14	1.18	1.96	4.6	First	15.98	
19	Ore 2 - 2T	169.34	3.26	1.16	2.10	8.8	Third	30.46	
20	Ore 2 - 3T	151.03	3.38	1.42	1.96	8.2	Second	29.46	25.9
21	Ore 2 - 4T	169.94	3.31	1.29	2.02	8.1	Second	26.62	
22	Ore 2 - 5T	165.35	3.24	1.22	2.02	8.0	Second	26.93	
23	Ore 5 - 1T	102.83	3.16	0.43	2.73	5.2	First	38.10	
24	Ore 5 - 2T	101.26	2.90	0.53	2.37	9.2	Third	59.72	
25	Ore 5 - 3T	91.48	3.25	0.73	2.52	9.0	Third	69.03	49.9
26	Ore 5 - 4T	77.27	3.12	1.48	1.64	10.4	Third	61.11	
27	Ore 5 - 5T	101.82	3.08	1.74	1.34	9.7	Third	35.43	
28	Ore 5 - 6T	106.59	3.07	1.72	1.35	10.2	Third	35.90	

8.2.4 Leaching Methodology

Five to six pairs of ore fragments (treated versus untreated) were leached in the 400-mL beakers (one fragment per beaker) using 160 mls of aqua regia in each beaker to ensure fragments are fully submerged, and no spillage due to bubbling occurs as leaching progresses. These samples were then heated on a hot plate capable of holding 10 beakers of 400 mls at a time (Figure 8.4). The leach solution temperature was maintained at about 65-70°C for 12 hours. To attain this temperature, the hot plate was set at 85-90°C using a surface temperature thermometer. The higher acid concentration and leach temperature were selected in this study to facilitate the leaching kinetics in order to achieve a significant metal extraction from such large particles within a few hours, given the refractory nature of copper sulphide ores via the conventional leaching approach. These leach conditions enabled rapid evaluation of the microwave treatment effect on the leaching performance of copper sulphide ores, which would have taken several months if typical leach conditions were used (e.g., leaching using weak sulphuric acid at ambient temperature).

During leaching, four aliquot samples of 2 mls were taken periodically at 0.5, 1, 4, and 12 hours to establish the leaching kinetics of copper and iron. An equivalent volume of aqua regia was added to replace the aliquot samples taken to keep the leach solution volume constant. The metal contents of the leachate were analysed using the Inductively Coupled Plasma Atomic Emission Spectroscopy (ICP-AES) technique described in Chapter 4.
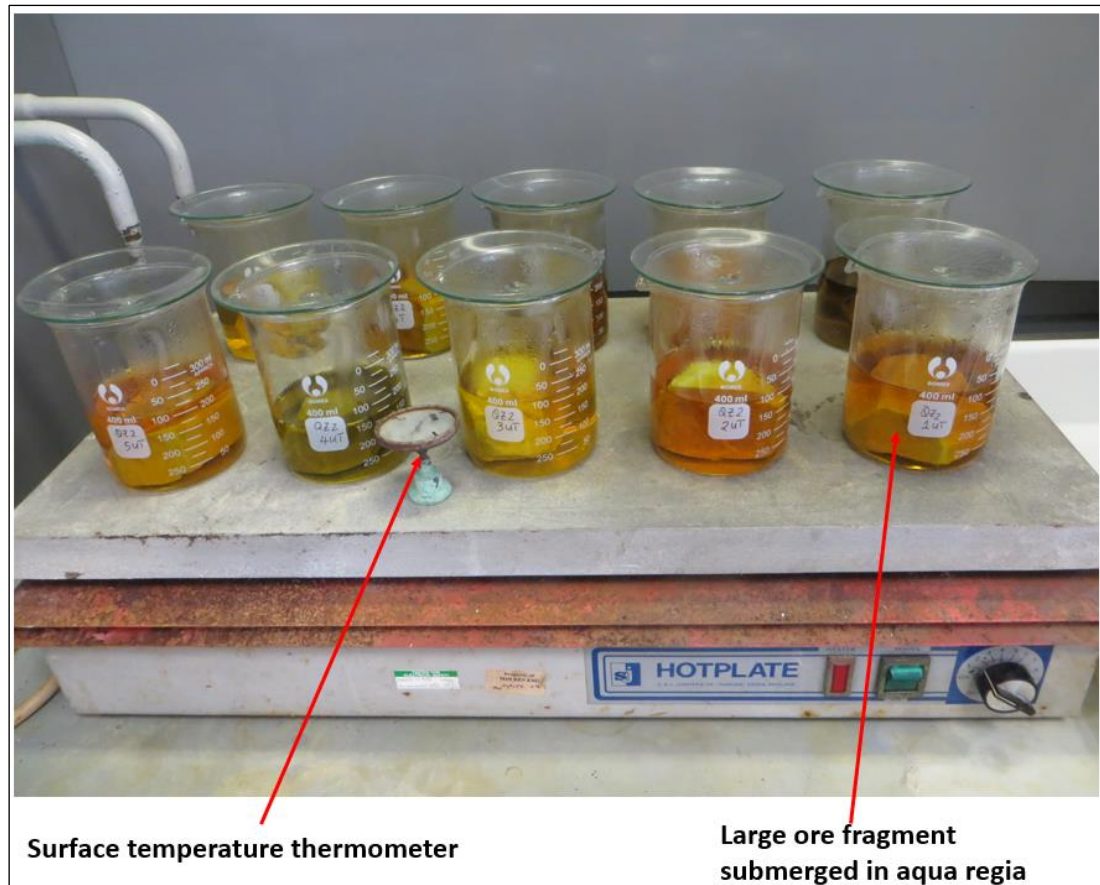
Figure 8.4. Leaching experimental set-up - large fragments

After leaching, the fragments were rinsed with tap water and dried in the oven before being subjected to the point load test, which helped to quantify the effect of microwave treatment on ore strength reduction by comparing the $Is_{(50)}$ strength index of the treated-leached fragments versus untreated-leached fragments. The broken fragments from the point load test were pulverised and acid digested to determine the metal content that remained in the fragment after leaching, allowing the ore head grades and metal leach extractions to be determined. The sample digestion was performed using the DigiPREP graphite block heater described in Section 7.4.1. The leaching performance was evaluated based on ultimate metal leach extraction and dissolution kinetics results.

273

8.3 Results and Discussion

8.3.1 Quantification of Microwave-induced Damage - UPV

Figures 8.5 to 8.9 show five fragments from each ore type before and after microwave treatment. The maximum, minimum, and average values of UPV reduction of each fragment are also shown to indicate the severity of microwave-induced damage based on the UPV testing performed at 5-10 different locations (marked spots) on sawn surfaces. Since the UPV testing was not performed on the entire fragment from multiple directions, the degree of induced damage in some fragments is probably underestimated to some extent, depending on fracture orientation relative to the pulse propagation path.

Based on visual observation and UPV results, these images show that the ores responded differently to microwave treatment, with Ores 4 and 1 exhibiting more significant induced damage than others. It can also be seen that, for a given ore type, some fragments (e.g., Ore 1-2T) were severely damaged compared to others (e.g., Ore 1-5T) as a result of microwave treatment. This variation in microwave treatment response between ore types or between fragments within an ore is largely attributed to ore mineralogy and texture properties, described later in more detail in the leaching results (Section 8.3.3). These properties include the abundance, grain size, and stiffness of microwave-absorbing phases, as well as the hardness of microwave-transparent gangue matrix.

	Ore 4-1T	Ore 4-2T	Ore 4-3T	Ore 4-4T	Ore 4-5T	
Max	87.8%	78.9%	89.9%	28.8%	74.4%	Overall
Min	4.8%	0.0%	3.6%	0.0%	0.3%	average
Average	50.7%	33.9%	47.9%	5.6%	55.4%	**39.0%**
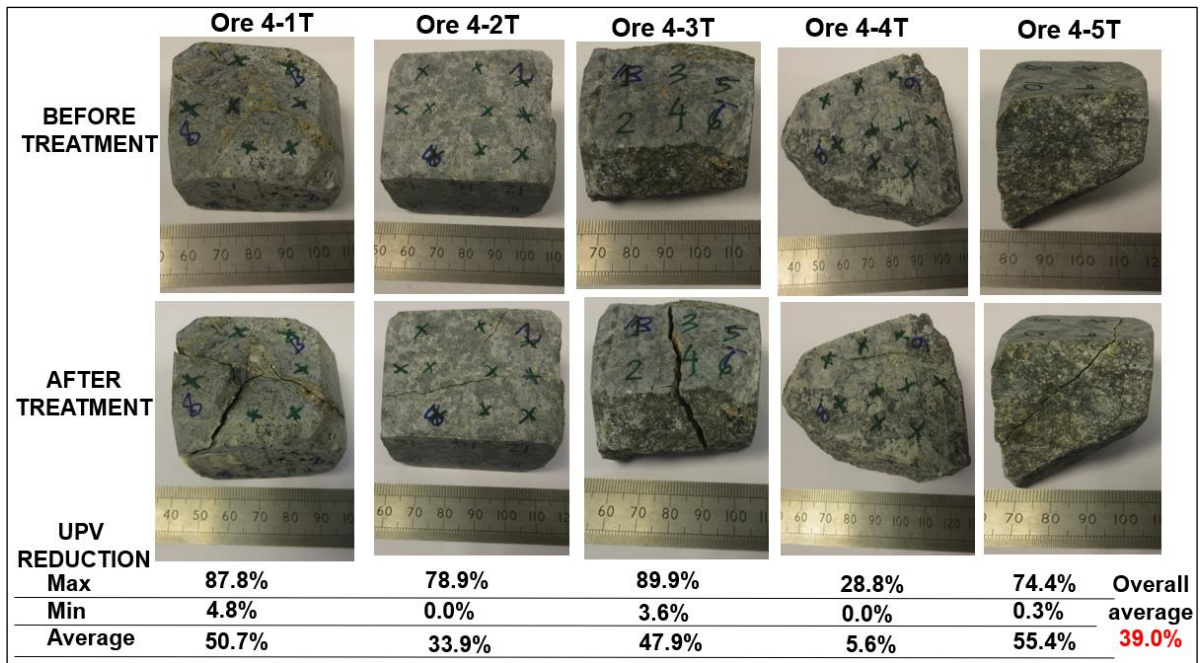
Figure 8.5. Pre- and post-treated fragments – Ore 4

	Ore 3-1T	Ore 3-2T	Ore 3-3T	Ore 3-4T	Ore 3-5T	
Max	10.8%	58.4%	25.2%	16.9%	49.8%	Overall
Min	3.5%	0.3%	0.0%	5.2%	7.7%	average
Average	6.9%	25.9%	7.9%	9.0%	29.7%	**16.5%**
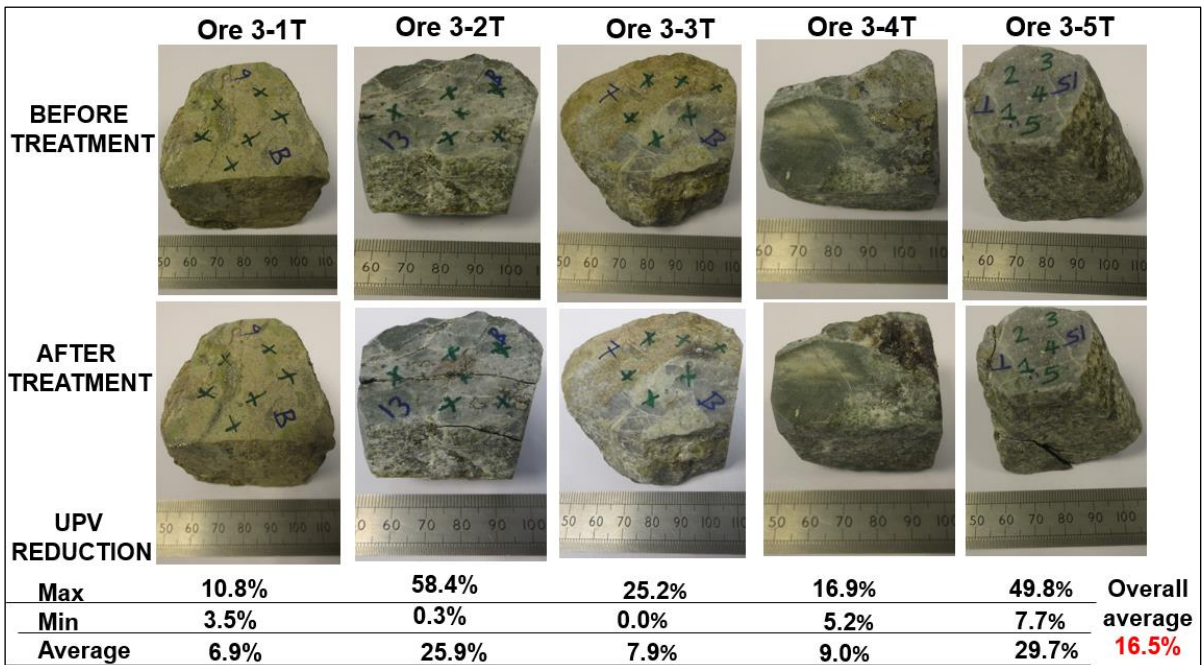
Figure 8.6. Pre- and post-treated fragments – Ore 3

275
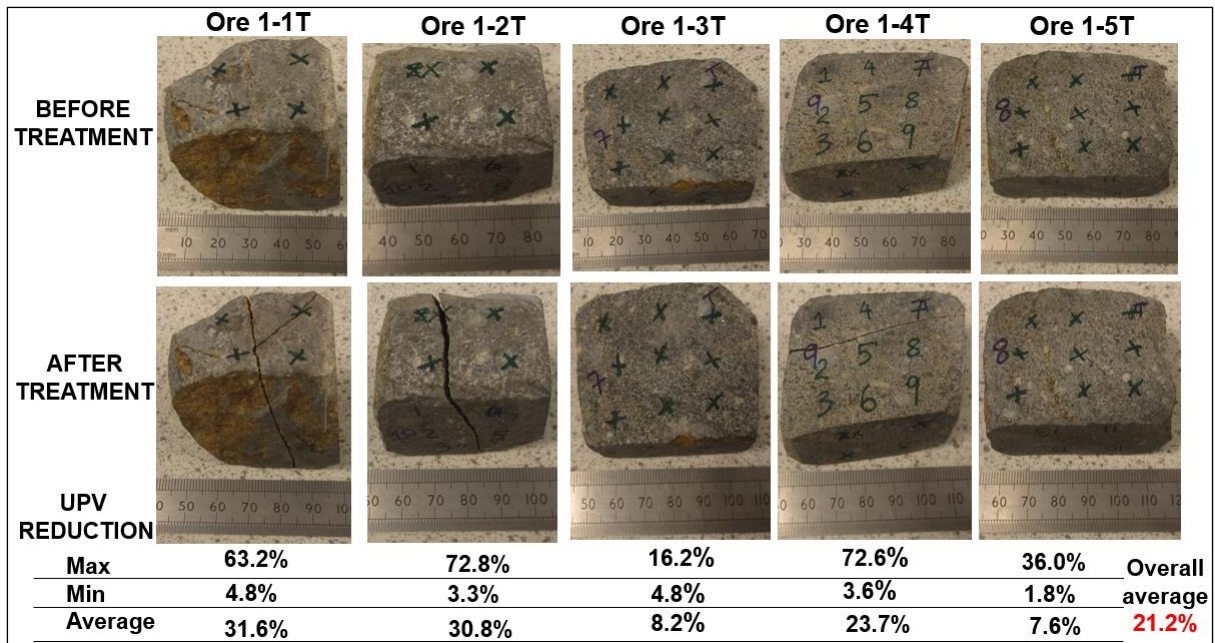
Figure 8.7. Pre- and post-treated fragments – Ore 1

	Ore 1-1T	Ore 1-2T	Ore 1-3T	Ore 1-4T	Ore 1-5T	
Max	63.2%	72.8%	16.2%	72.6%	36.0%	Overall
Min	4.8%	3.3%	4.8%	3.6%	1.8%	average
Average	31.6%	30.8%	8.2%	23.7%	7.6%	**21.2%**
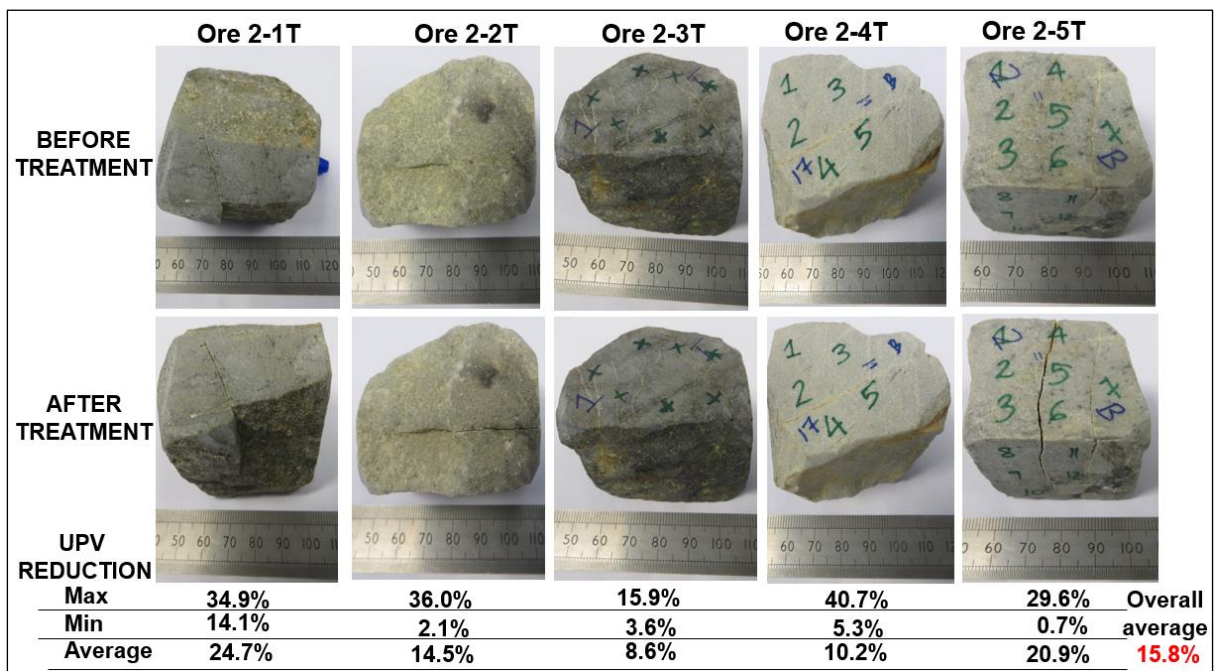
Figure 8.8. Pre- and post-treated fragments – Ore 2

	Ore 2-1T	Ore 2-2T	Ore 2-3T	Ore 2-4T	Ore 2-5T	
Max	34.9%	36.0%	15.9%	40.7%	29.6%	Overall
Min	14.1%	2.1%	3.6%	5.3%	0.7%	average
Average	24.7%	14.5%	8.6%	10.2%	20.9%	**15.8%**

276

UPV REDUCTION	Ore 5-1T	Ore 5-2T	Ore 5-3T	Ore 5-4T	Ore 5-5T	
Max	54.5%	10.1%	16.6%	7.8%	6.2%	Overall
Min	46.8%	4.5%	8.1%	3.5%	1.9%	average
Average	51.4%	6.4%	13.6%	5.3%	4.1%	15.9%
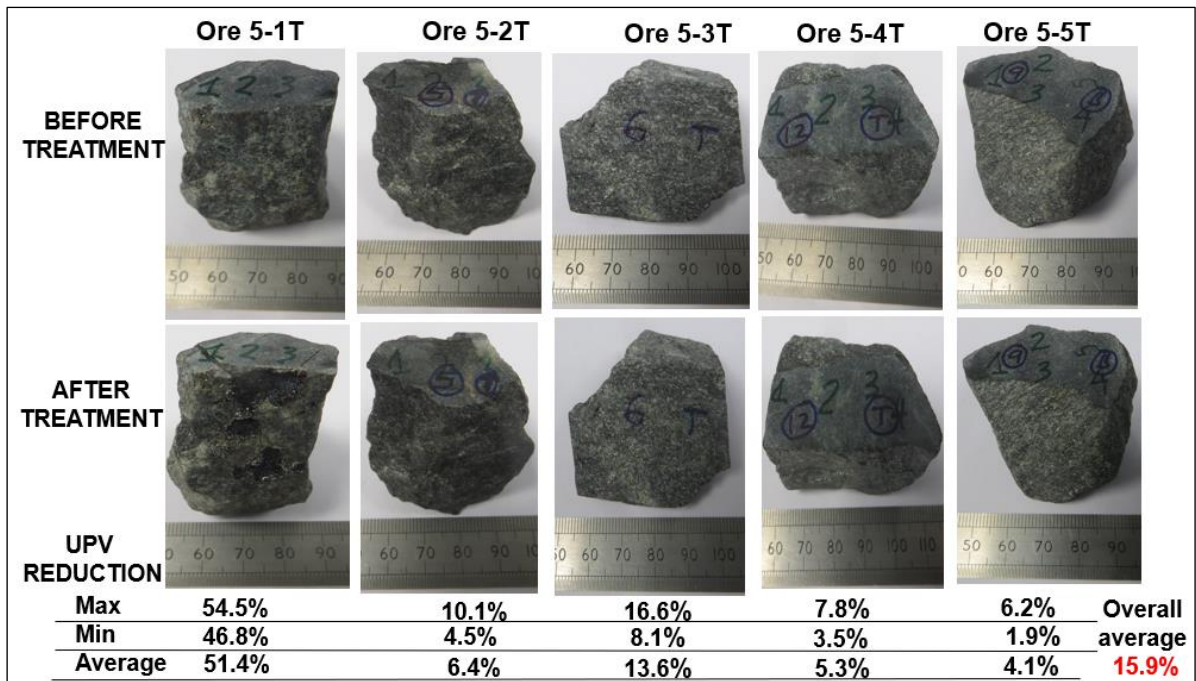
Figure 8.9. Pre- and post-treated fragments – Ore 5

Figure 8.10 shows the average UPV reduction of all fragments tested in each ore type and their corresponding microwave energy input. The error bars indicate the maximum and minimum UPV values. It can be seen that Ore 4 is the best performer in terms of microwave-induced damage, as indicated by the highest average UPV reduction of 39%, which was achieved at a microwave energy input of about 21 kWh/t. Ores 5 and 2, on the other hand, performed poorly, with both indicating lower UPV reductions of about 16% at higher microwave energy inputs of 50 and 26 kWh/t, respectively. Although Ore 5 had a maximum UPV value of 51%, the overall average was relatively low (nearly 16%), indicating that most fragments did not exhibit significant damage, with the exception of a few fragments (e.g., Ore 5-1T) that had suitable mineralogy and texture properties for microwave-induced fractures. This observation suggests that the proportion of amenable fragments for microwave treatment in a sample dictates the overall extent of ore pre-damage.

277
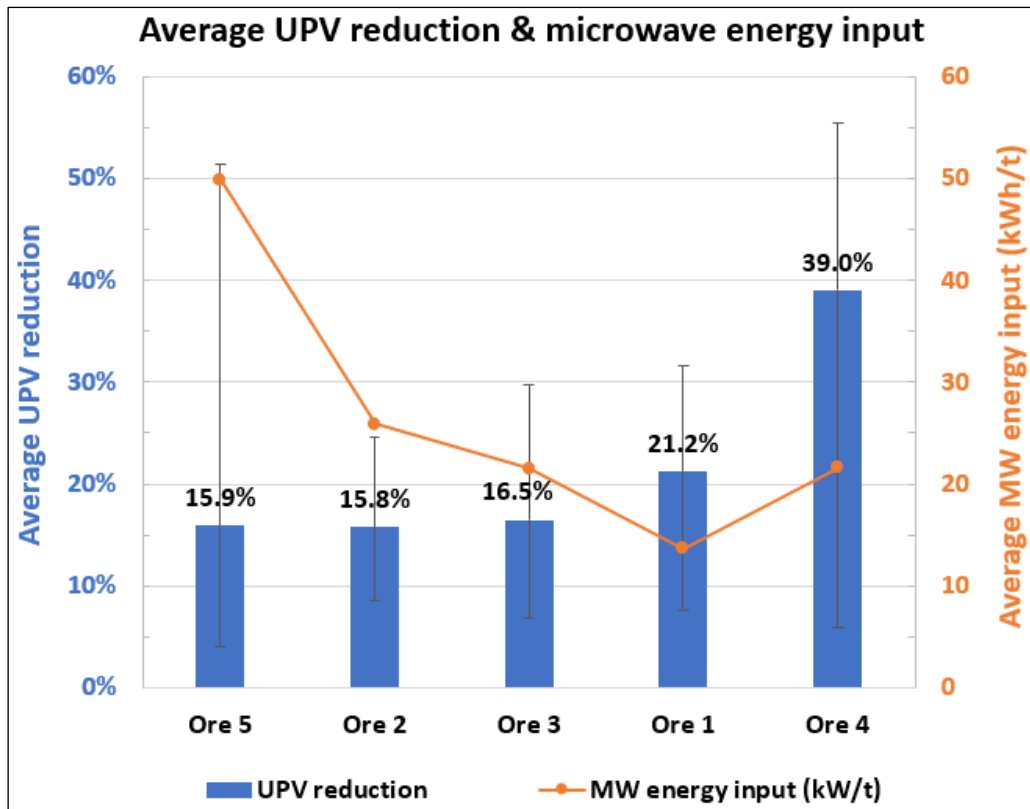
Figure 8.10. Average UPV reduction versus microwave energy input

8.3.2 Quantification of Microwave-induced Damage - PLT

In addition to UPV testing, the magnitude of microwave-induced damage was quantified using the PLT technique, which was performed after leaching due to the destructive nature of this method. The baseline (fresh) sample was subjected to the PLT without leaching. Although the number of fragments subjected to PLT was small (i.e., 5-6 in each subsample), it was sufficient to provide an indication of the effect of microwave treatment on the extent of ore pre-damage. Figures 8.11 - 8.15 compare the $Is_{(50)}$ strength indices of untreated-unleached (UT) (i.e., fresh) fragments to those of treated-leached (T&L) and untreated-leached (UT&L) fragments, arranged in ascending order. A summary of the PLT results is also shown in each figure to provide more information about the data set.

Generally, these results show that T&L fragments are significantly weaker (softer) than UT or UT&L for all ore types tested, achieving an average strength reduction of about 47-75% at >90% confidence level. The ore strength reduction of UT&L was not statistically significant for all ores tested. This suggests that the observed strength reduction in the treated fragments is mainly due to microwave-induced fractures. It is also possible that some of the induced fractures were exacerbated to some extent by the acid during leaching, making treated fragments much weaker. The widening of microwave-induced fractures as a result of mineral dissolution was observed in the X-ray CT results presented in Chapter 7.
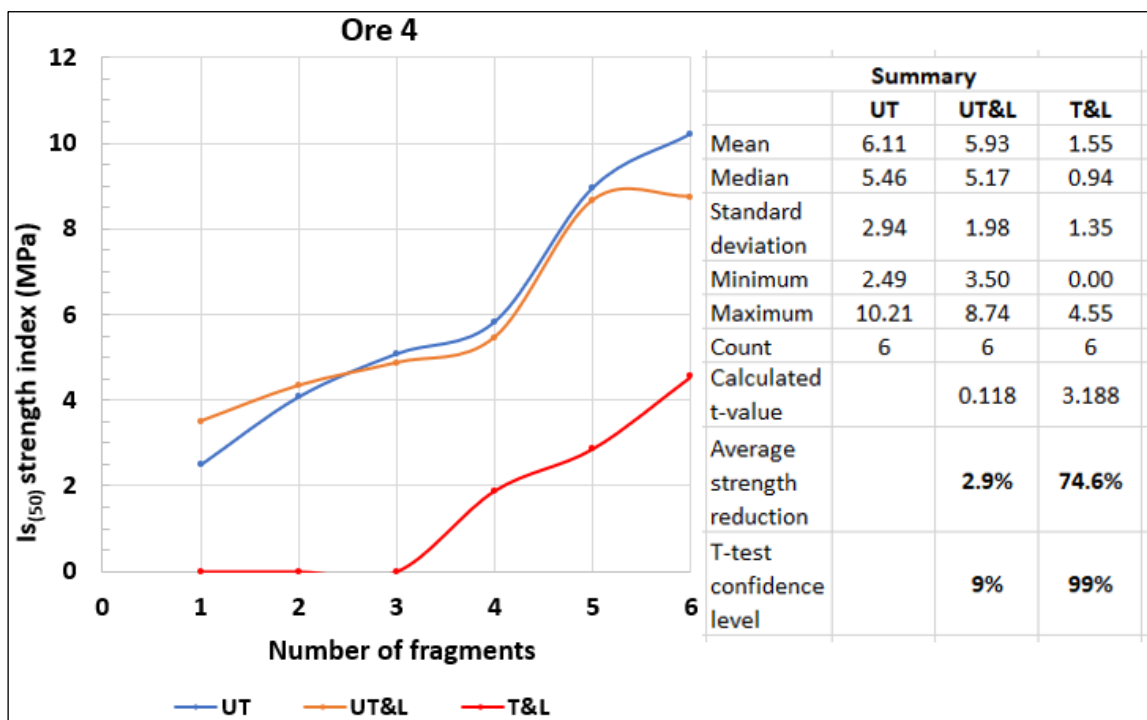
Figure 8.11. PLT results – Ore 4
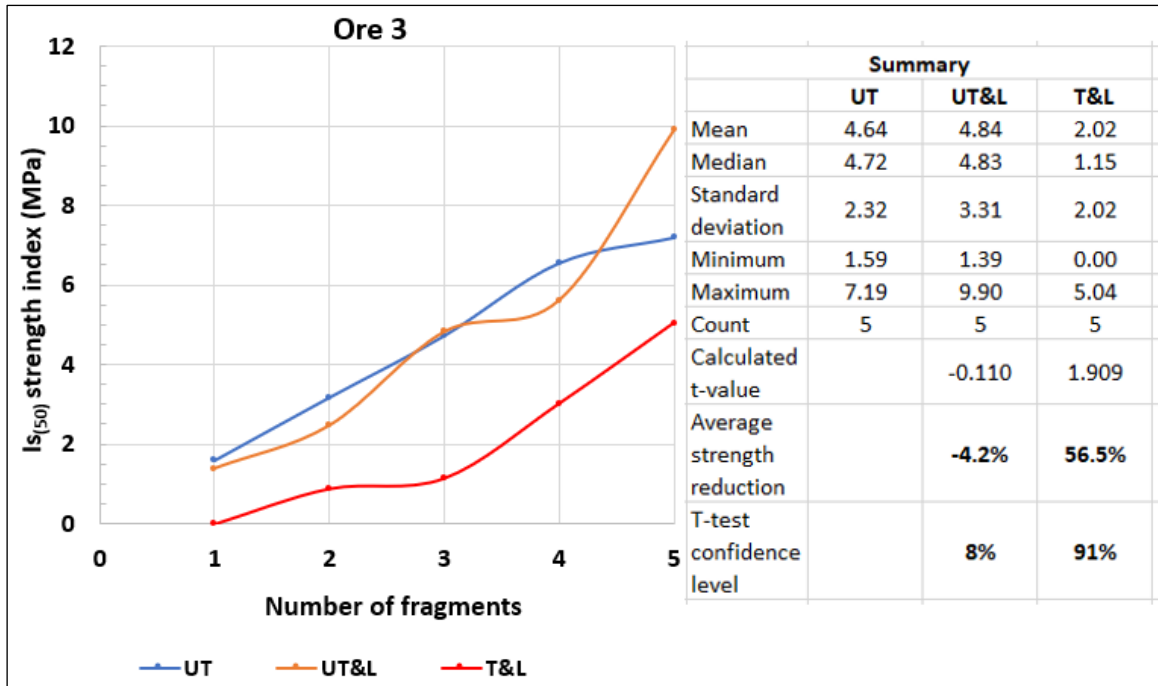
Figure 8.12. PLT results – Ore 3
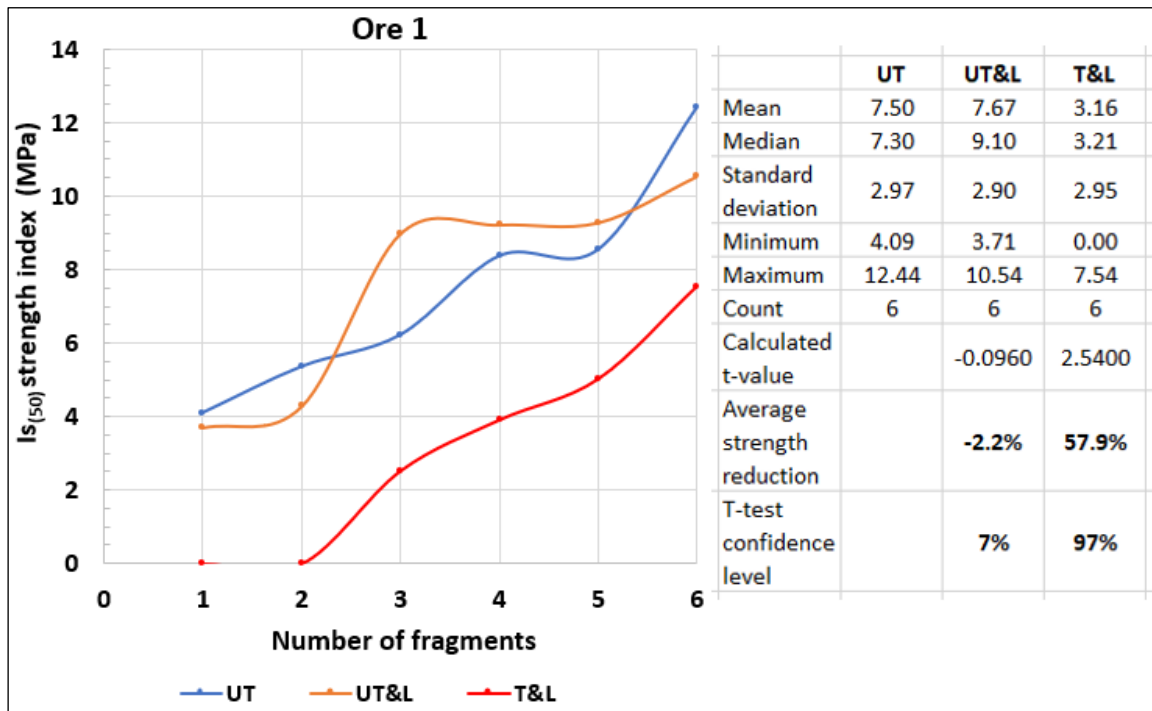
Figure 8.13. PLT results – Ore 1

280
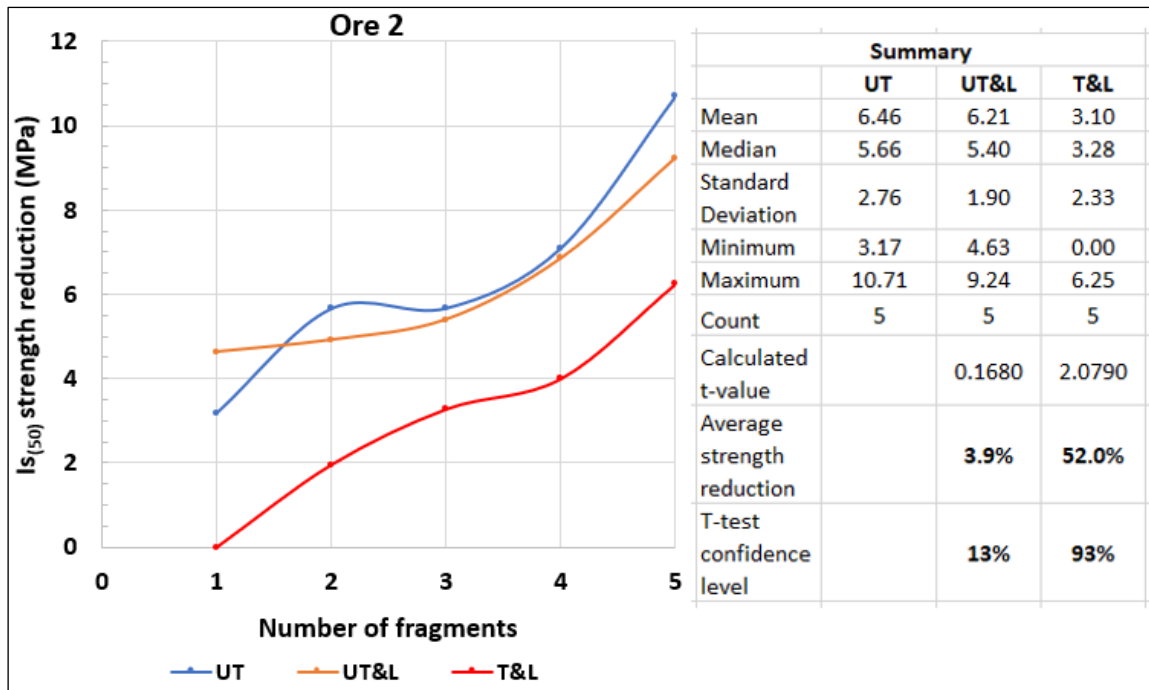
Figure 8.14. PLT results – Ore 2
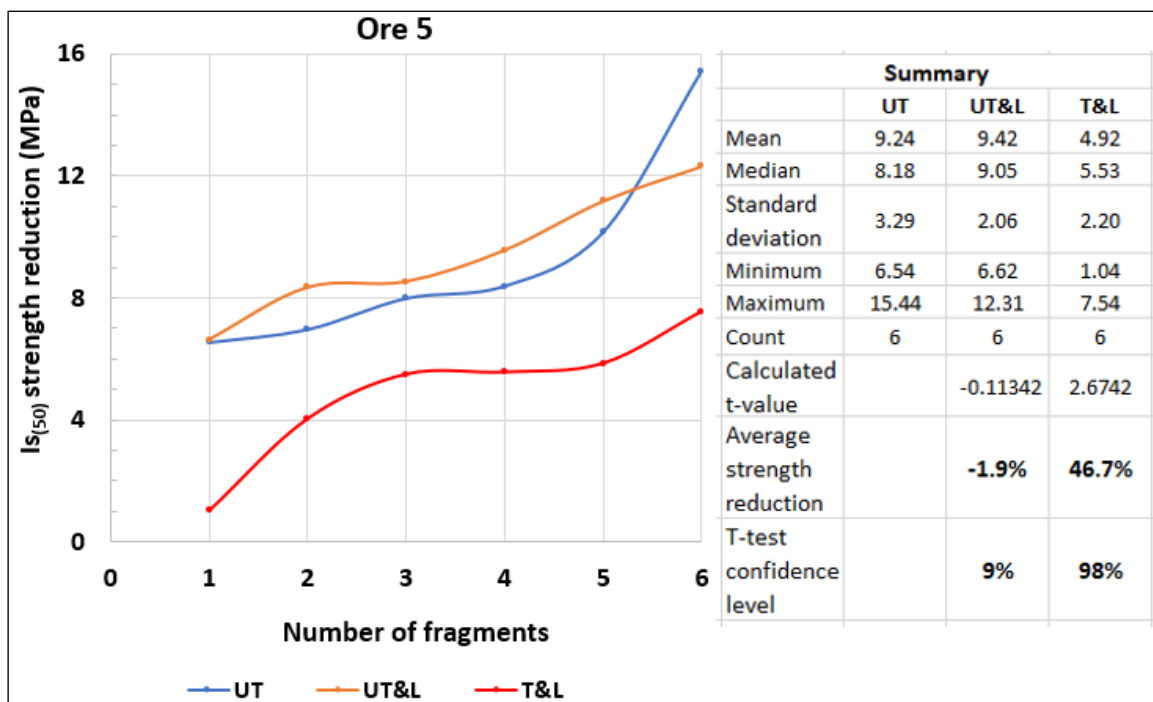
Figure 8.15. PLT results – Ore 5

281

Figure 8.16 compares the average strength Is$_{(50)}$ reductions of UT&L fragments to those of T&L fragments for all ore types tested, using the average strength index of fresh (UT) fragments as a baseline. It is evident that treated-leached (T&L) fragments achieved greater strength reductions than untreated-leached (UT&L) fragments, with Ore 4 achieving the greatest strength reduction of up to 75% and Ore 5 achieving the lowest strength reduction of approximately 47%. These results follow a similar pattern to the UPV results shown in the previous section, indicating that ores with favourable mineralogy and texture have demonstrated greater strength reduction due to microwave treatment than those with unfavourable properties, as detailed in the following section.
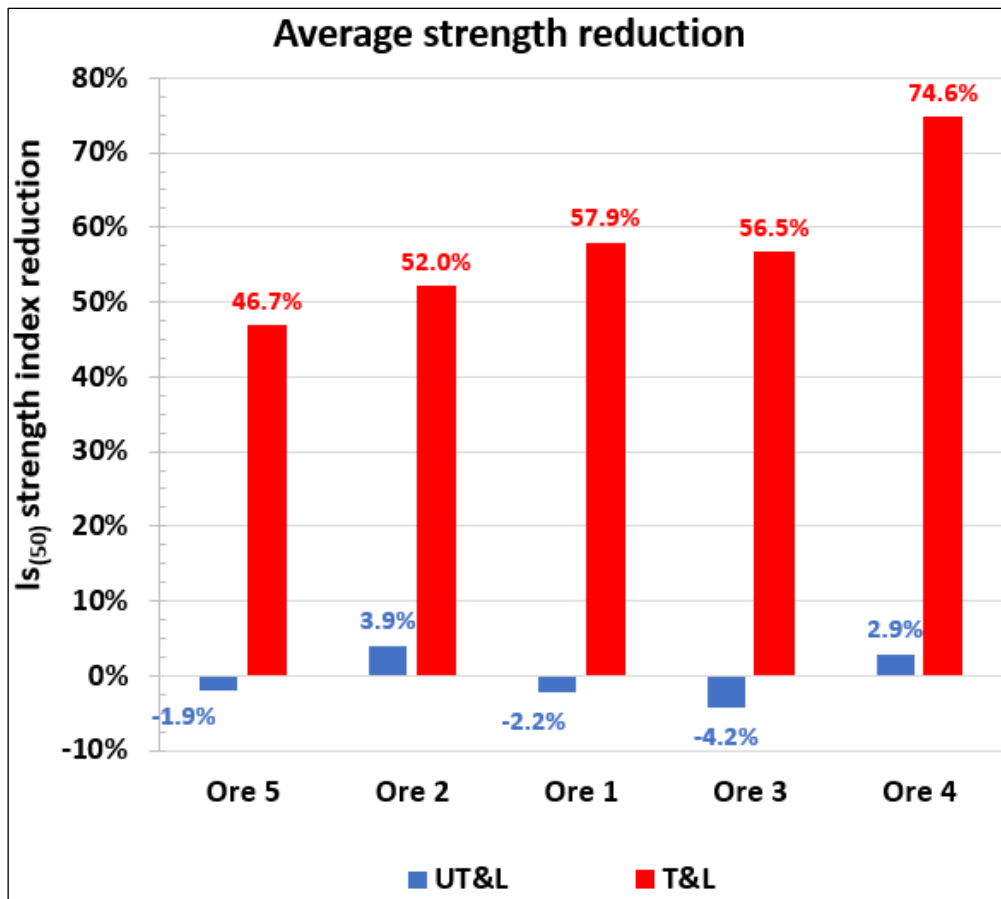
Figure 8.16. PLT results - large fragments

8.3.3 Overall Leach Extraction

Figures 8.17 to 8.26 show the copper and iron extractions after 12 hours of leaching for all pairs of fragments tested. Their corresponding copper and iron head grades are also indicated for comparison of initial metal contents, as these can influence leaching results to some extent. Despite significant differences in copper and/or iron grades in some pairs, the average grades of all treated fragments in each ore type are comparable to those of untreated fragments (as observed in Figure 8.3), given the smaller number of fragments used in each test. It can be seen that the effect of microwave treatment on leaching performance varies greatly between ore types, with some (e.g., Ore 4) performing better than others (e.g., Ore 2). It is also apparent that some pairs exhibited significant leaching improvement compared to others within a single ore type. This variation is mainly due to mineralogy or/and textural differences that exist between ore types or fragments within an individual ore.

As shown in Figures 8.17 and 8.18, Ore 4 demonstrated significant leaching improvements of both copper and iron for all six pairs tested, with the first pair achieving the highest copper extraction enhancement of about 64% (absolute) due to microwave treatment, i.e., 73.1% (treated) versus 9.3% (untreated). The improved leaching performance observed in this ore is due to increased mineral exposure, which is attributed to the high modal abundance of good microwave heaters (~14%) and the coarse grain size of these heaters (max D_{50} ~600 µm). This mineralogy and texture promote rapid heating and higher differential thermal stresses within shorter irradiation times, resulting in significant ore fracturing and increased mineral exposure for lixiviant interaction.

Furthermore, the magnitude of microwave-induced fractures and the extent of leaching improvement observed in Ore 4 results is enhanced by the high pyrite content. As discussed in Chapter 5, pyrite is a good microwave heater with a higher modulus of elasticity (stiffer) than the common gangue minerals found in copper ores (e.g., quartz). Hence, pyrite transfers the

induced stresses more effectively to the gangue matrix during microwave heating, resulting in significant ore fracturing that exposes more sulphide grains to the leach solution, increasing the leach extraction of both copper and iron even further.
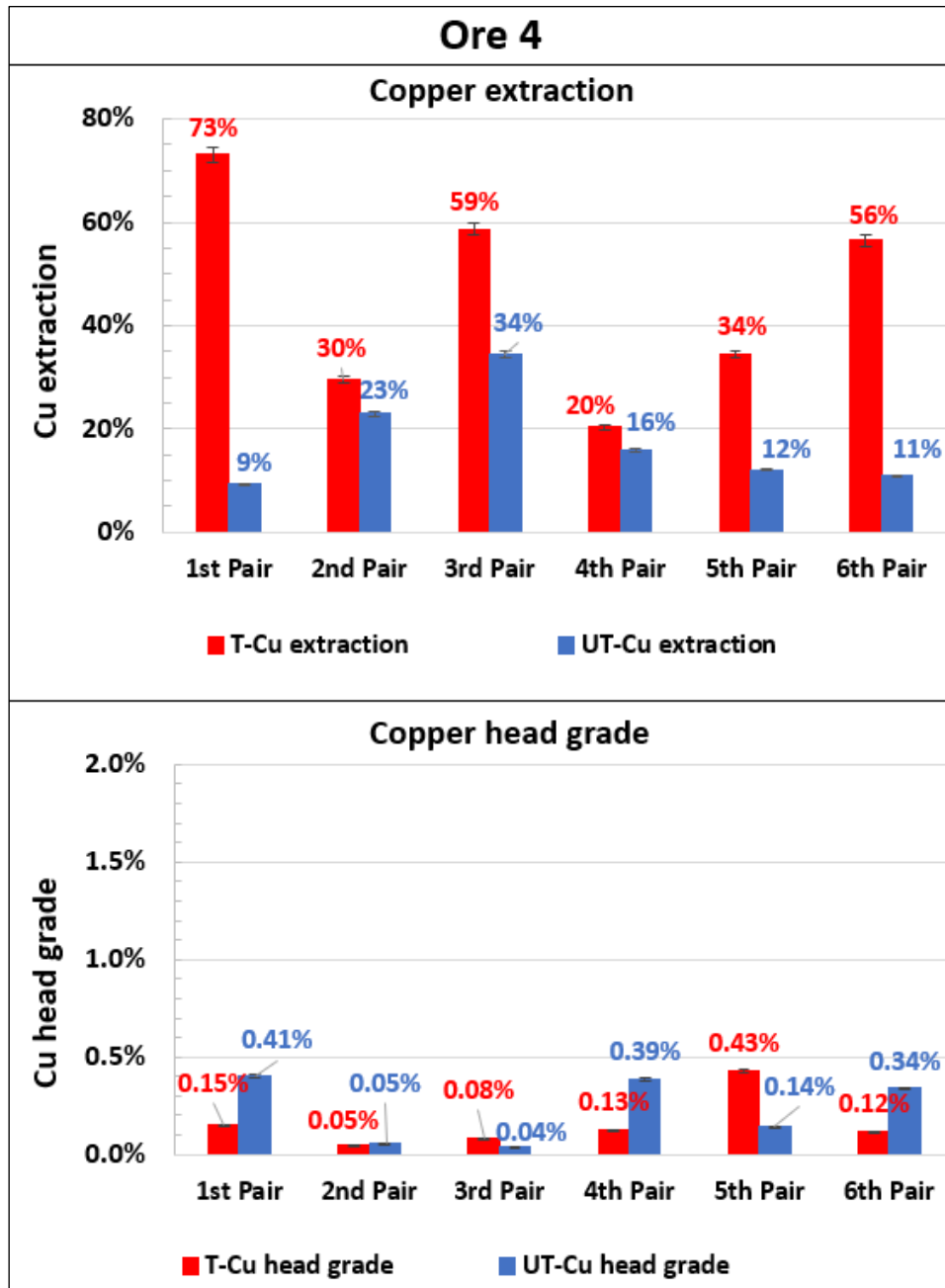
Figure 8.17. Copper extraction and head grade – Ore 4
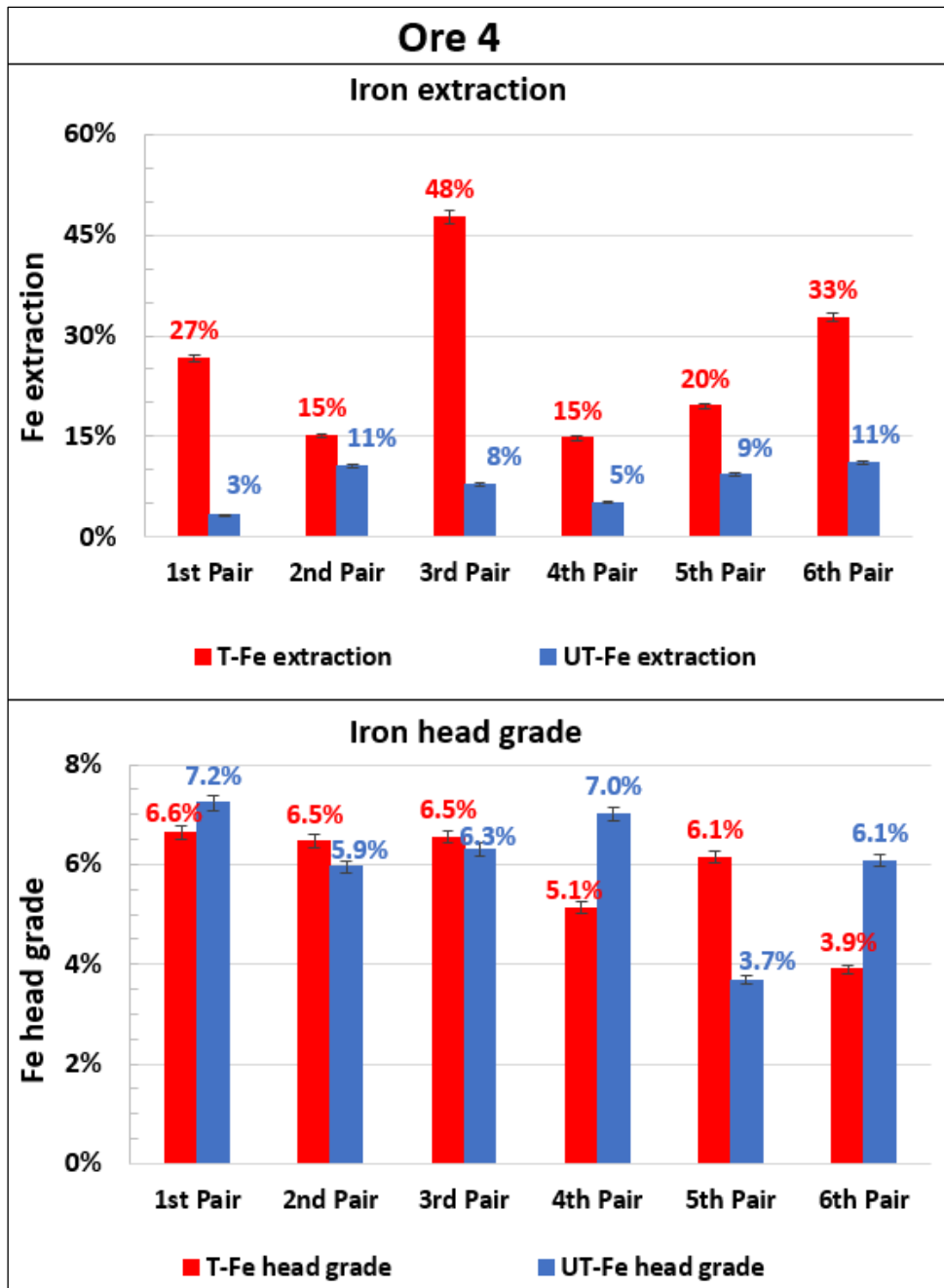
Figure 8.18. Iron extraction and head grade – Ore 4

Similarly, the improved leaching performance observed in Ore 3 results (Figures 8.19 and 8.20) is due to increased mineral exposure, which is attributed to a high modal abundance of good microwave heaters (7.3%) and the coarse grain size of these heaters (max D_{50} ~500 µm), as well as a high pyrite content of 5.3%. However, the magnitude of microwave-induced damage and subsequent leach improvement is lower compared to that of Ore 4. This could be due to a

higher content of the softer gangue matrix (Ore 3 - 59% versus Ore 4 - 41%), which absorbs thermal shock and undergoes ductile deformation, lowering the stresses available for ore fracturing and resulting in a comparatively lower leaching improvement.
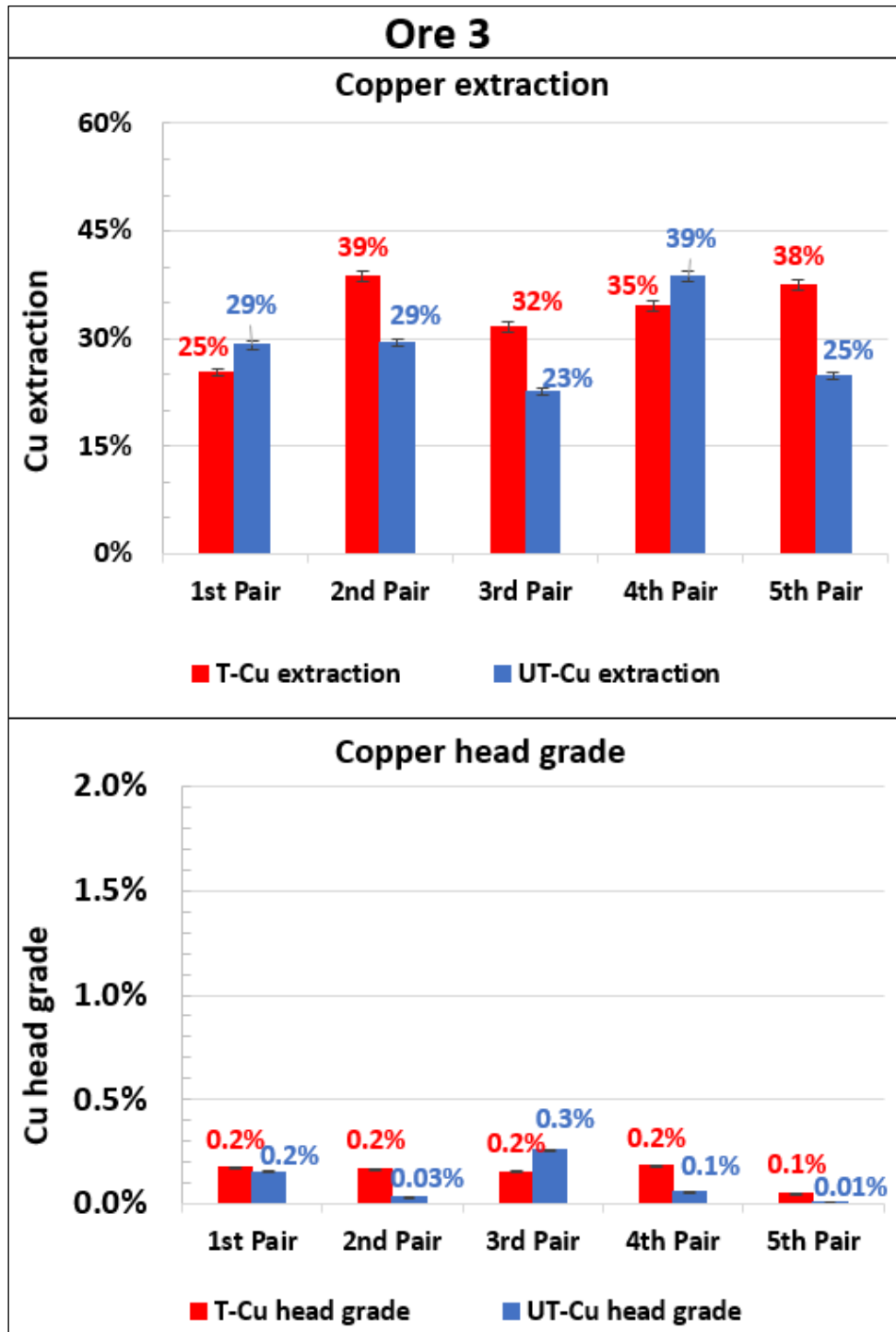
Figure 8.19. Copper extraction and head grade – Ore 3
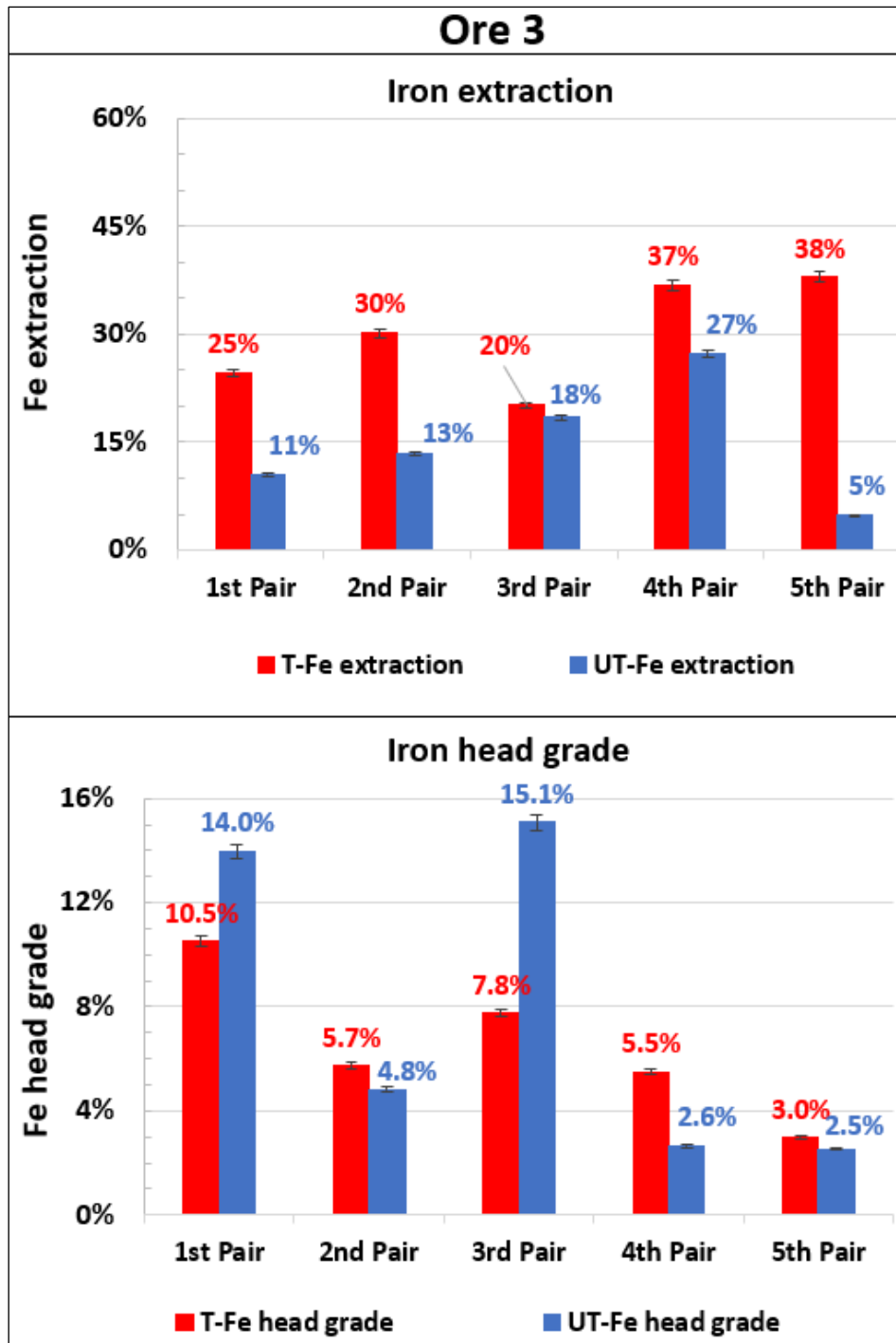
Figure 8.20. Iron extraction and head grade – Ore 3

The copper and iron leaching results of Ore 1 are shown in Figures 8.21 and 8.22, respectively. Although the iron or copper head grades varied greatly between treated and untreated fragments in some pairs, the general trend shows that treated fragments achieved higher leach extractions than untreated fragments. The observed leaching improvement is due to enhanced mineral

exposure, which is attributed to a combination of a high modal abundance of good microwave heaters (6%) dominated by pyrite (2.8%) and the moderate coarse grain size of these heaters (max D_{50} ~190 µm). Furthermore, Ore 1 contains a large proportion of the hard (brittle) gangue microwave-transparent matrix, dominated by quartz and feldspar (66% by weight), which does not undergo ductile deformation to absorb the thermal expansion of microwave heaters. As a result, more fractures are induced, resulting in improved copper and iron leaching extractions.
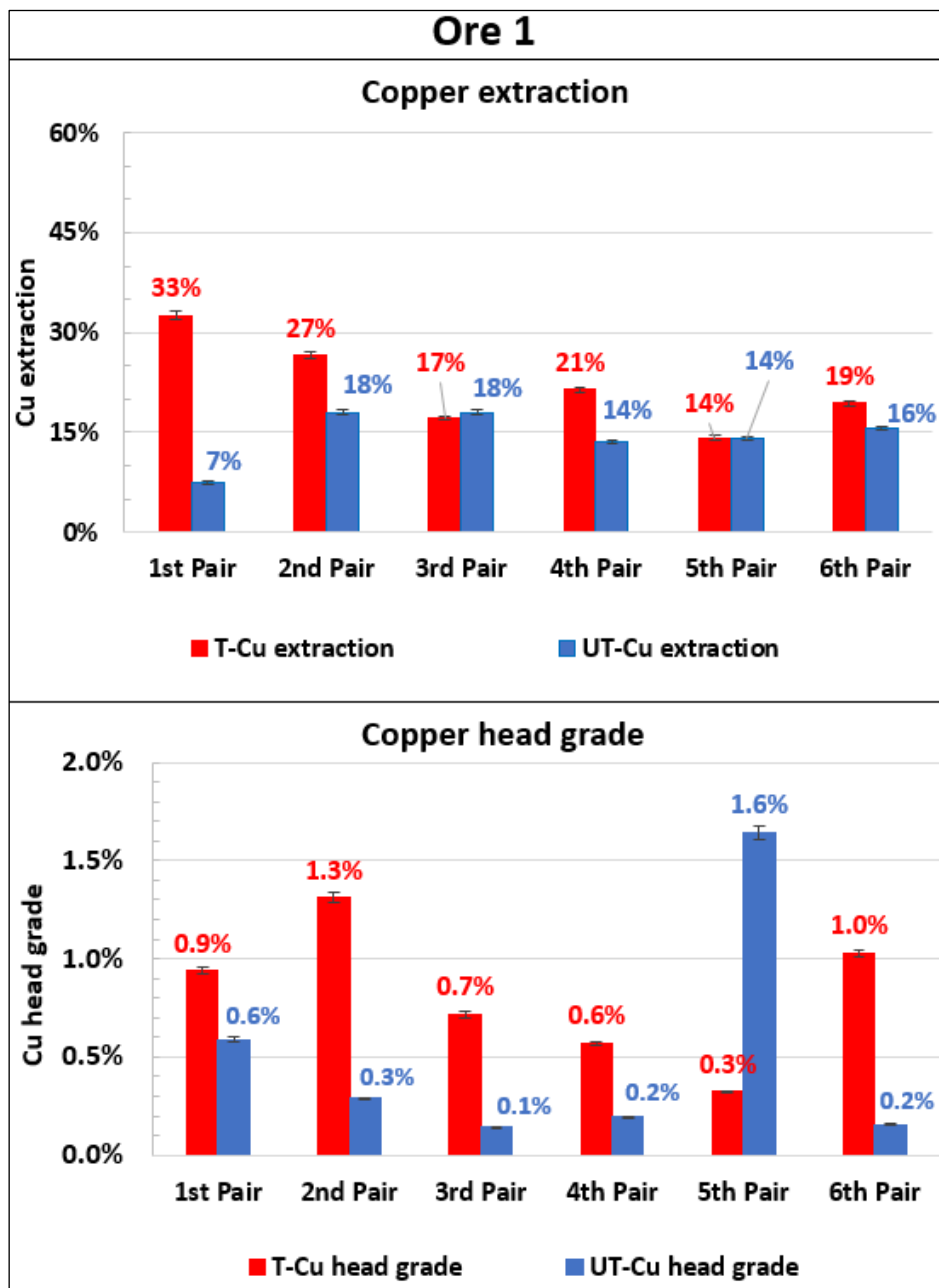
Figure 8.21. Copper extraction and head grade – Ore 1

288
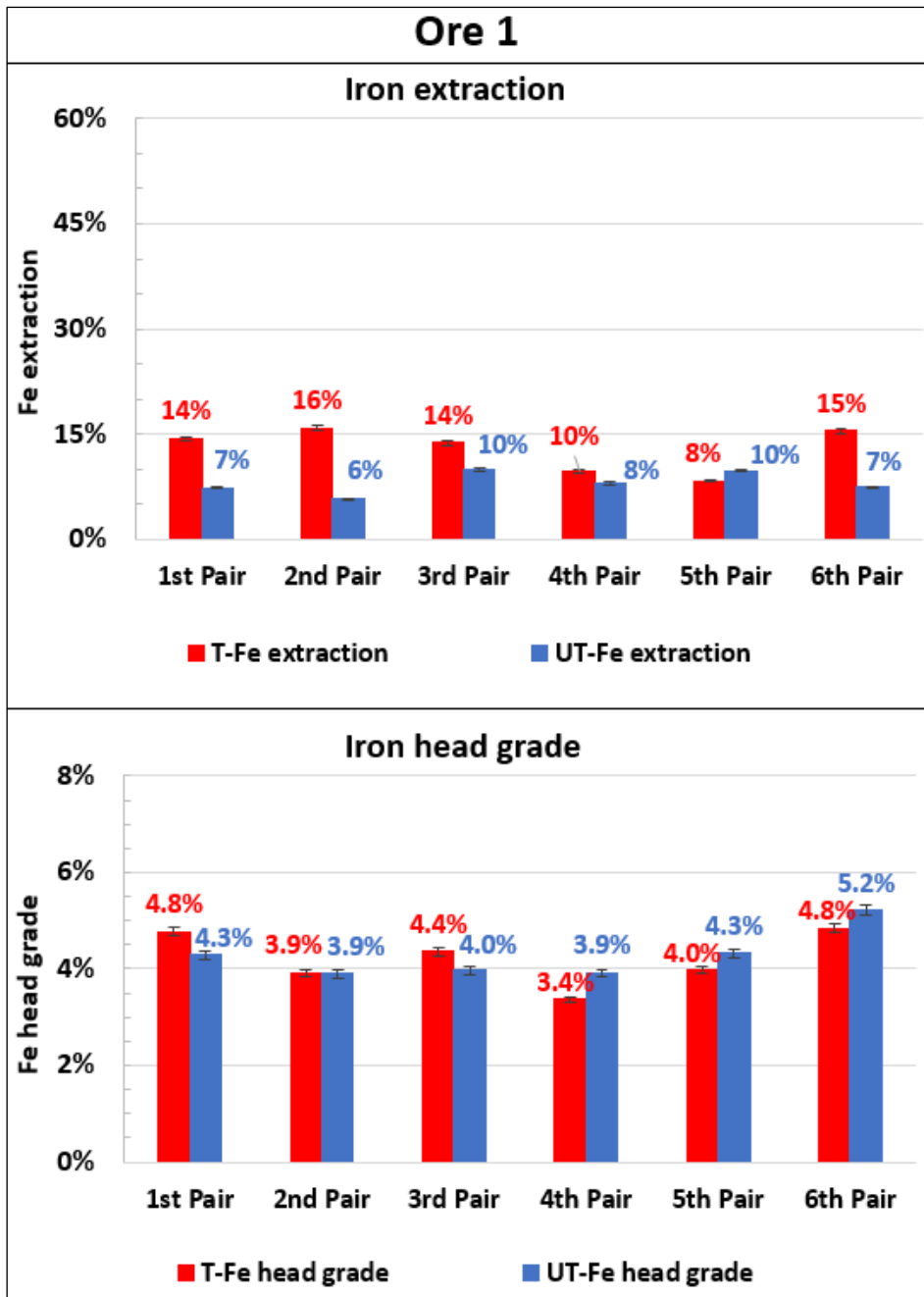
Figure 8.22. Iron extraction and head grade – Ore 1

Figures 8.23 and 8.24 show the copper and iron leaching results of Ore 2 fragments. In general, these results show that microwave treatment had little or no effect on leaching in most of the fragments. The poor leaching performance achieved by this ore is due to limited mineral exposure to the leach solution, which is attributed to a low content of microwave heaters (2%)

and the finer grain size of these heaters (D_{50} = 38-170 µm), as well as a low proportion of stiffer microwave heaters, such as pyrite of about 0.5%.
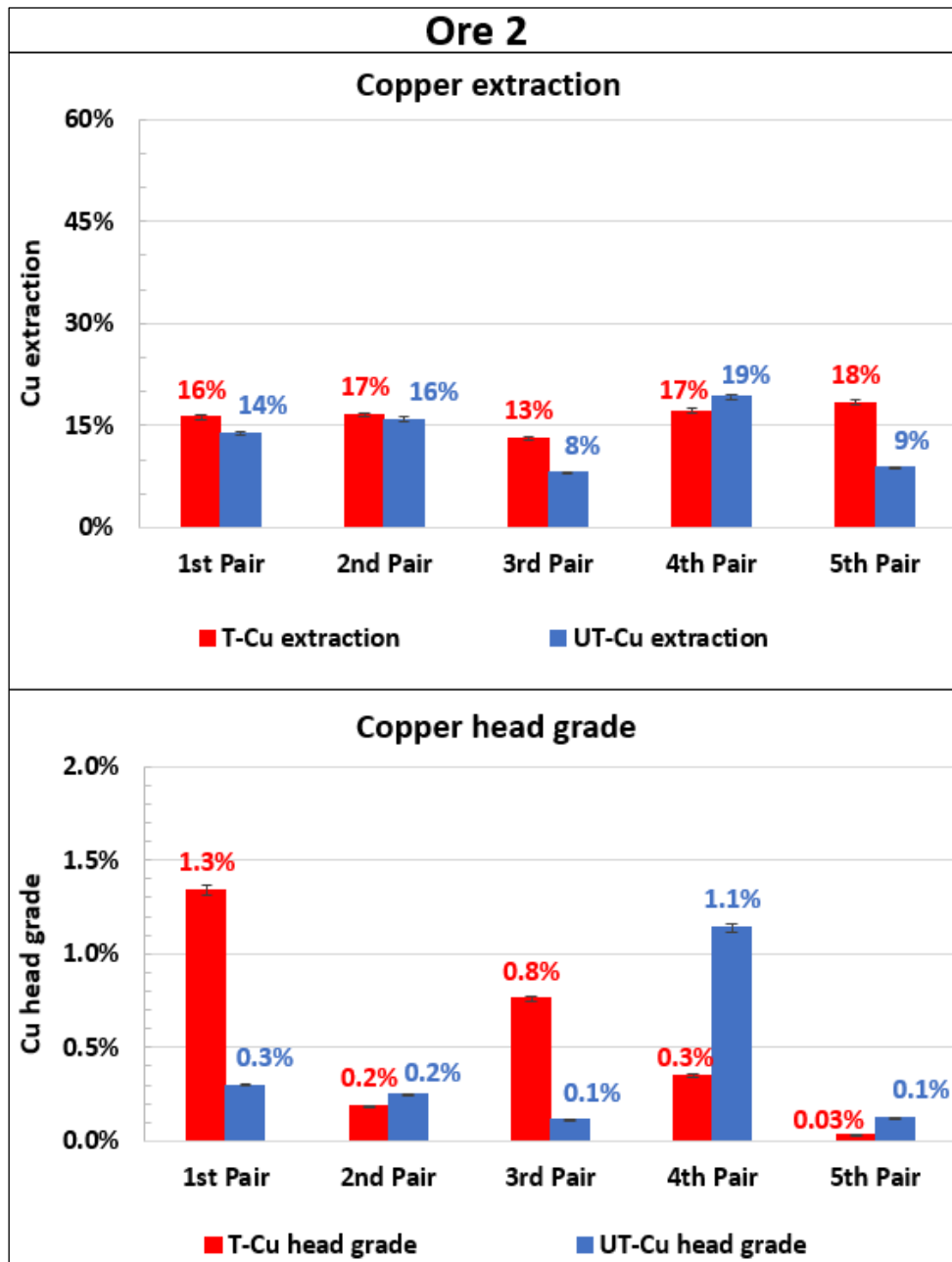
Figure 8.23. Copper extraction and head grade – Ore 2
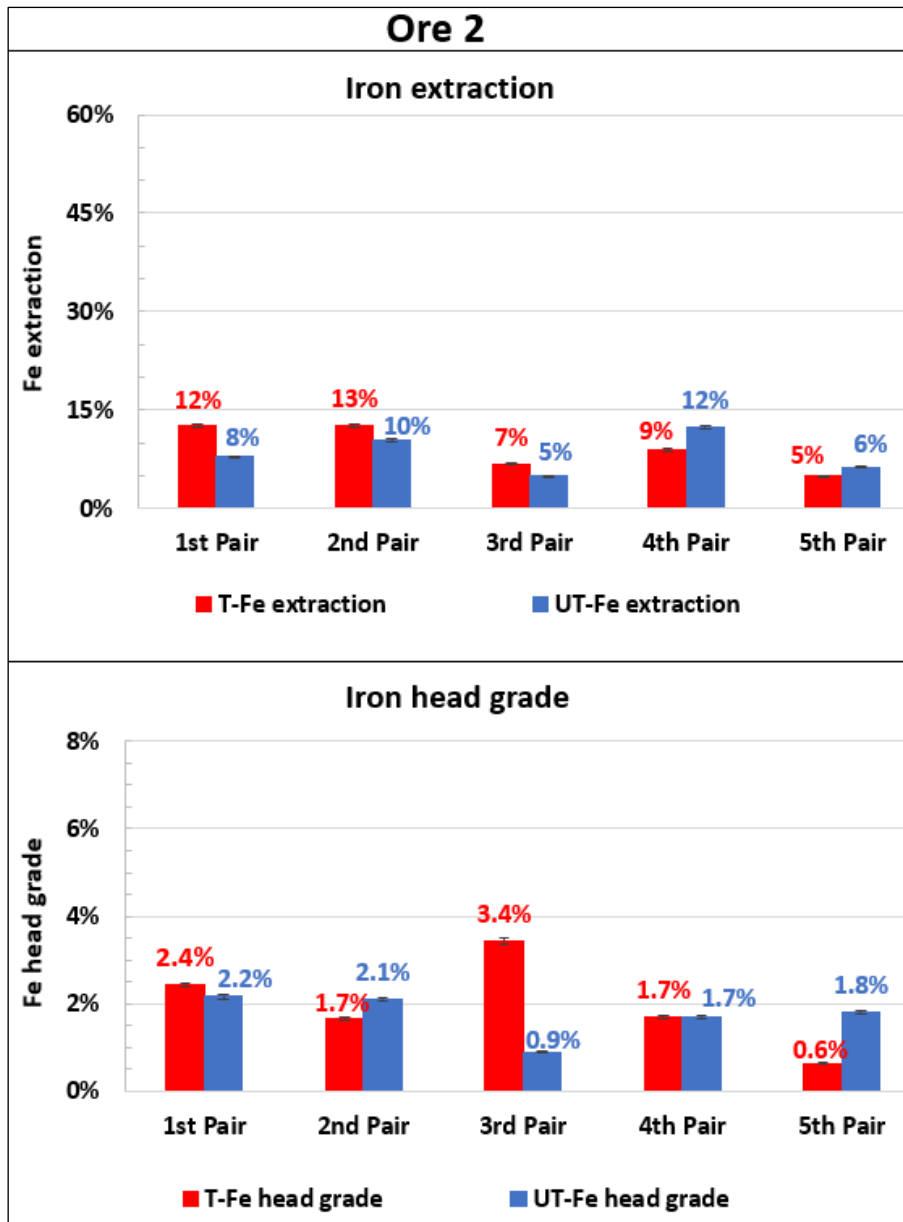
Figure 8.24. Iron extraction and head grade – Ore 2

The copper and iron leaching results of Ore 5 fragments are shown in Figures 8.25 and 8.26, respectively. This ore is highly variable in terms of copper head grade, with some fragments having significantly higher copper content than others. It can be seen that microwave treatment improved leaching performance in some pairs (e.g., 1st pair). According to the MLA results presented in Chapter 5, the observed leaching improvement could be attributed to favourable ore properties, such as a high modal abundance of good microwave heaters (5.1%), the moderate grain size of these heaters (up to $D_{50} \sim 212$ µm), and the presence of stiffer microwave

heaters dominated by magnetite (3%). However, the majority of the fragments in this ore consist of finely and highly disseminated microwave-absorbing grains, which promote conduction heat losses to the adjacent gangue matrix. Consequently, reducing the induced thermal stresses and ore fracturing, potentially lowering the leaching performance. The higher copper extraction of untreated fragments observed in the second and sixth pairs can be attributed to the higher copper head grade of untreated fragments in these pairs.
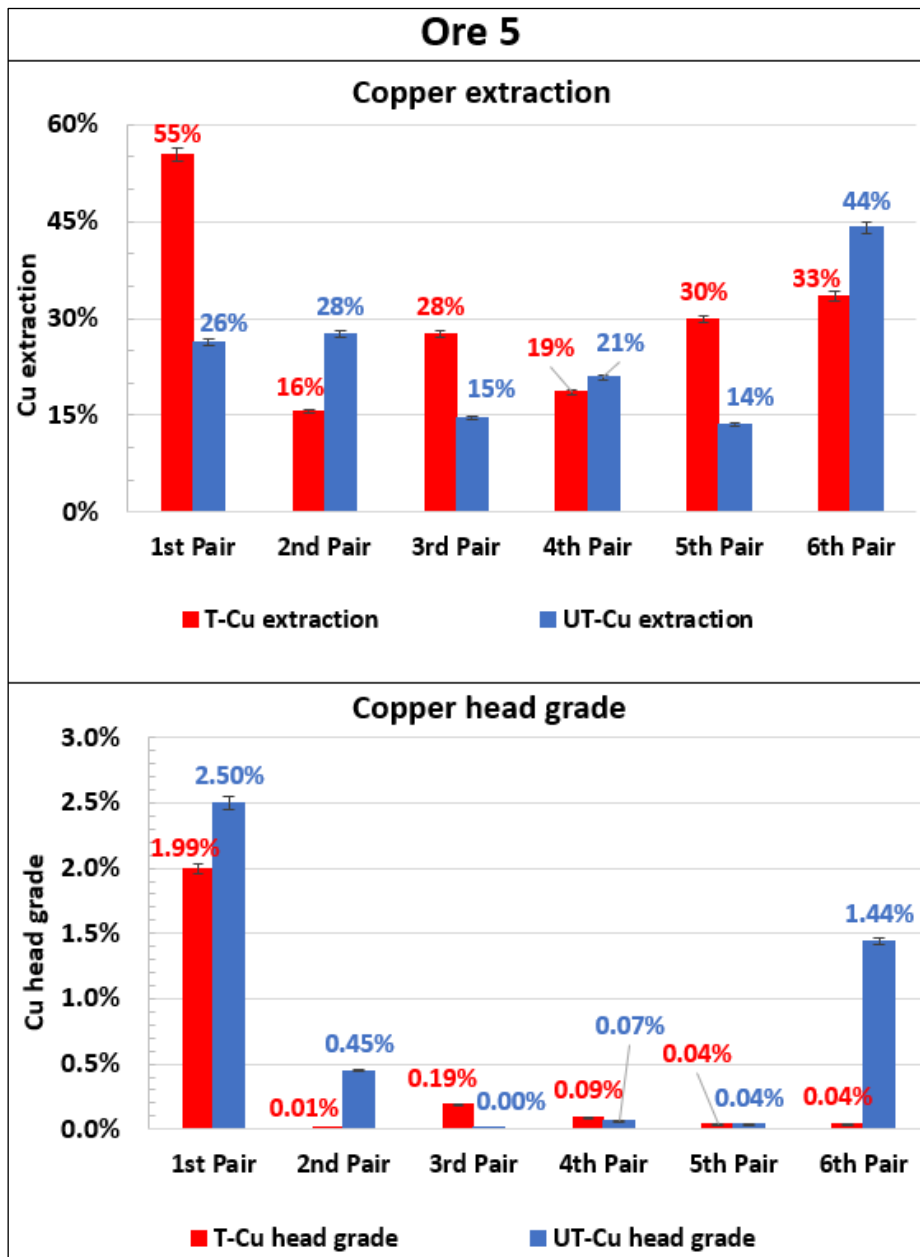
Figure 8.25. Copper extraction and head grade – Ore 5
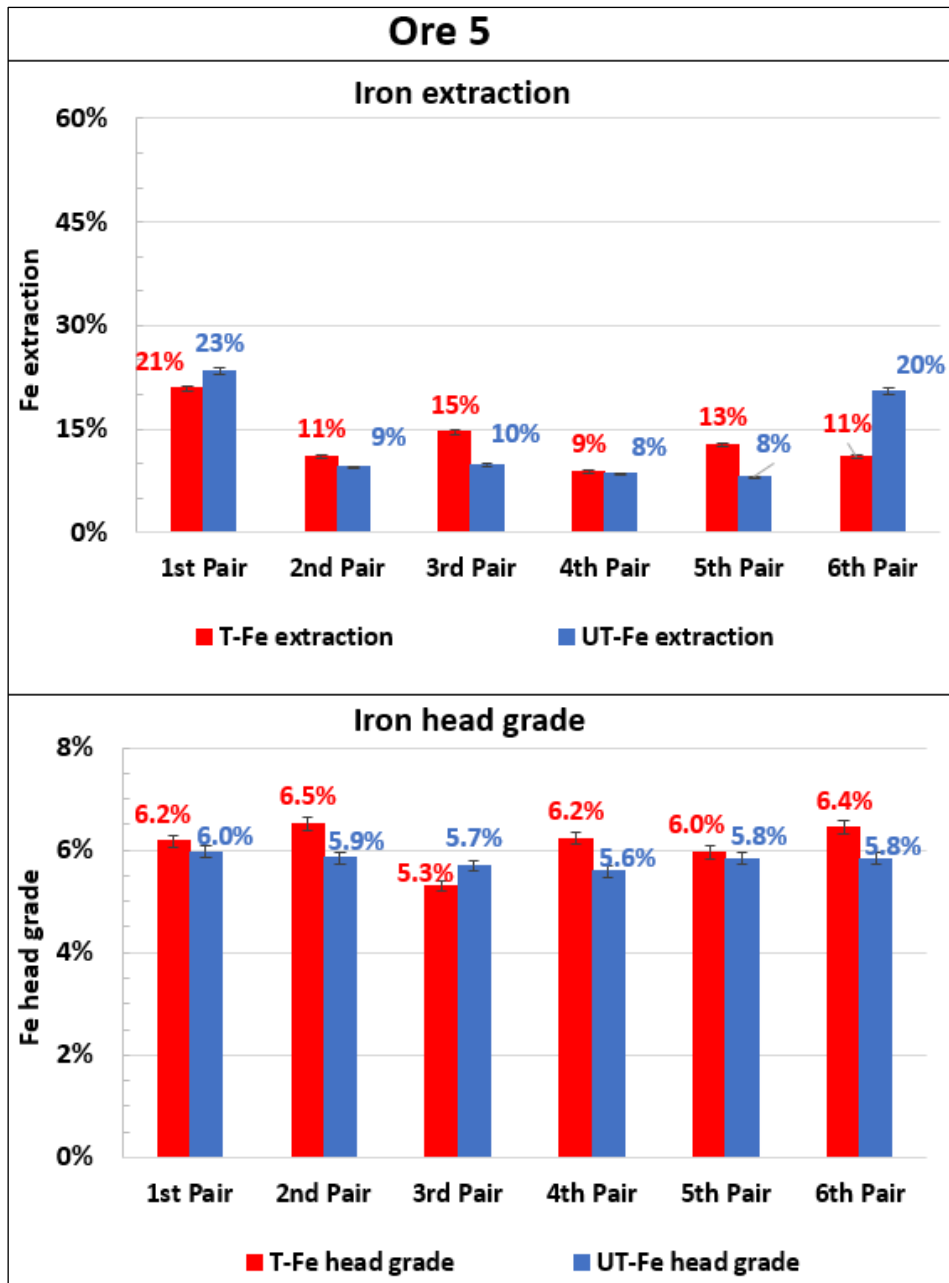
Figure 8.26. Iron extraction and head grade – Ore 5

Figures 8.27 and 8.28 show the average copper and iron leach extractions of all pairs of fragments tested in each ore type, as well as the corresponding metal head grades. The error bars indicate the maximum and minimum values. Despite greater variability of metal head grades between fragments within an ore (indicated by the long error bars of head grades in some ores), it is evident that microwave treatment improved leaching performance to varying degrees, with some ores performing better (e.g., Ore 4) than others (e.g., Ore 2).
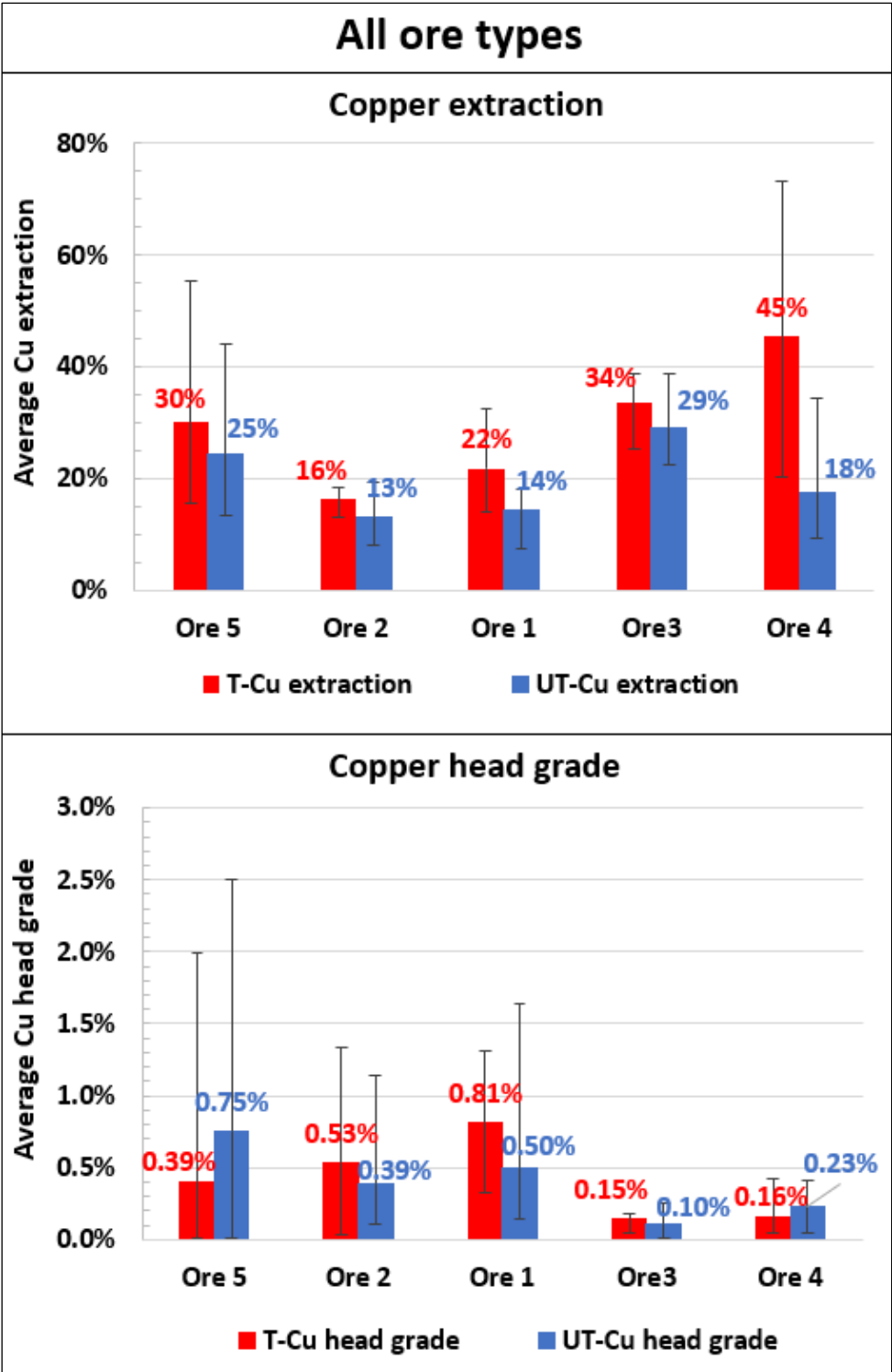
Figure 8.27. Copper extraction and head grade – All ore types

294
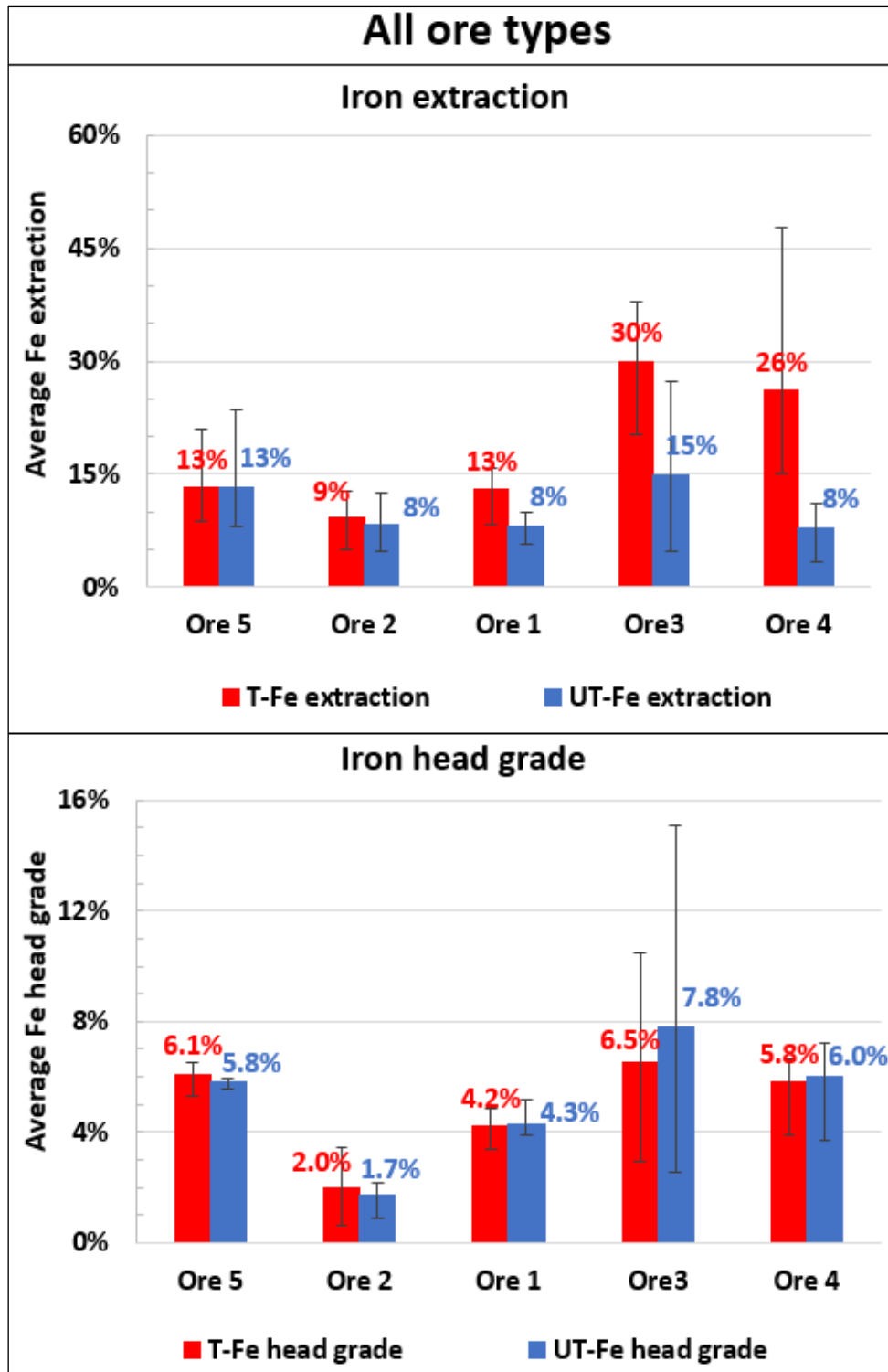
Figure 8.28. Iron extraction and head grade – All ore types

Figure 8.29 shows the absolute leach extraction enhancements due to microwave treatment (the difference between treated and untreated extractions) and the corresponding microwave energy inputs. It is clear that Ore 4 is the best performer, with an average leaching enhancement of about 28% (copper) and 18% (iron) at a microwave energy input of about 22 kWh/t. Ores 3 and 1 are the second-best performers, achieving enhancements of approximately 5-7% (copper) and 5-15% (iron) at a microwave energy input of 13-22 kWh/t. Ore 5 performed better in terms of copper extraction, achieving an average enhancement of 5.6% with negligible iron extraction enhancement, but at the expense of a higher microwave energy dose of about 50 kWh/t. Ore 2 performs the worst, with insignificant extraction enhancement of both copper (3.1%) and iron (0.8%) at 25 kWh/t microwave energy dose. These results can be linked with the UPV and PLT results presented in Sections 8.3.1 and 8.3.2, indicating that ores with significant induced damage (e.g., Ore 4) exhibited greater leaching improvement than those with little damage (e.g., Ore 2). The leaching extraction kinetics are evaluated in the next section.
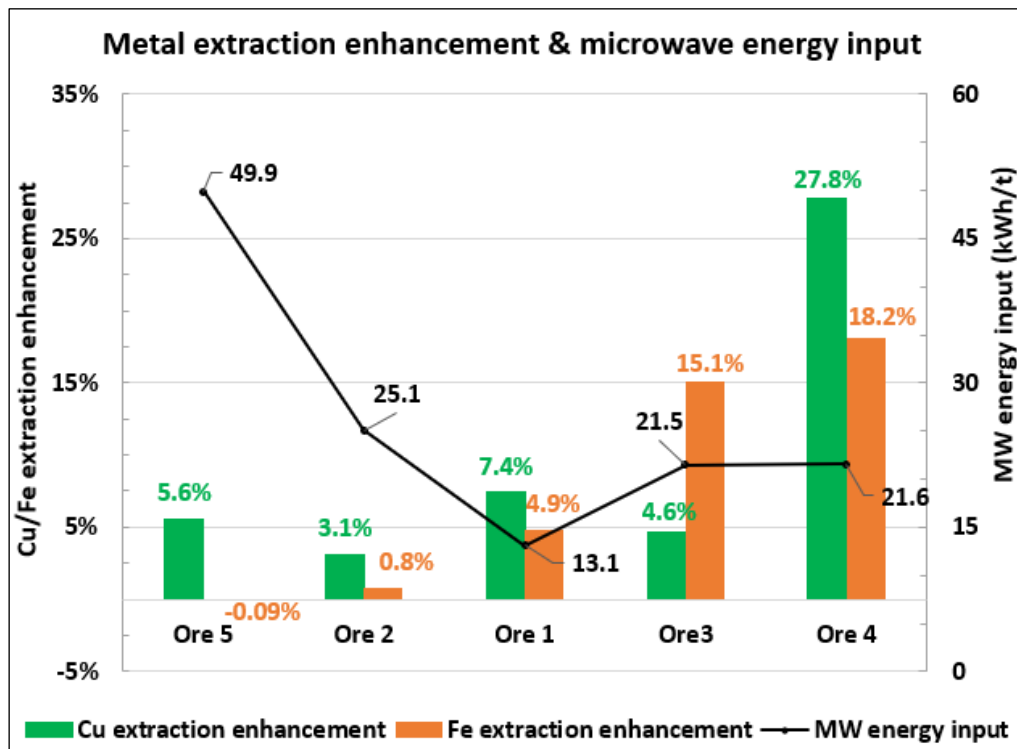
Figure 8.29. Average metal extraction enhancement vs microwave energy input

8.3.4 Leaching Kinetics

Figures 8.30 to 8.34 show the effect of microwave treatment on the leaching kinetics of copper and iron. It should be noted that the leaching extraction of each ore type indicated here is the average of leaching extractions determined from five/six treated fragments, which are compared to their corresponding untreated fragments of relatively similar ore grade. The error bars represent the maximum and minimum leach extractions at each data point. The raw data are presented in Appendix 11.3.1.

Results displayed a typical profile of leach extraction versus time which exhibited an initial fast leaching rate, then followed by a slow leaching rate as leaching progresses. The decrease in dissolution rate with time results from the depletion of accessible sulphide minerals to the leach solution. It can also be linked to the saturation of dissolved metals in the leach solution to the extent of inhibiting further mass transport. The colour of the pregnant solution changed from colourless at the start to dark brown or deep green near the end of the leaching process. Replacing this highly concentrated solution with a fresh solution was avoided because it could alter the overall dissolution kinetics. Another observation that supports the leach extraction profile is that the leach reaction was very aggressive at the start, with more bubbling and fizzing, which decreased gradually as leaching progressed. In the case of treated fragments, streams of small bubbles continued to evolve from the induced fractures till the end of leaching, suggesting that some mineral grains along fractured planes were not completely dissolved. Thus, given more time, these grains could have been dissolved, resulting in further leaching improvement.

Results show that microwave treatment can significantly improve the dissolution kinetics of minerals in certain ore types (e.g., Ores 4, 3, and 1). Figures 8.30-8.32 show that the rates of copper and iron extractions of treated fragments in these ores are significantly higher than those of untreated fragments, indicating that dissolution time is reduced by a factor of four or more

to achieve equivalent copper extraction. This implies that in heap leaching, multiple leach cycles can be performed on treated materials in these ores to achieve equivalent metal extraction as untreated materials, potentially increasing overall metal production and improving heap leaching economics.

The effect of microwave treatment on leaching kinetics exhibited by each ore type is dependent on the magnitude of microwave-induced fractures, which is dictated by ore mineralogy and texture properties, as described in the previous section. Furthermore, it is important to mention that although pyrite is a gangue mineral, its high content in the ore accelerates the dissolution of accessible copper minerals due to galvanic interaction. Essentially, the galvanic effect occurs when two semiconducting minerals with different rest potentials are in direct contact with each other in an acid-aqueous solution, such as pyrite (0.66V) and chalcopyrite (0.56V) (Mehta & Murr, 1983). In such a system, a mineral with a more negative rest potential (in this case chalcopyrite) will act as anode and will dissolve preferentially. The overall galvanic reaction proceeds according to chemical Equation 8.1 (Y. Li et al., 2013). The higher copper dissolution kinetics observed on the treated samples containing high pyrite content (3-11%), such as Ores 4, 3, and 1, can be partly attributed to the galvanic effect, due to improved mineral exposure (e.g., chalcopyrite and pyrite) via a network of microwave-induced fractures.

$$CuFeS_2 + O_2 + 4H^+ \rightarrow Cu^{2+} + Fe^{2+} + 2S + 2H_2O \qquad (8.1)$$
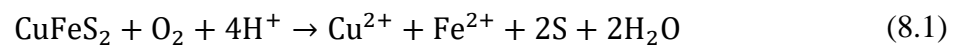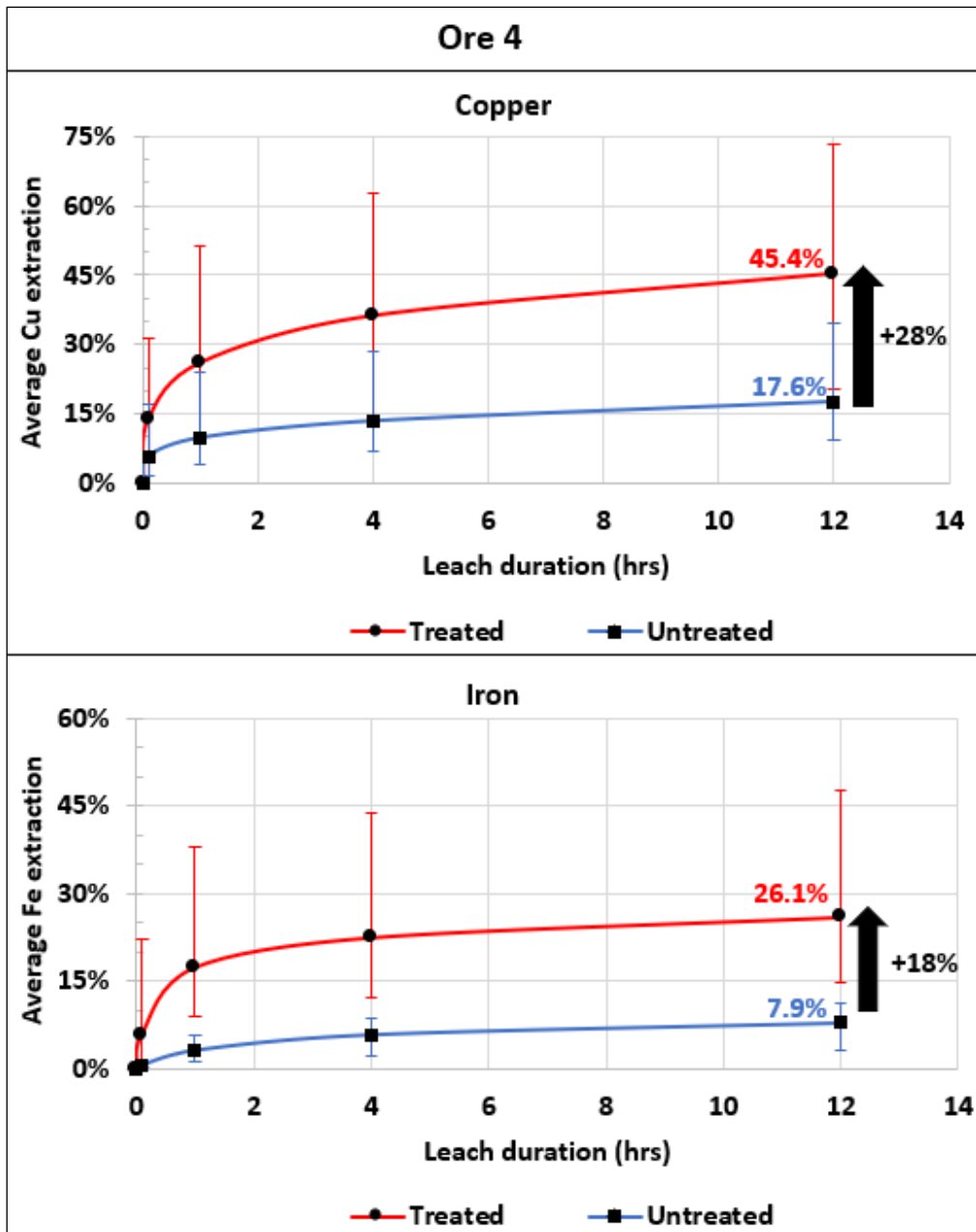
Figure 8.30. Effect of microwave treatment on leaching kinetics – Ore 4
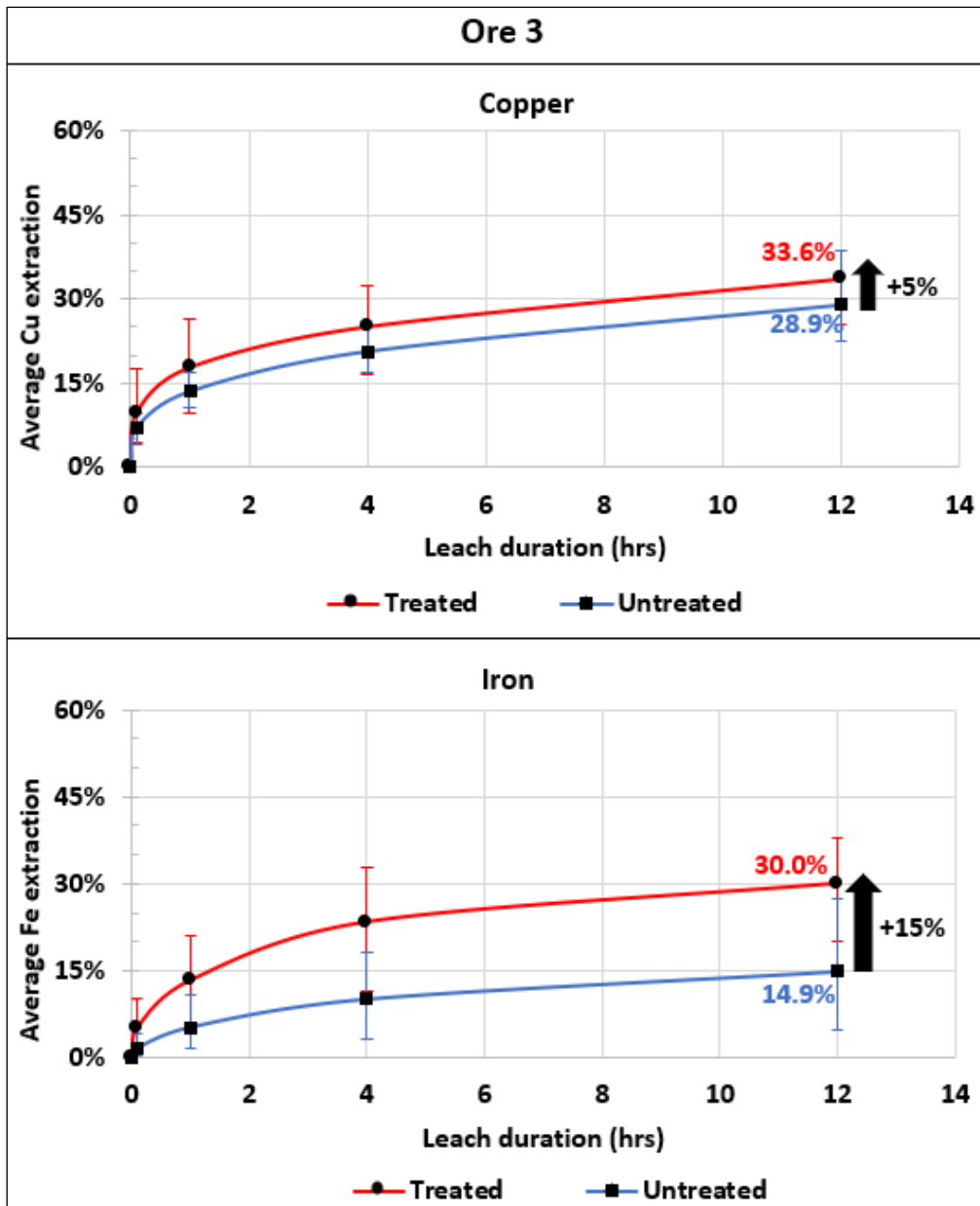
Figure 8.31. Effect of microwave treatment on leaching kinetics – Ore 3
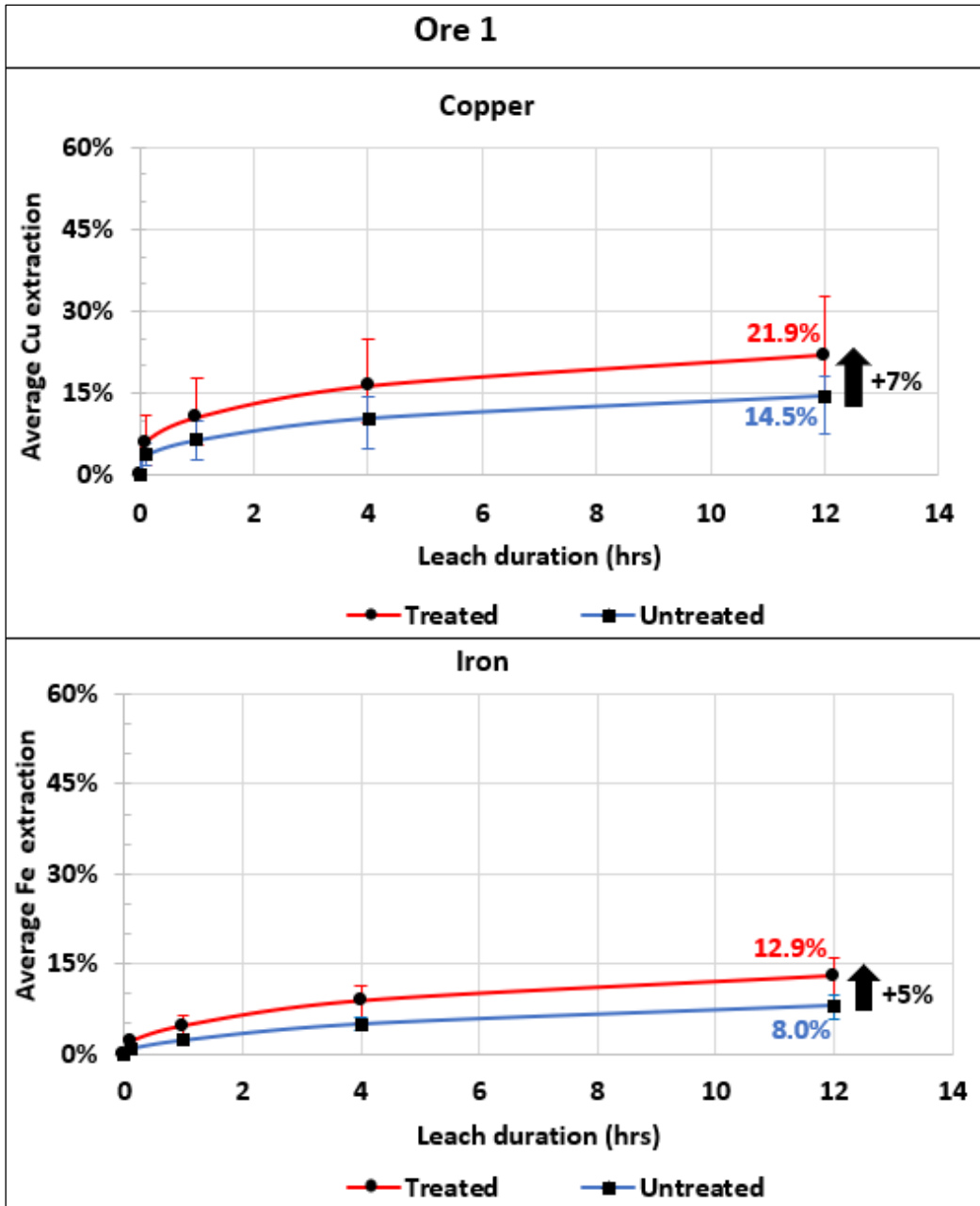
Figure 8.32. Effect of microwave treatment on leaching kinetics – Ore 1
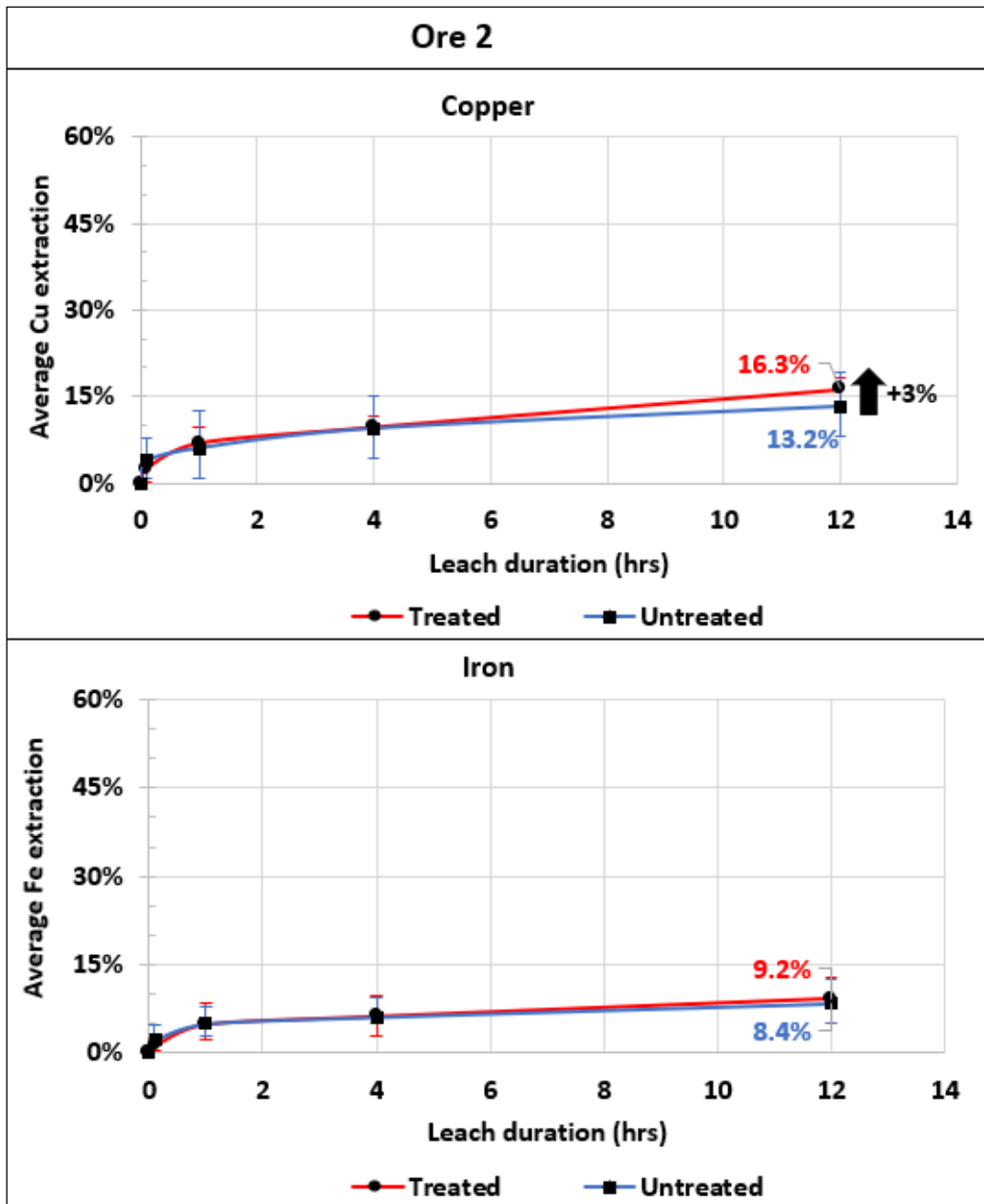
Figure 8.33. Effect of microwave treatment on leaching kinetics – Ore 2
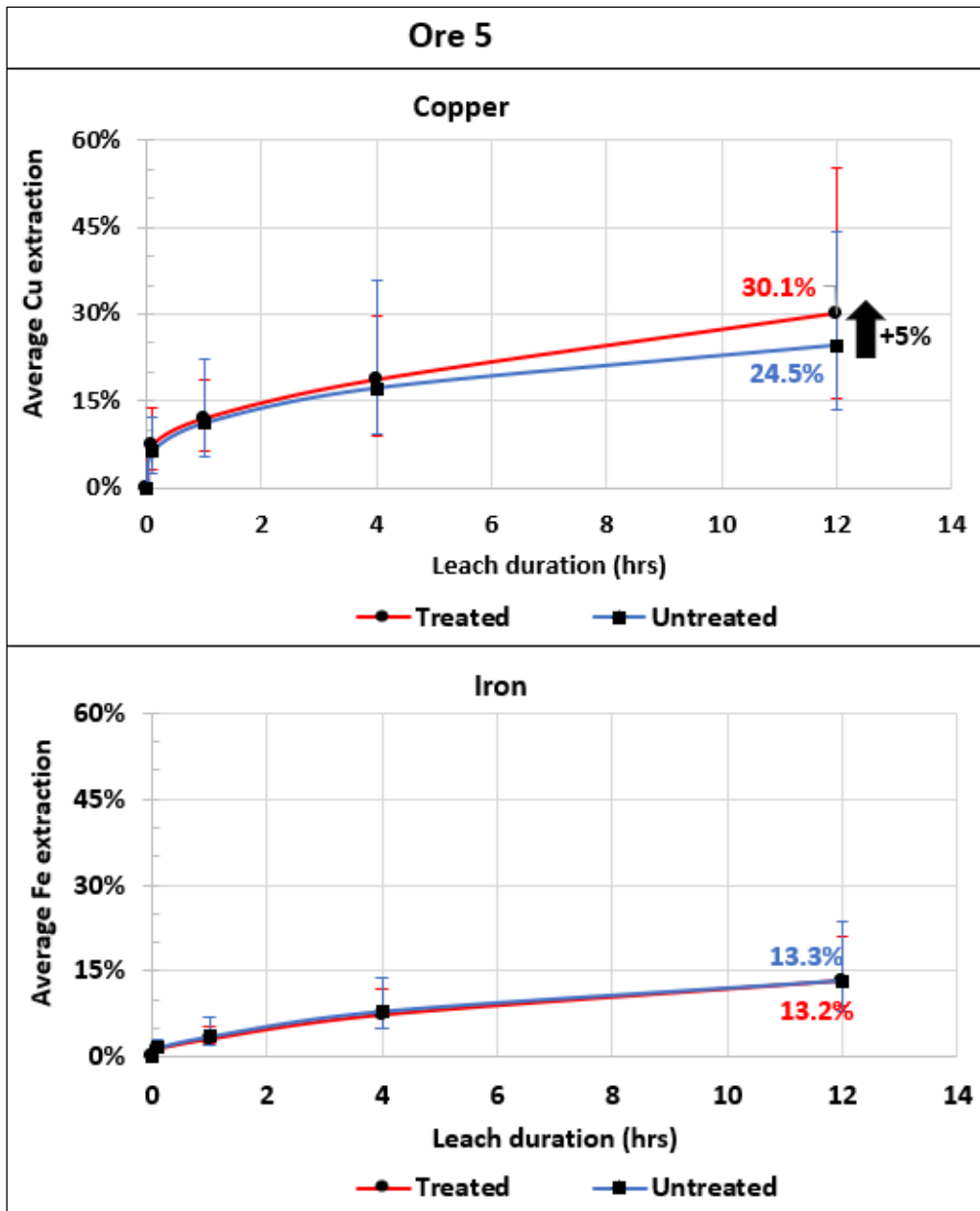
Figure 8.34. Effect of microwave treatment on leaching kinetics – Ore 5

8.3.5   Results Summary

Tables 8.2 and 8.3 summarise the statistical data of copper and iron leach extractions for the five ore types tested, respectively. It can be seen that Ores 4, 1, and 3 exhibited significant leaching improvement in copper and/or iron (up to 28% absolute) at >95% confidence level. Due to little induced fractures and thus limited mineral exposure, Ores 5 and 2 exhibited little

leaching improvement of both copper and iron (<6%) at a low confidence level of <80%. It is worth noting that Ore 2 had a relatively low iron head grade (1.7-2.0%) in comparison to other ore types (4.2-7.8%). This indicates a low content of iron sulphide (e.g., pyrite) or iron oxide (e.g., magnetite), the stiffer microwave-absorbing grains that can potentially promote significant ore fracturing and leaching improvement.

Table 8.2. Copper results – statistical analysis summary

Copper results							
Ore type	Sample type	Number of fragments tested	Average Cu head grade (%)	Mean ± SD Cu extraction (%)	Degrees of freedom	Calculated t-value	t-test confidence level
Ore 4	T	6	0.16	45.40 ± 20.33			
	UT	6	0.23	17.62 ± 9.58	10	3.028	98.7%
Ore 3	T	5	0.15	33.56 ± 5.33			
	UT	5	0.10	28.94 ± 6.19	8	1.263	76.0%
Ore 1	T	6	0.81	21.89 ± 6.70			
	UT	6	0.50	14.47 ± 3.92	10	2.341	95.9%
Ore 2	T	5	0.53	16.30 ± 1.96			
	UT	5	0.39	13.20 ± 4.77	8	1.344	78.6%
Ore 5	T	6	0.39	30.07 ± 14.13			
	UT	6	0.75	24.51 ± 11.20	10	0.755	53.4%

Table 8.3. Iron results – statistical analysis summary

Iron results							
Ore type	Sample type	Number of fragments tested	Average Fe head grade (%)	Mean ± SD Fe extraction (%)	Degrees of freedom	Calculated t-value	t-test confidence level
Ore 4	T	6	5.80	26.06 ± 12.65			
	UT	6	6.04	7.89 ± 3.10	10	3.415	99.3%
Ore 3	T	5	6.49	29.98 ± 7.66			
	UT	5	7.82	14.92 ± 8.54	8	2.938	98.1%
Ore 1	T	6	4.21	12.90 ± 3.13			
	UT	6	4.27	8.05 ± 1.60	10	3.385	99.3%
Ore 2	T	5	1.97	9.17 ± 3.42			
	UT	5	1.73	8.36 ± 3.06	8	0.396	30.8%
Ore 5	T	6	6.10	13.19 ± 4.24			
	UT	6	5.79	13.28 ± 6.83	10	-0.026	2.0%

Table 8.4 summarises the mineralogy and texture of the five ore types tested in this study, as well as their microwave treatment response in terms of strength reduction and leaching performance. The microwave energy input required to achieve the observed improvements is also indicated to identify the potential ore candidates for microwave-assisted leaching of coarse fragments (e.g., heap leaching). It is apparent that ore mineralogy and texture greatly influence the extent of microwave-induced damage and subsequent leaching performance.

These results are consistent with those presented in Chapter 7, indicating that ores with amenable textures for microwave-induced fractures (e.g., Ores 4, 3, and 1) exhibited greater fractures and leaching improvement as a result of microwave treatment. However, as expected, the large fragments (30-50 mm) required less microwave energy input (in the multiple of 4-5) than the small cores (21 mm diameter by 19-22 mm height) used in Chapter 7 to achieve relatively the same metal extraction enhancement. This is because the microwave-absorbing grains in coarse particles are mostly enclosed within a large volume of microwave-transparent gangue matrix, which supports more induced stresses and fracture propagation, resulting in improved mineral exposure and leaching performance at lower microwave energy input.

It can be seen in Table 8.4 that ores with some of the following properties are more likely to be the best candidates for microwave-assisted comminution and microwave-assisted heap leaching:

i.   A high modal abundance of good microwave heaters of ~6-14% wt, with a certain proportion of stiffer heaters (2.8-11%), such as pyrite and magnetite.

ii. Coarse discrete grains and/or mineralised veins of good microwave heaters (D_{50} ~0.5-0.6 mm).

iii. A high modal abundance of hard (brittle) gangue matrix (e.g., quartz) of at least 45% wt.

iv.   A consistent texture of microwave-absorbing phases (containing a high proportion of fragments with amenable texture).

v.   Natural flaws with microwave-absorbing grains deposited in them, which can be exacerbated by microwaves during treatment.

These observations are consistent with the previous studies on microwave-assisted comminution reported in the literature (Kingman et al., 2000; Batchelor et al., 2015).

Table 8.4. Assessment of potential ore candidates for microwave-assisted heap leaching

Ore type	Ore mineralogy and texture properties			MW- induced damage (average)		Absolute leaching enhancement due to MW treatment (average)		Average MW energy input (kWh/t)	Potential ore candidate for MW-assisted leaching?
	Ore description summary	Total MW heaters (wt%)	MW heater grain size max D_{50} (μm)	UPV reduction (%)	PLT strength reduction (%)	Cu (%)	Fe (%)		
Ore 4	A porphyry copper ore with pyrite and chalcopyrite as the dominant MW heaters, which occurs as macro-veins or coarse discrete grains. The texture of microwave-absorbing phases is consistent, with most fragments containing amenable texture. Contains a 45% wt hard gangue matrix dominated by quartz.	14	600	39.0	74.6	27.8	18.2	21.6	More likely
Ore 3	A limestone skarn low-grade copper ore. The ore has some mineralogical and textural properties that are similar to those of the AA sample. However, the ore has a relatively low proportion of hard gangue matrix (33% wt), which is dominated by quartz and orthoclase.	7.3	500	16.5	56.5	4.6	15.1	21.5	More likely
Ore 1	A quartz monzonite porphyry copper ore. The ore is dominated by the sulphide MW heaters (chalcopyrite and pyrite) and the non-sulphide MW heater (montmorillonite). Contains a high abundance of hard gangue matrix (66% wt), which is dominated by quartz and feldspar.	6.2	190	21.2	57.9	7.4	4.9	13.7	More likely
Ore 2	A quartzite copper ore containing chalcopyrite and pyrite as the main sulphide MW heaters, which are mostly disseminated. The ore contains a high proportion of non-heating gangue (92% wt), which is dominated by quartz. Some fragments had natural flaws with sulphide grains deposited in them.	2.0	170	15.8	52.0	3.1	0.8	25.9	Less likely
Ore 5	An alkalic porphyry copper ore consisting of bornite, chalcopyrite, and magnetite as the dominant MW heaters. These heaters mostly occur as finely disseminated grains or micro-veins. Few fragments had amenable texture (e.g., coarse MW heaters). The ore contains a high proportion of hard gangue matrix (64% wt), which is dominated by feldspar.	5.1	212	15.9	46.7	5.6	-0.1	49.9	Less likely

This dissertation has demonstrated that microwave heating technology can significantly improve leaching performance, but the energy required to achieve the observed leaching improvement exceeds the probable economic range (1-5 kWh/t) suggested by Bradshaw et al. (2005) based on energy savings in the comminution circuit. However, in order to understand the true economic value of microwave technology in heap leaching against the crush-grind-float circuit, all stages of metal production should be evaluated, not just the energy savings in the comminution circuit; this includes grinding (energy + grinding consumables), flotation, dewatering, and tailings disposal circuits, as well as copper concentrate smelting.

8.4 Conceptual Flowsheets Possibilities

This section describes conceptual flowsheets that incorporate microwave heating technology to assist the leaching of copper sulphide ores (e.g., heap leaching). These flowsheets show several possible options for exploiting microwave-induced fractures to improve mineral exposure and leaching performance of coarsely crushed materials while also reducing comminution energy and grinding media requirements by avoiding grinding the material to fine sizes. In addition, microwave-induced fractures in heaps can serve as preferential sites for microbial activities, which promote mineral dissolution kinetics (Olubambi, 2009).

Figure 8.35 illustrates a typical heap leaching flowsheet; this is the base-case scenario (without microwave treatment). Essentially, the run-of-mine ore (typically -1000 mm) is subjected to several stages of crushing to a top size of about 25 mm (Petersen, 2016). The crushed materials are then agglomerated with acid curing, stacked into heaps, and leached. The pregnant solution is sent to the solvent extraction-electrowinning (SX-EW) unit, where copper is recovered, and the barren solution is recycled to the heap. Despite longer leach durations of several months to a year or more, this flowsheet suffers from poor metal extraction (>70%) (Brierley, 2008; Petersen, 2016). Such a poor leaching performance is mainly caused by inadequate mineral

exposure for interaction with the leach solution. Based on this conventional flowsheet, alternative flowsheets incorporating a microwave treatment unit to assist leaching are proposed.
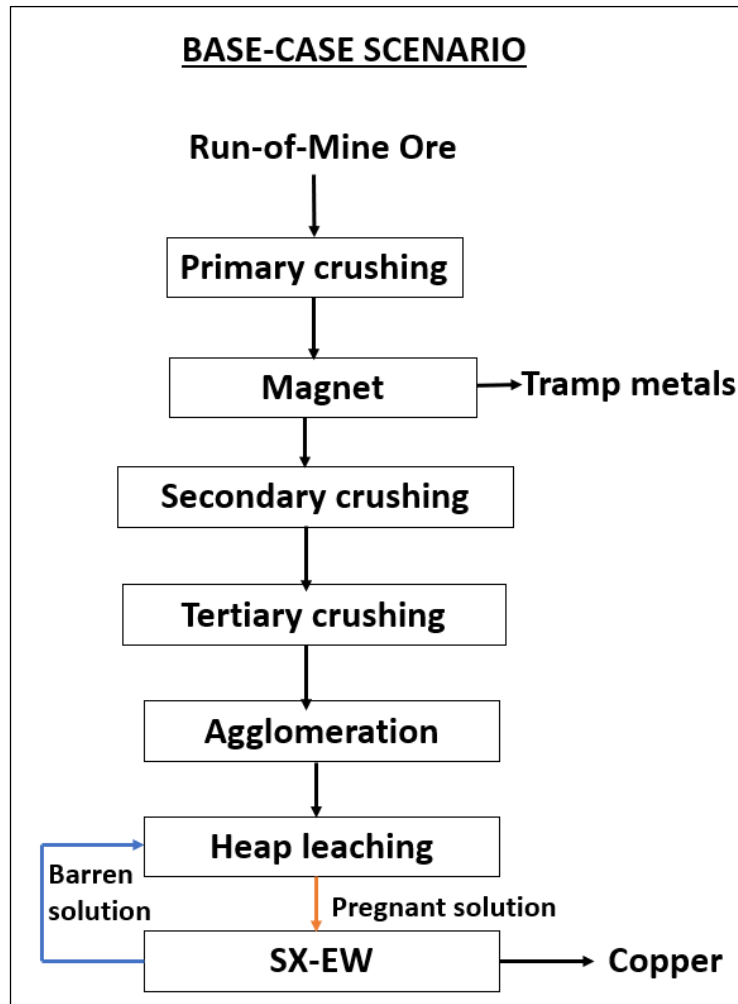
Figure 8.35. Conventional heap leaching flowsheet

Typically, tramp metals from mining tools and crushers (e.g., chains, bucket teeth, crusher plates, drill rods, bolts, and nuts) may find their way into crushed ore as it moves along conveyors. These metallic objects should be rejected (sorted) from the ore because they can significantly reflect microwave energy and disrupt the electric field distribution within the microwave cavity. Hence, reducing the efficiency of the treatment process, and ultimately lowering the expected leaching improvement. Also, the high reflected microwave power

caused by metallic objects in the ore can cause electrical arcing, which can potentially damage the microwave treatment components, including the magnetron. This necessitates the installation of metal detectors and magnetic separators to remove tramp metals from the ore prior to microwave treatment.

8.4.1 Option 1

The first option for utilising microwave energy in heap leaching operations is illustrated in Figure 8.36. The aim is to reduce ore competency and improve mineral exposure through preferential (selective) breakage along grain boundaries and mineralised veins at the coarsest particle size possible. In this case, crushed materials from the primary crusher (e.g., -100 mm) are microwave pre-treated before being subjected to a secondary crusher to expose internal valuable mineralisation along the fractures induced by microwaves. The secondary crushed materials are screened (e.g., through a 10 mm screen), and the fine particles (-10 mm) are agglomerated to prevent them from blocking the fractures and facilitating effective percolation of the leach solution within the heap, thereby improving leaching performance.

The advantage of this option is that significant fractures are more likely to be induced on ores with mineralised veins and coarse sulphide grains (such as Ores 3 and 4), which have coarse sulphide mineralisation (up to $D_{50}\sim0.5$ mm). This is because the microwave-absorbing grains in the coarse fragments are mostly enclosed within a large volume of microwave-transparent gangue matrix. This texture promotes the effective generation of microwave-induced stresses within the ore, as well as crack propagation through mineralised veins and grain boundaries, as observed in Chapter 7 in the X-ray CT scans of the treated fragments in Ores 4 and 3, potentially lowering comminution energy and improving mineral dissolution. One of the challenges in this flowsheet is that coarse fragments necessitate a large microwave cavity,

which may result in non-homogeneous material treatment if the cavity is not properly designed and integrated with the material handling system, potentially leading to minimal ore fracturing and poor leaching improvement.
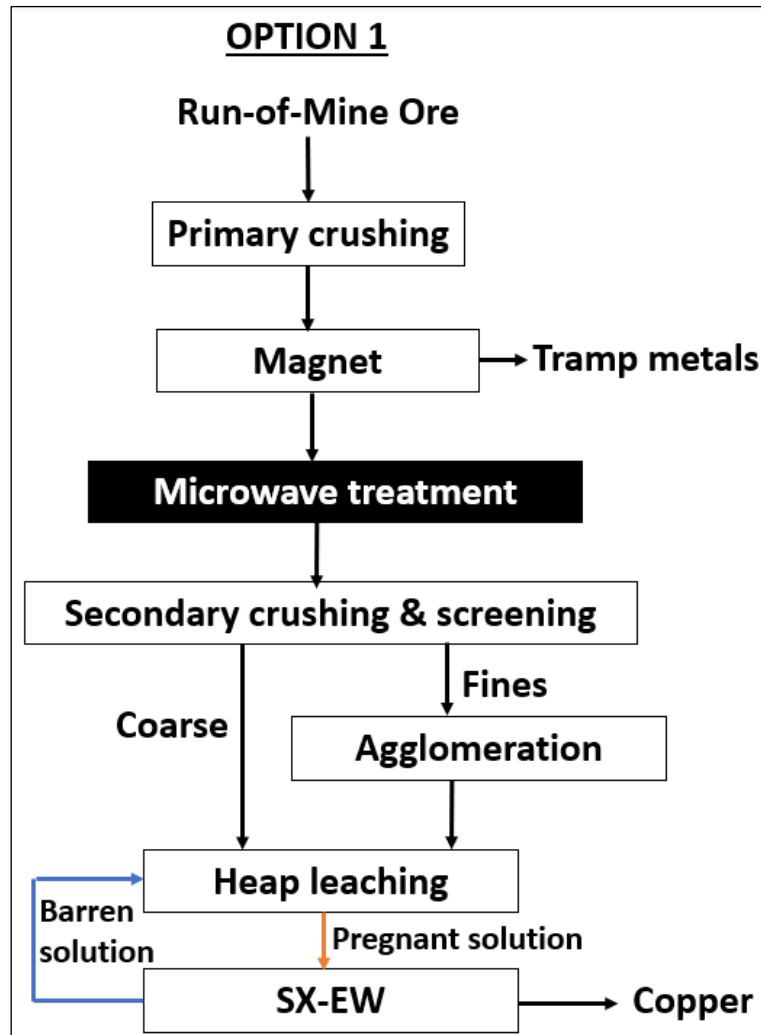
Figure 8.36. Conceptual flowsheet - Option 1

8.4.2 Option 2

Figure 8.37 illustrates the second option for exploiting microwave energy in heap leaching operations. The aim is to improve the leaching performance of crushed materials through microwave-induced fractures (providing leaching pathways) without subsequent comminution processes. In this flowsheet, the secondary crushed materials (for example, 40 mm top size)

are microwave treated followed by screening (e.g., through a 10 mm screen). The fine particles (-10 mm) are agglomerated and then combined with coarse particles prior to leaching. Similar to Option 1, it can be noticed in this circuit that crushed materials are not screened before microwave treatment. The fine particles help to fill the air gaps between coarse fragments during microwave treatment, lowering the possibility of electrical arcing, as described in detail in Section 2.9. As stated in the previous section, the screening and agglomeration stages are performed after microwave treatment to improve the percolation of the leach solution within the heap and prevent blockage of microwave-induced fractures in individual fragments during leaching.
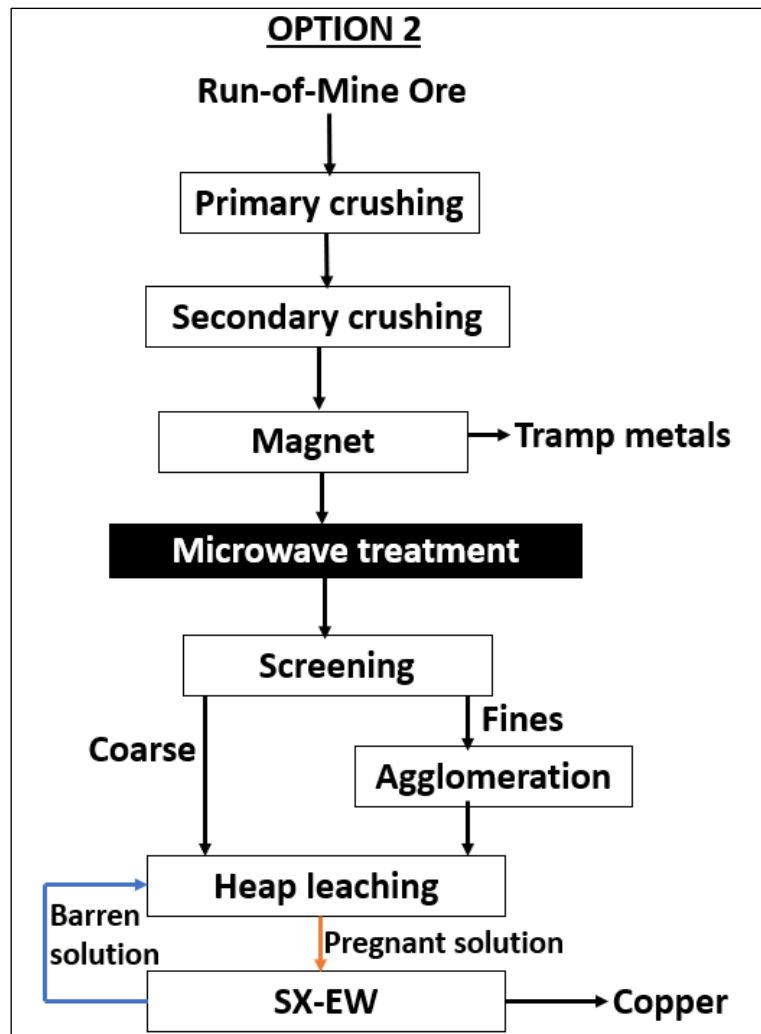
Figure 8.37. Conceptual flowsheet - Option 2

The advantage of this circuit is that higher mineral exposure and leaching improvement can be achieved even with a texture that lacks mineralised veins, such as the one observed in the Ore 1 fragments, which consists of coarse to fine discrete sulphide grains (e.g., $D_{50}<0.19$ mm). However, higher microwave energy and overall comminution energy will most likely be required to achieve the same leaching improvement as that of Option 1 due to a reduced effect of microwave-induced fractures with decreasing particle size.

8.4.3   Option 3

Figure 8.38 illustrates another way of exploiting microwave energy in improving heap leaching operations. The aim is to improve the extent and kinetics of mineral dissolution while also reducing microwave energy consumption by treating a small portion of the feed with microwave-amenable texture properties. This flowsheet incorporates a sorter after the secondary crusher that separates the low- and high-mineralised fragments (including those with high pyrite mineralisation) using sorting techniques, such as X-ray or MW-IR (microwave heating with infrared imaging). The high-mineralised fragments are microwave-treated to improve mineral exposure, then screened (e.g., through a 10 mm screen) and the fine particles agglomerated. Thereafter, the coarse fragments and agglomerated particles are stacked and leached. In contrast, the low-mineralised fragments are not microwave treated before leaching.
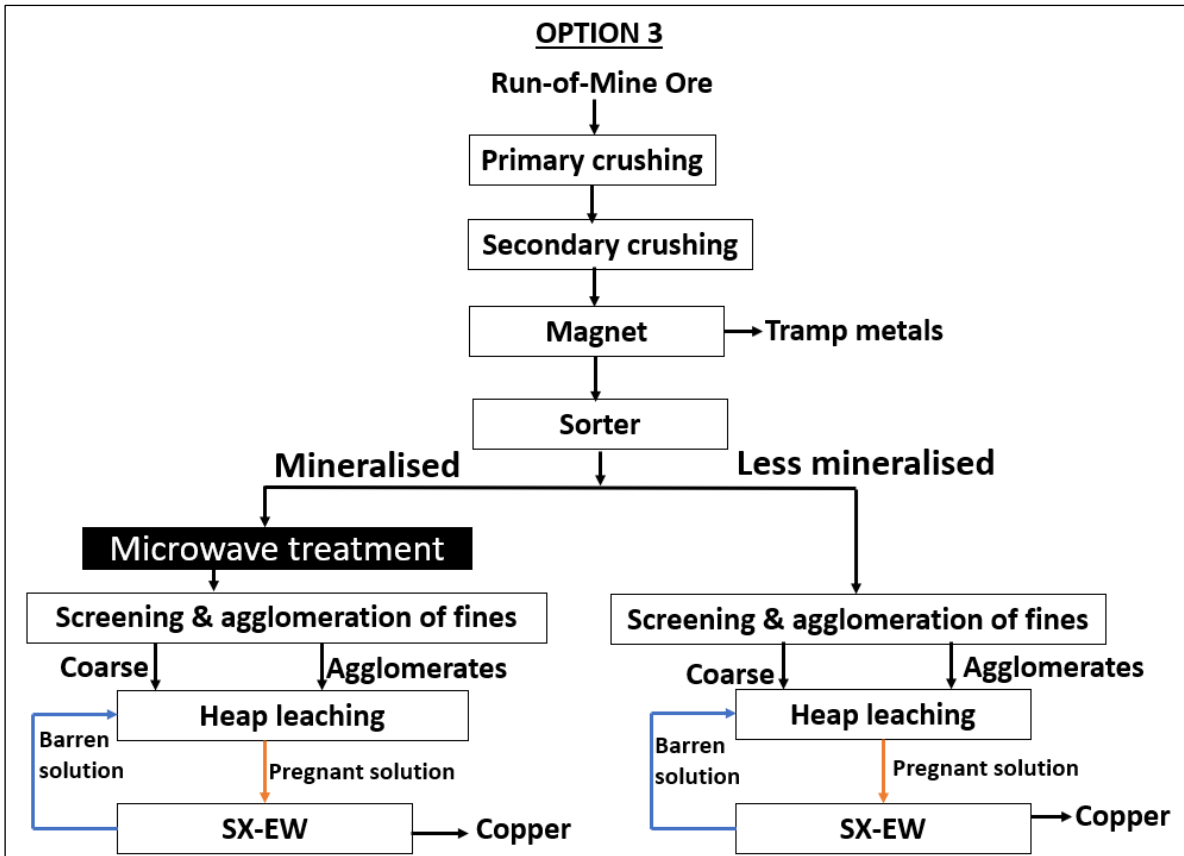
Figure 8.38. Conceptual flowsheet - Option 3

The advantage of this flowsheet is that instead of treating the whole ore, which requires more microwave energy and a larger microwave heating system for effective treatment, only a small portion of the feed with favourable mineralogy and texture properties is treated. Potentially, maximizing leaching performance at relatively low microwave energy input. It can also be noticed in this flowsheet that microwave-treated and untreated materials are leached separately, giving the flexibility to perform multiple leach cycles on treated materials without disrupting the operation of untreated materials (in the case of on-off leach pads), potentially paying back much faster at the start of the operation. This decision is based on the leaching kinetics results presented in Section 8.3.4, which demonstrated that microwave ore pre-treatment can significantly improve mineral leaching kinetics. In the case of permanent leach pads, the treated

and untreated materials can be combined in the screening and agglomeration stages prior to leaching.

The disadvantage of this flowsheet is that a sorter imposes an extra cost (for installation and operation). Also, if the ore contains significantly more hydrated clays than valuable microwave-absorbing minerals, the MW-IR sorter should not be used because these gangue minerals will most likely be misplaced to the high-grade materials due to their better microwave heating response. As a result, the high-grade material is diluted to some extent, lowering copper production. Furthermore, particle presentation to the sorter must be well controlled for effective separation, necessitating monolayer presentation in the case of belt-based sorting systems, which reduces the plant throughput rate and delays the leach cycle, potentially lowering copper production.

Table 8.5 compares and contrasts the proposed conceptual flowsheets for using microwave treatment technology to improve heap leaching operations. The next section highlights the scale-up developments of microwave ore pre-treatment systems since the 2000s. The lessons learnt from those studies, as well as the microwave treatment and leaching results from this dissertation, have been used to propose potential ore treatment systems that can be utilised at the mine to improve heap leaching operations, indicating opportunities and challenges.

Table 8.5. Conceptual flowsheets incorporating microwave ore pre-treatment to improve heap leaching operations

Flowsheet Option	Flowsheet Description Summary	Opportunity	Challenge
1	Microwave treatment is performed on the primary crushed materials (e.g., 100 mm top size). Treated materials are then subjected to a secondary crusher (to expose internal sulphide mineralization along the microwave-induced fractures) prior to leaching.	Significant fractures are more likely to be induced on fragments with mineralized veins and coarse sulphide (including pyrite) grains (for example, $D_{50}\sim0.5$ mm), potentially lowering comminution energy and improving metal leach recovery and kinetics.	Coarse ore fragments necessitate a large microwave cavity system, which may result in non-homogeneous material treatment if the cavity is not properly designed to confine microwave fields (to maximize power delivery), potentially leading to minimal ore fracturing and poor leaching improvement.
2	Microwave treatment is performed on the secondary crushed materials (e.g., 40 mm top size) to induce fractures (which enable deeper penetration of the leach solution) without subsequent comminution processes.	Higher mineral exposure and leaching improvement can be achieved even with a texture that lacks mineralized veins, which consists of coarse to fine discrete sulphide grains (e.g., $D_{50}<0.19$ mm).	Higher microwave energy will most likely be required compared to Option 1 to achieve the same leaching improvement due to a reduced effect of microwave-induced fractures with decreasing particle size.
3	Microwave treatment is performed on a small portion of the secondary crushed materials that have suitable mineralogy and texture properties for microwave-induced fractures, followed by screening/agglomeration before leaching. Unlike Option 2, this flowsheet requires a sorter that separates the mineralized and less-mineralized fragments prior to microwave treatment.	Treating only a small portion of the feed with suitable texture properties lowers microwave energy input and maximizes treatment performance, which leads to significant ore fracturing. Potentially, maximizing leaching recovery and mineral dissolution kinetics.	A sorting system imposes additional costs. Also, particle presentation to the sorter must be well controlled for effective separation, such as monolayer presentation in belt-based sorting systems, which reduces throughput rate and potentially lowers metal production.

8.5 Scale-up Developments - Opportunities and Challenges

As mentioned in the literature review (Chapter 3), studies in microwave treatment of ores to assist comminution have been reported since the 1990s, with the earliest studies published by Walkiewicz et al. (1991;1993). Most of these studies are carried out in small batches (typically <1 kg) using low-intensity multimode applicators (such as standard or modified kitchen microwave ovens) at low powers of less than 3 kW and for longer irradiation times (up to >10 minutes).

For the first time in the 2000s, single mode cavities with higher power levels of up to 15 kW were used for ore pre-treatment to assist comminution (Kingman et al., 2004a; 2004b). The use of single mode cavities demonstrated significant comminution improvements at economically feasible energy inputs (<5 kWh/t) by exposing the sample to high electric field intensity for less than 1 sec. Following this work, the first continuous belt-based treatment system was tested around 2006, in which a microwave-transparent plastic tube containing the ore was instantaneously moved through the applicator (at a throughput equivalent to 10-20 t/h) with a microwave power of up to 30 kW at 2.45 GHz. One of the key learning outcomes from this work was the issue of power spread in conveyor systems and gradual warming of the load, which minimizes the thermal shock and ore fracturing, indicating the importance of confining the electric field within the applicator. One possible solution is to use a vertically aligned tube through which materials flow as a packed bed to interact with well-confined microwave fields.

Around 2010, a pilot-scale treatment system was developed in which ore fragments packed in a vertically aligned tube were moved through the applicator using a belt and pulley system. The key development arising from this work was the design of circular chokes above and below the applicator, which helped to confine the electric field in a relatively small region to minimise gradual warming of the load, thereby maximizing thermal shock and ore fracturing. From 2010 to 2015, a large-scale continuous system capable of treating coarsely crushed ore fragments

(up to 50 mm) at a throughput rate of up to 150 t/hr (yielding 0.1-20 kWh/t) in a laboratory-based environment was designed, constructed, and evaluated by metallurgical testing, as described in the literature review in Section 3.5.4 (Buttress et al., 2017; Batchelor et al., 2017). One of the key learning outcomes from this work was the significance of ensuring that more ore fragments are exposed in a region of higher electric field strength, resulting in more homogeneous and effective treatment. Results showed that a dual treatment system of two single mode applicators connected in series exhibited significant improvements in comminution compared to a single applicator system.

Based on the knowledge gained from these studies, conceptual designs of microwave ore treatment systems are proposed for heap leaching operations, with the possibility of treating a portion of the feed with amenable texture or the whole ore, as described in the previous section.

In the first possibility, a low throughput of 10 t/hr crushed materials (up to 40 mm) is assumed, which is to be treated at a microwave power of 100-200 kW (10-20 kW/t) in order to achieve a significant copper leaching enhancement of 7-28% (absolute) observed on the leaching results. A treatment system consisting of a single mode cavity surrounding a vertically aligned tube can be adopted here to maximise ore fracturing by minimising the gradual warming of the ore during treatment. Based on the size of the fragments of 40 mm (top size), the diameter of the tube is chosen to be 200 mm (i.e., 5 times larger than the coarsest particle size) for effective material flow in the tube. This tube should span the entire width of the applicator to effectively treat all fragments, but this is limited by the waveguide's broad face dimensions in (TE_{10}) single mode cavities. The waveguide dimensions are determined by the ISM frequency of the applied microwave energy. Therefore, a tube diameter of 200 mm requires a waveguide of approximately 248x124 mm (WR975) at 896/915/922 MHz ISM frequency. Currently, the highest power microwave generators available commercially at this frequency are 100 kW. Thus, up to two generators are required to provide 100-200 kW to achieve (10-20 kWh/t), and

these generators should be connected in series to increase the chance of effectively treating more ore fragments.

Another possibility is to treat the whole ore, such as secondary crusher product (40 mm top size), at a higher throughput of 100 t/hr with a microwave power of 1-2 MW to achieve 10-20 kWh/t. Similar to the first conceptual design, a treatment system consisting of a single mode cavity surrounding a vertically aligned tube can be used, using the same tube dimension (200 mm diameter) and microwave frequency (896/915/922 MHz). However, at least ten units of 100 kW are required to achieve 1 MW microwave power. The possible approach is to split the feed to a microwave treatment system composed of 5 treatment tubes, with each tube consisting of two applicators connected in series. This approach reduces plant height and gives the flexibility of operating several units while repairing others in the event of unplanned maintenance, avoiding a complete shutdown. However, a thorough techno-economic analysis should be performed to check the feasibility of this undertaking.

It is important to mention that treating large fragments, such as primary crusher product (e.g., -100 mm), requires a large tube of nearly 500 mm in diameter for the effective flow of such coarse particles. A large waveguide, such as the WR2300, with standard dimensions of 584x292mm at 350/433 MHz ISM frequency, can be chosen to accommodate a cylindrical cavity containing this tube. Since there are currently no high-power (magnetron-based) sources capable of generating up to 1 MW, a new technology using a low microwave frequency of 350/433 MHz should be considered for potential application in the mining industry. In addition to magnetrons, other microwave sources such as klystrons and gyrotrons should be considered in the future due to their ability to generate high microwave power (up to hundreds of kilowatts to a few megawatts), though their power conversion efficiency is lower than that of magnetrons.

8.6 Conclusions

The influence of ore mineralogy and texture on the extent of microwave-induced fractures and subsequent leaching improvement has been investigated using coarse fragments of five copper sulphide ores with varying mineralogy and texture. Five to six pairs of ore fragments, each with similar metal content (copper and/or iron) were selected from each ore type by thermal imaging based on microwave heating response at low power. One fragment from each pair was subjected to microwave treatment before leaching, while the other was leached without treatment. The pairing of fragments was done to reduce the influence of ore head grade variability on leaching results, allowing the effect of microwave ore pre-treatment on leaching performance to be determined. Microwave treatment tests were carried out using a single mode cavity (TE_{10}), and no attempt was made to minimise the microwave treatment energy input. The extent of microwave-induced damage was quantified using the UPV and PLT techniques. Leaching tests were carried out at 65-70°C for 12 hours with aqua regia as a leaching agent, and four aliquot samples were taken to establish the mineral dissolution kinetics.

Results showed that ores with some of these properties exhibited significant fractures and higher leaching improvement: a high modal abundance of microwave heaters (6-14%) containing a certain proportion of stiffer heaters (e.g., pyrite), coarse/clustered grain size of microwave heaters (D_{50} ~0.5-0.6 mm), and consistent texture of microwave-absorbing phases. These ore types exhibited a significant $Is_{(50)}$ strength reduction of 57- 75%, a UPV reduction of about 17-39%, and a leaching enhancement of copper of up to 28% (absolute) at a specific microwave energy input of approximately 10-20 kWh/t. Also, these ores exhibited higher leaching kinetics, reducing the leach duration by a factor of four or more to achieve equivalent metal extraction. This suggests that in heap leaching, multiple leach cycles can be performed on treated materials to achieve the same copper recovery as untreated materials, hence maximising overall copper production. It is also clear that the microwave energy input required

to achieve the observed leaching improvement in the coarse particles is much lower than that used in the small cores tested in Chapter 7 (i.e., 4-8 times lower). This is due to an increased volume of microwave transparent gangue matrix surrounding the microwave-absorbing grains in coarse fragments, which acts as crack propagation sites for microwave-induced thermal stresses.

Several conceptual flowsheets for exploiting microwave-induced fractures to improve leaching of coarsely crushed materials have been proposed. These flowsheets have indicated that microwave treatment systems can potentially be incorporated into existing heap leaching flowsheets by treating the whole ore or a portion of the feed with amenable texture. However, the energy required to achieve significant leaching improvement is relatively higher (10-20 kWh/t), beyond the probable economic range based on comminution energy savings in the crush-grind-float circuit (<5 kWh/t). Such higher energy may require several units of 100 kW generators for ore pre-treatment at a throughput of 100 t/hr or higher. This undertaking requires a thorough techno-economic analysis to assess whether the benefit of microwave ore pre-treatment on leaching kinetics and overall copper extraction outweighs the capital expenditures and energy costs incurred to achieve the observed benefits. Furthermore, in order to understand the true economic value of microwave ore pre-treatment in heap leaching against the crush-grind-float circuit, all stages of metal production should be evaluated (e.g., grinding, flotation, dewatering, and tailings disposal), not just energy savings in comminution.

9. CONCLUSIONS AND FUTURE WORK

Over the past thirty years, studies have demonstrated that microwave energy can potentially reduce ore competency and improve mineral liberation (Walkiewicz et al., 1991; Kingman et al., 2000; Batchelor et al., 2016). Other researchers have shown that microwave treatment of ores can improve leaching performance by increasing mineral exposure to the leach solution through a network of induced fractures (Schmuhl et al. 2011; Charikinya & Bradshaw 2017). However, since these studies only used one copper sulphide ore, the effect of mineralogy and texture on microwave-assisted leaching has not been fully investigated. This research seeks to fill the gap in knowledge by assessing five porphyry copper ores with varying mineralogy and texture. Therefore, for the first time, allowing potential ore candidates for microwave treatment in leaching processes (e.g., heap leaching) to be identified.

The ore characterisation and evaluation performed in Chapter 5 were critical in understanding and predicting the microwave treatment effect on the magnitude of induced fractures and subsequent leaching improvement. The ores were characterised using the Mineral Liberation Analyser (MLA) and X-ray diffraction (XRD) techniques. The key mineralogical and textural features derived from the MLA analysis include: 1. The modal abundance of minerals, 2. The grain size distribution of microwave-absorbent minerals, and 3. The association of microwave-absorbent phases with each other (e.g., copper sulphides with iron sulphides) and with other phases (soft/hard gangue matrix, free space). The XRD analysis was used as an alternative method to quickly check the major mineral phases present in each ore.

Following ore characterisation, the effect of microwave treatment on the extent of ore pre-damage and subsequent leaching improvement was investigated using mixed-size fragments, small-cored fragments, and large-sawn fragments, as described in the following Sections. Finally, the knowledge gained from this investigation allowed recommendations to be made for future research.

9.1 Microwave Treatment of Mixed-Size Fragments (Chapter 6)

The aim of this preliminary work was to evaluate the influence of microwave energy input on the extent of ore pre-damage. Microwave treatment tests were carried out in batches of single or multiple fragments (depending on particle size) at three different microwave energy levels ranging from 2 to 7 kWh/t using a TE_{10} single mode cavity, and the extent of ore pre-damage was quantified using the point load test (PLT) technique. In addition, the broken ore fragments collected from the PLT were crushed using a jaw crusher to evaluate the microwave-induced damage left on these fragments after PLT measurement by comparing the crusher product particle size distributions (PSD) of treated and untreated samples.

The PLT results showed that the extent of ore pre-damage (strength reduction) increases with increasing microwave energy input. As expected, the effect is more pronounced for ores with suitable mineralogy and texture properties for microwave-induced fractures, which demonstrated higher strength reductions of 7-23% at a microwave energy input of approximately 2-7 kWh/t, compared to lower reductions of 0.6-10% achieved by ores with unfavourable texture at the same energy. The best ore candidates in this initial investigation (e.g., Ores 3 and 1) have the following properties: a coarser grain size of microwave heaters (D_{50} = 190-500 µm), a high modal abundance of good microwave heaters (6-7%), and a certain proportion of stiffer microwave heaters (e.g., pyrite) of approximately >3%. This type of mineralogy and texture promotes intense heating and thermal stresses within the ore, resulting in micro/macro-fractures. The presence of stiffer microwave heaters in the ore facilitates the effective transfer of stresses to the gangue matrix even further, resulting in an increased degree of ore fracturing. The effect is more pronounced when the ore contains a hard (brittle) gangue matrix (e.g., quartz) that does not undergo ductile deformation when thermal stresses are induced, and thus more stresses are available for fracture propagation.

The crushing results of Ore 3 fragments showed a slight increase in crusher product fineness from 10% to 20% passing through 4 mm due to microwave treatment. Since this ore exhibited significant microwave-induced damage compared to other ore types (due to higher modal abundance and coarser grain size of microwave heaters), it is possible that the jaw crusher extended some of the induced fractures left after PLT measurements, resulting in a finer size distribution of crushed materials observed in the treated samples. However, the microwave-induced damage left in other ore types (Ores 1, 2, and 5) was not large enough to be detected in the crushing results.

9.2 Microwave Treatment and Leaching of Small Cores (Chapter 7)

This work aimed to assess the influence of ore mineralogy and texture on the extent of microwave-induced fractures and leaching performance using small cores of 21 mm diameter by 19-22 mm height. The cores of similar metal content (copper and/or iron) were paired by thermal imaging based on microwave heating response at low power of 250 Watts (for 10 sec) to minimize the effect of ore grade variation on leaching results. Thereafter, each core was irradiated at a forward power of 1 kW for 6-11 sec in a TE_{10} single mode cavity, and the leaching tests were performed in the 50-mL leaching tubes using aqua regia as a leaching chemical. The high microwave energy input was selected in this investigation to induce macro-factures that can be detected and compared between ore samples (with varying mineralogy and texture properties) using the X-ray Computed Tomography (XRCT) technique; thus, no attempt was made to reduce the microwave energy input.

The use of XRCT imaging in this study enabled non-destructive 3D visualisation and quantification of internal structures of ore specimens (e.g., cracks and sulphide grains). The magnitude of microwave-induced fractures was determined by comparing the fracture size (volume and thickness) of pre-treated and post-treated scans. The disappearance of sulphide grains along the microwave-induced fractures on post-leached scans was linked to the leaching

enhancement (caused by microwave treatment) determined from the ICP assay results. This observation is useful because it provides both qualitative and quantitative information that directly links the magnitude of microwave-induced fractures and the resulting metal recovery improvement.

The results were consistent with those from Chapter 6, showing that ores with favourable mineralogy and texture properties for microwave-induced fractures exhibited significant damage due to microwave treatment. These ore types achieved a crack volume increase of over 500%, larger fracture openings of up to 1.0-2.5 mm wide, and higher UPV reductions of approximately 28-31% as a result of microwave treatment. A close examination of the XRCT images revealed that microwave-induced fractures occur in the vicinity of mineralised regions such as grain boundaries or microveins. In terms of leaching, this fracture pattern improves mineral exposure for lixiviant interaction (via a network of microwave-induced fractures) without further size reduction, or low comminution energy can be applied to expose internal mineralisation through grain boundary fractures induced by microwaves. The post-leached scans revealed that larger (wider) fractures allow deeper acid penetration, facilitating the dissolution of more sulphide grains. A significant copper extraction enhancement of 10-12% (absolute) was achieved for ores with suitable properties for microwave treatment. In contrast, a low copper extraction enhancement of 2% was achieved for ores with unfavourable properties, indicating the importance of mineralogy and texture in the leaching performance of microwave-treated ores.

9.3 Microwave Treatment and Leaching of Large-Sawn Fragments (Chapter 8)

The aim of this work was to assess the effect of microwave treatment on the leaching performance (ultimate extraction and dissolution kinetics) of coarse ore fragments (30-50 mm) in order to identify potential ore candidates for microwave-assisted leaching (e.g., heap leaching). Microwave treatment tests were performed using a single mode cavity (TE_{10}) at 13-

22 kWh/t, with no attempt made to minimise or optimise the microwave energy input. The magnitude of microwave-induced damage was quantified using the UPV and PLT techniques. Leaching tests were carried out in the 400-mL beakers with aqua regia as a leaching chemical, and four aliquot samples were taken over a 12-hour period to evaluate mineral dissolution kinetics.

It was found that ores with some of the following properties achieved more induced fractures and higher leaching improvement, and thus they are more likely to be the best candidates for microwave-assisted heap leaching:

i.   High modal abundance of microwave heaters of up to 5-14% wt.

ii. Containing a certain proportion of stiffer microwave heaters such as pyrite or magnetite of up to 2.8-11%.

iii. Coarse discrete or clustered grains (e.g., microveins) of microwave heaters of up to D_{50} ~0.5-0.6 mm.

iv. High modal abundance of hard (brittle) gangue matrix (e.g., quartz) of at least 45% wt.

v.   Consists of naturally fractured planes (with microwave-absorbing grains deposited in them) that can be exacerbated by microwave-induced thermal stresses.

vi. Consistent texture of microwave-absorbing phases in most fragments.

These ore types achieved a significant strength reduction $Is_{(50)}$ of 57-75%, and a higher UPV reduction of approximately 17-39%. In terms of leaching performance, they demonstrated higher copper dissolution enhancements of up to 28% (absolute) and faster leaching kinetics by reducing leaching time by a factor of four or more to achieve equivalent metal extraction. This was achieved at a microwave energy input of ~10-20 kWh/t, which is significantly lower than that used in the small cores tested in Chapter 7 (i.e., 4-8 times lower) to achieve equivalent leaching improvement. The lower energy consumption in coarse fragments is greatly attributed

to a large volume of microwave transparent gangue matrix surrounding the microwave-absorbing grains in large particles, which serves as crack propagation sites when thermal stresses are induced.

Several conceptual flowsheets that employ microwave heating technology to assist the leaching of copper sulphide ores (coarse fragments) have been proposed. These flowsheets indicate that a microwave treatment unit can potentially be incorporated into an existing heap leaching flowsheet to treat the whole ore or a portion of the feed with amenable texture. Microwave treatment can be performed on the coarsest size possible, such as primary crushed materials (e.g., -100 mm), followed by secondary crushing to expose internal sulphide mineralisation along microwave-induced fractures, thereby improving leaching performance at low comminution energy. Alternatively, microwave treatment can be performed on secondary crushed materials (e.g., 40 mm top size) to induce fractures that serve as leaching pathways into the interior of the particles, improving mineral dissolution without further comminution.

To improve treatment performance, ore fragments must be exposed to a region of high electric field strength for a short duration (a few seconds) to maximise thermal shock. One possible solution is to use a vertically aligned tube through which materials flow as a packed bed to interact with well-confined microwave fields in a TE_{10} single mode cavity. To ensure homogeneous and effective treatment, a dual treatment system of two single mode applicators connected in series can be used.

9.4 Recommendations for Future Research

The results presented in this dissertation show that microwave energy can induce fractures in copper sulphide ores, and that these fractures can enhance metal leach recoveries to varying but also significant degrees, depending on ore mineralogy and texture properties. Although encouraging results were obtained under laboratory conditions, further research work should

be conducted in order to exploit the microwave ore pre-treatment technology in full-scale heap leaching operations.

Higher microwave energy input of 10-20 kWh/t was required to achieve significant copper leaching enhancement of up to 28% in coarse fragments (30-50 mm). However, several units of 100 kW microwave generators may be required to treat ores at higher throughputs (e.g., 100 t/hr) in order to achieve such a higher leaching improvement. A thorough techno-economic analysis should be performed to assess whether the benefit of microwave ore pre-treatment on leaching kinetics and overall copper extraction outweighs the capital expenditures and energy costs incurred to achieve the observed benefits. Further research should also be conducted at lower microwave energies (e.g., <10 kWh/t) to strike a balance between microwave energy consumption and leaching improvement.

Moreover, in order to determine the true economic value of microwave ore pre-treatment in heap leaching versus the crush-grind-float circuit, a thorough techno-economic analysis should be performed in all stages of metal production, including comminution, flotation or metal concentration, dewatering, and tailings disposal.

To maximize treatment efficiency, higher throughput rates (e.g., >100-1000 t/hr) may necessitate multiple cavities, as well as high microwave power sources capable of generating more than 1 MW at 350/433 MHz ISM frequency. Since there are currently no high-power (magnetron-based) sources capable of generating up to 1 MW, other technologies (e.g., klystrons and gyrotrons) should be considered in the future that can potentially be used to generate high microwave powers for treating ores at higher throughputs in mining operations.

The single-particle microwave treatment tests carried out in this study were used to identify potential ore candidates for microwave-assisted leaching. However, the magnitude of microwave-induced fractures and leaching improvement achieved in this study does not

accurately represent the actual performance that can be achieved using multiple fragments. This is because the single fragment was positioned right in the hot spot (at the centre of the TE_{10} single mode cavity), whereas in a bulk sample, fragments are in different electric field intensity zones, with fragments at the periphery of the cavity receiving less microwave dose than those in the centre. As a result, the overall fracture inducement achieved in multiple fragments is lower than in single-fragment testworks. Therefore, further microwave treatment studies should be conducted using bulk samples of multiple fragments, followed by leaching.

The single-particle leach tests were performed using aqua regia to rapidly check the leaching performance of microwave pre-treated ores within a few hours. Since these tests were carried out using high acid strength, the leach recovery enhancement achieved in this research is overestimated to some extent. Therefore, further microwave-assisted leaching studies should be conducted using typical lixiviants for copper sulphide leaching, such as sulphuric acid with ferric chloride as an oxidant, utilizing leach columns to more accurately represent the conditions found in industrial heaps. Several heap-leach design parameters, such as leach solution flowrate application, acid consumption, and leach duration, can be investigated and optimised using column tests. Also, the ore can be inoculated with bacteria in the column tests to improve leaching kinetics, because microwave-induced fractures provide preferential sites for microbial activities, resulting in faster mineral dissolution.

In terms of image analysis, further research should be conducted to determine the extent of mineral exposure caused by microwave treatment, which can be linked to mineral dissolution improvement. In this case, the shortest distance of the mineral grains from the edge of the particle or cracks in the pre-treated and post-treated X-ray CT scanning results can be determined using the distance map techniques (e.g., Euclidean Distance Map - EDM). This helps in effectively quantifying the extent of mineral exposure and leaching improvement resulting from microwave treatment.

10.REFERENCES

Adams, M. (2005). *Advances in gold ore processing* (First Edit). Elsevier.

Agilent. (2005). *Basics of Measuring the Dielectric Properties of Materials Application Note*. *2007*, 1–32.

Ali, A. Y., & Bradshaw, S. M. (2009). Quantifying damage around grain boundaries in microwave treated ores. *Chemical Engineering and Processing: Process Intensification*, *48*(11–12), 1566–1573. https://doi.org/10.1016/j.cep.2009.09.001

Ali, A. Y., & Bradshaw, S. M. (2010). Bonded-particle modelling of microwave-induced damage in ore particles. *Minerals Engineering*, *23*(10), 780–790. https://doi.org/10.1016/j.mineng.2010.05.019

Ali, Abubeker Yimam. (2010). *Understanding the Effects of Mineralogy , Ore Texture and Microwave Power Delivery on Microwave Treatment of Ores*. PhD Thesis - University of Stellenbosch.

Als-Nielsen, J., & McMorrow, D. (2011). *Elements of Modern X-ray Physics. Chapter 1 - X-rays and their Interaction with Matter* (Second Edi). John Wiley & Sons.

Amankwah, R. K., Khan, A. U., Pickles, C. A., & Yen, W. T. (2005). Improved grindability and gold liberation by microwave pretreatment of a free-milling gold ore. *Transactions of the Institutions of Mining and Metallurgy, Section C: Mineral Processing and Extractive Metallurgy*, *114*(1), 30–36. https://doi.org/10.1179/037195505X28447

Amankwah, R. K., & Ofori-Sarpong, G. (2011). Microwave heating of gold ores for enhanced grindability and cyanide amenability. *Minerals Engineering*, *24*(6), 541–544. https://doi.org/10.1016/j.mineng.2010.12.002

Amankwah, R. K., & Ofori-Sarpong, G. (2020). Microwave roasting of flash flotation concentrate containing pyrite, arsenopyrite and carbonaceous matter. *Minerals Engineering*, *151*, 106312.

Amankwah, R. K., & Pickles, C. A. (2009). Microwave roasting of a carbonaceous sulphidic gold concentrate. *Minerals Engineering*, *22*(13), 1095–1101.

Andriese, M. D., Hwang, J. Y., Bell, W., Peng, Z., Upadhyaya, A., & Borkar, S. A. (2011). *Microwave assisted breakage of metallic sulfide bearing ore*.

ASTM. (1995). Standard test method for determination of the point load strength index of rock. *Am. Soc. Test. Mater*, *22*, 1–9.

ASTM E1441, A. (1992). *Standard Guide for Computed Tomography (CT) Imaging, ASTM Designation E 1441-92a. Section 3*(Annual Book of ASTM Standards), 690–713. https://doi.org/10.1520/G0161-00R06.2

Atwater, J. E., & Wheeler Jr, R. R. (2003). Complex permittivities and dielectric relaxation of granular activated carbons at microwave frequencies between 0.2 and 26 GHz. *Carbon*, *41*(9), 1801–1807.

Bain, A. K., & Chand, P. (2017). *Ferroelectrics: Principles and applications. Chapter 1 - Dielectric Properties of Materials*. John Wiley & Sons.

Barani, K., Azadi, M. R., & Moradpouri, F. (2021). Microwave Pretreatment on Copper Sulfide Ore: Comparison of Ball Mill Grinding and Bed Breakage Mechanism. *Mining, Metallurgy & Exploration*, *38*(5), 2209–2216.

Barrett, J. F., & Keat, N. (2004). Artifacts in CT: recognition and avoidance. *Radiographics*, *24*(6), 1679–1691.

Batchelor, A. R. (2013). *Microwave Treatment of Ores*. PhD Thesis - University of Nottingham.

Batchelor, A. R., Buttress, A. J., Jones, D. A., Katrib, J., Way, D., Chenje, T., Stoll, D., Dodds, C., & Kingman, S. W. (2017). Towards large scale microwave treatment of ores: Part 2 – Metallurgical testing. *Minerals Engineering*, *111*(September 2016), 5–24. https://doi.org/10.1016/j.mineng.2017.05.003

Batchelor, A. R., Ferrari-John, R. S., Dodds, C., & Kingman, S. W. (2016). Pilot scale microwave sorting of porphyry copper ores: Part 2 – Pilot plant trials. *Minerals Engineering*, *98*, 328–338. https://doi.org/10.1016/j.mineng.2016.07.009

Batchelor, A. R., Jones, D. A., Plint, S., & Kingman, S. W. (2015). Deriving the ideal ore texture for microwave treatment of metalliferous ores. *Minerals Engineering*, *84*, 116–129. https://doi.org/10.1016/j.mineng.2015.10.007

Batchelor, A. R., Jones, D. A., Plint, S., & Kingman, S. W. (2016). Increasing the grind size for effective liberation and flotation of a porphyry copper ore by microwave treatment. *Minerals Engineering*, *94*, 61–75.

Berry, T. F., & Bruce, R. W. (1966). A simple method of determining the grindability of ores. *Can. Min. J*, *87*, 63–65.

Bilik, V., & Bezek, J. (2010). High power limits of waveguide stub tuners. *Journal of Microwave Power and Electromagnetic Energy*, *44*(4), 178–186.

Bobicki, E. R., Pickles, C. A., Forster, J., Marzoughi, O., & Hutcheon, R. (2020). High temperature permittivity measurements of selected industrially relevant ores: Review and analysis. *Minerals Engineering*, *145*(August 2019), 106055. https://doi.org/10.1016/j.mineng.2019.106055

Bobicki, Erin R., Liu, Q., & Xu, Z. (2018). Microwave treatment of ultramafic nickel ores: Heating behavior, mineralogy, and comminution effects. *Minerals*, *8*(11), 1–19. https://doi.org/10.3390/min8110524

Bond, F. C. (1961). Crushing and grinding calculations. *British Chemical Engineering*, *16*, 543–548.

Borgefors, G., Nyström, I., & Di Baja, G. S. (1997). Connected components in 3D neighbourhoods. *Proceedings of The Scandinavian Conference on Image Analysis*, *2*, 567–572.

Bradshaw, S., Louw, W., Merwe, C. van der, Reader, H., Kingman, S., Celuch, M., & Kijewska, W. (2005). Techno-economic considerations in the commercial microwave processing of mineral ores. *Journal of Microwave Power and Electromagnetic Energy*, *40*(4), 228–240.

Brierley, C. L. (2008). How will biomining be applied in future? *Transactions of Nonferrous Metals Society of China*, *18*(6), 1302–1310.

British-Standards. (2011). *BSI Standards Publication Safety in electroheat installations*. *BS EN 60519-6:2011*.

Broch, E., & Franklin, J. A. (1972). The point-load strength test. *International Journal of Rock Mechanics and Mining Sciences & Geomechanics*, *9*(6), 669–676.

Brook, N. (1985). The equivalent core diameter method of size and shape correction in point load testing. *International Journal of Rock Mechanics and Mining Sciences And*, *22*(2), 61–70. https://doi.org/10.1016/0148-9062(85)92328-9

Bunaciu, A. A., UdriŞTioiu, E. G., & Aboul-Enein, H. Y. (2015). X-ray diffraction: instrumentation and applications. *Critical Reviews in Analytical Chemistry*, *45*(4), 289–299.

Bushberg, J. T. (1998). The AAPM/RSNA physics tutorial for residents. X-ray interactions. *Radiographics*, *18*(2), 457–468.

Buttress, A. J., Katrib, J., Jones, D. A., Batchelor, A. R., Craig, D. A., Royal, T. A., Dodds, C., & Kingman, S. W. (2017). Towards large scale microwave treatment of ores: Part 1 – Basis of design, construction and commissioning. *Minerals Engineering*, *109*, 169–183. https://doi.org/10.1016/j.mineng.2017.03.006

Cai, X., Qian, G., Zhang, B., Chen, Q., & Hu, C. (2018). Selective liberation of high-phosphorous oolitic hematite assisted by microwave processing and acid leaching [Article]. *Minerals*, *8*(6). https://doi.org/10.3390/min8060245

Catalá-Civera, J. M., Soto, P., Boria, V. E., Balbastre, J. V, & de los Reyes, E. (2006). Design parameters of multiple reactive chokes for open ports in microwave heating systems. In *Advances in Microwave and Radio Frequency Processing* (pp. 39–47). Springer.

Charikinya, E., Bradshaw, S., & Becker, M. (2015). Characterising and quantifying microwave induced damage in coarse sphalerite ore particles. *Minerals Engineering*, *82*, 14–24. https://doi.org/10.1016/j.mineng.2015.07.020

Charikinya, E., & Bradshaw, S. M. (2017). An experimental study of the effect of microwave treatment on long term bioleaching of coarse, massive zinc sulphide ore particles. *Hydrometallurgy*, *173*(August), 106–114. https://doi.org/10.1016/j.hydromet.2017.08.001

Chen, T. T., Dutrizac, J. E., Haque, K. E., Wyslouzil, W., & Kashyap, S. (1984). The relative transparency of minerals to microwave radiation. *Canadian Metallurgical Quarterly*, *23*(3), 349–351.

Cheremisinoff, N. P. (1989). *Handbook of polymer science and technology* (Vol. 4). CRC Press.

Cherevko, S., & Mayrhofer, K. J. J. (2018). *On-Line Inductively Coupled Plasma Spectrometry in Electrochemistry: Basic Principles and Applications*.

Choi, N.-C., Kim, B.-J., Cho, K., Lee, S., & Park, C.-Y. (2017). Microwave pretreatment for thiourea leaching for gold concentrate. *Metals*, *7*(10), 404.

Chunpeng, L., Yousheng, X., & Yixin, H. (1990). Application of microwave radiation to extractive metallurgy. *China. J. Met. Sci. Technol., 6, 2, Pp.121–124.*, *2*, 121–124.

Church, R. H., Webb, W. E., & Salsman, J. B. (1988). *Dielectric properties of low-loss*

minerals (Vol. 9194). US Department of the Interior.

Clark, D. E., Folz, D. C., & West, J. K. (2000). Processing materials with microwave energy. *Materials Science and Engineering: A*, *287*(2), 153–158.

Clark, D. E., & Sutton, W. H. (1996). Microwave processing of materials. *Annual Review of Materials Science*, *26*(1), 299–331.

CNS Farnell. (2006). *Operating Instructions PUNDIT7 Model PC1012*.

Cnudde, V., & Boone, M. N. (2013). High-resolution X-ray computed tomography in geosciences: A review of the current technology and applications. *Earth-Science Reviews*, *123*, 1–17.

Collin, R. E. (2007). Foundations for Microwave Engineering. In *Electronics and Power* (Vol. 13, Issue 1). The Institute of Electrical and Electronics Engineers. Inc., New York. https://doi.org/10.1049/ep.1967.0023

Crundwell, F. K. (1995). Progress in the mathematical modelling of leaching reactors. *Hydrometallurgy*, *39*(1–3), 321–335.

Cumbane, A. J. (2003). *Microwave treatment of mirerals and Ores*. PhD Thesis - University of Nottingham.

Davis, G. R., & Elliott, J. C. (2006). Artefacts in X-ray microtomography of materials. *Materials Science and Technology*, *22*(9), 1011–1018.

De Winter, J. C. F. (2013). Using the Student's t-test with extremely small sample sizes. *Practical Assessment, Research, and Evaluation*, *18*(1), 10.

Der Sarkissian, H., Lucka, F., van Eijnatten, M., Colacicco, G., Coban, S. B., & Batenburg, K. J. (2019). A cone-beam X-ray computed tomography data collection designed for machine learning. *Scientific Data*, *6*(1), 1–8.

Dixon, D. G., & Tshilombo, A. F. (2010). *Leaching process for copper concentrates* (Patent No. US 7,846,233 B2). United states patent.

Djordjevic, N. (2014). Recovery of copper sulphides mineral grains at coarse rock fragments size. *Minerals Engineering*, *64*, 131–138.

Dobson, K. J., Harrison, S. T. L., Lin, Q., Ní Bhreasail, A., Fagan-Endres, M. A., Neethling, S. J., Lee, P. D., & Cilliers, J. J. (2017). Insights into ferric leaching of low grade metal sulfide-containing ores in an unsaturated ore bed using X-ray computed tomography. *Minerals*, *7*(5), 85.

Dutrizac, J. E. (1989). Elemental sulphur formation during the ferric sulphate leaching of chalcopyrite. *Canadian Metallurgical Quarterly*, *28*(4), 337–344.

Dutrizac, J. E., & MacDonald, R. J. C. (1974). Ferric ion as a leaching medium. *Minerals Science and Engineering*, *6*(2), 59–95.

Elshkaki, A., Graedel, T. E., Ciacci, L., & Reck, B. K. (2016). Copper demand, supply, and associated energy use to 2050. *Global Environmental Change*, *39*, 305–315.

Elton, L. R. B., & Jackson, D. F. (1966). X-ray diffraction and the Bragg law. *American Journal of Physics*, *34*(11), 1036–1038.

Ferrari-John, R. S., Batchelor, A. . ., Katrib, J., Dodds, C., & Kingman, S. W. (2016).

Understanding selectivity in radio frequency and microwave sorting of porphyry copper ores. *International Journal of Mineral Processing*, *155*, 64–73.

Fonseca, J. (2011). *The evolution of morphology and fabric of a sand during shearing*. PhD Thesis - Imperial College London.

Ford, J. D., & Pei, D. C. T. (1967). High temperature chemical processing via microwave absorption. *Journal of Microwave Power*, *2*(2), 61–64.

Fraser, K. S., Walton, R. H., & Wells, J. A. (1991). Processing of refractory gold ores. *Minerals Engineering*, *4*(7–11), 1029–1041.

Garcia, D., Lin, C. L., & Miller, J. D. (2009). Quantitative analysis of grain boundary fracture in the breakage of single multiphase particles using X-ray microtomography procedures. *Minerals Engineering*, *22*(3), 236–243. https://doi.org/10.1016/j.mineng.2008.07.005

Ghadiri, M., Harrison, S. T. L., & Fagan-Endres, M. A. (2020). Quantitative X-ray µCT Measurement of the Effect of Ore Characteristics on Non-Surface Mineral Grain Leaching. *Minerals*, *10*(9), 746.

Ghorbani, Y., Becker, M., Mainza, A., Franzidis, J. P., & Petersen, J. (2011). Large particle effects in chemical/biochemical heap leach processes - A review. *Minerals Engineering*, *24*(11), 1172–1184. https://doi.org/10.1016/j.mineng.2011.04.002

Ghorbani, Y., Becker, M., Petersen, J., Mainza, A. N., & Franzidis, J. P. (2013b). Investigation of the effect of mineralogy as rate-limiting factors in large particle leaching. *Minerals Engineering*, *52*, 38–51. https://doi.org/10.1016/j.mineng.2013.03.006

Ghorbani, Y., Petersen, J., Becker, M., Mainza, A. N., & Franzidis, J.-P. (2013a). Investigation and modelling of the progression of zinc leaching from large sphalerite ore particles. *Hydrometallurgy*, *131*, 8–23.

Goh, T. Y., Basah, S. N., Yazid, H., Safar, M. J. A., & Saad, F. S. A. (2018). Performance analysis of image thresholding: Otsu technique. *Measurement*, *114*, 298–307.

Gupta, M., & Leong, E. W. W. (2008). *Microwaves and metals*. John Wiley & Sons.

Haase, J. R., & Go, D. B. (2016). Analysis of thermionic and thermo-field emission in microscale gas discharges. *Journal of Physics D: Applied Physics*, *49*(5), 55206.

Hafner, B. (2007). Scanning electron microscopy primer. *Characterization Facility, University of Minnesota-Twin Cities*, 1–29.

Haque, K E. (1987). Microwave irradiation pretreatment of a refractory gold concentrate. In *Proceedings of the Metallurgical Society of the Canadian Institute of Mining and Metallurgy* (pp. 327–339). Elsevier.

Haque, Kazi E. (1999). Microwave energy for mineral treatment processes—a brief review. *International Journal of Mineral Processing*, *57*(1), 1–24.

Harder, J. (2020). *Trends in the mining industry - AT Mineral Processing*. https://www.at-minerals.com/en/artikel/at_Trends_in_der_Minenindustrie-3596021.html, viewed 20th October 2022

He, C., Zhao, J., Su, X., Ma, S., Fujita, T., Wei, Y., Yang, J., & Wei, Z. (2021). Thermally Assisted Grinding of Cassiterite Associated with Pollimetallic Ore: A Comparison

between Microwave and Conventional Furnaces. *Minerals*, *11*(7), 768.

Hellier, C. J. (2003). *Handbook of Nondestructive Evaluation, Chapter 7 - Ultrasonic Testing*. The McGraw-Hill Companies.

Helliwell, J. R., Sturrock, C. J., Grayling, K. M., Tracy, S. R., Flavel, R. J., Young, I. M., Whalley, W. R., & Mooney, S. J. (2013). Applications of X-ray computed tomography for examining biophysical interactions and structural development in soil systems: a review. *European Journal of Soil Science*, *64*(3), 279–297.

Helm, M., Vaughan, J., Staunton, W. P., & Avraamides, J. (2009). An investigation of the carbonaceous component of preg-robbing gold ores. *World Gold Conference*, 139–144.

Heneka, M. J. (2019). SEM-EDX Guide for Buyers, Chapter 3 - Imaging and Spectroscopy Detectors. *RJL Micro & Analytic GmbH*, *c*, 1–4.

Hildebrand, T., & Rüegsegger, P. (1997). A new method for the model-independent assessment of thickness in three-dimensional images. *Journal of Microscopy*, *185*(1), 67–75.

Hotta, M., Hayashi, M., Lanagan, M. T., Agrawal, D. K., & Nagata, K. (2011). Complex permittivity of graphite, carbon black and coal powders in the ranges of X-band frequencies (8.2 to 12.4 GHz) and between 1 and 10 GHz. *ISIJ International*, *51*(11), 1766–1772.

Hotta, M., Hayashi, M., Nishikata, A., & Nagata, K. (2009). Complex permittivity and permeability of SiO2 and Fe3O4 powders in microwave frequency range between 0.2 and 13.5 GHz. *ISIJ International*, *49*(9), 1443–1448.

Hua, Y., Cai, C., & Cui, Y. (2006). Microwave-enhanced roasting of copper sulfide concentrate in the presence of CaCO3. *Separation and Purification Technology*, *50*(1), 22–29.

Hua, Y., & Liu, C. (1996). Heating rate of minerals and compounds in microwave field. *Transactions-Nonferrous Metals Society of China-English Edition*, *6*, 35–40.

Huang, L., Lai, H., Lu, C., Fang, M., Ma, W., Xing, P., Li, J., & Luo, X. (2016). Enhancement in extraction of boron and phosphorus from metallurgical grade silicon by copper alloying and aqua regia leaching. *Hydrometallurgy*, *161*, 14–21.

ICSG. (2021). The World Copper Factbook 2021. *International Copper Study Group*, 63. http://www.icsg.org/

Jenike, A. W. (1964). Storage and flow of solids. *Bulletin No. 123, Utah State University*.

Jiawang, H. A. O., Qingwen, L. I., Lan, Q., & Naifu, D. (2020). Effects of microwave irradiation on impact comminution and energy absorption of magnetite ore. *IOP Conference Series: Earth and Environmental Science*, *570*(5), 52003.

Jin, J., Han, Y., Li, H., Huai, Y., Peng, Y., Gu, X., & Yang, W. (2019). Mineral phase and structure changes during roasting of fine-grained carbonaceous gold ores and their effects on gold leaching efficiency. *Chinese Journal of Chemical Engineering*, *27*(5), 1184–1190.

Jones, D. A., Kingman, S. W., Whittles, D. N., & Lowndes, I. S. (2005). Understanding microwave assisted breakage. *Minerals Engineering*, *18*(7), 659–669.

https://doi.org/10.1016/j.mineng.2004.10.011

Jones, D. A., Kingman, S. W., Whittles, D. N., & Lowndes, I. S. (2007). The influence of microwave energy delivery method on strength reduction in ore samples. *Chemical Engineering and Processing: Process Intensification*, *46*(4), 291–299. https://doi.org/10.1016/j.cep.2006.06.009

Jones, Dafydd Aled. (2005a). *Understanding microwave treatment of ores*. *November*. http://etheses.nottingham.ac.uk/2161/

Jones, Dafydd Aled. (2005b). *Understanding microwave treatment of ores* [Unknown]. *November*. http://etheses.nottingham.ac.uk/2161/

Kapur, J. N., Sahoo, P. K., & Wong, A. K. C. (1985). A new method for gray-level picture thresholding using the entropy of the histogram. *Computer Vision, Graphics, and Image Processing*, *29*(3), 273–285.

Karjodkar, F. R. (2019). *Essentials of oral & maxillofacial radiology. Chapter 4 - Production of X-rays*. Jaypee Brothers Medical Publishers.

Ketcham, R. A., & Carlson, W. D. (2001). Acquisition, optimization and interpretation of x-ray computed tomographic imagery: Applications to the geosciences. *Computers and Geosciences*, *27*(4), 381–400. https://doi.org/10.1016/S0098-3004(00)00116-3

Kingman, S. W., Jackson, K., Bradshaw, S. M., Rowson, N. A., & Greenwood, R. (2004a). An investigation into the influence of microwave treatment on mineral ore comminution. *Powder Technology*, *146*(3), 176–184.

Kingman, S. W., Jackson, K., Cumbane, A., Bradshaw, S. M., Rowson, N. A., & Greenwood, R. (2004b). Recent developments in microwave-assisted comminution. *International Journal of Mineral Processing*, *74*(1–4), 71–83. https://doi.org/10.1016/j.minpro.2003.09.006

Kingman, S. W., Vorster, W., & Rowson, N. A. (2000). Influence of mineralogy on microwave assisted grinding. *Minerals Engineering*, *13*(3), 313–327. https://doi.org/10.1016/S0892-6875(00)00010-8

Kitchen, R. (2001). *RF and microwave radiation safety*. Butterworth - Heinemann.

Klauber, C. (2008). A critical review of the surface chemistry of acidic ferric sulphate dissolution of chalcopyrite with regards to hindered dissolution. *International Journal of Mineral Processing*, *86*(1–4), 1–17.

Kobusheshe, J. (2010). *Microwave Enhanced Processing of Ores*. PhD Thesis - University of Nottingham.

Kocabag, D., & Smith, M. R. (1985). The effect of grinding media and galvanic interactions upon the flotation of sulfide minerals. *Complex Sulfides--Processing of Ores, Concentrates and By-Products*, 55–81.

Kodali, P., Dhawan, N., Depci, T., Lin, C. L., & Miller, J. D. (2011). Particle damage and exposure analysis in HPGR crushing of selected copper ores for column leaching. *Minerals Engineering*, *24*(13), 1478–1487. https://doi.org/10.1016/j.mineng.2011.07.010

Kojovic, T., Michaux, S. P., & Walters, S. (2010). Development of new comminution testing

methodologies for geometallurgical mapping of ore hardness and throughput. *XXV International Mineral Processing Congress 2010, IMPC 2010*, *2*, 891–899.

Koleini, S. M. J., & Barani, K. (2008). The effect of microwave radiation upon grinding energy of an iron ore. *Microwave Technology Conference, Cape Town, South Africa*.

Komnitsas, C., & Pooley, F. D. (1989). Mineralogical characteristics and treatment of refractory gold ores. *Minerals Engineering*, *2*(4), 449–457.

Konstantinidis, K., Sirakoulis, G. C., & Andreadis, I. (2009). Ant Colony Optimization for Use in Content Based Image Retrieval. In *Handbook of Research on Artificial Immune Systems and Natural Computing: Applying Complex Adaptive Technologies* (pp. 384–404). IGI Global.

Krautkrämer, J., & Krautkrämer, H. (2013). *Ultrasonic testing of materials*. Springer Science & Business Media.

Kruth, J. P., Bartscher, M., Carmignato, S., Schmitt, R., De Chiffre, L., & Weckenmann, A. (2011). Computed tomography for dimensional metrology. *CIRP Annals*, *60*(2), 821–842.

Kumar, P., Sahoo, B. K., De, S., Kar, D. D., Chakraborty, S., & Meikap, B. C. (2010). Iron ore grindability improvement by microwave pre-treatment. *Journal of Industrial and Engineering Chemistry*, *16*(5), 805–812. https://doi.org/10.1016/j.jiec.2010.05.008

Kyle, J. R., & Ketcham, R. A. (2015). Application of high resolution X-ray computed tomography to mineral deposit origin, evaluation, and processing. *Ore Geology Reviews*, *65*(P4), 821–839. https://doi.org/10.1016/j.oregeorev.2014.09.034

La Brooy, S. R., Linge, H. G., & Walker, G. S. (1994). Review of gold extraction from ores. *Minerals Engineering*, *7*(10), 1213–1241.

Li, H., Long, H., Zhang, L., Yin, S., Li, S., Zhu, F., & Xie, H. (2020). Effectiveness of microwave-assisted thermal treatment in the extraction of gold in cyanide tailings. *Journal of Hazardous Materials*, *384*, 121456.

Li, H., Peng, J., Ma, P., Zhou, Z., Long, H., Li, S., & Zhang, L. (2021). Application of diagnostic roasting method in thermochemical treatment for Au recovery from gold-containing tailings in microwave field. *Minerals Engineering*, *163*, 106773.

Li, Y., Kawashima, N., Li, J., Chandra, A. P., & Gerson, A. R. (2013). A review of the structure, and fundamental mechanisms and kinetics of the leaching of chalcopyrite. *Advances in Colloid and Interface Science*, *197*, 1–32.

Limentani, G. B., Ringo, M. C., Ye, F., Bergquist, M. L., & McSorley, E. O. (2005). *Beyond the t-test: statistical equivalence testing*. ACS Publications.

Lin, Q., Neethling, S. J., Courtois, L., Dobson, K. J., & Lee, P. D. (2016). Multi-scale quantification of leaching performance using X-ray tomography. *Hydrometallurgy*, *164*, 265–277.

Maier, A., Steidl, S., Christlein, V., & Hornegger, J. (2018). *Medical imaging systems: An introductory guide*.

Makins, S. R. (2014). Artifacts interfering with interpretation of cone beam computed tomography images. *Dental Clinics*, *58*(3), 485–495.

Marion, C., Jordens, A., Maloney, C., Langlois, R., & Waters, K. E. (2016). Effect of microwave radiation on the processing of a Cu-Ni sulphide ore. *Canadian Journal of Chemical Engineering*, *94*(1), 117–127. https://doi.org/10.1002/cjce.22359

Marsden, J., & House, I. (2006). *The chemistry of gold extraction*. Society for Mining, Metallurgy and Exploration, Inc (SME).

Mavko, G., Mukerji, T., & Dvorkin, J. (2009). *The Rock Physics Handbook*. Cambridge University Press.

McGill, S. L., Walkiewicz, J. W., & Smyres, G. A. (1988). The effects of power level on the microwave heating of selected chemicals and minerals. *MRS Online Proceedings Library (OPL)*, *124*.

Mehdizadeh, M. (2015). Microwave/RF Applicators and Probes for Material Heating, Sensing, and Plasma Generation: Second Edition. In *Microwave/RF Applicators and Probes for Material Heating, Sensing, and Plasma Generation: Second Edition*. https://doi.org/10.1016/C2014-0-00010-X

Meng, B., Booske, J., & Cooper, R. (1995). Extended cavity perturbation technique to determine the complex permittivity of dielectric materials. *IEEE Transactions on Microwave Theory and Techniques*, *43*(11), 2633–2636.

Meredith, R. (1998). Engineers' Handbook of Industrial Microwave Heating. In *Engineers' Handbook of Industrial Microwave Heating*. https://doi.org/10.1049/pbpo025e

Metaxas, A. C., & Meredith, R. J. (1983). *Industrial microwave heating* (Issue 4). IEE Power Engineering.

Michael, G. (2001). X-ray computed tomography. *Physics Education*, *36*(6), 442.

Microwaves101. (2011). *Directional couplers*. https://www.microwaves101.com/encyclopedias/directional-couplers, viewed 10th January 2023.

Mishra, R. R., & Sharma, A. K. (2016). Microwave–material interaction phenomena: heating mechanisms, challenges and opportunities in material processing. *Composites Part A: Applied Science and Manufacturing*, *81*, 78–97.

Mohammed, A., & Abdullah, A. (2018). Scanning electron microscopy (SEM): A review. *Proceedings of the 2018 International Conference on Hydraulics and Pneumatics— HERVEX, Băile Govora, Romania*, 7–9.

Montgomery, D. C., Runger, G. C., & Hubele, N. F. (2009). *Engineering statistics*. John Wiley & Sons.

Moore, W. C. (1911). Aqua Regia: Preliminary Paper. *Journal of the American Chemical Society*, *33*(7), 1091–1099.

Müller, P., Hiller, J., Dai, Y., Andreasen, J. L., Hansen, H. N., & De Chiffre, L. (2015). Quantitative analysis of scaling error compensation methods in dimensional X-ray computed tomography. *CIRP Journal of Manufacturing Science and Technology*, *10*, 68–76.

Murray, R. W., Miller, D. J., & Kryc, K. A. (2000). *Analysis of major and trace elements in rocks, sediments, and interstitial waters by inductively coupled plasma–atomic emission*

spectrometry (ICP-AES).

Nanthakumar, B., Pickles, C. A., & Kelebek, S. (2007). Microwave pretreatment of a double refractory gold ore. *Minerals Engineering*, *20*(11), 1109–1119. https://doi.org/10.1016/j.mineng.2007.04.003

Napier-Munn, T. J., Morrell, S., Morrison, R. D., & Kojovic, T. (1996). *Mineral comminution circuits: their operation and optimisation.*

Nave, C. R. (2021). *The Magnetron. Department of Physics and Astronomy, Georgia State University*. http://hyperphysics.phyastr.gsu.edu/hbase/Waves/magnetron.html, viewed 22nd August 2021.

Nelson, S. O. (1994). Measurement of microwave dielectric properties of particulate materials. *Journal of Food Engineering*, *21*(3), 365–384.

Nelson, S. O. (2006). Agricultural applications of dielectric measurements. *IEEE Transactions on Dielectrics and Electrical Insulation*, *13*(4), 688–702.

Nikl, M. (2006). Scintillation detectors for x-rays. *Measurement Science and Technology*, *17*(4), R37.

Olubambi, P. A. (2009). Influence of microwave pretreatment on the bioleaching behaviour of low-grade complex sulphide ores. *Hydrometallurgy*, *95*(1–2), 159–165. https://doi.org/10.1016/j.hydromet.2008.05.043

Olubambi, P. A., Potgieter, J. H., Hwang, J. Y., & Ndlovu, S. (2007). Influence of microwave heating on the processing and dissolution behaviour of low-grade complex sulphide ores. *Hydrometallurgy*, *89*(1–2), 127–135. https://doi.org/10.1016/j.hydromet.2007.07.010

Omran, M., Fabritius, T., & Mattila, R. (2015). Thermally assisted liberation of high phosphorus oolitic iron ore: A comparison between microwave and conventional furnaces. *Powder Technology*, *269*, 7–14. https://doi.org/10.1016/j.powtec.2014.08.073

Orumwense, O. A., Negeri, T., & Lastra, R. (2004). Effect of microwave pretreatment on the liberation characteristics of a massive sulfide ore. *Mining, Metallurgy & Exploration*, *21*(2), 77–85.

Otsu, N. (1979). A threshold selection method from gray-level histograms. *IEEE Transactions on Systems, Man, and Cybernetics*, *9*(1), 62–66.

Pandey, S., & Bright, C. L. (2008). What are degrees of freedom? *Social Work Research*, *32*(2), 119–128.

Peng, Z., & Hwang, J.-Y. (2015). Microwave-assisted metallurgy. *International Materials Reviews*, *60*(1), 30–63.

Petersen, J. (2016). Heap leaching as a key technology for recovery of values from low-grade ores–A brief overview. *Hydrometallurgy*, *165*, 206–212.

Pickles, C. A., Mouris, J., & Hutcheon, R. M. (2005). High-temperature dielectric properties of goethite from 400 to 3000 MHz. *Journal of Materials Research*, *20*(1), 18–29.

Pickles, C., & Lu, T. (2022). Microwave Dewatering of Gibbsite-Type Bauxite Ores: Permittivities, Heating Behavior and Strength Indices. *Minerals*, *12*(5), 648.

Powell, M., & Bye, A. (2009). Beyond mine-to-mill: Circuit design for energy efficient resource utilisation. *Tenth Mill Operators Conference 2009, Proceedings*, *11*, 357–364.

Pridmore, D. F., & Shuey, R. T. (1976). The electrical resistivity of galena, pyrite, and chalcopyrite. *American Mineralogist*, *61*(3–4), 248–259.

Pszonka, J., & Sala, D. (2018). Application of the mineral liberation analysis (MLA) for extraction of grain size and shape measurements in siliciclastic sedimentary rocks. *E3S Web of Conferences*, *66*, 2002.

Pyke, B. L., Johnston, R. F., & Brooks, P. (1999). The characterisation and behaviour of carbonaceous material in a refractory gold bearing ore. *Minerals Engineering*, *12*(8), 851–862.

Reyes, F., Lin, Q., Udoudo, O., Dodds, C., Lee, P. D., & Neethling, S. J. (2017). Calibrated X-ray micro-tomography for mineral ore quantification. *Minerals Engineering*, *110*(January), 122–130. https://doi.org/10.1016/j.mineng.2017.04.015

Rizmanoski, V. (2011). The effect of microwave pretreatment on impact breakage of copper ore. *Minerals Engineering*, *24*(14), 1609–1618. https://doi.org/10.1016/j.mineng.2011.08.017

Robinson, D. W. (2008). Entropy and uncertainty. *Entropy*, *10*(4), 493–506.

Rötzer, N., & Schmidt, M. (2018). Decreasing metal ore grades—is the fear of resource depletion justified? *Resources*, *7*(4), 88.

Rouquerol, J., Baron, G. V., Denoyel, R., Giesche, H., Groen, J., Klobes, P., Levitz, P., Neimark, A. V., Rigby, S., Skudas, R., Sing, K., Thommes, M., & Unger, K. (2012). The characterization of macroporous solids: An overview of the methodology. *Microporous and Mesoporous Materials*, *154*, 2–6. https://doi.org/10.1016/j.micromeso.2011.09.031

Sahyoun, C., Kingman, S.W., Rowson, N. A. (2004). High powered microwave treatment of carbonate copper ore. *European Journal of Mineral Processing and Environmental Protection*, *4*(3), 175–182.

Salsman, J. B., Williamson, R. L., Tolley, W. K., & Rice, D. A. (1996). Short-pulse microwave treatment of disseminated sulfide ores. *Minerals Engineering*, *9*(1), 43–54.

Scarfe, W. C., & Farman, A. G. (2008). What is cone-beam CT and how does it work? *Dental Clinics of North America*, *52*(4), 707–730.

Schmuhl, R., Smit, J. T., & Marsh, J. H. (2011). The influence of microwave pre-treatment of the leach behaviour of disseminated sulphide ore. *Hydrometallurgy*, *108*(3–4), 157–164. https://doi.org/10.1016/j.hydromet.2011.04.001

Schneider, C. A., Rasband, W. S., & Eliceiri, K. W. (2012). NIH Image to ImageJ: 25 years of image analysis. *Nature Methods*, *9*(7), 671–675.

Schulze, R., Heil, U., Groß, D., Bruellmann, D. D., Dranischnikow, E., Schwanecke, U., & Schoemer, E. (2011). Artefacts in CBCT: a review. *Dentomaxillofacial Radiology*, *40*(5), 265–273.

Schwenk, K., & Huber, F. (2015). Connected component labeling algorithm for very complex and high-resolution images on an FPGA platform. *High-Performance Computing in*

Remote Sensing V, *9646*, 9–22.

Scott, G. (2006). *Microwave pretreatment of a low grade copper ore to enhance milling performance and liberation*. Master's Thesis: University of Stellenbosch.

Seibert, J. A. (2004). X-ray imaging physics for nuclear medicine technologists. Part 1: Basic principles of x-ray production. *Journal of Nuclear Medicine Technology*, *32*(3), 139–147.

Semenov, V. E., & Zharova, N. A. (2006). Thermal runaway and hot spots under controlled microwave heating. In *Advances in Microwave and Radio Frequency Processing* (pp. 482–490). Springer.

Shannon, C. E., & Weaver, W. (1949). The mathematical theory of communication. University of Illinois. *Urbana*, *117*.

Shefer, E., Altman, A., Behling, R., Goshen, R., Gregorian, L., Roterman, Y., Uman, I., Wainer, N., Yagil, Y., & Zarchin, O. (2013). State of the art of CT detectors and sources: a literature review. *Current Radiology Reports*, *1*(1), 76–91.

Shi, F., Kojovic, T., Larbi-Bram, S., & Manlapig, E. (2009). Development of a rapid particle breakage characterisation device - The JKRBT. *Minerals Engineering*, *22*(7–8), 602–612. https://doi.org/10.1016/j.mineng.2009.05.001

Singh, V., Venugopal, R., Tripathy, S. K., & Saxena, V. K. (2017). Comparative analysis of the effect of microwave pretreatment on the milling and liberation characteristics of mineral matters of different morphologies. *Minerals and Metallurgical Processing*, *34*(2), 65–75. https://doi.org/10.19150/mmp.7506

Smith, A. D., Lester, E., Thurecht, K. J., El Harfi, J., Dimitrakis, G., Kingman, S. W., Robinson, J. P., & Irvine, D. J. (2010). Dielectric properties of free-radical polymerizations: molecularly symmetrical initiators during thermal decomposition. *Industrial & Engineering Chemistry Research*, *49*(4), 1703–1710.

Spahn, M. (2013). X-ray detectors in medical imaging. *Nuclear Instruments and Methods in Physics Research Section A: Accelerators, Spectrometers, Detectors and Associated Equipment*, *731*, 57–63.

Speakman, S. A. (2011). Basics of X-ray powder diffraction. *Massachusetts-USA, 2011a. Disponível Em:< Http://Prism. Mit. Edu/Xray/Basics% 20of% 20X-Ray% 20Powder% 20Diffraction. Pdf.*

Staebler, P. (2017). *Human exposure to electromagnetic fields: from extremely low frequency (ELF) to radiofrequency*. John Wiley & Sons.

Stauber, M., & Müller, R. (2008). Micro-computed tomography: a method for the non-destructive evaluation of the three-dimensional structure of biological specimens. In *Osteoporosis* (pp. 273–292). Springer.

Stenebråten, J. F., Johnson, W. P., & McMullen, J. (2000). Characterization of Goldstrike ore carbonaceous material. *Mining, Metallurgy & Exploration*, *17*(1), 7–15.

Stuchly, M. A., & Stuchly, S. S. (1983). Industrial, scientific, medical and domestic applications of microwaves. *IEE Proceedings A-Physical Science, Measurement and Instrumentation, Management and Education-Reviews*, *130*(8), 467–503.

Stutzman, P. E., & Clifton, J. R. (1999). Specimen preparation for scanning electron microscopy. *Proceedings of the International Conference on Cement Microscopy*, *21*, 10–22.

Sun, J., Wang, W., Yue, Q., Ma, C., Zhang, J., Zhao, X., & Song, Z. (2016). Review on microwave–metal discharges and their applications in energy and industrial processes. *Applied Energy*, *175*, 141–157.

Sun, W., Brown, S. B., & Leach, R. K. (2012). *An overview of industrial X-ray computed tomography*.

Tabor, D. (1970). The hardness of solids. *Review of Physics in Technology*, *1*(3), 145.

Tavares, L. M., & King, R. P. (1999). Evaluation of thermally-assisted fracture of particles using microscale fracture measurements. *KONA Powder and Particle Journal*, *17*(May), 163–172. https://doi.org/10.14356/kona.1999023

Tebbs, J. M., & Bower, K. M. (2003). Some comments on the robustness of student t procedures. *Journal of Engineering Education*, *92*(1), 91–94.

Thostenson, E. T., & Chou, T.-W. (1999). Microwave processing: fundamentals and applications. *Composites Part A: Applied Science and Manufacturing*, *30*(9), 1055–1071.

Toriwaki, J., & Yonekura, T. (2002). Euler number and connectivity indexes of a three dimensional digital picture. *Forma-Tokyo-*, *17*(3), 183–209.

Tromans, D. (2008). Mineral comminution: Energy efficiency considerations. *Minerals Engineering*, *21*(8), 613–620. https://doi.org/10.1016/j.mineng.2007.12.003

Tyler, G., & Jobin Yvon, S. (1995). ICP-OES, ICP-MS and AAS Techniques Compared. *ICP Optical Emission Spectroscopy Technical Note*, *5*.

Unruh, D. K., & Forbes, T. Z. (2019). X-ray diffraction techniques. *Analytical Geomicrobiology: A Handbook of Instrumental Techniques (Eds Alessi DS, Veeramani H, Kenney L)*, 215–237.

Ure, A. (2017). *Understanding the influence of mineralogy and microwave energy input on the microwave treatment of copper ores*. PhD Thesis - University of Nottingham.

Valenta, R. K., Kemp, D., Owen, J. R., Corder, G. D., & Lèbre, É. (2019). Re-thinking complex orebodies: Consequences for the future world supply of copper. *Journal of Cleaner Production*, *220*, 816–826.

Van Geet, M., Swennen, R., & Wevers, M. (2000). Quantitative analysis of reservoir rocks by microfocus X-ray computerised tomography. *Sedimentary Geology*, *132*(1–2), 25–36.

Van Weert, G., & Kondos, P. (2007). Infrared recognition of high sulphide and carbonaceous rocks after microwave heating. *39th Annual Meeting of the Canadian Mineral Processors, Ottowa, Ontario, Canada*, 345–363.

Varley, T., Barrett, E. P., Stevenson, C. C., Bradford, R. H., Croasdale, S., Howe, B., & Schmidt, W. A. (1923). *The Chloride Volatilization Process of Ore Treatment.* (p. 116). https://digicoll.manoa.hawaii.edu/techreports/PDF/USBM-211.pdf

Vernon-Parry, K. D. (2000). Scanning electron microscopy: an introduction. *III-Vs Review*, *13*(4), 40–44.

Vorster, W., Rowson, N. A., & Kingman, S. W. (2001). The effect of microwave radiation upon the processing of Neves Corvo copper ore. *International Journal of Mineral Processing*, *63*(1), 29–44.

Vriezinga, C. A., Sanchez-Pedreno, S., & Grasman, J. (2002). Thermal runaway in microwave heating: a mathematical analysis. *Applied Mathematical Modelling*, *26*(11), 1029–1038.

Walkiewicz, J W, Kazonich, G., & McGill, S. L. (1988). Microwave heating characteristics of selected minerals and compounds. *Minerals & Metallurgical Processing*, *5*(1), 39–42.

Walkiewicz, J W, Lindroth, D. P., & Clark, A. E. (1993). Grindability of taconite rod mill feed enhanced by microwave-induced cracking. *Preprints-Society of Mining Engineers of AIME*.

Walkiewicz, John W, Clark, A. E., & Mcgill, S. L. (1991). *Microwave-Assisted Grinding*. *27*(2).

Wang, J., Wang, W., Dong, K., Fu, Y., & Xie, F. (2019). Research on leaching of carbonaceous gold ore with copper-ammonia-thiosulfate solutions. *Minerals Engineering*, *137*, 232–240.

Wang, J., Xie, F., Wang, W., Bai, Y., Fu, Y., & Dreisinger, D. (2020). Eco-friendly leaching of gold from a carbonaceous gold concentrate in copper-citrate-thiosulfate solutions. *Hydrometallurgy*, *191*, 105204.

Wang, Y., & Forssberg, E. (2005). Dry comminution and liberation with microwave assistance. *Scandinavian Journal of Metallurgy*, *34*(1), 57–63. https://doi.org/10.1111/j.1600-0692.2005.00718.x

Wellington, S. L., & Vinegar, H. J. (1987). X-ray computerized tomography. *Journal of Petroleum Technology*, *39*(08), 885–898.

Westlake, P., Siozos, P., Philippidis, A., Apostolaki, C., Derham, B., Terlixi, A., Perdikatsis, V., Jones, R., & Anglos, D. (2012). Studying pigments on painted plaster in Minoan, Roman and Early Byzantine Crete. A multi-analytical technique approach. *Analytical and Bioanalytical Chemistry*, *402*(4), 1413–1432.

Whittaker, G. (1997). A basic introduction to microwave chemistry. *Accessed*, *1*, 2–20.

Whittles, D. N., Kingman, S. W., & Reddish, D. J. (2003). Application of numerical modelling for prediction of the influence of power density on microwave-assisted breakage. *International Journal of Mineral Processing*, *68*(1–4), 71–91. https://doi.org/10.1016/S0301-7516(02)00049-2

Wills, B. A., & Atkinson, K. (1993). Some observations on the fracture and liberation of mineral assemblies. *Minerals Engineering*, *6*(7), 697–706. https://doi.org/10.1016/0892-6875(93)90001-4

Wilschefski, S. C., & Baxter, M. R. (2019). Inductively coupled plasma mass spectrometry: introduction to analytical aspects. *The Clinical Biochemist Reviews*, *40*(3), 115.

Yang, W., Pickles, C. A., & Forster, J. (2020). Microwave fragmentation of a synthetic alundum-pyrite ore. *Mineral Processing and Extractive Metallurgy*, *129*(3–4), 251–266.

Yu, Q., Ding, D., Chen, W., Hu, N., Wu, L., Zhang, Q., Liu, Y., Zhang, Z., Li, F., & Xue, X.

(2021). Effect of Microwave Pretreatment on Grindability of Lead-Zinc Ore. *Geofluids*, *2021*.

Zhang, J., & Hu, J. (2008). Image segmentation based on 2D Otsu method with histogram analysis. *2008 International Conference on Computer Science and Software Engineering*, *6*, 105–108.

Zhu, F., Zhang, L., Li, H., Yin, S., Koppala, S., Yang, K., & Li, S. (2018). Gold extraction from cyanidation tailing using microwave chlorination roasting method. *Metals*, *8*(12), 1025.

Zink, F. E. (1997). X-ray tubes. *Radiographics*, *17*(5), 1259–1268.

Zuo, W., & Shi, F. (2016). Ore impact breakage characterisation using mixed particles in wide size range. *Minerals Engineering*, *86*, 96–103. https://doi.org/10.1016/j.mineng.2015.12.007

11. APPENDICES

11.1 Mixed-Size Fragments – Raw Data

11.1.1 Microwave Energy Profiles

Energy profiles at low energy level

Energy profiles at medium energy level

Energy profiles at high energy level
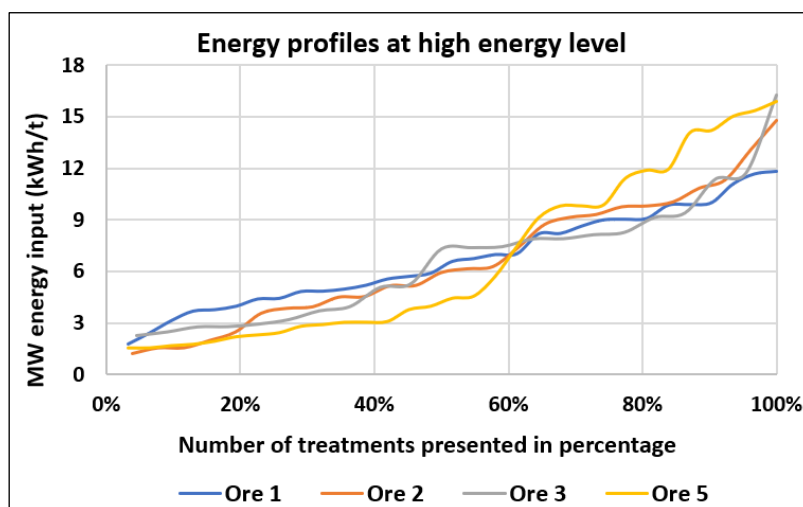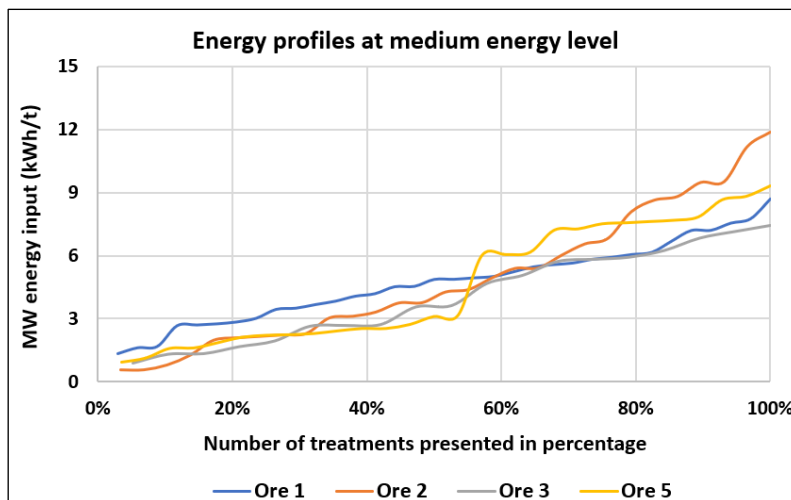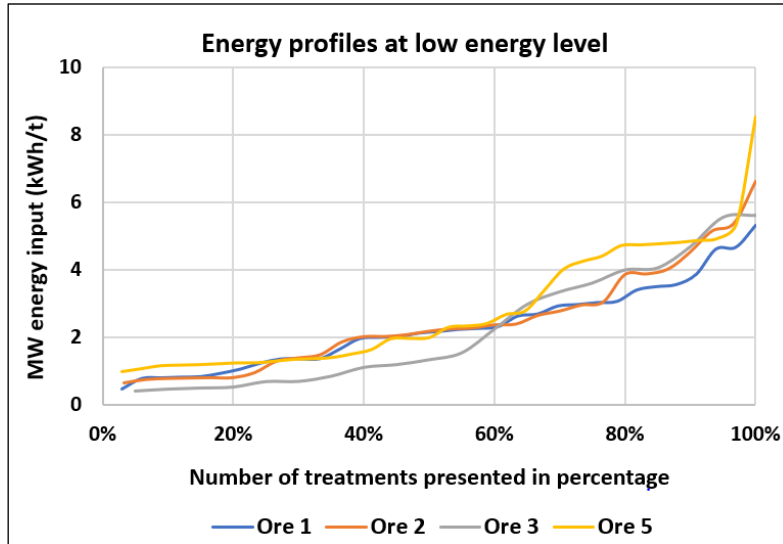
11.1.2 Point Load Test Data

11.1.2.1   Ore 1

POINT LOAD TEST						
Ore type:		Ore 1				
Description:		Untreated				
Sample ID	Count No.	Mass (g)	Depth (mm)	Width (mm)	Load (kN)	De	$Is_{(50)}$ (MPa)
1f	1	109.62	28.49	42.60	12.355	39.32	7.17
2f	2	82.73	22.35	33.12	7.775	30.71	6.62
3f	3	92.38	29.38	38.05	9.215	37.74	5.70
4f	4	101.10	27.29	48.05	5.451	40.87	2.98
5f	5	78.63	25.33	39.29	12.906	35.61	8.74
6f	6	79.33	24.97	33.63	7.761	32.71	5.99
7f	7	94.63	32.80	24.83	9.274	32.21	7.33
8f	8	89.39	29.31	35.57	7.662	36.44	5.00
9f	9	75.33	24.95	26.87	6.536	29.22	6.01
10f	10	74.78	18.78	31.59	4.264	27.49	4.31
11f	11	57.92	23.18	36.30	7.110	32.74	5.48
12f	12	54.86	18.41	30.81	4.289	26.88	4.49
13f	13	60.10	29.90	30.34	5.548	33.99	4.04
14f	14	63.66	20.89	45.47	8.714	34.79	6.12
15f	15	56.94	27.86	30.19	3.192	32.73	2.46
16f	16	48.65	18.34	27.47	3.224	25.33	3.70
17f	17	64.90	23.23	35.42	9.554	32.38	7.50
18f	18	71.02	19.24	37.23	5.804	30.21	5.07
19f	19	51.25	24.34	28.03	9.662	29.48	8.76
20f	20	48.93	23.39	30.54	2.114	30.17	1.85
21f	21	65.65	18.15	40.07	6.601	30.44	5.70
22f	22	52.49	15.92	30.71	9.167	24.96	10.77
23f	23	58.99	21.74	26.42	7.920	27.05	8.21
24f	24	48.48	13.40	34.80	4.291	24.37	5.23
25f	25	51.25	19.08	26.24	7.179	25.25	8.28
26f	26	33.93	20.85	20.62	3.752	23.40	4.87
27f	27	43.66	18.80	27.71	8.463	25.76	9.46
28f	28	40.48	16.08	34.33	3.729	26.52	3.99
29f	29	42.97	18.89	27.69	4.112	25.81	4.58
30f	30	39.89	14.60	37.20	4.555	26.30	4.93

Table continues next page

31f	31	39.21	23.64	27.95	3.194	29.01	2.97
32f	32	53.25	17.26	30.98	1.131	26.10	1.24
33f	33	30.90	14.08	33.46	2.212	24.50	2.67
34f	34	25.52	14.88	31.20	5.275	24.32	6.45
35f	35	30.02	20.13	23.58	5.239	24.59	6.30
36f	36	17.68	16.74	21.15	3.201	21.24	4.83
37f	37	25.82	14.77	26.74	6.229	22.43	8.63
Mean							5.63
Median							5.48
Standard Deviation							2.19
Minimum							1.24
Maximum							10.77
Count							37

POINT LOAD TEST							
Ore type:		Ore 1					
Description:		Treated at 2.4 kWh/t					
Sample ID	Count No.	Mass (g)	Depth (mm)	Width (mm)	Load (kN)	De	$Is_{(50)}$ (MPa)
1c	1	64.73	19.91	37.99	4.778	31.04	4.00
2c	2	66.22	23.92	37.3	9.383	33.71	6.91
3c	3	57.09	16.40	27.83	6.600	24.11	8.18
4c	4	45.05	26.71	28.78	3.500	31.29	2.89
5c	5	29.89	12.57	24.92	3.324	19.98	5.51
6c	6	28.30	10.43	20.08	2.341	16.33	5.30
7c	7	107.93	27.12	50.09	12.531	41.60	6.67
8c	8	83.23	23.41	34.53	7.261	32.09	5.78
9c	9	84.18	25.54	37.92	11.599	35.12	8.02
10c	10	71.15	19.17	35.68	3.820	29.52	3.46
11c	11	80.41	26.26	39.06	8.389	36.15	5.55
12c	12	60.72	13.61	42.40	1.118	27.11	1.15
13c	13	93.97	21.79	33.85	7.632	30.65	6.52
14c	14	95.56	26.96	28.54	6.452	31.31	5.33
15c	15	80.31	20.08	40.20	6.564	32.07	5.23
16c	16	53.40	18.10	21.86	3.996	22.45	5.53
17c	17	46.35	18.84	23.39	7.920	23.69	10.08
18c	18	45.75	20.70	31.14	4.202	28.66	3.98
19c	19	55.71	16.48	35.10	1.141	27.15	1.18
20c	20	67.37	20.93	31.39	11.025	28.93	10.30
21c	21	45.48	13.44	30.17	4.062	22.73	5.52
22c	22	50.93	16.88	34.75	4.742	27.34	4.84
23c	23	43.63	15.50	26.11	2.449	22.71	3.33
24c	24	39.59	22.17	23.58	6.652	25.81	7.42
25c	25	39.97	20.93	24.13	3.872	25.36	4.43
26c	26	42.57	21.91	28.35	5.808	28.13	5.67
27c	27	39.81	23.10	26.67	6.027	28.01	5.92
28c1	28	30.98	11.70	31.15	3.192	21.55	4.71
28c2	29	38.01	18.64	24.95	8.394	24.34	10.25
29c1	30	37.42	17.20	33.58	2.296	27.12	2.37

Table continues next page

29c2	31	35.02	23.06	29.09	6.919	29.23	6.36
30c1	32	32.22	18.18	27.80	7.517	25.37	8.60
30c2	33	23.85	15.70	19.05	3.102	19.52	5.33
31c1	34	33.88	19.37	15.74	5.840	19.71	9.89
31c2	35	37.54	14.58	35.59	2.834	25.71	3.18
32c1	36	32.72	22.00	25.60	2.224	26.79	2.34
32c2	37	32.31	16.65	30.04	2.150	25.24	2.48
33c1	38	43.44	23.10	27.68	4.183	28.54	3.99
33c2	39	35.52	18.08	22.01	2.761	22.52	3.80
34c1	40	35.81	16.92	23.53	1.337	22.52	1.84
34c2	41	33.73	11.96	31.76	1.029	22.00	1.47
Mean							5.25
Median							5.33
Standard Deviation							2.44
Minimum							1.15
Maximum							10.30
Count							41

POINT LOAD TEST						
Ore type:		Ore 1				
Description:		Treated at 4.8 kWh/t				
Sample ID	Count No.	Mass (g)	Depth (mm)	Width (mm)	Load (kN)	De	$Is_{(50)}$ (MPa)
1d	1	74.44	24.44	39.97	8.589	35.28	5.90
2d	2	49.65	25.20	27.56	5.314	29.74	4.75
3d	3	66.88	19.60	30.46	4.222	27.58	4.25
4d	4	53.21	16.42	31.01	3.834	25.47	4.36
5d	5	68.72	17.81	44.66	7.823	31.83	6.30
6d	6	61.05	22.80	24.30	2.021	26.57	2.15
7d	7	95.16	22.67	32.25	2.021	30.52	1.74
8d	8	96.66	27.26	37.80	2.564	36.23	1.69
9d	9	69.99	24.02	26.27	7.535	28.35	7.26
10d	10	79.26	22.12	33.20	6.869	30.59	5.89
11d	11	64.29	21.75	41.44	5.272	33.88	3.85
12d	12	58.59	16.22	30.83	7.048	25.24	8.13
13d	13	66.72	19.40	32.62	6.965	28.39	6.70
14d	14	69.91	23.36	29.77	2.573	29.76	2.30
15d	15	109.11	29.77	49.32	15.403	43.25	7.71
16d	16	64.00	22.30	37.45	4.944	32.62	3.83
17d	17	74.41	20.43	36.93	5.920	31.00	4.97
18d	18	110.16	22.62	40.43	9.354	34.13	6.76
19d	19	63.17	20.11	34.78	8.151	29.85	7.25
20d	20	58.97	25.22	28.22	9.129	30.11	8.01
21d	21	44.23	23.03	26.58	5.045	27.92	4.98
22d	22	38.46	13.53	25.70	3.493	21.05	5.34
23d	23	42.79	17.80	20.52	2.344	21.57	3.45
24d	24	47.02	17.29	38.38	1.585	29.07	1.47
25d	25	48.46	19.23	33.08	1.480	28.47	1.42
26d	26	50.80	18.83	33.71	2.047	28.44	1.96
27d	27	37.40	16.59	27.66	3.024	24.18	3.73
28d	28	38.69	21.30	25.45	4.756	26.28	5.16
29d	29	38.10	16.60	37.80	3.175	28.27	3.07
30d1	30	28.96	9.33	24.44	2.424	17.04	5.14

Table continues next page

350

30d2	31	31.69	17.37	30.88	3.745	26.14	4.09
31d1	32	31.54	23.17	26.92	4.263	28.19	4.15
31d2	33	40.38	21.44	33.10	5.523	30.07	4.86
32d1	34	15.54	16.19	28.30	2.969	24.16	3.67
32d2	35	28.58	11.93	23.17	2.816	18.76	5.15
33d1	36	27.04	19.49	22.83	5.620	23.81	7.10
33d2	37	30.22	16.82	25.20	3.609	23.24	4.73
34d1	38	37.97	15.20	27.26	5.424	22.97	7.24
34d2	39	28.56	16.17	29.35	4.704	24.59	5.65
Mean							**4.77**
Median							**4.86**
Standard Deviation							**1.94**
Minimum							**1.42**
Maximum							**8.13**
Count							**39**

POINT LOAD TEST							
Ore type:		Ore 1					
Description:		Treated at 6.9 kWh/t					
Sample ID	Count No.	Mass (g)	Depth (mm)	Width (mm)	Load (kN)	De	Is$_{(50)}$ (MPa)
1e	1	72.71	15.93	33.97	3.970	26.26	4.31
2e	2	101.64	28.50	35.84	5.588	36.07	3.71
3e	3	118.44	31.15	41.16	7.109	40.41	3.96
4e	4	84.21	23.47	41.68	11.690	35.30	8.02
5e	5	81.69	22.14	32.98	1.486	30.50	1.28
6e	6	98.41	29.42	30.90	3.978	34.03	2.89
7e	7	80.32	25.57	36.28	2.704	34.38	1.93
8e	8	76.39	22.11	33.10	5.476	30.53	4.70
9e	9	61.18	15.50	35.57	5.054	26.50	5.41
10e	10	58.90	13.83	32.76	3.711	24.02	4.62
11e	11	61.96	18.20	34.07	2.497	28.11	2.44
12e	12	52.09	18.37	34.53	4.172	28.43	4.00
13e	13	53.25	19.20	27.15	2.140	25.77	2.39
14e	14	54.92	20.50	28.63	4.417	27.34	4.50
15e	15	65.05	28.74	34.86	10.774	35.73	7.26
16e	16	59.53	23.69	28.01	0.227	29.07	0.21
17e	17	55.51	24.22	28.70	4.253	29.76	3.80
18e	18	50.70	15.69	32.72	5.782	25.57	6.54
19e	19	53.46	22.70	32.67	8.047	30.74	6.84
20e	20	57.79	20.26	37.75	2.134	31.21	1.77
21e	21	60.25	15.00	41.87	3.260	28.29	3.15
22e	22	53.54	19.06	29.32	7.930	26.68	8.40
23e1	23	43.58	21.39	29.77	11.306	28.48	10.82
23e2	24	17.72	9.84	25.17	2.082	17.76	4.14
24e1	25	45.02	16.61	23.30	1.443	22.20	2.03
24e2	26	24.76	13.82	34.17	4.368	24.53	5.27
25e1	27	27.49	13.15	25.42	2.637	20.64	4.16
25e2	28	29.62	12.10	29.13	2.640	21.19	4.00
26e1	29	34.65	17.05	27.11	4.811	24.27	5.90
26e2	30	41.28	21.09	33.15	6.298	29.84	5.61

Table continues next page

27e1	31	45.08	15.74	24.59	5.146	22.20	7.24
27e2	32	33.65	21.73	29.24	3.565	28.45	3.42
28e1	33	31.61	18.04	32.65	1.841	27.39	1.87
28e2	34	30.58	18.56	22.65	4.844	23.14	6.40
29e1	35	33.76	11.35	29.12	0.994	20.52	1.58
29e2	36	40.29	19.16	27.82	4.137	26.06	4.54
30e	37	44.96	16.70	30.70	5.667	25.56	6.42
31e1	38	42.32	22.60	31.70	2.148	30.21	1.88
31e2	39	19.66	9.68	20.82	0.738	16.02	1.72
Mean							4.34
Median							4.14
Standard Deviation							2.31
Minimum							0.21
Maximum							10.82
Count							39

11.1.2.2   Ore 2

POINT LOAD TEST							
Ore type:		Ore 2					
Description:		Untreated					
Sample ID	Count No.	Mass (g)	Depth (mm)	Width (mm)	Load (kN)	De	$Is_{(50)}$ (MPa)
1q	1	99.84	22.51	41.18	7.5	34.36	5.37
2q	2	113.62	32.46	37.13	19.0	39.18	11.09
3q	3	105.25	23.68	31.87	11.5	31.01	9.65
4q	4	127.74	27.46	48.00	12.0	40.98	6.53
5q	5	83.56	17.97	39.94	4.0	30.24	3.49
6q	6	121.04	30.67	39.46	10.5	39.26	6.11
7q	7	92.30	21.25	39.36	2.5	32.64	1.94
8q	8	73.33	21.73	36.70	6.5	31.87	5.22
9q	9	65.12	25.55	34.44	12.0	33.48	8.94
10q	10	79.83	24.56	37.25	5.5	34.14	3.97
11q	11	65.03	20.30	31.34	8.0	28.47	7.66
12q	12	72.50	23.93	33.06	9.0	31.75	7.28
13q	13	55.01	21.50	25.71	7.0	26.54	7.48
14q	14	58.30	18.95	37.67	5.0	30.16	4.38
15q	15	64.23	28.03	32.41	6.5	34.02	4.72
16q	16	41.46	20.48	34.61	6.5	30.05	5.72
17q	17	39.06	16.61	32.39	7.5	26.18	8.18
18q	18	41.32	14.52	23.88	3.5	21.02	5.36
19q	19	65.26	24.26	33.40	8.0	32.13	6.35
20q	20	37.37	15.30	30.97	4.0	24.57	4.81
21q	21	36.24	17.75	28.84	4.0	25.54	4.53
22q	22	34.35	22.08	24.35	7.5	26.17	8.18
23q	23	26.46	10.70	26.93	3.0	19.16	5.31
24q	24	26.78	11.72	28.49	3.0	20.62	4.73
25q	25	29.43	20.85	24.42	3.5	25.47	3.98
26q	26	21.56	10.78	25.13	2.0	18.58	3.71
27q	27	20.19	10.20	26.77	4.0	18.65	7.38
28q	28	24.26	17.59	23.84	2.0	23.11	2.65
29q	29	16.08	14.20	16.20	2.5	17.12	5.27
30q	30	15.25	11.86	20.25	2.5	17.49	5.09
31q	31	26.37	18.57	22.71	4.0	23.18	5.27
32q	32	27.46	14.00	32.36	2.5	24.02	3.11
Mean							5.73
Median							5.29
Standard Deviation							2.07
Minimum							1.94
Maximum							11.09
Count							32

354

POINT LOAD TEST							
Ore type:		Ore 2					
Description:		Treated at 2.3 kWh/t					
Sample ID	**Count No.**	**Mass (g)**	**Depth (mm)**	**Width (mm)**	**Load (kN)**	**De**	**Is$_{(50)}$ (MPa)**
1r	1	110.68	28.28	43.67	13.0	39.66	7.45
2r	2	86.34	18.40	40.98	7.5	30.99	6.30
3r	3	89.08	17.50	34.68	5.0	27.81	4.97
4r	4	116.86	31.56	37.00	9.5	38.57	5.68
5r	5	84.23	26.38	29.49	14.0	31.48	11.47
6r	6	74.52	20.63	33.94	10.5	29.87	9.34
7r	7	93.68	24.36	38.36	3.5	34.50	2.49
8r	8	68.30	22.37	35.53	6.5	31.82	5.24
9r	9	68.77	17.24	38.83	9.0	29.20	8.29
10r	10	78.56	24.97	34.30	8.5	33.03	6.46
11r	11	55.83	21.66	31.72	11.0	29.58	9.92
12r	12	55.08	23.43	30.65	1.5	30.25	1.31
13r	13	62.90	25.40	34.29	8.0	33.31	6.01
14r	14	55.41	22.48	37.04	10.5	32.57	8.16
15r	15	55.06	23.34	27.62	7.0	28.66	6.64
16r	16	53.64	23.67	28.35	9.0	29.24	8.27
17r	17	55.85	22.82	30.01	5.0	29.54	4.52
18r	18	43.15	15.94	30.80	5.0	25.01	5.85
19r	19	39.92	21.03	22.03	8.0	24.29	9.80
20r	20	45.33	17.37	29.59	6.0	25.59	6.78
21r	21	41.11	24.03	25.49	9.5	27.93	9.37
22r	22	44.51	16.33	33.01	1.5	26.20	1.63
23r	23	75.76	22.20	36.80	2.0	32.26	1.58
24r	24	41.44	23.10	26.64	3.5	28.00	3.44
25r	25	39.38	15.76	31.05	2.5	24.97	2.93
26r	26	36.20	16.94	23.25	1.0	22.40	1.39
27r1	27	32.56	22.30	25.22	4.5	26.77	4.74
27r2	28	18.49	12.68	25.84	1.5	20.43	2.40
28r1	29	27.12	12.71	30.00	2.5	22.04	3.56
28r2	30	19.81	11.02	28.91	1.5	20.15	2.46
29r	31	40.26	19.03	25.78	2.0	25.00	2.34
30r1	32	22.86	8.76	24.71	3.0	16.61	6.63
30r2	33	17.90	15.89	17.97	2.5	19.07	4.45
30r3	34	9.25	12.45	15.00	1.0	15.42	2.48
Mean							5.42
Median							5.46
Standard Deviation							2.83
Minimum							1.31
Maximum							11.47
Count							34

355

POINT LOAD TEST							
Ore type:		Ore 2					
Description:		Treated at 4.2 kWh/t					
Sample ID	**Count No.**	**Mass (g)**	**Depth (mm)**	**Width (mm)**	**Load (kN)**	**De**	**Is(50) (MPa)**
1s	1	130.72	25.65	46.53	15.5	38.99	9.12
2s	2	91.33	22.58	37.40	12.0	32.80	9.23
3s	3	109.35	27.32	45.61	12.0	39.84	6.83
4s	4	62.74	22.63	39.39	6.5	33.70	4.79
4s	5	99.70	34.05	37.46	1.5	40.31	0.84
6s	6	74.13	17.90	35.56	8.0	28.48	7.66
7s	7	68.63	18.59	35.71	11.5	29.08	10.66
8s	8	75.89	19.54	34.68	5.0	29.38	4.56
9s	9	63.50	26.47	33.13	4.0	33.42	2.99
10s	10	73.90	21.43	38.35	7.5	32.36	5.89
11s	11	44.63	20.70	24.01	2.5	25.16	2.90
12s	12	45.59	18.63	29.17	7.5	26.31	8.12
13s	13	44.92	16.91	36.07	7.5	27.87	7.42
14s	14	52.65	20.32	30.48	3.5	28.09	3.42
15s	15	49.53	18.08	27.29	7.0	25.07	8.16
16s	16	41.93	17.51	28.85	5.0	25.37	5.73
17s	17	69.73	25.18	34.37	1.5	33.20	1.13
18s	18	41.01	18.66	30.79	10.5	27.05	10.88
19s	19	41.47	21.03	33.42	8.5	29.92	7.54
20s	20	41.36	20.60	32.85	10.0	29.36	9.13
21s1	21	41.39	17.58	29.24	4.5	25.59	5.08
21s2	22	16.95	13.60	18.64	1.0	17.97	1.95
22s1	23	43.10	22.30	24.25	3.0	26.25	3.26
22s2	24	27.39	11.87	29.74	3.5	21.21	5.29
23s1	25	30.05	15.98	24.87	3.0	22.50	4.14
23s2	26	16.67	15.78	23.10	2.5	21.55	3.69
24s1	27	25.05	13.46	28.46	2.5	22.09	3.55
24s2	28	20.99	18.63	20.01	4.0	21.79	5.80
25s1	29	20.60	10.80	28.06	3.0	19.65	5.10
25s2	30	17.28	12.23	25.68	2.0	20.00	3.31
25s3	31	14.22	6.73	23.30	1.5	14.13	4.25
26s1	32	21.83	12.33	28.60	0.5	21.19	0.76
26s2	33	20.24	19.74	24.53	2.0	24.84	2.37
27s1	34	18.71	16.85	22.98	2.0	22.21	2.81
27s2	35	16.91	15.49	22.08	2.5	20.87	3.87
27s3	36	13.77	15.55	17.34	3.0	18.53	5.59
28s	37	68.20	20.32	35.47	4.5	30.30	3.91
29s	38	43.43	15.97	30.10	3.0	24.75	3.57
Mean							5.14
Median							4.68
Standard Deviation							2.65
Minimum							0.76
Maximum							10.88
Count							38

POINT LOAD TEST							
Ore type:		Ore 2					
Description:		Treated at 6.3 kWh/t					
Sample ID	Count No.	Mass (g)	Depth (mm)	Width (mm)	Load (kN)	De	Is(50) (MPa)
1t	1	78.51	16.89	49.38	6.5	32.60	5.05
2t	2	101.92	21.81	48.62	2.0	36.75	1.29
3t	3	111.28	25.37	34.82	12.0	33.55	8.91
4t	4	100.97	31.66	35.59	10.0	37.89	6.15
5t	5	80.13	23.22	30.08	12.5	29.83	11.13
6t	6	110.71	26.49	35.84	3.5	34.78	2.46
7t	7	71.03	18.13	33.96	10.0	28.01	9.82
8t	8	111.70	29.90	33.86	11.0	35.91	7.35
9t	9	93.36	22.68	42.69	4.5	35.12	3.11
10t	10	64.80	19.87	35.13	10.5	29.82	9.36
11t	11	87.88	31.34	34.59	14.5	37.16	9.19
12t	12	53.76	15.55	30.66	7.5	24.64	8.98
13t	13	59.41	21.36	25.50	5.0	26.34	5.40
14t	14	78.81	27.14	34.73	4.0	34.65	2.82
15t	15	62.96	16.51	36.10	3.5	27.55	3.53
16t	16	46.51	18.17	32.85	4.5	27.57	4.53
17t	17	43.72	12.38	26.37	5.0	20.39	8.03
18t	18	47.50	24.54	27.16	3.5	29.14	3.23
19t	19	45.79	14.62	37.79	7.0	26.53	7.48
20t	20	54.74	15.97	32.49	2.0	25.71	2.24
21t	21	46.46	18.35	27.52	4.5	25.36	5.15
22t1	22	28.95	13.44	21.88	5.5	19.35	9.58
22t2	23	24.32	21.40	23.60	1.5	25.36	1.72
23t1	24	27.19	13.11	22.47	3.0	19.37	5.22
23t2	25	10.87	8.41	27.29	1.5	17.10	3.17
23t3	26	13.00	13.24	18.29	1.5	17.56	3.04
24t1	27	19.27	12.20	25.54	3.0	19.92	5.00
24t2	28	11.89	8.47	24.75	1.5	16.34	3.40
24t3	29	13.55	13.09	22.32	1.5	19.29	2.63
24t4	30	22.81	11.08	26.15	2.5	19.21	4.40
25t1	31	25.10	15.20	24.59	2.0	21.82	2.89
25t2	32	22.24	15.54	22.42	4.5	21.07	6.87
25t3	33	13.19	12.10	19.43	1.5	17.31	3.11
26t1	34	24.08	15.55	23.89	2.5	21.75	3.63
26t2	35	18.61	18.09	19.80	3.0	21.36	4.48
26t3	36	13.61	6.54	28.39	0.5	15.38	1.24
Mean							5.16
Median							4.51
Standard Deviation							2.76
Minimum							1.24
Maximum							11.13
Count							36

11.1.2.3 Ore 3

POINT LOAD TEST							
Ore type:		Ore 3					
Description:		Untreated					
Sample ID	Count No.	Mass (g)	Depth (mm)	Width (mm)	Load (kN)	De	Is(50) (MPa)
1h	1	119.71	28.93	38.87	3.00	37.85	1.85
2h	2	117.12	25.13	45.62	4.00	38.22	2.43
3h	3	115.61	22.58	47.93	5.50	37.13	3.49
4h	4	67.39	21.91	36.42	3.50	31.88	2.81
5h	5	149.10	22.15	50.55	2.00	37.77	1.24
6h	6	92.30	26.66	40.24	4.00	36.97	2.56
7h	7	51.61	26.88	31.81	4.50	33.00	3.43
8h	8	46.26	21.46	36.43	2.00	31.56	1.63
9h	9	41.92	18.50	33.91	3.00	28.27	2.90
10h	10	68.69	20.87	40.3	2.00	32.73	1.54
11h	11	67.23	20.91	32.99	3.00	29.64	2.70
12h	12	48.68	15.00	31.91	4.50	24.69	5.37
13h	13	67.10	28.80	25.52	3.50	30.60	3.00
14h	14	65.50	23.70	30.40	2.50	30.30	2.17
15h	15	37.50	18.23	27.68	2.50	25.35	2.87
16h	16	44.63	17.93	33.23	3.50	27.55	3.53
17h	17	28.07	18.45	31.08	1.50	27.03	1.56
18h	18	29.60	16.31	25.20	0.50	22.88	0.67
19h	19	31.66	15.49	24.48	1.50	21.98	2.15
20h	20	33.50	15.65	23.16	3.50	21.49	5.18
21h	21	28.58	17.17	30.36	2.50	25.77	2.79
22h	22	27.31	20.97	21.50	2.50	23.97	3.13
23h	23	23.90	19.11	20.12	1.50	22.13	2.12
24h	24	34.80	13.80	28.95	1.50	22.56	2.06
25h	25	22.84	9.14	34.59	1.00	20.07	1.65
26h	26	18.23	8.86	31.43	1.50	18.83	2.73
27h	27	21.66	14.45	21.13	0.50	19.72	0.85
28h	28	16.44	12.01	23.07	2.50	18.79	4.56
29h	29	16.68	20.37	19.14	1.00	22.29	1.40
30h	30	11.92	10.90	19.87	2.00	16.61	4.41
31h	31	11.01	13.00	16.50	1.00	16.53	2.22
Mean							2.61
Median							2.56
Standard Deviation							1.14
Minimum							0.67
Maximum							5.37
Count							31

POINT LOAD TEST							
Ore type:		Ore 3					
Description:		Treated at 2.2 kWh/t					
Sample ID	Count No.	Mass (g)	Depth (mm)	Width (mm)	Load (kN)	De	Is(50) (MPa)
1a	1	131.98	27.92	37.47	6.50	36.51	4.23
2a	2	130.05	34.53	39.39	3.00	41.63	1.59
3a1	3	47.10	18.40	32.71	1.50	27.69	1.50
3a2	4	18.75	15.75	25.53	1.50	22.63	2.05
4a	5	129.11	28.11	40.02	5.50	37.86	3.39
5a1	6	32.01	18.68	29.42	3.50	26.46	3.75
5a2	7	31.13	17.30	31.06	3.50	26.16	3.82
6a1	8	32.52	20.76	26.67	2.50	26.56	2.67
6a2	9	27.53	17.01	23.78	0.50	22.70	0.68
7a	10	86.87	26.44	31.11	5.50	32.37	4.32
8a	11	65.70	25.95	41.17	2.50	36.89	1.60
9a1	12	53.32	16.83	36.18	1.50	27.85	1.49
9a2	13	22.70	16.73	20.18	0.50	20.74	0.78
10a	14	53.37	14.61	34.11	1.50	25.20	1.74
11a	15	47.19	21.58	31.02	3.50	29.20	3.22
12a1	16	44.78	25.35	39.42	4.00	35.68	2.70
12a2	17	131.50	30.85	38.46	4.50	38.88	2.66
13a	18	87.88	22.45	39.77	1.50	33.72	1.10
14a1	19	38.12	12.41	41.17	1.50	25.51	1.70
14a2	20	18.00	16.71	22.29	1.50	21.78	2.18
15a1	21	36.01	17.27	22.71	1.50	22.35	2.09
15a2	22	31.39	17.98	29.20	2.50	25.86	2.78
16a	23	89.65	28.80	34.60	1.50	35.63	1.01
17a1	24	47.07	24.47	30.40	1.00	30.78	0.85
17a2	25	18.15	14.04	17.29	1.00	17.59	2.02
18a1	26	41.90	41.90	35.96	1.50	43.81	0.74
18a2	27	39.47	39.47	29.63	1.00	38.60	0.60
19a	28	58.59	58.59	25.05	3.00	43.24	1.50
20a	29	144.39	31.69	45.44	5.50	42.83	2.80
Mean							2.12
Median							2.02
Standard Deviation							1.07
Minimum							0.60
Maximum							4.32
Count							29

POINT LOAD TEST							
Ore type:		Ore 3					
Description:		Treated at 4.1 kWh/t					
Sample ID	Count No.	Mass (g)	Depth (mm)	Width (mm)	Load (kN)	De	Is(50) (MPa)
1b1	1	72.14	28.29	26.65	2.00	30.99	1.68
1b2	2	20.80	14.63	25.7	1.50	21.89	2.16
2b	3	95.35	30.00	39.63	2.50	38.92	1.47
3b1	4	54.72	27.54	27.56	2.00	31.09	1.67
3b2	5	20.16	15.60	26.29	0.50	22.86	0.67
4b	6	69.02	28.09	41.24	2.00	38.41	1.20
5b1	7	49.05	19.13	34.22	4.00	28.88	3.75
5b2	8	28.48	21.92	22.11	2.00	24.85	2.36
6b1	9	57.08	29.46	30.69	2.50	33.94	1.82
6b2	10	19.96	15.00	25.35	1.50	22.01	2.14
7b	11	81.16	22.98	48.25	2.50	37.58	1.56
8b	12	79.39	28.29	41.38	2.50	38.62	1.49
9b1	13	38.56	16.24	34.60	2.00	26.75	2.11
9b2	14	43.19	18.82	33.64	4.00	28.40	3.85
10b1	15	43.16	22.96	28.88	0.50	29.06	0.46
10b2	16	47.43	21.24	30.25	2.00	28.61	1.90
11b	17	102.41	30.46	43.32	3.00	41.00	1.63
12b	18	63.86	30.31	34.18	3.00	36.33	1.97
13b1	19	59.33	25.25	32.38	1.50	32.27	1.18
13b2	20	34.40	13.88	29.62	1.00	22.89	1.34
14b1	21	41.17	21.68	34.00	4.00	30.64	3.42
14b2	22	24.19	13.54	25.93	0.50	21.15	0.76
15b	23	66.44	27.13	28.37	4.00	31.31	3.30
16b1	24	28.42	16.56	28.71	2.00	24.61	2.40
16b2	25	18.79	15.24	27.55	1.50	23.13	1.98
16b3	26	23.86	18.04	16.39	2.50	19.41	4.34
17b	27	54.19	16.28	29.68	4.00	24.81	4.74
18b	28	54.19	12.31	26.41	1.50	20.35	2.42
19b1	29	49.13	20.88	26.39	0.50	26.49	0.54
19b2	30	33.77	20.28	21.46	1.50	23.55	1.93
Mean							2.08
Median							1.91
Standard Deviation							1.07
Minimum							0.46
Maximum							4.74
Count							30

360

POINT LOAD TEST							
Ore type:		Ore 3					
Description:		Treated at 6.9 kWh/t					
Sample ID	Count No.	Mass (g)	Depth (mm)	Width (mm)	Load (kN)	De	Is(50) (MPa)
1g	1	120.68	22.52	50.34	3.347	38.00	2.05
2g	2	110.19	25.08	44.27	4.329	37.61	2.69
3g	3	71.72	27.83	31.14	5.407	33.23	4.07
4g	4	98.56	22.08	36.02	1.321	31.83	1.06
5g	5	104.41	30.27	39.87	2.418	39.21	1.41
6g	6	112.02	25.73	38.89	1.986	35.70	1.34
7g	7	94.27	30.54	39.02	7.031	38.96	4.14
8g	8	106.40	29.28	28.11	7.540	32.38	5.91
9g	9	71.60	18.54	44.74	2.027	32.51	1.58
10g	10	61.60	23.90	34.45	3.714	32.39	2.91
11g	11	56.22	14.69	30.21	1.349	23.78	1.71
12g	12	59.04	23.84	33.61	0.718	31.95	0.58
13g	13	53.67	14.25	35.21	0.846	25.28	0.97
14g1	14	36.30	13.53	36.60	4.326	25.12	5.03
14g2	15	45.89	20.07	29.06	0.590	27.26	0.60
15g1	16	36.68	12.23	30.00	0.866	21.62	1.27
15g2	17	26.30	16.77	25.06	2.427	23.14	3.21
16g1	18	43.56	20.95	27.18	3.324	26.93	3.47
16g2	19	15.26	5.53	24.02	0.635	13.01	2.05
17g1	20	36.56	20.21	26.97	3.000	26.35	3.24
17g2	21	13.85	8.34	27.25	0.624	17.01	1.33
17g3	22	14.86	15.05	21.30	0.957	20.21	1.56
18g1	23	39.32	22.42	22.99	0.730	25.62	0.82
18g2	24	18.63	8.85	25.69	0.704	17.02	1.50
19g1	25	33.82	14.90	25.99	1.700	22.21	2.39
19g2	26	25.88	18.11	25.51	0.938	24.26	1.15
20g1	27	34.35	14.81	29.50	0.665	23.59	0.85
20g2	28	23.07	15.26	17.30	0.439	18.34	0.83
21g1	29	28.48	13.68	29.20	1.149	22.56	1.58
21g2	30	21.88	12.70	21.01	0.862	18.44	1.62
22g1	31	19.27	17.07	17.42	1.439	19.46	2.48
22g2	32	28.11	13.45	25.58	0.853	20.94	1.32
Mean							2.09
Median							1.58
Standard Deviation							1.30
Minimum							0.58
Maximum							5.91
Count							32

11.1.2.4   Ore 5

POINT LOAD TEST							
Ore type:		Ore 5					
Description:		Untreated					
Sample ID	Count No.	Mass (g)	Depth (mm)	Width (mm)	Load (kN)	De	$Is_{(50)}$ (MPa)
1j	1	154.70	36.05	43.23	21.5	44.56	10.28
2j	2	164.96	27.34	51.46	20.0	42.33	10.35
3j	3	91.81	18.30	48.56	14.5	33.65	10.72
4j	4	144.47	23.28	46.31	18.5	37.06	11.77
5j	5	88.54	17.60	35.61	20.5	28.26	19.86
6j	6	81.96	20.73	37.27	9.0	31.37	7.41
7j	7	98.11	26.42	35.27	14.5	34.45	10.33
8j	8	96.57	19.28	37.70	14.0	30.43	12.09
9j	9	87.05	27.08	35.18	19.0	34.84	13.31
10j	10	124.24	32.66	48.00	18.0	44.69	8.57
11j	11	70.68	20.50	30.14	9.5	28.06	9.31
12j	12	66.35	20.65	32.00	10.0	29.01	9.30
13j	13	55.71	21.70	26.01	4.5	26.81	4.73
14j	14	51.51	17.93	30.26	14.0	26.29	15.17
15j	15	35.19	16.16	32.56	5.0	25.89	5.55
16j	16	46.64	16.13	30.47	7.5	25.02	8.77
17j	17	35.61	10.29	34.14	6.0	21.15	9.10
18j	18	27.26	13.60	27.00	7.5	21.63	11.00
19j	19	36.93	19.32	24.75	4.5	24.68	5.38
20j	20	27.40	14.91	23.26	3.5	21.02	5.36
21j	21	26.12	10.61	21.03	4.5	16.86	9.71
22j	22	20.82	16.20	19.61	6.5	20.12	10.66
23j	23	23.46	13.64	18.82	5.0	18.08	9.67
24j	24	26.89	17.21	19.41	8.5	20.63	13.41
25j	25	22.17	11.42	18.58	3.0	16.44	6.73
26j	26	21.27	14.47	21.35	4.0	19.84	6.71
27j	27	25.86	18.19	21.41	7.0	22.27	9.81
28j	28	28.09	13.10	27.88	1.5	21.57	2.21
29j	29	23.54	13.72	21.66	1.5	19.46	2.59
30j	30	21.50	13.48	20.87	4.5	18.93	8.11
31j	31	18.57	9.70	27.36	3.5	18.39	6.60
32j	32	21.66	17.87	28.65	3.0	25.54	3.40

Table continues next page

33j	33	23.19	15.15	23.40	5.5	21.25	8.29
34j	34	24.10	15.54	21.68	8.5	20.72	13.32
35j	35	16.57	14.92	22.04	2.0	20.47	3.19
36j	36	19.45	14.20	25.86	3.0	21.63	4.40
37j	37	21.41	14.85	29.53	8.0	23.64	10.22
38j	38	13.65	8.51	22.75	2.5	15.70	6.02
39j	39	17.22	14.23	22.44	4.0	20.17	6.54
40j	40	13.17	7.27	28.48	3.0	16.24	6.86
41j	41	16.78	12.1	24.86	2.5	19.58	4.28
42j	42	13.17	12.86	14.43	3.5	15.38	8.71
43j	43	17.53	13.23	20.69	2.5	18.67	4.60
44j	44	11.08	10.09	24.34	1.5	17.69	3.00
45j	45	14.57	12.11	22.71	6.0	18.72	11.01
46j	46	10.91	6.04	25.45	2.0	13.99	5.76
47j	47	14.07	9.07	29.41	6.0	18.43	11.27
48j	48	7.46	7.88	21.53	2.0	14.70	5.33
Mean							8.35
Median							8.64
Standard Deviation							3.60
Minimum							2.21
Maximum							19.86
Count							48

POINT LOAD TEST							
Ore type:		**Ore 5**					
Description:		**Treated at 2.7 kWh/t**					
Sample ID	**Count No.**	**Mass (g)**	**Depth (mm)**	**Width (mm)**	**Load (kN)**	**De**	**Is$_{(50)}$ (MPa)**
1L	1	108.62	25.65	40.04	13.50	36.17	8.92
2L	2	92.61	28.28	31.84	19.50	33.87	14.27
3L	3	72.51	18.05	40.90	5.50	30.67	4.69
4L	4	101.59	24.10	42.30	19.50	36.04	12.96
5L	5	74.41	17.14	40.34	8.50	29.68	7.63
6L	6	63.52	21.45	39.83	16.50	32.99	12.57
7L	7	56.59	22.31	33.74	8.50	30.97	7.15
8L	8	64.56	17.54	31.94	9.50	26.71	10.04
9L	9	45.93	13.98	33.17	9.50	24.30	11.62
10L	10	69.48	28.19	31.61	5.50	33.69	4.06
11L	11	43.43	23.07	38.06	5.50	33.44	4.10
12L	12	62.35	21.32	34.12	10.50	30.44	9.06
13L	13	40.83	15.96	32.51	13.00	25.71	14.58
14L1	14	36.62	19.34	25.73	5.50	25.18	6.37
14L2	15	17.12	10.57	21.62	5.00	17.06	10.59
14L3	16	13.19	9.99	24.42	4.00	17.63	8.05
15L	17	54.76	17.64	30.47	12.50	26.17	13.64
16L1	18	26.21	13.24	22.92	3.00	19.66	5.10
16L2	19	24.87	14.37	26.84	10.50	22.17	14.82
17L1	20	41.38	16.17	26.96	8.50	23.57	10.91
17L2	21	16.78	14.08	23.78	2.00	20.65	3.15
18L1	22	35.02	14.15	32.66	4.00	24.26	4.91
18L2	23	18.60	13.64	23.20	4.00	20.08	6.58
19L1	24	36.75	14.34	29.21	7.50	23.10	9.93
19L2	25	27.45	18.15	21.08	5.50	22.08	7.81
20L1	26	46.11	25.89	30.85	10.00	31.90	8.03
20L2	27	11.75	10.55	23.41	3.00	17.74	5.98
21L1	28	42.89	15.06	31.60	6.50	24.62	7.80
21L2	29	16.96	15.41	23.07	8.50	21.28	12.78
22L1	30	35.73	14.97	28.30	2.00	23.23	2.62
22L2	31	20.66	14.81	22.38	1.50	20.55	2.38
23L1	32	29.00	13.80	23.84	5.50	20.47	8.78

Table continues next page

23L2	33	23.40	17.36	22.30	4.50	22.21	6.33
24L1	34	30.45	16.68	16.36	7.50	18.64	13.84
24L2	35	26.91	14.11	28.96	5.50	22.82	7.42
25L1	36	36.42	12.41	19.21	3.00	17.43	6.15
25L2	37	19.41	12.98	24.93	5.00	20.30	8.09
26L1	38	36.55	15.50	26.92	7.00	23.06	9.30
26L2	39	19.82	11.45	31.37	5.50	21.39	8.20
27L1	40	27.78	15.71	25.30	8.50	22.50	11.72
27L2	41	22.79	13.17	21.13	5.50	18.83	10.00
28L1	42	31.10	17.79	25.21	3.00	23.90	3.77
28L2	43	28.72	17.00	31.81	4.00	26.25	4.34
29L1	44	27.95	17.36	25.02	6.50	23.52	8.37
29L2	45	26.93	14.58	28.90	5.50	23.17	7.25
30L1	46	31.15	16.44	20.74	7.00	20.84	10.87
30L2	47	24.56	12.84	25.76	5.50	20.53	8.74
31L1	48	41.60	18.27	30.99	2.50	26.86	2.62
31L2	49	15.14	16.26	22.10	6.00	21.40	8.95
32L1	50	34.53	21.14	24.87	8.50	25.88	9.44
32L2	51	12.60	9.00	20.66	3.00	15.39	7.45
33L1	52	28.75	10.70	18.05	2.50	15.69	6.03
33L2	53	12.92	8.31	23.38	3.00	15.73	7.20
33L3	54	17.84	11.97	27.38	5.50	20.43	8.81
34L1	55	20.23	15.80	19.66	5.50	19.89	9.18
34L2	56	14.75	5.07	34.35	1.50	14.89	3.92
34L3	57	13.10	6.49	21.56	2.00	13.35	6.19
Mean							8.18
Median							8.05
Standard Deviation							3.22
Minimum							2.38
Maximum							14.82
Count							57

365

POINT LOAD TEST						
Ore type:		Ore 5				
Description:		Treated at 4.7 kWh/t				
Sample ID	**Count No.**	**Mass (g)**	**Depth (mm)**	**Width (mm)**	**Load (kN)**	**De**	**Is$_{(50)}$ (MPa)**
1i	1	86.30	22.94	27.70	12.0	28.45	11.50
2i	2	111.93	19.39	38.00	19.5	30.64	16.67
3i	3	91.86	24.92	42.84	13.0	36.88	8.34
4i	4	90.22	16.75	48.86	9.0	32.29	7.09
5i	5	67.09	23.21	31.27	13.5	30.41	11.67
6i	6	60.60	20.38	39.41	9.5	31.99	7.59
7i	7	59.05	24.92	25.26	11.0	28.32	10.62
8i1	8	53.85	15.60	28.73	8.5	23.89	10.68
8i2	9	19.84	15.76	20.95	5.5	20.51	8.76
9i1	10	57.56	15.58	39.53	10.5	28.01	10.31
9i2	11	15.99	12.23	20.07	5.5	17.68	11.02
10i1	12	54.04	20.15	37.90	6.5	31.19	5.40
10i2	13	10.55	6.25	25.71	2.0	14.31	5.56
11i1	14	45.75	17.05	27.40	5.5	24.40	6.69
11i2	15	17.13	15.04	16.14	5.0	17.58	10.10
12i1	16	46.85	24.36	25.43	1.5	28.09	1.47
12i2	17	34.67	17.87	27.87	2.5	25.19	2.89
13i1	18	51.29	18.18	32.67	9.5	27.51	9.60
13i2	19	23.58	16.18	25.63	5.5	22.98	7.34
14i1	20	47.63	19.33	29.64	12.5	27.02	12.98
14i2	21	21.55	15.42	22.50	7.5	21.02	11.49
15i1	22	41.84	12.73	36.74	9.5	24.41	11.55
15i2	23	39.95	17.64	28.62	17.0	25.36	19.48
16i1	24	43.42	13.40	29.29	7.0	22.36	9.75
16i2	25	30.49	12.92	28.52	3.5	21.67	5.12
16i3	26	25.87	12.29	28.88	3.5	21.26	5.27
17i1	27	36.16	11.98	35.66	7.5	23.33	9.78
17i2	28	35.94	15.34	23.91	4.5	21.62	6.60
18i1	29	32.32	15.78	24.29	7.0	22.10	9.93
18i2	30	26.26	10.46	32.34	4.5	20.76	7.03
18i3	31	11.57	6.86	25.74	2.0	15.00	5.17
19i1	32	35.14	13.51	23.79	3.5	20.23	5.69

Table continues next page

19i2	33	32.10	15.73	21.42	8.0	20.72	12.54
19i3	34	22.00	12.20	23.51	3.0	19.11	5.33
20i1	35	27.36	12.62	27.43	6.5	21.00	9.98
20i2	36	28.72	14.15	29.65	2.5	23.12	3.31
20i3	37	15.90	12.00	21.07	2.0	17.95	3.92
21i1	38	23.85	10.50	29.56	3.5	19.88	5.85
21i2	39	19.60	12.66	23.45	4.5	19.45	7.78
21i3	40	23.66	11.66	27.96	4.0	20.38	6.43
22i1	41	29.03	14.65	26.57	7.0	22.27	9.81
22i2	42	21.21	12.93	19.80	3.0	18.06	5.82
22i3	43	10.57	10.41	21.83	2.5	17.01	5.32
23i1	44	30.66	16.90	23.64	14.5	22.56	19.91
23i2	45	33.69	18.01	24.08	2.5	23.50	3.22
23i3	46	15.14	14.12	18.48	5.0	18.23	9.55
24i1	47	35.90	16.47	34.52	11.5	26.91	12.02
24i2	48	16.71	7.00	24.76	3.0	14.86	7.87
24i3	49	15.07	12.43	24.84	3.5	19.83	5.87
25i1	50	28.20	14.69	23.45	6.0	20.95	9.24
25i2	51	22.89	13.94	24.96	4.0	21.05	6.11
25i3	52	20.74	11.31	29.92	6.0	20.76	9.37
26i1	53	45.06	22.18	28.62	5.0	28.44	4.80
26i2	54	11.67	10.50	19.18	2.5	16.02	5.84
26i3	55	14.03	14.65	18.69	1.5	18.68	2.76
27i1	56	15.19	13.70	20.95	3.5	19.12	6.21
27i2	57	20.33	16.57	26.47	5.0	23.64	6.39
27i3	58	18.42	16.16	20.19	4.5	20.39	7.23
28i1	59	18.76	12.30	27.19	2.0	20.64	3.15
28i2	60	23.81	15.10	28.46	2.5	23.40	3.24
28i3	61	11.43	13.70	21.11	1.0	19.19	1.76
Mean							7.93
Median							7.23
Standard Deviation							3.80
Minimum							1.47
Maximum							19.91
Count							61

POINT LOAD TEST							
Ore type:		Ore 5					
Description:		Treated at 6.9 kWh/t					
Sample ID	Count No.	Mass (g)	Depth (mm)	Width (mm)	Load (kN)	De	$Is_{(50)}$ (MPa)
1k	1	113.38	26.33	38.44	19.5	35.91	13.03
2k	2	101.35	28.27	44.88	10.5	40.20	5.89
3k	3	85.16	22.19	42.76	11.0	34.77	7.73
4k	4	117.51	31.92	44.85	12.5	42.70	6.38
5k	5	94.38	21.86	48.86	7.5	36.89	4.81
6k	6	60.70	17.12	28.71	8.0	25.02	9.36
7k	7	62.72	21.30	40.88	12.0	33.31	9.01
8k	8	70.16	19.96	30.68	12.0	27.93	11.84
9k	9	71.94	20.30	29.71	7.5	27.72	7.49
10k	10	72.11	22.85	36.24	7.5	32.48	5.86
11k	11	71.60	17.14	41.60	10.0	30.14	8.77
12k	12	67.87	19.67	28.71	7.0	26.82	7.35
13k	13	57.45	14.41	37.15	2.5	26.11	2.74
14k	14	65.47	15.36	37.18	4.5	26.97	4.69
15k1	15	47.54	19.25	28.97	10.0	26.65	10.61
15k2	16	19.82	12.74	23.94	2.0	19.71	3.39
16k	17	53.76	22.43	39.41	3.0	33.56	2.23
17k1	18	48.84	20.32	32.86	13.5	29.16	12.45
17k2	19	19.65	16.58	27.26	7.5	23.99	9.36
18k1	20	41.59	19.95	23.61	8.5	24.50	10.28
18k2	21	18.11	12.27	27.32	4.0	20.66	6.29
19k1	22	47.10	25.70	22.24	12.5	26.98	13.01
19k2	23	35.91	15.17	23.81	6.0	21.45	8.91
20k1	24	37.37	20.80	28.73	7.5	27.59	7.54
20k2	25	25.53	16.55	25.14	9.0	23.02	11.98
21k1	26	33.18	19.75	27.80	9.0	26.45	9.66
21k2	27	19.46	16.90	19.42	6.5	20.45	10.40
22k1	28	34.27	15.70	21.53	5.5	20.75	8.60
22k2	29	25.27	9.76	23.69	4.0	17.16	8.39
23k1	30	31.39	17.05	22.12	11.5	21.92	16.52
23k2	31	19.39	11.03	28.64	6.0	20.06	9.89
24k1	32	35.55	19.35	26.02	2.5	25.33	2.87

Table continues next page

24k2	33	17.04	15.41	19.58	8.0	19.61	13.66
24k3	34	12.90	13.40	23.19	9.5	19.90	15.85
25k1	35	26.17	17.70	22.19	4.5	22.37	6.26
25k2	36	22.23	16.54	20.69	4.0	20.88	6.19
25k3	37	15.95	13.91	21.94	9.0	19.72	15.23
26k1	38	27.52	15.98	30.28	9.0	24.83	10.66
26k2	39	20.32	12.07	21.82	3.0	18.32	5.69
26k3	40	15.48	10.98	22.45	3.5	17.72	6.99
27k1	41	23.10	12.62	21.02	7.5	18.38	14.15
27k2	42	23.76	20.63	21.36	6.0	23.69	7.64
27k3	43	13.75	14.21	20.24	1.5	19.14	2.66
28k1	44	18.40	11.49	23.96	3.0	18.73	5.50
28k2	45	17.96	8.49	25.85	2.5	16.72	5.46
28k3	46	15.24	9.39	20.70	2.5	15.74	6.00
29k1	47	22.88	8.00	35.54	3.5	19.03	6.26
29k2	48	23.42	13.93	23.00	8.0	20.20	13.04
29k3	49	13.25	13.87	18.60	4.5	18.13	8.67
30k1	50	19.71	10.32	26.22	3.5	18.57	6.50
30k2	51	17.01	13.74	23.18	3.5	20.14	5.73
30k3	52	13.11	15.27	19.41	5.5	19.43	9.52
31k1	53	17.51	13.53	21.11	4.5	19.07	8.02
31k2	54	14.79	8.82	23.79	3.0	16.35	6.79
31k3	55	11.97	12.10	20.94	4.0	17.97	7.82
31k4	56	17.15	13.15	26.56	2.0	21.09	3.05
Mean							8.30
Median							7.77
Standard Deviation							3.46
Minimum							2.23
Maximum							16.52
Count							56

11.1.2.5   PLT Results Statistical Summary

Ore type	Sample type	Number of fragments	Mean $Is_{(50)}$	Mean $Is_{(50)}$ difference	Degrees of Freedom	Standard deviation	Standard error of difference	Calculated t-value	Confidence level
Ore 1	UT	37	5.63			2.19			
	T- at low energy	41	5.25	0.38	76	2.44	0.527	0.72081	**52%**
	T- at medium energy	39	4.77	0.86	74	1.94	0.474	1.81434	**93%**
	T - at high energy	39	4.34	1.29	74	2.31	0.517	2.49555	**99%**
Ore 2	UT	32	5.73			2.07			
	T- at low energy	34	5.42	0.31	64	2.83	0.614	0.50528	**39%**
	T- at medium energy	38	5.14	0.59	68	2.65	0.577	1.02332	**69%**
	T - at high energy	36	5.16	0.57	66	2.76	0.598	0.95365	**66%**
Ore 3	UT	31	2.61			1.14			
	T- at low energy	29	2.12	0.49	58	1.07	0.286	1.71375	**90%**
	T- at medium energy	30	2.08	0.53	59	1.07	0.283	1.87085	**93%**
	T - at high energy	32	2.09	0.52	61	1.30	0.308	1.68590	**90%**
Ore 5	UT	48	8.35			3.60			
	T- at low energy	57	8.18	0.17	103	3.22	0.666	0.25533	**60%**
	T- at medium energy	61	7.93	0.42	107	3.80	0.716	0.58619	**72%**
	T - at high energy	56	8.30	0.05	102	3.46	0.693	0.07211	**53%**
Total		640							

11.1.3   Crushing Test Data

11.1.3.1   Ore 1

Crusher feed - Ore 1								
	Untreated				**2.4 kWh/t**			
Sieve size (µm)	Weight rtn (g)	Weight rtn (%)	Cum weight rtn (%)	Cum passing (%)	Weight rtn (g)	Weight rtn (%)	Cum weight rtn (%)	Cum passing (%)
37500	0	0	0	100	0	0	0	100
31500	275.1	12.9	12.9	87.1	189.2	9.3	9.3	90.7
26500	870.6	41.0	53.9	46.1	610.4	29.9	39.2	60.8
22400	577.7	27.2	81.1	18.9	796.5	39.0	78.2	21.8
19000	287.5	13.5	94.6	5.4	342.6	16.8	95.0	5.0
16000	115.0	5.4	100.0	0.0	101.9	5.0	100.0	0.0
Pan	0	0			0	0		
Sum	2125.9	100			2040.6	100		
	4.8 kWh/t				**6.9 kWh/t**			
Sieve size (µm)	Weight rtn (g)	Weight rtn (%)	Cum weight rtn (%)	Cum passing (%)	Weight rtn (g)	Weight rtn (%)	Cum weight rtn (%)	Cum passing (%)
37500	0	0	0	100	0	0	0	100
31500	197.2	9.3	9.3	90.7	235.5	11.3	11.3	88.7
26500	851.9	40.4	49.7	50.3	573.5	27.6	39.0	61.0
22400	564.6	26.8	76.5	23.5	801.5	38.6	77.6	22.4
19000	361.9	17.1	93.6	6.4	341.1	16.4	94.0	6.0
16000	134.9	6.4	100.0	0.0	124.6	6.0	100.0	0.0
Pan	0	0			0	0		
Sum	2110.5	100			2076.1	100		

Crusher product - Ore 1							
	Untreated				**2.4 kWh/t**		
Sieve size (µm)	Weight rtn (g)	Weight rtn (%)	Cum weight rtn (%)	Cum passing (%)	Weight rtn (g)	Weight rtn (%)	Cum weight rtn (%)	Cum passing (%)
16000	0.0	0.0	0.0	100.0	31.7	1.6	1.6	98.4
13200	98.2	4.6	4.6	95.4	157.3	7.7	9.3	90.7
9500	681.0	32.1	36.7	63.3	663.4	32.5	41.8	58.2
6700	555.1	26.1	62.8	37.2	493.7	24.2	66.0	34.0
4750	251.1	11.8	74.6	25.4	215.0	10.5	76.6	23.4
3350	118.8	5.6	80.2	19.8	96.0	4.7	81.3	18.7
pan	420.2	19.8			381.2	18.7		
Sum	2124.5	100.0			2038.3	100.0		
	4.8 kWh/t				**6.9 kWh/t**		
Sieve size (µm)	Weight rtn (g)	Weight rtn (%)	Cum weight rtn (%)	Cum passing (%)	Weight rtn (g)	Weight rtn (%)	Cum weight rtn (%)	Cum passing (%)
16000	21.5	1.0	1.0	99.0	0.0	0.0	0.0	100.0
13200	104.2	4.9	6.0	94.0	135.1	6.5	6.5	93.5
9500	731.7	34.7	40.7	59.3	739.0	35.6	42.1	57.9
6700	553.9	26.3	66.9	33.1	466.3	22.5	64.6	35.4
4750	220.2	10.4	77.4	22.6	206.3	9.9	74.5	25.5
3350	87.4	4.1	81.5	18.5	86.6	4.2	78.7	21.3
pan	389.9	18.5			441.8	21.3		
Sum	2108.9	100.0			2075.0	100.0		

11.1.3.2 Ore 2

Crusher feed - Ore 2							
	Untreated				2.3 kWh/t		
Sieve size (µm)	Weight rtn (g)	Weight rtn (%)	Cum weight rtn (%)	Cum passing (%)	Weight rtn (g)	Weight rtn (%)	Cum weight rtn (%)	Cum passing (%)
37500	0	0	0	100	0	0	0	100
31500	424.6	24.0	24.0	76.0	310.4	17.1	17.1	82.9
26500	596.2	33.7	57.7	42.3	474.0	26.2	43.3	56.7
22400	348.2	19.7	77.4	22.6	698.4	38.6	81.9	18.1
19000	272.7	15.4	92.8	7.2	177.7	9.8	91.7	8.3
16000	88.4	5.0	97.8	2.2	107.0	5.9	97.6	2.4
13200	39.6	2.2	100.0	0.0	43.8	2.4	100.0	0.0
Pan	0.0	0.0			0	0		
Sum	1769.7	100.0			1811.4	100.0		

	4.2 kWh/t				6.3 kWh/t		
Sieve size (µm)	Weight rtn (g)	Weight rtn (%)	Cum weight rtn (%)	Cum passing (%)	Weight rtn (g)	Weight rtn (%)	Cum weight rtn (%)	Cum passing (%)
37500	0	0	0	100	0	0	0	100
31500	521.5	29.7	29.7	70.3	213.0	11.7	11.7	88.3
26500	427.1	24.3	54.1	45.9	800.3	44.1	55.8	44.2
22400	392.6	22.4	76.5	23.5	494.0	27.2	83.1	16.9
19000	233.9	13.3	89.8	10.2	75.9	4.2	87.2	12.8
16000	167.7	9.6	99.3	0.7	154.3	8.5	95.7	4.3
13200	11.5	0.7	100.0	0.0	77.2	4.3	100.0	0.0
Pan	0	0	100		0.0	0.0		
Sum	1754.2	100.0			1814.7	100.0		

Crusher product - Ore 2							
	Untreated				2.3 kWh/t		
Sieve size (µm)	Weight rtn (g)	Weight rtn (%)	Cum weight rtn (%)	Cum passing (%)	Weight rtn (g)	Weight rtn (%)	Cum weight rtn (%)	Cum passing (%)
16000	0	0	0	100	0	0	0	100
13200	94.2	5.4	5.4	94.6	62.8	3.5	3.5	96.5
9500	567.4	32.6	38.1	61.9	594.2	32.7	36.2	63.8
6700	505.6	29.1	67.1	32.9	542.9	29.9	66.1	33.9
4750	196.5	11.3	78.4	21.6	220.5	12.2	78.3	21.7
3350	85.7	4.9	83.4	16.6	91.8	5.1	83.3	16.7
pan	289.3	16.6			302.23	16.7		
Sum	1738.7	100.0			1814.37	100.0		

	4.2 kWh/t				6.3 kWh/t		
Sieve size (µm)	Weight rtn (g)	Weight rtn (%)	Cum weight rtn (%)	Cum passing (%)	Weight rtn (g)	Weight rtn (%)	Cum weight rtn (%)	Cum passing (%)
16000	0	0	0	100	0	0	0	100
13200	55.3	3.2	3.2	96.8	76.4	4.2	4.2	95.8
9500	567.2	32.4	35.6	64.4	562.4	31.0	35.2	64.8
6700	536.0	30.6	66.2	33.8	565.2	31.2	66.4	33.6
4750	201.9	11.5	77.7	22.3	221.3	12.2	78.6	21.4
3350	89.9	5.1	82.9	17.1	88.4	4.9	83.5	16.5
pan	299.5	17.1			300.0	16.5		
Sum	1749.8	100.0			1813.7	100		

11.1.3.3 Ore 3

Sieve size (µm)	Weight rtn (g)	Weight rtn (%)	Cum weight rtn (%)	Cum passing (%)	Weight rtn (g)	Weight rtn (%)	Cum weight rtn (%)	Cum passing (%)
	Untreated				**2.2 kWh/t**			
37500	0	0	0	100	0	0	0	100
31500	69.2	4.6	4.6	95.4	351.3	20.5	20.5	79.5
26500	498.2	33.3	37.9	62.1	473.6	27.7	48.2	51.8
22400	411.8	27.5	65.4	34.6	438.6	25.6	73.8	26.2
19000	235.9	15.8	81.2	18.8	265.7	15.5	89.3	10.7
16000	140.9	9.4	90.6	9.4	101.3	5.9	95.3	4.7
13200	93.0	6.2	96.8	3.2	56.2	3.3	98.6	1.4
Pan	48.4	3.2			24.8	1.4		
Sum	1497.3	100			1711.5	100		
	4.1 kWh/t				**6.9 kWh/t**			
37500	0	0	0	100	0	0	0	100
31500	0.0	0.0	0.0	100.0	353.3	21.7	21.7	78.3
26500	518.9	34.9	34.9	65.1	584.2	35.9	57.6	42.4
22400	445.1	29.9	64.8	35.2	191.7	11.8	69.4	30.6
19000	240.4	16.2	80.9	19.1	268.6	16.5	86.0	14.0
16000	198.1	13.3	94.2	5.8	183.5	11.3	97.2	2.8
13200	48.2	3.2	97.5	2.5	34.4	2.1	99.4	0.6
Pan	37.9	2.5			10.6	0.6		
Sum	1488.6	100			1626.3	100		

Crusher feed - Ore 3

Sieve size (µm)	Weight rtn (g)	Weight rtn (%)	Cum weight rtn (%)	Cum passing (%)	Weight rtn (g)	Weight rtn (%)	Cum weight rtn (%)	Cum passing (%)
	UT crusher				**2.2 kWh/t**			
13200	71.0	4.8	4.8	95.2	74.6	4.4	4.4	95.6
9500	516.6	34.6	39.3	60.7	536.9	31.4	35.8	64.2
6700	498.4	33.4	72.7	27.3	494.8	29.0	64.8	35.2
4750	189.3	12.7	85.4	14.6	192.1	11.2	76.0	24.0
3350	83.2	5.6	91.0	9.0	81.1	4.7	80.8	19.2
pan	135.1	9.0	100.0	0.0	328.3	19.2	100.0	0.0
Sum	1493.7	100			1707.8	100.0		
	4.1 kWh/t				**6.9 kWh/t**			
13200	53.8	3.6	3.6	96.4	50.8	3.1	3.1	96.9
9500	431.2	29.1	32.7	67.3	506.9	31.3	34.4	65.6
6700	466.2	31.4	64.1	35.9	499.7	30.8	65.2	34.8
4750	183.7	12.4	76.5	23.5	176.9	10.9	76.1	23.9
3350	86.1	5.8	82.3	17.7	82.5	5.1	81.2	18.8
pan	263.0	17.7	100.0	0.0	305.3	18.8	100.0	0.0
Sum	1484.0	100.0			1621.9	100.0		

Crusher product - Ore 3

11.1.3.4   Ore 5

Crusher feed - Ore 5							
	Untreated				2.7 kWh/t		
Sieve size (μm)	Weight rtn (g)	Weight rtn (%)	Cum weight rtn (%)	Cum passing (%)	Weight rtn (g)	Weight rtn (%)	Cum weight rtn (%)	Cum passing (%)
37500	0	0	0	100	0	0	0	100
31500	269.2	13.1	13.1	86.9	120.2	6.0	6.0	94.0
26500	442.3	21.5	34.6	65.4	504.0	25.0	31.0	69.0
22400	630.4	30.7	65.3	34.7	374.4	18.6	49.6	50.4
19000	294.1	14.3	79.6	20.4	450.5	22.4	71.9	28.1
16000	252.9	12.3	91.8	8.2	380.0	18.9	90.8	9.2
13200	148.3	7.2	99.1	0.9	162.6	8.1	98.8	1.2
Pan	19.4	0.9			23.4	1.2		
Sum	2056.53	100			2015.2	100		
	4.7 kWh/t				6.9 kWh/t		
Sieve size (μm)	Weight rtn (g)	Weight rtn (%)	Cum weight rtn (%)	Cum passing (%)	Weight rtn (g)	Weight rtn (%)	Cum weight rtn (%)	Cum passing (%)
37500	0	0	0	100	0	0	0	100
31500	61.5	3.0	3.0	97.0	161.7	7.8	7.8	92.2
26500	238.8	11.7	14.7	85.3	606.0	29.1	36.8	63.2
22400	551.4	27.0	41.7	58.3	427.9	20.5	57.3	42.7
19000	578.0	28.3	70.0	30.0	363.2	17.4	74.8	25.2
16000	387.9	19.0	89.0	11.0	351.1	16.8	91.6	8.4
13200	158.8	7.8	96.8	3.2	157.3	7.5	99.1	0.9
Pan	65.7	3.2			17.9	0.9		
Sum	2042.01	100			2085.14	100		

Crusher product - Ore 5							
	Untreated				2.7 kWh/t		
Sieve size (μm)	Weight rtn (g)	Weight rtn (%)	Cum weight rtn (%)	Cum passing (%)	Weight rtn (g)	Weight rtn (%)	Cum weight rtn (%)	Cum passing (%)
16000	0	0	0	100	0	0	0	100
13200	128.7	6.3	6.3	93.7	0.0	0.0	0.0	100.0
9500	752.6	36.6	42.8	57.2	869.9	43.1	43.1	56.9
6700	460.4	22.4	65.2	34.8	458.3	22.7	65.9	34.1
4750	187.2	9.1	74.3	25.7	177.9	8.8	74.7	25.3
3350	77.3	3.8	78.0	22.0	78.2	3.9	78.6	21.4
pan	452.4	22.0			432.6	21.4		
Sum	2058.7	100.0			2016.8	100.0		
	4.7 kWh/t				6.9 kWh/t		
Sieve size (μm)	Weight rtn (g)	Weight rtn (%)	Cum weight rtn (%)	Cum passing (%)	Weight rtn (g)	Weight rtn (%)	Cum weight rtn (%)	Cum passing (%)
16000	0	0	0	100	0	0	0	100
13200	100.3	4.9	4.9	95.1	89.7	4.3	4.3	95.7
9500	815.3	39.9	44.8	55.2	775.9	37.2	41.5	58.5
6700	469.6	23.0	67.8	32.2	451.6	21.6	63.1	36.9
4750	173.8	8.5	76.4	23.6	182.6	8.8	71.9	28.1
3350	82.5	4.0	80.4	19.6	91.1	4.4	76.3	23.7
pan	400.2	19.6			495.4	23.7		
Sum	2041.7	100.0			2086.2	100.0		

11.2 Cores - Raw Data

11.2.1 UPV Repeatability Data

	Core X										
	Transit times (µs)						Statistical data				
							A	B	C	D	E= C*B/SQRT(D)	F=E/A*100
Locati on ID	Run 1	Run 2	Run 3	Run 4	Run 5	Run 6	Avera ge	Standard Dev	Z-score at 95% CI	Number of runs	Margin error at 95% CI	% Margin error at 95% CI
1	5.0	4.9	5.0	4.9	4.8	4.9	4.92	0.075	1.96	6	0.0602	1.23%
2	4.4	4.3	4.2	4.2	4.3	4.2	4.27	0.082	1.96	6	0.0653	1.53%
3	4.4	4.5	4.4	4.3	4.4	4.3	4.38	0.075	1.96	6	0.0602	1.37%
4	4.3	4.4	4.3	4.2	4.4	4.3	4.32	0.075	1.96	6	0.0602	1.40%
5	4.4	4.3	4.4	4.3	4.4	4.3	4.35	0.055	1.96	6	0.0438	1.01%
6	5.0	5.1	5.0	5.1	5.2	5.1	5.08	0.075	1.96	6	0.0602	1.18%
7	4.9	4.8	4.9	5.0	4.8	5.0	4.90	0.089	1.96	6	0.0716	1.46%

	Core Y										
	Transit times (µs)						Statistical data				
							A	B	C	D	E= C*B/SQRT(D)	F=E/A*100
Locati on ID	Run 1	Run 2	Run 3	Run 4	Run 5	Run 6	Avera ge	Standard Dev	Z-score at 95% CI	Number of runs	Margin error at 95% CI	% Margin error at 95% CI
1	4.8	4.8	4.7	4.7	4.6	4.7	4.72	0.075	1.96	6	0.0602	1.28%
2	4.0	4.1	3.9	4.2	4.0	4.4	4.10	0.179	1.96	6	0.1431	3.49%
3	4.1	4.1	4.2	4.3	4.3	4.2	4.20	0.089	1.96	6	0.0716	1.70%
4	4.1	3.9	4.0	4.0	4.1	4.2	4.05	0.105	1.96	6	0.0839	2.07%
5	4.2	4.2	4.3	4.2	4.4	4.2	4.25	0.084	1.96	6	0.0669	1.58%
6	4.3	4.4	4.2	4.3	4.3	4.2	4.28	0.075	1.96	6	0.0602	1.41%
7	4.1	4.2	4.0	4.1	4.2	4.1	4.12	0.075	1.96	6	0.0602	1.46%

Note: Other cores in all ore types tested had a margin of error of less than 3.5%

11.2.2 UPV Reductions

		Pre-treated		Post-treated		
	A	B	X=A/B	C	Y=A/C	Z=(X-Y)/X*100
Location tested on the specimen	Distance between probes (mm)	Average transit time (µs)	Average velocity mm/µs	Average transit time (µs)	Average velocity (mm/µs)	Average UPV reduction (%)
1	23.2	4.92	4.71	5.30	4.37	7.2%
2	21.0	4.27	4.92	4.58	4.58	6.9%
3	21.0	4.38	4.79	4.57	4.60	4.0%
4	21.0	4.32	4.86	4.75	4.42	9.1%
5	21.0	4.35	4.83	21.17	1.00	79.3%
6	21.0	5.08	4.13	19.17	1.10	73.5%
7	21.0	4.90	4.29	5.45	3.85	10.1%
Mean			4.65		3.42	
STD deviation			0.31		1.64	
Overall induced damage						**27.2%**
Calculated t-value						1.95432
T-test confidence level						**92.56%**

Core ID: Ore 1-1T

		Pre-treated		Post-treated		
	A	B	X=A/B	C	Y=A/C	Z=(X-Y)/X*100
Location tested on the specimen	Distance between probes (mm)	Average transit time (µs)	Average velocity mm/µs	Average transit time (µs)	Average velocity (mm/µs)	Average UPV reduction (%)
1	23.6	5.03	4.69	5.40	4.37	6.8%
2	21.0	4.47	4.70	4.48	4.68	0.4%
3	21.0	4.32	4.86	4.50	4.67	4.1%
4	21.0	4.28	4.90	4.78	4.39	10.5%
5	21.0	4.05	5.19	12.82	1.64	68.4%
6	21.0	4.12	5.10	12.35	1.70	66.7%
7	21.0	4.10	5.12	4.57	4.60	10.2%
Mean			4.94		3.72	
STD deviation			0.20		1.41	
Overall induced damage						**23.9%**
Calculated t-value						2.26262
T-test confidence level						**95.70%**

Core ID: Ore 1-2T

376

Core 1D: Ore 1-3T						
		Pre-treated		Post-treated		
Location tested on the specimen	A Distance between probes (mm)	B Average transit time (µs)	X=A/B Average velocity mm/µs	C Average transit time (µs)	Y=A/C Average velocity (mm/µs)	Z=(X-Y)/X*100 Average UPV reduction (%)
1	23.0	5.27	4.37	6.38	3.60	17.5%
2	21.0	4.60	4.57	5.32	3.95	13.5%
3	21.0	4.77	4.41	5.68	3.70	16.1%
4	21.0	4.68	4.48	5.55	3.78	15.6%
5	21.0	4.57	4.60	5.55	3.78	17.7%
6	21.0	4.62	4.55	5.55	3.78	16.8%
7	21.0	4.62	4.55	5.17	4.06	10.6%
Mean			4.50		3.81	
STD deviation			0.09		0.15	
Overall induced damage						15.4%
Calculated t-value						10.47265
T-test confidence level						99.90%

Core ID: Ore 1-4T						
		Pre-treated		Post-treated		
Location tested on the specimen	A Distance between probes (mm)	B Average transit time (µs)	X=A/B Average velocity mm/µs	C Average transit time (µs)	Y=A/C Average velocity (mm/µs)	Z=(X-Y)/X*100 Average UPV reduction (%)
1	22.2	4.72	4.72	6.32	3.52	25.3%
2	21.0	4.12	5.10	4.97	4.23	17.1%
3	21.0	4.20	5.00	5.62	3.74	25.2%
4	21.0	4.05	5.19	5.23	4.01	22.6%
5	21.0	4.25	4.94	5.00	4.20	15.0%
6	21.0	4.28	4.90	6.23	3.37	31.3%
7	21.0	4.12	5.10	5.88	3.57	30.0%
Mean			4.99		3.81	
STD deviation			0.16		0.34	
Overall induced damage						23.8%
Calculated t-value						8.31402
T-test confidence level						99.90%

377

Core ID: Ore 2-1T						
		Pre-treated		Post-treated		
Location tested on the specimen	A	B	X=A/B	C	Y=A/C	Z=(X-Y)/X*100
	Distance between probes (mm)	Average transit time (µs)	Average velocity mm/µs	Average transit time (µs)	Average velocity (mm/µs)	Average UPV reduction (%)
1	22.7	4.30	5.27	5.20	4.36	17.3%
2	21.0	3.97	5.29	5.28	3.97	24.9%
3	21.0	4.03	5.21	5.65	3.72	28.6%
4	21.0	4.57	4.60	5.45	3.85	16.2%
5	21.0	3.95	5.32	5.40	3.89	26.9%
6	21.0	3.77	5.58	5.35	3.93	29.6%
7	21.0	3.80	5.53	5.17	4.06	26.5%
Mean			5.26		3.97	
STD deviation			0.32		0.20	
Overall induced damage						**24.3%**
Calculated t-value						8.98919
T-test confidence level						**99.99%**

Core ID: Ore 2-2T						
		Pre-treated		Post-treated		
Location tested on the specimen	A	B	X=A/B	C	Y=A/C	Z=(X-Y)/X*100
	Distance between probes (mm)	Average transit time (µs)	Average velocity mm/µs	Average transit time (µs)	Average velocity (mm/µs)	Average UPV reduction (%)
1	22.9	4.43	5.16	5.82	3.93	23.8%
2	21.0	3.75	5.60	4.22	4.98	11.1%
3	21.0	3.95	5.32	4.18	5.02	5.6%
4	21.0	3.95	5.32	4.47	4.70	11.6%
5	21.0	3.83	5.48	4.50	4.67	14.8%
6	21.0	3.87	5.43	4.55	4.62	15.0%
7	21.0	4.20	5.00	4.45	4.72	5.6%
Mean			5.33		4.66	
STD deviation			0.20		0.36	
Overall induced damage						**12.5%**
Calculated t-value						4.29121
T-test confidence level						**99.90%**

Core ID: Ore 2-3T						
		Pre-treated		Post-treated		
Location tested on the specimen	A	B	X=A/B	C	Y=A/C	Z=(X-Y)/X*100
	Distance between probes (mm)	Average transit time (µs)	Average velocity (mm/µs)	Average transit time (µs)	Average velocity (mm/µs)	Average UPV reduction (%)
1	23.6	5.35	4.41	5.93	3.98	9.8%
2	21.0	4.23	4.96	4.43	4.74	4.5%
3	21.0	4.17	5.04	4.42	4.75	5.7%
4	21.0	4.23	4.96	4.35	4.83	2.7%
5	21.0	4.32	4.86	4.55	4.62	5.1%
6	21.0	4.43	4.74	4.87	4.32	8.9%
7	21.0	4.62	4.55	4.97	4.23	7.0%
Mean			4.79		4.49	
STD deviation			0.24		0.32	
Overall induced damage						6.3%
Calculated t-value						1.94861
T-test confidence level						92.49%

Core ID: Ore 3-1T						
		Pre-treated		Post-treated		
Location tested on the specimen	A	B	X=A/B	C	Y=A/C	Z=(X-Y)/X*100
	Distance between probes (mm)	Average transit time (µs)	Average velocity mm/µs	Average transit time (µs)	Average velocity (mm/µs)	Average UPV reduction (%)
1	23.4	6.60	3.54	8.28	2.82	20.3%
2	21.0	5.23	4.01	7.53	2.79	30.5%
3	21.0	4.95	4.24	6.70	3.13	26.1%
4	21.0	5.08	4.13	5.43	3.87	6.4%
5	21.0	5.07	4.14	7.23	2.90	30.0%
6	21.0	5.05	4.16	6.35	3.31	20.5%
7	21.0	4.42	4.75	5.12	4.10	13.7%
Mean			4.14		3.27	
STD deviation			0.36		0.52	
Overall induced damage						21.1%
Calculated t-value						3.61613
T-test confidence level						99.65%

Core ID: Ore 3-2T						
		Pre-treated		Post-treated		
Location tested on the specimen	A Distance between probes (mm)	B Average transit time (µs)	X=A/B Average velocity (mm/µs)	C Average transit time (µs)	Y=A/C Average velocity (mm/µs)	Z=(X-Y)/X*100 Average UPV reduction (%)
1	20.7	7.15	2.90	14.37	1.44	50.2%
2	21.0	5.12	4.10	6.27	3.35	18.4%
3	21.0	5.38	3.90	6.87	3.06	21.6%
4	21.0	5.55	3.78	7.73	2.72	28.2%
5	21.0	5.65	3.72	7.57	2.78	25.3%
6	21.0	5.98	3.51	7.80	2.69	23.3%
7	21.0	5.78	3.63	7.93	2.65	27.1%
Mean		3.65		2.67		
STD deviation		0.38		0.60		
Overall induced damage						27.7%
Calculated t-value						3.65413
T-test confidence level						99.67%

Core ID: Ore 3-3T						
		Pre-treated		Post-treated		
Location tested on the specimen	A Distance between probes (mm)	B Average transit time (µs)	X=A/B Average velocity (mm/µs)	C Average transit time (µs)	Y=A/C Average velocity (mm/µs)	Z=(X-Y)/X*100 Average UPV reduction (%)
1	21.6	5.00	4.31	6.18	3.49	19.1%
2	21.0	4.92	4.27	7.77	2.70	36.7%
3	21.0	4.85	4.33	9.20	2.28	47.3%
4	21.0	4.85	4.33	9.00	2.33	46.1%
5	21.0	4.88	4.30	6.77	3.10	27.8%
6	21.0	4.90	4.29	7.75	2.71	36.8%
7	21.0	4.88	4.30	6.93	3.03	29.6%
Mean		4.30		2.81		
STD deviation		0.02		0.43		
Overall induced damage						34.8%
Calculated t-value						9.13233
T-test confidence level						99.99%

Core ID: Ore 4-1T						
		Pre-treated		Post-treated		
Location tested on the specimen	A Distance between probes (mm)	B Average transit time (µs)	X=A/B Average velocity (mm/µs)	C Average transit time (µs)	Y=A/C Average velocity (mm/µs)	Z=(X-Y)/X*100 Average UPV reduction (%)
1	23.2	4.40	5.27	14.03	1.65	68.6%
2	21.0	4.20	5.00	4.68	4.48	10.3%
3	21.0	3.85	5.45	5.00	4.20	23.0%
4	21.0	3.87	5.43	4.33	4.85	10.8%
5	21.0	3.85	5.45	9.12	2.30	57.8%
6	21.0	3.83	5.48	6.77	3.10	43.3%
7	21.0	3.48	6.03	4.28	4.90	18.7%
Mean			5.44		3.64	
STD deviation			0.31		1.30	
Overall induced damage						**33.2%**
Calculated t-value						3.57626
T-test confidence level						**99.62%**

Core ID: Ore 4-2T						
		Pre-treated		Post-treated		
Location tested on the specimen	A Distance between probes (mm)	B Average transit time (µs)	X=A/B Average velocity (mm/µs)	C Average transit time (µs)	Y=A/C Average velocity (mm/µs)	Z=(X-Y)/X*100 Average UPV reduction (%)
1	23.0	4.17	5.52	8.53	2.70	51.2%
2	21.0	3.57	5.89	4.15	5.06	14.1%
3	21.0	3.50	6.00	5.02	4.19	30.2%
4	21.0	3.50	6.00	4.55	4.62	23.1%
5	21.0	3.78	5.55	4.37	4.81	13.4%
6	21.0	3.68	5.70	5.00	4.20	26.3%
7	21.0	3.67	5.73	4.58	4.58	20.0%
Mean			5.77		4.31	
STD deviation			0.20		0.78	
Overall induced damage						**25.5%**
Calculated t-value						4.83468
T-test confidence level						**99.96%**

Core ID: Ore 4-3T						
		Pre-treated		Post-treated		
	A	B	X=A/B	C	Y=A/C	Z=(X-Y)/X*100
Location tested on the specimen	Distance between probes (mm)	Average transit time (μs)	Average velocity (mm/μs)	Average transit time (μs)	Average velocity (mm/μs)	Average UPV reduction (%)
1	23.3	4.02	5.80	14.72	1.58	72.7%
2	21.0	3.55	5.92	4.78	4.39	25.8%
3	21.0	3.53	5.94	9.85	2.13	64.1%
4	21.0	3.55	5.92	4.37	4.81	18.7%
5	21.0	3.63	5.78	4.48	4.68	19.0%
6	21.0	3.53	5.94	4.68	4.48	24.6%
7	21.0	3.65	5.75	4.20	5.00	13.1%
Mean			5.86		3.87	
STD deviation			0.08		1.40	
Overall induced damage						34.0%
Calculated t-value						3.77221
T-test confidence level						99.73%

11.2.3 Pairing of Cores (Ores 1, 2, and 4)
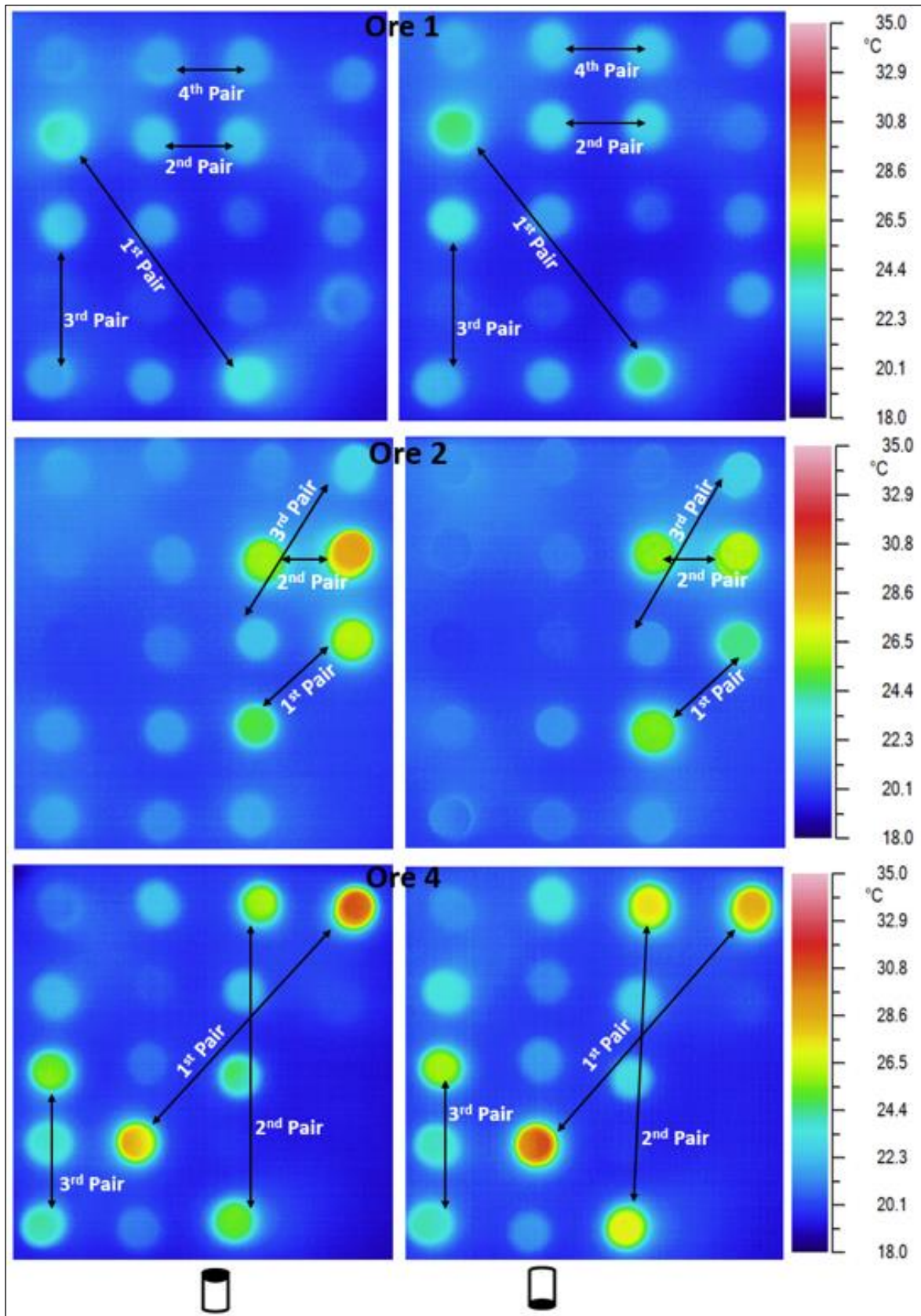
11.2.4 Temperature Profiles – Pairing of Cores

Ore 1

Ore 2
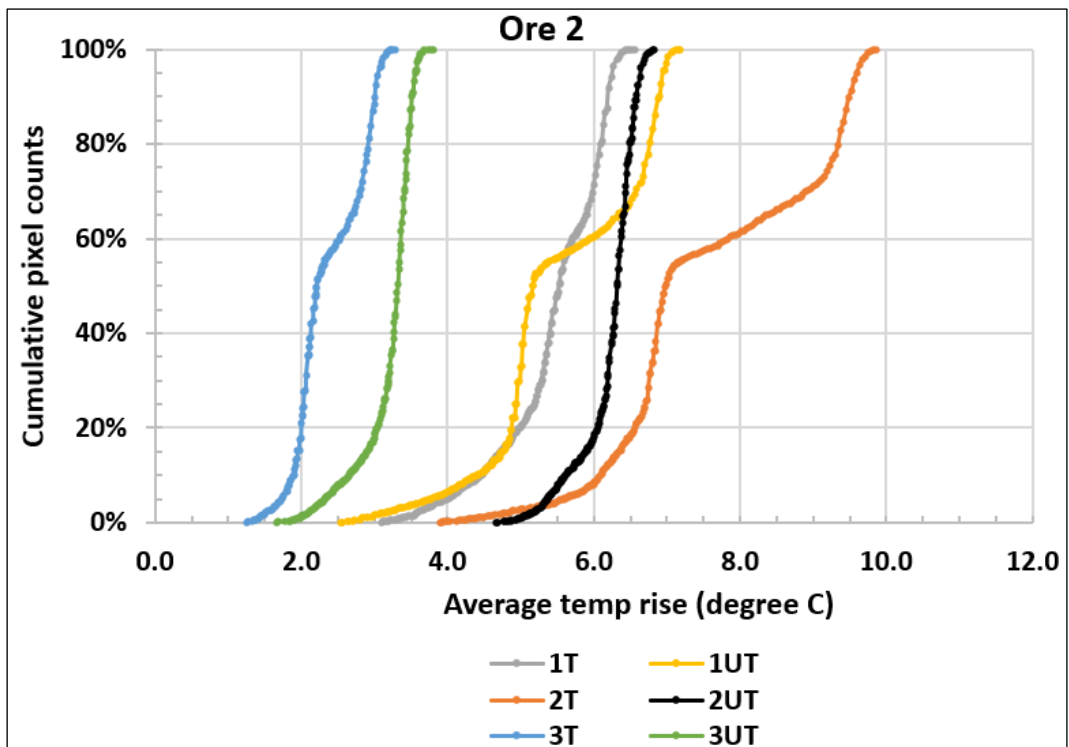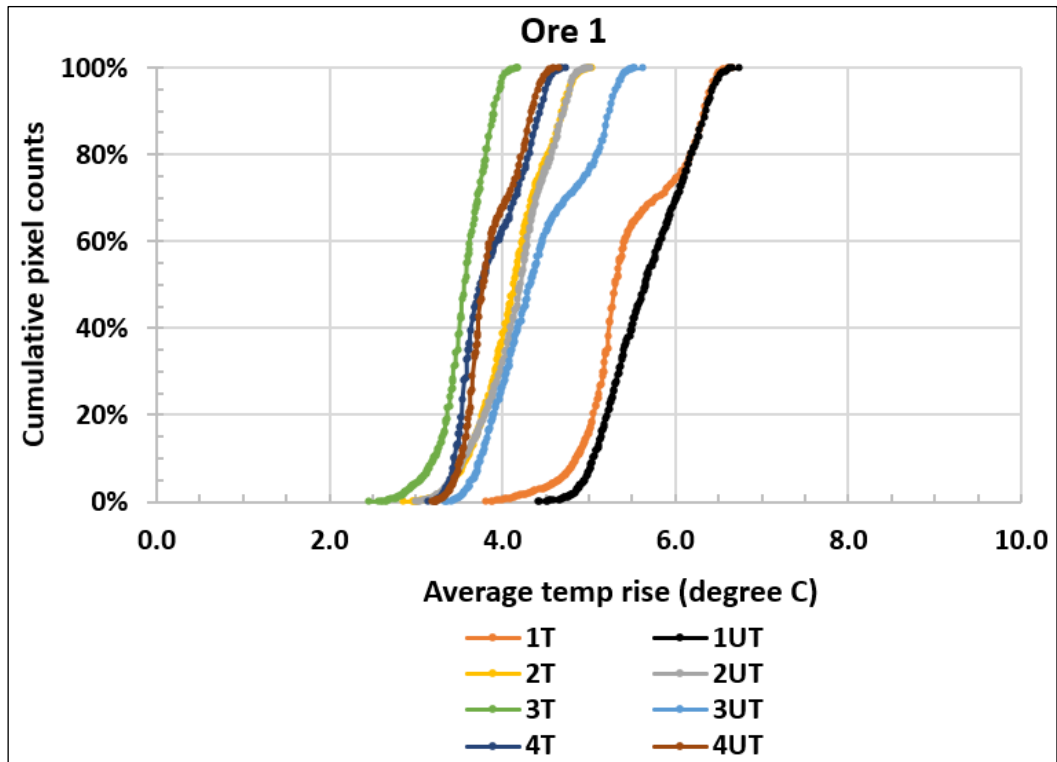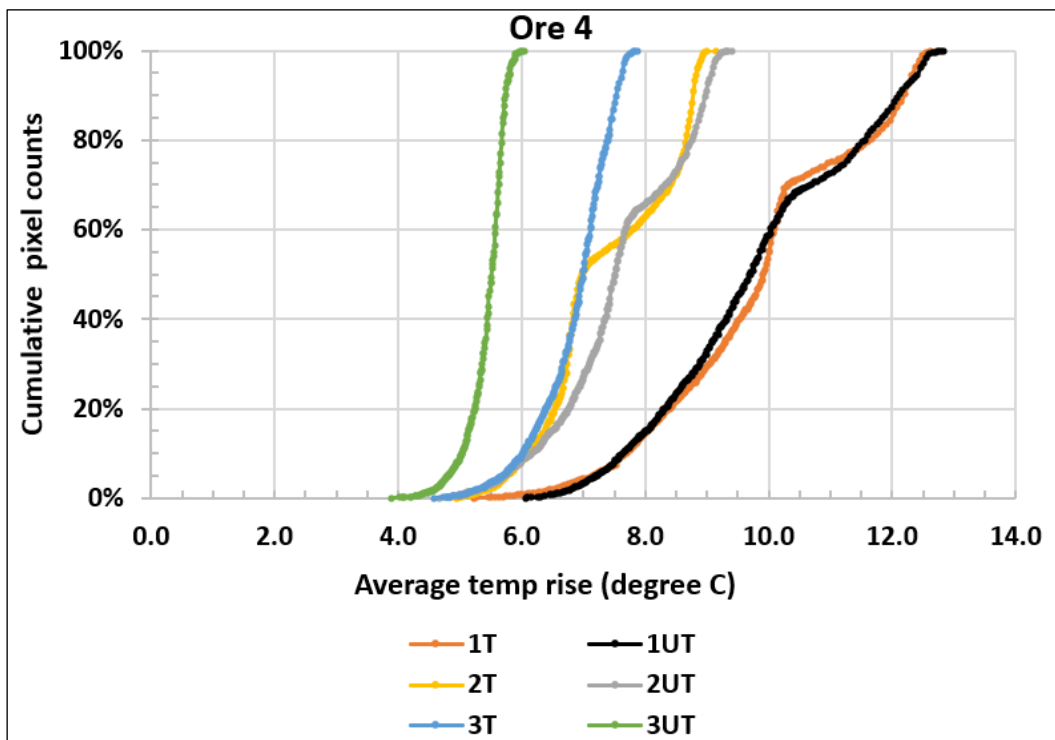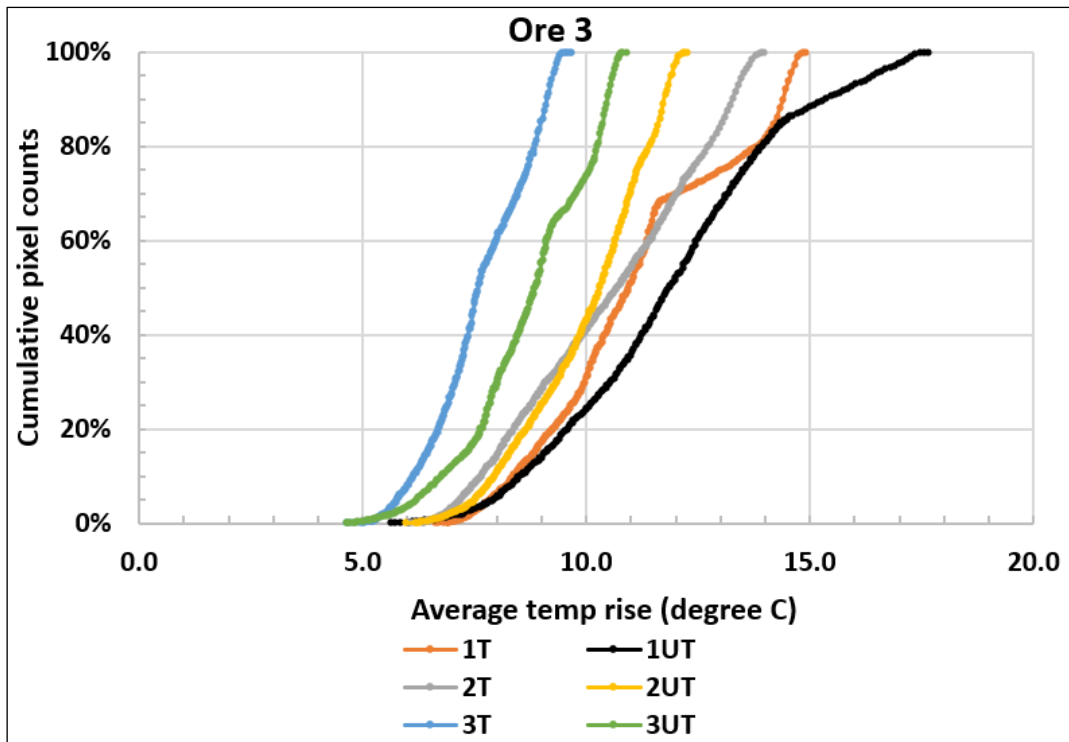
11.2.5 ICP Statistical Results (three repeats) - Several Wavelengths

Sample	Cu (324.754 nm) ppm	Cu (327.395 nm) ppm	Cu II (213.598 nm) ppm	Cu II (224.700 nm) ppm	Fe (273.358 nm) ppm	Fe (370.792 nm) ppm	Fe II (234.350 nm) ppm	Fe II (238.204 nm) ppm	Fe II (259.940 nm) ppm
1B run 1	90.5	89.0	87.8	91.0	2206.5	2208.1	2075.3	2070.9	2085.3
1B run 2	93.5	92.0	90.1	93.6	2278.3	2292.4	2139.1	2134.1	2149.6
1B run 3	91.0	89.3	87.4	90.9	2212.7	2234.7	2076.6	2069.6	2089.7
Mean	91.7	90.1	88.4	91.8	2232.5	2245.1	2097.0	2091.5	2108.2
STD	1.61	1.65	1.46	1.53	39.78	43.10	36.47	36.87	35.92
Margin error (95% CI)	**2.0**	**2.1**	**1.9**	**1.9**	**2.0**	**2.2**	**2.0**	**2.0**	**1.9**

11.2.6 ICP Assay Results Comparison Lab A versus Lab B

	Cu (ppm)			
	Lab A			Lab B
Label	Run 1	Run2	Average	Average
Sample 1	23	22.7	22.9	23.0
Sample 2	40.1	39.1	39.6	37.0
Sample 3	213.6	212.2	212.9	204.0
Sample 4	20.2	19.7	20.0	19.0
Sample 5	1.3	1.3	1.3	<10
Sample 6	1.7	1.7	1.7	<10
Sample 7	1279.9	1271.6	1275.8	1231.0
Sample 8	163.4	148.5	156.0	142.0
Sample 9	2.2	2.2	2.2	<10
Sample 10	11.1	10.3	10.7	10.0
	Fe (ppm)			
	Lab A			Lab B
Label	Run 1	Run2	Average	Average
Sample 1	1072.8	1048.4	1060.6	1150
Sample 2	917.4	889.4	903.4	949
Sample 3	485.8	482.9	484.35	522
Sample 4	482.2	465.9	474.05	517
Sample 5	1125.4	1102.3	1113.85	1235
Sample 6	800.8	786.7	793.75	886
Sample 7	1416	1398.4	1407.2	1503
Sample 8	1608.5	1462.5	1535.5	1571
Sample 9	4807.5	4790.8	4799.15	5156
Sample 10	2573.8	2377.5	2475.65	2602
Note: Only the average results were reported by Lab B				

11.2.7 Copper and Iron Extraction Results - ICP-AES

	Pregnant solution			Acid degistion of residue core			Back-calculated total copper content		
	Soln concentration	Copper content in 24 mls AR		1 gram sample, soln concentration	Copper content in 10 mls AR, 1 gram sample	Copper content whole fragment		Back-calculated head grade	Copper extraction (%)
	**A	B=A*0.024	C	**D	E=D*0.01	F=E*C	G=B+F	H=G/(1000*C)*100	I=(B/G)*100
Core ID	Cu (mg/L)	Cu (mg)	Mass of core (g)	Cu (mg/L)	Cu (mg)	Cu (mg)	Cu (mg)	Cu (%)	Cu (%)
Ore 1-1T	1118.1	26.84	20.38	324.0	3.24	66.03	92.87	0.46	**28.9**
Ore 1-UT	127.3	3.06	19.63	87.5	0.875	17.18	20.23	0.10	**15.1**
Ore 1-2T	352.9	8.47	21.37	228.0	2.28	48.72	57.19	0.27	**14.8**
Ore 1-2UT	305.0	7.32	20.58	302.5	3.025	62.25	69.57	0.34	**10.5**
Ore 1-3T	227.3	5.46	20.5	114.0	1.14	23.37	28.83	0.14	**18.9**
Ore 1-3UT	812.9	19.51	19.13	580.0	5.8	110.95	130.46	0.68	**15.0**
Ore 1-4T	1821.5	43.72	19.88	474.0	4.74	94.23	137.95	0.69	**31.7**
Ore 1-4UT	165.8	3.98	18.78	149.0	1.49	27.98	31.96	0.17	**12.5**
Ore 4-1T	19.8	0.48	22.0	4.0	0.04	0.88	1.35	0.01	**35.1**
Ore 4-1UT	19.8	0.48	20.1	8.5	0.085	1.71	2.18	0.01	**21.8**
Ore 4-2T	382.5	9.18	22.6	115.0	1.15	25.96	35.14	0.16	**26.1**
Ore 4-2UT	351.0	8.43	22.5	200.5	2.005	45.01	53.44	0.24	**15.8**
Ore 4-3T	412.1	9.89	23.7	156.0	1.56	36.93	46.82	0.20	**21.1**
Ore 4-3UT	40.0	0.96	23.0	24.5	0.245	5.62	6.58	0.03	**14.6**
Ore 2-1T	4050.8	97.22	20.7	1337.5	13.375	276.86	374.08	1.81	**26.0**
Ore 2-1UT	3157.7	75.79	19.7	1402.5	14.025	276.29	352.08	1.79	**21.5**
Ore 2-2T	4661.0	111.87	22.0	1763.5	17.635	387.97	499.84	2.27	**22.4**
Ore 2-2UT	2650.2	63.61	20.0	1170.0	11.7	234.00	297.61	1.49	**21.4**
Ore 2-3T	3678.5	88.29	21.3	1595.5	15.955	339.68	427.97	2.01	**20.6**
Ore 2-3UT	3856.9	92.57	20.5	1732.5	17.325	355.34	447.90	2.18	**20.7**
Ore 3-1T	655.8	15.74	19.6	201.0	2.01	39.34	55.08	0.28	**28.6**
Ore 3-1UT	350.6	8.42	22.0	308.0	3.08	67.88	76.30	0.35	**11.0**
Ore 3-2T	403.3	9.68	22.1	174.5	1.745	38.63	48.31	0.22	**20.0**
Ore 3-2UT	515.0	12.36	22.3	267.0	2.67	59.57	71.93	0.32	**17.2**
Ore 3-3T	566.7	13.60	21.6	125.5	1.255	27.16	40.76	0.19	**33.4**
Ore 3-3UT	375.0	9.00	24.8	179.0	1.79	44.30	53.30	0.22	**16.9**

**A - The values have been multiplied by 50/24 because the 24 mls leach solution was diluted with DI water to 50 mls before ICP analysis

**D - The values have beenmultiplied by 50/10 because the 10 mls leach solution was diluted with DI water to 50 mls before ICP analysis

	Iron raw data								
	Pregnant solution			Acid degistion of residue core					
	Soln concentration	Iron content in 24 mls AR		1 gram sample, soln concentration	Iron content in 10 mls AR, 1 gram sample	Iron content whole fragment	Back-calculated total iron content	Back-calculated head grade	Iron extraction (%)
	**A	B=A*0.024	C	**D	E=D*0.01	F=E*C	G=B+F	H=G/(1000*C)*100	I=(B/G)*100
Core ID	Fe (mg/L)	Fe (mg)	Mass of core (g)	Fe (mg/L)	Fe (mg)	Fe (mg)	Fe (mg)	Fe (%)	Fe (%)
Ore 1-1T	4017.5	96.42	20.38	2569.0	25.69	523.56	619.98	3.042	15.6
Ore 1-UT	3552.7	85.27	19.63	3581.0	35.81	702.95	788.22	4.015	10.8
Ore 1-2T	4768.8	114.45	21.37	3287.5	32.875	702.54	816.99	3.823	14.0
Ore 1-2UT	3357.5	80.58	20.58	3682.0	36.82	757.76	838.34	4.074	9.6
Ore 1-3T	4008.8	96.21	20.5	3497.0	34.97	716.89	813.10	3.966	11.8
Ore 1-3UT	3293.8	79.05	19.13	3388.5	33.885	648.22	727.27	3.802	10.9
Ore 1-4T	4353.5	104.49	19.88	3316.5	33.165	659.32	763.81	3.842	13.7
Ore 1-4UT	3421.5	82.12	18.78	3396.0	33.96	637.77	719.88	3.833	11.4
Ore 4-1T	22698.5	544.77	22.0	6188.5	61.885	1358.38	1903.14	8.670	28.6
Ore 4-1UT	16438.3	394.52	20.1	5440.0	54.4	1093.44	1487.96	7.403	26.5
Ore 4-2T	6351.7	152.44	22.6	5364.0	53.64	1210.65	1363.09	6.039	11.2
Ore 4-2UT	13836.7	332.08	22.5	4587.0	45.87	1029.78	1361.86	6.066	24.4
Ore 4-3T	6983.3	167.60	23.7	5538.5	55.385	1310.96	1478.56	6.247	11.3
Ore 4-3UT	3288.8	78.93	23.0	5129.0	51.29	1177.11	1256.04	5.473	6.3
Ore 2-1T	5032.1	120.77	20.7	2919.5	29.195	604.34	725.11	3.503	16.7
Ore 2-1UT	3381.3	81.15	19.7	2976.0	29.76	586.27	667.42	3.388	12.2
Ore 2-2T	4778.1	114.68	22.0	3249.5	32.495	714.89	829.57	3.771	13.8
Ore 2-2UT	2909.8	69.84	20.0	2673.0	26.73	534.60	604.44	3.022	11.6
Ore 2-3T	3646.3	87.51	21.3	2993.5	29.935	637.32	724.83	3.405	12.1
Ore 2-3UT	3900.4	93.61	20.5	2991.5	29.915	613.56	707.17	3.448	13.2
Ore 3-1T	20389.6	489.35	19.6	4720.0	47.2	923.70	1413.05	7.221	34.6
Ore 3-1UT	22334.8	536.04	22.0	10982.5	109.825	2420.54	2956.58	13.415	18.1
Ore 3-2T	23198.5	556.77	22.1	9872.0	98.72	2185.66	2742.43	12.387	20.3
Ore 3-2UT	13276.0	318.63	22.3	11357.0	113.57	2533.75	2852.37	12.785	11.2
Ore 3-3T	28357.9	680.59	21.6	4740.5	47.405	1025.84	1706.43	7.886	39.9
Ore 3-3UT	23630.8	567.14	24.8	14090.0	140.9	3487.28	4054.42	16.381	14.0

**A - The values have been multiplied by 50/24 because the 24 mls leach solution was diluted with DI water to 50 mls before ICP analysis

**D - The values have been multiplied by 50/10 because the 10 mls leach solution was diluted with DI water to 50 mls before ICP analysis

11.2.8 X-ray CT Data

11.2.8.1   Cracks/voids and Sulphide Grains

	Core ID	Total voxel	Total volume (mm³)	Labelled voxels count	Volume of labelled voxels (mm³)	Volume of labelled voxels (%)
			Voids/cracks			
			Pre-treated cores			
1C	Ore 1-1T	3,626,079,600	12,237.04	25,288,116	85.34	0.70%
1D	Ore 1-1UT	3,269,303,856	11,033.02	9,349,295	31.55	0.29%
2C	Ore 1-2T	3,794,266,224	12,804.62	11,927,261	40.25	0.31%
2D	Ore 1-2UT	3,531,567,600	11,918.09	27,087,093	91.41	0.77%
3C	Ore 1-3T	3,594,935,288	12,131.94	14,780,493	49.88	0.41%
3D	Ore 1- 3UT	3,203,826,080	10,812.05	27,846,239	93.97	0.87%
4C	Ore 1-4T	3,279,388,464	11,067.05	7,248,147	24.46	0.22%
4D	Ore 1-4UT	3,204,022,560	10,812.71	29,247,856	98.70	0.91%
1E	Ore 4-1T	3,797,505,640	12,815.56	9,113,781	30.76	0.24%
1F	Ore 4-1UT	3,556,840,688	12,003.38	42,294,860	142.73	1.19%
2E	Ore 4-2T	3,571,647,600	12,053.35	3,231,144	10.90	0.09%
2F	Ore 4-2UT	3,660,712,833	12,353.92	57,669,403	194.62	1.58%
3E	Ore 4-3T	3,640,545,440	12,285.86	5,956,337	20.10	0.16%
3F	Ore 4-3UT	3,626,276,160	12,237.70	23,772,937	80.23	0.66%
1G	Ore 2-1T	3,510,718,848	11,847.73	19,293,595	65.11	0.55%
1H	Ore 2-1UT	3,283,259,826	11,080.12	40,492,769	136.65	1.23%
2G	Ore 2-2T	3,430,135,072	11,575.78	51,950,588	175.32	1.51%
2H	Ore 2-2UT	3,321,728,430	11,209.94	53,618,457	180.95	1.61%
3G	Ore 2-3T	3,451,503,672	11,647.89	31,333,576	105.74	0.91%
3H	Ore 2-3UT	3,430,707,184	11,577.71	80,206,540	270.68	2.34%
1I	Ore 3-1T	3,639,151,425	12,282.05	6,452,657	21.78	0.18%
1J	Ore 3-1UT	3,243,463,860	10,945.81	153,203,655	517.02	4.72%
2I	Ore 3-2T	3,084,229,440	10,408.44	34,458,539	116.29	1.12%
2J	Ore 3-2UT	3,230,122,752	10,900.79	76,878,004	259.44	2.38%
3I	Ore 3-3T	3,274,539,696	11,050.69	1,415,197	4.78	0.04%
3J	Ore 3- 3UT	3,418,214,040	11,535.55	64,002,462	215.99	1.87%

| | | | Voids/cracks | | | |
| | | | Post- treated cores | | | |
	Core ID	Total voxel	Total volume (mm^3)	Labelled voxels count	Volume of labelled voxels (mm^3)	Volume of labelled voxels (%)
1C	Ore 1-1T	3,626,079,600	12,236.55	57,169,984	192.93	1.58%
1D	Ore 1-1UT					
2C	Ore 1-2T	3,781,891,157	12,788.70	45,760,883	154.42	1.21%
2D	Ore 1-2UT					
3C	Ore 1-3T	3,594,935,288	12,131.45	16,621,120	56.09	0.46%
3D	Ore 1- 3UT					
4C	Ore 1-4T	3,279,388,464	11,067.05	8,580,775	28.96	0.26%
4D	Ore 1-4UT					
1E	Ore 4-1T	3,797,505,640	12,815.04	54,279,734	183.17	1.43%
1F	Ore 4-1UT					
2E	Ore 4-2T	3,571,647,600	12,052.86	12,739,372	42.99	0.36%
2F	Ore 4-2UT					
3E	Ore 4-3T	3,640,545,440	12,285.86	42,910,037	144.81	1.18%
3F	Ore 4-3UT					
1G	Ore 2-1T	3,510,718,848	11,847.25	28,927,744	97.62	0.82%
1H	Ore 2-1UT					
2G	Ore 2-2T	3,430,135,072	11,575.32	54,870,237	185.16	1.60%
2H	Ore 2-2UT					
3G	Ore 2-3T	3,451,503,672	11,647.43	31,915,146	107.70	0.92%
3H	Ore 2-3UT					
1I	Ore 3-1T	3,639,151,425	12,282.05	17,704,513	59.75	0.49%
1J	Ore 3-1UT					
2I	Ore 3-2T	3,084,229,440	10,408.03	63,671,301	214.86	2.06%
2J	Ore 3-2UT					
3I	Ore 3-3T	3,265,989,984	11,021.39	23,559,624	79.50	0.72%
3J	Ore 3- 3UT					

| | | | Voids/cracks | | | |
| | | | Leached cores | | | |
	Core ID	Total voxel	Total volume (mm^3)	Labelled voxels count	Volume of labelled voxels (mm^3)	Volume of labelled voxels (%)
1C	Ore 1-1T	3,626,079,600	12,236.55	67,319,584	227.18	1.86%
1D	Ore 1-1UT	3,269,303,856	11,032.58	16,152,148	54.51	0.49%
2C	Ore 1-2T	3,789,700,320	12,788.70	57,546,332	194.20	1.52%
2D	Ore 1-2UT	3,531,567,600	11,917.61	29,031,749	97.97	0.82%
3C	Ore 1-3T	3,594,935,288	12,131.94	23,923,079	80.73	0.67%
3D	Ore 1- 3UT	3,203,826,080	10,811.62	33,001,505	111.37	1.03%
4C	Ore 1-4T	3,279,388,464	11,067.94	14,833,511	50.06	0.45%
4D	Ore 1-4UT	3,204,022,560	10,812.28	43,148,545	145.61	1.35%
1E	Ore 4-1T	3,797,505,640	12,815.04	117,520,964	396.59	3.09%
1F	Ore 4-1UT	3,556,840,688	12,002.90	79,031,925	266.70	2.22%
2E	Ore 4-2T	3,571,647,600	12,052.86	22,544,007	76.08	0.63%
2F	Ore 4-2UT	3,660,712,833	12,353.42	70,125,602	236.65	1.92%
3E	Ore 4-3T	3,640,545,440	12,285.37	45,168,146	152.42	1.24%
3F	Ore 4-3UT	3,626,276,160	12,237.21	35,247,396	118.95	0.97%
1G	Ore 2-1T	3,510,718,848	11,847.73	52,199,512	176.16	1.49%
1H	Ore 2-1UT	3,283,259,826	11,079.67	53,291,980	179.84	1.62%
2G	Ore 2-2T	3,430,135,072	11,575.32	55,558,865	187.49	1.62%
2H	Ore 2-2UT	3,321,728,430	11,209.49	62,953,135	212.44	1.90%
3G	Ore 2-3T	3,451,503,672	11,647.43	38,342,063	129.39	1.11%
3H	Ore 2-3UT	3,430,707,184	11,577.25	86,897,310	293.24	2.53%
1I	Ore 3-1T	3,641,585,640	12,288.88	67,210,550	226.81	1.85%
1J	Ore 3-1UT	3,243,463,860	10,945.38	181,941,301	613.98	5.61%
2I	Ore 3-2T	3,084,229,440	10,408.03	93,991,693	317.18	3.05%
2J	Ore 3-2UT	3,230,122,752	10,900.36	116,040,053	391.59	3.59%
3I	Ore 3-3T	3,278,814,552	11,064.67	47,076,775	158.87	1.44%
3J	Ore 3- 3UT	3,418,214,040	11,535.55	103,084,472	347.88	3.02%

| | | | Sulphide grains | | | |
| | | | pre-treated cores | | | |
	Core ID	Total voxel	Total volume (mm^3)	Labelled voxels count	Volume of labelled voxels (mm^3)	Volume of labelled voxels (%)
1C	Ore 1-1T	3,626,079,600	12,237.04	112,169,229	378.54	3.09%
1D	Ore 1-1UT	3,282,049,680	11,076.03	63,122,425	213.02	1.92%
2C	Ore 1-2T	3,798,832,128	12,820.03	50,530,821	170.53	1.33%
2D	Ore 1-2UT	3,531,567,600	11,918.09	42,622,699	143.84	1.21%
3C	Ore 1-3T	3,594,935,288	12,131.94	34,441,693	116.23	0.96%
3D	Ore 1- 3UT	3,216,624,320	10,856.11	77,606,643	261.92	2.41%
4C	Ore 1-4T	3,279,388,464	11,067.05	82,990,267	280.07	2.53%
4D	Ore 1-4UT	3,216,847,200	10,855.99	23,305,118	78.65	0.72%
1E	Ore 4-1T	3,811,231,564	12,861.88	309,854,021	1,045.67	8.13%
1F	Ore 4-1UT	3,569,885,336	12,047.40	277,430,282	936.25	7.77%
2E	Ore 4-2T	3,575,966,400	12,067.92	221,043,061	745.96	6.18%
2F	Ore 4-2UT	3,673,872,975	12,398.33	215,408,667	726.95	5.86%
3E	Ore 4-3T	3,640,545,440	12,285.86	222,310,775	750.24	6.11%
3F	Ore 4-3UT	3,639,543,024	12,282.48	230,181,412	776.80	6.32%
1G	Ore 2-1T	3,510,718,848	11,847.73	234,354,674	790.88	6.68%
1H	Ore 2-1UT	3,293,968,436	11,116.25	235,533,709	794.86	7.15%
2G	Ore 2-2T	3,438,673,056	11,604.59	172,246,240	581.28	5.01%
2H	Ore 2-2UT	3,334,334,610	11,252.48	148,085,374	499.75	4.44%
3G	Ore 2-3T	3,451,503,672	11,647.89	141,802,512	478.55	4.11%
3H	Ore 2-3UT	3,443,304,640	11,620.22	178,172,030	601.28	5.17%
1I	Ore 3-1T	3,639,151,425	12,282.05	181,629,899	613.00	4.99%
1J	Ore 3-1UT	3,258,579,870	10,996.83	345,817,985	1,167.04	10.61%
2I	Ore 3-2T	3,092,796,744	10,438.12	232,067,936	783.22	7.50%
2J	Ore 3-2UT	3,243,008,880	10,945.15	263,800,074	890.33	8.13%
3I	Ore 3-3T	3,278,814,552	11,065.11	165,170,757	557.41	5.04%
3J	Ore 3- 3UT	3,426,717,060	11,565.17	399,076,919	1,346.88	11.65%

	Core ID	Total voxel	Total volume (mm^3)	Labelled voxels count	Volume of labelled voxels (mm^3)	Volume of labelled voxels (%)
				Sulphide grains		
				Leached cores		
1C	Ore 1-1T	3,626,079,600	12,236.55	85,027,269	286.93	2.34%
1D	Ore 1-1UT	3,282,049,680	11,075.59	50,708,480	171.12	1.55%
2C	Ore 1-2T	3,798,832,128	12,819.52	39,558,836	133.50	1.04%
2D	Ore 1-2UT	3,531,567,600	11,917.61	37,976,883	128.16	1.08%
3C	Ore 1-3T	3,594,935,288	12,131.94	30,180,272	101.85	0.84%
3D	Ore 1- 3UT	3,216,624,320	10,854.80	70,670,220	238.48	2.20%
4C	Ore 1-4T	3,279,388,464	11,067.94	68,822,097	232.27	2.10%
4D	Ore 1-4UT	3,216,847,200	10,855.99	20,362,616	68.72	0.63%
1E	Ore 4-1T	3,811,231,564	12,861.36	205,971,343	695.07	5.40%
1F	Ore 4-1UT	3,569,885,336	12,046.92	222,935,138	752.32	6.24%
2E	Ore 4-2T	3,575,966,400	12,067.44	185,423,191	625.73	5.19%
2F	Ore 4-2UT	3,673,872,975	12,397.83	175,950,133	593.76	4.79%
3E	Ore 4-3T	3,640,545,440	12,285.37	186,009,433	627.71	5.11%
3F	Ore 4-3UT	3,639,543,024	12,281.98	178,473,771	602.28	4.90%
1G	Ore 2-1T	3,510,718,848	11,847.73	169,635,516	572.47	4.83%
1H	Ore 2-1UT	3,293,968,436	11,115.81	184,949,511	624.13	5.61%
2G	Ore 2-2T	3,438,673,056	11,604.13	135,027,779	455.66	3.93%
2H	Ore 2-2UT	3,334,334,610	11,252.03	123,621,223	417.17	3.71%
3G	Ore 2-3T	3,451,503,672	11,619.76	110,977,081	374.50	3.22%
3H	Ore 2-3UT	3,443,304,640	11,619.76	139,817,160	471.83	4.06%
1I	Ore 3-1T	3,641,585,640	12,288.88	99,109,761	334.46	2.72%
1J	Ore 3-1UT	3,258,579,870	10,996.39	253,806,804	856.50	7.79%
2I	Ore 3-2T	3,092,796,744	10,436.94	171,434,065	578.52	5.54%
2J	Ore 3-2UT	3,243,008,880	10,943.84	229,181,753	773.40	7.07%
3I	Ore 3-3T	3,278,814,552	11,064.67	93,594,095	315.84	2.85%
3J	Ore 3- 3UT	3,426,717,060	11,564.24	366,395,995	1,236.49	10.69%

11.2.8.2   Cracks/voids Thickness Map – Ore 1-4T
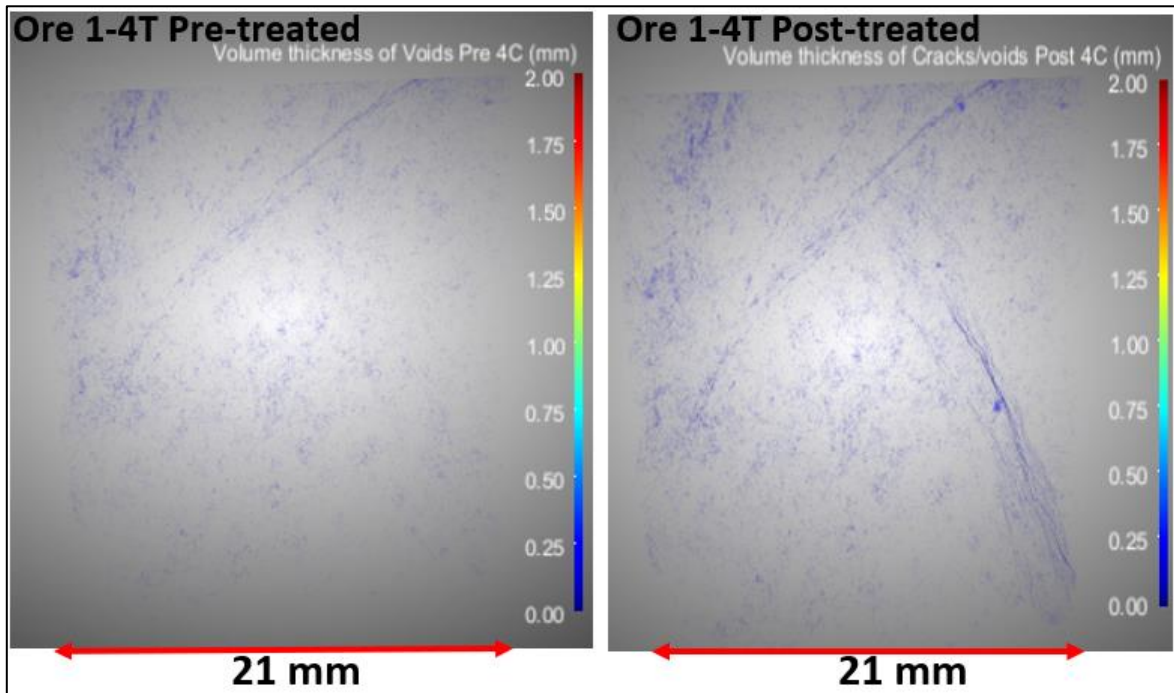
11.2.8.3   Cracks/voids Thickness Size Distributions
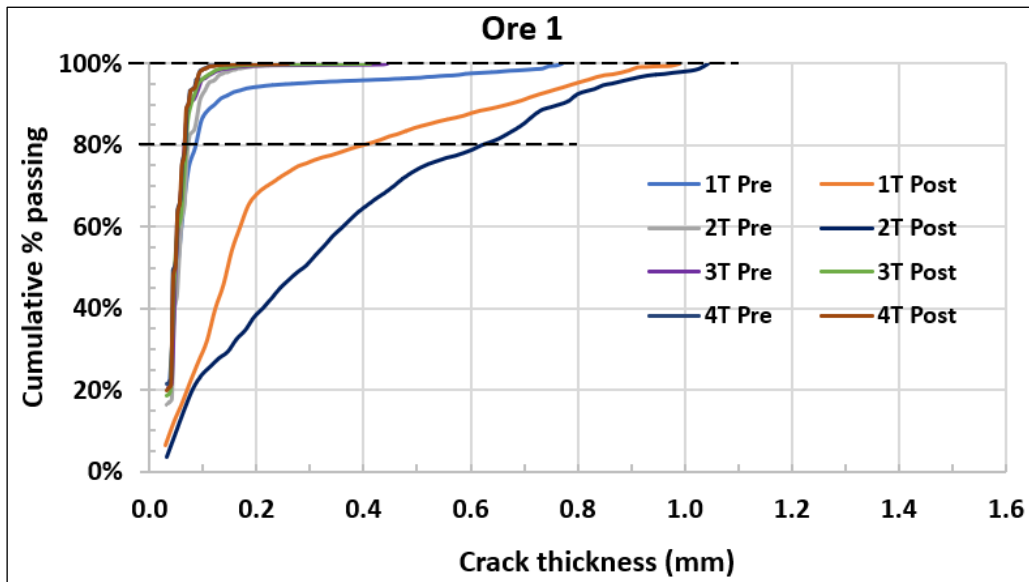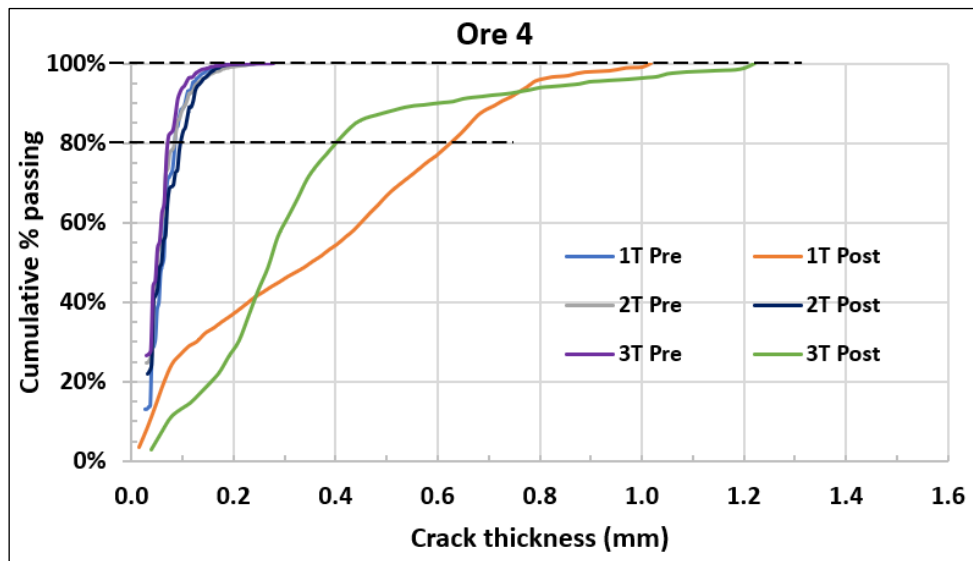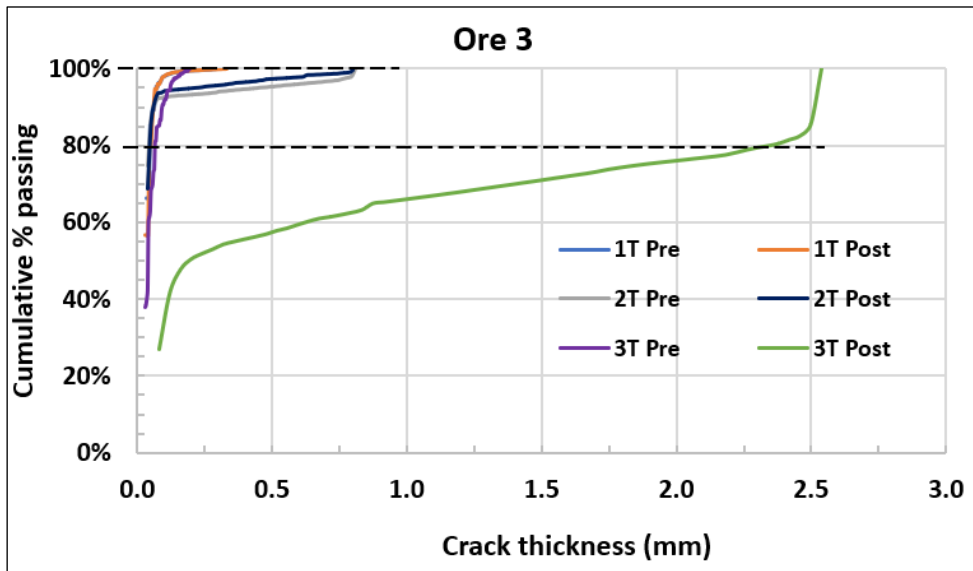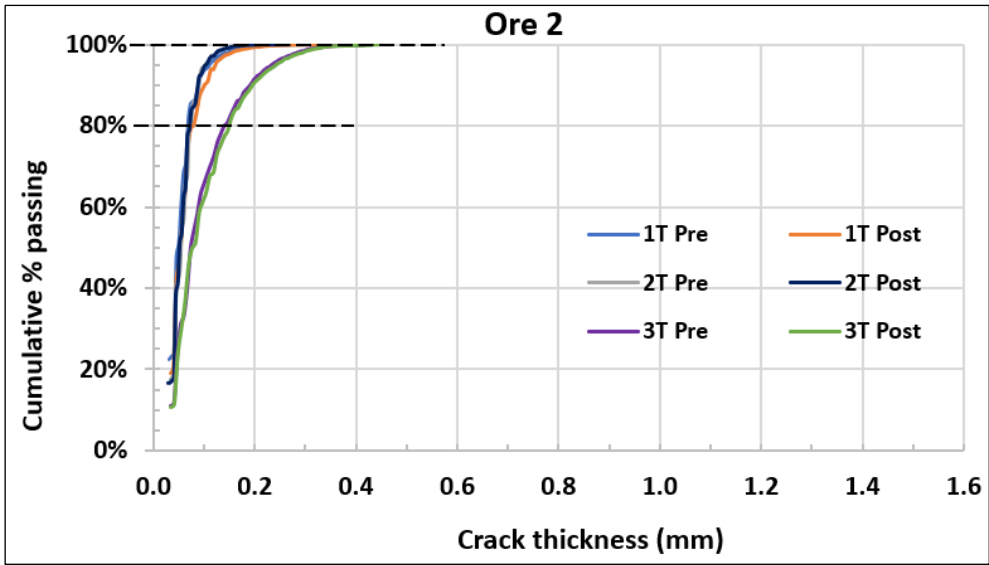
11.3 Large Fragments - Raw Data

11.3.1 Leach Kinetics Data

Ore type	Leach Duration (hrs)	Treated fragments-copper extraction (%)								Untreated fragments-copper extraction (%)								Abs Enhancement (%)	t-value calculated	t-test conf level
		1T	2T	3T	4T	5T	6T	Average	STD dev	1UT	2UT	3UT	4UT	5UT	6UT	Average	STD dev			
Ore 4	0	0.0	0.0	0.0	0.0	0.0	0.0	0.0	0.0	0.0	0.0	0.0	0.0	0.0	0.0	0.0	0.0			
	0.5	31.4	9.9	22.4	3.6	7.8	7.3	13.7	10.8	2.8	7.4	17.0	3.3	2.6	1.8	5.8	5.8			
	1	51.2	20.0	35.7	9.1	20.1	19.9	26.0	15.0	4.5	13.0	24.1	6.7	6.1	4.2	9.8	7.7			
	4	62.6	25.6	48.5	14.4	28.0	38.1	36.2	17.4	6.8	18.2	28.5	9.8	8.9	8.3	13.4	8.4			
	12	73.1	29.6	58.6	20.3	34.4	56.4	**45.4**	20.3	9.3	23.0	34.4	15.9	12.1	10.9	**17.6**	9.6	27.8	3.028	98.7%
Ore 3	0	0.0	0.0	0.0	0.0	0.0		0.0	0.0	0.0	0.0	0.0	0.0	0.0		0.0	0.0			
	0.5	4.3	9.6	7.7	9.7	17.7		9.8	4.9	7.2	7.0	4.1	9.6	7.8		7.1	2.0			
	1	9.7	19.6	17.0	16.5	26.4		17.8	6.0	15.1	13.6	10.7	16.8	11.7		13.6	2.5			
	4	16.7	29.1	24.2	23.0	32.3		25.1	6.0	23.5	20.2	17.4	25.3	17.0		20.7	3.7			
	12	25.4	38.7	31.6	34.6	37.6		**33.6**	5.3	29.1	29.5	22.6	38.7	24.8		**28.9**	6.2	4.6	1.263	76.0%
Ore 1	0	0.0	0.0	0.0	0.0	0.0	0.0	0.0	0.0	0.0	0.0	0.0	0.0	0.0	0.0	0.0	0.0			
	0.5	10.9	5.4	5.5	8.4	1.9	3.7	6.0	3.2	1.7	5.1	5.9	3.4	2.3	3.5	3.6	1.6			
	1	17.6	11.2	8.7	12.6	5.6	7.5	10.5	4.3	2.7	8.5	9.9	6.1	4.8	6.6	6.4	2.6			
	4	24.9	19.5	12.8	16.4	9.7	14.2	16.2	5.4	4.8	13.6	14.2	9.7	9.0	11.0	10.4	3.4			
	12	32.6	26.6	17.2	21.4	14.2	19.4	**21.9**	6.7	7.4	18.0	18.0	13.6	14.1	15.6	**14.5**	3.9	7.4	2.341	95.9%
Ore 2	0	0.0	0.0	0.0	0.0	0.0		0.0	0.0	0.0	0.0	0.0	0.0	0.0		0.0	0.0			
	0.5	0.1	2.8	3.9	3.0	2.5		2.5	1.4	0.7	7.4	1.8	7.9	1.4		3.8	3.5			
	1	9.6	5.9	6.7	6.9	5.6		7.0	1.6	0.9	10.1	3.0	12.6	3.5		6.0	5.0			
	4	11.6	9.3	9.0	10.1	8.7		9.7	1.2	9.9	12.4	4.4	15.0	5.4		9.4	4.5			
	12	16.3	16.6	13.1	17.2	18.3		**16.3**	2.0	13.9	15.9	8.1	19.3	8.8		**13.2**	4.8	3.1	1.344	78.6%
Ore 5	0	0.0	0.0	0.0	0.0	0.0	0.0	0.0	0.0	0.0	0.0	0.0	0.0	0.0	0.0	0.0	0.0			
	0.5	11.8	4.4	5.7	3.3	5.2	13.8	7.4	4.3	4.2	11.4	4.9	2.7	2.5	12.3	6.3	4.4			
	1	18.6	6.7	10.6	6.3	10.8	18.6	11.9	5.5	8.2	15.2	9.7	5.7	5.5	22.2	11.1	6.5			
	4	29.6	8.9	17.3	12.0	19.8	24.1	18.6	7.6	15.6	20.5	9.7	12.0	9.2	35.8	17.1	10.1			
	12	55.4	15.6	27.6	18.6	29.9	33.4	**30.1**	14.1	26.3	27.6	14.6	20.9	13.5	44.1	**24.5**	11.2	5.6	0.755	53.4%

| Ore type	Leach Duration (hrs)	Treated fragments-iron extraction (%)								Untreated fragments-iron extraction (%)								Abs Enhancement (%)	t-value calculated	t-test conf level
		1T	2T	3T	4T	5T	6T	Average	STD dev	1UT	2UT	3UT	4UT	5UT	6UT	Average	STD dev			
Ore 4	0	0.0	0.0	0.0	0.0	0.0	0.0	0.0	0.0	0.0	0.0	0.0	0.0	0.0	0.0	0.0	0.0			
	0.5	5.9	2.6	22.4	1.8	1.1	1.4	5.9	8.3	0.5	0.9	0.9	0.6	0.4	0.3	0.6	0.3			
	1	19.5	11.1	38.2	8.9	12.0	14.7	17.4	10.8	1.2	4.3	3.4	1.7	5.6	2.7	3.1	1.7			
	4	23.7	13.2	43.9	12.1	16.3	26.0	22.5	11.9	2.3	7.7	5.4	3.1	7.8	8.6	5.8	2.7			
	12	26.6	15.1	47.6	14.8	19.5	32.7	**26.1**	12.7	3.3	10.6	7.9	5.2	9.3	11.1	**7.9**	3.1	18.2	3.415	99.3%
Ore 3	0	0.0	0.0	0.0	0.0	0.0		0.0	0.0	0.0	0.0	0.0	0.0	0.0		0.0	0.0			
	0.5	0.8	4.6	3.1	7.5	10.1		5.2	3.6	0.9	1.1	0.6	4.2	0.4		1.4	1.6			
	1	6.8	13.9	6.0	18.5	21.1		13.3	6.8	3.2	4.9	5.2	10.7	1.7		5.1	3.4			
	4	17.7	22.4	11.6	32.1	32.9		23.3	9.2	7.4	8.7	13.1	18.3	3.0		10.1	5.8			
	12	24.7	30.2	20.2	36.8	38.0		**30.0**	7.7	10.5	13.5	18.5	27.4	4.8		**14.9**	8.5	15.1	2.938	98.1%
Ore 1	0	0.0	0.0	0.0	0.0	0.0	0.0	0.0	0.0	0.0	0.0	0.0	0.0	0.0	0.0	0.0	0.0			
	0.5	2.7	2.2	2.1	1.9	0.4	2.7	2.0	0.9	0.9	0.9	0.8	0.4	1.1	0.6	0.8	0.2			
	1	6.0	6.0	4.5	3.3	1.7	6.4	4.6	1.8	2.1	2.1	2.7	1.6	2.5	2.4	2.2	0.4			
	4	10.3	11.2	8.6	6.2	5.1	11.2	8.8	2.6	4.3	3.9	6.2	4.5	5.9	4.8	4.9	0.9			
	12	14.4	15.8	13.7	9.7	8.3	15.4	**12.9**	3.1	7.4	5.8	9.9	8.0	9.8	7.4	**8.0**	1.60	4.9	3.385	99.3%
Ore 2	0	0.0	0.0	0.0	0.0	0.0		0.0	0.0	0.0	0.0	0.0	0.0	0.0		0.0	0.0			
	0.5	0.4	2.5	1.1	0.9	0.9		1.2	0.8	0.9	3.2	1.0	4.6	0.8		2.1	1.7			
	1	8.5	5.8	2.9	4.6	2.2		4.8	2.5	4.8	7.0	2.0	7.8	3.0		4.9	2.5			
	4	9.7	8.1	4.2	6.0	2.8		6.2	2.8	5.4	8.4	2.9	9.5	4.1		6.1	2.8			
	12	12.5	12.7	6.8	9.0	5.0		**9.2**	3.4	7.8	10.4	4.9	12.4	6.3		**8.4**	3.1	0.8	0.396	30.8%
Ore 5	0	0.0	0.0	0.0	0.0	0.0	0.0	0.0	0.0	0.0	0.0	0.0	0.0	0.0	0.0	0.0	0.0			
	0.5	2.5	1.5	1.2	1.2	1.1	0.7	1.4	0.6	2.8	1.2	1.4	1.0	1.0	1.6	1.5	0.7			
	1	5.3	2.9	3.4	2.2	2.8	2.2	3.1	1.2	6.8	2.7	2.9	2.3	2.1	4.5	3.5	1.8			
	4	12.0	6.3	7.6	5.0	6.9	6.0	7.3	2.4	13.7	5.4	6.2	5.0	4.9	12.4	7.9	4.0			
	12	20.9	11.0	14.6	8.9	12.8	11.0	**13.2**	4.2	23.5	9.4	9.9	8.5	8.0	20.4	**13.3**	6.8	-0.1	-0.026	2.0%

11.3.2 Overall Leach Extractions

		Pregnant solution at t= 12 hours		Mass of fragment	Acid degistion of residue			Back-calculated total metal content	Back-calculated head grade	Metal extraction (%)
		Soln concentration	Metal content in 160 mls AR		1 gram sample, soln concentration	Metal content in 10 mls AR, 1 gram sample	Metal content whole fragment			
		**A	B=A*0.16 L	C	**D	E=D*0.01 L	F=E*C	G=B+F	H=G/(1000*C)*100	I=(B/G)*100
Pair #	Sample	Cu (mg/L)	Cu (mg)	Grams	Cu (mg/L)	Cu (mg)	Cu (mg)	Cu (mg)	Cu (%)	Cu (%)
1st pair	1T	3109.0	497.4	162.81	632.0	6.32	1029.0	1526.4	0.94	**32.6**
	1UT	430.0	68.8	157.49	544.0	5.44	856.7	925.5	0.59	**7.4**
2nd pair	2T	2724.0	435.8	125.33	961.0	9.61	1204.4	1640.3	1.31	**26.6**
	2UT	623.0	99.7	191.8	236.5	2.365	453.6	553.3	0.29	**18.0**
3rd pair	3T	1186.0	189.8	154.59	592.0	5.92	915.2	1104.9	0.71	**17.2**
	3UT	252.0	40.3	157.61	116.5	1.165	183.6	223.9	0.14	**18.0**
4th pair	4T	1221.0	195.4	160.71	446.0	4.46	716.8	912.1	0.57	**21.4**
	4UT	221.0	35.4	134.63	166.5	1.665	224.2	259.5	0.19	**13.6**
5th pair	5T	517.0	82.7	180.52	277.0	2.77	500.0	582.8	0.32	**14.2**
	5UT	1900.0	304.0	131.09	1409.0	14.09	1847.1	2151.1	1.64	**14.1**
6th pair	6T	2015.0	322.4	161.84	828.5	8.285	1340.8	1663.2	1.03	**19.4**
	6UT	194.0	31.0	126.99	132.0	1.32	167.6	198.7	0.16	**15.6**

** A - The values have been multiplied by 10 because the aliquot sample was diluted 10 times with DI water before ICP analysis
** D - The values have been multipled by 5 because the 10 mL AR was diluted to 50 mL with DI water before ICP analysis

Ore 1 - copper raw data *(table title)*

		Pregnant solution at t= 12 hours		Mass of fragment	Acid degistion of residue			Back-calculated total metal content	Back-calculated head grade	Metal extraction (%)
		Soln concentration	Metal content in 160 mls AR		1 gram sample, soln concentration	Metal content in 10 mls AR, 1 gram sample	Metal content whole fragment			
		**A	B=A*0.16 L	C	**D	E=D*0.01 L	F=E*C	G=B+F	H=G/(1000*C)*100	I=(B/G)*100
Pair #	Sample	Fe (mg/L)	Fe (mg)	Grams	Fe (mg/L)	Fe (mg)	Fe (mg)	Fe (mg)	Fe (%)	Fe (%)
1st pair	1T	6969.0	1115.0	162.8	4084.5	40.8	6650.0	7765.0	4.77	**14.4**
	1UT	3111.0	497.8	157.5	3979.5	39.8	6267.3	6765.1	4.30	**7.4**
2nd pair	2T	4859.0	777.4	125.3	3296.0	33.0	4130.9	4908.3	3.92	**15.8**
	2UT	2693.0	430.9	191.8	3670.0	36.7	7039.1	7469.9	3.89	**5.8**
3rd pair	3T	5784.0	925.4	154.6	3761.0	37.6	5814.1	6739.6	4.36	**13.7**
	3UT	3887.0	621.9	157.6	3572.0	35.7	5629.8	6251.7	3.97	**9.9**
4th pair	4T	3284.0	525.4	160.7	3038.0	30.4	4882.4	5407.8	3.36	**9.7**
	4UT	2636.0	421.8	134.6	3597.0	36.0	4842.6	5264.4	3.91	**8.0**
5th pair	5T	3749.0	599.8	180.5	3657.0	36.6	6601.6	7201.5	3.99	**8.3**
	5UT	3468.0	554.9	131.1	3896.5	39.0	5107.9	5662.8	4.32	**9.8**
6th pair	6T	7563.0	1210.1	161.8	4099.5	41.0	6634.6	7844.7	4.85	**15.4**
	6UT	3061.0	489.8	127.0	4820.0	48.2	6120.9	6610.7	5.21	**7.4**

** A - The values have been multiplied by 10 because the aliquot sample was diluted 10 times with DI water before ICP analysis
** D - The values have been multipled by 5 because the 10 mL AR was diluted to 50 mL with DI water before ICP analysis

Ore 1 - iron raw data *(table title)*

Ore 2 - copper raw data

Pair #	Sample	Pregnant solution at t= 12 hours		Mass of fragment	Acid degistion of residue			Back-calculated total metal content	Back-calculated head grade	Metal extraction (%)
		Soln concentration	Metal content in 160 mls AR		1 gram sample, soln concentration	Metal content in 10 mls AR, 1 gram sample	Metal content whole fragment			
		**A	B=A*0.16 L	C	**D	E=D*0.01 L	F=E*C	G=B+F	H=G/(1000*C)*100	I=(B/G)*100
		Cu (mg/L)	Cu (mg)	Grams	Cu (mg/L)	Cu (mg)	Cu (mg)	Cu (mg)	Cu (%)	Cu (%)
1st pair	1T	2123.0	339.7	155.9	1123.0	11.2	1750.3	2090.0	1.34	16.3
	1UT	454.0	72.6	173.9	258.0	2.6	448.7	521.3	0.30	13.9
2nd pair	2T	330.0	52.8	169.3	156.5	1.6	265.0	317.8	0.19	16.6
	2UT	360.0	57.6	146.4	207.5	2.1	303.7	361.3	0.25	15.9
3rd pair	3T	942.0	150.7	151.0	662.0	6.6	999.8	1150.5	0.76	13.1
	3UT	102.0	16.3	178.8	104.0	1.0	186.0	202.3	0.11	8.1
4th pair	4T	638.0	102.1	169.9	289.5	2.9	492.0	594.1	0.35	17.2
	4UT	1385.0	221.6	100.7	921.0	9.2	927.6	1149.2	1.14	19.3
5th pair	5T	65.0	10.4	165.4	28.0	0.3	46.3	56.7	0.03	18.3
	5UT	118.0	18.9	168.9	116.0	1.2	195.9	214.8	0.13	8.8

** A - The values have been multipled by 10 because the aliquot sample was diluted 10 times with DI water before ICP analysis

** D - The values have been multipled by 5 because the 10 mL AR was diluted to 50 mL with DI water before ICP analysis

Ore 2 - iron raw data

Pair #	Sample	Pregnant solution at t= 12 hours		Mass of fragment	Acid degistion of residue			Back-calculated total metal content	Back-calculated head grade	Metal extraction (%)
		Soln concentration	Metal content in 160 mls AR		1 gram sample, soln concentration	Metal content in 10 mls AR, 1 gram sample	Metal content whole fragment			
		**A	B=A*0.16 L	C	**D	E=D*0.01 L	F=E*C	G=B+F	H=G/(1000*C)*100	I=(B/G)*100
		Fe (mg/L)	Fe (mg)	Grams	Fe (mg/L)	Fe (mg)	Fe (mg)	Fe (mg)	Fe (%)	Fe (%)
1st pair	1T	2955.0	472.8	155.9	2123.5	21.2	3309.7	3782.5	2.43	12.5
	1UT	1832.0	293.1	173.9	1994.0	19.9	3467.6	3760.7	2.16	7.8
2nd pair	2T	2236.0	357.8	169.3	1456.0	14.6	2465.6	2823.4	1.67	12.7
	2UT	2011.0	321.8	146.4	1887.0	18.9	2761.8	3083.6	2.11	10.4
3rd pair	3T	2205.0	352.8	151.0	3204.5	32.0	4839.8	5192.6	3.44	6.8
	3UT	487.0	77.9	178.8	846.5	8.5	1513.5	1591.5	0.89	4.9
4th pair	4T	1609.0	257.4	169.9	1540.5	15.4	2617.9	2875.4	1.69	9.0
	4UT	1323.0	211.7	100.7	1482.5	14.8	1493.2	1704.9	1.69	12.4
5th pair	5T	324.0	51.8	165.4	601.5	6.0	994.6	1046.4	0.63	5.0
	5UT	1194.0	191.0	168.9	1691.0	16.9	2856.3	3047.3	1.80	6.3

** A - The values have been multipled by 10 because the aliquot sample was diluted 10 times with DI water before ICP analysis

** D - The values have been multipled by 5 because the 10 mL AR was diluted to 50 mL with DI water before ICP analysis

Ore 3 - copper raw data

Pair #	Sample	Pregnant solution at t= 12 hours		Mass of fragment	Acid degistion of residue			Back-calculated total metal content	Back-calculated head grade	Metal extraction (%)
		Soln concentration	Metal content in 160 mls AR		1 gram sample, soln concentration	Metal content in 10 mls AR, 1 gram sample	Metal content whole fragment			
		**A	B=A*0.16 L	C	**D	E=D*0.01 L	F=E*C	G=B+F	H=G/(1000*C)*100	I=(B/G)*100
		Cu (mg/L)	Cu (mg)	Grams	Cu (mg/L)	Cu (mg)	Cu (mg)	Cu (mg)	Cu (%)	Cu (%)
1st pair	1T	384.0	61.4	140.0	129.0	1.29	180.6	242.0	0.17	25.4
	1UT	443.0	70.9	157.7	109.5	1.10	172.7	243.6	0.15	29.1
2nd pair	2T	604.0	96.6	148.2	103.5	1.04	153.4	250.0	0.17	38.7
	2UT	76.0	12.2	132.4	22.0	0.22	29.1	41.3	0.03	29.5
3rd pair	3T	476.0	76.2	156.1	105.5	1.06	164.7	240.9	0.15	31.6
	3UT	512.0	81.9	141.0	198.5	1.99	279.9	361.8	0.26	22.6
4th pair	4T	476.0	76.2	120.5	119.5	1.20	144.0	220.2	0.18	34.6
	4UT	231.0	37.0	155.8	37.5	0.38	58.4	95.4	0.06	38.7
5th pair	5T	142.0	22.7	116.3	32.5	0.33	37.8	60.5	0.05	37.6
	5UT	19.0	3.0	184.6	5.0	0.05	9.2	12.3	0.01	24.8

** A - The values have been multipled by 10 because the aliquot sample was diluted 10 times with DI water before ICP analysis

** D - The values have been multipled by 5 because the 10 mL AR was diluted to 50 mL with DI water before ICP analysis

		Ore 3 - iron raw data								
		Pregnant solution at t= 12 hours			Acid degistion of residue			Back-calculated total metal content		Metal extraction (%)
		Soln concentration	Metal content in 160 mls AR	Mass of fragment	1 gram sample, soln concentration	Metal content in 10 mls AR, 1 gram sample	Metal content whole fragment		Back-calculated head grade	
		**A	B=A*0.16 L	C	**D	E=D*0.01 L	F=E*C	G=B+F	H=G/(1000*C)*100	I=(B/G)*100
Pair #	Sample	Fe (mg/L)	Fe (mg)	Grams	Fe (mg/L)	Fe (mg)	Fe (mg)	Fe (mg)	Fe (%)	Fe (%)
1st pair	1T	22714.0	3634.2	140.0	7911.0	79.1	11075.4	14709.6	10.51	24.7
	1UT	14480.0	2316.8	157.7	12510.5	125.1	19730.3	22047.1	13.98	10.5
2nd pair	2T	16032.0	2565.1	148.2	3997.0	40.0	5922.8	8487.9	5.73	30.2
	2UT	5384.0	861.4	132.4	4177.5	41.8	5530.6	6392.0	4.83	13.5
3rd pair	3T	15265.0	2442.4	156.1	6185.5	61.9	9656.2	12098.6	7.75	20.2
	3UT	24543.0	3926.9	141.0	12307.5	123.1	17356.0	21282.9	15.09	18.5
4th pair	4T	15265.0	2442.4	120.5	3476.0	34.8	4189.6	6632.0	5.50	36.8
	4UT	7060.0	1129.6	155.8	1925.0	19.3	2999.5	4129.1	2.65	27.4
5th pair	5T	8165.0	1306.4	116.3	1835.0	18.4	2133.4	3439.8	2.96	38.0
	5UT	1400.0	224.0	184.6	2417.5	24.2	4462.0	4686.0	2.54	4.8

** A - The values have been multiplied by 10 because the aliquot sample was diluted 10 times with DI water before ICP analysis
** D - The values have been multiplied by 5 because the 10 mL AR was diluted to 50 mL with DI water before ICP analysis

		Ore 4 - copper raw data								
		Pregnant solution at t= 12 hours			Acid degistion of residue			Back-calculated total metal content		Metal extraction (%)
		Soln concentration	Metal content in 160 mls AR	Mass of fragment	1 gram sample, soln concentration	Metal content in 10 mls AR, 1 gram sample	Metal content whole fragment		Back-calculated head grade	
		**A	B=A*0.16 L	C	**D	E=D*0.01 L	F=E*C	G=B+F	H=G/(1000*C)*100	I=(B/G)*100
Pair #	Sample	Cu (mg/L)	Cu (mg)	Grams	Cu (mg/L)	Cu (mg)	Cu (mg)	Cu (mg)	Cu (%)	Cu (%)
1st pair	1T	1312.0	209.9	192.9	40.0	0.40	77.2	287.1	0.15	73.1
	1UT	400.0	64.0	168.6	368.0	3.68	620.6	684.6	0.41	9.3
2nd pair	2T	188.0	30.1	207.8	34.5	0.35	71.7	101.8	0.05	29.6
	2UT	124.0	19.8	158.0	42.0	0.42	66.4	86.2	0.05	23.0
3rd pair	3T	523.0	83.7	168.9	35.0	0.35	59.1	142.8	0.08	58.6
	3UT	140.0	22.4	155.0	27.5	0.28	42.6	65.0	0.04	34.4
4th pair	4T	245.0	39.2	153.6	100.0	1.00	153.6	192.8	0.13	20.3
	4UT	672.0	107.5	174.8	325.0	3.25	568.0	675.6	0.39	15.9
5th pair	5T	1263.0	202.1	136.9	282.0	2.82	386.2	588.3	0.43	34.4
	5UT	167.0	26.7	155.1	125.0	1.25	193.9	220.6	0.14	12.1
6th pair	6T	703.0	112.5	166.9	52.0	0.52	86.8	199.3	0.12	56.4
	6UT	483.0	77.3	208.9	302.5	3.03	631.9	709.1	0.34	10.9

** A - The values have been multiplied by 10 because the aliquot sample was diluted 10 times with DI water before ICP analysis
** D - The values have been multiplied by 5 because the 10 mL AR was diluted to 50 mL with DI water before ICP analysis

		Ore 4 - iron raw data								
		Pregnant solution at t= 12 hours			Acid degistion of residue			Back-calculated total metal content		Metal extraction (%)
		Soln concentration	Metal content in 160 mls AR	Mass of fragment	1 gram sample, soln concentration	content in 10 mls AR, 1 gram sample	Metal content whole fragment		Back-calculated head grade	
		**A	B=A*0.16 L	C	**D	E=D*0.01 L	F=E*C	G=B+F	H=G/(1000*C)*100	I=(B/G)*100
Pair #	Sample	Fe (mg/L)	Fe (mg)	Grams	Fe (mg/L)	Fe (mg)	Fe (mg)	Fe (mg)	Fe (%)	Fe (%)
1st pair	1T	21277.0	3404.3	192.9	4869.0	48.7	9391.8	12796.1	6.63	26.6
	1UT	2510.0	401.6	168.6	6994.5	69.9	11794.8	12196.4	7.23	3.3
2nd pair	2T	12669.0	2027.0	207.8	5481.0	54.8	11386.8	13413.8	6.46	15.1
	2UT	6240.0	998.4	158.0	5316.0	53.2	8401.4	9399.8	5.95	10.6
3rd pair	3T	32936.0	5269.8	168.9	3428.0	34.3	5789.9	11059.7	6.55	47.6
	3UT	4797.0	767.5	155.0	5805.5	58.1	8998.5	9766.0	6.30	7.9
4th pair	4T	7276.0	1164.2	153.6	4377.5	43.8	6724.3	7888.4	5.14	14.8
	4UT	3964.0	634.2	174.8	6641.5	66.4	11608.0	12242.3	7.00	5.2
5th pair	5T	10254.0	1640.6	136.9	4937.0	49.4	6760.7	8401.4	6.14	19.5
	5UT	3317.0	530.7	155.1	3338.0	33.4	5176.6	5707.3	3.68	9.3
6th pair	6T	13280.0	2124.8	166.9	2621.5	26.2	4375.8	6500.6	3.89	32.7
	6UT	8791.0	1406.6	208.9	5400.0	54.0	11279.5	12686.1	6.07	11.1

** A - The values have been multiplied by 10 because the aliquot sample was diluted 10 times with DI water before ICP analysis
** D - The values have been multiplied by 5 because the 10 mL AR was diluted to 50 mL with DI water before ICP analysis

		Pregnant solution at t=12 hours		Mass of fragment	Acid degistion of residue			Back-calculated total metal content	Back-calculated head grade	Metal extraction (%)

Ore 5 - copper raw data

		Pregnant solution at t=12 hours		Mass of fragment	Acid degistion of residue			Back-calculated total metal content	Back-calculated head grade	Metal extraction (%)
		Soln concentration	Metal content in 160 mls AR		1 gram sample, soln concentration	Metal content in 10 mls AR, 1 gram sample	Metal content whole fragment			
		**A	B=A*0.16 L	C	**D	E=D*0.01 L	F=E*C	G=B+F	H=G/(1000*C)*100	I=(B/G)*100
Pair #	Sample	Cu (mg/L)	Cu (mg)	Grams	Cu (mg/L)	Cu (mg)	Cu (mg)	Cu (mg)	Cu (%)	Cu (%)
1st pair	1T	7084.0	1133.4	102.83	889.0	8.89	914.2	2047.6	1.99	**55.4**
	1UT	2584.0	413.4	62.87	1844.0	18.44	1159.3	1572.8	2.50	**26.3**
2nd pair	2T	7.0	1.1	101.26	6.0	0.06	6.1	7.2	0.01	**15.6**
	2UT	796.0	127.4	102.41	325.5	3.255	333.3	460.7	0.45	**27.6**
3rd pair	3T	296.0	47.4	91.48	136.0	1.36	124.4	171.8	0.19	**27.6**
	3UT	3.0	0.5	70.08	4.0	0.04	2.8	3.3	0.00	**14.6**
4th pair	4T	85.0	13.6	77.27	77.0	0.77	59.5	73.1	0.09	**18.6**
	4UT	117.0	18.7	131.34	54.0	0.54	70.9	89.6	0.07	**20.9**
5th pair	5T	80.0	12.8	101.82	29.5	0.295	30.0	42.8	0.04	**29.9**
	5UT	22.0	3.5	70.28	32.0	0.32	22.5	26.0	0.04	**13.5**
6th pair	6T	97.0	15.5	106.59	29.0	0.29	30.9	46.4	0.04	**33.4**
	6UT	2891.0	462.6	72.71	807.0	8.07	586.8	1049.3	1.44	**44.1**

** A - The values have been multipled by 10 because the aliquot sample was diluted 10 times with DI water before ICP analysis
** D - The values have been multipled by 5 because the 10 mL AR was diluted to 50 mL with DI water before ICP analysis

Ore 5 - iron raw data

		Pregnant solution at t=12 hours		Mass of fragment	Acid degistion of residue			Back-calculated total metal content	Back-calculated head grade	Metal extraction (%)
		Soln concentration	Metal content in 160 mls AR		1 gram sample, soln concentration	Metal content in 10 mls AR, 1 gram sample	Metal content whole fragment			
		**A	B=A*0.16 L	C	**D	E=D*0.01 L	F=E*C	G=B+F	H=G/(1000*C)*100	I=(B/G)*100
Pair #	Sample	Fe (mg/L)	Fe (mg)	Grams	Fe (mg/L)	Fe (mg)	Fe (mg)	Fe (mg)	Fe (%)	Fe (%)
1st pair	1T	8292.0	1326.7	102.8	4878.5	48.8	5016.6	6343.3	6.17	**20.9**
	1UT	5508.0	881.3	62.9	4564.5	45.6	2869.7	3751.0	5.97	**23.5**
2nd pair	2T	4544.0	727.0	101.3	5802.0	58.0	5875.1	6602.1	6.52	**11.0**
	2UT	3535.0	565.6	102.4	5300.0	53.0	5427.7	5993.3	5.85	**9.4**
3rd pair	3T	4419.0	707.0	91.5	4527.5	45.3	4141.8	4848.8	5.30	**14.6**
	3UT	2457.0	393.1	70.1	5132.0	51.3	3596.5	3989.6	5.69	**9.9**
4th pair	4T	2663.0	426.1	77.3	5677.0	56.8	4386.6	4812.7	6.23	**8.9**
	4UT	3886.0	621.8	131.3	5113.5	51.1	6716.1	7337.8	5.59	**8.5**
5th pair	5T	4842.0	774.7	101.8	5198.0	52.0	5292.6	6067.3	5.96	**12.8**
	5UT	2046.0	327.4	70.3	5368.5	53.7	3773.0	4100.3	5.83	**8.0**
6th pair	6T	4731.0	757.0	106.6	5726.0	57.3	6103.3	6860.3	6.44	**11.0**
	6UT	5419.0	867.0	72.7	4640.5	46.4	3374.1	4241.1	5.83	**20.4**

** A - The values have been multipled by 10 because the aliquot sample was diluted 10 times with DI water before ICP analysis
** D - The values have been multipled by 5 because the 10 mL AR was diluted to 50 mL with DI water before ICP analysis